12-16-2013

Synthesis, Structural Variations and Trends In the Properties of Unique Dinuclear and Polynuclear Complexes of Bis(Pyrazolyl)Methane Ligands In Solid State and Solution

Andrea Eva Pascui
University of South Carolina - Columbia

SYNTHESIS, STRUCTURAL VARIATIONS AND TRENDS IN THE PROPERTIES OF UNIQUE DINUCLEAR AND POLYNUCLEAR COMPLEXES OF BIS(PYRAZOLYL)METHANE LIGANDS IN SOLID STATE AND SOLUTION

by

Andrea Éva Pascui

Bachelor of Science
"Babeş-Bolyai" University Cluj-Napoca, 2008

Master of Science
"Babeş-Bolyai" University Cluj-Napoca, 2009

Submitted in Partial Fulfillment of the Requirements

For the Degree of Doctor of Philosophy in

Chemistry

College of Arts and Sciences

University of South Carolina

2013

Accepted By:

Daniel L. Reger, Major Professor

Richard D. Adams, Committee Member

Linda S. Shimizu, Committee Member

Michael A. Matthews, Committee Member

Lacy Ford, Vice Provost and Dean of Graduate Studies

Dedication

To the “giants” of science.

“If I have seen further it is by standing on the shoulders of giants.”

— Isaac Newton

Acknowledgements

"It is the story that matters, not just the ending" - it is for this reason that I would like to acknowledge and thank all the people who have contributed to this "story" that ends with this dissertation.

First I thank Dr. Daniel L. Reger for being an excellent mentor and assigning me to a very fruitful project. By allowing me scientific freedom, being always helpful when I needed insight, advice and support, you contributed significantly to my professional growth.

I thank Dr. Monica M. Venter, my undergraduate adviser, for the time spent with me in the laboratory, teaching me the basics of scientific research. Thank you for encouraging me to pursue a doctorate at the University of South Carolina (USC).

I am indebted to all the collaborators and co-workers that helped in the realization of this work: Dr. Mark D. Smith, who solved all the crystal structures presented in this dissertation, Dr. Perry J. Pellechia for helping me with numerous NMR experiments, Dr. Andrew Ozarowski for the EPR measurements and DFT calculations, Dr. Julia Jezierska for the magnetic measurements, Dr. William E. Cotham and Dr. Mike Walla for recording the mass spectra of my compounds.

I am also grateful for the support of my doctoral committee: Dr. Richard D. Adams, Linda S. Shimizu and Dr. Michael A. Matthews.

Additional thanks are due to Dr. zur Loye and the entire zur Loye group for generously allowing the use of their equipment.

I would like to express appreciation to the past and present members of the Reger group for a great graduate school experience: Dr. Elizabeth A. Foley and Dr. Jacob Horger for getting me started in the laboratory; to Andrew P. Leitner for the good conversations about science and not only; Dr. Ágota Debreczeni, without whom I would not have come to USC, a good friend and support from the very beginning both in the laboratory and outside of it.

I owe thanks to Olga Kalló and her daughters Éva, Rozi and Mari for the moral and financial support that got me to USC.

To my mother, Kati Pascui, I have to thank for supporting me and letting me go when she saw that I am ready to leave home. To my late family members, István Pascui, Viola Gál-Szabó, István Gál-Szabó, people who molded me into the person I am today. My close friends and second family: Bea L., Timi, Oti, Bogi, Bea B., Attila, Zoli, Cucu, Levi and Kemi for finding time to spend with me whenever possible.

To my husband, Filip George Stamate, thank you for the nice designs and animations used in the artwork of my publications. On a more personal note, I thank you for being considerate, supportive and most importantly for accompanying me to USC.

Abstract

The semi-rigid ligands, *p*-$[CH(pz)_2]_2C_6H_4$, $\mathbf{L}_{\boldsymbol{p}}$, *m*-$[CH(pz)_2]_2C_6H_4$, $\mathbf{L}_{\boldsymbol{m}}$, and *m*-$[CH(3,5\text{-}Me_2pz)_2]_2C_6H_4$, $\mathbf{L}_{\boldsymbol{m}}$***** (pz = pyrazolyl ring), link two bis(pyrazolyl)methane units into a single molecule by a rigid phenylene spacer and are used to study the structural variations and magnetic interactions in self-assembled first row, divalent transition metal complexes in polymeric, dinuclear and dinuclear metallacyclic settings. The formation of these architectures highly depend on the geometry of these ligands: *anti*, the two -$CH(pz)_2$ units are on the opposite side of the plane defined by the phenylene spacer, or *syn*, both -$CH(pz)_2$ units are on the same side of the phenylene spacer.

The first chapter focuses on structural modifications in dinuclear or polymeric copper(II) complexes of $\mathbf{L}_{\boldsymbol{p}}$, in *anti* conformation, induced by slight changes in the solvent of crystallization, and the effect of these changes on the supramolecular organization and weak hydrogen bonding patterns in these complexes.

Opposite to the structural diversity generated with $\mathbf{L}_{\boldsymbol{p}}$ in *anti* conformation, $\mathbf{L}_{\boldsymbol{m}}$ and $\mathbf{L}_{\boldsymbol{m}}$***** prefer to self-assemble into dinuclear metallacycles, by adopting *syn* conformation. In these units the divalent metal centers are also linked by a small anionic bridge, $X = F^-$, Cl^-, Br^-, OH^-, CN^-, N_3^-, to generate $[M_2(\mu\text{–}X)(\mu\text{–}\mathbf{L})_2]^{3+}$, where $\mathbf{L} = \mathbf{L}_{\boldsymbol{m}}$ or $\mathbf{L}_{\boldsymbol{m}}$*****.

The tendency of these ligands to form a single structural type prompted us to tackle a fundamental problem in magnetism: carefully designed systems that control the geometry around the metal centers are lacking, therefore magneto-structural correlations

are based on compounds where several structural parameters vary simultaneously. As demonstrated in chapters II-V, this $[M_2(\mu\text{–}X)(\mu\text{–}\mathbf{L})_2]^{3+}$ metallacyclic system, for the first time, uniquely allows the overall structure to be maintained constant while a single structural feature, directly affecting the antiferromagnetic superexchange interactions, is selectively altered.

The copper(II) series, $[Cu_2(\mu\text{–}X)(\mu\text{–}\mathbf{L_m*})_2](ClO_4)_3$, represents the first series of dinuclear complexes with a strict linear Cu–X–Cu bridging arrangement, enabling extremely strong antiferromagnetic superexchange pathways. The magnetic susceptibilities of the copper(II) complexes are close to 0, even at room temperature, allowing the study of these compounds in solution by different NMR techniques. In chapter VI, I show that the structure, geometry and magnetic interactions in solution and solid state are similar.

Chapter VII is centered around the dynamic behavior of $[Zn_2(\mu\text{-}OH)(\mu\text{-}\mathbf{L_m})_2](ClO_4)_3$ in solution. The VT-NMR and spin saturation transfer experiments reveal an unprecedented example of concerted Berry pseudorotation at two metal sites accompanied by the simultaneous 180° ring flip of the phenylene spacer - termed the "Carolina Twist and Flip" mechanism. This process is hindered by the methyl groups on the pyrazolyl rings for $[M_2(\mu\text{-}OH)(\mu\text{-}\mathbf{L_m*})_2](ClO_4)_3$, M = Zn(II), Cd(II).

Chapter VIII discusses the synthesis and characterization of an unusual cubane type structure, $[M_4(\mu\text{-}OH)_4(\mu\text{-}\mathbf{L_m})_2(Solvent)_4](ClO_4)_4$ where M = Ni(II) or Cd(II). The nickel(II) centers are ferromagnetically coupled and the cadmium(II) compound undergoes a similar rearrangement to $[Zn_2(\mu\text{-}OH)(\mu\text{-}\mathbf{L_m})_2](ClO_4)_3$.

Table of Contents

List of Tables

List of Figures

List of Schemes

Chapter I

Structural Variations in Copper(II) Complexes of a Ditopic Bis(pyrazolyl)methane Ligand[1]

[1]Adapted with permission from Reger, D. L.; Pascui, A. E.; Smith, M. D. *Eur. J. Inorg. Chem.* **2012**, 4593-4604. DOI:10.1002/ejic.201200118. Copyright 2012 John Wiley and Sons.

Introduction

Molecular self-assembly has gained an ever increasing importance in coordination chemistry and materials science as it is a valuable tool that can generate diversity and great complexity in the structure of compounds.[1] Supramolecules can be carefully tailored for different applications, giving rise to the field of molecular nanotechnology.[2] A main goal of this field is to generate well organized functional systems for a higher level of miniaturization through bottom-up strategies.

A large number of supramolecules have been designed based on metal-ligand interactions, from discrete molecular architectures[3] to coordination polymers[4] (CPs). The metal centers and connecting ligands can be modified to obtain magnetic and electronic properties for future applications such as molecular information storage and microelectronic systems. A representative class of CPs are 1-dimensional (1D) chain type structures[5] generated by the periodical repetition of organic ligands and inorganic building blocks. An intriguing and novel aspect of the design and synthesis of 1D and 2D CPs is their potential for being used as nanowires.[2a,5c]

Although coordination polymers are favored subjects of research, most studies focus on the covalent assembly of the structures; only a smaller number of examples target the synergistic effect of coordination bonds, anion and/or noncovalent interactions.[6] The role of the anions in the definition of the overall structure only recently gained significant attention.[7] The anions can have a dramatic role in the preorganization of the building blocks either by direct coordination or spatial templating effects.

The Reger group has reported the synthesis and structural characterization of self-assembled supramolecules, both metallacycles[8] and coordination polymers,[9] using semi-

rigid, multitopic, third generation poly(pyrzolyl)methane ligands. Second generation poly(pyrazolyl)methane ligands are substituted with bulky groups at the 3-position so as to impact the coordination sphere of the metal, third generation ligands are substituted at the "backbone" position away from the coordination sites of the metal. Recently, the design and synthesis of supramolecules using two bis(pyrazolyl)methane units linked by a phenylene spacer substituted in the 1,4-, *p*-bis[bis(1-pyrazolyl)methyl]benzene (**L**$_{p}$) or 1,3-, *m*-bis[bis(1-pyrazolyl)methyl]benzene (**L**$_{m}$), positions became of great interest (Scheme 1.1). These ligands are best described as "fixed" but not necessarily "rigid." The distances between the central methine carbon atoms of the bis(pyrazolyl)methane units remain essentially constant for complexes of each of these ligands, but rotation of the bis(pyrazolyl)methane units about the methine–arene carbon (*ipso*) bond allows variation in the way the ligands bind metal centers.

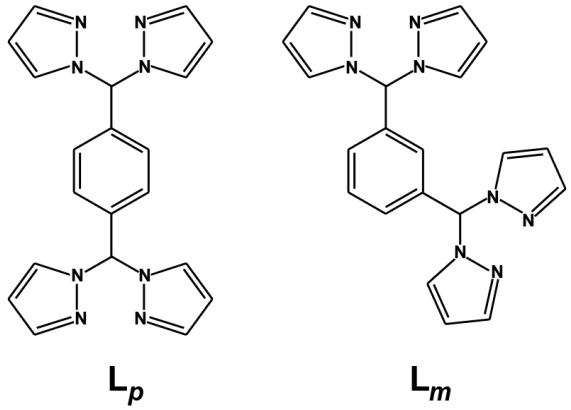

Scheme 1.1. The structures of **L**$_{p}$ and **L**$_{m}$.

It was shown in several cases that **L**$_{m}$ supports the formation of binuclear metallacycles[8,9] (e.g. [Ag$_2$(μ-**L**$_{m}$)$_2$](BF$_4$)$_2$) with monovalent transition metal cations, Figure 1.1a) with both bis(pyrazolyl)methane units on the same side (*syn*) of the linking arene ring, while **L**$_{p}$ tends to form 1-dimensional coordination polymers, such as [Ag(μ-

$\mathbf{L}_p$)](BF$_4$), in which the bis(pyrazolyl)methane units are on opposite sides (*anti*) of the linking arene ring (Figure 1.1c).[8] The 2- and 3-dimensional frameworks have also been isolated with the same ligand, [Ag$_2$(μ-$\mathbf{L}_p$)$_{1.5}$(NO$_3$)](NO$_3$) and Ag(μ-$\mathbf{L}_p$)(NO$_3$), by Wang *et al.*[10] The ligand $\mathbf{L}_p$, was also used for the synthesis of dinuclear organometallic compounds of the heavier Group 8 metals by the Messerle and Rao groups (Figure 1.1d).[11]

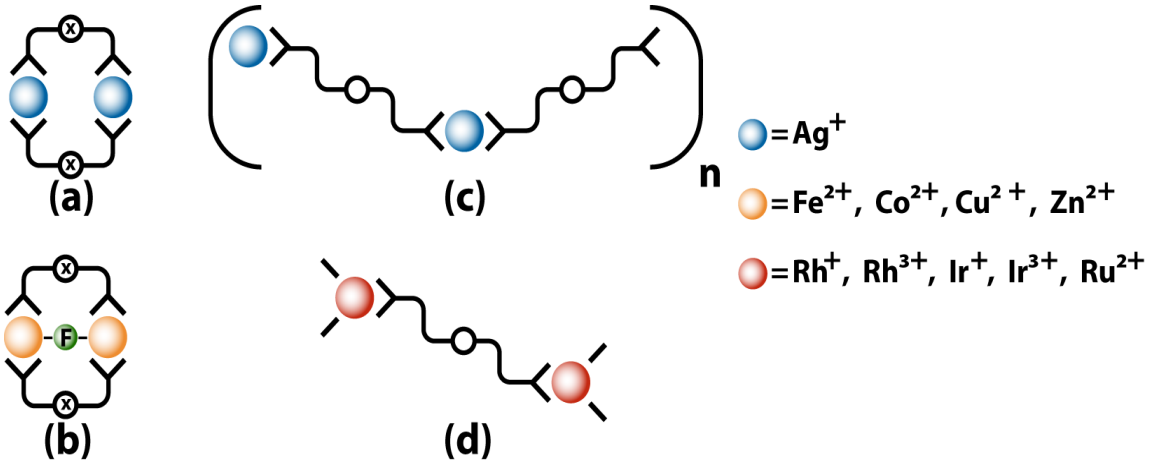

Figure 1.1. Schematic representation of the cations in (a) [M$_2$(μ-$\mathbf{L}_m$)$_2$](BF$_4$)$_2$, (b) [M$_2$(μ-F)(μ-$\mathbf{L}_m$)$_2$](BF$_4$)$_3$, (c) [M(μ-$\mathbf{L}_p$)](BF$_4$)$_n$ (d) [M$_2$(μ-$\mathbf{L}_p$)(L$_1$)$_2$(L$_2$)$_2$](PF$_6$)$_n$.

Interestingly, the use of the $\mathbf{L}_m$ ligand with divalent cations, where M = Fe(II), Co(II), Cu(II), Zn(II), leads to the formation of metallacyclic complexes bridged by a fluoride abstracted from the BF_4^- anion, of the formula [M$_2$(μ-F)(μ-$\mathbf{L}_m$)$_2$](BF$_4$)$_3$ (Figure 1.1b).[9] Based on these results, there was an interest in determining the types of complexes that would form with divalent metals and the semi-rigid $\mathbf{L}_p$ ligand. In this chapter the synthesis and characterization of 1-dimensional coordination polymers and dinuclear complexes of copper(II) that form with $\mathbf{L}_p$ are discussed. The crystal packing of both structural types is influenced by the charge compensating anions and/or solvent

molecules. The effect of non-coordinating anions on the extended structure, organized through strong and weaker noncovalent interactions will be highlighted.

Experimental Section

General Considerations. The synthesis of the compounds was carried out in open atmosphere. The ligand, $\mathbf{L}_{\boldsymbol{p}}$,[12] was prepared following our reported procedures. All other chemicals were purchased from Sigma-Aldrich and were used as received. Reported melting points are uncorrected.

Crystals used for elemental analysis and mass spectrometry were removed from the mother liquor and rinsed with ether. Mass spectrometric measurements were obtained on a MicroMass QTOF spectrometer in an acid-free environment. Elemental analyses were performed by Robertson Microlit Laboratories (Ledgewood, NJ) on samples dried to constant weight (105˚C vacuum), which removes both the free and coordinated solvents, except when the solvent is the high boiling DMSO.

Thermogravimetric analysis was performed using a Thermal Analysis (TA) SDT-Q600 simultaneous DTA/TGA system. The samples were heated in air to 800 ˚C with a heating rate of 10˚C/min.

XSEED and POV-RAY were used for the preparation of figures.[13]

$[Cu(\mu\text{-}L_p)(CH_3OH)](BF_4)_2\cdot(CH_3OH)_{0.62}$ (1). In a test tube, $Cu(BF_4)_2\cdot 3H_2O$ (19.5 mg, 0.067 mmol) was dissolved in MeOH (3 mL) followed by addition of a buffer layer of pure MeOH (5 mL). The ligand, $\mathbf{L}_{\boldsymbol{p}}$ (24.8 mg, 0.067 mmol) was dissolved in hot MeOH (6 mL), allowed to cool to room temperature and added as a third layer. The tube was capped and in a few weeks crystals (20 mg, 45%), suitable for X-ray diffraction, were collected. Anal. Calcd.(Found) for $C_{20}H_{18}B_2CuF_8N_8$ ($[Cu(\mu\text{-}\mathbf{L}_{\boldsymbol{p}})](BF_4)_2$): C, 39.54

(39.49); H, 2.99 (2.77); N, 18.44 (18.16). MS ESI(+) *m*/*z* (rel. % abund.) [assgn] acetonitrile solution: 890 (18) $[Cu(\mathbf{L}_p)_2BF_4]^+$, 803 (9) $[Cu(\mathbf{L}_p)_2]^+$, 553 (7) $[Cu_2(\mathbf{L}_p)_2(CH_3OH)_2(BF_4)_2]^{2+}$, 474 (18) $[Cu\mathbf{L}_p(CH_3CN)]^+$, 433 (40) $[Cu\mathbf{L}_p]^+$, 401 (100) $[Cu(\mathbf{L}_p)_2]^{2+}$, 371 (11) $[\mathbf{L}_p+H]^+$; methanol solution: 803 (100) $[Cu(\mathbf{L}_p)_2]^+$, 433 (32) $[Cu\mathbf{L}_p]^+$, 371 (78) $[\mathbf{L}_p+H]^+$.

$[Cu(\mu\text{-}L_p)(CH_3OH)]_2(SiF_6)(BF_4)_2\cdot 2CH_3OH$ (2). In a test tube, $Cu(BF_4)_2\cdot 3H_2O$ (19.5 mg, 0.067 mmol) was dissolved in 3 mL H_2O followed by addition of a buffer layer of pure methanol (6 mL). $\mathbf{L}_p$ (24.8 mg, 0.067 mmol), dissolved in MeOH (6 mL) was layered on top of the buffer layer. In a few weeks crystals (18 mg, 41%), suitable for X-ray diffraction were collected. Anal. Calcd.(Found) for $C_{40}H_{36}B_2Cu_2F_{14}N_{16}Si$ ($[Cu(\mu\text{-}\mathbf{L}_p)]_2(SiF_6)(BF_4)_2$): C, 40.59 (40.44); H, 3.07 (2.99); N, 18.93 (18.54). MS ESI(+) *m*/*z* (rel. % abund.) [assgn] acetonitrile solution: 803 (9) $[Cu(\mathbf{L}_p)_2]^+$, 474 (73) $[Cu\mathbf{L}_p(CH_3CN)]^+$, 433 (100) $[Cu\mathbf{L}_p]^+$, 371 (20) $[\mathbf{L}_p+H]^+$.

$[Cu_2(\mu\text{-}L_p)(H_2O)_6](SiF_6)_2\cdot(H_2O)_4$ (3). In a test tube, $Cu(BF_4)_2\cdot 3H_2O$ (39.0 mg, 0.134 mmol) was dissolved in H_2O (3 mL). A buffer layer of pure ethanol was added to the test tube before $\mathbf{L}_p$ (24.8 mg, 0.067 mmol), dissolved in ethanol (8 mL), was layered on the top of it. In a month, dichroic crystals (20 mg, 31%) of **3**, suitable for X-ray analysis, were grown. Anal. Calcd.(Found) for $C_{20}H_{18}Si_2Cu_2F_{12}N_8$ ($[Cu_2(\mu\text{-}\mathbf{L}_p)](SiF_6)_2$): C, 30.73 (30.45); H, 2.32 (3.04); N, 14.34 (14.13). MS ESI(+) *m*/*z* (rel. % abund.) [assgn] acetonitrile solution: 803 (9) $[Cu(\mathbf{L}_p)_2]^+$, 474 (73) $[Cu\mathbf{L}_p(CH_3CN)]^+$, 433 (100) $[Cu\mathbf{L}_p]^+$, 371 (20) $[\mathbf{L}_p+H]^+$; water solution: 803 (30) $[Cu(\mathbf{L}_p)_2]^+$, 433 (100) $[Cu\mathbf{L}_p]^+$, 402 (20) $[Cu(\mathbf{L}_p)_2]^{2+}$.

[Cu(μ-$\mathbf{L}_p$)(H_2O)](BF_4)$_2$·2CH_3CH_2OH (4). In a test tube, Cu(BF_4)$_2$·3H_2O (19.5 mg, 0.067 mmol) was dissolved in H_2O (3 mL), followed by a buffer layer of pure EtOH and an ethanolic solution (6 mL) of $\mathbf{L}_p$ (24.8 mg, 0.067 mmol). In a few weeks both **3** and **4** formed in the same test tube. Crystals of **3** were found at the bottom of the test tube. The identity of crystals of **4**, collected from the wall of the test tube was confirmed by elemental analyses. Anal. Calcd.(Found) for $C_{20}H_{18}B_2CuF_8N_8$ ([Cu(μ-$\mathbf{L}_p$)](BF_4)$_2$): C, 39.54 (39.79); H, 2.99 (2.61); N, 18.44 (18.59).

[Cu$_2$(μ-$\mathbf{L}_p$)(DMSO)$_6$](BF_4)$_4$·(DMSO)$_2$·C_6H_6·(H_2O)$_{0.5}$ (5). Both $\mathbf{L}_p$ (49.6 mg, 0.134 mmol) and Cu(BF_4)$_2$·3H_2O (39.0 mg, 0.134 mmol) were dissolved separately in THF (8 mL). The ligand solution was canula transferred into the copper solution. A blue precipitate formed immediately. The reaction mixture was stirred overnight, and then the system was filtered by cannula, washed with 5 mL THF and dried under vacuum. Greenish blue single crystals suitable for X-ray studies were obtained by dissolving the blue compound (the PXRD spectrum of this solid is broad, indicating low crystallinity, but shows three features that more closely match the spectrum of the coordination polymer **1** than that predicted for **5**, see figure 1.2) in DMSO and layering it with benzene to afford 54 mg (52%) of **5**. Anal. Calcd.(Found) for $C_{32}H_{54}B_4Cu_2F_{16}N_8O_6S_6$ ([Cu$_2$(μ-$\mathbf{L}_p$)(DMSO)$_6$](BF_4)$_4$): C, 29.26 (29.61); H, 4.14 (3.63); N, 8.53 (8.93). MS ESI(+) *m*/*z* (rel. % abund.) [assgn] acetonitrile solution: 890 (19) [Cu($\mathbf{L}_p$)$_2$$BF_4$]$^+$, 803 (80) [Cu($\mathbf{L}_p$)$_2$]$^+$, 441 (60) [Cu($\mathbf{L}_p$)$_2$DMSO)]$^+$, 433 (35) [Cu$\mathbf{L}_p$]$^+$, 402 (72) [Cu($\mathbf{L}_p$)$_2$]$^{2+}$.

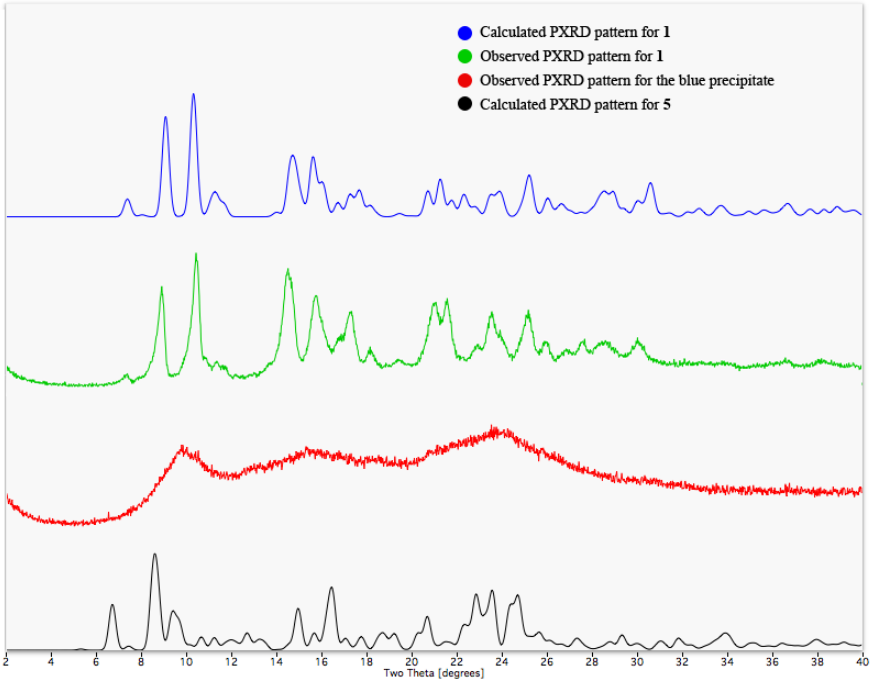

Figure 1.2. The observed and predicted PXRD patterns of **1**, the predicted pattern of **5**, and the blue precipitate isolated from the reaction of $Cu(BF_4)_2{\cdot}xH_2O$ with $\mathbf{L}_{\boldsymbol{p}}$ in THF.

$[Cu_2(\mu\text{-}L_p)(DMSO)_6](BF_4)_4{\cdot}(DMSO)_2{\cdot}C_6H_6$ (6). Layering benzene on top of the DMSO solution of compound **1** (30 mg, 0.046 mmol) results in crystals of **6** (21 mg, 60%). Anal. Calcd.(Found) for $C_{32}H_{54}B_4Cu_2F_{16}N_8O_6S_6$ ($[Cu_2(\mu\text{-}\mathbf{L}_{\boldsymbol{p}})(DMSO)_6](BF_4)_4$): C, 29.26 (29.47); H, 4.14 (3.73); N, 8.53 (8.46).

Crystallographic studies. X-ray diffraction intensity data for compounds **1-6** were collected on a Bruker SMART APEX CCD-based diffractometer (Mo Kα radiation, λ = 0.71073 Å).[14] Raw area detector data frame processing was performed with the SAINT+ and SADABS programs.[14] Final unit cell parameters were determined by least-squares refinement of large sets of strong reflections taken from each data set. Direct methods structure solution, difference Fourier calculations and full-matrix least-squares refinement against F^2 were performed with SHELXTL.[15] Non-hydrogen atoms were refined with anisotropic displacement parameters, the exception being disordered species.

Table 1.1. Selected crystal and structure refinement data for **1-6.**

	1	**2**	**3**	**4**	**5**	**6**
Formula	$C_{21.62}H_{24.46}B_2CuF_8N_8O_{1.62}$	$C_{44}H_{52}B_2Cu_2F_{14}N_{16}O_4Si$	$C_{20}H_{38}Cu_2F_{12}N_8O_{10}Si_2$	$C_{24}H_{32}B_2CuF_8N_8O_3$	$C_{42}H_{73}B_4Cu_2F_{16}N_8O_{8.50}S_8$	$C_{42}H_{72}B_4Cu_2F_{16}N_8O_8S_8$
Fw, g mol^{-1}	659.47	1311.81	961.84	717.74	1556.88	1547.88
Cryst. Syst.	Monoclinic	Triclinic	Triclinic	Triclinic	Triclinic	Monoclinic
Space group	C2/c	$P\bar{1}$	$P\bar{1}$	$P\bar{1}$	$P\bar{1}$	$P2_1/c$
T, K	150(2)	150(2)	150(2)	150(2)	150(2)	100(2)
a, Å	20.7649(8)	11.6662(10)	8.6391(4)	12.0337(9)	10.7590(6)	11.8973(5)
b, Å	15.1386(6)	11.8615(10)	9.8509(5)	12.2725(9)	17.3133(10)	10.1467(5)
c, Å	18.2841(7)	12.1415(10)	11.6019(6)	12.7401(9)	18.9502(11)	27.3244(13)
α, deg	90	61.879(1)	74.158(1)	107.546(1)	83.935(1)	90
β, deg	110.599(1)	66.786(1)	74.315(1)	110.906(1)	88.427(1)	91.979(1)
γ, deg	90	82.483(2)	77.460(1)	103.401(1)	74.054(1)	90
V, Å^3	5380.2(4)	1358.7(2)	903.47(8)	1549.5(2)	3375.1(3)	3296.6(3)
Z	8	1	1	2	2	2
R1[I>2σ(I)]	0.0530	0.0418	0.0302	0.0545	0.0625	0.0598
wR2[I>2σ(I)]	0.1519	0.0954	0.0764	0.1498	0.1622	0.1565

The hydrogen atoms were placed in geometrically idealized positions and included as riding atoms. The space groups were confirmed by the successful solution and refinement of the structure. Details of the data collection are given in Table 1.1.

Compound **1** crystallizes in the space group C2/c. The asymmetric unit consists of one copper atom, half each of two ligands located on inversion centers, one coordinated methanol molecule, three independent sites occupied by BF_4^- anions, and two independent sites containing fractionally populated methanol molecules. One BF_4^- anion (B1) is located on a site of general crystallographic symmetry and refines normally. Anion B2 is located on and is disordered about a two-fold rotational axis; only half is present in the asymmetric unit. The disorder of this anion was modeled with one boron atomic position on the C_2 axis and six 1/3-occupied fluorine atomic positions. Anion B3 is disordered about an inversion center; there are two independent BF_4^- units per asymmetric unit with occupancies B3A/B3B = 0.298(7)/0.202(7). Electron density in the vicinity of the B3 disorder assembly was modeled as two methanol sites with populations 0.33(1) and 0.29(1). No hydrogen atoms were located or calculated for these species. 38 geometric restraints were applied to maintain chemically reasonable geometries for the disordered groups. The proton H1A of the coordinated methanol molecule was located in a difference map and refined freely.

Compound **2** crystallizes in the space group P $\bar{1}$ of the triclinic system. The asymmetric unit consists of one copper atom, half each of two ligands located on inversion centers, one coordinated methanol molecule, half of a SiF_6^{2-} anion located on an inversion center, one BF_4^- anion and one uncoordinated methanol molecule. The uncoordinated methanol is disordered equally over two closely separated positions and

was refined isotropically with the aid of two C-O distance restraints. The hydrogen on the coordinated methanol was located and refined isotropically with a d(O-H) = 0.84(2) Å distance restraint. Reasonable positions for the oxygen-bound hydrogens of the uncoordinated methanol were located, adjusted to give d(O-H) = 0.84 Å and subsequently treated as riding of the parent oxygen atom. The adventitious SiF_6^{2-} species was assigned on the basis of geometry, Si-F bond distances and evaluation of the central atom displacement parameter.

Compound **3** crystallizes in the space group P $\bar{1}$ of the triclinic system. The asymmetric unit consists of half of one $[Cu_2(\mu\text{-}\mathbf{L_p})(H_2O)_6]^{4+}$ cation located on an inversion center, one SiF_6^{2-} anion and two interstitial water molecules. The SiF_6^{2-} anion is rotationally disordered about the F1-Si1-F2 vector with a major population of 0.849(4). The disorder affects only atoms F3-F6. All water hydrogen atoms were located in difference maps and refined isotropically with all O-H distances restrained to be approximately equal.

Compound **4** crystallizes in the space group P $\bar{1}$ of the triclinic system. The asymmetric unit consists of one copper atom, half each of two ligands located on inversion centers, one coordinated water molecule, two independent BF_4^- anions, and two independent ethanol molecules. Both BF_4^- anions are disordered and were refined with either two (B1) or three (B2) orientations, with the total site occupancy constrained to sum to unity. Sixty restraints were applied to these species to maintain chemically reasonable geometries. One of the two independent ethanol molecules (O3) is disordered over two orientations. The proton bonded to O3 could not be located and was not

calculated for this molecule. The oxygen-bound water and ethanol (O2) hydrogen atoms were located in difference maps and refined with O-H and H-H distance restraints.

Compound **5** crystallizes in the space group P $\bar{1}$ of the triclinic system. The asymmetric unit consists of one $[Cu_2(\mu\text{-}\mathbf{L}_p)(DMSO)_6]^{4+}$ complex, four independent BF_4^- anions, two uncoordinated DMSO molecules, one benzene molecule and half of a water molecule (O1S) disordered over an inversion center. The three DMSO molecules bonded to Cu(2) (S4, S5, S6) and one uncoordinated DMSO (S8) are disordered over two orientations. Two BF_4^- anions (B3, B4) are also disordered. The geometries of these disordered species were restrained to be similar to that of an ordered counterpart, using the SHELX SAME instruction (316 total restraints). Their populations were constrained to sum to unity. All non-hydrogen atoms were refined with anisotropic displacement parameters except for some atoms of minor disorder components (isotropic). Hydrogen atoms were placed in geometrically idealized positions and included as riding atoms. No hydrogen atoms were located or calculated for the disordered water molecule.

Compound **6** crystallizes in the space group $P2_1/c$ as determined by the pattern of systematic absences in the intensity data. The asymmetric unit consists of half of one $[Cu_2(\mu\text{-}\mathbf{L}_p)(DMSO)_6]^{4+}$ cation located on a crystallographic inversion center, two independent tetrafluoroborate anions, half of one benzene molecule also located on an inversion center, and one uncoordinated DMSO molecule. Two-fold positional disorder was modeled for two of the coordinated DMSO molecules (S2 and S3) and for the uncoordinated DMSO (S4). Total DMSO populations were constrained to sum to unity. The minor populations refined to: S2B = 0.369(3), S3B = 0.067(4), S4B = 0.078(5). Minor component geometry was restrained to be similar to that of major.

Results

Synthesis. Six complexes are prepared by the reaction of $Cu(BF_4)_2{\cdot}3H_2O$ with *p*-$[CH(pz)_2]_2C_6H_4$, $\mathbf{L_p}$, under different conditions, mainly changes in solvent, as outlined in Scheme 1.2.

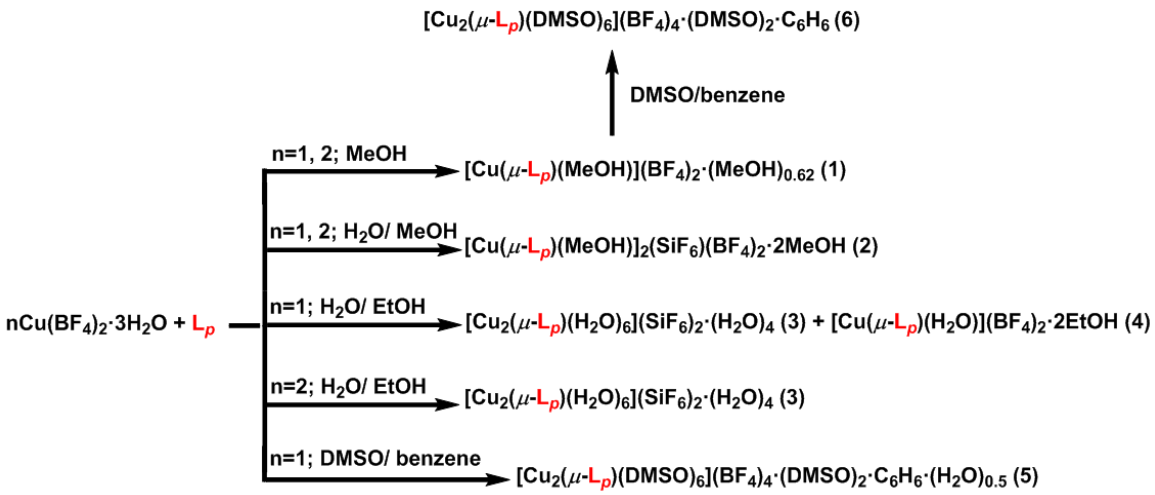

Scheme 1.2. Synthesis of $\mathbf{L_p}$ complexes.

Layering equal molar methanol solutions (or 2/1) of the two components yields over a few weeks $[Cu(\mu\text{-}\mathbf{L_p})(CH_3OH)](BF_4)_2{\cdot}(CH_3OH)_{0.62}$ (**1**), whereas if water is used for the $Cu(BF_4)_2{\cdot}3H_2O$ layer $[Cu(\mu\text{-}\mathbf{L_p})(CH_3OH)]_2(SiF_6)(BF_4)_2{\cdot}2CH_3OH$ (**2**) is produced. The similar use of water/ethanol layering solutions produces in the same tube both $[Cu_2(\mu\text{-}\mathbf{L_p})(H_2O)_6](SiF_6)_2{\cdot}(H_2O)_4$ (**3**), which forms in the water rich bottom part of the tube, and $[Cu(\mu\text{-}\mathbf{L_p})(H_2O)](BF_4)_2{\cdot}2CH_3CH_2OH$ (**4**), which forms in the ethanol rich upper part of the tube. A similar reaction starting from a 2/1 Cu(II)/$\mathbf{L_p}$ mixture of the reactants produces only compound **3**. In the case of compound **2** some and in the case of **3** all of the anions are SiF_6^{2-}. The formation of SiF_6^{2-} is promoted by the presence of H_2O, which may lead to the formation of small amounts of HF, capable of etching the glassware.

Hydrolysis of the BF_4^- anions and the subsequent reaction of the F^- anions with SiO_2 have been observed previously.[16] Even though the partial exchange of the counter ions by SiF_6^{2-} is more commonly observed, a few examples of the formation of only SiF_6^{2-} salts were also reported upon use of BF_4^- starting materials.[17] $[Cu_2(\mu\text{-}\mathbf{L_p})(DMSO)_6](BF_4)_4\cdot(DMSO)_2\cdot C_6H_6\cdot(H_2O)_{0.5}$ (**5**) was obtained by layering benzene on top of the DMSO solution of the product from the reaction of $\mathbf{L_p}$ and $Cu(BF_4)_2\cdot 3H_2O$ in THF. Recrystallizing **1** from benzene layered on top of the DMSO solution resulted in $[Cu_2(\mu\text{-}\mathbf{L_p})(DMSO)_6](BF_4)_4\cdot(DMSO)_2\cdot C_6H_6$ (**6**).

Compounds **1**-**6** are barely soluble in acetonitrile or water, which impeded solution characterization. No solution NMR were observed. The positive-ion electrospray mass spectra (ESI^+-MS) of **1** is typical of an oligomeric structure, as observed in the solid phase, vide infra. Surprisingly, so are the spectra of compounds **3** and **5**, indicating the soluble species may not hold the dimeric solid state structures in solution.

Solid State Structures. The structure of **1** is shown in Figure 1.3; compounds **2** and **4** have similar structures and the numbering scheme in Figure 1.3 is correct for all three. The structure of **3** is shown in Figure 1.4a; complex **6** has a similar structure and numbering scheme. Figure 1.4b shows the structure, which is similar to **3** and **6,** and numbering scheme for compound **5**. Selected bond lengths and angles are gathered in Table 1.2 and 1.3.

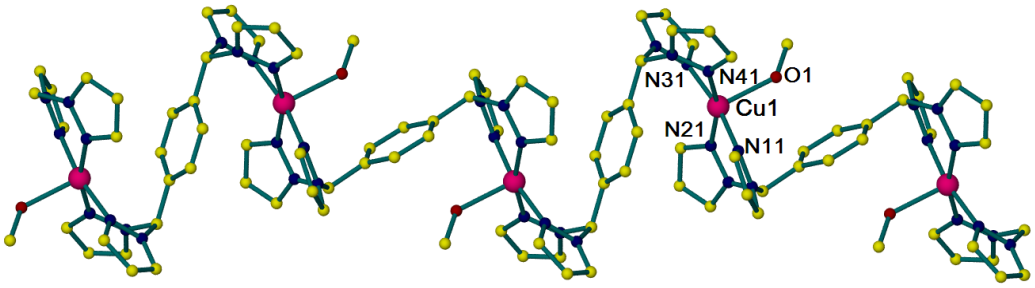

Figure 1.3. Structure of the 1-dimensional cationic coordination polymer of [Cu(μ-**L**$_p$)(CH$_3$OH)](BF$_4$)$_2$·(CH$_3$OH)$_{0.62}$ (**1**). Hydrogen atoms are omitted for clarity.

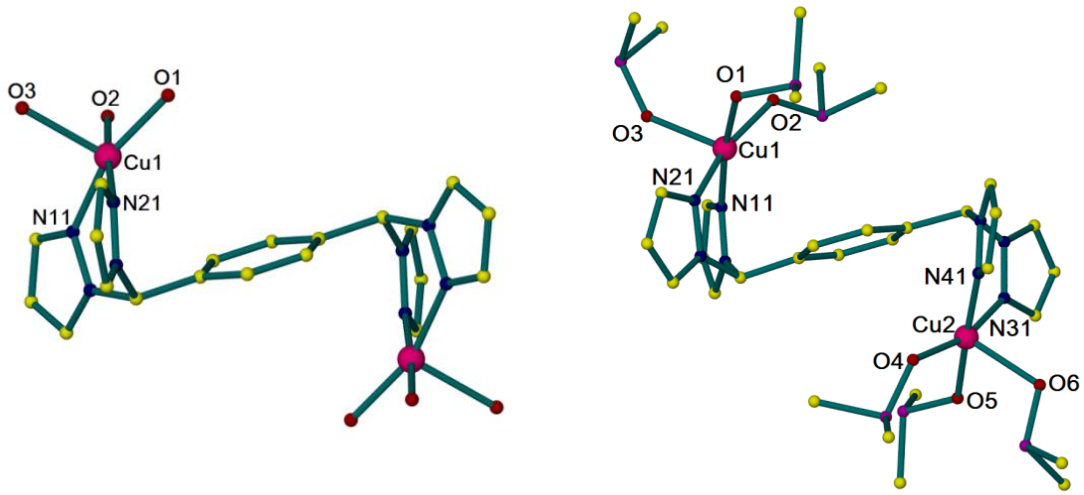

(a) (b)

Figure 1.4. (a) Structure of the cationic units in [Cu$_2$(μ-**L**$_p$)(H$_2$O)$_6$](SiF$_6$)$_2$·(H$_2$O)$_4$ (**3**) and (b) [Cu$_2$(μ-**L**$_p$)(DMSO)$_6$](BF$_4$)$_4$·(DMSO)$_2$·C$_6$H$_6$·(H$_2$O)$_{0.5}$ (**5**). Hydrogen atoms and one set of disordered atoms for **5** are omitted for clarity.

In the structures of all six compounds, the ligand adopts the *anti* conformation where the two bis(pyrazolyl)methane units are on opposite sides of the plane formed by the phenylene spacer. The copper(II) ions are five-coordinate. The τ_5[18] values, shown in Table 1.1 and 1.2, indicate an almost perfect square pyramidal arrangement (τ_5 value of 0, where τ_5 = 1 is a perfect trigonal bipyramid) of the coordinated atoms, the least distorted being **4** (τ_5 = 0.02) and the most distorted being **3** (τ_5 = 0.24).

Table 1.2. Selected bond lengths (Å) and angles (deg) for **1**, **2** and **4**.

	1	**2**	**4**
		Bond Lengths (Å)	
Cu(1)-N(11)	2.011(3)	2.020(3)	2.023(3)
Cu(1)-N(21)	2.004(3)	2.013(3)	2.019(3)
Cu(1)-N(31)	2.026(3)	2.027(3)	2.033(3)
Cu(1)-N(41)	2.016(3)	2.025(3)	2.022(3)
Cu(1)-O(1)	2.206(2)	2.200(2)	2.188(3)
		Bond Angles (deg)	
N(21)-Cu(1)-N(11)	89.24(11)	91.21(10)	90.14(12)
N(21)-Cu(1)-N(41)	162.63(10)	164.13(10)	164.60(12)
N(11)-Cu(1)-N(41)	91.39(11)	90.86(10)	90.05(13)
N(21)-Cu(1)-N(31)	90.66(11)	89.88(10)	89.84(12)
N(11)-Cu(1)-N(31)	168.64(10)	166.01(10)	163.37(12)
N(41)-Cu(1)-N(31)	85.35(11)	84.39(10)	85.62(12)
N(21)-Cu(1)-O(1)	106.72(10)	103.82(10)	97.78(12)
N(11)-Cu(1)-O(1)	96.90(10)	92.60(10)	107.65(11)
N(41)-Cu(1)-O(1)	90.43(10)	91.80(10)	96.83(12)
N(31)-Cu(1)-O(1)	94.00(10)	100.68(10)	88.82(11)
τ_5	0.10	0.03	0.02

Table 1.3. Selected bond lengths (Å) and angles (deg) for **3**, **5** and **6**.

	3	**5**	**6**
		Bond Lengths (Å)	
Cu(1)-O(1)	1.9638(17)	1.962(3)	1.965(3)
Cu(1)-O(2)	1.9484(18)	1.983(3)	1.9595[a]
Cu(1)-O(3)	2.1870(15)	2.142(3)	2.1685[a]
Cu(1)-N(11)	1.9898(16)	1.982(3)	2.018(4)
Cu(1)-N(21)	1.9837(18)	1.989(3)	1.984(3)
		Bond Angles (deg)	
O(2)-Cu(1)-O(1)	90.58(9)	86.98(12)	87.4[a]
O(2)-Cu(1)-N(21)	175.23(8)	164.87(13)	172.5[a]
O(1)-Cu(1)-N(21)	89.90(8)	87.17(13)	93.29(14)
O(2)-Cu(1)-N(11)	88.70(7)	94.34(12)	89.35[a]
O(1)-Cu(1)-N(11)	161.00(7)	171.71(13)	160.56(14)
N(21)-Cu(1)-N(11)	89.29(7)	89.52(13)	88.86(15)
O(2)-Cu(1)-O(3)	90.27(7)	98.08(12)	93.85[a]
O(1)-Cu(1)-O(3)	99.00(7)	96.98(12)	91.03[a]
N(21)-Cu(1)-O(3)	94.34(7)	96.47(12)	98.585[a]
N(11)-Cu(1)-O(3)	100.00(6)	90.95(11)	107.44[a]
τ_5	0.24	0.11	0.19

[a]Due to the disorder of the coordinated DMSO molecules average bond lengths and average bond angles are shown.

In compounds **1**, **2** and **4** the $\mathbf{L}_{p}$ ligands bridge two neighboring copper(II) centers by coordination to the equatorial sites of the square pyramid, forming 1-dimensional zigzag coordination polymers running parallel to each other. The overall shapes of the three coordination polymers are very similar; as shown in Figure 1.5, they overlap nearly perfectly. The Cu-N bond lengths vary between 2.004 and 2.033 Å with the axial position occupied by a solvent molecule (**1** and **2** MeOH, **4** H_2O); Cu-O bond lengths are in the range 2.142 - 2.187 Å.[19]

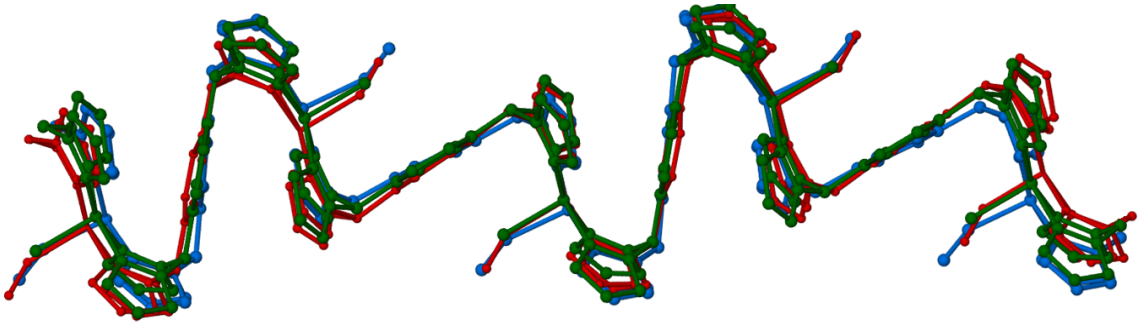

Figure 1.5. Overlay of the 1-dimensional polymeric chains of compounds **1** (red), **2** (blue) and **4** (dark green).

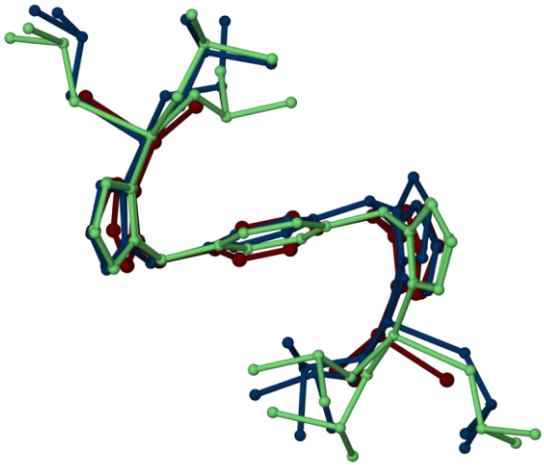

Figure 1.6. Overlay of the cations of dinuclear **3** (garnet), **5** (dark blue) and **6** (green).

Compounds **3**, **5** and **6** were isolated in the presence of a large excess of H_2O (**3**) or DMSO (**5**, **6**), which fill three of the coordination sites. All three compounds are dinuclear. Two equatorial positions about copper(II) are occupied by the $\mathbf{L}_{\boldsymbol{p}}$ nitrogen donors (Cu-N 1.98-2.02 Å), while the other two equatorial positions are taken by solvent molecules (Cu-O 1.95-1.98 Å). The axial position is occupied by the third solvent molecule with longer Cu-O lengths (2.14-2.19 Å), as observed above with **1**, **2** and **4**. Again, the overlap of the structures of **3**, **5** and **6** (Figure 1.6) is almost perfect, emphasizing that the type of coordinated solvent molecule and the anion has little to no effect on the covalent structures of these complexes.

Supramolecular Structure. Compounds **1-4** form a variety of noncovalent interactions with neighboring cations, anions and interstitial solvent molecules. The dominant interactions are different types of hydrogen bonding interactions. It is generally accepted that there is a direct correlation between hydrogen bond strength and crystallographically determined distances between hydrogen bond donors and acceptors.[20] A hydrogen bond of the general formula A-H···B is considered strong if it has a major covalent component (d(H···B) ~ 1.2 - 1.5 Å and the A-H···B angle is 175-180º), moderate if the interaction is mainly electrostatic (d(H···B) ~ 1.5 – 2.2 Å and the A-H···B angle is 130-180º), and weak if d(H···B) ~ 2.2 – 3.2 Å and the A-H···B angle is 90-150º.[21]

Based on the classification above, along the covalent chains of compound **1** two types of hydrogen bonds (Table 1.4, Figure 1.7) are formed with the BF_4^- anions: a stronger O(1)-H(1A)···F(14) hydrogen bond (2.024 Å, 158.55º), through the involvement of coordinated methanol, and a somewhat weaker C(5)-H(5)···F(32A) interaction (2.310

Å, 147.17º), through the methine hydrogen. Although weaker, these C-H···F interactions are unusually strong; more generally d(H···F) = 2.4-2.6 Å are observed.[22, 23] The strength observed here can be attributed to the cooperative effect of the increased acidity of the methine C-H bond and charge assistance (the fact that the fluorine atom is part of an anion) from the BF_4^- anion.

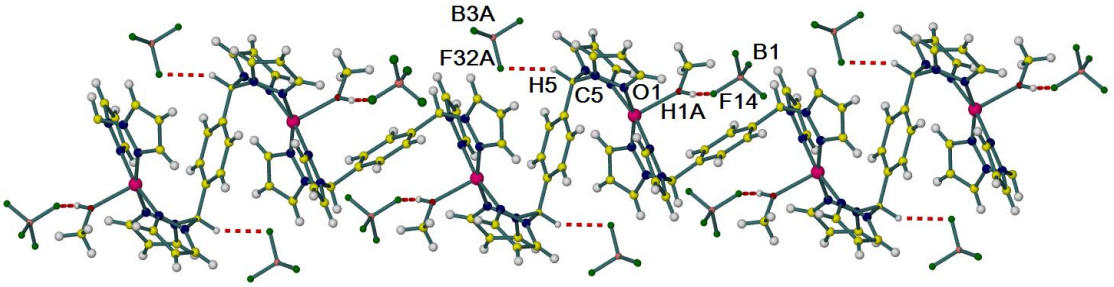

Figure 1.7. Hydrogen bonding interactions along the CP chain in the structure **1**.

Table 1.4. Noncovalent interactions in the structures of **1** and **2**.

	1		**2**	
	Distance (Å)[a]	**Angle (deg)**	**Distance (Å)[a]**	**Angle (deg)**
O(1)-H(1A)···F	2.024 (2.811)	158.55	1.909 (2.729)	168.13
C(5)-H(5)···F	2.310 (3.197)	147.17	2.008 (2.965)	159.40

[a] H···X (Y···X), where Y-H···X is a hydrogen bond of the general formula, X = F or O, Y = O, C.

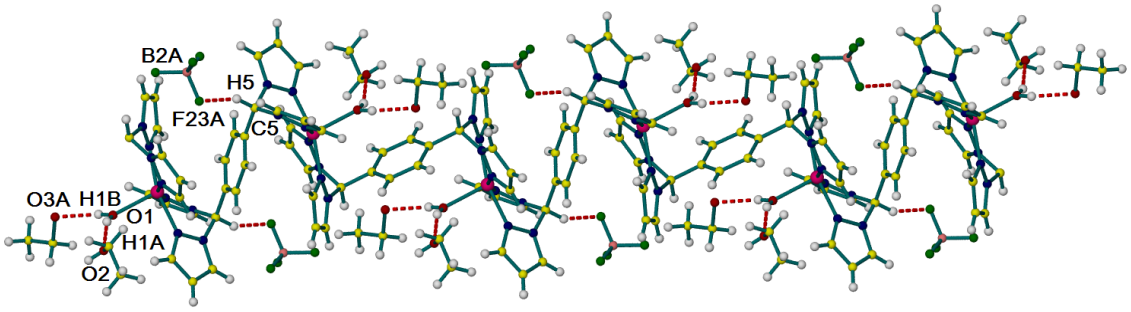

Figure 1.8. Hydrogen bonding interactions in the structure of **4**.

Similarly, the polymeric chains in the structure of **4** form C(5)-H(5)···F(23) interactions (2.151 Å, 152.70º) of the BF_4^- anions with the methine hydrogen atoms. The coordinated water hydrogen bonds with the two interstitial ethanol molecules, O(1)-H(1)···O 2.027 and 2.122 Å (Figure 1.8). The hydrogen bonding of interstitial solvent molecules to coordinated solvent is observed only in the structure of **4,** probably because of the small size of the coordinated water molecule, which allows the EtOH to access the "pocket" (space) formed between adjacent parallel polymeric chains, Table 1.5.

Table 1.5. Noncovalent interactions in the structures of **4**.

	4	
	Distance (Å)[a]	**Angle (deg)**
O(1)-H(1A)···O(2)	2.027 (2.812)	157.91
O(1)-H(1B)···O(3A)	2.122 (2.916)	166.77
C(5)-H(5)···F(23A)	2.151 (3.073)	152.70

[a]H···X (Y···X), where Y-H···X is a hydrogen bond of the general formula, X = F or O, Y = O, C.

In the structure of **2**, the axially coordinated methanol forms the same type of hydrogen bond with BF_4^- as **1,** O(1)-H(1A)···F(1) 1.909 Å. The methine hydrogens of the ligand selectively participate in hydrogen bonds with SiF_6^{2-}, C(5)-H(5)···F(5) 2.008 Å and 159.40º. The size and geometry of the SiF_6^{2-} allows it to reach out to a parallel polymeric chain, subsequently generating a 2-dimensional, sheet like supramolecular structure (Figure 1.9).

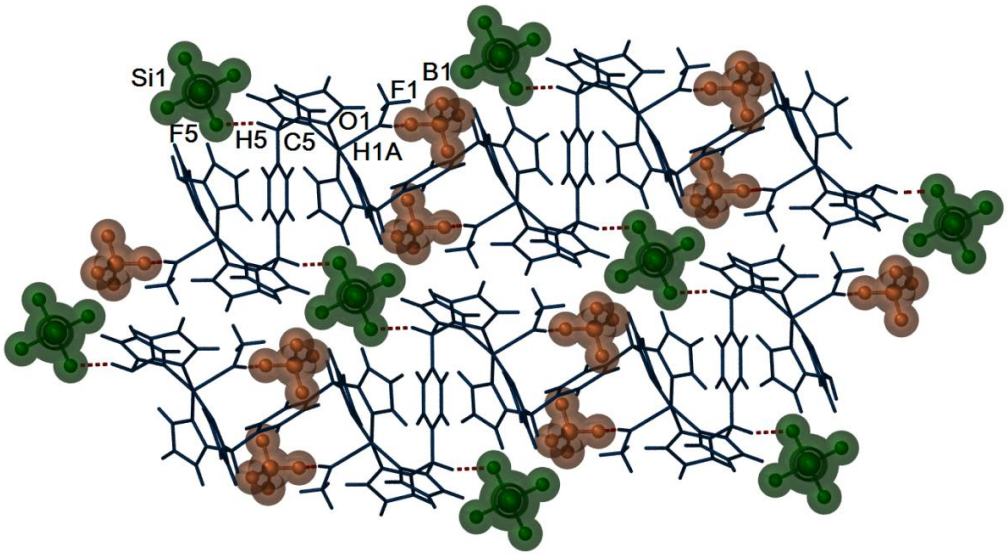

Figure 1.9. The sheet like structure of **2** generated by O-H···F and C-H···F interactions (CP blue, BF_4^- orange, SiF_6^{2-} green).

While the crystal packing of compounds **1**, **2** and **4** are very similar at first glance (the coordination polymers run parallel to each other and the anions separate the chains), there are major differences. Figure 1.10 shows the crystal packing of compounds **1**, **2** and **4**, where the CP chains go into the plane of the figure. In the structure of **1**, the chains are surrounded by BF_4^- anions. In **2**, the rotation of the supramolecular sheets (Figure 1.9) by 90˚ show the polymeric chains linked by SiF_6^{2-} in the vertical direction, and separated by BF_4^- anions perpendicular to them. The SiF_6^{2-} anions interact with two MeOH molecules located at the corners of the coordination polymeric chains. Compound **4** packs differently than **1**, even though there are only BF_4^- anions in the structure. The anion forms only C-H···F interactions with the chain, which modifies the crystal packing. The BF_4^- are located at the sides of the chains, while the O-H···O hydrogen bonds, between the coordinated water and the interstitial EtOH put the solvent molecules at the corners of the coordination polymer.

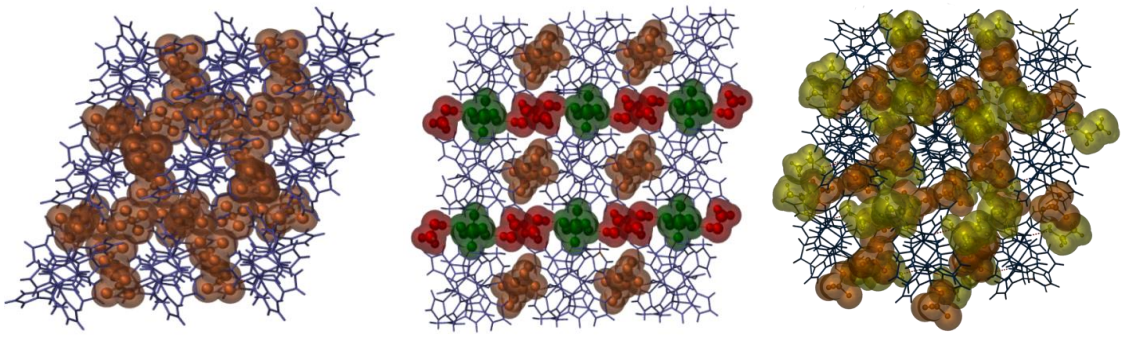

(a) (b) (c)

Figure 1.10. Crystal packing of compound **1** (a)*, **2** (b) and **4** (c). Color code: CP blue (goes into the plane of the paper), BF_4^- orange, SiF_6^{2-} green, MeOH red, EtOH yellow. *Disordered methanol is excluded.

While **5** and **6** do not form supramolecular networks, the coordination and inclusion of water in the structure of **3** results in the formation of nine different hydrogen bonds. These interactions, between coordinated and uncoordinated water and the SiF_6^{2-} anion propagate the supramolecular structure in three dimension (Figure 1.11, Table 1.6).

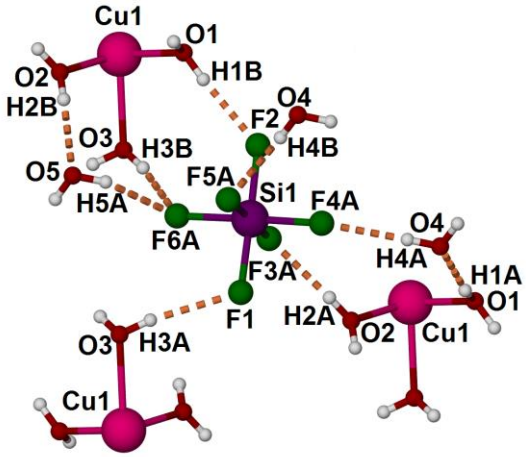

Figure 1.11. Hydrogen bonded water network in the structure of $[Cu_2(\mu\text{-}L_p)(H_2O)_6](SiF_6)_2\cdot(H_2O)_4$ (**3**): nine different hydrogen bonds.

One dimension of the supramolecular structure is generated by hydrogen bonding of two coordinated water molecules from different dinuclear cations to the same SiF_6^{2-} (Figure 1.12a). The neighboring $[Cu_2(\mu\text{-}\mathbf{L}_p)(H_2O)_6]^{4+}$ cations are connected via two of

these bridging SiF_6^{2-} through O-H···F hydrogen bonds: O(2)-H(2A)···F(3A) (1.898 Å) and O(3)-H(3A)···F(1) (2.103 Å). The interaction involves 16 atoms, forming a hydrogen bonded inorganic ring colored in green on Figure 1.12a, and link the dinuclear cations into chains.

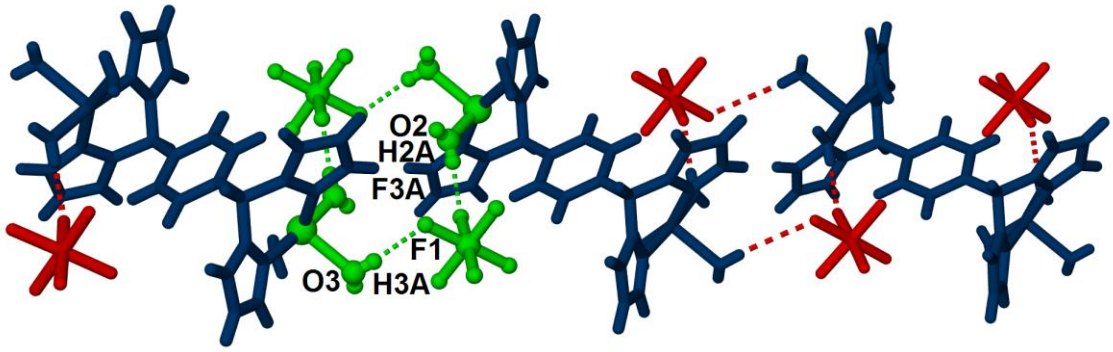

(a)

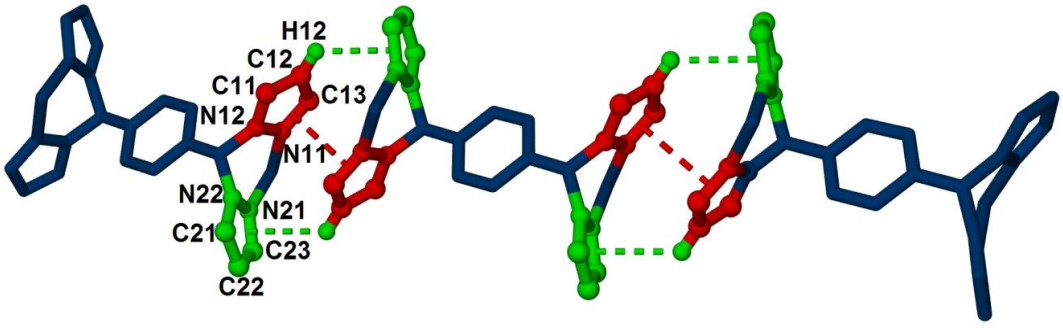

(b)

Figure 1.12. (a) Hydrogen bonds in **3** connecting two dinuclear cations into chains, the involved atoms and bonds are colored in green, (b) Pyrazolyl "embrace" supporting the chains. Hydrogen atoms and water molecules are omitted for clarity, except the ones forming the "embrace".

This dimension of the supramolecular structure is also supported by the "pyrazolyl embrace" supramolecular synthon, which is frequently observed in poly(pyrazolyl)borate and poly(pyrazolyl)methane complexes.[24] It is constructed of π···π stacking and C-H···π interactions between two pairs of pyrazolyl rings from neighbouring dinuclear units (Figure 1.12b). The metrics for this interaction (Table 1.6) fit well with previously

reported values,[24] where the centroid···centroid distance is in the range 3.4 – 3.8 Å, and the C-H···centroid distance 2.4 - 3.2 Å with an angle between 120-170˚.

Table 1.6. Noncovalent interactions in the structure of **3**.

	Distance (Å)[a]	**Angle (deg)**	**Generated supramolecular dimension**
Coordinated H_2O to SiF_6^{2-}			
O(2)-H(2A)···F(3A)	1.898 (2.445)	171.13	1D
O(3)-H(3A)···F(1)	2.103 (2.848)	171.53	1D
O(3)-H(3B)···F(6A)	1.963 (2.701)	167.42	2D
O(1)-H(1B)···F(2)	1.898 (2.637)	167.70	2D
Interstitial H_2O to SiF_6^{2-}			
O(5)-H(5A)···F(6A)	2.145 (2.791)	145.74	Supports 2D
O(4)-H(4A)···F(4A)	1.970 (2.711)	173.77	3D
O(4)-H(4B)···F(5A)	2.038 (2.786)	175.07	3D
Coordinated H_2O to interstitial H_2O			
O(2)-H(2B)···O(5)	1.907 (2.647)	172.12	Supports 2D
O(1)-H(1A)···O(4)	1.894 (2.637)	167.13	Supports 3D
Pyrazolyl Embrace			
Centroid···Centroid	3.633	⊥ Angle: 92.78	Supports 1D
C-H···Centroid	2.881	124.86	Supports 1D

[a] H···X (O···X); where X = F or O.

These infinite chains of dinuclear cations and SiF_6^{2-} further participate in hydrogen bonding in a second direction. Two pairs of O-H···F hydrogen bonds [O(3)-H(3B)···F(6A) 1.963 Å, and O(1)-H(1B)···F(2) 1.898 Å], with the participation of four $[Cu_2(\mu\text{-}\mathbf{L}_p)(H_2O)_6]^{4+}$ cations and two SiF_6^{2-}, connect the parallel chains into hydrogen bonded sheets. These hydrogen bonds generate new 8 and 12 membered hydrogen bonded rings, shown as magenta in Figure 1.13. In the same plane one of the two interstitial water molecules also bridges the cation to the anion. This water molecule forms hydrogen bond with the anion, O(5)-H(5A)···F(6A) 2.145 Å and the coordinated water molecule O(2)-H(2B)···O(5) 1.907 Å and supports the second dimension of the supramolecular structure. These hydrogen bonds are not shown on the pictures.

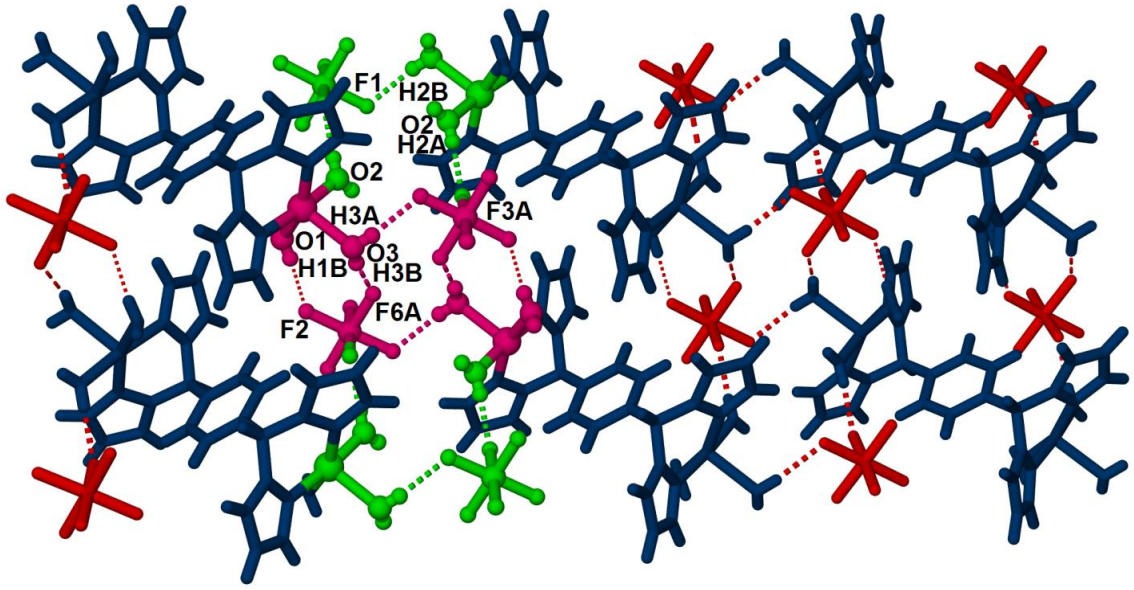

Figure 1.13. Hydrogen bonding interactions in **3** that join the chains into a 2-dimensional supramolecular structure. The hydrogen atoms and bonds involved in these interactions that form the second dimension are colored magenta.

Rotation of these sheets by 90˚ reveals the third dimension of the supramolecular structure. This dimension is realized through hydrogen bonding of the second interstitial water with SiF_6^{2-} anions from parallel layers [O(4)-H(4A)···F(4A) 1.970 Å and O(4)-H(4B)···F(5A) 2.038 Å]. Figure 1.14 shows the parallel sheets, going into the plane of the paper (colored green, violet and blue) connected *via* hydrogen bonded interstitial waters and SiF_6^{2-} anions connected to different sheets. The O-H···O hydrogen bond between the coordinated and interstitial water [O(1)-H(1A)···O(4) 1.894 Å] supports the third dimension of the supramolecular structure.

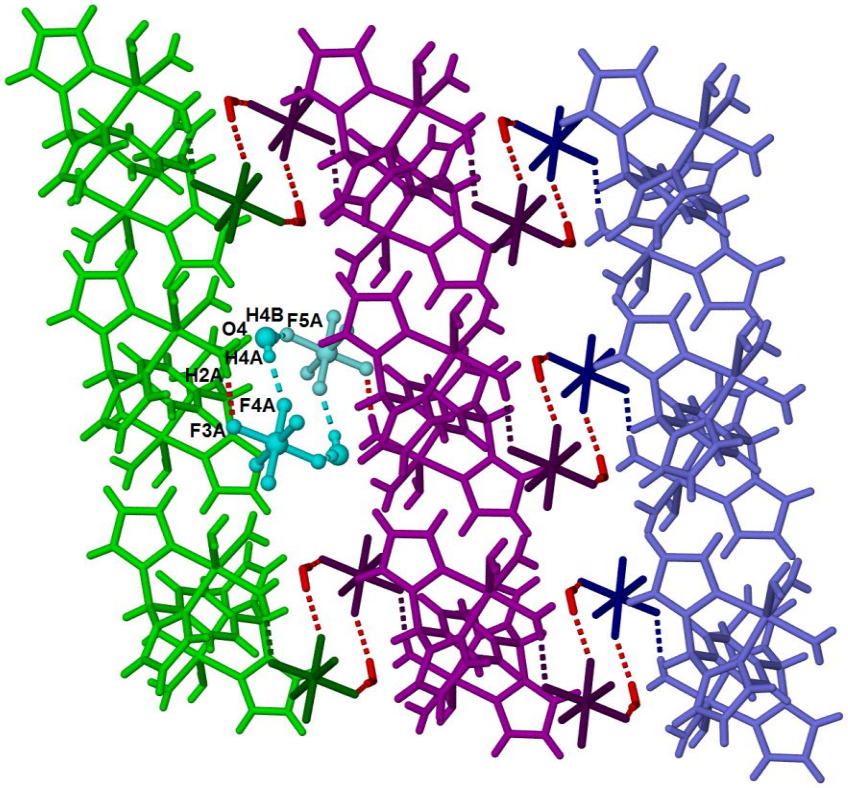

Figure 1.14. Dimers from three layers in **3** shown on Figure 1.13, colored green, violet and blue, are linked by additional hydrogen bonding interactions between the SiF_6^{2-} and interstitial water.

Thermogravimetric Analysis. To monitor the loss of solvent molecules and the stability of the compounds, thermogravimetric analysis was carried out on crystals of **1- 3** and **6**.

The TGA/DTA curves show multistep decomposition for each compound. Compound **1** (Figure 1.15) gradually loses the solvent of crystallization (exp. and calcd. 3.0%) up to 71˚C, followed by the loss of coordinated MeOH (4.6%; calcd. 4.9%). This step is completed at 140˚C. The decomposition of $\mathbf{L}_p$ in three steps (1. pyrazolyl rings; 2. methines; 3. phenylene spacer) and the BF_4^- (77.3%, calcd. 82.5%) occurs between 195 and 670˚C. The final residual weight of the remaining black powder corresponds to CuO. A similar TGA-DTA curve was observed for **2**.

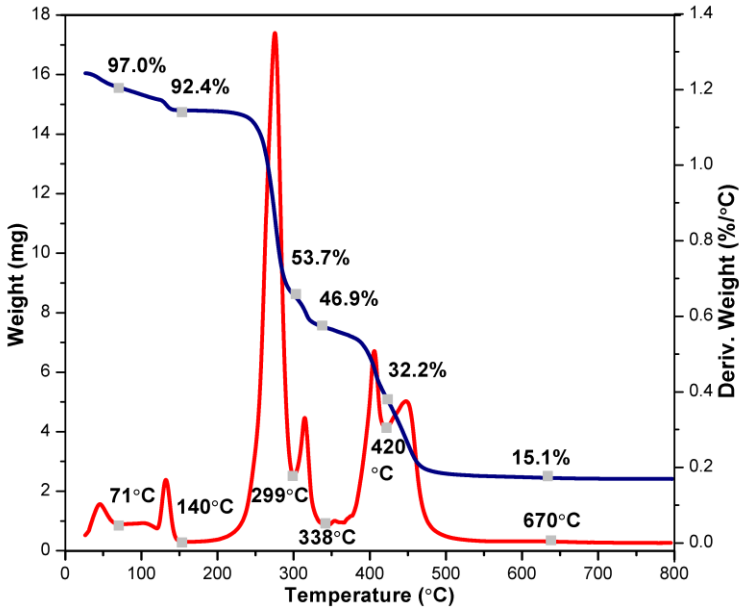

Figure 1.15. TGA/DTA curves for $[Cu(\mu\text{-}\mathbf{L}_p)(CH_3OH)](BF_4)_2\cdot(CH_3OH)_{0.62}$ (**1**).

Similarly, **3** loses the water of crystallization at 104˚C (7.9%, calcd. 7.5%), followed by the loss of coordinated water molecules (11.1%, calcd. 11.2%). The ligand and the SiF_6^{2-} decompose in four steps between 150 and 430˚C, resulting in CuO (14.7%, calcd. 16.3%). Compound **6** ($[Cu_2(\mu\text{-}L_p)(DMSO)_6](BF_4)_4\cdot(DMSO)_2\cdot C_6H_6$), interestingly, loses the two DMSO and benzene of crystallization in the same step at 233˚C (15.2%, calcd. 15.1%). This step is followed by the loss of coordinated DMSO molecules, which is completed at 278˚C (30.1%, calcd. 30.3%). This step is followed by the three step decomposition of the ligand and BF_4^- resulting in CuO (13.2%, calcd. 10.3%).

The elemental analyses reflect the results of the TGA/ DTA. The elemental analyses of crystals of **1-4** dried to constant weight indicate the loss of interstitial and coordinated solvent molecules under the drying conditions (105˚C, vacuum). The TGA/DTA curves show that for **1-3** the coordinated solvent molecules are lost under 140˚C, which indicates that under reduced pressure this temperature may decrease to less than 105˚C. Compound

6 loses the coordinated DMSO above 278˚C, these solvent molecules were not removed by the drying process used for the elemental analyses.

Discussion and Conclusions

Six copper(II) complexes, with the metal in square pyramidal geometry, were synthesized by the layering technique of $Cu(BF_4)_2 \cdot 3H_2O$ with $\mathbf{L}_{\boldsymbol{p}}$, a ligand that links two bis(pyrazolyl)methane units through a 1,4-phenylene spacer. Subtle changes in the preparations lead to substantial changes in the products of these reactions. When MeOH is the solvent, the coordination polymers **1** and **2** form, with or without the addition of a water layer, in which MeOH is the axial ligand. The main impact of the additional water is the conversion of the BF_4^- to SiF_6^{2-} during the slow crystallization procedures; the SiF_6^{2-} is clearly derived from the glass of the crystallization tube. Even when the reaction of $Cu(BF_4)_2 \cdot 3H_2O$ and $\mathbf{L}_{\boldsymbol{p}}$ is carried out in MeOH in a 2/1 ratio, the 1/1 polymers **1** and **2** form. In contrast, a 2/1 reaction in EtOH results in the dinuclear compound **3**, where the metal to ligand ratio matches the reaction conditions and water is coordinated in two equatorial and the axial positions. A 1/1 reaction leads to both **3** and polymeric **4**, where again water is located in the axial position. The use of DMSO as part of the recrystallization solvent system leads to dinuclear **5** and **6**, where DMSO is coordinated in two equatorial and the axial positions.

While the isomeric $\mathbf{L}_{\boldsymbol{m}}$ ligand, which uses a 1,3-phenylene spacer, generates metallacycles in similar reactions through self-assembly,[8,9] $\mathbf{L}_{\boldsymbol{p}}$ forms 1-dimensional coordination polymers or dinuclear copper(II) complexes where the ligand simply bridges two metals.[8,10,11] In this new chemistry of $\mathbf{L}_{\boldsymbol{p}}$ with copper(II), there is no indication of fluoride abstraction from the BF_4^- counterions, as observed in complexes of divalent

metals with $\mathbf{L}_{m,}$[9] in one case with the more flexible bitopic ligand $[H_2C(pz)_2]_2(CH_2CH_2)_2$[25] and in complexes of simple bis(pyrazolyl)methane ligands.[26]

The copper(II) centers show a strong preference towards the five-coordinate, square pyramidal geometry, where the axial ligand has a longer bond length. Copper(II) ions in five coordination tend to adopt an apically elongated square pyamidal geometry due to the pseudo Jahn-Teller electronic effect.[19] In the cases of the coordination polymers, which have N_4O coordination spheres, this weak axial ligation is clearly noticed in the TGA analyses where the axial ligand (a solvent molecule) can be removed at low temperatures upon heating of the crystals. It is interesting to compare the coordination behavior of $\mathbf{L}_p$ in the 1-dimensional polymeric compounds (**1**, **2** and **4**) with other simple Cu(II)[bis(pyrazolyl)methane]$_2$-compounds. With the parent $H_2C(pz)_2$ ligand, six-coordinate $[Cu[H_2C(pz)_2]_2Cl(H_2O)]^+$ forms[27] rather than the five-coordinate polymers formed here with the "linked" parent ligand. The use of the more bulky $H_2C(3,5\text{-}Me_2pz)_2$ ligand does produce axial elongated, five-coordinate $[Cu[H_2C(pz)_2]_2X]^+$ species similar to those observed here, although the τ_5 values range from 0.04 to 0.47, depending on the fifth ligand, indicating a more distorted coordination sphere.[28]

The three CP covalent structures are very similar to each other. As shown in Figure 1.5, the three structures nearly overlap. Even with these similarities, variations in the strong (O-H···F and O-H···O) and weaker (C-H···F) hydrogen bonding interactions in the so called "secondary sphere of coordination"[29] of the complex cations do impact the overall structures of the coordination polymers. Two trends are important. First, in the absence of stronger hydrogen bonds the importance of weaker interactions increases[30] and can even compete with the strength of hydrogen bonds conventionally considered

strong.[31] For example, in compound **2** the C-H···F (2.008 Å, 159.4˚) and O-H···F (1.909 Å, 168.13˚) hydrogen bonds are of similar strength. Second, the strength of C-H···F interactions, d(H···F) 2.0-2.3 Å, are remarkable when compared to H···F distances measured for other compounds [generally d(H···F) = 2.4-2.6 Å].[22,23] In fact, in compounds **1-4** the C-H···F distances are only 0.1-0.3 Å longer than the O-H···F and O-H···O bond distances. The strength of these interactions is probably the concerted effect of two phenomena: the electron withdrawing pyrazolyl groups of the ligand increases the polarization of the methine C-H bond[29] and different ionic charges carried by the cationic metal complexes and the anion, a process called "charge assistance".[23]

As shown in Figure 1.6, the three dinuclear structures are also very similar. Only complex **3** has a supramolecular structure, where a series of hydrogen bonding interactions lead to a fully 3-dimensional structure. Two factors dominate these interactions: the abundance of water in the structure to form hydrogen bonds and the presence of the larger SiF_6^{2-} ion. Both of these factors support the formation of the $H_2O\cdots SiF_6^{2-}$ clusters that in combination with a pyrazolyl "embrace" organize the 3D structure. In contrast, the other two dinuclear complexes **5** and **6**, which contain DMSO as the additional ligands, a group that does not contain highly polarized hydrogen atoms, do not form supramolecular structures.

References

(1) Selected reviews: (a) Schalley, C. A.; Lützen, A.; Albrecht, M. *Chem. Eur. J.* **2004**, *10*, 1072. (b) Zaworotko, M. J. *Cryst. Growth Des.* **2007**, *7*, 1740. (c) Lehn, J. M. *Science*, **2002**, *295*, 2400. (d) Desiraju, G. *Angew. Chem. Int. Ed.* **2007**, *46*, 8342. (e) Friese, V. A.; Kurth, D. G. *Coord. Chem. Rev.* **2008**, *252*, 199. (f) Braga, D.; Brammer, L.; Champness, N. R. *CrystEngComm* **2005**, *7*, 1. (g) O'Keeffe, M. *Chem. Soc. Rev.* **2009**, *38*, 1215.

(2) (a) Mas-Ballesté, R.; Gómez-Herrero, J.; Zamora, F. *Chem. Soc. Rev*. **2010**, *39*, 4220. (b) Barth, J. V.; Constantini, G.; Kern, K. *Nature* **2005**, *437*, 671. (c) de Ruiter, G.; Van der Boom, M. E. *Acc. Chem. Res.* **2011**, *44*, 563. (d) Talham, D. R.; Meisel, M. W. *Chem. Soc. Rev*. **2011**, *40*, 3356. (e) Karlin, K. D.; Toma, H. E.; Araki, K. *Prog. Inorg. Chem.*, **2009**, *56*, 379. (f) Pettinari, C.; Masciocchi, N.; Pandolfo, L.; Pucci, D. *Chem. Eur. J.* **2010**, *11*, 1106.

(3) Selected reviews: (a) Chakrabarty, R.; Mukherjee, P. S.; Stang, P. J. *Chem. Rev.* **2011**, 111(11), 6810. (b) Zhao, D.; Timmons, D. J.; Yuan, D.; Zhou, H.-C. *Acc. Chem. Res.* **2011**, *44*, 123. (c) Chen, C.-L.; Zhang, J.-Y.; Su, C.-Y. *Eur. J. Inorg. Chem.* **2007**, 2997. (d) Northrop, B. H.; Yang, H.-B.; Stang, P. J. *Chem. Commun.* **2008**, *45*, 5896. (e) Lee, S. J.; Lin, W. *Acc. Chem. Res.* **2008**, *41*, 521. (f) Holliday, B. J.; Mirkin, C. A. *Angew. Chem. Int. Ed.* **2001**, *40*, 2022.

(4) Selected reviews: (a) Robson, R. *Dalton Trans.* **2008**, 5113. (b) Kitagawa, S.; Kitaura, R.; Noro, S.-I. *Angew. Chem. Int. Ed.* **2004**, 43, 2334. (c) Kitagawa, S.; Uemura, K. *Chem. Soc. Rev.* **2005**, *34*, 109. (d) Blake, A. J.; Champness, N. R.; Hubberstey, P.; Li, W.-S.; Whitersby, M. A.; Schröder, M. *Coord. Chem. Rev.* **1999**, *183*, 117. (e) Biradha, K.; Madhushree, S.; Rajput, L. *Chem. Commun.* **2006**, 4169.

(5) Recent examples: (a) Leong, W. L.; Vittal, J. J. *Chem. Rev.* **2011**, *111*, 688. (b) Fromm, K. M.; Sagué, J. L.; Mirolo, L. *Macromol. Symp.* **2010**, *291-292*, 75. (c) Mas-Ballesté, R.; Castillo, O.; Sanz Miguel, P. J.; Olea, D.; Gómez-Herrero, J.; Zamora, F. *Eur. J. Inorg. Chem.* **2009**, 2885. (d) Aakeröy, C. B.; Scott, B. M. T.; Smith, M. M.; Urbina, J. F.; Desper, J. *Inorg. Chem.* **2009**, *48*, 4052. (e) Chesman, A. S. R.; Turner, D. R.; Deacon, G. B.; Batten, S. R. *Chem. Commun.* **2010**, *46*, 4899. (f) Drabent, K.; Ciunik, Z.; Ozarowski, A. *Inorg. Chem.* **2008**, *47*, 3358. (g) Jia, L.; Tang, N.; Vittal, J. J. *Inorg. Chim. Acta* **2009**, *362*, 2525. (h) Hu, S.; He, K.-H.; Zeng, M.-H.; Zou, H.-H.; Ylang, Y.-M. *Inorg. Chem.* **2008**, *47*, 5218. (i) Chu, Z.; You, W.; Huang, W. *J. Mol. Struct.* **2009**, *920*, 277. (j) Khlobystov, A. N.; Blake, A. J.; Champness, N. R.; Lemenovskii, D. A.; Majouga, A. G.; Zyk, N. V.; Schröder, M. *Coord. Chem. Rev.* **2001**, *222*, 155.

(6) (a) Li, C.-P.; Du, M. *Chem. Commun.* **2011**, *47*, 5958. (b) Blondeau, P.; van der Lee, A.; Barboiu, M. *Inorg. Chem.* **2005**, *44*, 5649. (c) Zhang, J.; Xu, X.; James, S. L. *Chem. Commun.* **2006**, 4218. (d) Janiak, C. *J. Chem. Soc. Dalton Trans.* **2000**, 3885. (e) Zhang, J.-P.; Huang, X.-C.; Chen, X.-M. *Chem. Soc. Rev.* **2009**, *38*, 2385.

(7) (a) Vilar, R. *Eur. J. Inorg. Chem.* **2008**, 357. (b) Desmartes, C.; Azcarate, I.; Gontard, G.; Amouri, H. *Eur. J. Inorg. Chem.* **2011**, 4558. (c) Ni, J.; Wei, K.-J.; Liu, Y.; Huang, X.-C.; Li, D. *Cryst. Growth Des.* **2010**, *10*, 3964. (d) Amouri, H.; Desmarets, C.; Bettoschi, A.; Rager, M. N.; Boubekeur, K.; Rabu, P.; Drillon, M. *Chem. Eur. J.* **2007**, *13*, 5401. (e) Užarević, K.; Đilović, I.; Matković-Kalogović, D.; Šišak, D.; Cindrić, M. *Angew. Chem. Int. Ed.* **2008**, *47*, 7022. (f) Campos-Fernández, C. S.; Schottel, B. L.; Chifotides, H. T.; Bera, J. K.; Bacsa, J.; Koomen, J. M.; Russell, D. H.; Dunbar, K. R. *J. Am. Chem. Soc.* **2005**, *127*, 12909.

(8) Reger, D. L.; Watson, R. P.; Smith, M. D. *Inorg. Chem.* **2006**, *45*, 10077.

(9) (a) Reger, D. L.; Foley, E. A.; Watson, R. P.; Pellechia, P. J.; Smith, M. D.; Grandjean, F.; Long, G. J. *Inorg. Chem.* **2009**, *48*, 10658. (b) Reger, D. L.; Watson, R. P.; Gardinier, J. R.; Smith, M. D.; Pellechia, P. J. *Inorg. Chem.* **2006**, *45*, 10088.

(10) (a) Wang, S.; Yuan, G.; Sun, C.; Yang, G.; Shao, K.; Wang, X. *Inorg. Chem. Comm.* **2011**, *14*, 347. (b) Wang, S.; Zang, H.; Sun, C.; Xu, G.; Wang, X.; Shao, K.; Lan, Y.; Su, Z. *CrystEngComm* **2010**, *12*, 3458.

(11) (a) Ho, J. H. H.; Wagler, J.; Willis, A. C.; Messerle, B. A. *Dalton Trans.* **2011**, *40*, 11031. (b) Prasad, K. T.; Therrein, B.; Rao, K. M. *J. Organomet. Chem.* **2010**, *695*, 1375.

(12) Reger, D. L.; Watson, R. P.; Smith, M. D.; Pellechia, P. J. *Organometallics* **2005**, *24*, 1544.

(13) (a) Barbour, L. J. *J. Supramol. Chem.* **2003**, *1*, 189. (b) *POV-RAY 3.6*, **2006**, Persistence of Vision Raytracer Pty Ltd., Williamstown, Vic., Australia.

(14) SMART Version 5.630, SAINT+ Version 6.45. Bruker Analytical X-ray Systems, Inc., Madison, Wisconsin, USA, **2003**.

(15) Sheldrick, G.M. SHELXTL Version 6.14, Bruker Analytical X-ray Systems, Inc., Madison, Wisconsin, USA, **2000**.

(16) (a) Galstyan, A.; Shen, W.-Z.; Freisinger, E.; Alkam, H.; Hiller, W.; Sanz Miguel, P. J.; Schürmann, M.; Lippert, B. *Chem. Eur. J.* **2011**, *17*, 10771. (b) Stephenson, A.; Argent, S. P.; Riis-Johannessen, T.; Tidmarsh, I. S.; Ward., M. D. *J. Am. Chem. Soc.* **2011**, *133*, 858. (c) Tang, J.; Sánchez Costa, J.; Pevec, A.; Kozlevčar, B.; Massera, C.; Roubeau, O.; Mutikainen, I.; Turpeinen, U.; Gamez, P.; Reedijk, J. *Cryst. Growth Des.* **2008**, *8*(3), 1005. (d) Mastropietro, T. F.; Armentano, D.; Grisolia, E.; Zanchini, C.; Lloret, F.; Julve, M.; De Munno, G. *Dalton Trans.* **2008**, *514*. (d) Huang, Y.-Q.; Ding, B.; Song, H.-B.; Zhao, B.; Ren, P.; Cheng, P.; Wang, H.-G.; Liao, D.-Z.; Yan, S.-P. *Chem. Commun.* **2006**, 4906. (c) Gamez, P.; Steensma, H.; Driessen, W. L.; Reedijk, J. *Inorg. Chim. Acta* **2002**, *333*, 51.

(17) (a) Chen, W.; Chu, J.; Mutikainen, I.; Reedijk, J.; Turpeinen, U.; Song, Y.-F. *CrystEngComm* **2011**, *13*, 7299. (b) Maekawa, M.; Tominaga, T.; Sugimoto, K.; Okubo, T.; Kuroda-Sowa, T.; Munakata, M.; Kitagawa, S. *CrystEngComm* **2012**, *14*, 1345. (c)

Whitersby, M. A.; Blake, A. J.; Champness, N. R.; Cooke, P. A.; Hubberstey, P.; Realf, A. L.; Teat, S. J.; Schröder, M. *J. Chem. Soc. Dalton Trans.* **2000**, 3261.

(18) Addison, A. W.; Rao, T. N.; J. Reedijk, Van Rijn, J.; Verschoor, G. C. *J. Chem. Soc., Dalton Trans*. **1984**, 1349. $\tau_5 = \frac{(\beta - \alpha)}{60°}$ Where α and β are the two largest angles measured around the metal centers. Perfect square pyramid: $\tau_5 = 0$; Perfect trigonal bipyramid: $\tau_5 = 1$.

(19) (a) Reinen, D.; Atanasov, M. *Chemical Physics* **1989**, *136*, 27. (b) Arriourtua, M. I.; Mesa, J. L.; Rojo, T.; Debaerdemaeker, T.; Beltrán-Porter, D.; Stratemeier, H.; Reinen, D. *Inorg. Chem.* **1988**, *27*, 2976. (c) D. Reinen, C. Friebel *Inorg. Chem.* **1984**, *23*, 791.

(20) Desiraju, G. R.; Steiner, T. in "*The Weak Hydrogen Bond: In structural Chemistry and Biology"*, Oxford Univ. Press, UK, 2001.

(21) Steed, J. W.; Atwood, J. L. in "*Supramolecular Chemistry"*, 2nd Ed., John Wiley & Sons, UK, 2009.

(22) (a) Custelcean, R. *Chem. Soc. Rev.* **2010**, *39*, 3675. (b) Alonso, J. L.; Antolínez, S.; Blanco, S.; Lessari, A.; López, J. C.; Caminati, W. *J. Am. Chem. Soc.* **2004**, *126*, 3244. (c) Brammer, L.; Bruton, E. A.; Sherwood, P. *Cryst. Growth Des.* **2001**, *1*, 277. (d) Reichenbächer, K.; Süss, H. I.; Hulliger, J. *Chem. Soc. Rev.* **2005**, *34*, 22. (e) Moussa, J.; Chamoreau, L.-M.; Boubekeur, K.; Amouri, H. *Organometallics* **2008**, *27*, 67. (f) Zhu, S.; Zhu, S.; Jin, G.; Li, Z. *Tetrahedron Lett.* **2005**, *46*, 2713.

(23) Grepioni, F.; Cojazzi, G.; Draper, S. M.; Scully, N.; Braga, D. *Organometallics* **1998**, *17*, 296.

(24) (a) Reger, D. L.; Gardinier, J. R.; Semeniuc, R. F.; Smith, M. D. *Dalton Trans.* **2003**, 1712. (b) Reger, D. L; Semeniuc, R. F.; Smith, M. D. *Dalton Trans.* **2008**, 2253. (c) Reger, D. L.; Semeniuc, R. F.; Smith, M. D. *Cryst. Growth Des.* **2003**, *5*, 1181.

(25) Reger, D. L.; Watson, R. P.; Smith, M. D.; Pellechia, P. J. *Cryst. Growth Des.* **2007**, 7, 1163.

(26) (a) Reedijk, J. *Comm. Inorg. Chem.* **1982**, *1*, 389. (b) Verbiest, J.; van Ooijen, J. A. C.; Reedijk, J. *Inorg. Nucl. Chem.* **1980**, *42*, 971.

(27) Machura, B.; Małecki, J. G.; Świtlicka, A.; Nawrot, I.; Kruszynski, R. *Polyhedron*, **2011**, *30*, 864.

(28) (a) Fujisawa, K.; Kanda, R.; Miyashita, Y.; Okamoto, K.-i. *Polyhedron* **2008**, *27*, 1432. (b) Zhai, B.; Shen, W.-Z.; Chen, X.-Y.; Song. H.-B.; Shi, W.; Cheng, P. *Inorg. Chem. Commun.* **2006**, *9*, 1293. (c) Machura, B.; Świtlicka, A.; Kruszynski, R.; Kusz, J.; Penczek, R. *Polyhedron* **2008**, 2513.

(29) Mercer, D. J.; Loeb, S. J. *Chem. Soc. Rev.* **2010**, *39*, 3612.

(30) Choudhury Roy, C. A.; Guru Row, T. N. *Cryst. Growth Des.* **2004**, *4*, 47.

(31) Hay, B. P.; Bryantsev, V. S. *Chem. Commun.* **2008**, 2417.

Chapter II

Dinuclear Complexes Containing Linear M-F-M [M = Mn(II), Fe(II), Co(II), Ni(II), Cu(II), Zn(II), Cd(II)] Bridges: Trends in Structures, Antiferromagnetic Superexchange Interactions and Spectroscopic Properties[2]

[2]Adapted with permission from Reger, D. L.; Pascui, A. E.; Smith, M. D.; Jezierska, J.; Ozarowski, A. *Inorg. Chem.* **2012**, *51*, 11820-11836. DOI: 10.1021/ic301757g. Copyright 2012 American Chemical Society.

Introduction

A major emphasis in inorganic chemistry is the preparation of new ligands that are designed to control the structures of metal complexes.[1] Much of our research has centered on the use of designed "third generation" poly(pyrazolyl)methane ligands.[2] While "second generation" poly(pyrazolyl)methane ligands control the metal coordination site with bulky groups located near the pyrazolyl nitrogen donor,[3] "third generation" poly(pyrazolyl)methane ligands control the overall structure by specific functionalization at the non-coordinating "back" position. An important class of these types of ligands links multiple poly(pyrazolyl)methane units into a single molecule. This linkage can be made with either "flexible" [2b,4] or "fixed"[5] central groups. Within the latter case of ligands, it was demonstrated that linking two bis(pyrazolyl)methane units through a meta-substituted arene spacer triggers the formation of dinuclear metallacycles.[6]

Using the fixed ligand *m*-bis[bis(1-pyrazolyl)methyl]benzene (*m*-$[CH(pz)_2]_2C_6H_4$, $\mathbf{L}_{\boldsymbol{m}}$, pz = pyrazolyl ring, Scheme 2.1), the syntheses of dinuclear metallacycles with silver(I)[6a] and, in the case of higher charged first row metals iron(II), cobalt(II), copper(II) and zinc(II), metallacyclic complexes of the formula $[M_2(\mu\text{-}F)(\mu\text{-}\mathbf{L}_{\boldsymbol{m}})_2]^{3+}$, which contain a linear or nearly linear bridging fluoride that arises from abstraction from tetrafluoroborate (BF_4^-) were reported.[6b,c] Such a metallacycle is exemplified by the fluoride bridged iron(II) compound shown in Figure 2.1. With nickel(II) and cadmium(II), difluoride bridged complexes form. While there were a number of examples of fluoride[7] bridged compounds in the literature, our monobridged compounds represent an almost unknown structural type and offer a unique opportunity to prepare and investigate the properties of a series of complexes with similar structures where the

metal can be extensively varied. The magnetic properties of these complexes are particularly interesting because theory[8] indicates that linear M–F–M fluoride bridges (and other bridges such as OH^- and Cl^-) would yield complexes that show strong intramolecular antiferromagnetic exchange interactions. In our initial work[6b,c] with $\mathbf{L}_{m}$, such strong antiferromagnetic properties were observed for the copper(II) complex, but only weakly antiferromagnetic properties were observed for the iron(II) and cobalt(II) complexes, and the monobridged nickel(II) complex could not be isolated for comparison.

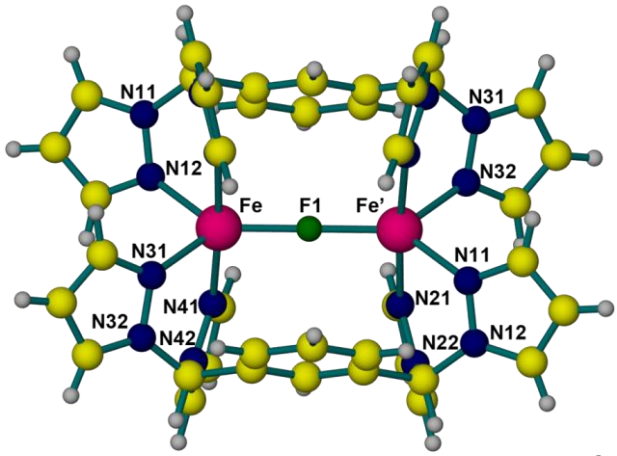

Figure 2.1. The structure of $[Fe_2(\mu\text{-}F)(\mu\text{-}\mathbf{L}_{m})_2]^{3+}$.

The new ligand *m*-bis[bis(3,5-dimethyl-1-pyrzolyl)methyl]benzene ($\mathbf{L}_{m}$**, Scheme 2.1) forms a series of monofluoride bridged metallacyclic complexes with first row transition metals from manganese(II) to zinc(II) and also cadmium(II) that all contain linearly bridged fluoride - the first extensive series of complexes with this bridging structural motif. Crystallographic, magnetic and EPR studies and DFT calculations of the paramagnetic complexes $[M_2(\mu\text{-}F)(\mu\text{-}\mathbf{L}_{m}\mathbf{*})_2](A)_3$ (M = Mn(II), Fe(II), Co(II), Ni(II), Cu(II), A= BF_4^- or ClO_4^-) allow us to carefully compare changes in the metal ions on

structure and the magnetic and EPR properties of these linearly fluoride bridged complexes.[9] The zinc(II) and cadmium(II) provide interesting NMR data.

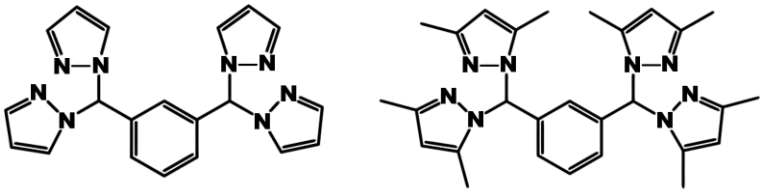

L_m L_m*

Scheme 2.1. Schematic drawing of *m*-$[CH(pz)_2]_2C_6H_4$ (**L_m**) and *m*-$[CH(3,5\text{-dimethyl-1-pz})_2]_2C_6H_4$ (**L_m***).

Experimental Section

General considerations. For the synthesis of the fluoride bridged compounds, standard Schlenk techniques were used. The solvents for the syntheses of metal complexes were not dried prior to use. The metal tetrafluoroborates and the manganese(II) perchlorate were purchased from Sigma-Aldrich or Strem Chemicals and were used as received. Reported melting points are uncorrected.

Crystals used for elemental analysis and mass spectrometry were removed from the mother liquor, rinsed with ether, and dried under vacuum, a process that removes solvent of crystallization, if present.

^1H, ^{13}C, ^{19}F and ^{113}Cd NMR spectra were recorded on a Varian Mercury/VX 300, Varian Mercury/VX 400, or Varian INOVA 500 spectrometer. All chemical shifts are in ppm and were referenced to residual undeuterated solvent signals (^1H), deuterated solvent signals (^{13}C), or externally to $CFCl_3$ (^{19}F) and $CdCl_2$ (^{113}Cd). Mass spectrometric measurements were obtained on a MicroMass QTOF spectrometer in an acid-free environment. Elemental analyses were performed on vacuum-dried samples by Robertson Microlit Laboratories (Ledgewood, NJ).

High-field, high-frequency EPR spectra at temperatures ranging from ca. 6K to 290 K were recorded on a home-built spectrometer at the EMR facility of the NHMFL.[10] The instrument is a transmission-type device in which microwaves are propagated in cylindrical lightpipes. The microwaves were generated by a phase-locked Virginia Diodes source generating frequency of 13 ± 1 GHz and producing its harmonics of which the 2^{nd}, 4^{th}, 6^{th}, 8^{th}, 16^{th}, 24^{th} and 32^{nd} were available. A superconducting magnet (Oxford Instruments) capable of reaching a field of 17 T was employed. The powder samples were not constrained and showed no magnetic torquing at high magnetic fields.

Magnetic susceptibility measurements over the temperature range 1.8-300 K were performed at a magnetic field of 0.5 T using a Quantum Design SQUID MPMSXL-5 magnetometer. Correction for the sample holder, as well as the diamagnetic correction χ_D which was estimated from the Pascal constants[11] was applied.

XSEED, POV-RAY and MESTRENOVA and GOpenMol were used for the preparation of figures.[12]

***m*-bis[bis(3,5-dimethyl-1-pyrazolyl)methyl]benzene (*m*-[CH(3,5-$Me_2pz)_2]_2C_6H_4$, L_m*)**. Under a nitrogen atmosphere, a 500 mL Schlenk flask containing sodium hydride (3.90 g, 163 mmol) suspended in anhydrous THF (350 mL) was cooled in an ice bath for 30 minutes. Solid 3,5-dimethylpyrazole (15.67 g, 163 mmol) was added over 10 minutes and the resulting solution was allowed to stir at 0ºC for 30 minutes. After the dropwise addition of thionyl chloride (5.94 mL, 81.4 mmol), the ice bath was removed and the suspension was allowed to warm to room temperature over 30 minutes. Isophthalaldehyde (2.73 g, 20.4 mmol) and anhydrous $CoCl_2$ (0.26 g, 2.0 mmol) were added at once and the reaction mixture was heated at reflux for 42 hours. After cooling to

room temperature, water (160 mL) was added and the resulting solution was left to stir for 30 minutes. The organic and aqueous layers were separated and the aqueous layer was extracted with CH_2Cl_2 (2 x 100 mL). The combined organic extracts were washed with water (100 mL) and dried over $MgSO_4$. Removal of the solvent leaves a beige solid that contains unreacted 3,5-dimethyl-pyrazole, which was removed by sublimation at 70-80 ºC under vacuum for 2 days. The remaining solid was dissolved in ethyl acetate and flushed through a plug of silica. Removal of solvent afforded 8.02 g (81%) of white product, melting point 152-153˚C. ^{1}H NMR (300 MHz, acetone-d_6): δ 7.67(s, 2H, *C*H(3,5-pz)$_2$), 7.37 (t, J = 6.0 Hz, 1H, 5-H C_6H_4), 6.97 (d, J = 9.0 Hz, 2H, 4,6-H C_6H_4), 6.57 (s, 1H, 2-H C_6H_4), 5.84 (s, 4H, 4-H 3,5-pz), 2.18/ 2.09 (s/s, 12H/12H, 3,5-CH_3). ^{13}C NMR (75.5 MHz, acetone-d_6): δ 148.3/141,6 (3,5-C pz), 138.3 (1,3-C C_6H_4), 129.0 (5-C C_6H_4), 127.8 (4,6-C C_6H_4), 126.9 (2-C C_6H_4), 107.22 (4-C pz), 74.4 (CH(pz)$_2$), 13.69/11.80 (CH_3). Anal. Calcd.(Found) for $C_{28}H_{34}N_8$: C, 69.68 (69.37); H, 7.10 (7.40); N, 23.22 (23.05). MS ES(+) *m*/*z* (rel. % abund.) [assgn]: 521 (28) [$\mathbf{L_m}$***** + K]$^+$, 505 (92) [$\mathbf{L_m}$***** + Na]$^+$, 483 (100) [$\mathbf{L_m}$***** + H]$^+$, 387 (70) [$\mathbf{L_m}$***** – 3,5-Me_2pz]$^+$. HRMS: ES$^+$ (*m*/*z*): [$\mathbf{L_m}$*****+ H]$^+$ calcd. for $[C_{28}H_{35}N_8]^+$ 483.2984; found 483.2988.

[Fe_2(μ-F)(μ-$\mathbf{L_m}$*)$_2$](BF_4)$_3$ (1). Both $\mathbf{L_m}$***** (0.241 g, 0.50 mmol) and $Fe(BF_4)_2 \cdot 6H_2O$ (0.169 g, 0.50 mmol) were separately dissolved in THF (10 mL) and the ligand solution transferred by cannula into the iron solution. An off-white precipitate formed immediately. The reaction mixture was stirred for 5 hours, after which time the system was cannula filtered, the remaining solid washed with THF (10 mL) and dried under vacuum overnight, affording 0.326 g (96%) of the crude product. Single crystals suitable for X-ray studies were grown by the vapor diffusion of Et_2O into 1 mL acetonitrile

solutions (20 mg/mL) of **1**. Anal. Calcd.(Found) for $C_{56}H_{68}B_3Fe_2N_{16}F_{13}$: C, 49.59 (49.75); H, 5.05 (4.81); N, 16.52 (16.75). MS ESI(+) *m/z* (rel. % abund.) [assgn]: 1269 (25) $[Fe_2(\mathbf{L_m^*})_2F(BF_4)_2]^+$, 591 (48) $[Fe_2(\mathbf{L_m^*})_2F(BF_4)]^{2+}$, 557 (87) $[Fe\mathbf{L_m^*}F]^+$, 483 (12) $[\mathbf{L_m^*} + H]^+$, 365 (100) $[Fe_2(\mathbf{L_m^*})_2F]^{3+}$. HRMS: ES^+ (*m/z*): $[Fe_2(\mathbf{L_m^*})_2F(BF_4)_2]^+$ calcd. for $[C_{56}H_{68}B_2Fe_2F_9N_{16}]^+$ 1269.4575; found 1269.4519.

$[Co_2(\mu\text{-}F)(\mu\text{-}L_m^*)_2](BF_4)_3$ (2). Compound **2** was prepared similarly to compound **1** starting from $Co(BF_4)_2{\cdot}6H_2O$ (0.170 g, 0.5 mmol). The reaction afforded 0.310 g (91%) of a pink solid. Single crystals suitable for X-ray studies were grown by the vapor diffusion of Et_2O into 1 mL acetonitrile solutions (30 mg/mL) of **2**. Anal. Calcd.(Found) for $C_{56}H_{68}B_3Co_2N_{16}F_{13}$: C, 49.37 (49.23); H, 5.03 (4.83); N, 16.45 (16.55). MS ESI(+) *m/z* (rel. % abund.) [assgn]: 1275 (28) $[Co_2(\mathbf{L_m^*})_2F(BF_4)_2]^+$, 594 (50) $[Co_2(\mathbf{L_m^*})_2F(BF_4)]^{2+}$, 560 (80) $[Co\mathbf{L_m^*}F]^+$, 483 (5) $[\mathbf{L_m^*} + H]^+$, 367 (100) $[Co_2(\mathbf{L_m^*})_2F]^{3+}$. HRMS: ES^+ (*m/z*): $[Co_2(\mathbf{L_m^*})_2F(BF_4)_2]^+$ calcd. for $[C_{56}H_{68}B_2Co_2F_9N_{16}]^+$ 1275.4486; found 1275.4537.

$[Ni_2(\mu\text{-}F)(\mu\text{-}L_m^*)_2](BF_4)_3$ (3). Compound **3** was prepared similarly to compound **1** starting from $Ni(BF_4)_2{\cdot}6H_2O$ (0.170 g, 0.5 mmol). The reaction afforded 0.280 g (82%) crude product. Compound **3** was crystallized as compound **2** and was taken directly from the mother liquor for the crystallographic studies as **3**·$2H_2O$. Anal. Calcd.(Found) for $C_{56}H_{68}B_3Ni_2N_{16}F_{13}$: C, 49.38 (49.27); H, 5.03 (4.81); N, 16.45 (16.62). MS ESI(+) *m/z* (rel. % abund.) [assgn]: 1273 (10) $[Ni_2(\mathbf{L_m^*})_2F(BF_4)_2]^+$, 593 (50) $[Ni_2(\mathbf{L_m^*})_2F(BF_4)]^{2+}$, 559 (10) $[Ni\mathbf{L_m^*}F]^+$, 366 (100) $[Ni_2(\mathbf{L_m^*})_2F]^{3+}$. HRMS: ES^+ (*m/z*): $[Ni_2(\mathbf{L_m^*})_2F(BF_4)_2]^+$ calcd. for $[C_{56}H_{68}B_2Ni_2F_9N_{16}]^+$ 1273.4557; found 1273.4583.

$[Cu_2(\mu\text{-}F)(\mu\text{-}L_m^*)_2](BF_4)_3$ (4). Compound **4** was prepared similarly to compound **1** starting from $Cu(BF_4)_2{\cdot}3H_2O$ (0.145 g, 0.5 mmol). The reaction afforded 0.245 g (72%) crude product. Compound **4** was crystallized as compound **2**. Anal. Calcd.(Found) for $C_{56}H_{68}B_3Cu_2N_{16}F_{13}$: C, 49.03 (48.78); H, 5.00 (4.76); N, 16.34 (16.36). MS ESI(+) *m*/*z* (rel. % abund.) [assgn]: 1283 (7) $[Cu_2(\mathbf{L_m^*})_2F(BF_4)_2]^+$, 1028 (18) $[Cu(\mathbf{L_m^*})_2]^+$, 599 (30) $[Cu_2(\mathbf{L_m^*})_2F(BF_4)]^{2+}$, 564 (12) $[Cu\mathbf{L_m^*}F]^+$, 545 (100) $[Cu\mathbf{L_m^*}]^+$, 483 (68) $[\mathbf{L_m^*} + H]^+$, 370 (60) $[Cu_2(\mathbf{L_m^*})_2F]^{3+}$. HRMS: ES^+ (*m*/*z*): $[Cu_2(\mathbf{L_m^*})_2F(BF_4)_2]^+$ calcd. for $[C_{56}H_{68}B_2Cu_2F_9N_{16}]^+$ 1273.4557; found 1273.4583.

$[Zn_2(\mu\text{-}F)(\mu\text{-}L_m^*)_2](BF_4)_3$ (5). Compound **5** was prepared similarly to compound **1** starting from $Zn(BF_4)_2{\cdot}5H_2O$ (0.165 g, 0.5 mmol). The reaction afforded 0.287 g (83%) crude product. Single crystals suitable for X-ray studies were grown by the vapor diffusion of Et_2O into 1 mL methanol solutions of **5** and were taken directly from the mother liquor for the crystallographic studies as **5**·$2H_2O$. ^1H NMR (300 MHz, acetonitrile-d_3): δ 7.62 (s, 4H, $CH(pz)_2$), 7.56 (t, *J* = 8.0 Hz, 2H, 5-H C_6H_4), 7.01 (d, *J* = 8.0 Hz, 4H, 4,6-H C_6H_4), 6.12/6.06 (s/s, 4H/4H, 4-H pz), 5.02 (s, 2H, 2-H C_6H_4), 2.55/2.37 (s/s, 12H/12H, 5-CH_3) 1.68/0.73 (s/s, 12H/12H, 3-CH_3). ^{13}C NMR (100.6 MHz, acetonitrile-d_3): *δ* 154.6/152.1/146.0/145.9 (3,5-C pz), 135.8 (1,3-C C_6H_4), 130.6 (5-C C_6H_4), 129.6 (4,6-C C_6H_4), 126.5 (2-C C_6H_4), 109.9/108.0 (4-C pz), 68.6 ($CH(pz)_2$), 16.9/11.5 (3-*C*H_3), 11.1/11.0 (5-*C*H_3). ^{19}F NMR (376 MHz, acetonitrile-d_3): *δ* -151 (s, BF_4^-), -173 (s, Zn-F-Zn). Anal. Calcd.(Found) for $C_{56}H_{68}B_3Zn_2N_{16}F_{13}$: C, 48.90 (49.12); H, 4.98 (4.74); N, 16.29 (16.43). MS ES(+) *m*/*z* (rel. % abund.) [assgn]: 1287 (8) $[Zn_2(\mathbf{L_m^*})_2F(BF_4)_2]^+$, 1115 (8) $[Zn(\mathbf{L_m^*})_2BF_4]^+$, 1047 (10) $[Zn(\mathbf{L_m^*})_2F]^+$, 873 (10) $[Zn_2\mathbf{L_m^*}(BF_4)_3]^+$, 565 (70) $[Zn\mathbf{L_m^*}F]^+$, 514 (100) $[Zn(\mathbf{L_m^*})_2]^{2+}$, 483 (52) $[\mathbf{L_m^*} + H]^+$,

371 (15) $[Zn_2(\mathbf{L}_m\mathbf{*})_2F]^{3+}$, 273 (55) $[Zn\mathbf{L}_m\mathbf{*}]^{2+}$. HRMS: ES^+ (*m/z*): $[Zn_2(\mathbf{L}_m\mathbf{*})_2F(BF_4)_2]^+$ calcd. for $[C_{56}H_{68}B_2Zn_2F_9N_{16}]^+$ 1287.4438; found 1287.4435.

$[Cd_2(\mu\text{-}F)(\mu\text{-}L_m\mathbf{*})_2](BF_4)_3$ (6). Compound **6** was prepared similarly to compound **1** starting from $Cd(BF_4)_2\cdot 6H_2O$ (0.147 g, 0.514 mmol). The reaction afforded 0.295 g (78%) of crude product. Single crystals suitable for X-ray studies were grown by the vapor diffusion of Et_2O into 1 mL acetonitrile solutions of **6** and were taken directly from the mother liquor for crystallographic studies as **6**·$2CH_3CN$. ^{1}H NMR (300 MHz, acetone-d_6): δ 8.03 (s, 4H, $CH(pz)_2$), 7.72 (t, J = 9.0 Hz, 2H, 5-H C_6H_4), 7.08 (d, J = 9.0 Hz, 4H, 4,6-H C_6H_4), 6.36/6.29 (s/s, 4H/4H, 4-H pz), 5.35 (s, 2H, 2-H C_6H_4), 2.68/2.60 (s/s, 12H/12H, 5-CH_3) 2.14/1.33 (s/s, 12H/12H, 3-CH_3). ^{13}C NMR (100.6 MHz, acetone-d_6): δ 153.4/151.7/146.1/145.4 (3,5-C pz, $J_{C\text{-}Cd}$ = 6-10 Hz, $J_{C\text{-}F}$ = 2 Hz), 135.2 (1,3-C C_6H_4), 130.1 (5-C C_6H_4), 129.0 (4,6-C C_6H_4), 126.6 (2-C C_6H_4), 108.3/106.9 (4-C pz), 68.1 ($CH(pz)_2$), 14.5/10.7 (3-CH_3), 10.3/9.9 (5-*C*H_3). ^{19}F NMR (376.2 MHz, acetone-d_6): δ -151 (s, 12F, BF_4^-), -223 (s, $J_{F\text{-}Cd}$ = 30 Hz, 1F, Cd-F-Cd), ^{113}Cd NMR (88.8 MHz, acetone-d_6): δ 25.1 (d, $J_{Cd\text{-}F}$ = 28 Hz). Anal. Calcd.(Found) for $C_{56}H_{68}B_3Cd_2N_{16}F_{13}$: C, 45.77 (45.74); H, 4.66 (4.40); N, 15.25 (15.05). MS ES(+) *m/z* (rel. % abund.) [assgn]: 1382 (12) $[Cd_2(\mathbf{L}_m\mathbf{*})_2F(BF_4)_2]^+$, 648 (7) $[Cd_2(\mathbf{L}_m\mathbf{*})_2F(BF_4)]^{2+}$, 614 (55) $[Cd\mathbf{L}_m\mathbf{*}F]^+$, 402 (100) $[Cd_2(\mathbf{L}_m\mathbf{*})_2F]^{3+}$. HRMS: ES^+ (*m/z*): $[Cd_2(\mathbf{L}_m\mathbf{*})_2F(BF_4)_2]^+$ calcd. for $[C_{56}H_{68}B_2Cd_2F_9N_{16}]^+$ 1383.3956; found 1383.4004.

$[Mn_2(\mu\text{-}F)(\mu\text{-}L_m\mathbf{*})_2](ClO_4)_3$ (7). Both $NaBF_4$ (0.028 g, 0.257 mmol) and $Mn(ClO_4)_2\cdot 6H_2O$ (0.186 g, 0.514 mmol) were dissolved in THF (4 mL). Water (500 μL) was added to the mixture of the metal salts to completely dissolve the $NaBF_4$. A THF (7 mL) solution of $\mathbf{L}_m\mathbf{*}$ (0.248 g, 0.514 mmol) was transferred by cannula into the metal

salts solution. The reaction mixture was stirred for 5 hours, after which time the solvents were removed by rotary evaporation. The white solid was washed with H_2O (20 mL) and dried under vacuum overnight, affording 0.274 g (77%) of the crude product. Single crystals suitable for X-ray studies were grown by the vapor diffusion of Et_2O into 1 mL acetonitrile (40 mg/mL) solutions of **7**. Anal. Calcd.(Found) for $C_{56}H_{68}Cl_3Mn_2N_{16}FO_{12}$: C, 48.30 (48.33); H, 4.92 (4.65); N, 16.09 (16.19). MS ESI(+) *m*/*z* (rel. % abund.) [assgn]: 1291 (5) $[Mn_2(\mathbf{L}_m\mathbf{*})_2F(ClO_4)_2]^+$, 596 (50) $[Mn_2(\mathbf{L}_m\mathbf{*})_2F(ClO_4)]^{2+}$, 556 (12) $[Mn\mathbf{L}_m\mathbf{*}F]^+$, 483 (93) $[\mathbf{L}_m\mathbf{*} + H]^+$, 364 (100) $[Mn_2(\mathbf{L}_m\mathbf{*})_2F]^{3+}$.

Crystallographic studies. X-ray diffraction intensity data for compounds **1-6** were measured on a Bruker SMART APEX CCD-based diffractometer (Mo Kα radiation, λ = 0.71073 Å).[13] Raw area detector data frame processing was performed with the SAINT+ and SADABS programs.[13] Final unit cell parameters were determined by least-squares refinement of large sets of strong reflections taken from each data set. Direct methods structure solution, difference Fourier calculations and full-matrix least-squares refinement against F^2 were performed with SHELXTL.[14] Non-hydrogen atoms were refined with anisotropic displacement parameters, the exception being disordered species. The hydrogen atoms were placed in geometrically idealized positions and included as riding atoms. Details of the data collection are given in Table 2.1.

Table 2.1. Selected Crystal Data and Structure Refinement.

	1	**2**	**3·2H$_2$O**	**4**	**4**	**5·2H$_2$O**	**6·2CH$_3$CN**	**7·2CH$_3$CN**
Formula	C_{56} H_{68} B_3 F_{13} N_{16} Fe_2	C_{56} H_{68} B_3 F_{13} N_{16} Co_2	C_{56} H_{72} B_3 F_{13} N_{16} O_2 Ni_2	C_{56} H_{68} B_3 F_{13} N_{16} Cu_2	C_{56} H_{68} B_3 F_{13} N_{16} Cu_2	C_{56} H_{72} B_3 F_{13} N_{16} O_2 Zn_2	C_{60} H_{74} B_3 F_{13} N_{18} Cd_2	C_{60} H_{74} Cl_3 F N_{18} O_{12} Mn_2
Fw, g·mol^{-1}	1356.39	1362.55	1398.15	1371.77	1371.77	1411.47	1551.60	1474.60
Cryst. Syst.	Triclinic	Triclinic	Monoclinic	Triclinic	Triclinic	Monoclinic	Monoclinic	Monoclinic
Space group	*P* $\bar{1}$	*P* $\bar{1}$	*P 2$_1$/n*	*P* $\bar{1}$	*P1*	*P 2$_1$/n*	*C 2/c*	*P 2$_1$/n*
T, K	296(2) K	296(2) K	150(2) K	296(2) K	150(2) K	150(2) K	100(2) K	100(2) K
a, Å	11.1007(4)	11.1049(13)	14.5757(9)	11.223(4)	12.5765(8)	14.6112(8)	18.0575(8)	22.1885(11)
b, Å	12.7715(5)	12.7328(15)	13.4631(8)	12.712(4)	13.5961(9)	13.5709(8)	18.7759(8)	14.1645(7)
c, Å	13.4497(5)	13.3656(15)	15.9731(9)	13.453(4)	27.8253(18)	15.9646(9)	20.6046(9)	22.5076(11)
α, deg	117.203(1)	116.666(2)	90	116.453(6)	82.997(1)	90	90	90
β, deg	99.415(1)	99.639(2)	95.171(1)	101.258(6)	88.741(1)	95.154(1)	100.845(1)	106.512(1)
γ, deg	104.248(1)	104.647(2)	90	103.926(6)	71.763(1)	90	90	90
V, Å^3	1557.13(10)	1545.3(3)	3121.7(3)	1563.6(9)	4484.5(5)	3152.8(3)	6861.1(5)	6782.2(6)
Z	1	1	2	1	3	2	4	4
R_1 (I >2σ(*I*))	0.0549	0.0532	0.0364	0.0627	0.0480	0.0361	0.0349	0.0391
wR_2 (I >2σ(*I*))	0.1497	0.1549	0.0876	0.1677	0.1167	0.0893	0.0970	0.0989

Compounds 1, 2 and 4, room-temperature structures. At room temperature the three compounds are isostructural, and crystallize in the triclinic system. The space group $P\ \bar{1}$ (No. 2) was confirmed in each case by the successful solution and refinement of the structures. The asymmetric unit of this structure type consists of half of one $[M_2(\mu\text{-F})(\mu\text{-}\mathbf{L_m^*})_2]^{3+}$ cation [M = Fe(II), Co(II), Cu(II)] that is located on a crystallographic inversion center, half of a BF_4^- anion that is disordered across an inversion center (B1), and one BF_4^- anion disordered on a general position (B2). Anion B1 is further disordered over two sites within the asymmetric unit. Because of its location near an inversion center, only half of tetrafluoroborate B1 is present per asymmetric unit. B1 was refined with two equally populated (25%) components, and B2 was refined with three disorder components, the occupancies of which were constrained to sum to unity. B-F and F-F distance restraints were used to maintain a chemically reasonable geometry for each component. Treatment of the tetrafluoroborate anion disorder was identical for the three structures.

Phase transitions: Examination of crystals of compounds **1**, **2** and **4** at different temperatures indicated a structural phase transition occurs in each system, with different onset temperatures. Transition temperatures were determined on the diffractometer by examination of sets of area detector data frames collected at various temperatures. Preliminary scans were conducted to indicate the approximate transition temperature, after which the crystal was either cooled from room temperature in increments of 5° around the transition temperature, or flash-cooled to 100 K followed by warming in increments of 5° around the transition temperature. The crystals were allowed to equilibrate for *ca*. five minutes at each temperature before collecting data for unit cell

determination. The data frames were carefully examined for weak reflections, and in general reflections with $I>3\sigma(I)$ were harvested for indexing. Upon cooling, the phase changes are signaled by the appearance of additional peaks in the diffraction pattern below the transition temperature.

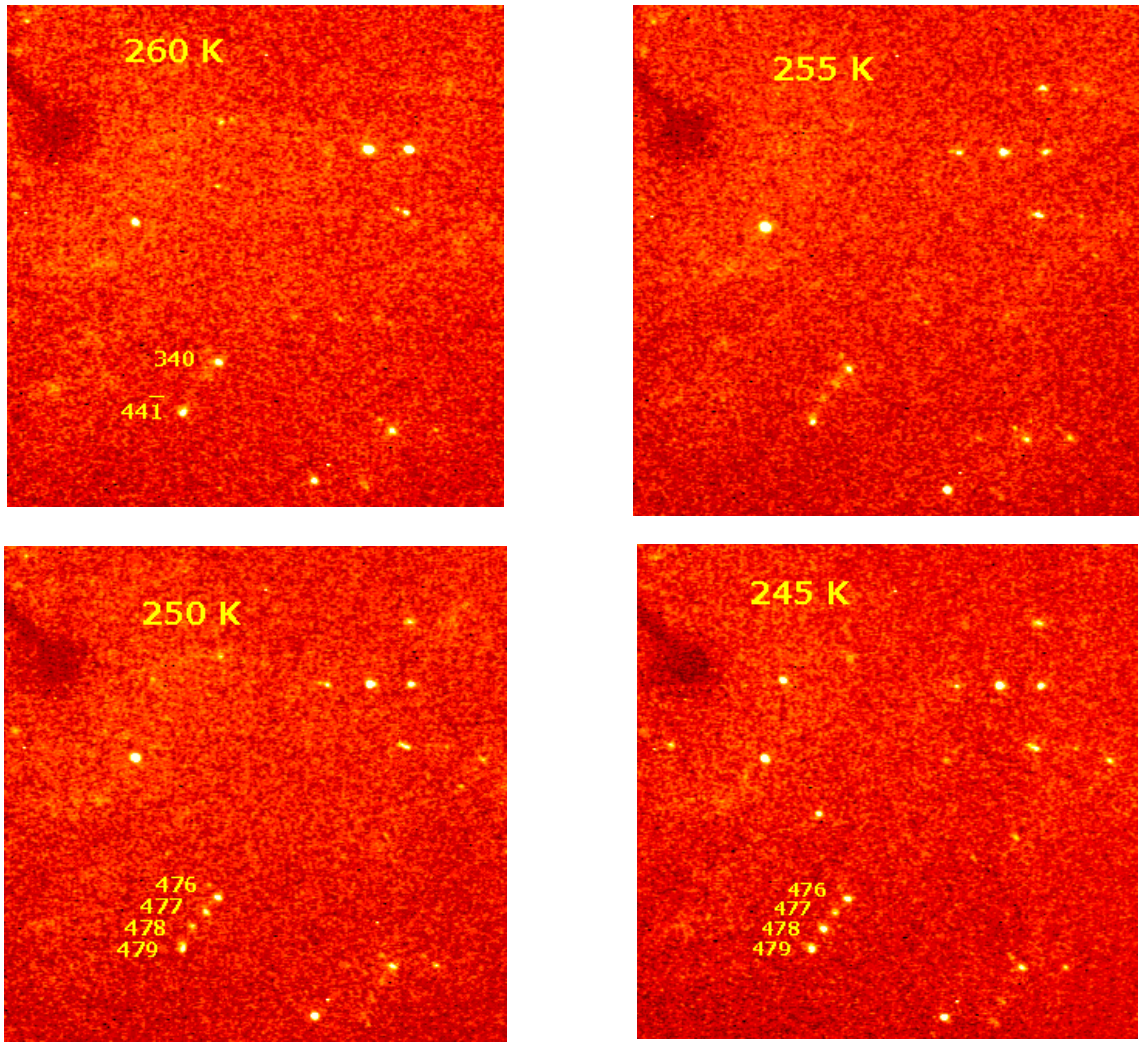

Figure 2.2. SMART area detector data frames at four temperatures, showing details of the change in diffraction patterns near the phase transition temperature. The hkl indices transform according to $(hkl)_{LT} = (k, h+k+l, 2h-l)_{HT}$.

For compound **4** (Cu) one phase transition occurs in the temperature range attainable with our equipment (90-300 K), having an onset temperature of T_{trans} = 250 K. Very weak reflections indicating a change in unit cell parameters appear near 255 K

(Figure 2.2). The spots are spaced roughly ⅓ and ⅔ between the dominant spots of the high temperature cell. At 250 K these diffraction spots become intense enough to center properly for indexing. Above T_{trans}, the diffraction pattern can be indexed to a triclinic unit cell with cell volume $V \approx 1560$ Å^3 (1563.6(9) Å^3 at 296 K). Below T_{trans}, the diffraction pattern can now be indexed entirely to a triclinic cell with $V \approx 4500$ Å^3(4484.5(5) Å^3 at 150 K), corresponding to a tripling of the unit cell volume allowing for thermal contraction. The relationship between the two triclinic cells (Table 2.1) is: $(abc)_{LT} = (b, a+b+c, 2a-c)_{HT}$ (LT = low temperature, HT = high temperature). The phase transition is moderately sudden, occurring over a temperature range of ca. 5K centered on T = 250 K, and may depend subtly on crystal size, inhomogeneity of the temperature stream, or impurities in the crystal. This transition temperature was verified by multiple warming/cooling cycles using three separate crystals. The phase changes are completely reversible, as warming the crystals above the transition temperature regenerates the HT unit cell with no apparent loss of crystal quality. There is little hysteresis evident as the transition temperature observed upon warming agrees with that observed upon cooling within 5 K. While diffraction maxima of compound **4** at both HT and LT are sharp and both phases could be characterized well, the low temperature structures of **1** and **2** could not be determined precisely. Below the transition temperatures for these crystals, the diffraction pattern is characterized by broadened peak maxima and diffuse scattering. Attempts to improve the crystallinity of the samples by flash-cooling below T_{trans}, or by soaking the crystal at 100 K overnight were unsuccessful. The reason for the different behavior of such similar systems is not clear. Several different crystals of the iron(II) and

cobalt(II) compounds, including those from different crystallizations, were studied with the same results.

150 K structure of 4: For data collection of the low-temperature form of **4**, data covering the full sphere in reciprocal space were collected at 150(2) K. The crystal system remains triclinic. Structure solutions initially attempted in the centric space group $P\ \bar{1}$ (No. 2) resulted in whole-cation disorder and were rejected (see below). The correct space group is the acentric group *P*1 (No. 1). The asymmetric unit in *P*1 consists of three crystallographically independent $[Cu_2(\mu\text{-}F)(\mu\text{-}\mathbf{L}_{\boldsymbol{m}}\mathbf{*})_2]^{3+}$cations and nine independent BF_4^- anions. All atoms of the three cations were refined anisotropically. The same atom labeling scheme was applied to each cation, with atoms distinguished by the label suffixes A, B or C. The displacement parameters of 20 atoms were restrained using the Shelx ISOR instruction to prevent non-positive definite ellipsoids. This result is likely due to the pseudosymmetry of the structure. The anion disorder observed in the 250 K form is partially resolved at 150 K, though still present to a lesser degree. Above 250 K, both inequivalent anion sites are heavily disordered, occupying four (B1, two unique orientations and two generated by inversion) or three orientations (B2) per site. These 1.5 unique anions transform into nine independent, partially ordered anions, transforming as: B1 (HT) > B1, B4, B7 (LT), and B2 (HT) > B2, B3, B5, B6, B7, B8 (LT). At 150 K, six of the nine independent anions are disordered but could be readily modeled in each case with only two components. Anions B2, B4, B5, B6, B7 and B8 were refined with two distinct orientations. Populations were constrained to unity and anion geometry was constrained to be similar to that of the ordered anions B1, B3, or B9. Only the ordered anions were refined with anisotropic displacement parameters; all disordered atoms were

refined isotropically, with minor components given a common displacement parameter. The low-temperature form is an inversion twin, as required by this form of symmetry-breaking structural transition. The inversion centers lost during the transition become the twin element in the lower symmetry form. The Flack parameter is 0.50(1), indicating a perfect two-component twin. The Flack parameter was included in the refinement as the twin fraction. The structure is pseudosymmetric, as the shifts in cation position upon structural transition are small. Trial solutions in the centric space group $P\ \bar{1}$ (No. 2) show that the asymmetric unit consists of one entire cation and half of another cation located on an inversion center. Both independent cations display a pattern of residual electron density peaks which are nearly superimposed upon the located atoms, but shifted by ca. 0.3 angstroms, implying whole cation disorder in $P\ \bar{1}$. In *P*1 these apparent small displacements away from average cation positions (disorder) is resolved and the structure solution is physically sensible and reasonably stable toward anisotropic refinement (i.e needing only 20 geometric restraints to calm high correlations). A data collection at 90 K showed the BF_4^- disorder still remains, and also that there were no improvement in refinement statistics compared to the 150 K data. In fact, the crystallinity appears to degrade somewhat below 150 K, as the Bragg reflection maxima appear sharpest at ca. 150 K. At temperatures below this approximate value, the unit cell does not alter except for the expected contraction, but there is a broadening of the peak profiles. This result may indicate the onset of another phase change below the lowest accessible temperature, or that further temperature contraction is damaging the crystallinity.

Compounds $3{\cdot}2H_2O$ and $5{\cdot}2H_2O$ crystallize in the space group $P2_1/n$ as determined by the pattern of systematic absences in the intensity data. The asymmetric

unit consists of half of one metal cation that is located on a crystallographic inversion center, 1.5 tetrafluoroborate anions (formally) and one water molecule. Both tetrafluoroborate anions are disordered. B1 was refined with three differently oriented components having refined populations A/B/C = 0.510(4)/0.341(5)/0.149(4), which were constrained to sum to unity. It was refined isotropically with all B-F distances restrained to be similar. B2 is disordered about an inversion center and was refined anisotropically with half-occupancy, and all B-F distances restrained to be similar. All non-hydrogen atoms were refined with anisotropic displacement parameters except atoms of the B1 anion. The water hydrogens were located in difference maps and refined isotropically with O-H = 0.85(2) Å and H···H = 1.40(2) Å distance restraints.

Compound 6·2CH$_3$CN crystallizes in the space group *C2/c* as determined by the pattern of systematic absences in the intensity data and by the successful solution and refinement of the structure. The asymmetric unit consists of half of one $[Cd_2(\mu\text{-F})(\mu\text{-}\mathbf{L}_m\mathbf{*})_2]^{3+}$ cation located on a crystallographic inversion center, 1.5 independent tetrafluoroborate anions, and one acetonitrile molecule of crystallization. One tetrafluoroborate ion (B2) is located on a crystallographic two-fold axis of rotation, and as such only half is present in the asymmetric unit.

Compound 7·2CH$_3$CN crystallizes in the monoclinic space group *P2$_1$/n* and the asymmetric unit consists of half of two independent $[Mn_2(\mu\text{-F})(\mu\text{-}\mathbf{L}_m\mathbf{*})_2]^{3+}$ cations, three perchlorate anions and two acetonitrile molecules. The manganese cations are located on crystallographic inversion centers. One perchlorate anion (Cl3) is disordered over two positions with refined populations A/B = 0.464(5) / 0.536(5).

Results

Synthesis of L_m*. The ligand was prepared by the cobalt(II) catalyzed Peterson rearrangement[15] between isophthalaldehyde and $SO(3,5\text{-}Me_2pz)_2$, according to Scheme 2.2. The $SO(3,5\text{-}Me_2pz)_2$ was synthesized in situ from sodium pyrazolate and thionyl chloride. In order to achieve high yields (81%), the reaction time was increased (42 h), compared to the preparation of L_m (24 h).[6a]

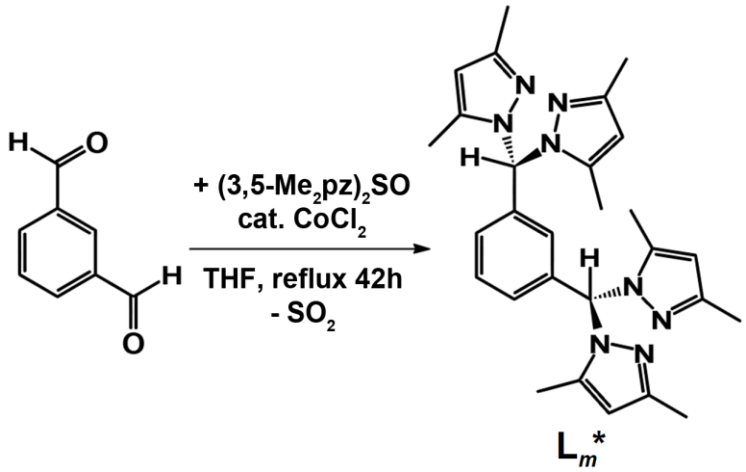

Scheme 2.2. Synthesis of L_m*.

Syntheses of the Metallacycles. Compounds **1-6** were prepared by mixing separate THF solutions of L_m* and $M(BF_4)_2 \cdot xH_2O$ ($M = Fe^{2+}$, Co^{2+}, Ni^{2+}, Cd^{2+} $x = 6$; Cu^{2+} $x = 3$; Zn^{2+} $x = 5$) as shown in the equation below.

$$2\ M(BF_4)_2 + 2\ L_m^* \xrightarrow{\text{THF}} [M_2(\mu\text{-F})(\mu\text{-}L_m^*)_2](BF_4)_3 + BF_3$$

M = Fe^{2+} (**1**), Co^{2+}(**2**), Ni^{2+}(**3**), Cu^{2+}(**4**), Zn^{2+}(**5**), Cd^{2+}(**6**)

Compound **7** was isolated from the reaction of $Mn(ClO_4)_2 \cdot 6H_2O$ and L_m* in the presence of $NaBF_4$, according to the following equation:

$$2\ Mn(ClO_4)_2 + NaBF_4 + 2\ \mathbf{L_m^*} \xrightarrow{THF} [Mn_2(\mu\text{-}F)(\mu\text{-}\mathbf{L_m^*})_2](ClO_4)_3 + NaClO_4 + BF_3$$

(**7**)

Solution Properties. A variety of NMR experiments (^{1}H, ^{13}C, ^{19}F, and in addition for **6** ^{113}Cd) were employed to study the solution behavior of the diamagnetic zinc(II) and cadmium(II) metallacycles. The ^{1}H NMR spectra of **5** and **6** (Figure 2.3) show one set of resonances for each type of hydrogen atoms in the *m*-phenylene spacers and the –CH(3,5-$Me_2pz)_2$ methine hydrogen atoms. In contrast, each type of hydrogen atom on the pyrazolyl rings show two equal intensity resonances, indicating two sets of non-equivalent pyrazolyl rings. Interestingly, the resonances for the *a**,*c**-methyl groups are at 2.55, 2.37, 1.68 and 0.73 ppm for **5**, and at 2.68, 2.60, 2.14 and 1.33 ppm for **6**, showing that one resonance in the second set for both compounds is highly shielded.

The assignment of the ^{13}C NMR signals in the spectra of **5** and **6** were made based on the Heteronuclear Single Quantum Coherence (HSQC) spectra of the compounds. As observed in the ^{1}H NMR, there is one set of resonances for each carbon atom type of the linking groups, but those on the pyrazolyl rings each show two.

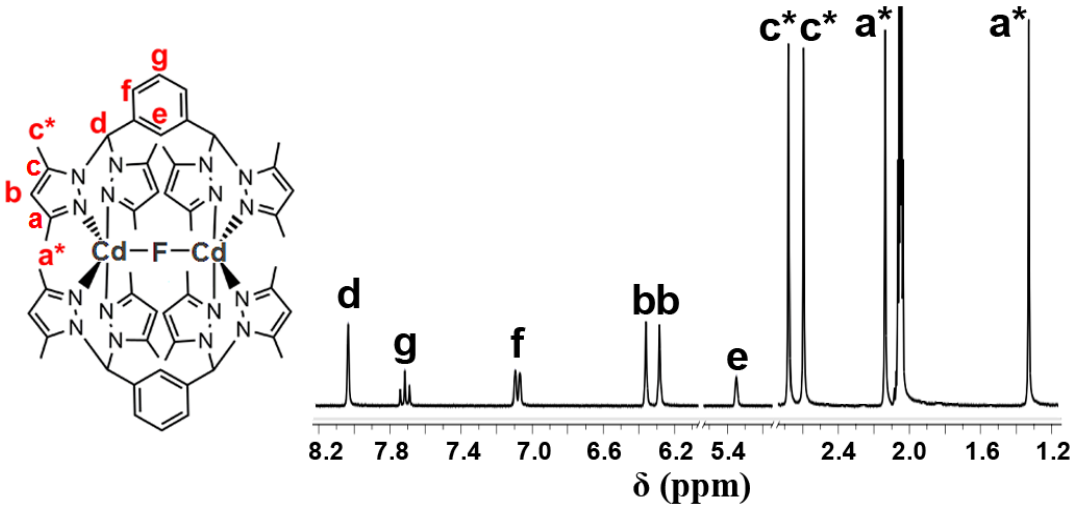

Figure 2.3. ^{1}H NMR spectrum of $[Cd_2(\mu\text{-}F)(\mu\text{-}\mathbf{L_m^*})_2](BF_4)_3$ (**6**).

For the *a**,*c**-methyl group carbon atoms on the pyrazolyl rings (16.9, 11.5, 11.1 and 11.0 ppm for **5**; 14.5, 10.7, 10.3 and 9.9 ppm for **6**), again one of the resonances, this time for the first pair, is more shielded than expected (11.1 for **5**; 10.7 for **6**). The HSQC spectra show these unusually shielded resonances correlate with the more shielded resonances in the ^{1}H spectra. The four distinct *a*- and *c*-pyrazolyl ring carbon resonances are at 154.6, 152.1, 146.0 and 145.9 ppm for **5**; 153.4, 151.7, 146.1 and 145.4 ppm for **6**. Cadmium satellites were observed with these resonances where $J_{C\text{-}Cd}$ varies between 6 and 10 Hz (Figure 2.4). The resonance at 145.4 ppm was a doublet due to coupling with the bridging fluorine with $J_{C\text{-}F}$ = 2Hz.

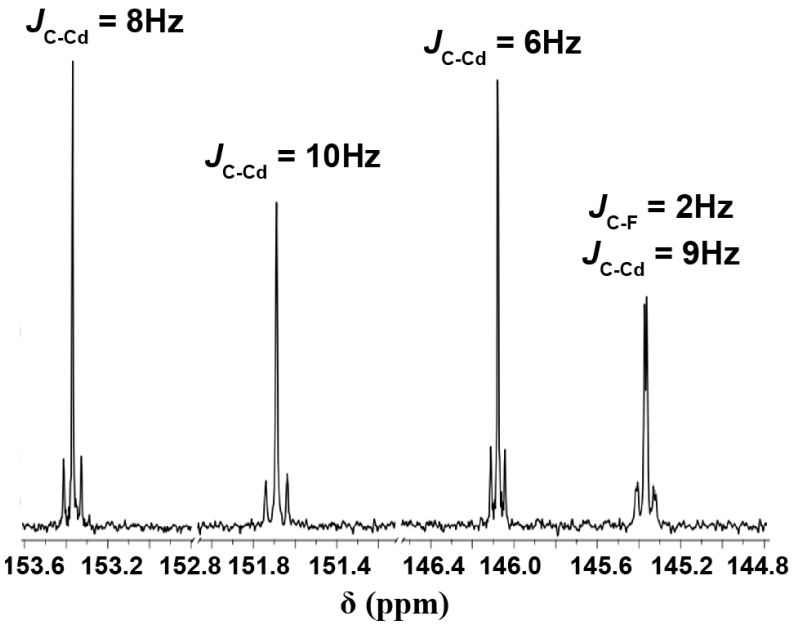

Figure 2.4. The *a*- and *c*-pyrazolyl ring carbon resonances in the ^{13}C NMR spectrum of $[Cd_2(\mu\text{-}F)(\mu\text{-}\mathbf{L}_{\boldsymbol{m}}\mathbf{*})_2](BF_4)_3$ (**6**).

The ^{19}F NMR spectra of both compounds show a resonance at -151.4 ppm, assigned to the BF_4^- anions. The smaller resonance at -151.3 can be associated with the isotopic distribution of the boron isotopes. The bridging fluoride gives rise to a resonance at -173 ppm for compound **5** and at -224 ppm for compound **6**. The signal of the bridging

fluoride in **6** is a singlet with $^{111/113}$Cd satellites, the *J* value being 30 Hz (Figure 2.5). Similarly, the ^{113}Cd NMR spectrum of **6** shows a doublet resonance split by a similar magnitude coupling from the bridging fluoride.

All of these results indicate that the dinuclear structures shown in the solid state (vide infra) are retained in acetonitrile or acetone solutions, respectively, for both **5** and **6**. Consideration of the solid state structures leads to the prediction that if the same structures are present in solution two pairs of resonances should be observed for each hydrogen and carbon of the pyrazolyl rings, one set for those oriented along the M–F–M axis (equatorial) and another set for those perpendicular to it (axial), as is reported above. In contrast, each type of hydrogen and carbon atom in the *m*-phenylene spacers and the –$CH(pz)_2$ methine group should be equivalent, again as observed. Importantly, the bridging fluoride ligand gives rise to a resonance in the ^{19}F NMR spectra of both complexes, a resonance for **6** that shows appropriate satellites for coupling to cadmium, with the reverse coupling to a single fluoride nucleus observed in the ^{113}Cd NMR spectrum. Coupling to both fluorine and cadmium is also observed in some of the ^{13}C resonances.

Finally, the hydrodynamic radius of **5** was measured from the diffusion coefficient of the complex in solution as determined by pulsed field-gradient spin-echo NMR (PFGSE-NMR). The radius determined from this experiment is 9.2 Å, while the hypothetical radius, calculated from the X-ray crystal structure of the dinuclear zinc(II) compound is 8.4 Å. The accuracy of this method is believed to be in the 20% range.

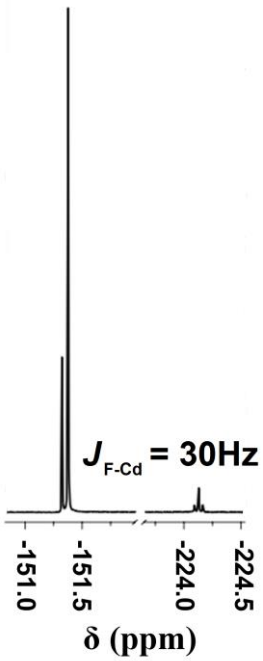

Figure 2.5. ^{19}F NMR spectrum of $[Cd_2(\mu\text{-}F)(\mu\text{-}\mathbf{L}_m\mathbf{*})_2](BF_4)_3$ (**6**).

Mass spectrometry. Positive-ion electrospray mass spectra (ESI^+-MS) of all seven complexes are similar. Clusters, such as $[M_2(\mathbf{L}_m\mathbf{*})_2F(BF_4)_2]^+$ and $[M_2(\mathbf{L}_m\mathbf{*})_2F]^{3+}$, where M = Fe(II), Co(II), Ni(II), Cu(II), Zn(II), Cd(II), are observed in all spectra that correspond to the fluoride bridged metallacycles. The ESI^+-MS spectra of **7** shows similar peaks with the corresponding ClO_4^- counterions. For **1**-**3, 6** and **7**, the base peak in the spectrum is $[M_2(\mathbf{L}_m\mathbf{*})_2F]^{3+}$; for compounds **4** and **5** it also has relatively high intensity. A set of peaks for $[M_2(\mathbf{L}_m\mathbf{*})_2F(A)]^{2+}$ (A = BF_4^- for **1**-**4** and **6** or ClO_4^- for **7**) is observed in all spectra except for **5**. Fragments of the metallacycles, like $[M\mathbf{L}_m\mathbf{*}F]^+$, were also detected with high intensities. In the ESI^+-MS spectra of compound **1**-**7**, no polymeric species were observed, indicating that the metallacycles are highly stable even in the gas phase. These observations are in good agreement with the structures determined in solid state and for **5** and **6** in solution.

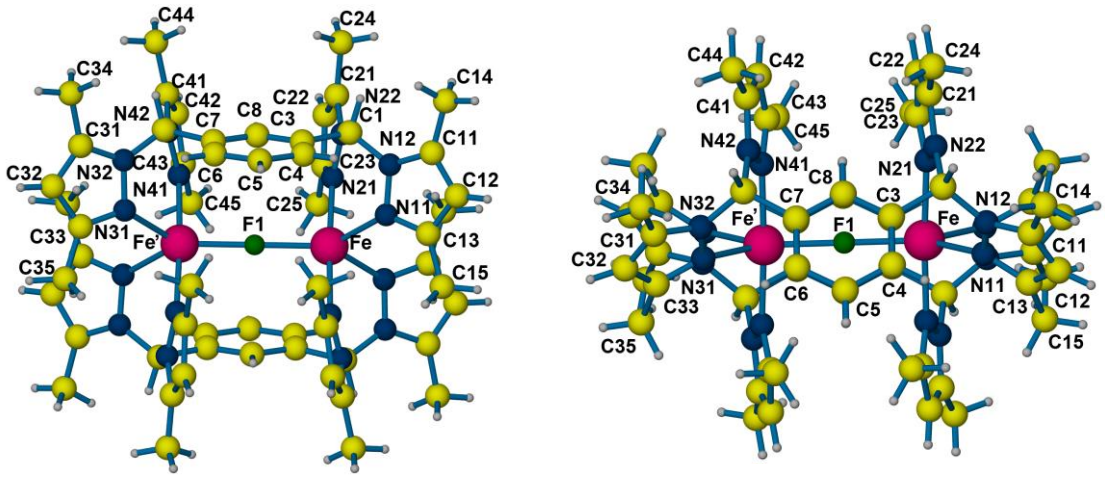

Figure 2.6. Structure of the cation in $[Fe_2(\mu\text{-}F)(\mu\text{-}\mathbf{L}_m\mathbf{*})_2](BF_4)_3$ (**1**) (**a**) front view, (**b**) top view.

Solid State Structures. Figure 2.6 shows the structure of the dinuclear fluoride bridged cation for compound **1**, $[Fe_2(\mu\text{-}F)(\mu\text{-}\mathbf{L}_m\mathbf{*})_2](BF_4)_3$, where the numbering scheme is correct for all of the structures of **1**-**6**, with the exception of the low temperature structure of the copper(II) complex **4**, vide infra. As shown in Table 2.2 and Table 2.3, which contains selected bond lengths, the structures of the cationic units are very similar.

The structures of **1**-**6** are centrosymmetric (center of symmetry at fluoride), except the low temperature structure of **4**, vide infra. The geometry around the metal centers is a distorted trigonal bipyramid; the fluoride (F1) and N11, N31 are equatorial and N21 and N41 are axial. The equatorial angles are distorted from the ideal values (120˚), e.g. **1**: N-M-F 135.94˚, 132.32˚; N-M-N 91.71˚, while the axial-axial angle is almost ideal (180˚), e.g. **1**: N-M-N 177.12˚. In addition, the trigonal bipyramidal geometry is indicated by the τ_5 values, a general descriptor of five coordinate systems[16] that is calculated according to the following equation: $\tau_5 = \frac{(\beta - \alpha)}{60°}$, where α and β are the two largest angles measured

Table 2.2. Important Structural Parameters for $[Fe_2(\mu\text{-}F)(\mu\text{-}\mathbf{L}_m\mathbf{*})_2](BF_4)_3$ (**1**), $[Co_2(\mu\text{-}F)(\mu\text{-}\mathbf{L}_m\mathbf{*})_2](BF_4)_3$ (**2**), $[Ni_2(\mu\text{-}F)(\mu\text{-}\mathbf{L}_m\mathbf{*})_2](BF_4)_3\cdot 2H_2O$ (**3**$\cdot 2H_2O$), $[Cu_2(\mu\text{-}F)(\mu\text{-}\mathbf{L}_m\mathbf{*})_2](BF_4)_3$ (**4**), $[Zn_2(\mu\text{-}F)(\mu\text{-}\mathbf{L}_m\mathbf{*})_2](BF_4)_3\cdot 2H_2O$ (**5**$\cdot 2H_2O$**)**, $[Cd_2(\mu\text{-}F)(\mu\text{-}\mathbf{L}_m\mathbf{*})_2](BF_4)_3\cdot 2CH_3CN$ (**6**$\cdot 2CH_3CN$**)** and $[Mn_2(\mu\text{-}F)(\mu\text{-}\mathbf{L}_m\mathbf{*})_2](ClO_4)_3$ (**7**$\cdot 2CH_3CN$).

Complex	T, K	Metal centers	M-F-M angle, deg	M-F distance, Å	Predicted M-F distance, Å[d]	Average M-N distance, Å	τ_5	M···M distance, Å
1	296	Fe(1)-Fe(1')	180.00	2.0231(4)	2.00	2.149	0.69	4.05
2	296	Co(1)-Co(1')	180.00(2)	2.0626(4)	1.96	2.099	0.74	4.13
3·2H$_2$O	150	Ni(1)-Ni(1')	180.00	2.0603(3)	1.92	2.057	0.71	4.12
4	296	Cu(1)-Cu(1')	180.00(2)	2.0631(8)	1.94	2.072	0.72	4.13
4	100	Cu(1A)-Cu(2A)	175.60(14)	2.025(3)/ 2.038(3)	1.94	2.058/2.059	0.74/0.68	4.061
		Cu(1B)-Cu(2B)	176.10(16)	2.013(3)/ 2.048(3)		2.058/2.057	0.67/0.75	4.058
		Cu(1C)-Cu(2C)	179.0(3)	2.027(5)/ 2.055(6)		2.066/2.054	0.70/0.69	4.082
5·2H$_2$O	150	Zn(1)-Zn(1')	180.00	2.0456(2)	1.97	2.113	0.77	4.09
6·2CH$_3$CN	100	Cd(1)-Cd(1')	180.00	2.1507(2)	2.16	2.307	0.78	4.30
7·2CH$_3$CN	100	Mn(1)-Mn(1')	180.00(1)	2.0293(3)	2.04	2.235	0.70	4.06
		Mn(2)-Mn(2')	180.00(1)	2.0669(3)		2.219	0.71	4.13

[a]Difference of the M-F distance in the $\mathbf{L}_m\mathbf{*}$ [$\mathbf{dL}_m\mathbf{*(M\text{-}F)}$]compounds and the M-F distance in the $\mathbf{L}_m$ compounds [$\mathbf{dL}_m\mathbf{(M\text{-}F)}$], see ref. 6b for $\mathbf{dL}_m\mathbf{(M\text{-}F)}$; [b]Two different $\mathbf{dL}_m\mathbf{*(M\text{-}F)\text{-}dL}_m\mathbf{(M\text{-}F)}$ differences**,** due to the fact that the $\mathbf{L}_m$ fluoride bridged compounds have two crystallographically independent cations in the unit cell; [c]Average of the $\mathbf{dL}_m\mathbf{*(M\text{-}F)\text{-}dL}_m\mathbf{(M\text{-}F)}$ differences; [d]Ref. 17.

around the metal centers. A perfect square pyramid is given by a τ_5 value of 0 and a perfect trigonal bipyramid has a value of 1. The τ_5 values for **1-7** are summarized in Table 2.2 and in all cases support the distorted trigonal bipyramidal geometry around the metal centers. The axial M-N bond lengths are shorter than the equatorial M-N bond lengths in the range 0.01-0.05 Å in all complexes except for the copper(II) complex **4**, an arrangement in disagreement with electrostatic predictions.[18] The compression of the axial bonds is very large with **4**, where the axial bond lengths are 0.175 Å shorter.

Table 2.3. M-F and M-N bond distances (Å).

	M-F(1)	**M-N(11)**	**M-N(21)**	**M-N(31)**	**M-N(41)**
1 (296 K)	2.0231(4)	2.162(3)	2.127(3)	2.164(3)	2.140(3)
2 (296 K)	2.0626(4)	2.104(2)	2.084(2)	2.108(2)	2.100(2)
3·2H$_2$O (150 K)	2.0603(3)	2.104(2)	2.029(2)	2.067(2)	2.029(2)
4 (296 K)	2.0631(8)	2.174(4)	1.977(4)	2.151(4)	1.985(4)
5·2H$_2$O (150 K)	2.0456(2)	2.181(2)	2.066(2)	2.129(2)	2.077(2)
6·2CH$_3$CN (100 K)	2.1508(2)	2.312(2)	2.310(2)	2.312(2)	2.293(2)
7·2CH$_3$CN (100 K)	2.0293(3)/ 2.0669(3)	2.231(2)/ 2.254(2)	2.239(2)/ 2.207(2)	2.242(2)/ 2.235(2)	2.228(2)/ 2.208(2)

In the structure of $[Mn_2(\mu\text{-}F)(\mu\text{-}\mathbf{L}_m\mathbf{*})_2](ClO_4)_3$ (**7**) there are two independent cationic units, Figure 2.7. Both cations reside on crystallographic inversion centers; the overall structures are similar to each other and compounds **1**-**6**. An unusual result observed for compound **7** is that the Mn-F bond length in one of the independent cations is smaller (2.029 Å) than the other (2.067 Å). As expected, the cation with the shorter M-F bond length shows longer Mn-N bond lengths than the other cation by an average of 0.016 Å.

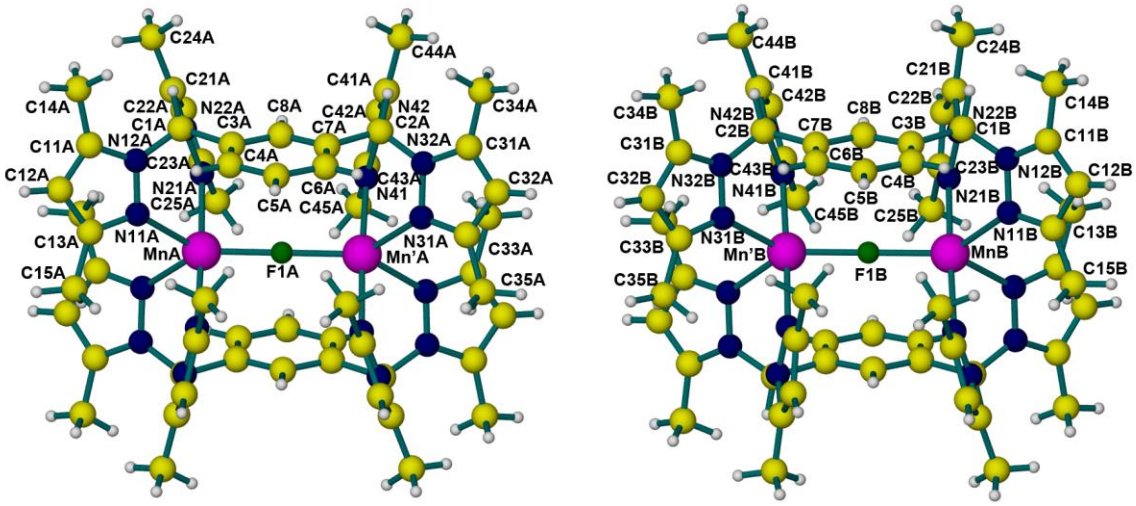

Figure 2.7. Structure of the two independent cationic units of $[Mn_2(\mu\text{-}F)(\mu\text{-}\mathbf{L}_m\mathbf{*})_2](ClO_4)_3$ (**7**).

Phase change of $[Cu_2(\mu\text{-}F)(\mu\text{-}L_m*)_2](BF_4)_3$, (4). Lowering the temperature of crystals of compounds **1**, **2** and **4** leads to a structural phase transition. Only in the case of **4**, where the phase transition takes place reversibly at 250 K (T_{trans}), could the lower temperature structure be properly determined. The phase transition involves partial ordering (cooling) or disordering (warming) of the tetrafluoroborate anions, and shifts in cation geometries and positions (Figure 2.8).

The cation geometry changes and their displacements within the unit cell are likely a response to the ordering movement of the anions below the transition temperature. Upon cooling below T_{trans}, the (half of) one unique, centrosymmetric cation in the asymmetric unit is transformed into three unique, non-centrosymmetric cations. A good indicator of the distortion of cation geometry in the low temperature form is given by the continuous symmetry measure (CSM S' value),[19] calculated by PLATON.[20] This parameter gives the measure of deviation from a given point symmetry, with a CSM

value of zero corresponding to ideal point symmetry, and higher values representing increasingly larger departures from ideal symmetry.

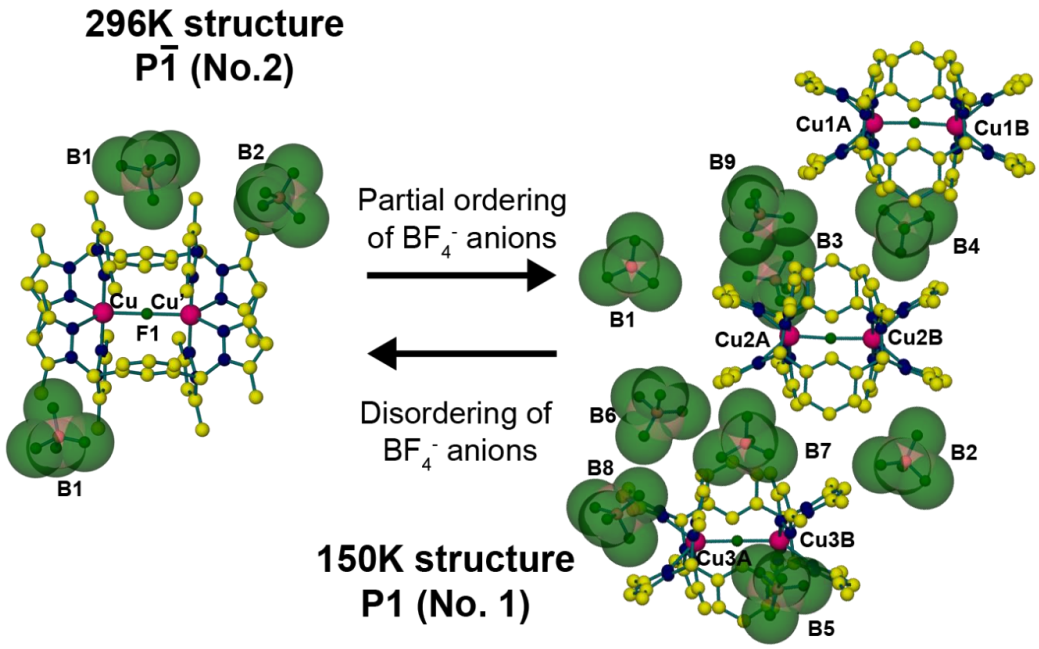

Figure 2.8. Phase change of $[Cu_2(\mu\text{-F})(\mu\text{-}\mathbf{L}_m\mathbf{*})_2](BF_4)_3$ (**4**). Hydrogen atoms and disordered BF_4^- anions were omitted for clarity (disordered BF_4^- species: high temperature structure: B1, B2; low temperature structure: B2, B4, B5, B6, B7, B8).

In the high temperature form, the single cation has crystallographically imposed C_i point symmetry (CSM ≡ 0). The CSM values for the three low temperature cations are: A = 1.0, B = 1.0, C = 0.1. The large deviations from inversion symmetry for cations A and B can be seen most obviously in their bent Cu-F-Cu angles of 175.6 and 176.1°, respectively. For cation C this angle is 179.0°. Figure 2.9 shows both forms viewed along corresponding directions ($[100]_{HT}$ = $[1\text{-}1\text{-}1]_{LT}$), showing misalignment of the cations and anions in the low temperature form in projection along this direction. Figure 2.10 shows both structures viewed along the equivalent directions $[010]_{HT}$ and $[100]_{LT}$. Figure 2.11 shows the equivalent views $[001]_{HT}$ and $[\text{-}22\text{-}1]_{LT}$.

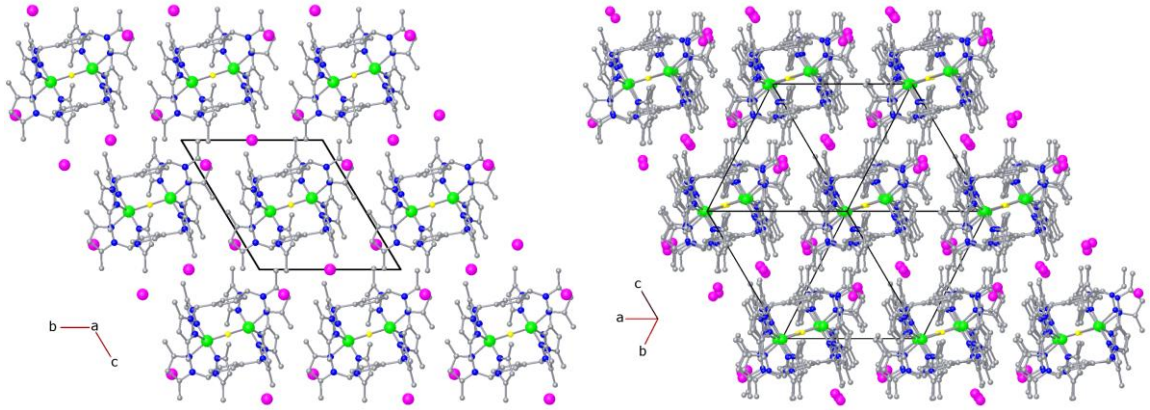

Figure 2.9. Equivalent views of the crystal packing (directions $[100]_{HT}$ and $[1\text{-}1\text{-}1]_{LT}$), showing the displacement of the cations and anions in the LT form (right) relative to the HT structure (left). In this view the three independent cations A, B, and C in the LT structure are superimposed in projection.

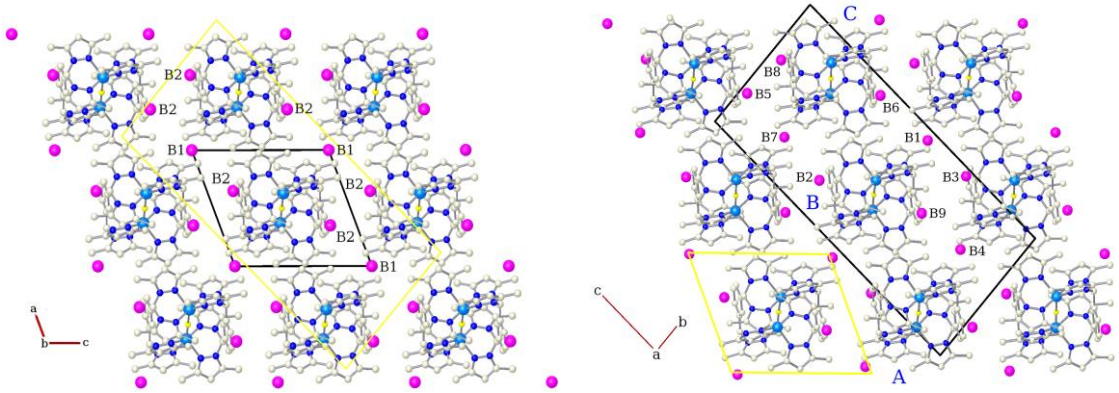

Figure 2.10. Views down equivalent directions $[010]_{HT}$ (left) and $[100]_{LT}$ (right). Average positions for the disordered BF_4^- anions are labeled. Only anions corresponding directly between the two cells are labeled. Columns of the three independent cations are labeled in blue. Unit cells corresponding to the other form are shown in yellow in each structure.

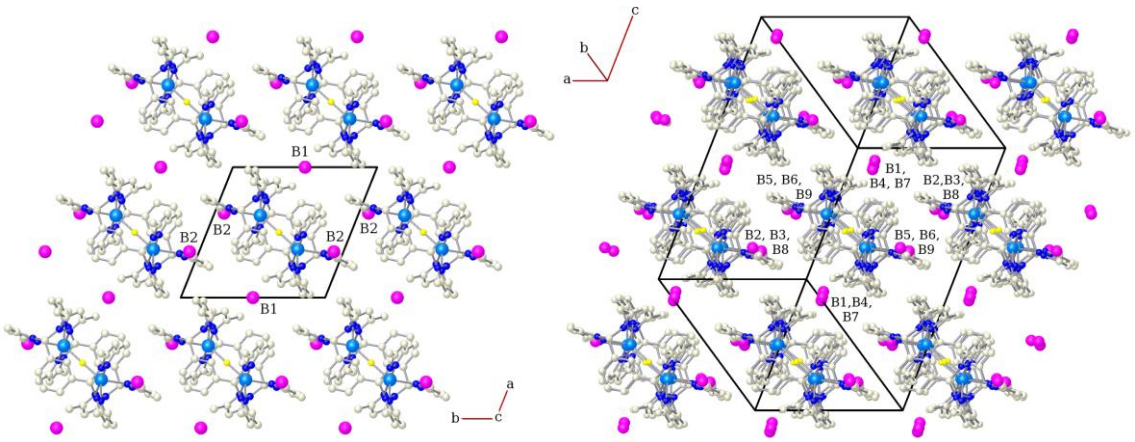

Figure 2.11. Views down equivalent directions $[001]_{HT}$ (left)and $[-22-1]_{LT}$ (right). Average positions for the disordered BF_4^- anions are labeled. Only anions corresponding directly between the two cells are labeled.

Magnetic properties and EPR spectra. The exchange coupling between two ions with spin $S_1 = S_2$ gives rise to a series of coupled spin states characterized by the total spin quantum number S ranging from 0 to $2S_1$. The Heisenberg-Dirac-Van Vleck Hamiltonian in the form:

$$\hat{\boldsymbol{H}} = - J \hat{\boldsymbol{S}}_1 \hat{\boldsymbol{S}}_2 \qquad (1)$$

has been typically applied to interpret the magnetic properties of the dinuclear complexes. The energies of the S levels are:

$$E(S) = -(J/2)\{S(S+1) - 2S_1(S_1+1)\} \qquad (2)$$

If the exchange coupling is sufficiently large, the S levels are 'pure' and the EPR as well as magnetic problems may be handled by using the coupled-spin representation (often called the 'giant spin' approximation), in which a separate spin Hamiltonian is defined for each of the different coupled S states:

$$\hat{\boldsymbol{H}}_S = \mu_B \boldsymbol{B}\cdot\{\boldsymbol{g}_S\}\cdot\hat{\boldsymbol{S}} + D_S\{\hat{\boldsymbol{S}}_z^2 - S(S+1)/3\} + E_S(\hat{\boldsymbol{S}}_x^2 - \hat{\boldsymbol{S}}_y^2) \qquad (3)$$

The zero-field splitting parameters D_S and E_S are different in each coupled spin state and they contain contributions due to the zero-field splitting on individual ions with $S_1>1/2$, D_1, D_2 and E_1, E_2, as well as a contributions D_{12} and E_{12} due to the anisotropic interactions between the metal ions:[21,22]

$$D_S= \alpha_S D_{12} + \beta_S (D_1+ D_2)$$

$$E_S= \alpha_S E_{12} + \beta_S (E_1+ E_2) \quad (4)$$

where $$\alpha_S = [S(S + 1)+2S_1(S_1 + 1) + 2S_2(S_2 + 1)]/[2(2S - 1)(2S + 3)] \quad (5)$$

$$\beta_S = [3S(S+1)-2S_1(S_1 + 1) - 2S_2(S_2 + 1)-3]/[2(2S - 1)(2S + 3)]$$

In the present case, large zero-field splitting, comparable to the exchange coupling is expected for the nickel(II), iron(II) and cobalt(II) complexes causing the S levels to mix. For this reason, the above treatment is not adequate and the spin Hamiltonian needs to be expressed by the spin operators of the individual ions:

$$\hat{\boldsymbol{H}} = - J \hat{\boldsymbol{S}}_1 \hat{\boldsymbol{S}}_2 + D_{12}\{ \hat{\boldsymbol{S}}_{z1} \hat{\boldsymbol{S}}_{z2} - \hat{\boldsymbol{S}}_1 \cdot \hat{\boldsymbol{S}}_2 /3\} + E_{12} (\hat{\boldsymbol{S}}_{x1} \hat{\mathbf{S}}_{x2} - \hat{\boldsymbol{S}}_{y1} \hat{\mathbf{S}}_{y2})$$

$$\mu_B B \{\boldsymbol{g}_1\} \hat{\boldsymbol{S}}_1 + D_1 \{ \hat{\boldsymbol{S}}_{z1}^2 - S_1(S_1 + 1)/3\} + E_1 (\hat{\boldsymbol{S}}_{x1}^2 - \hat{\boldsymbol{S}}_{y1}^2) +$$

$$\mu_B B \{\boldsymbol{g}_2\} \hat{S}_2 + D_2 \{ \hat{\boldsymbol{S}}_{z2}^2 - S_2(S_2 + 1)/3\} + E_2 (\hat{\boldsymbol{S}}_{x2}^2 - \hat{\boldsymbol{S}}_{y2}^2) \quad (6)$$

In the centrosymmetric complexes studied here $D_1 = D_2$, $E_1 = E_2$ and the $\{g\}$ tensors of the two ions are equal and coaxial. For that reason, the $\{g\}$ tensors in each coupled state must be equal to each other and equal to $\{g\}$ on individual ions. Both the dipole-dipole and anisotropic exchange interactions contribute to D_{12} and E_{12}. The spin Hamiltonian above may be used to explain both the magnetic properties and EPR spectra. Its application is much more difficult than using the 'giant spin' method. For example, in the case of a Fe(II) dinuclear system the spin Hamiltonian matrices of dimension 25x25

have to be diagonalised, while the coupled representation method would use matrices 3x3, 5x5, 7x7 and 9x9 for the total spin states 1, 2, 3 and 4, respectively.

Since no analytical formulas are available for the energy levels of the manganese(II), iron(II), cobalt(II) and nickel(II) dinuclear compounds if the zero-field splitting on individual metal ions as well as and the Zeeman term need to be included, their magnetic susceptibility χ_d has to be evaluated from the basic relation:

$$\chi_d = -\frac{N}{B}\frac{\sum_i \frac{\partial E_i}{\partial B}\exp(-E_i/kT)}{\sum_i \exp(-E_i/kT)} + 2TIP \qquad (7)$$

where the summation runs over all states in the system. The energies were found by diagonalising the matrix of spin Hamiltonian (6) The derivatives $\delta E_i/\delta B$ were calculated numerically, by evaluating energies E_i 5 Gauss below and 5 Gauss above the magnetic field of the the SQUID instrument (5000 G). As in other dinuclear complexes, a contribution to magnetic susceptibility due to mononuclear impurities was observed, which was taken into account by fitting experimental data to

$$\chi = (1-f)\,\chi_d + 2f\,\chi_m \qquad (8)$$

where f is the fraction of a mononuclear impurity and χ_m is its molar magnetic susceptibility. For the Mn(II), Fe(II), Co(II) and Ni(II) compounds, χ_d was calculated from eq. 7 and χ_m was expressed as:

$$\chi_m = -\frac{N\mu_B g}{B}\frac{\sum_{M_S=-S}^{S} M_S \exp(-g\mu_B B M_S/kT)}{\sum_{M_S=-S}^{S} \exp(-g\mu_B B M_S/kT)} + TIP \qquad (9)$$

In the much simpler case of the copper(II) complexes, where the 'giant spin' method and spin Hamiltonian (3) are applicable, χ_d was evaluated from the well-known Bleaney-Bowers expression:[22]

$$\chi_d = \frac{N\mu_B^2 g^2}{3kT}\frac{6\exp(J/kT)}{1+3\exp(J/kT)} + 2TIP \qquad (10)$$

and χ_m from Curie's law:

$$\chi_m = (N\mu^2{}_B{}^2 g^2/3kT)\cdot 0.75 + TIP \qquad (11)$$

Figure 2.12 shows the magnetic susceptibility for compounds **1**-**4** and **7** and Table 2.4 shows the "spin Hamiltonian parameters". All of the compounds are antiferromagnetically coupled, although the magnitude of the coupling changes dramatically. An interesting feature of the susceptibilities of the nickel(II), iron(II) and cobalt(II) complexes is that they do not drop to zero at the lowest temperatures (even if the monomer contribution is subtracted), a result caused by very large zero-field splitting in the excited paramagnetic states. The magnetic susceptibility of the nickel(II) complex **3** calculated with or without the D_1 term is shown in Figure 2.13. The manganese(II) complex susceptibility does not reach zero at 1.8 K because of the small -*J*. The magnitude of the antiferromagnetic coupling increases across the periodic table from left to right; the copper(II) complex **4** is dramatically larger than the other metals, 322 cm^{-1}.

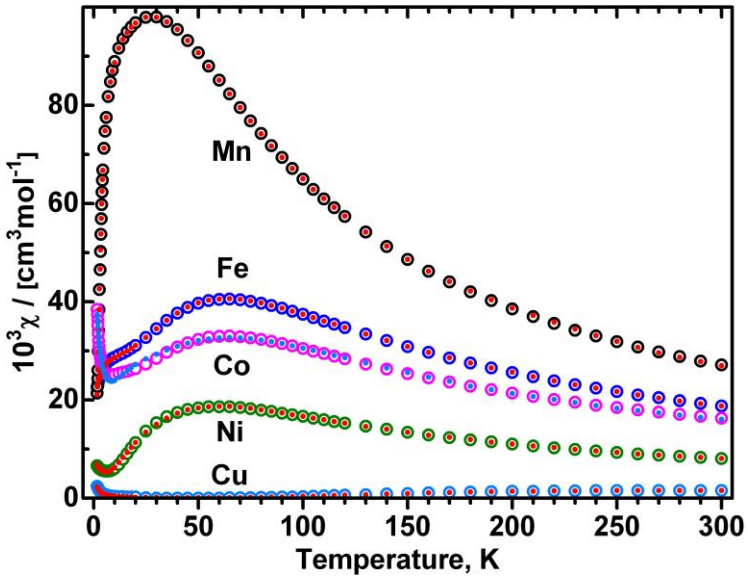

Figure 2.12. Magnetic susceptibility of $[Mn_2(\mu\text{-}F)(\mu\text{-}\mathbf{L_m}^*)_2](ClO_4)_3{\cdot}2CH_3CN$ (**7**·2CH$_3$CN), $[Fe_2(\mu\text{-}F)(\mu\text{-}\mathbf{L_m}^*)_2](BF_4)_3$ (**1**), $[Co_2(\mu\text{-}F)(\mu\text{-}\mathbf{L_m}^*)_2](BF_4)_3$ (**2**), $[Ni_2(\mu\text{-}F)(\mu\text{-}\mathbf{L_m}^*)_2](BF_4)_3{\cdot}2H_2O$ (**3**·2H$_2$O) and $[Cu_2(\mu\text{-}F)(\mu\text{-}\mathbf{L_m}^*)_2](BF_4)_3$ (**4**) - listed top to bottom. Circles: experimental data; dots: calculated. The g, $-J$ and D_1 values for the Fe(II), Co(II) and Ni(II) complexes were determined from the magnetic data (Table 2.4), while for Mn(II) the EPR values of D_1 = -0.3254 cm^{-1}, E_1 = -0.0153 cm^{-1}, D_{12} = 0.0302 cm^{-1}, E_{12} = 0 were fixed while g and $-J$ were fitted. See Figure 2.16 for an expansion and details on $[Cu_2(\mu\text{-}F)(\mu\text{-}\mathbf{L_m}^*)_2](BF_4)_3$.

Table 2.4. Experimental spin Hamiltonian parameters and results of DFT calculations.

	1 (Fe)	**2 (Co)**	**3·2H$_2$O (Ni)**	**7·2CH$_3$CN (Mn)**	**4 (Cu)**
g_{avg} **(magnetic)**	2.11	2.26	2.31	2.02	2.22
g_x, g_y, g_z **(EPR)**	2.26, 2.29, 1.99	-	-	2.00, 2.00 2.00	2.15, 2.33, 2.01
$-J$ **cm^{-1} (exp)**	16.3(3)	24.1(5)[a]	39.0(1)[a]	6.7(2)[a]	322(5)[a]
$-J$ **cm^{-1} (DFT)**	28	-	55	12 long 14 short[c]	380
D_1**, cm^{-1}**	-10.0(3)[a], -9.89(2)[b]	20(2)[a]	36(1)[a]	-0.325(2)[b]	0.173(2)[b,d]
E_1**, cm^{-1}**	0	0	0	-0.0153(2)[b]	0.089(2)[b,d]

[a]Parameters from magnetic susceptibility; [b]Parameters from EPR; [c]Data for two molecules with slightly different Mn-F bond length; [d] D and E refer to the coupled-spin Hamiltonian (eq. 3), other D and E values are for the spin Hamiltonian (eq. 6).

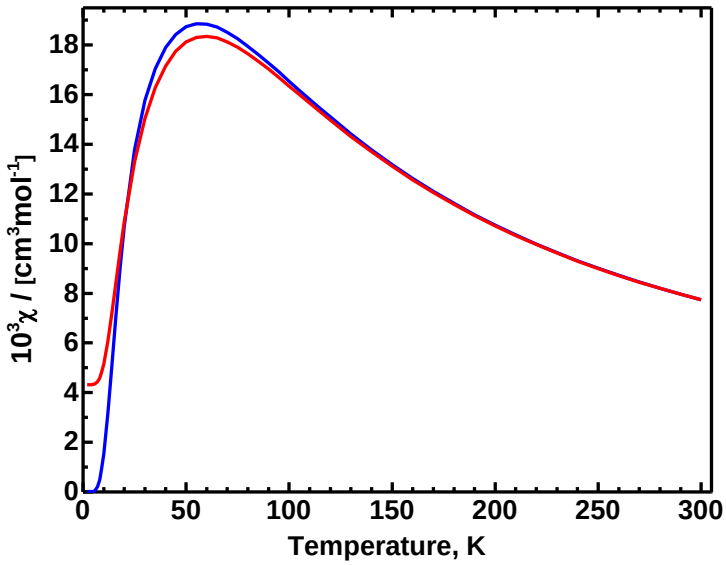

Figure 2.13. Magnetic susceptibility of the dinuclear Ni(II) system calculated with g_{avg} = 2.31,-J = 39 cm^{-1}, D_1 = 36 cm^{-1}, (red) and with g_{avg} = 2.31, -J = 39 cm^{-1}, D_1 = 0, (blue).

Magnetic properties and EPR spectra of $[Mn_2(\mu\text{-}F)(\mu\text{-}\mathbf{L}_m\mathbf{*})_2](ClO_4)_3\cdot 2CH_3CN$, **7.**

The exchange integral was determined from fitting of the magnetic susceptibility using eqs 7-9. The zfs parameters were fixed at the values found from EPR (see below) and only -J and g were allowed to change. Small differences between the g from EPR and from magnetic susceptibility (Table 2.4) are often observed. The temperature-independent paramagnetism (TIP) was assumed to be 0 and the fraction of mononuclear impurities of 0.2% was obtained. The complex exhibits well resolved high-field EPR spectra in which the positions of the resonance lines which can be assigned to the S = 1 and S = 2 states are almost temperature independent over the temperature range 3 – 50 K. Although the 'giant spin' model is not strictly applicable, it is still useful to classify the EPR transitions according to the total spin state in which they occur. Comparison of calculations using the spin Hamiltonian (3) versus (6) indicates that with -J of ca 7 cm^{-1}, and D_1 on individual manganese(II) ions of ~-0.3 cm^{-1}, the spin state mixing affects only

marginally the S = 1 state of the dinuclear system, while its effect on the S = 2 state is significant. The spin state mixing causes a shift of the M_S = 0 level of S = 2, so that the energies of the M_S levels no longer follow the $E(M_S) = D_S M_S^2$ dependence. However, the energy difference between levels M_S = ±1 and M_S = ±2 remains largely unaffected. In an S = 2 state there are 4 'allowed' transitions at each orientation of the magnetic field. The outer of the four resonances at Z orientation (labeled 2z in Figure 2.14), which correspond to transitions (-2)↔(-1) and (2)↔(1) could therefore be used to determine the $D_{S=2}$ magnitude of 0.341 cm^{-1}.

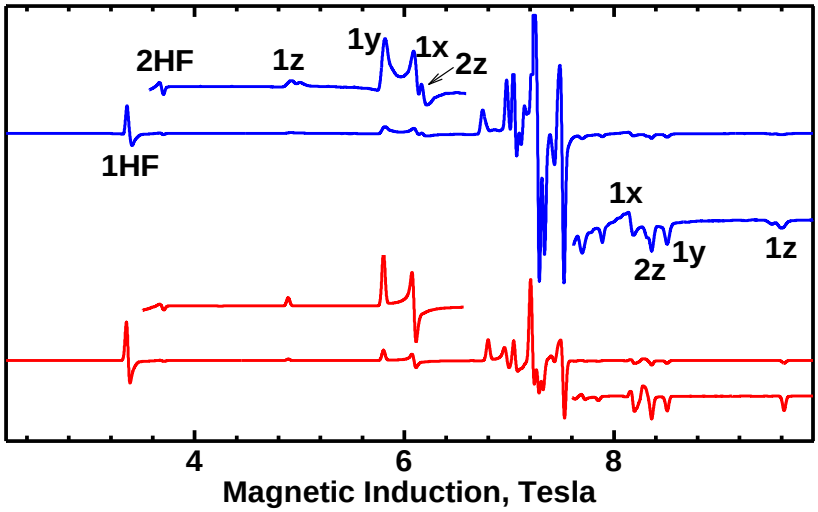

Figure 2.14. EPR spectra of $[Mn_2(\mu\text{-}F)(\mu\text{-}\mathbf{L_m}^*)_2](ClO_4)_3 \cdot 2CH_3CN$. Top (blue): experimental, recorded at 10 K with ν = 203.2 GHz. Bottom (red): simulated by using Hamiltonian (6) with $g_x = g_y = g_z = 2.00$, D_1 = -0.325 cm^{-1}, E_1 = -0.0153 cm^{-1}, $-J$ = 6.7 cm^{-1}, D_{12} = 0.0302 cm^{-1}, E_{12} = 0. Note the doubling of some resonances in the experimental spectrum (at 4.8 and at 9.6 T) is presumably due to two dinuclear species with slightly different Mn-F bond lengths (see the crystallographic section). The numbers 1, 2 indicate the spin states in which transitions occur, letters x, y, and z mark the molecular orientations. HF means the half-field, "forbidden transition", $\Delta M_S = 2$. The HF transition in S = 1 is at a lower magnetic field than that in S = 2 because of much larger zfs parameters in the former.

The S = 1 spectrum can be very well simulated at each microwave frequency according to the 'giant spin' (i.e. coupled representation) model (eq 3) with S = 1, $g_x = g_y$ = 2.005, g_z=2.000, $D_{S=1}$ = 2.187 cm^{-1}, $E_{S=1}$ = 0.0935 cm^{-1}. The intensity of the low-field

ΔM_S = 1 resonance (1z at 4.9 T in Figure 2.14) is suppressed when the temperature is lowered, while the intensity of the high-field 1z resonance (9.6 T) increases. These trends prove that $D_{S=1}$ is positive.[23] $D_{S=2}$ is also positive (high-field 2z line becomes stronger with the temperature lowering, while the low-field 2z line disappears). Determination of D in both S = 1 and S = 2 states allows calculation of D_1 = -0.320 cm^{-1} and D_{12} = 0.036 cm^{-1} (eqs. 4 and 6). This analysis assumes that the coordinate systems for D_1 and D_{12} are parallel (or exactly orthogonal), which is likely to be obeyed by our molecules. Density Functional Theory (DFT) calculations were performed using the TZVPP basis set for copper(II) and SVP for other atoms, combined with the B3LYP functional, of D_1 on individual ions by using the software package ORCA.[24] The calculations were performed on a fragment containing one metal ion with its ligands and the bridging atom. In the case of **7**·2CH_3CN, the DFT method gave D_1 = -0.06 cm^{-1} with the Z axis of the zfs (zero-field splitting) tensor along the bipyramid vertical axis. It is known that DFT does not produce reliable D_1 values. In the present case, D_1 = -0.10 cm^{-1}, still much less than the experimental value was obtained from UHF (available within ORCA as well). In general, the orientation of the zero-field splitting tensor is calculated more properly than its magnitude. With the Mn···Mn distance of 4.1 Å, the dipolar contribution to D_{12} of eq. 6 is $D_{12}^{dipolar}=-3\mu_B^2g^2/r_{Mn\text{-}Mn}^3$ = -0.075 cm^{-1}. This value should be considered as an upper limit, since the formula takes no electron delocalization into account, and $E_{12}^{dipolar}$ is 0. The Z component of the dipolar interaction lies along the Mn···Mn direction, while the Z axis of D_1 is along the trigonal bipyramid axis, roughly perpendicular. Rotation of the dipolar interaction tensor into the D_1 system produces $D_{12}^{dipolar}$ of +0.037 cm^{-1}, $E_{12}^{dipolar}$ =

0.037 cm^{-1}. Thus, the dipolar part appears to account for the magnitude of D_{12} found above from the EPR spectra analysis.

The parameters above were used as seed values in a procedure fitting the dependence of the resonance fields versus frequency, which is explained in a more detailed way below (for **1**). The spectrum in Figure 2.14 was simulated with the parameters refined in this way. The magnetic susceptibility in Figure 2.13 was calculated using the same zfs parameters.

Mantel *et al.*[26] have investigated with HF EPR some mononuclear trigonal-bipyramidal manganese(II) complexes and observed negative D (-0.3 cm^{-1}) in axially elongated molecules, while our manganese(II) complex is axially compressed. These complexes, however, are too dissimilar from ours to make a direct comparison.

Magnetic properties and EPR spectra of $[Fe_2(\mu\text{-}F)(\mu\text{-}\mathbf{L_m}^*)_2](BF_4)_3$, **1.** The magnetic susceptibility of **1** could be very well reproduced using the spin Hamiltonian (eq. 6) in which the anisotropic metal-metal interactions were neglected. The zero-field splitting in this dinuclear compound is expected to be dominated by the $D_1 = D_2$, $E_1 = E_2$ terms, which are typically very large in iron(II). Fitting with eqs. 7-9 resulted in $-J = 16$ cm^{-1}, $D_1 = 10$ cm^{-1}, which are similar to those observed in the unsubstituted complex.[6] Similar $-J$ and D_1 were also found in other dinuclear iron(II) complexes.[23] The fraction of mononuclear impurities was 0.04% and TIP was 0. It is known that magnetic susceptibility fitting is often insensitive to the sign of D_1 on single metal ions, even in the mononuclear systems. Somewhat surprisingly, this insensitivity is not true in the present case, as no reasonable fit was possible with $D_1 > 0$. This result may be understood by inspection of the energy diagrams calculated for positive or negative $D_1 = D_2$.

With D_1 = D_2 = -10 cm^{-1} and -J = 16 cm^{-1}, the lowest level of the dinuclear compound is S = 0, M_S = 0, followed by S = 1, M_S = 0 at 2.6 cm^{-1} above it and the S = 1, M_S = ±1 pair at 44.4 cm^{-1} above the ground level. With D_1 positive, the S = 1, M_S = ±1 pair lies 13.8 cm^{-1} above the S = 0, M_S = 0 state and the S = 1, M_S = 0 is 49.8 cm^{-1} above the diamagnetic ground level. These two energy diagrams predict very different magnetic behavior with only the negative sign of D_1 fitting the data, thus clearly establishing the sign.

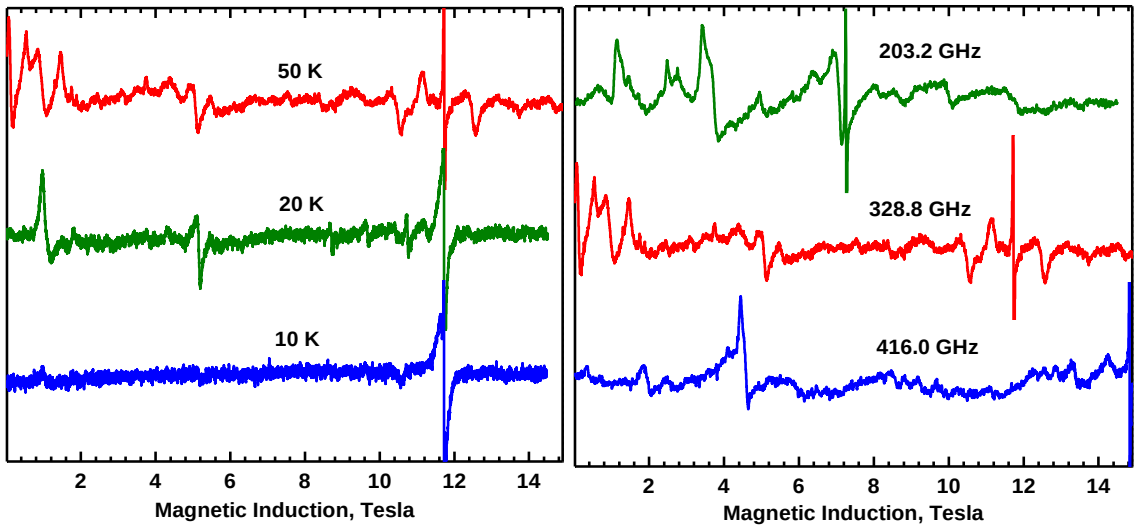

Figure 2.15. Left: EPR spectrum of $[Fe_2(\mu\text{-}F)(\mu\text{-}\mathbf{L_m}^*)_2](BF_4)_3$, **1**, at the temperatures indicated on the figure and ν = 328.8 GHz. The sharp resonance at 11.74 T (g ~ 2.003) is a free-radical contamination. The spectrum intensity decreases with temperature lowering as expected for this antiferromagnetic iron(II) compound. Right: EPR spectrum of **1** recorded at 50 K with microwave frequencies indicated. Note that a resonance near to zero magnetic field is observed at ν = 328.8 GHz.

High-field EPR spectra of **1**, recorded with frequencies 50-420 GHz were very weak and noisy, yet well reproducible and contained large number of resonance lines. Spectra shown in Figure 2.15 are presumably the *first ever observed for an iron(II) dinuclear system where the 'allowed' transitions between states split by D are directly observed.* X-Band spectra of diferrous systems can sometimes be detected even at X-

band. In cases, where E is small compared to D, the X-band active transitions occur between levels like $M_S = 4$ and $M_S = -4$, within an $S = 4$ state, which are split in zero magnetic field by $\sim E^2/D$ (second-order perturbation calculation). Being forbidden, $\Delta M_S = 8$ transitions, they appear at very high effective g values and carry only limited information of the zero-field splitting.[27]

In the present case, the HF EPR spectra could be observed at temperatures as high as 120 K, had best quality at about 50 K and disappeared completely below 10 K, in agreement with the energy diagram derived for $-J = 16$ cm^{-1} and $D_1 = -10$ cm^{-1}. If the 'giant spin' method is applied, $D_1 = -10$ cm^{-1} results in $D_{S=1} = +42$ cm^{-1} in the triplet state ($S = 1$) of the dinuclear compound, $D_{S=2} = +4.28$ cm^{-1} in the $S = 2$ state and $D_{S=3} = -2$ cm^{-1} in the $S = 3$ state. In the present case $-J$ is not large enough compared to D_1 and these relations are somewhat altered due to the spin state mixing – the distance between the $M_S = 0$ and $M_S = \pm 1$ pair of the nominal triplet state is 41.77 cm^{-1} when calculated with Hamiltonian (eq. 6), instead of 42 cm^{-1}. These relatively small differences affect strongly the EPR spectra. With $-J$ and D_1, as determined from the magnetic susceptibility, a resonance at nearly zero magnetic field is expected at 328.8 GHz and it is indeed observed (Figure 2.15). This resonance corresponds to an 'allowed' transition M_S=-2 to M_S=-1 within the nominal $S = 3$ state. A method frequently used in this lab was employed to determine the spin Hamiltonian parameters. Instead of attempting simulation of the powder EPR spectra which is extremely time consuming (the spin Hamiltonian matrix has a size of 25x25 and a powder simulation requires calculation of many thousands of single-crystal type spectra), the frequency dependencies of some well defined resonances were fitted. In the present case, the best defined canonical resonances (at X, Y and Z

orientations) were observed in the 295-334 GHz range and mainly those were used in the fitting procedure.

The fitting did not change much the D_1 and $-J$ values found from the magnetic susceptibility. $g_x = 2.26$, $g_y = 2.29$, $g_z = 1.99$, $-J = 16.0$ cm^{-1}, $D_1 = -9.89$ cm^{-1}, $D_{12} = -0.065$ cm^{-1} were obtained. DFT calculations, like those for the Mn(II) complex above, resulted in $D_1 = -3.6$ cm^{-1} with the largest component of the zfs tensor along the Fe-F axis and therefore there is no need of rotating the D_{12}^{dipolar} tensor. D_{12}^{dipolar} calculated from the point-dipole formula is -0.086 cm^{-1} and compares well to D_{12} above. The UHF calculations ended with error (crashing in the phase of calculating D). The most interesting result here is that D_1 on the iron(II) ions is negative and that the largest zfs component is directed towards the bridge. Negative D_1 values have been reported in strongly elongated trigonal pyramidal iron(II) compounds.[28] Unfortunately, no direction of zfs has been reported, but it is likely to be along the pyramid axis. Those complexes are actually trigonal, having three N atoms in the equatorial plane. Indeed, it is the axially elongated iron(II) trigonal bipyramid which is supposed to exhibit negative D_1.[29] However, the coordination sphere symmetry in our compounds is not perfectly trigonal, but resembles rather C_{2v}, which is responsible for the negative D_1 and its orientation, as confirmed by the DFT results.

Magnetic properties of $[Co_2(\mu\text{-}F)(\mu\text{-}\mathbf{L}_m\mathbf{*})_2](BF_4)_3$ (**2**), $[Ni_2(\mu\text{-}F)(\mu\text{-}\mathbf{L}_m\mathbf{*})_2](BF_4)_3\cdot 2H_2O$ (**3**$\cdot 2H_2O$)**.** No EPR spectra were observed at any temperature and frequency. Large D_1 values, comparable to $-J$ were obtained from the magnetic data fitting. The sign of zfs appears to be well determined, as in the case above for **1**. Large D_1 magnitudes are expected in nickel(II) complexes of low symmetry (idealized C_{2v} here),

yet the D_1 value of 36 cm^{-1} in **3** is surprisingly high, but in the absence of EPR data it has to be accepted. The absence of the HF EPR actually indicates a very large zfs. Besides the parameters in Table 3, the magnetic fit yielded TIP of $150 \cdot 10^{-6}$ emu and mononuclear fraction f = 0.11%. DFT and UHF calculations of D in the nickel(II) complex were unsuccessful. The UHF calculation ended in error and DFT produced a senseless, very small value. The cobalt(II) complex **3** was the most problematic in this series. In the magnetic fitting, a large TIP of $1360 \cdot 10^{-6}$ emu had to be allowed and the fraction on mononuclear impurities (1.0 %) was the highest. The Self-Consistent Field (SCF) procedure did not converge and thus not even a rough estimate of $-J$ or D is available. DFT calculations of the exchange integrals are described separately below. Cobalt(II) may be in an orbitally degenerate state or there may be low-lying excited states, and the entire spin Hamiltonian concept may be not applicable, like in octahedral high-spin cobalt(II) compounds.

Magnetic properties and EPR spectra of the $[Cu_2(\mu\text{-}F)(\mu\text{-}L_m^*)_2](BF_4)_3$, **4** and $[Cu_2(\mu\text{-}F)(\mu\text{-}\mathbf{L_m})_2](BF_4)_3$. Fitting of the magnetic susceptibility data (Figure 2.16) with equations (8) and (10) resulted in $-J$ = 322 cm^{-1} for $[Cu_2(\mu\text{-}F)(\mu\text{-}\mathbf{L_m^*})_2](BF_4)_3$, **4**, $-J$ = 340 cm^{-1} for its perchlorate analogue[9] and 370 cm^{-1} for $[Cu_2(\mu\text{-}F)(\mu\text{-}\mathbf{L_m})_2](BF_4)_3 \cdot 1.5CH_3CN$.[6] Note that equation (10) and spin Hamiltonian (3) with S = 1 were used to interpret the magnetic susceptibility and EPR spectra, respectively, of the copper(II) complexes, opposite to the Mn(II), Fe(II), Co(II) and Ni(II) systems described above which required more advanced treatment by using eqs. 7-9 and spin Hamiltonian (6).

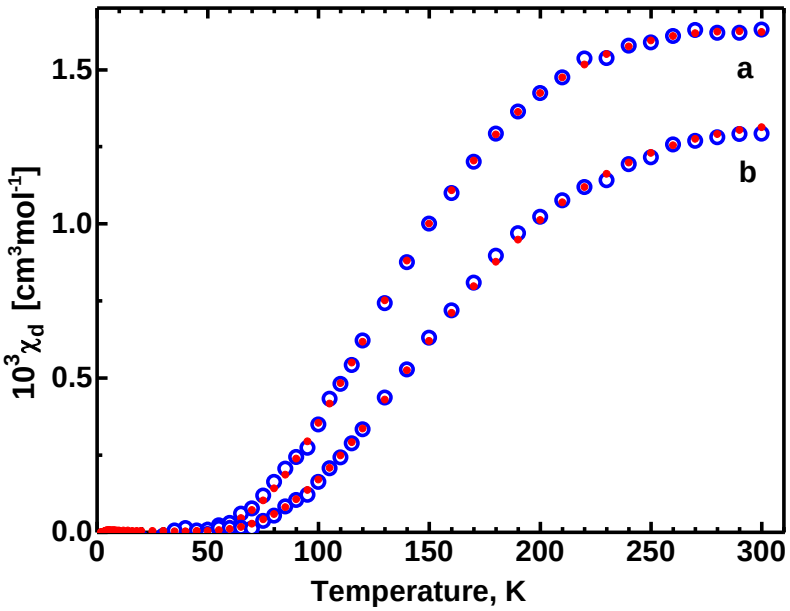

Figure 2.16. Magnetic susceptibility of $[Cu_2(\mu\text{-}F)(\mu\text{-}\mathbf{L}_m\mathbf{*})_2](BF_4)_3$ (a) and $[Cu_2(\mu\text{-}F)(\mu\text{-}\mathbf{L}_m)_2](BF_4)_3$ (b). Circles: experimental, dots: calculated with g_{avg} = 2.22, $-J$ = 322 cm^{-1}, for (a); g_{avg} = 2.16, $-J$ = 370 cm^{-1} for (b). Contributions due to mononuclear impurities were removed from experimental data according to $\chi_d = [\chi_{exp}\text{-}2f\cdot(Ng^2\mu_B{}^2/\,3kT)\cdot 0.75]/(1\text{-}f)$ (see eq. 8). The f values of 0.015 and 0.005 were used for (a) and (b), respectively.

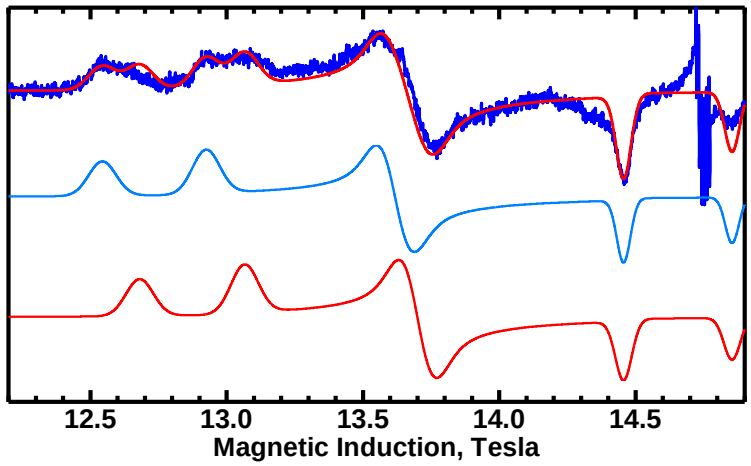

Figure 2.17. Top blue trace: EPR spectrum of $[Cu_2(\mu\text{-}F)(\mu\text{-}\mathbf{L}_m)_2](BF_4)_3\cdot 1.5CH_3CN$ recorded at 150K with ν = 412.8 GHz. The spectrum consists of two components with the following parameters of spin Hamiltonian (eq 3) with S = 1: species 1: g_x = 2.159, g_y = 2.316, g_z = 2.013, D = 0.187 cm^{-1}, E = 0.075 cm^{-1}; species 2: g_x = 2.152, g_y = 2.291, g_z = 2.013, D = 0.187 cm^{-1}, E = 0.075 cm^{-1}. Spectra simulated for species 1 and 2 are plotted as blue and red traces, respectively at the bottom. The top red trace is their sum. Spectrum of Mn(II) centered at 14.77 T (g = 2) is due to the gelatin capsule used as a sample container.

The powder samples of $[Cu_2(\mu\text{-}F)(\mu\text{-}\mathbf{L}_m)_2](BF_4)_3 \cdot 1.5CH_3CN$ exhibit very weak and noisy EPR spectra in which the presence of two $S = 1$ species can be recognized (Figure 2.17), in agreement with the X-ray structure in which two independent species were detected differing in symmetry.[6b] Minuscule differences in the g parameters of the two species can only be seen thanks to the very high microwave frequency. Signals of these two species would collapse into one in standard EPR.

The spectra of **4** were of yet lower quality, possibly due to the presence of several disordered molecules. Powder spectra of **4** proved to be non-interpretable, but fortunately spectra of its frozen solution in CH_3CN at 150 K (Figure 2.18) allowed the extraction of the parameters: $g_x = 2.15$, $g_y = 2.33$, $g_z = 2.01$, $D = 0.173$ cm^{-1}, $E = 0.084$ cm^{-1}, similar to other copper(II) complexes in this family, including that with $\mathbf{L}_m$.

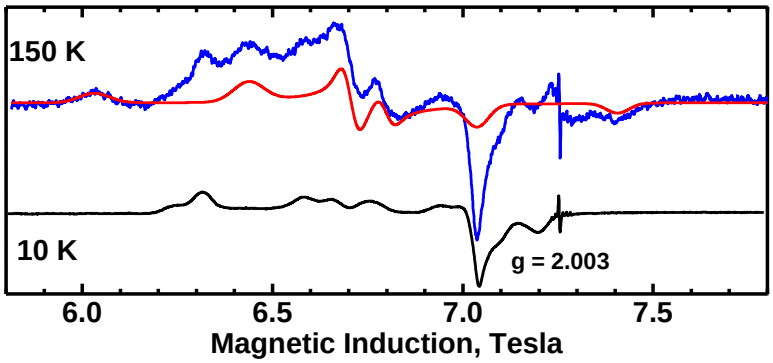

Figure 2.18. EPR spectra of a frozen solution of **4** in CH_3CN. Blue: experimental at 150 K, 203.2 GHz. Red: simulated with $g_x = 2.150$, $g_y = 2.329$, $g_z = 2.010$, $D = 0.173$ cm^{-1}, $E = 0.089$ cm^{-1}. Signals due to paramagnetic impurities are seen, which remain in the low-temperature spectrum (10 K, black trace), whereas signals of the dinuclear species disappear. A sharp line due to traces of a free radical is seen at $g = 2.003$.

One of the g components in these copper(II) complexes, g_z, is very close to 2, indicating that the ground state of Cu(II) is d_{z^2}. This rarely encountered electronic configuration of copper(II) was also confirmed by DFT calculations. Very different

magnitudes of the g_x and g_y components indicate large energy difference between the excited d_{xz} and d_{yz} orbitals of copper(II), according to the approximate formulas below:

$$g_x = 2.0023 - \frac{6\xi}{E(d_{z^2}) - E(d_{yz})}$$

$$g_y = 2.0023 - \frac{6\xi}{E(d_{z^2}) - E(d_{xz})}$$

$$g_z = 2.0023$$

In these formulas, ξ is the spin-orbit coupling constant which may be reduced from its free-ion value of -828 cm^{-1} for copper(II) by the covalence effects. The zero-field splitting in a dinuclear copper(II) complex originates from the magnetic dipole-dipole interactions and from the anisotropic exchange interactions. In the present case, with the Cu···Cu distance of ca. 4 Å, the dipole-dipole contribution to *D* cannot be more negative than -0.045 cm^{-1} (this value is appropriate for spin Hamiltonian (3) and was calculated from the point-dipole model)[23,30a] and the zero-field splitting must originate from the anisotropic exchange like in other dinuclear copper(II) systems.[21-23,30] The zero-field splitting parameters, with relatively large *E* compared to *D* in the copper(II) complexes reported here as well as in reference 9 are unusual compared to other dinuclear copper systems. For example, in the well-known dinuclear copper(II) carboxylates, the *E* parameter ranges from 0 to ~*D*/20. It is now well understood that the exchange-related contribution to zfs in dinuclear complexes is related to the exchange coupling in the single-excited states of a dinuclear molecule, in which one of the copper(II) ions is in its ground state while the other one is in one of the excited states. Only those excited states need be considered which have non-zero matrix elements of the angular momentum operator **L** with the ground state. Maurice et al. performed a sophisticated DFT analysis

of such interactions in copper acetate and derived formulas for the exchange-related D and E.[30a]

$$D = 2\frac{\xi^2 J_{x^2-y^2,xy}}{\Delta E^2_{x^2-y^2,xy}} - \frac{1}{4}\frac{\xi^2 J_{x^2-y^2,xz}}{\Delta E^2_{x^2-y^2,xz}} - \frac{1}{4}\frac{\xi^2 J_{x^2-y^2,yz}}{\Delta E^2_{x^2-y^2,yz}}$$

$$E = \frac{1}{4}\frac{\xi^2 J_{x^2-y^2,xz}}{\Delta E^2_{x^2-y^2,xz}} - \frac{1}{4}\frac{\xi^2 J_{x^2-y^2,yz}}{\Delta E^2_{x^2-y^2,yz}}$$

Symbols like $J_{x2\text{-}y2,xz}$ are the exchange integrals between the $d_{x2\text{-}y2}$ ground orbital of one copper ion and the d_{xz} orbital of another Cu(II). (Note that in the above formulas positive J is considered antiferromagnetic).[30] In the copper acetate case, axis Z joins the two copper ions and the d_{xz} and d_{yz} orbitals of one copper are oriented similarly versus the $d_{x2\text{-}y2}$ orbital of another copper atom. Accordingly, the terms in equations above involving $J_{x2\text{-}y2,xz}$ and $J_{x2\text{-}y2,yz}$ must be of similar magnitude[30a] resulting in a small or equal to zero E parameter. Also, the g_x and g_y components are close to each other because of the similarity of the d_{xz} and d_{yz} arrangenment.

In our case, with d_{z2} being the ground state, only the d_{xz} and d_{yz} orbitals may play a role (as they have non-zero matrix elements of **L** with d_{z2}). The Z axis is along the vertical bipyramid axis, while X joins the copper ions. The d_{xz} orbital of one copper extends two of its lobes towards the bridge and forms a π bond to F^-, but the d_{yz} orbital (perpendicular to the Cu-F direction) cannot form bonds with F^-. It seems thus logical to assume that the d_{xz}-d_{z2} interaction affects the zfs in our copper complex more than d_{yz}-d_{z2}. These two interactions contribute to the D_{yy} and the D_{xx} components of the interaction tensor, respectively (because $|\langle d_{z2}|\mathbf{L}_y|d_{xz}\rangle|^2 = |\langle d_{z2}|\mathbf{L}_x|d_{yz}\rangle|^2 = 3$). To extract the exchange related part of zfs parameters, one subtracts the calculated dipole-dipole contribution from the experimental EPR parameters. This requires knowledge of the sign of the

experimental D parameter,[23] which could not be determined here. Also, the point-dipole model gives very inaccurate results.[30a] Nevertheless, assuming negative D, it is possible to estimate the exchange-related components of the zfs tensor $D_{xx}(ex) = 0.13$ cm^{-1}, $D_{yy}(ex) = 0.26$ cm^{-1}, $D_{zz}(ex) = 0$ which result in the scalar $D_{ex} = -0.195$ cm^{-1} and $E_{ex} = -0.065$ cm^{-1} [pertinent to the spin Hamiltonian (3)].

DFT calculation of the exchange integrals. Estimation of the exchange integrals by "broken symmetry" Density Functional Theory calculations was attempted.[31] The molecules were simplified by removing the methyl groups on pyrazole fragments as well as the benzene rings and placing hydrogen atoms at appropriate positions. All remaining atoms were retained at the positions determined by the X-ray structures. The system of coordinates was chosen so that the X axis was along the M-F vector and the Z axis was perpendicular to the plane of the fluoride and two equatorial nitrogen atoms. The "broken symmetry" procedure applied to a system of two metal ions, A and B, each containing N unpaired spins, first performs a Self-Consistent Field (SCF) calculation for a high-spin molecule (HS) with spin equal to N. In the next stage, another SCF calculation is performed taking all spins on atom A 'up' and all spins on atom B 'down', which is referred to as the broken symmetry solution (BS). Finally, the magnitude of J [for Hamiltonian (1)] is evaluated as $-J = 2(E_{HS} - E_{BS}) / (\langle S^2\rangle_{HS} - \langle S^2\rangle_{BS})$, where E are the energies and $\langle S\rangle^2$ are the expectation values of the spin-squared operator in the HS and BS states.

Ahlrichs-type basis set TZVPP[32a] for copper(II) and SVP[33] for other atoms were used, combined with the B3LYP[33] functional. Ahlrichs polarisation functions from basis H - Kr R and auxiliary bases from the TurboMole library were also used.[32c] The SCF

calculations did not converge in the case of the cobalt(II) complex. The results obtained in other cases appear to be reasonable. Correct sign of -*J* was found while the magnitude of -*J* was overestimated except for the copper(II) complex (Table 2.4). The interactions which contribute to antiferromagnetism of dinuclear complexes involve pairs of overlapping 'magnetic orbitals' localized on both metal ions. Various metal orbitals have very different ability, dictated by symmetry, to interact with the bridging atom, and as a result their relative importance in transmitting the exchange interactions, measured by the overlap integral[34] of the magnetic orbitals, is also very unequal.

The d^9, copper(II) complex **4** is best to describe first. As has been treated previously by Hoffmann[8b] for a different bridging system, in this trigonal bipyramidal geometry with the coordinates chosen as above, the magnetic orbital has mainly d_{z^2} character. The calculations show that the key orbitals influencing the magnetic properties are the symmetric antibonding combination formed by the "magnetic orbitals" of the metal (mainly consisting of the metal d orbitals, but delocalized onto the ligands) with the s orbitals and the antisymmetric antibonding combination with the p_x orbital of the bridging group (Figure 2.19). The p_x orbital interacts more strongly, so the antisymmetric orbital is relatively high in energy, stabilizing the singlet state and producing the large –*J* values. The calculated energy difference between the antisymmetric and symmetric orbitals containing the d_{z^2} orbitals of two copper(II) ions is 0.532 eV (4290 cm^{-1}, average for the spin-up and spin-down energies).

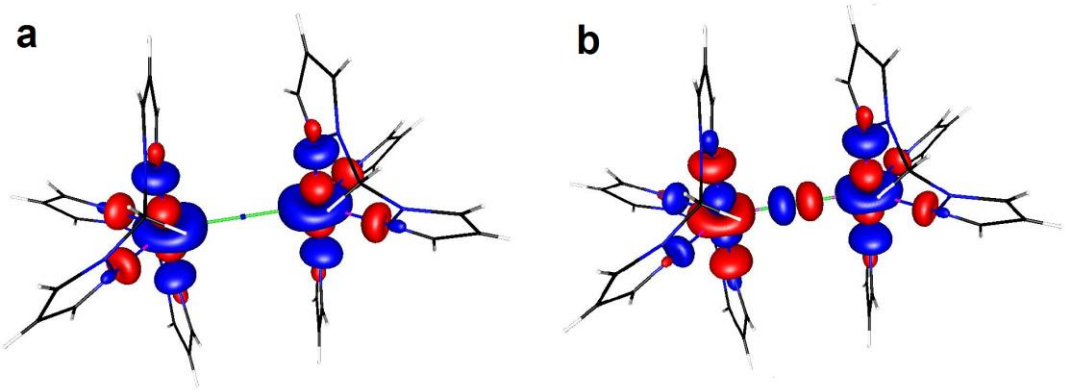

Figure 2.19. The symmetric (a) and antisymmetric (b) combination of the copper(II) d_{z^2} orbitals with the bridging F^- orbitals of appropriate symmetry (s and p, respectively) in the model compound $[Cu_2(\mu\text{-}F)(\text{bis(1-pyrazolyl)methane})_4]^{3+}$.

In the multi-electron ions Mn(II), Fe(II), Co(II) and Ni(II) studied here, there are more contributions to the exchange interactions, which are associated with the symmetric and antisymmetric combinations involving other d orbitals of the two metal ions; the four combinations for nickel(II) are shown in Figure 2.20.

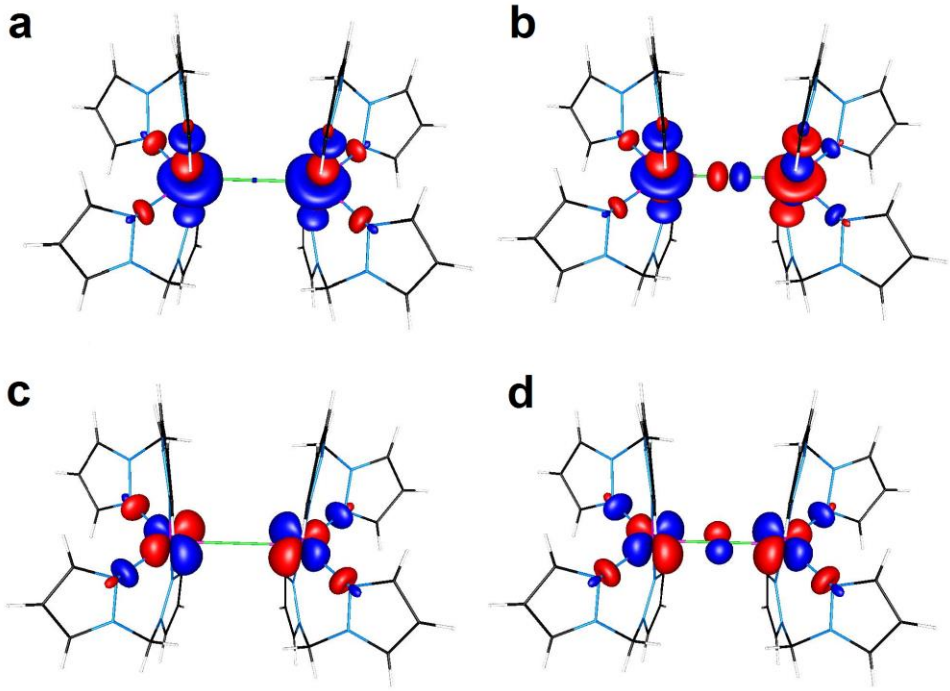

Figure 2.20. The symmetric (a, c) and antisymmetric (b, d) combination of the nickel(II) d_z^2 and $d_{x^2-y^2}$ orbitals with the bridging F^- orbitals of appropriate symmetry (s and p, respectively) in the model compound $[Ni_2(\mu\text{-}F)(\text{bis(1-pyrazolyl)methane})_4]^{3+}$.

Analysis of the "broken symmetry" results indicates that the energy of the symmetric and antisymmetric orbitals increase in the sequence yz(s) < yz(a) < x^2-y^2(s) < xz(s) < x^2-y^2(a) < xz(a) < xy(s) < xy(a) < z^2(s) < z^2(a) for the manganese(II) complex and yz(s) < yz(a) < x^2-y^2(s) < xz(s) < xz(a) < x^2-y^2(a) < xy(s) < xy(a) < z^2(s) < z^2(a) for the iron(II) complex. Only the last of the orbitals listed here contain unpaired electron in the case of copper(II), while xy and z^2 are the SOMOs (singly occupied molecular orbitals) for nickel(II), all except yz are SOMOs for iron(II) and finally each of the five d orbitals contains one unpaired electron in manganese(II). The cobalt(II) complex will not be discussed here since the DFT calculations failed in this case. The d_{yz} metal orbitals cannot interact with the bridging atom and thus the energy of the symmetric and antisymmetric combinations will be almost the same resulting in no contribution to the antiferromagnetic exchange. The only case where d_{yz} has to be considered is in the manganese(II) complex.

The situation is relatively simple in the nickel(II) complex, since the d_z^2 and d_{xy} SOMOs do not interfere with each other, the former only engaging in the σ bonds and the latter only in π bonds to the bridging ligand. The two magnetic orbitals are pure and their respective d_z^2 and d_{xy} character is easily recognizable (Figure 2.20).

In the iron(II) and manganese(II) complexes, a d_{x2-y2} SOMO is also present. It engages in σ bonds with the bridging fluoride and the resulting magnetic orbital, being a mixture of d_{z2} and d_{x2-y2}, does not possess a readily recognizable shape, Figure 2.21 and 2.22.

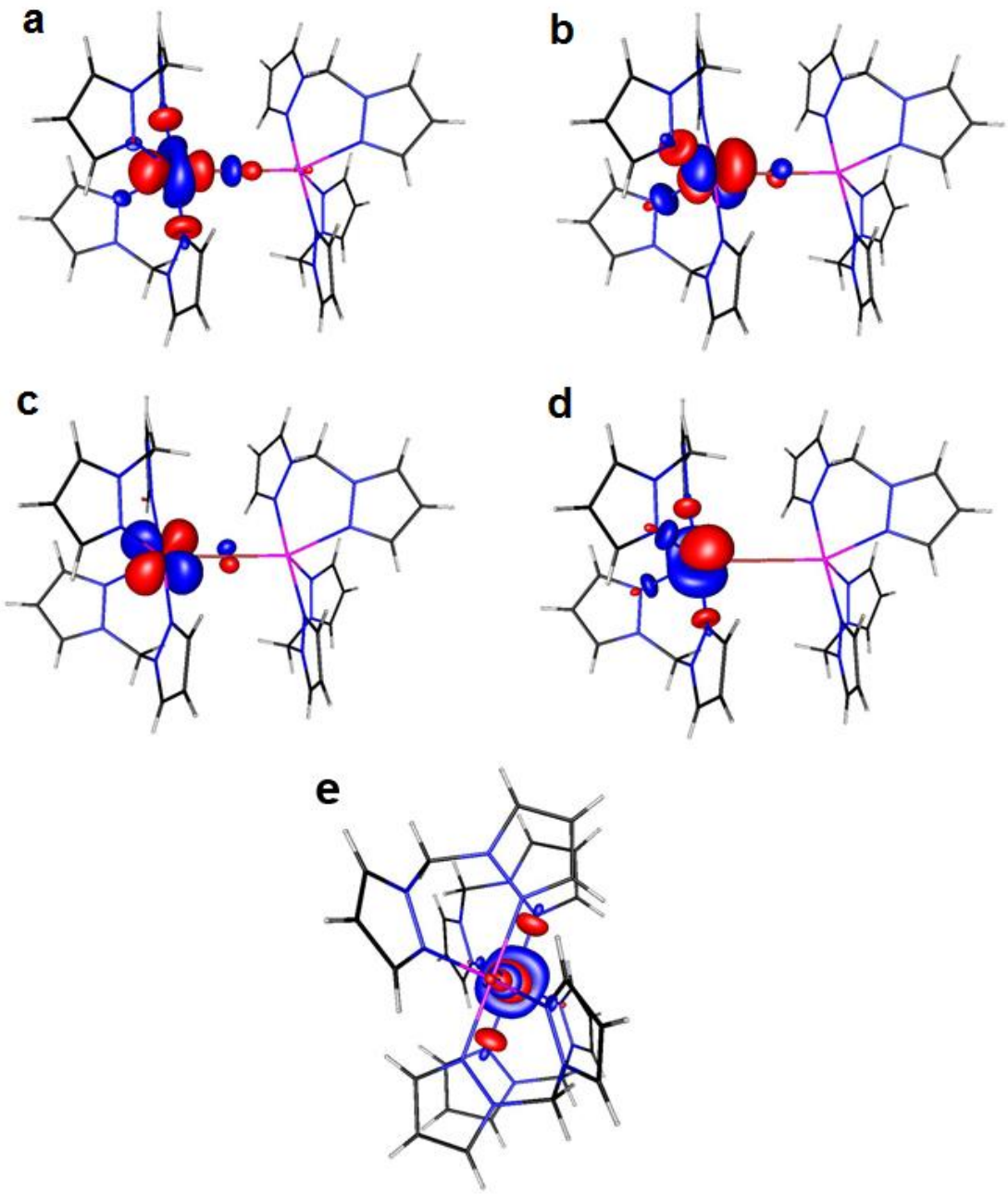

Figure 2.21. The magnetic orbitals for the model compound $[Fe_2(\mu\text{-}F)(bis(1\text{-}pyrazolyl)methane)_4]^{3+}$: (a) S = 0.100, mixed d_z^2 and $d_{x^2-y^2}$ character; (b) S = 0.046, d_{xy} character; (c) S = 0.032, d_{xz} character; (d) S = 0, mixed d_z^2 and $d_{x^2-y^2}$ character; (e) head-on view of magnetic orbital (a), it looks like d_z^2 along the Fe-F direction, but is actually a mixture of d_z^2 along the trigoanl bipyramid main axis and the $d_{x^2-y^2}$ in the trigonal plane.

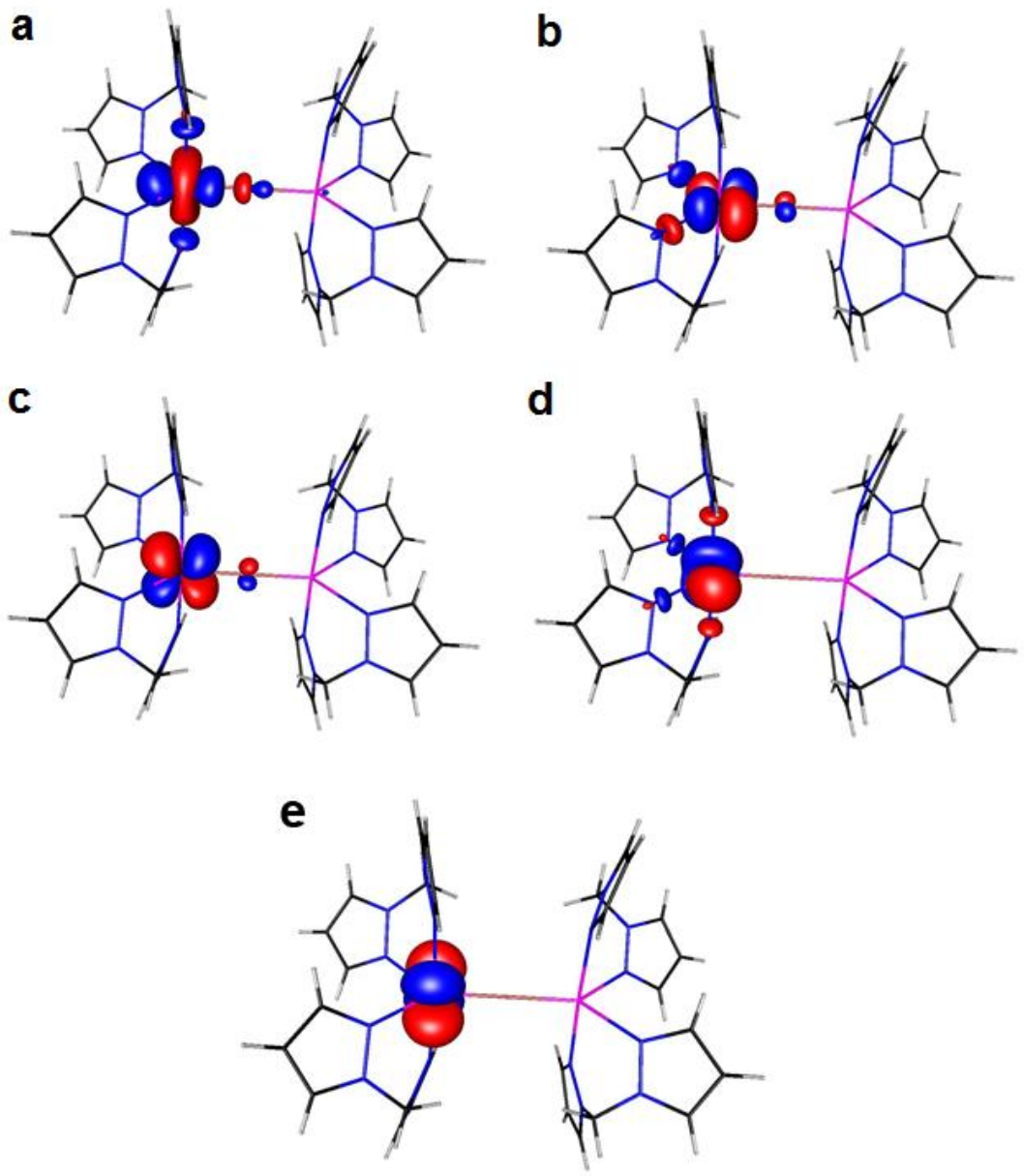

Figure 2.22. The magnetic orbitals for the model compound $[Mn_2(\mu\text{-F})(\text{bis(1-pyrazolyl)methane})_4]^{3+}$: (a) S = 0.084, mixed d_z^2 and $d_{x^2-y^2}$ character; (b) S = 0.049, d_{xy} character; (c) S = 0.037, d_{xz} character; (d) S = 0.003, mixed d_z^2 and $d_{x^2-y^2}$ character; (e) S = 0.001, d_{yz} character.

Note that the magnetic orbitals in (a) and (d) in Figure 2.21 for iron(II) and Figure 2.22 for manganese(II) are those mixed ones. In the antisymmetric or symmetric combinations, the d_{z2} and d_{x2-y2} shapes are seen, but in the magnetic orbitals they are

combined. An important quantity allowing assessing the contribution of an exchange pathway to the overall antiferromagnetic interaction is the overlap integral between the magnetic orbitals of two interacting metal ions. Table 2.5 shows that the magnetic orbitals engaged in σ bonds to the bridging ligand contribute the most to the exchange interactions.

Table 2.5. Spin densities and orbital interactions as calculated from the "broken symmetry" DFT method.

Complex of	**Mn(II)**	**Fe(II)**	**Ni(II)**	**Cu(II)**
		Spin density		
Metal d_{yz}	0.979	0.080	0.008	0.008
Metal d_{xz}	0.967	0.960	0.005	0.001
Metal d_{x2-y2}	0.951	0.910	0.019	0.025
Metal d_{xy}	0.927	0.908	0.867	0.009
Metal d_{z2}	0.904	0.851	0.791	0.663
F p_x	0.013	0.027	0.030	0.035
F p_y	0.021	0.024	0.030	0.000
F p_z	0.018	0.020	0.000	0.000
		E_{anti}-E_{sym} **(eV)**[a]		
yz	0.014	-	-	-
xz	0.267	0.299	-	-
x^2-y^2	0.176	0.336	-	-
xy	0.339	0.303	0.265	-
z^2	0.417	0.276	0.421	0.532
		Overlap integral between the magnetic orbitals (*S*)		
yz	0	-	-	-
xz	0.037	-	-	-
x^2-y^2	[b]	[b]	-	-
xy	0.049	0.046	0.042	-
z^2	0.084[b]	0.100[b]	0.075	0.125
		Exchange Integral (-*J*)		
Calc., DFT	14	28	55	380
Exp.	6.7	16.3	39	322

[a]Calculated from the averages of the spin-up and spin-down energies of the respective antisymmetric and symmetric orbitals. [b]The x^2-y^2 and z^2 magnetic orbitals are combined.

The calculated exchange integrals were in a half-quantitative agreement with the experiment, being significantly too large (except for the copper(II) case). Often, an

empirical factor of 0.5 is applied to the exchange integral values calculated from DFT,[35] and indeed this would result in a better agreement between our calculated and experimental -*J* values (except for the copper(II) complex **4**). This correction was not introduced here.

The differences between the antisymmetric and symmetric combinations in Table 2.5 are similar for all metals (for the orbitals of the same type) and the overlap integrals are similar, yet the exchange integrals are very different. The relations between the exchange integrals and the orbital energies involve the square of the number of the unpaired electrons, n^2.[8b] When the -*J* values in Table 2.5 are multiplied by n^2 then the resulting numbers are of the same order of magnitude.

Discussion

The preparation of the new third-generation $\mathbf{L_m}$***** ligand, containing 3,5-dimethyl group substitution on the pyrazolyl rings, has allowed the syntheses of seven dinuclear cations of the formula $[M_2(\mu\text{-}F)(\mu\text{-}\mathbf{L_m}\mathbf{*})_2]^{3+}$ [M = Mn(II), Fe(II), Co(II), Ni(II), Cu(II) and Zn(II) and Cd(II)], all with essentially the same metallacyclic structure containing a linear M-F-M core, a virtually unknown arrangement in dinuclear complexes prior to this work. While previously analogous complexes with the unsubstituted ligand $\mathbf{L_m}$ was prepared, only the M = Fe(II), Co(II), Cu(II) and Zn(II) complexes could be isolated; dibridged $[M_2(\mu\text{-}F)_2(\mu\text{-}\mathbf{L_m}\mathbf{*})_2]^{2+}$ form with the metals Ni(II) and Cd(II). Clearly the difference in the two systems relates to the steric influence of the 3,5-dimethyl groups, where space filling models (Figure 2.23) show the methyl groups in the metallacycles are close to each other and the linking arene groups. This conclusion is supported by the

unusual chemical shifts reported for one set of methyl resonances in both the ^{1}H and ^{13}C NMR spectra. In this substituted system, dibridging fluoride is sterically blocked. Steric effects also support the axially compressed, trigonal bipyramidal geometry around the metal centers over the more favored apically elongated square pyramidal,[36,37] where the severe compression of the axial bond lengths in $[Cu_2(\mu\text{-}F)(\mu\text{-}\mathbf{L}_m\mathbf{*})_2]^{3+}$ is explained, in addition, by the pseudo Jahn-Teller (PJT) effect.[38]

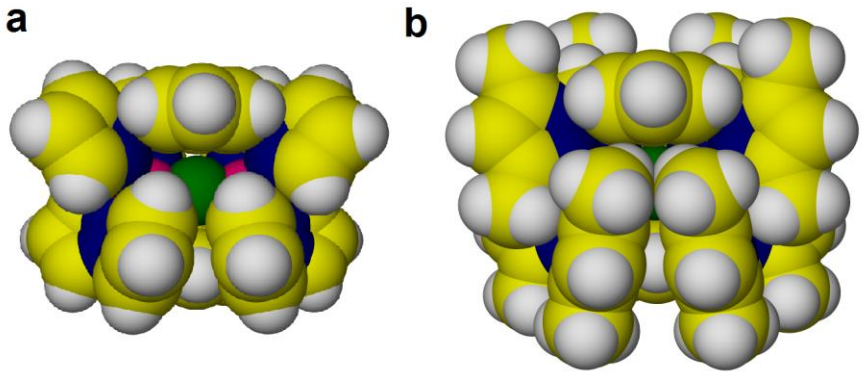

Figure 2.23. Space filling model of $[Zn_2(\mu\text{-}F)(\mu\text{-}\mathbf{L}_m)_2](BF_4)_3$ (a) and $[Zn_2(\mu\text{-}F)(\mu\text{-}\mathbf{L}_m\mathbf{*})_2](BF_4)_3$ (b).

The most obvious trend in comparing the $[M_2(\mu\text{-}F)(\mu\text{-}\mathbf{L}_m\mathbf{*})_2]^{3+}$ structures of the six first row metals is the *lack of trends* in the overall geometry of the metals and the M-F bond lengths. Scheme 2.3 shows plots of the predicted[17] and actual M-F and average M-N bond lengths. The changes in the M-N bond lengths track those predicted from the change in ionic radii of the metal(II) cation, although with the exception of manganese(II) all are somewhat shorter. In contrast, the actual M-F bond lengths are *nearly constant* within 0.04 Å with the longest recorded for nickel(II), even though it is the smallest cation.[17] Clearly, the M-F or more exactly M-F-M lengths are being slightly elongated, with the exception of the largest metal manganese(II), and held constant by the bridging $\mathbf{L}_m\mathbf{*}$ ligands. The same trends were observed previously in the $\mathbf{L}_m$ system, where the M-F bond lengths also vary by only 0.04 Å and did not track the metal ionic radii.

Importantly, the overall M-F average in the $\mathbf{L}_m$ system is 1.96 Å, 0.09 Å shorter than the 2.05 Å average for the $\mathbf{L}_m$* system. This difference is again explained by the increased steric crowding in the $\mathbf{L}_m$* system. As with manganese(II), the Cd-F bond length in $[Cd_2(\mu\text{-F})(\mu\text{-}\mathbf{L}_m\text{*})_2]^{3+}$ matches that predicted for the larger cadmium(II) ion. The larger size of these two metals "fits" the favored M-F-M distance of the $\mathbf{L}_m$* ligands. It is the elongated M-F distances for the other metals, forced by the $\mathbf{L}_m$* ligands, that explains the observed contracted M-N distances shown in Scheme 3.

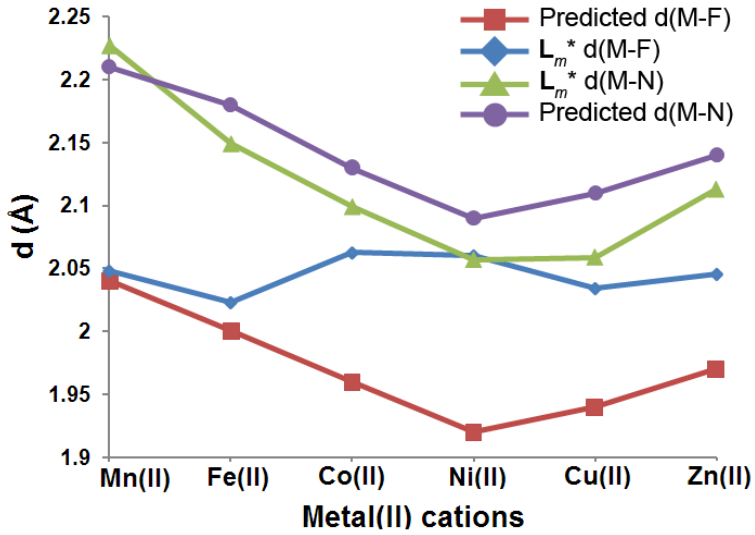

Scheme 2.3. Plot of the metal(II) cations (listed in order of increasing Z) vs. predicted M-F and M-N (based on ionic radii) and observed the M-F [average for Mn(II)] and average M-N bond distances in compounds **1-5** and **7**.

There are very few previous examples of dinuclear complexes with linear or nearly linear single fluoride bridges for comparison. A zinc(II) dimetallic complex bonded to a ligand containing a 1,3-substituted pyridine with bis(imidazolyl)methylene donor groups contains a linear M–F–M arrangement in a discrete dinuclear complexes where the Zn-F distance is 1.99 Å, close to the predicted value.[39] Three other octahedral complexes, one of copper(II)[40] and two of nickel(II)[41,42] with M-F-M angles ranging from 161 to 177°

have been reported. Our ability to prepare this extensive series of complexes with this unique linear M-F-M arrangement is forced/supported by the third-generation bis(pyrazolyl)methane ligand reported in this work, the bulky $\mathbf{L}_{m}$**.

It is interesting to compare the structural behavior of the copper(II) $\mathbf{L}_{m}$ and $\mathbf{L}_{m}$* compounds with other Cu(II)[bis(pyrazolyl)methane]$_2$-compounds, the metal that has the largest number of known complexes of these types. The parent $H_2C(pz)_2$ ligand forms six-coordinate $[Cu[H_2C(pz)_2]_2Cl(H_2O)]^+$ with all four pyrazolyl rings in the equatorial positions of an octahedron.[43] Copper(II) compounds with bulkier bis(pyrazolyl)methane ligands, e.g. $[Cu[H_2C(3,5\text{-}Me_2pz)_2]_2Cl]_2(CuCl_4)$,[44] $[Cu[H_2C(3,5\text{-}Me_2pz)_2]_2(CH_3OH)](ClO_4)_2$,[44] and $[Cu_2[H_2C(3,5\text{-}Me_2pz)_2]_4(ta)](ClO_4)_2$[45] ($H_2ta$ = terephthalic acid) form axially elongated square pyramidal geometries around the copper(II) center, with three pyrazolyl rings in the equatorial plane and one in the axial position (τ_5 values are between 0.04 to 0.47). As the steric crowding of the complex is increased, upon using *iso*-propyl substituted pyrazolyl groups, e.g. $[Cu([H_2C(3\text{-}i\text{-}Pr\text{-}pz)_2])_2(H_2O)]_2(ClO_4)_2$,[44] the geometry around the copper(II) changes from axially elongated square pyramidal to axially compressed trigonal bipyramidal geometry (τ_5 = 0.64, Cu-N_{ax} = 1.940 Å, Cu-N_{eq} = 2.174 Å). Thus, as the steric interactions built into the ligands increase the copper(II) coordination changes from octahedral, to square pyramidal to trigonal bipyramidal geometry. The bulky third generation bis(pyrazolyl)methane ligands $\mathbf{L}_{m}$ and especially $\mathbf{L}_{m}$* stabilize the metallacycle and the less stable compressed trigonal bipyramidal arrangement.

The NMR studies clearly indicate these metallacycles hold structure in solution. Most definitive on this issue are the ^{19}F and ^{113}Cd spectra of the $[Cd_2(\mu\text{-}F)(\mu\text{-}\mathbf{L}_{m}\text{*})_2]^{3+}$

cation that show appropriate chemical shift[3d] and coupling as expected for the Cd-F-Cd core arrangement and the two sets of ^{1}H and ^{13}C pyrazolyl ring resonaces expected from the solid state structures. The stability of the metallacycles is also highlighted by the positive-ion electrospray mass spectra of all seven complexes that show clusters such as $[M_2(\mathbf{L}_m\mathbf{*})_2F(A)_2]^+$ (A = BF_4^- or ClO_4^-) and $[M_2(\mathbf{L}_m\mathbf{*})_2F]^{3+}$.

Both copper(II) $[Cu_2(\mathbf{L})_2F]^{3+}$ metallacycles, with **L** = $\mathbf{L}_m$ and $\mathbf{L}_m\mathbf{*}$, represent the first examples of linear single fluoride bridged dinuclear compounds, where copper(II) is in this unusual, axially compressed trigonal bipyramidal coordination environment. This architecture leads to substantial antiferromagnetic interactions, $-J$ = 322 and 370 cm^{-1} respectively, comparable with the ones measured in copper(II) acetate dimers[46] (usually $-J$ = 300-350 cm^{-1}). For comparison, Noro and co-workers[40] recently reported $[Cu_2F(BF_4)_3(4\text{-phpy})_7]$ (4-phpy = 4-phenylpyridine) where the axially elongated octahedral Cu(II) centers, linearly bridged by F^- (Cu1···Cu2 4.12 Å; Cu1-F-Cu2 177.5˚), are orthogonally positioned with respect to each other (Jahn-Teller axes of Cu1 and Cu2 are not parallel) resulting in ferromagnetic interactions (J = 13.2 cm^{-1}). Another example of a bent monofluoride bridged copper(II) compound (Cu1-F-Cu2 115.12˚) from the Christou group,[47] $[Cu_2F(OAc)_2L]BF_4$, L = 1,2-bis(2,2'-bipyridil-6-yl)ethane, places the copper(II) centers in square pyramidal coordination environment. Due to the counter complementarity of the bridging ligands, ferromagnetic behavior was again observed (J = 15.6 cm^{-1}).

Little data exists for the other metals. Antiferromagnetic superexchange interactions of similar magnitude to **3**·$2H_2O$ ($-J$ = 39.0 cm^{-1}) were reported for $[Ni_2(L)_2F](BF_4)_3$,[41] L = 2,5,8-trithia[9],(2,9)-1,10-phenanthro-linophane, one of the two[42] dinuclear compounds

with almost linear fluoride bridges with other metals. The nickel(II) centers are in a distorted octahedral coordination environment (Ni···Ni' 3.887 Å; Ni-F-Ni' 161.31°) and -*J* is 40 cm^{-1}.

The theory of the isotropic exchange interactions in dinuclear and polynuclear complexes is well understood. Antiferromagnetic interactions are transmitted through the magnetic orbitals localized on individual metal ions, provided that these magnetic orbitals overlap. Interactions between non-overlapping orbitals lead to ferromagnetic contributions. The "broken symmetry" method, developed to calculate the exchange integrals, is becoming a standard tool of coordination chemistry. DFT calculations in this work reproduced the experimental -*J* values semi-quantitatively and allowed identification of the orbital interactions which contribute to the exchange interactions. The magnetic results reported here represent the first test of the theory for a series of complexes of different metals in dinuclear complexes with linear M-F-M bridges. Both theory and experimental results show the trend is increasing antiferromagnetic coupling interactions as one moves to the right across the periodic table from manganese(II) to copper(II), with the interaction for copper(II) being much larger.

The zero-field splitting (zfs) is a much more complicated problem. Even in mononuclear complexes of metal ions with S > 1/2, the theoretical calculation of the zfs parameters is still a challenge. This zfs in a form of D_1, provides the bulk of the zero-field splitting in dinuclear complexes of multi-electron ions, as seen in our manganese(II) and iron(II) complexes. Because of its magnitude, it also renders such complexes unsuitable for the standard X or Q-band EPR techniques. The spectrum of our iron(II) complex

appears to be the first ever observed, thanks to the very high microwave frequencies and magnetic fields applied in this study.

In the theoretical calculations, the interaction term D_{12} is a greater challenge yet than D_1. It contains both the magnetic dipolar interaction and the anisotropic exchange interaction, which is a contribution mediated by the spin-orbit coupling and is the most difficult to evaluate by theory. To our knowledge, only one successful calculation of D_{12} (in copper acetate) has been reported so far.[30a]

Conclusion

The new ditopic ligand *m*-bis[bis(3,5-dimethyl-1-pyrazolyl)methyl]benzene (**L*m****) has been prepared and used to synthesis the series of metal complexes $[M_2(\mu\text{-F})(\mu\text{-}\mathbf{L}_{\boldsymbol{m}}\mathbf{*})_2]^{3+}$ (M = Mn(II), Fe(II), Co(II), Ni(II), Cu(II) and Zn(II) and Cd(II)) that have metallacyclic structures and are the first series with the *linear M-F-M core*. The metal ions are all in a distorted trigonal bipyramidal geometry in the solid state, an arrangement that is maintained in solution. The bridging ditopic ligands causes the M-F bond lengths to remain nearly constant despite the changes in the ionic radii of the cations along the series. The paramagnetic compounds with the metals from manganese(II) to copper(II) are antiferromagnetically coupled, with the magnitude of the coupling increasing along the series from left to right across the periodic table; the coupling is very large for copper(II), at 322 cm^{-1}. The spin Hamiltonian parameters, determined from the high-frequency EPR spectra of the manganese(II) and iron(II) complexes showed that the zero-field splitting in the dinuclear systems is mainly caused by the zfs splitting on single ions. In the copper(II) complexes, the zfs is dominated by the anisotropic exchange interactions. The lack of axial symmetry of the latter and of the EPR *g* factor can be

understood by considering the arrangement of the copper d_{xz} and d_{yz} orbitals versus the bridging fluoride. Both the magnetic and EPR data are supported by DFT calculations.

References

(1) (a) Zhao, D.; Timmons, D. J.; Yuan, D.; Zhou, H.-C.; *Acc. Of Chem. Res.* **2011**, *44*, 123. (b) Northrop, B. H.; Yang, H.-B.; Stang, P. J. *Chem. Commun.* **2008**, *45*, 5896. (c) Chen, C.-L; Zhang, J.-Y.; Su, C.-Y *Eur. J. Inorg. Chem.* **2007**, 2997. (d) Dul, M.-C.; Pardo, E.; Lescouëzec, R.; Journaux, Y.; Ferrando-Soria, J.; Ruiz-García, R.; Cano, J.; Julve, M.; Lloret, F.; Cangussu, D.; Pereira, C. L. M.; Stumpf, H. O.; Pasán, J.; Ruiz-Pérez, C. *Coord. Chem. Rev.* **2010**, *254*, 2281. (e) Pariya, C.; Fronczek, F. R.; Maverick, A. W. *Inorg. Chem.* **2011**, *50*, 2748. (f) Clegg, J. K.; Bray, D. J.; Gloe, K.; Hayter, M. J.; Jolliffe, K.; Lawrance, G. A.; Meehan, G. V.; McMurtrie, J. C.; Lindoy, L. F.; Wenzel, M. *Dalton Trans.* **2007**, 1719. (g) Su, C.-Y.; Cai, Y.-P.; Chen, C.-L.; Smith, M. D.; Kaim, W.; zur Loye, H.-C. *J. Am. Chem. Soc.* **2003**, *125*, 8595.

(2) (a) Reger, D. L.; Foley, E. A.; Smith, M. D. *Inorg. Chem. Comm.* **2010**, *13*, 568. (b) Reger, D. L.; Foley, E. A.; Semeniuc, R. F.; Smith, M. D. *Inorg. Chem.* **2007**, *46*, 11345. (c) Reger, D. L.; Gardinier, J. R.; Bakbak, S.; Semeniuc, R. F.; Bunz, U. H.; Smith, M. D. *New J. Chem.* **2005**, *29*, 1035.

(3) (a) Titze, C.; Hermann, J.; Vahrenkamp, H. *Chem. Ber.* **1995**, *128*, 1095. (b) Reger, D. L.; Elgin, J. D.; Foley, E. A.; Smith, M. D.; Grandjean, F.; Long, G. J. *Inorg. Chem.* **2009**, *48*, 9393. (c) Reger, D. L.; Grattan, T. C.; Brown, K. J.; Little, C. A.; Lamba, J. J. S.; Rheingold, A. L.; Sommer, R. D. J. *Organomet. Chem.* **2000**, *607*, 120. (d) Weis, K.; Vahrenkamop, H. *Inorg. Chem.* **1997**, *36*, 5592.

(4) (a) Reger, D. L.; Watson, R. P.; Smith, M. D.; Pellechia, P. J. *Cryst. Growth Des.* **2007**, 7, 1163. (b) Reger, D. L.; Watson, R. P.; Gardinier, J. R.; Smith, M. D. *Inorg. Chem.* **2004**, *43*, 6609. (c) Reger, D. L.; Watson, R. P.; Smith, M. D. *J. Chem. Crystallogr.* **2008**, *38*, 17. (d) Reger, D. L.; Semeniuc, R. F.; Smith, M. D. *Dalton Trans.* **2008**, 2253.

(5) (a) Reger, D. L.; Watson, R. P.; Smith, M. D. *J. Organomet. Chem.* **2007**, *692*, 5414. (b) Reger, D. L.; Watson, R. P.; Smith, M. D. *J. Organomet. Chem.* **2007**, *692*, 3094. (c) Reger, D. L.; Watson, R. P.; Smith, M. D.; Pellechia, P. J. *Organometallics*, **2005**, *24*, 1544.

(6) (a) Reger, D. L.; Watson, R. P.; Smith, P. J. *Inorg. Chem.* **2006**, *45*, 10077. (b) Reger, D. L.; Foley, E. A.; Watson, R. P.; Pellechia, P. J.; Smith, M. D., Grandjean, F.; Long, G. J. *Inorg. Chem.* **2009**, *48*, 10658. (c) Reger, D. L.; Foley, E. A.; Watson, R. P.; Pellechia, P. J.; Smith, M. D. *Inorg. Chem.* **2011**, *50*, 2704. (d) Reger, D. L.; Watson, R. P.; Gardinier, J. R.; Smith, M. D.; Pellechia, P. J. *Inorg. Chem.* **2006**, *45*, 10088. (e) Reger, D. L.; Foley, E. A.; Smith, M. D. *Inorg. Chem.* **2009**, *48*, 936.

(7) Selected examples: (a) Nadeem, M. A.; Bhadbhade, M; Stride, J. A. *Dalton Trans.* **2010**, *39*, 9860. (b) Ding, K.; Dugan, T. R.; Brennessel, E. B.; Holland, P. L. *Organometallics* **2009**, *28*, 6650. (c) Vela, J.; Smith, J. M.; Yu, Y.; Ketterer, N. A.; Flaschenriem, C. J.; Lachicotte, R. J.; Holland, P. L. *J. Am. Chem. Soc.* **2005**, *127*, 7857.

(d) Zhu, Q.; Nelson, K. J.; Shum, W. W.; DiPasquale, A.; Rheingold, A. L.; Miller, J. S. *Inorg. Chim. Acta* **2009**, *362*, 595. (e) Birk, T.; Magnussen, M. J.; Piligkos, S.; Weihe, H.; Holten, A.; Benidx, J. *J. Fluor. Chem.* **2010**, *131*, 898. (f) Tomat, E.; Cuesta, L.; Lynch, V. M.; Sessler, J. L. *Inorg. Chem.* **2007**, *46*, 6224. (g) Casellas, H.; Pevec, A.; Kozlevčar; Gamez, P.; Reedijk, J. *Polyhedron* **2005**, *24*, 1549. (h) Wang, C.-M.; Liao, C.-H.; Kao, H.-M.; Lii, K.-H. *Inorg. Chem.* **2005**, *44*, 6294. (i) Leo, R.; Massa, W.; Pebler, J. *J. Fluor. Chem.* **2004**, *125*, 923. (j) Choudhury, A.; Rao, C. N. R. *J. Struct. Chem.* **2002**, *43*, 632. (k) Worm, K.; Chu, F.; Matsumoto, K; Best, M. D.; Lynch, V.; Anslyn, E. V. *Chem. Eur. J.* **2003**, *9*, 741. (l) Blake, A. J., Devillanova, F. A.; Garau, A.; Harrison, A.; Isaia, F.; Lippolis, V.; Tiwary, S. K.; Schröder, M.; Verani, G.; Whittaker, G. *J. Chem. Soc. Dalton Trans.* **2002**, 4389.

(8) (a) Kahn, O. *Molecular Magnetism*; VCH Publishers, Inc.: New York, **1993**. (b) Hay, P. J.; Thibeault, J. C.; Hoffmann, R. *J. Am. Chem. Soc.* **1975**, *97*, 4884.

(9) Reger, D. L.; Pascui, A. E.; Smith, M. D.; Jezierska, J.; Ozarowski, A. *Inorg. Chem.* **2012,** *51*, 7966.

(10) Hassan, A. K.; Pardi, L. A.; Krzystek, J.; Sienkiewicz, A.; Goy, P.; Rohrer, M.; Brunel, L.-C. *J. Magn. Reson.* **2000**, *142*, 300.

(11) (a) O'Connor, C. J. *Prog. Inorg. Chem.* **1982**, *29*, 203. (b) Bain, G. A.; Berry, J. F. *J. Chem. Ed.* **2008**, *85*, 532.

(12) (a) Barbour, L. J *J. Supramol. Chem.* **2003**, *1*, 189. (b) *POV-RAY 3.6*, **2006**, Persistence of Vision Raytracer Pty Ltd, Williamstown, Vic., Australia. (c) MestReNOVA v.5.2.5, Mesrelab Research S. L. **2008**. (d) Laaksonen, L. gOpenMol version 3.00 www.csc.fi/english/pages/g0penMol.

(13) SMART Version 5.630, SAINT+ Version 6.45 and SADABS Version 2.10. Bruker Analytical X-ray Systems, Inc., Madison, Wisconsin, USA, 2003.

(14) Sheldrick, G. M. *Acta Cryst*. **2008**, *A64*, 112.

(15) Peterson, L. K.; Kiehlmann, E.; Sanger, A. R.; Thé, K. I. *Can. J. Chem.* **1974**, *52*, 2367.

(16) Addison, A. W.; Rao, T. N.; Reedijk, J.; Van Rijn, J.; Verschoor, G. C. *J. Chem. Soc. Dalton Trans*. **1984**, 1349.

(17) Shannon, R. D. *Acta Crystallogr.* **1976**, *A32*, 751.

(18) (a) Kepert, D. L. in "*Inorganic Chemistry Concepts*" Springer-Verlag, New York 1982, Vol. *6*, 36. (b) Pearson, R. G. *J. Am. Chem. Soc.* **1969**, *91*, 4947. (c) Pearson, R. G. *Proc. Nat. Acad. Sci. USA* **1975**, *72*, 2104. (d) Bartell, L. S. *J. Chem. Educ.* **1963**, *45*, 754.

(19) Zabrodsky, H.; Peleg, S.; Avnir, D. *J. Am. Chem. Soc.* **1993**, 115, 8278.

(20) (a) Spek, A. L. *ActaCrystallogr., Sect A* **1990**, *46*, C34. (b) PLATON, A Multipurpose Crystallographic Tool, Utrecht University, Utrecht, The Netherlands, Spek, A. L. **1998**.

(21) Bencini, A.; Gatteschi, D. In *EPR of Exchange Coupled Systems*; Springer Verlag: Berlin-Heidelberg, 1990.

(22) Bleaney, B. in "*Electron Spin Resonance of Transition Ions",* Clarendon Press: London, 1970.

(23) Ozarowski, A. *Inorg. Chem*. **2008**, 47, 9760.

(24) Neese, F. ORCA-An Ab Initio Density Functional and Semiempirical Program Package, version 2.8; Universität Bonn: Bonn, Germany, **2008**; free download from http://www.thch.uni-bonn.de/tc/orca/, registration required.

(25) (a) Krzystek, J.; Ozarowski, A.; Zvyagin, S.A.; Telser, J. *Inorg. Chem.* **2012**, 51, 4954. (b) Wojciechowska, A.; Daszkiewicz, M.; Staszak, Z.; Trusz-Zdybek, A.; Bienko, A.; Ozarowski, A. *Inorg. Chem.* **2011**, 50, 11532. (c) Garribba, E.; Micera, G. *J. Chem. Ed*. **2006**, *83*, 1229.

(26) Mantel, C.; Baffert, C.; Romero I., Deronzier, A.; Pecaut, J.; Collomb, M.-N.; Duboc, C. *Inorg. Chem.* **2004**, 43, 6455.

(27) Hendrich, M. P.; Day, E. P.; Wang, C.-P.; Synder, B. S.; Holm, R. H.; Münck, E. *Inorg. Chem.* **1994**, *33*, 2848.

(28) Harman, W. H.; Harris, T.D.; Freedman, D. E.; Fong, H.; Chang, A.; Rinehart, J. D.; Ozarowski, A.; Sougrati, M. T.; Grandjean, F.; Long, G. J.; Chang, C. J. *J. Am. Chem. Soc.* **2010**, *132*, 18115.

(29) (a) Solomon, E. I.; Brunold, T. C.; Davis, M. I., Kemsley, J. N.; Lee, S. K.; Lehnert, N.; Neese, F.; Skulan, A. J.; Yang, Y. S.; Zhou, J. *Chem. Rev.* **2000**, 100, 235. (b) Yang, Yi-S.; Broadwater, J. A.; Coates Pulver, S.; Fox, B. G.; Solomon, E. I. *J. Am. Chem. Soc*. **1999,** *121,* 2770. (c) Solomon, E. I.; Pavel, E. G.; Loeb, K. E.; Campochiaro, C. *Coord. Chem. Rev.* **1995**, 144, 369.

(30) (a) Maurice, R.; Sivalingam, K.; Ganyushin, D.; Guihery, N.; de Graaf, C.; Neese, F. *Inorg. Chem.* **2011**, *50*, 6229. (b) Ozarowski, A.; Szymanska, I. B.; Muziol, T.; Jezierska, J. *J. Am. Chem. Soc.* **2009**, *131*, 10279. (c) Gribnau, M. C. M.; Keijzers, C. P. *Inorg. Chem.* **1987**, *26*, 3413. (d) Ross, P. K.; Allendorf, M. D.; Solomon, E. I. *J. Am. Chem. Soc.* **1989**, *111*, 4009. (e) Garribba, E.; Micera, G. *J. Chem. Ed*. **2006**, *83*, 1229.

(31) Neese, F. *J. Phys. Chem. Solids*, **2004**, 65, 781.

(32) (a) Schaefer, A.; Horn, H.; Ahlrichs, R. *J. Chem. Phys.* **1992**, *97*, 2571. (b) Ahlrichs, R. *et al*., unpublished. (c) The Ahlrichs auxiliary basis sets were obtained from the TurboMole basis set library under ftp.chemie.uni-karlsruhe.de/pub/jbasen. (d) Eichkorn, K.; Treutler, O.; Ohm, H.; Haser, M.; Ahlrichs, R. *Chem. Phys. Lett.* **1995**, *240*, 283. (e) Eichkorn, K.; Weigend, F.; Treutler, O.; Ahlrichs, R. *Theor. Chem. Acc.* **1997**, *97*, 119.

(33) (a) Becke, D. A.; *Phys. Rev. A* **1988**, *38*, 3098. (b) Perdew, J. P. *Phys. Rev. B* **1986**, *33*, 8822. (c) Perdew, J. P. *Phys. Rev. B.* **1986**, *34*, 7406. (d) Kendall, R. A.; Früchtl, H. A. *Theor. Chem. Acc.* **1997**, 97, 158.

(34) Kahn, O.; Briat, B. J. *Chem. Soc. Faraday Trans 2* **1976**, *72*, 268.

(35) Onofrio, N; Mouesca, J.-M. *Inorg. Chem.* **2011**, *50*, 5577. Rodríguez-Fortea, A.; Alemany, P.; Alvarez, S.; Ruiz, E. *Inorg. Chem.* **2002**, *41*, 3769.

(36) Bianchi, A.; Fallani, D. G.; Ghilardi, C. A.; Sacconi, L. *J. Chem. Soc. Dalton Trans.* **1973**, 641.

(37) (a) Reinen, D.; Friebel, C. *Inorg. Chem.* **1984**, *23*, 791. (b) Arriortua, M. I.; Mesa, J. L.; Rojo, T.; Debaerdemaeker, T.; Beltrán-Porter, D.; Stratemeier, H.; Reinen, D. *Inorg. Chem.* **1987**, *27*, 2976.

(38) (a) Bersuker, I. B. in "*The Jahn–Teller Effect*" Univ. Press Cambridge, UK, 2006. (b) Harrison, D.; Kennedy D.; Hathaway, B. *Inorg. Nucl. Chem. Lett*. **1981**, *17*, 87.

(39) Worm, K.; Chu, F.; Matsumoto, K; Best, M. D.; Lynch, V.; Anslyn, E. V. *Chem. Eur. J.* **2003**, *9*, 741.

(40) Noro, S.-i.; Akutagawa, T.; Nakamura, T. *Chem. Commun.* **2010**, 4619.

(41) Blake, A. J.; Devillanova, F. A.; Garau, A.; Harrison, A.; Isaia, F.; Lippolis, V.; Tiwary, S. K.; Schröder, M.; Verani, G.; Whittaker, G. *J. Chem. Soc. Dalton Trans.* **2002**, 4389.

(42) Emsley, J.; Arif, M.; Bates, P. A.; Hursthouse, M. B. *J. Chem. Soc. Dalton Trans.* **1989**, 1273.

(43) Machura, B.; Małecki, J. G.; Świtlicka, A.; Nawrot, I.; Kruszynski, R. *Polyhedron*, **2011**, *30*, 864.

(44) (a) Fujisawa, K.; Kanda, R.; Miyashita, Y.; Okamoto, K.-i. *Polyhedron* **2008**, *27*, 1432. (b) Machura, B.; Świtlicka, A.; Kruszynski, R.; Kusz, J.; Penczek, R. *Polyhedron* **2008**, 2513.

(45) Zhai, B.; Shen, W.-Z.; Chen, X.-Y.; Song. H.-B.; Shi, W.; Cheng, P. *Inorg. Chem. Commun.* **2006**, *9*, 1293.

(46) (a) Melnik, M. Coord. Chem. Rev. **1981**, *36*, 1. (b) Harcourt, R. D.; Skrezenek, F. L.; Maclagan R. G. A. R. *J. Am. Chem. Soc.* **1986**, 108(18), 5403. (c) De Loth, P.; Cassoux, P.; Daudey, J. P.; Malrieu J. P. *J. Am. Chem. Soc.* **1981**, 103(14), 4007.

(47) Grant, C. M.; Stamper, B. J.; Knapp, M. J.; Folting, K.; Huffman, J. C.; Hendrickson, D. N.; Christou, G. *J. Chem. Soc. Dalton Trans.* **1999**, 3399.

Chapter III

Dinuclear Metallacycles with Single M-O(H)-M Bridges [M = Fe(II), Co(II), Ni(II), Cu(II)]: Effects of Large Bridging Angles on Structure and Antiferromagnetic Superexchange Interactions[3]

[3]Adapted with permission from Reger, D. L.; Pascui, A. E.; Smith, M. D.; Jezierska, J.; Ozarowski, A. *Inorg. Chem.* **2013**. Copyright 2013 American Chemical Society.

Introduction

Extensive efforts have been made to synthesize ligands designed to direct the organization of new metal complexes at the molecular and supramolecular level as a way to control different properties of the resulting materials.[1] One important class of ligands is based on poly(pyrazolyl)methane units, first introduced in 1970 by Trofimenko.[2] More recently, a series of second generation tris(pyrazolyl)methane ligands, compounds with bulky groups substituted near the metal coordination site of the pyrazolyl nitrogen donor[3] were synthesized. These ligands impact the coordination environment around the metal centers. This ligand family was then expanded to include third-generation poly(pyrazolyl)methane ligands, where the non-coordinating "back" position of the poly(pyrazolyl)methane unit is functionalized.[4] One class of third-generation ligands have several poly(pyrazolyl)methane units directionally oriented by linking with a designed central core. It has been shown that the number of poly(pyrazolyl)methane groups as well as the type of linker influence the structure of the metal complexes.[4-6]

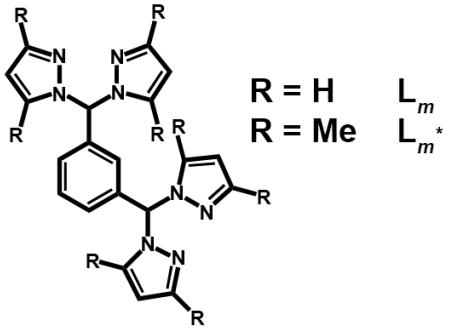

Scheme 3.1. Schematic drawing of the structure of $\mathbf{L}_m$ and $\mathbf{L}_m$*.

Of particular interest are the ditopic ligands, $\mathbf{L}_m$ and $\mathbf{L}_m$* (Scheme 3.1) that act as fixed, but not completely rigid ligands. The fixed *meta*-orientation of the bis(pyrazolyl)methane units coupled with the free rotation around the arene-methine bond supports the formation of dinuclear metallacycles, such as $[Ag_2(\mu\text{-}\mathbf{L}_m)_2](BF_4)_2$. These

types of complexes have Ag···Ag non-bonding distances ranging from 4.1 to 5.3 Å.[4] With metals in higher oxidation state [Mn(II), Fe(II), Co(II), Cu(II), and Zn(II)], dinuclear complexes still form, but abstraction of fluoride from the BF_4^- counterion, if present, leads to the formation of monobridged $[M_2(\mu\text{-}F)(\mu\text{-}\mathbf{L})_2]^{3+}$ complexes (**L** = $\mathbf{L}_m$ or $\mathbf{L}_m$*****).[5,6] Interestingly, with M = Ni(II), Cd(II) difluoride bridged complexes, $[M_2(\mu\text{-}F)_2(\mu\text{-}\mathbf{L}_m)_2](BF_4)_2$ formed with the less bulky $\mathbf{L}_m$,[5] while the monofluoride bridged species were isolated with $\mathbf{L}_m$*****.[6] These complexes with the bulky $\mathbf{L}_m$***** ligand nearly always have linear M-F-M bridging units, an arrangement that is uniquely important for magnetic studies,[7] with the complexes M = Mn(II), Fe(II), Co(II) and Ni(II) showing moderate intramolecular antiferromagnetic exchange coupling between the two metal ions, while $[Cu_2(\mu\text{-}F)_2(\mu\text{-}\mathbf{L}_m^*)_2](BF_4)_2$ shows strong antiferromagnetic coupling, $-J$ = 322 cm^{-1}.[6a]

In this chapter the syntheses and characterization of analogous complexes will be discussed with bridging hydroxide rather than fluoride, $[M_2(\mu\text{-}OH)(\mu\text{-}\mathbf{L})_2](ClO_4)_3$, [$\mathbf{L}_m$: M = Fe(II), Co(II), Cu(II); $\mathbf{L}_m$*****: M = Co(II), Ni(II), Cu(II)]. Complexes containing a bridging hydroxide group are particularly important because this arrangement is frequently observed in biological systems.[8] The uniqueness of this linear or nearly linear bridged system allows us, for the first time, to maintain the overall structure relatively constant while altering a single structural feature of the complexes through selective modification of the bridging group (F^- vs. OH^-), the divalent metal ion and/or the ligand (**$\mathbf{L}_m$** vs. **$\mathbf{L}_m$***). Reported are detailed structural, magnetic and EPR studies, supported by DFT calculations, of these complexes, with focus on the strength of the superexchange interactions.[6b]

Experimental Section

General Considerations. For the synthesis of the hydroxide bridged compounds, standard Schlenk techniques were used. The solvents were not dried prior to use, except for compound **1**, $[Fe_2(\mu\text{-}OH)(\mu\text{-}\mathbf{L}_m)_2](ClO_4)_3$. The ligands $\mathbf{L}_m$[5] and $\mathbf{L}_m$*[6a] were prepared following reported procedures. All other chemicals were purchased from Sigma-Aldrich or Strem Chemicals and used as received.

Crystals used for elemental analysis and mass spectrometry were removed from the mother liquor, rinsed with ether, and dried under vacuum, a process that removes the solvent of crystallization, if present. Mass spectrometric measurements were obtained on a MicroMass QTOF spectrometer in an acid-free environment. For all reported peaks, the isotopic patterns match those calculated for the assignment. Elemental analyses were performed on vacuum-dried samples by Robertson Microlit Laboratories (Ledgewood, NJ).

High-field, high-frequency EPR spectra at temperatures ranging from ca. 6K to 290 K were recorded on a home-built spectrometer at the EMR facility of the NHMFL.[9] The instrument is a transmission-type device in which microwaves are propagated in cylindrical lightpipes. The microwaves were generated by a phase-locked Virginia Diodes source generating frequency of 13 ± 1 GHz and producing its harmonics of which the 2nd, 4th, 6th, 8th, 16th, 24th and 32nd were available. A superconducting magnet (Oxford Instruments) capable of reaching a field of 17 T was employed. The powder samples were not constrained and showed no magnetic torqueing at high magnetic fields.

Magnetic susceptibility measurements over the temperature range 1.8-300 K were performed at a magnetic field of 0.5 T using a Quantum Design SQUID MPMSXL-5

magnetometer. Correction for the sample holder, as well as the diamagnetic correction χ_D which was estimated from the Pascal constants[10] was applied.

XSEED, POV-RAY and MESTRENOVA and GOpenMol were used for the preparation of figures.[11]

CAUTION! *Perchlorate salts of metal complexes with organic ligands are potentially explosive.*[12] *The behavior of a few crystals of* **2**·CH_3CN *under physical stress was tested and did not show any sign of explosive decomposition, but proper precautions should be taken when handling these complexes.*

$[Fe_2(\mu\text{-}OH)(\mu\text{-}L_m)_2](ClO_4)_3$, 1. To the ligand, $\mathbf{L}_m$ (0.190 g, 0.514 mmol), dissolved in methanol (10 mL), triethylamine (0.070 mL, 0.51 mmol) was added. The $Fe(ClO_4)_2 \cdot 7H_2O$ (0.196 g, 0.514 mmol) was separately dissolved in methanol (5 mL) and the ligand/amine solution was added by cannula. A dark, air sensitive green precipitate formed immediately. The reaction mixture was stirred for 3 hours, after which time the system was filtered by cannula and dried in vacuum. The green precipitate was transported to the drybox and dissolved in methanol. Vapor diffusion tubes (methanol/Et_2O) set up in the drybox gave a green precipitate and a few white crystals after several days. Colorless crystals suitable for X-ray studies were mounted directly from the mother liquor as **1**·1.5CH_3OH. Anal. Calcd (Found) for $C_{40}H_{37}Cl_3Fe_2N_{16}O_{13}$: C, 41.14 (40.76); H, 3.19 (3.04); N, 19.19 (19.28). The green precipitate turns orange in open atmosphere and was not identified.

$[Co_2(\mu\text{-}OH)(\mu\text{-}L_m)_2](ClO_4)_3$, 2. To the ligand $\mathbf{L}_m$ (0.380 g, 1.03 mmol) dissolved in methanol (25 mL) triethylamine (0.143 mL, 1.03 mmol) was added. The $Co(ClO_4)_2 \cdot 6H_2O$ (0.374 g, 1.03 mmol) was dissolved separately in methanol (6 mL) and the ligand/amine

solution was added by cannula. A pink precipitate formed immediately. The reaction mixture was stirred for 5 hours, after which time the system was filtered by cannula, washed with 5 mL ether and dried in vacuum overnight, affording 0.382 g (63%) of pink solid. Single crystals suitable for X-ray studies were grown by vapor diffusion of Et_2O into 1 mL acetonitrile solutions of the pink solid and were mounted directly from the mother liquor as **2**·CH_3CN. Anal. Calcd (Found) for $C_{40}H_{37}Cl_3Co_2N_{16}O_{13}$: C, 40.92 (40.72); H, 3.18 (3.07); N, 19.09 (19.22). MS ES(+) *m/z* (rel. % abund.) [assgn]: 1073 (1) $[Co_2(\mathbf{L}_m)_2(OH)(ClO_4)_2]^+$, 898 (23) $[Co(\mathbf{L}_m)_2(ClO_4)]^+$, 528 (53) $[Co_2(\mathbf{L}_m)_2(ClO_4)_2]^{2+}$, 487 (19) $[Co_2(\mathbf{L}_m)_2(OH)(ClO_4)]^{2+}$, 446 (10) $[Co\mathbf{L}_mOH]^+$, 400 (90) $[Co(\mathbf{L}_m)_2]^{2+}$, 292 (22) $[Co_2(\mathbf{L}_m)_2(OH)]^{3+}$. HRMS: ES^+ (*m/z*): $[Co_2(\mathbf{L}_m)_2(OH)(ClO_4)]^{2+}$ calcd. for $[C_{40}H_{37}Co_2N_{16}ClO_5]^{2+}$ 487.0737; found 487.0697. Preliminary X-ray diffraction studies indicated that the acetone solvate of the compound can be obtained by slow diffusion of Et_2O into the acetone solution of the pink solid.

$[Cu_2(\mu\text{-}OH)(\mu\text{-}L_m)_2](ClO_4)_3$, 3. This compound was prepared similarly to **2** starting from $\mathbf{L}_m$ (0.37 g, 1.0 mmol) dissolved in 12 mL of methanol, triethylamine (0.14 mL, 1.0 mmol) and $Cu(ClO_4)_2·6H_2O$ (0.37 g, 1.0 mmol) dissolved in 4 mL of methanol. The resulting blue solid weighed 0.354 g (58%). A 40 mg sample of the blue solid was gently heated in a mixture of 6 mL water and 3 mL acetone until the solid completely dissolved. In 3-5 days at 5˚C blue crystals of **3**·$2H_2O$ were isolated. Vapor diffusion of Et_2O into 1 mL acetonitrile solutions of the blue solid results in crystals of **3**·$1.5CH_3CN$. Anal. Calcd (Found) for $C_{40}H_{37}Cl_3Cu_2N_{16}O_{13}$: C, 40.60 (40.84); H, 3.15 (3.05); N, 18.94 (19.03). MS ES(+) *m/z* (rel. % abund.) [assgn]: 1083 (22) $[Cu_2(\mathbf{L}_m)_2(OH)(ClO_4)_2]^+$, 902 (40) $[Cu(\mathbf{L}_m)_2(ClO_4)]^+$, 532 (48) $[Co_2(\mathbf{L}_m)_2(ClO_4)_2]^{2+}$, 492 (40) $[Cu_2(\mathbf{L}_m)_2(OH)(ClO_4)]^{2+}$, 450

(25) [Cu$\mathbf{L}_m$OH]$^+$, 433 (100) [Cu($\mathbf{L}_m$)$_2$]$^{2+}$, 371 (28) [$\mathbf{L}_m$ + H]$^+$, 294 (22) [Cu$_2$($\mathbf{L}_m$)$_2$(OH)]$^{3+}$. HRMS: ES$^+$ (*m/z*): [Cu$_2$($\mathbf{L}_m$)$_2$(OH)(ClO$_4$)$_2$]$^+$ calcd. for [$C_{40}H_{37}Cu_2N_{16}Cl_2O_9$]$^+$ 1081.0898; found 1081.0896.

[Co$_2$(μ-OH)(μ-L$_m$*)$_2$](ClO$_4$)$_3$, 4. This compound was prepared similarly to **2** starting from $\mathbf{L}_m$***** (0.25 g, 0.51 mmol) dissolved in 10 mL of methanol, triethylamine (0.070 mL, 0.51 mmol) and Co(ClO$_4$)$_2$·6H$_2$O (0.19 g, 0.51 mmol) dissolved in 4 mL of methanol. The resulting pink solid weighed 0.235 g (65%). Single crystals suitable for X-ray studies were grown by the vapor diffusion of Et$_2$O into 1 mL acetonitrile solutions of the pink solid and were mounted directly from the mother liquor as **4**. Anal. Calcd (Found) for $C_{56}H_{69}Cl_3Co_2O_{13}N_{16}$: C, 48.10 (48.21); H, 4.97 (4.98); N, 16.03 (16.08). MS ES(+) *m/z* (rel. % abund.) [assgn]: 1297 (32) [Co$_2$($\mathbf{L}_m$*)$_2$(OH)(ClO$_4$)$_2$]$^+$, 599 (100) [Co$_2$($\mathbf{L}_m$*****)$_2$(OH)(ClO$_4$)]$^{2+}$, 416 (10) [Co$_2$$\mathbf{L}_m$*****(ClO$_4$)$_2$]$^{2+}$, 366 (80) [Co$_2$($\mathbf{L}_m$*****)$_2$(OH)]$^{3+}$. HRMS: ES$^+$ (*m/z*): [Co$_2$($\mathbf{L}_m$*****)$_2$(OH)(ClO$_4$)$_2$]$^+$ calcd. for [$C_{56}H_{69}Cl_2Co_2O_9N_{16}$]$^+$ 1297.3474; found 1297.3420.

[Ni$_2$(μ-OH)(μ-L$_m$*)$_2$](ClO$_4$)$_3$, 5. This compound was prepared similarly to **2** starting from $\mathbf{L}_m$***** (0.25 g, 0.51 mmol) dissolved in 10 mL of methanol, triethylamine (0.070 mL, 0.51 mmol) and Ni(ClO$_4$)$_2$·6H$_2$O (0.19 g, 0.51 mmol) dissolved in 4 mL of methanol. The cloudy solution was cannula filtered and the solvent was removed by rotary evaporation. The resulting green solid weighed 0.267 g (74%). Compound **5** was crystallized the same way as compound **2**. Anal. Calcd (Found) for $C_{56}H_{69}Cl_3Ni_2O_{13}N_{16}$: C, 48.11 (47.75); H, 4.97 (5.04); N, 16.03 (15.90). MS ES(+) *m/z* (rel. % abund.) [assgn]: 1297 (31) [Ni$_2$($\mathbf{L}_m$*****)$_2$(OH)(ClO$_4$)$_2$]$^+$, 599 (100) [Ni$_2$($\mathbf{L}_m$*****)$_2$(OH)(ClO$_4$)]$^{2+}$, 511 (15)

$[Ni(\mathbf{L_m*})_2]^{2+}$, 366 (95) $[Ni_2(\mathbf{L_m*})_2(OH)]^{3+}$. HRMS: ES^+ (*m/z*): $[Ni_2(\mathbf{L_m*})_2(OH)(ClO_4)_2]^+$ calcd. for $[C_{56}H_{69}Cl_2Ni_2O_9N_{16}]^+$ 1295.3517; found 1295.3478.

$[Cu_2(\mu\text{-}OH)(\mu\text{-}L_m*)_2](ClO_4)_3$, 6. This compound was prepared similarly to **2** starting from $\mathbf{L_m*}$ (0.25 g, 0.51 mmol) dissolved in 10 mL of methanol, triethylamine (0.070 mL, 0.51 mmol) and $Cu(ClO_4)_2{\cdot}6H_2O$ (0.19 g, 0.51 mmol) dissolved in 4 mL of methanol. The cloudy solution was cannula filtered and the solvent was removed by rotary evaporation. The resulting green solid weighed 0.300 g (83%). Compound **6** was crystallized the same way as compound **2**, and was taken directly from the mother liquor for the crystallographic studies as $\mathbf{6}{\cdot}2H_2O$. The 65 mg green precipitate remaining after the cannula filtration and crystallized in the same way as **6** also proved to be $\mathbf{6}{\cdot}2H_2O$ by single crystal X-ray diffraction. An analogous synthesis carried out in THF instead of methanol yields 0.342 g (95%) of a green precipitate. Single crystals grown with the same method proved be $\mathbf{6}{\cdot}2H_2O$. Anal. Calcd (Found) for $C_{56}H_{69}Cl_3Cu_2O_{13}N_{16}$: C, 47.78 (47.79); H, 4.94 (5.03); N, 15.92 (15.84). MS ES(+) *m/z* (rel. % abund.) [assgn]: 1307 (5) $[Cu_2(\mathbf{L_m*})_2(OH)(ClO_4)_2]^+$, 604 (42) $[Cu_2(\mathbf{L_m*})_2(OH)(ClO_4)]^{2+}$, 562 (10) $[Cu(\mathbf{L_m*})_2(ClO_4)]^+$, 545 (100) $[Cu(\mathbf{L_m*})]^+$, 514 (5) $[Cu(\mathbf{L_m*})_2]^{2+}$, 483 (95) $[\mathbf{L_m*} + H]^+$, 370 (80) $[Cu_2(\mathbf{L_m*})_2(OH)]^{3+}$.

Crystallographic Studies. X-ray diffraction intensity data for compounds **1-6** was measured on a Bruker SMART APEX CCD-based diffractometer (Mo Kα radiation, λ = 0.71073 Å).[13,14]

For $\mathbf{2}{\cdot}CH_3CN$ all of several surveyed crystals were found to be twinned. The selected data crystal was composed of two domains related to each other by a 180º rotation around the reciprocal space [10-1] vector. Raw area detector data frame

processing was performed with the SAINT+[13] and TWINABS[15] programs. Identification of the twin law was performed with the Bruker CellNow program.[15] Twin refinement with an HKLF-5 format reflection file created by TWINABS was performed with SHELXL. The major twin fraction refined to 0.526(1).

In the case of all the other crystals raw area detector data frame processing was performed with the SAINT+[13] and SADABS[14] programs. Final unit cell parameters were determined by least-squares refinement of large sets of strong reflections taken from each data set. Direct methods structure solution, difference Fourier calculations and full-matrix least-squares refinement against F^2 were performed with SHELXTL[16] for **2**-**6** and SHELXS/L as implemented in OLEX2[17] for **1**. Non-hydrogen atoms were refined with anisotropic displacement parameters, the exception being disordered species. The hydrogen atoms were placed in geometrically idealized positions and included as riding atoms. Details of the data collection are given in Table 3.1.

Compound **1**·1.5CH_3OH crystallizes in the space group $P2_1/m$. The asymmetric unit consists half each of two di-iron cations, three ClO_4^- anions and two independent regions of solvent species, which were modeled as disordered methanol molecules. Cation Fe1 resides on an inversion center; cation Fe2 is on a mirror plane. The bridging hydroxide oxygen atom of each cation showed a highly elongated displacement ellipsoid if refined with a single position; these atoms were modeled with split positions. Hydroxide oxygen O1 is equally disordered over two inversion-related sites; hydroxide O2 occupies two sites with occupancies O2A/O2B = 0.58(4)/0.42(4). These atoms were refined isotropically, and their hydroxide protons could not be located and were not calculated. Perchlorate anions Cl1/O11-O14 and Cl3/O31-O34 are disordered and each was modeled

as occupying two distinct orientations. The disordered methanol molecules were modeled with three (O1S/C1S, O2S/C2S, O3S/C3S) or two (O4S/C4S, O5S/C5S) components, whose total site occupancies were restrained to sum to unity. C-O distance restraints (1.45(2) Å) were applied and each set was refined with a common displacement parameter. No hydrogen atoms were located or calculated for these species.

Compound **2**·CH_3CN crystallizes in the space group $P\ \bar{1}$ of the triclinic system. The unit cell consists of two independent $[Co_2(\mu\text{-OH})(\mu\text{-}\mathbf{L_m})_2]^{3+}$ cations, six independent perchlorate anions and two independent acetonitrile molecules. Positional disorder was modeled for two (Cl1 and Cl3) of the six perchlorates. The oxygen atom of the bridging hydroxide group of Co1B/Co2B is disordered over two equally populated sites. Reliable positions for either of the two independent hydroxide protons could not be located, and were not calculated.

Compound **3**·$2H_2O$ crystallizes in the space group $P\ \bar{1}$ of the triclinic system. The asymmetric unit consists of one di-copper complex, two water molecules and three perchlorate anions. One perchlorate (Cl3) is disordered over two orientations. The bridging hydroxide proton was located in a difference map and refined freely. The water hydrogens were also located in difference maps. They were refined with d(O-H) = 0.85(2) Å restraints, and $U_{iso,H} = 1.5U_{eq,O}$. The largest residual electron density peak of 1.45 e-/$Å^3$ is located near Cl2.

Compound **3**·$1.5CH_3CN$ crystallizes in the space group $P2_1/m$. The asymmetric unit consists of half each of two independent $[Cu_2(\mu\text{-OH})(\mu\text{-}\mathbf{L_m})_2]^{3+}$ cations, three independent perchlorate anions and 1.5 independent acetonitrile molecules. Cation Cu1 is located on a crystallographic inversion center; cation Cu2 is located on a crystallographic

Table 3.1. Selected Crystal Data and Structure Refinement for **1-6**.

	1·1.5CH_3OH	**2**·CH_3CN	**3**·2H_2O	**3**·1.5CH_3CN	**4**	**4**	**5**	**6**·2H_2O
Formula	$C_{41.5}H_{43}Cl_3Fe_2N_{16}O_{14.5}$	$C_{42}H_{40}Cl_3Co_2N_{17}O_{13}$	$C_{40}H_{41}Cl_3Cu_2N_{16}O_{15}$	$C_{43}H_{41.5}Cl_3Cu_2N_{17.5}O_{13}$	$C_{56}H_{69}Cl_3Co_2N_{16}O_{13}$	$C_{56}H_{69}Cl_3Co_2N_{16}O_{13}$	$C_{56}H_{69}Cl_3Ni_2N_{16}O_{13}$	$C_{56}H_{73}Cl_3Cu_2N_{16}O_{15}$
Fw, g mol^{-1}	1215.97	1215.12	1219.32	1244.87	1398.48	1398.48	1398.04	1443.73
Cryst. Syst.	Monoclinic	Triclinic	Triclinic	Monoclinic	Triclinic	Triclinic	Triclinic	Monoclinic
Space group	*P* $2_1/m$	*P* $\bar{1}$	*P* $\bar{1}$	*P* $2_1/m$	*P* $\bar{1}$	*P* $\bar{1}$	*P* $\bar{1}$	*P*$2_1/n$
T, K	150(2)	295(2)	100(2)	150(2)	295(2)	100(2)	295(2)	150(2)
a, Å	10.3203(10)	14.2961(11)	11.6805(5)	10.6154(4)	11.3744(7)	12.6577(10)	11.395(6)	14.7236(7)
b, Å	42.774(4)	16.9353(13)	14.0720(6)	42.3862(16)	12.8037(8)	13.6991(11)	12.762(6)	13.6600(7)
c, Å	11.9508(12)	22.0270(17)	15.4802(6)	11.5326(4)	13.3320(8)	18.7180(14)	13.222(6)	15.8038(8)
α, deg	90	97.085(2)	93.721(1)	90	116.545(1)	92.443(1)	116.338(8)	90
β, deg	102.136(2)	102.730(2)	103.333(1)	101.648(1)	99.203(1)	99.717(2)	99.724(9)	95.017(1)
γ, deg	90	94.027(2)	101.286(1)	90	105.900(1)	106.747(1)	105.896(9)	90
V, $Å^3$	5157.7(9)	5135.9(7)	2411.79(17)	5082.2(3)	1577.94(17)	3049.1(4)	1560.5(13)	3166.4(3)
Z	4	4	2	4	1	2	1	2
$R_1(I > 2\sigma(I))$	0.0529	0.0538	0.0411	0.0489	0.0508	0.0531	0.0480	0.0385
$wR_2(I > 2\sigma(I))$	0.1176	0.1213	0.1043	0.0931	0.1440	0.1465	0.1382	0.1010

mirror plane. The half-acetonitrile lies in a mirror plane. The hydroxide group of the centrosymmetric cation Cu1 is disordered across the inversion center and was refined as half-occupied. Perchlorate anion Cl3 is disordered and was modeled with two distinct orientations. The geometry of both disorder components was restrained to be similar to that of the ordered perchlorate Cl1. Reasonable positions for both hydroxyl protons H1A and H2A were located in difference maps, but could not be refined freely. Their coordinates were adjusted to give d(O-H) = 0.84 Å and they were refined as riding on the parent oxygen atom with $U_{iso,H} = 1.5U_{eq,O}$.

Compound **4** undergoes a structural phase transition at lower temperatures. Both the high- and low-temperature structures adopt the space group $P\ \bar{1}$ of the triclinic system. **295 K form**: The asymmetric unit consists of half of one $[Co_2(\mu\text{-OH})(\mu\text{-}\mathbf{L_m}\mathbf{*})_2]^{3+}$ cation located on an inversion center, one disordered ClO_4^- anion on a general position (Cl2), and half of another ClO_4^- anion which is disordered across an inversion center (Cl1). Because of its location on an inversion center, only half of perchlorate Cl1 is present in the asymmetric unit. The Cl1 anion is further disordered within the asymmetric unit, and was refined with two equally populated (25%) components. Perchlorate Cl2 was refined with three disorder components, the occupancies of which were constrained to sum to unity. The hydroxide proton of the cobalt(II) cation is disordered across the inversion center and was refined isotropically with half-occupancy. The O-H distance was restrained to 0.85(2) Å, and Co-H distances were restrained to be approximately equal. **100 K form**: The diffraction pattern showed broad peaks, indicating low crystallinity. This suggests the structural transition may not be complete at 100K. Lower temperatures are not accessible with our instrumentation. The unit cell volume has approximately

doubled in size allowing for temperature contraction, and the inversion symmetry of the cation has been lost. All species are now on positions of general crystallographic symmetry. The asymmetric unit consists of one complete cobalt(II) complex and three independent perchlorate anions. All three perchlorate anions were refined with a minor disorder component (0.069(3) occupancy for Cl1B, 0.046(2) occupancy for Cl2B, 0.083(2) occupancy for Cl3B). The bridging hydroxide group oxygen occupies a single ordered position, but a reliable position (or positions) for its proton could not be located from difference maps and was not calculated.

The high temperature structure of compound **5** is isostructural with the cobalt(II) analog. A reasonable position for the hydroxide proton was located by difference synthesis, and it was refined isotropically with the O-H distance restrained to 0.85(2) Å and the H···Ni distances restrained to be approximately equal. This proton is disordered across the inversion center at O1, and was refined with half-occupancy.

Compound **6**·2H_2O crystallizes in the space group $P2_1/n$. The asymmetric unit consists of half of one $[Cu_2(\mu\text{-OH})(\mu\text{-}\mathbf{L_m}\mathbf{*})_2]^{3+}$ cation located on an inversion center, one ClO_4^- anion on a general position, half of another ClO_4^- anion which is disordered across an inversion center, and a water molecule disordered over two closely separated sites. The hydroxide proton of the copper(II) cation is disordered across the inversion center and was refined isotropically with half-occupancy. The O-H distance was restrained to 0.85(2) Å, and Cu-H distances were restrained to be approximately equal.

Results

Syntheses. The reactions of $M(ClO_4)_2 \cdot 6H_2O$ with the corresponding ligand $\mathbf{L}_m$ [M = Fe(II), Co(II), Cu(II)] or $\mathbf{L}_m$***** [M = Co(II), Ni(II), Cu(II)] in the presence of triethylamine resulted in the formation of the monohydroxide bridged dinuclear metallacycles. The base was used to deprotonate the water molecules according to Scheme 3.2.

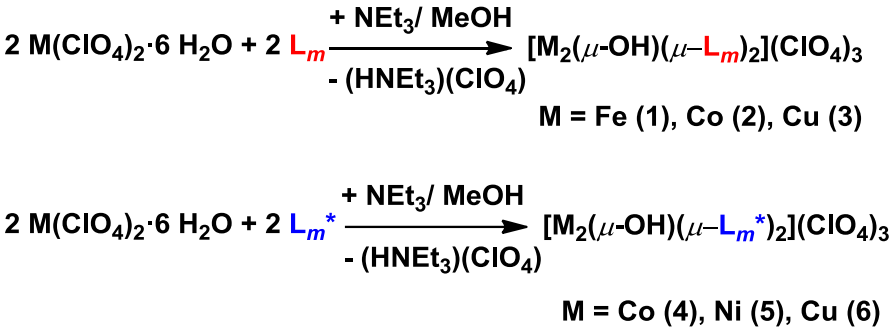

Scheme 3.2. Synthesis of the hydroxide bridged metallacycles.

Even in the presence of excess NEt_3, the monohydroxide bridged compounds formed in all cases. Only a few colorless crystals of **1** were isolated; in the reaction the major product is a very air sensitive green powder that was not characterized.

Mass Spectrometry. Positive-ion electrospray mass spectra (ESI^+-MS) of complexes **2**-**6** are similar. In all spectra, clusters such as $[M_2(\mathbf{L})_2OH(ClO_4)_2]^+$, $[M_2(\mathbf{L})_2OH(ClO_4)]^{2+}$ and $[M_2(\mathbf{L})_2OH]^{3+}$ corresponding to the complete hydroxide bridged metallacycles are observed. Figure 3.1 shows these peaks for $[Co_2(\mu\text{-}OH)(\mu\text{-}\mathbf{L}_m\mathbf{*})_2](ClO_4)_3$, **4**, where the isotope patterns coupled with the high resolution data definitively characterize these complexes. In the spectra of **2** and **3**, metallacycles formed with $\mathbf{L}_m$, the $[M(\mathbf{L}_m)_2]^{2+}$ type peaks have the highest intensities. For compounds **4**-**6**, the base peak is $[M_2(\mathbf{L}_m\mathbf{*})_2OH(ClO_4)]^{2+}$ and the $[M_2(\mathbf{L}_m\mathbf{*})_2OH]^{3+}$ species have very high

intensities. The increase of the signal intensities for the metallacyclic species in the spectra of $\mathbf{L}_m$* compounds, especially for $[M_2(\mathbf{L})_2OH]^{3+}$ (22% for **2**, **3** vs. 80-95% for **4-6**), indicate that these metallacycles are more stable than the metallacycles formed with $\mathbf{L}_m$ under the conditions of these experiments.

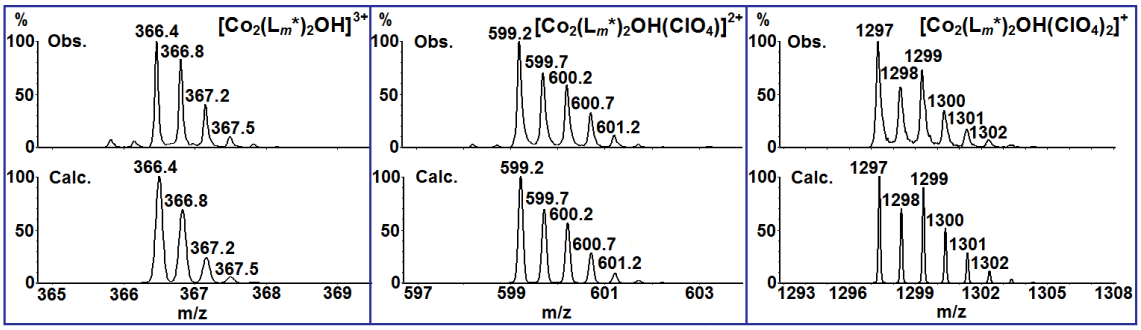

Figure 3.1. Observed (top) and calculated ESI$^+$-MS peaks corresponding to $[Co_2(\mathbf{L}_m*)_2OH(ClO_4)_2]^+$, $[Co_2(\mathbf{L}_m*)_2OH(ClO_4)]^{2+}$ and $[Co_2(\mathbf{L}_m*)_2OH]^{3+}$ cationic units of $[Co_2(\mu\text{-}OH)(\mu\text{-}\mathbf{L}_m*)_2](ClO_4)_3$, **4**.

Solid State Structures. Figure 3.2-3.5 show the structure of the dinuclear hydroxide bridged cations $[M_2(\mu\text{-}OH)(\mu\text{-}\mathbf{L})_2]^{3+}$, compounds **1-6**. The numbering scheme on Figure 3.4 is also correct for compound **1** and similarly, Figure 3.5 is correct for **5** and **6**·2H_2O. Selected bond distances and bond angles are shown in Table 3.2-3.6.

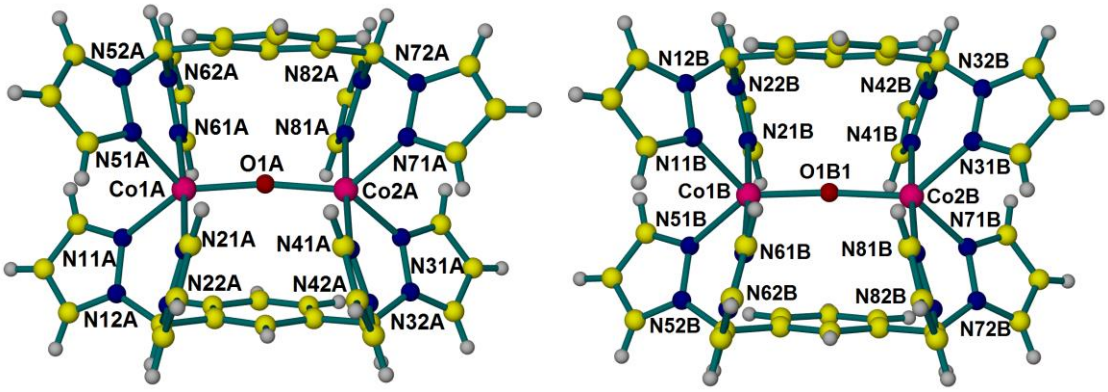

Figure 3.2. Structure of the two independent $[Co_2(\mu\text{-}OH)(\mu\text{-}\mathbf{L}_m)_2]^{3+}$ units of **2**.

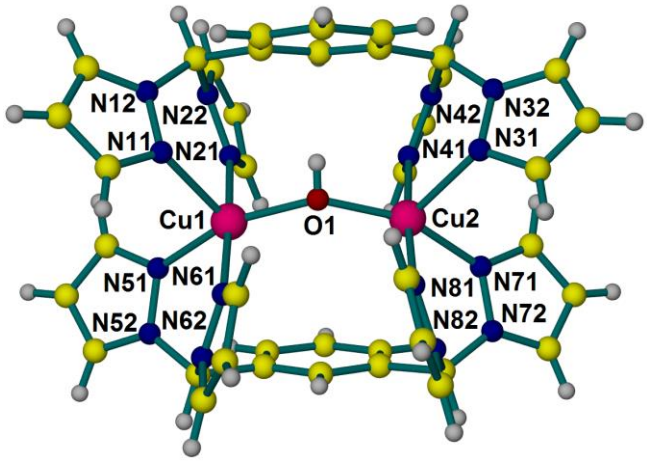

Figure 3.3. Structure of the $[Cu_2(\mu\text{-OH})(\mu\text{-}\mathbf{L}_m)_2]^{3+}$ unit of $\mathbf{3}\cdot 2H_2O$.

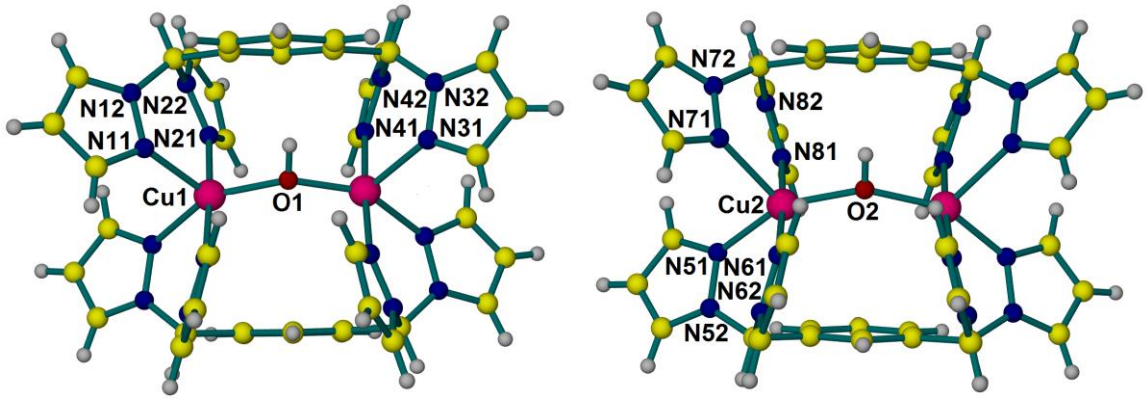

Figure 3.4. Structure of the two independent $[Cu_2(\mu\text{-OH})(\mu\text{-}\mathbf{L}_m)_2]^{3+}$ units of $\mathbf{3}\cdot 1.5CH_3CN$. Disorder is removed for clarity of the figure.

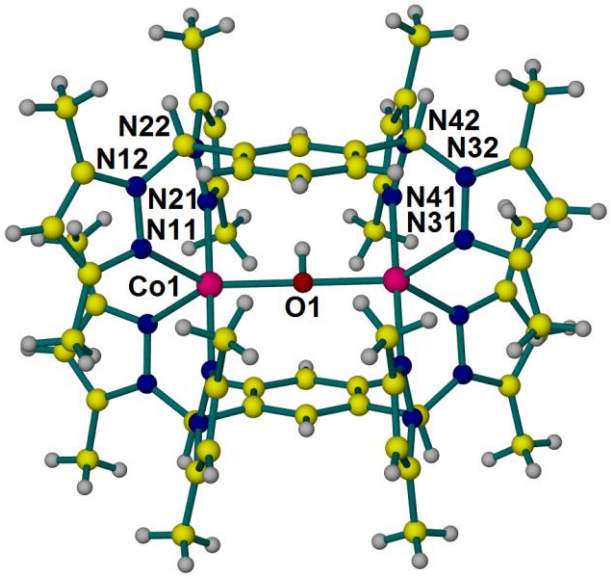

Figure 3.5. Structure of $[Co_2(\mu\text{-OH})(\mu\text{-}\mathbf{L}_m\mathbf{*})_2]^{3+}$ unit of **4** at 295K. Disorder was removed for clarity of the figure. At 100 K the inversion center is lost.

In the structure of all compounds, except **3**·2H_2O and **3**·1.5CH_3CN, the geometry around the metal centers is a distorted trigonal bipyramid, supported by the unusually large M-O-M angles (**1**: 156.4(4) Å, 161.7(17) Å; **2**: 166.8(2)˚, 165.8(4)˚) or perfectly linear M-O-M angles (**4-6**: 180˚). Two pyrazolyl nitrogens and the hydroxide oxygen occupy the equatorial positions of the trigonal bipyramid, with N-M-N and N-M-O angles between 94.0-138.7˚. In the axial positions the two remaining pyrazolyl nitrogens can be found enclosing N-M-N angles between 173.72 and 179.30˚. The τ_5[19] values also indicate distorted trigonal bipyramidal geometry around the metal centers.

In the distorted trigonal bipyramidal structures of **1**·1.5CH_3OH, **2**, **4** and **5**, the axial and equatorial M-N bond distances are similar; for the first three the distances on average are 0.04 Å longer in the axial position whereas for **5** they are 0.015 Å shorter. In contrast, for the copper(II) complex **6**·2H_2O, as expected because of the pseudo Jahn-Teller effect, the structures are substantially axially compressed (Tables 3.4 and 3.5); axial Cu-N 1.9875(18) Å, 1.9854(17) Å; equatorial Cu-N 2.2579(18) Å, 2.1218(18) Å.

The Cu-O-Cu angles in the two copper(II) metallacycles with $\mathbf{L}_{\boldsymbol{m}}$ are significantly lower than 180° (141.2˚ for **3**·2H_2O, 141.2˚ and 151.0˚ for **3**·1.5CH_3CN). This change in bridging angle results in two larger bond angles around the copper(II) centers [e.g. **3**·2H_2O: N(61)-Cu(1)-N(21) 175.81(8)˚ and O(1)-Cu(1)-N(51) 158.52(7)˚] generating τ_5 values between 0.3 and 0.4, typical of distorted square pyramidal geometry. This change is also reflected by the Cu-N bond lengths with one longer axial, **3**·2H_2O: Cu(1)-N(11) 2.2264(18) Å, and three shorter equatorial bond lengths, Cu(1)-N(21) 2.045(2) Å, Cu(1)-N(51) 2.0165(19) Å, Cu(1)-N(61) 2.017(2) Å. The oxygen from the bridging hydroxide group completes the equatorial plane.

Table 3.2. Important Structural Parameters for $[Fe_2(\mu\text{-}OH)(\mu\text{-}\mathbf{L_m})_2](ClO_4)_3\cdot 1.5CH_3OH$ (**1**·1.5CH_3OH), $[Co_2(\mu\text{-}OH)(\mu\text{-}\mathbf{L_m})_2](ClO_4)_3\cdot CH_3CN$ (**2**·CH_3CN), $[Cu_2(\mu\text{-}OH)(\mu\text{-}\mathbf{L_m})_2](ClO_4)_3\cdot 2H_2O$ (**3**·2H_2O), $[Cu_2(\mu\text{-}OH)(\mu\text{-}\mathbf{L_m})_2](ClO_4)_3\cdot 1.5CH_3CN$ (**3**·1.5 CH_3CN), $[Co_2(\mu\text{-}OH)(\mu\text{-}\mathbf{L_m}^*)_2](ClO_4)_3$ (**4**), $[Ni_2(\mu\text{-}OH)(\mu\text{-}\mathbf{L_m}^*)_2](ClO_4)_3$ (**5**), and $[Cu_2(\mu\text{-}OH)(\mu\text{-}\mathbf{L_m}^*)_2](ClO_4)_3\cdot 2H_2O$ (**6**·2H_2O).

Complex	Temp, K	Metal centers	M-O-M angle, deg	M-O distance, Å	Predicted M-O distance, Å[b]	Average M-N distance, Å	τ_5	M···M distance, Å
1·1.5CH_3OH	150	Fe(1)-Fe(1')	156.4(4)	1.961[a]	2.03	2.136	0.59	3.839
		Fe(2)-Fe(2')	161.7(17)	1.995(5)	2.03	2.152	0.61	3.939
2·CH_3CN	296	Co(1A)-Co(2A)	166.8(2)	1.969(3)/ 1.945(3)	1.99	2.108/ 2.103	0.71/0.72	3.888
		Co(1B)-Co(2B)	165.8(4)	1.962/ 1.983[a]	1.99	2.119/ 2.114	0.63/0.65	3.908
3·2H_2O	100	Cu(1)-Cu(2)	141.04(9)	1.9328(16)/ 1.9413(16)	1.97	2.076/ 2.071	0.30	3.652
3·1.5CH_3CN	150	Cu(1)-Cu(1')	141.2(3)	1.932[a]	1.97	2.112	0.42	3.644
		Cu(2)-Cu(2')	151.0(2)	1.9653(11)	1.97	2.083	0.40	3.805
4	295	Co(1)-Co(1')	180	2.0673(4)	1.99	2.118	0.74	4.135
4	100	Co(1)-Co(2)	177.61(10)	2.0655(18)/ 2.0490(18)	1.99	2.109/ 2.107	0.73/0.72	4.114
5	295	Ni(1)-Ni(1')	180	2.0640(10)	1.95	2.070	0.72	4.128
6·2H_2O	150	Cu(1)-Cu(1')	180	2.0230(3)	1.97	2.088	0.68	4.046

[a]Average bond length, due to disorder. [b]Ref. 18.

Table 3.3. Selected Bond Lengths (Å) for **1** and **2**.

	1		**2**			
M	**Fe1**	**Fe2**	**Co1A**	**Co1B**	**Co2A**	**Co2B**
M-N11	2.114(5)	-	2.079(4)	2.084(4)	-	-
M-N21	2.159(5)	-	2.130(4)	2.147(4)	-	-
M-N31	2.118(5)	-	-	-	2.065(4)	2.088(4)
M-N41	2.153(5)	-	-	-	2.120(4)	2.157(4)
M-O	1.961*	1.995(5)	1.969(3)	1.962*	1.945(3)	1.983*
M-N51	-	2.152(4)	2.068(4)	2.093(4)	-	-
M-N61	-	2.150(5)	2.153(4)	2.150(4)	-	-
M-N71	-	2.153(5)	-	-	2.071(4)	2.079(4)
M-N81	-	2.152(5)	-	-	2.157(4)	2.133(4)

*Average bond length, due to disorder.

Table 3.4. Selected Bond Lengths (Å) for **3**·$2H_2O$**, 3**·$1.5CH_3CN$**, 4** (100K).

	3·$2H_2O$		**3**·$1.5CH_3CN$		**4** (100K)	
M	**Cu1**	**Cu2**	**Cu1**	**Cu2**	**Co1**	**Co2**
M-N11	2.2264(18)	-	2.119(4)	-	2.111(3)	-
M-N21	2.045(2)	-	2.019(3)	-	2.127(2)	-
M-N31	-	2.2426(19)	2.128(4)	-	-	2.109(3)
M-N41	-	2.021(2)	2.011(3)	-	-	2.111(2)
M-O	1.9328(16)	1.9413(16)	1.932*	1.9653(11)	2.0655(18)	2.0490(18)
M-N51	2.0165(19)	-	-	2.066(4)	2.088(2)	-
M-N61	2.017(2)	-	-	1.982(3)	2.110(2)	-
M-N71	-	2.0456(19)	-	2.275(4)	-	2.092(3)
M-N81	-	1.976(2)	-	2.009(3)	-	2.114(2)

*Average bond length, due to disorder.

Table 3.5. Selected Bond Lengths (Å) for **4** (295 K), **5, 6**·$2H_2O$.

	4 (295K)	**5**	**6**·$2H_2O$
M	**Co1**	**Ni1**	**Cu1**
M-N11	2.107(2)	2.080(2)	2.2579(18)
M-N21	2.117(2)	2.053(2)	1.9875(18)
M-N31	2.116(2)	2.080(2)	2.1218(18)
M-N41	2.133(2)	2.066(2)	1.9854(17)
M-O	2.0673(4)	2.0640(10)	2.0230(3)

Table 3.6. Selected Bond Angles (°) for **3**·$2H_2O$ and **3**·$1.5CH_3CN$.

	3·$2H_2O$		**3**·$1.5CH_3CN$	
	Cu1	**Cu2**	**Cu1**	**Cu2**
N-Cu-O eq	110.45/157.70	106.28/158.52	113.62/151.21	116.16/152.14
N-Cu-N eq	91.67	95.21	94.52	91.69
N-Cu-N ax	175.38	175.81	176.67	176.39
N(ax)-Cu-N(eq)	85-95	87-94	86-97	85-93

The M-O distances for the $\mathbf{L}_{m}$ compounds are slightly shorter than predicted from the sum of the ionic radii,[18] while for the more sterically hindered $\mathbf{L}_{m}$***** metallacycles the M-O distances are longer than predicted (Table 3.2). This trend was previously noted in analogous fluoride bridged complexes. In the data presented here, the only true direct comparison between the two ligands is with the cobalt(II) complexes where the average Co-O distance in **2**·CH_3CN is 1.96 Å compared to the 2.0655(18) distance in the structure of **4** at the same temperature.

Compounds **4** and **5** undergo a phase change of order-disorder type at lower temperatures, but only the structure of **4** could be solved at 100 K (see crystallographic section for details and Figure 3.6). The phase change does not cause major structural changes that would significantly alter the properties of these compounds.

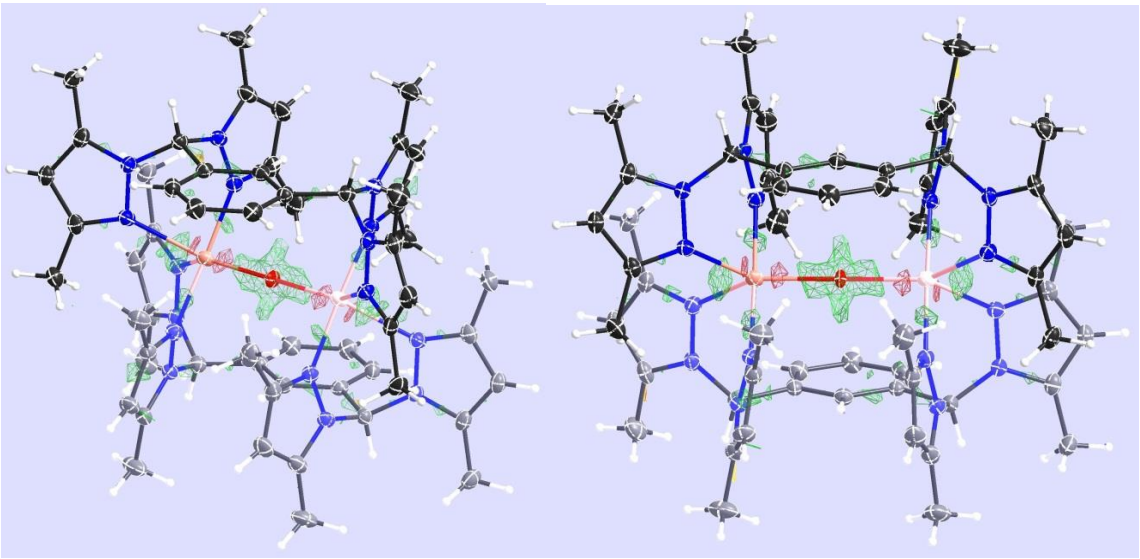

Figure 3.6. Electron density map calculated near the bridging hydroxide (positive electron density = green cage) of $[Cu_2(\mu\text{-}OH)(\mu\text{-}\mathbf{L}_{m}\mathbf{*})_2](ClO_4)_3\cdot 2H_2O$. Peak assigned as bridging hydroxyl proton has a magnitude of 0.35 $e^-/Å^3$ and required O-H and Cu-H distance restraints for stability. It refined isotropically with a reasonable displacement parameter.

Magnetic Properties of the Copper(II) Complexes. The magnetic susceptibility data for the copper(II) complexes were interpreted using the standard Heisenberg-Dirac-Van Vleck Hamiltonian: $\hat{\mathbf{H}} = -J\ \hat{\mathbf{S}}_1\hat{\mathbf{S}}_2$. In this notation, J is negative in the case of antiferromagnetic superexchange interactions. The magnetic susceptibility of a dinuclear copper(II) system is:

$$\chi_d = \frac{N\mu_B^2 g^2}{3kT}\frac{6\exp(J/kT)}{1+3\exp(J/kT)} + 2TIP \qquad (1)$$

As it is usually observed, the samples contained small amounts (less than 1%) of monomeric impurities. The monomer susceptibility can be calculated from:

$$\chi_m = (N\mu^2{}_B{}^2 g^2/3kT)\cdot 0.75 + TIP \qquad (2)$$

At low temperatures these impurities dominated the magnetic susceptibility owing to very strong antiferromagnetic exchange interactions in the dinuclear species. For this reason, the monomeric contributions were removed from the experimental data (Figure 3.7) using:

$$\chi_d = (\chi_{exp} - 2f\cdot\chi_m)/(1-f) \qquad (3)$$

where f is the fraction of monomeric copper(II) species. The value for f was found from the low-temperature data and subsequently the $-J$ values were extracted from the altered experimental data above 100 K, as the dinuclear susceptibility is near zero at lower temperatures.

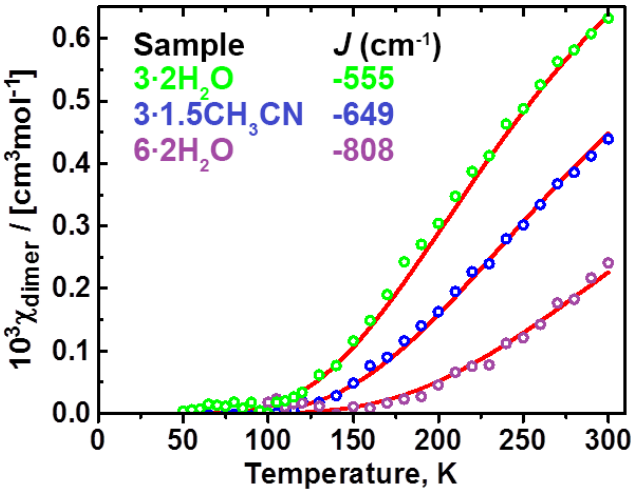

Figure 3.7. Magnetic susceptibility of the copper(II) complexes. Green circles: $Cu_2(\mu\text{-}OH)(\mu\text{-}\mathbf{L}_m)_2](ClO_4)_3\cdot 2H_2O$ (**3**·2H$_2$O), blue circles: $[Cu_2(\mu\text{-}OH)(\mu\text{-}\mathbf{L}_m)_2](ClO_4)_3\cdot 1.5CH_3CN$ (**3**·1.5H$_2$O), purple circles: $[Cu_2(\mu\text{-}OH)(\mu\text{-}\mathbf{L}_m\mathbf{*})_2](ClO_4)_3\cdot 2H_2O$ (**6**·2H$_2$O)**.** Contribution from the monomeric impurities to the magnetic susceptibility was removed from the experimental data (see text). Solid red lines are calculated with parameters in Table 3.7.

Table 3.7. Spin Hamiltonian parameters for the $[Cu_2(\mu\text{-}OH)(\mu\text{-}\mathbf{L})_2](ClO_4)_3$ complexes, where **L** = $\mathbf{L}_m$ (**3**) or $\mathbf{L}_m$***** (**6**).

Complex	$-J$ (cm^{-1})	g_x	g_y	g_z	$\lvert D\rvert$ (cm^{-1})	$\lvert E\rvert$ (cm^{-1})
3·1.5CH$_3$CN	649(1)	2.14[a]	2.03[a]	2.27[a]	0.28	0.047
3·2H$_2$O	555(3)	2.130[a]	2.048[a]	2.263[a]	0.299	0.028
		2.083[b]	2.048[b]	2.310[b]		
		2.130[c]	2.263[c]	2.048[c]	0.191[c]	0.136[c]
6·2H$_2$O	808(50)	2.123[d]	2.310[d]	2.019[d]	0.235	0.142

[a]Coupled-spin state g values. [b]Single-ion g values. [c]An equivalent parameter set allowing a direct comparison to the parameters of **6**·2H$_2$O. [d]The coupled-spin and the single-ion g values are equal in a centrosymmetric dinuclear system. Note: The errors in $-J$ (in parentheses) were calculated by the fitting software. However, there are experimental uncertainties, like the Pascal corrections, errors in the molar mass, etc., which may significantly affect the fitting results. The errors in such magnetic fittings of $-J$ are often estimated to be of the order of 5-10 %.

For the three $[Cu_2(\mu\text{-}OH)(\mu\text{-}\mathbf{L})_2](ClO_4)_3$ complexes, where **L** = $\mathbf{L}_m$ or $\mathbf{L}_m$***,** χ_M decreases with the temperature demonstrating strong antiferromagnetic superexchange interactions between the copper(II) centers, Figure 3.7, Table 3.7. The magnetic moment [per one copper(II)] at 300 K is 0.98 B.M. for **3**·2H$_2$O 0.75 B.M. for **3**·1.5CH$_3$CN and

0.68 B.M. for **6**·2H_2O, very small compared to the magnetic moment for a non-interacting copper(II) center (ca. 1.82 B.M). The antiferromagnetic exchange coupling constant, -*J*, is 555 cm^{-1} for **3**·2H_2O, -649 cm^{-1} for **3**·1.5CH_3CN, and 808 cm^{-1} for **6**·2H_2O.

Single crystal X-ray diffraction data showed that there are two crystallographically independent $[Cu_2(\mu\text{-OH})(\mu\text{-}\mathbf{L_m})_2]^{3+}$ cations in the unit cell of **3**·1.5CH_3CN, with Cu-O-Cu angles of 141.2º and 151.0º, respectively. The -*J* value of 649 cm^{-1} obtained from the magnetic data fitting represents an average of the two species.

Magnetic Properties of the Cobalt(II) Complexes. Zero-field splitting (zfs) exists on separate multi-electron ions like cobalt(II) and it affects the magnetic properties of the dinuclear complexes. To account for zfs, the magnetic data for the cobalt(II) systems were interpreted using the Hamiltonian:

$$\hat{\boldsymbol{H}} = -J\,\hat{\boldsymbol{S}}_1\,\hat{\boldsymbol{S}}_2 + D\{\hat{\boldsymbol{S}}_{z1}{}^2 - S_1\cdot(S_1+1)/3\} + E(\hat{\boldsymbol{S}}_{x1}{}^2 - \hat{\mathbf{S}}_{y1}{}^2) + D\{\hat{\boldsymbol{S}}_{z2}{}^2 - S_2\cdot(S_2+1)/3\} + E(\hat{\boldsymbol{S}}_{x2}{}^2 - \hat{\mathbf{S}}_{y2}{}^2) + \mu_B B\,\{\boldsymbol{g_1}\}\,\hat{\boldsymbol{S}}_1 + \mu_B B\,\{\boldsymbol{g_2}\}\,\hat{\boldsymbol{S}}_2 \qquad (4)$$

The spin Hamiltonian matrix was diagonalised to find the energy levels and the magnetic susceptibility per mole of dimer was calculated from:

$$\chi_d = -\frac{N}{B}\frac{\sum_i \frac{\partial E_i}{\partial B}\exp(-E_i/kT)}{\sum_i \exp(-E_i/kT)} \qquad (5)$$

The derivatives $\delta E_i/\delta B$ were evaluated numerically by calculating the energy levels slightly below and slightly above (±5 Gauss) the operational magnetic field of a SQUID magnetometer (5000 G).

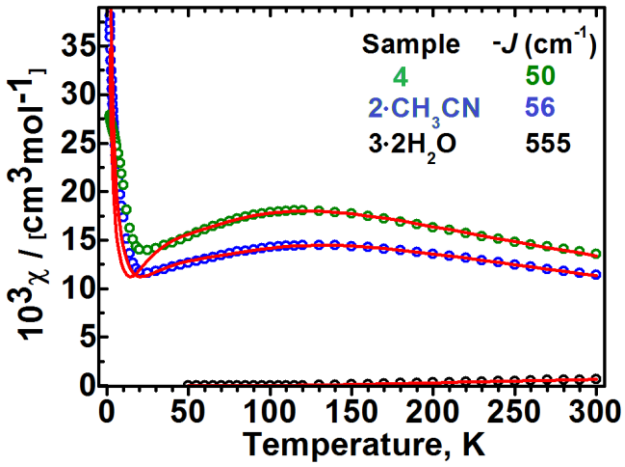

Figure 3.8. Magnetic susceptibility of $[Co_2(\mu\text{-OH})(\mu\text{-}\mathbf{L}_m)_2](ClO_4)_3\cdot CH_3CN$ (**2**·CH_3CN) and $[Co_2(\mu\text{-OH})(\mu\text{-}\mathbf{L}_m\mathbf{*})_2](ClO_4)_3$ (**4**). Circles experimental data, solid lines calculated. Data for $[Cu_2(\mu\text{-OH})(\mu\text{-}\mathbf{L}_m)_2](ClO_4)_3\cdot 2H_2O$ (**3**·$2H_2O$) are also shown for comparison.

As clearly indicated in Figure 3.8, that includes data for one of the copper(II) complexes, and Table 3.8, the antiferromagnetic interactions for the cobalt(II) complexes are weaker than for the copper(II) compounds, but still substantial. Relatively high contents of monomeric impurities, 2% in **2**·CH_3CN and 1.4% in **4**, were observed, impacting on the quality of the low-temperature susceptibility data. The monomeric cobalt(II) impurities are likely to have large zero-field splitting, complicating the low-temperature magnetic behavior; attempts of taking that kind of zfs into account were not successful. Higher-temperature data, above ~30K, were sufficient to determine the -*J* values in these dinuclear species. Contrary to what have been observed in our recent paper on analogous fluoride bridged compounds of the type $[Co_2(\mu\text{-F})(\mu\text{-}\mathbf{L}_m\mathbf{*})_2]^{3+}$,[6b] the sign of the *D* parameters could not be determined from the magnetic data and the reported results of the fitting is with either positive or negative *D*. The effect of the sign of *D* on -*J* is moderate. The magnitude of *D* is not surprising, as high-spin cobalt(II) was found to exhibit even larger zero-field splitting.[20] The data for the nickel(II) complex were not interpretable, presumably due to the high contents of monomeric impurities with

large zfs. The small sample size available for $[Fe_2(\mu\text{-}OH)(\mu\text{-}\mathbf{L}_m)_2](ClO_4)_3\cdot 1.5CH_3OH$ prevented collection of magnetic data.

Table 3.8. Spin Hamiltonian Parameters for the $[Co_2(\mu\text{-}OH)(\mu\text{-}\mathbf{L})_2](ClO_4)_3$ Complexes, where **L** = $\mathbf{L}_m$ or $\mathbf{L}_m$*.

Complex	$-J$ (cm^{-1})	D (cm^{-1})	g_{ave}
2·CH_3CN	56	-30	2.33
	51	67	2.29
4	50	-30	2.47
	48	47	2.45

EPR. Only the copper(II) complexes showed EPR spectra (Figure 8 and 9), while the cobalt(II) and nickel(II) analogues were EPR-silent at any frequency and temperature. In a coupled cobalt(II) system, the *D* parameter on a single ion (eq. 4) of 30 cm^{-1} (Table 3) contributes 72 cm^{-1} to the *D* parameter of the coupled triplet state (eq. 6),[21] far above the possibilities of our high field EPR instrument, where the maximum microwave quantum energy is about 14 cm^{-1}. This effect is not so strong in the case of nickel(II) dinuclear systems, but all complexes studied here exhibited strong non-resonant microwave absorption affecting even the quality of the spectra of the copper(II) complexes. Spectra of the copper(II) compounds were very weak and noisy even at 309 K, yet well reproducible, but could not be recorded at low temperatures as a result of the strong antiferromagnetic interactions. Standard spin Hamiltonian for $S = 1$ was used to interpret these spectra:

$$\hat{\boldsymbol{H}}_{\boldsymbol{S}} = \mu_B \boldsymbol{B}\cdot\{\boldsymbol{g}\}\cdot\hat{\boldsymbol{S}} + D\{\hat{\boldsymbol{S}}_z^2 - S(S+1)/3\} + E(\hat{\boldsymbol{S}}_x^2 - \hat{\boldsymbol{S}}_y^2) \qquad (6)$$

Presence of two different species in **3**·$1.5CH_3CN$ causes very broad and ill-defined resonances in its spectrum and the parameters above represent an average of the two species. Sample **6**·$2H_2O$ produced spectra of much better quality than **3**·$2H_2O$ and **3**·$1.5CH_3CN$ in the 200 GHz frequency range, but no spectrum could be recorded in the

400 GHz range. Opposite to this, the best spectrum of **3**·2H_2O was obtained with 412.8 GHz at 309 K, the highest temperature possible in our experimental setup. While very weak and noisy, this spectrum (Figure 3.9) is very well reproducible.

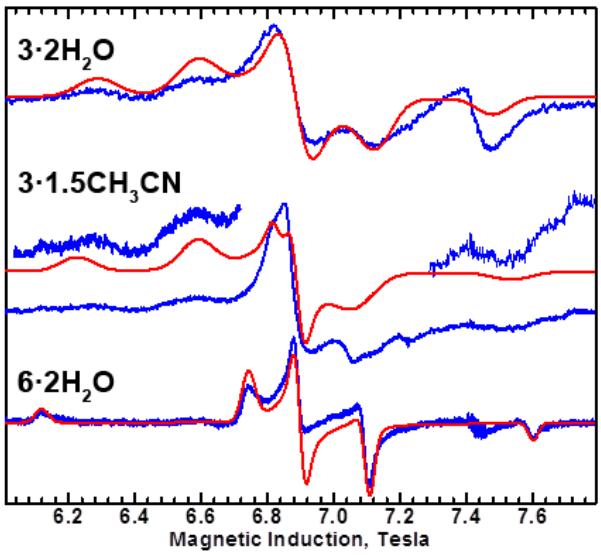

Figure 3.9. High-Frequency EPR spectra of the copper(II) complexes recorded with ν = 208.00 GHz at 305 K. The red lines are simulated with g_x = 2.16, g_y = 2.31, g_z = 2.035, D = 0.168 cm^{-1}, E = 0.051 cm^{-1} for **3**·2H_2O, g_x = 2.16, g_y = 2.32, g_z = 2.035, D = 0.224 cm^{-1}, E = 0.056 $cm^{-1}$for **3**·1.5CH_3CN and g_x = 2.123, g_y = 2.310, g_z = 2.019, D = 0.235 cm^{-1}, E = 0.142 cm^{-1} for **6**·2H_2O.

The signs of the D and E parameters could not be determined and the absolute values are listed in Table 2. However, E must have the same sign as D in each case. An interesting feature of the complex **6**·2H_2O is the low value, 2.02, of one of its g components. Analogous complexes such as $[Cu_2(\mu\text{-}F)(\mu\text{-}\mathbf{L})_2](BF_4)_3$, **L** = $\mathbf{L}_m$ or $\mathbf{L}_m$*, have one of the g components exactly 2, indicating that the ground state orbital of copper(II) is d_{z^2} instead of the more commonly encountered among copper(II) complexes $d_{x^2-y^2}$. This appears to be not fully realized in **6**·2H_2O. DFT calculations (vide infra) indicate that the ground state in our OH^- bridged species is a mixture of d_{z^2} and $d_{x^2-y^2}$. The $d_{x^2-y^2}$ character is most pronounced in **3**·2H_2O, while the d_{z^2} character is prevalent in **6**·2H_2O. Another

characteristic feature is the very strong "rhombicity" of the EPR parameters - three very different *g* values and *E* parameter comparable to *D*. The mixed character of the ground state, particularly in **6**·2H_2O, introduces an ambiguity in assigning the *g* values – it must be decided which of the *g* components will be labeled "z". In a pure d_{z^2} case, the smallest *g* should be named g_z, and also it should be closer to 2 than that found in **6**·2H_2O (2.019). In **3**·2H_2O there is less ambiguity because the smallest *g* component is significantly larger than that in **6**·2H_2O and calls for the $d_{x^2-y^2}$–type parameters. When choosing g_z = 2.019, one obtains the parameter set for **6**·2H_2O: g_x = 2.123, g_y = 2.310, g_z = 2.019, *D* = 0.235 cm^{-1}, *E* = 0.142 cm^{-1} (Figure 3.9). A choice of the 2.310 component as g_z results in a parameter set g_x = 2.123, g_y = 2.019, g_z = 2.310, *D* = 0.330 cm^{-1}, *E* = 0.046 cm^{-1}. These two sets are equivalent and result in the same EPR simulation. By convention, one would be tempted to choose the latter parameter set with $|E| < |D/3|$, but the former one is useful in discussing the zero-field splitting parameters in **6**·2H_2O and even more so in similar linear M-X-M bridged complexes.[6]

"Broken symmetry" DFT Calculation of the Exchange Integrals (-*J*). "Broken symmetry" Density Functional Theory calculations were performed by using the software ORCA[21] to estimate and rationalize the magnitude of the exchange integral. A self-consistent field (SCF) calculation is first performed for the maximum spin state of the dinuclear species. Next, a "broken symmetry" state is set up with all unpaired electrons being spin-up on one metal and spin-down on the other, and another SCF calculation is ran. The energies of the high-spin and broken symmetry states are finally used to estimate the exchange integral value, -*J* (for Hamiltonian $\hat{\mathbf{H}} = -J\,\hat{\mathbf{S}}_1\hat{\mathbf{S}}_2$) based on the equation $-J = 2(\boldsymbol{E}_{HS}-\boldsymbol{E}_{BS})/(\langle \boldsymbol{S}^2\rangle_{HS}-\langle \boldsymbol{S}^2\rangle_{BS})$, where $\boldsymbol{E}_{HS}$ and $\boldsymbol{E}_{BS}$ are the energies of the high-spin (HS)

and the broken-symmetry (BS) states and $<\boldsymbol{S}>^2$ are the expectation values of the spin-squared operator in the HS and BS states. Ahlrichs-type basis set TZVPP for copper(II) and SVP for other atoms were used, combined with the B3LYP functional.[22] Ahlrichs polarisation functions from basis H - Kr R and auxiliary bases from the TurboMole library were also used.[23]

The molecules were simplified by removal of the pyrazolyl methyl groups and benzene rings and placement of hydrogens at appropriate locations. All remaining atoms were retained at the positions determined by the X-ray structures. The coordinate system for the complexes with d_z^2 ground state, representing all but one case (**3**·2H_2O), was chosen with the X axis along the metal-O vector and the Z axis perpendicular to the plane of oxygen and two equatorial nitrogen atoms. For **3**·2H_2O, with a d_x^2-$_y^2$ ground state, the Z axis was the least-squares plane of the bridging O atom and the three short-distance N atoms. The Y axis was perpendicular to both Z and Cu-O.

Table 3.9 shows the results of these calculations. Although the Cu-O-Cu angle in **3**·2H_2O (141.0^o) is the same as in one of the species in **3**·1.5CH_3CN (141.2^o), the -*J* value calculated from DFT for the latter is much smaller than the one calculated for the former. This difference appears to be associated with the character of the ground state, which is more of the d_{x2-y2} type in **3**·2H_2O than in **3**·1.5CH_3CN, allowing for a stronger overlap of the magnetic orbitals. The ground state character is reflected in the spin densities on the axial and equatorial nitrogen ligands (Figure 3.10 and Table 3.10).

Table 3.9. Spin Densities and Orbital Interactions for the Copper(II) Complexes as Calculated from the "Broken Symmetry" DFT method in the High-Spin State.

Complex	**3**·2H_2O[a]	**3**·1.5CH_3CN[b]	**3**·1.5CH_3CN[b]	**6**·2H_2O[b]
Cu-O-Cu(°)	141.0	141.2	151.2	180
Spin density				
Cu[c]	0.658	0.665	0.664	0.667
O	0.153	0.157	0.144	0.136
N on trigonal axis	0.094	0.098	0.095	0.102
	0.085	0.089	0.089	0.084
N in trigonal plane	0.074	0.051	0.065	0.049
	0.005	0.016	0.010	0.024
Overlap integral	0.172	0.156	0.191	0.203
$E_{antisym}$-E_{sym} **(cm^{-1})**[d]	5710	5280	6430	6730
Exchange integral, -*J* (cm^{-1})				
Calc., DFT	700	514	916	994
Exp.	555	649		808

[a]Z axis along the tetragonal pyramid axis and X axis close to Cu-O. [b]Z axis along the trigonal bipyramid axis and X axis close to Cu-O. [c]Average of two copper(II) ions. [d]Calculated from the averages of the spin-up and spin-down energies of the respective antisymmetric and symmetric orbitals.

The ratio of -*J* calculated from DFT (Table 3.9) to the experimental -*J* in **3**·2H_2O and in **6**·2H_2O are 1.26 and 1.23, respectively, therefore the factor ~1.24 was taken as the systematic overestimation error in these DFT calculations. The corrected DFT values of -*J* for the two molecules in **3**·1.5CH_3CN would then be -415 cm^{-1} for the molecule with the 141.2° Cu-O-Cu angle and -739 cm^{-1} for that with the 151.2° Cu-O-Cu angle. The average of these two numbers, 577 cm^{-1}, compares reasonably with the experimental -*J* value, 649 cm^{-1} for **3**·1.5CH_3CN.

As shown in Table 3.10, the calculations match the measured weaker, but still substantial, antiferromagnetic interactions for the cobalt(II) complexes. Similar trends were observed previously for the fluoride bridged analogues.

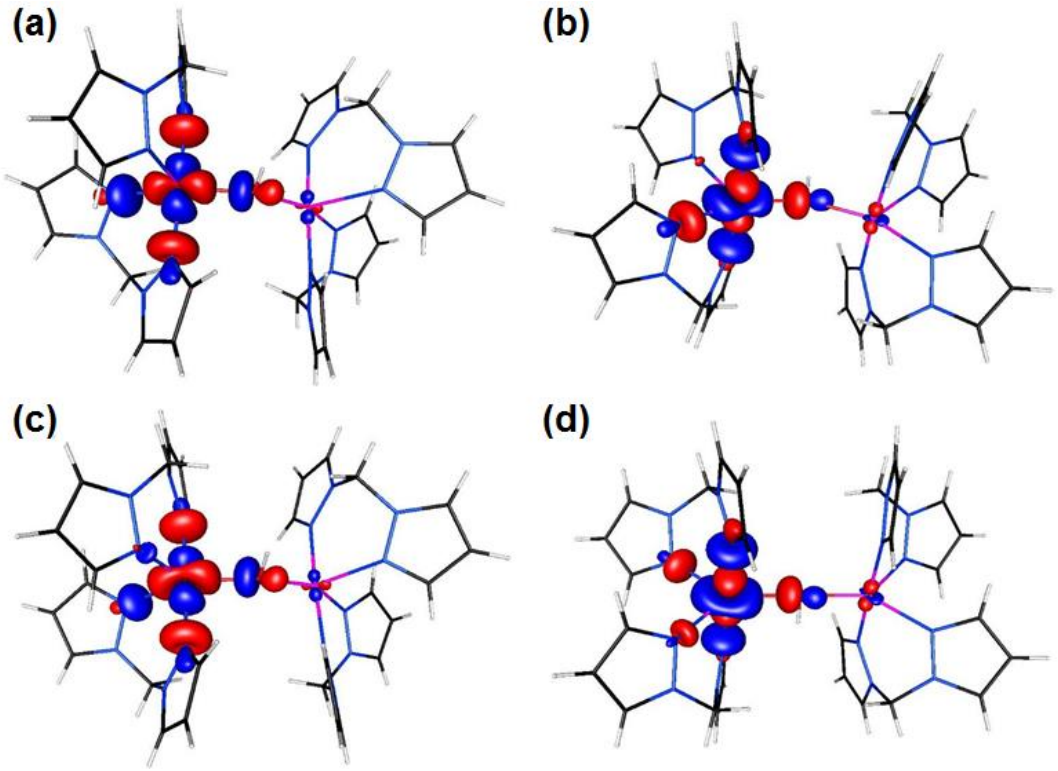

Figure 3.10. Change of the ground state character from predominatly d_{x2-y2} character to predominatly d_{z2} character: **3**·2H_2O (a), **3**·1.5CH_3CN, Cu-O-Cu 151˚ (b), **3**·1.5CH_3CN Cu-O-Cu 141˚ (c) and **6**·2H_2O (d). The participation in the magnetic orbital of one of the equatorial nitrogen ligands (using the trigonal bipyramid nomenclature) is increasing from (a) to (d) and correlates with the τ_5 values (0.30, 0.42, 0.40 and 0.68 respectively) indicating increasing d_{z2} character.

Table 3.10. Spin densities and overlap integrals of the three magnetic orbitals for the cobalt(II) complexes as calculated from the "broken symmetry" DFT.

Complex	**4**	**2**·CH_3CN
M-O-M (°)	180	166.8
Spin density		
M	2.767	2.748
O	0.098	0.119
N on trigonal axis	0.034	0.034
	0.039	0.040
N in trigonal plane	0.034	0.035
	0.034	0.032
Overlap integral	0.111	0.139
	0.066	0.083
	0.001	0.006
Exchange integral, -*J*, cm^{-1}		
Calc., DFT	58	99
Exp.	50, 48	56, 51

Discussion

Two series of $[M_2(\mu\text{-OH})(\mu\text{-}\mathbf{L})_2](ClO_4)_3$ complexes with $\mathbf{L}_m$ and $\mathbf{L}_m$* were synthesized by deprotonation of the water of crystallization of the starting perchlorate salts, in order to probe the effects of changing the metal centers, or bridging ligands, on the geometry and therefore on the magnetic properties of the metallacycles. Previous work has demonstrated that the geometry of the metal coordination environment and the position and type of bridging groups greatly affect the magnetic interactions between the metal centers,[7] but the complexes reported here represent the first extensive series of monohydroxide bridged compounds where the M-O-M angle is large or in some cases exactly 180°.

The M-O-M angle is the main metric that defines the geometry around the metal centers: distorted trigonal bipyramidal for large or linear angles (156-180˚), or distorted square pyramidal for bent M-O-M angles (141-151˚). As previously demonstrated with the analogous $[M_2(\mu\text{-F})(\mu\text{-}\mathbf{L})_2]^{3+}$ complexes, these (pyrazolyl)methane ligands favor the trigonal bipyramidal geometry over the generally more favored square pyramidal,[24] especially the more bulky $\mathbf{L}_m$* ligand. The copper(II) compounds with both ligands undergo pseudo Jahn-Teller distortions that cause the expected bond length anomalies (axially elongated square pyramid for $\mathbf{3}\cdot 2H_2O$ and axially compressed trigonal bipyramid for $\mathbf{6}\cdot 2H_2O$).[25]

For compounds **4**-**6**, the M-O-M angle is exactly 180°. These and previous results suggest that the metallacycles of the bulkier $\mathbf{L}_m$* favor a structure where the M-O-M angle is 180°. While a large number of hydroxide bridged compounds have been synthesized[26] examples of a perfectly linear M-O(H)-M bridge were not found in the

literature, and only a couple of examples of nearly linear hydroxide bridges.[27,28] Some of these bridges are supported by sterically protecting, large porphyrin ligands. The Fe-O-Fe angle of 173.6˚, close to perfect linearity, was measured for [(tpp)Fe-O(H)-Fe-(tpp)]($CB_{11}H_6Cl_6$)·toluene (tpp = tetraphenylporphyrinate).[27a] Another example of a monohydroxide bridged compound [$Cu_2(L^{21})(OH)$](CF_3SO_3)$_3$·H_2O, L^{21} = amino-cryptand, with M-O-M angle close to 180˚ was reported by the Nelson group where the hydroxide bridge is supported by aminocryptands; the Cu-O-Cu is 174.0˚.[28]

Hoffmann and co-workers[7b] worked with theoretical models investigating the relationship between structure and magnetism of a model five-coordinate copper(II) compound $[Cl_4CuClCuCl_4]^{5-}$ in both trigonal bipyramidal and square pyramidal geometry. The result showed that in the trigonal bipyramidal geometry, the unpaired electron of each copper(II) is located in a d_{z^2} shaped orbital. The singlet-triplet energy gap, which corresponds to -*J*, the intramolecular exchange coupling constant, involves the sideways symmetric antibonding combination of the copper(II) $3d_{z^2}$ shaped orbitals with the Cl s orbital and sideways antisymmetric combination of the same metal orbitals with a Cl $3p_x$ orbital. Consequently the -*J* values are excellent descriptors of the strength of the antiferromagnetic exchange interactions. Upon distortion of the trigonal bipyramidal geometry into square pyramidal, the highest energy orbital becomes a $d_{x^2-y^2}$ type orbital (basal plane of the square pyramid) and the bridging ligand becomes axial. The bridging ligand has no orbitals with the proper symmetry to interact with the $d_{x^2-y^2}$ type orbitals. The symmetric and antisymmetric combinations of the two orbitals remain degenerate in such a dinuclear compound and there is no expected magnetic interaction of the unpaired electrons, $-J = 0$. As the geometry is distorted from square pyramidal to

trigonal bipyramidal the degeneracy of these states is lifted, allowing better interactions between the metal centers, and increasing the singlet-triplet energy gap.

Although the change in the Cu-O-Cu angle of the $[Cu_2(\mu\text{-}OH)(\mu\text{-}\mathbf{L})_2](ClO_4)_3$, **L** = $\mathbf{L}_{\boldsymbol{m}}$ or $\mathbf{L}_{\boldsymbol{m}}$*****, compounds from 180° for **6**·$2H_2O$ to 151.0-141.0° in **3**·$2H_2O$ and **3**·$1.5CH_3CN$ results in the distortion of the geometry around copper(II) from a geometry resembling more a trigonal bipyramid into one more square pyramidal, in contrast to the similar distortion presented by Hoffmann,[7b] in **3**·$2H_2O$ the hydroxide remains in the equatorial position of the distorted square pyramid. Therefore, significant antiferromagnetic superexchange interactions are still promoted through the $d_{x^2-y^2}$ and the oxygen s and p_x orbitals. The axial site is occupied by one of the four nitrogen atoms of $\mathbf{L}_{\boldsymbol{m}}$. The "broken-symmetry" DFT calculations for **3**·$2H_2O$ and **3**·$1.5CH_3CN$ show increasing participation of one of the equatorial nitrogen ligands (using the trigonal bipyramidal nomenclature) in the magnetic orbital of copper(II) in the sequence **3**·$2H_2O$ < **3**·$1.5CH_3CN$ (151°) < **3**·$1.5CH_3CN$ (141°) < **6**·$2H_2O$, which may be used as a measure of the increasing d_{z^2} character of the magnetic orbital. (Table 3.10, Figure 3.10). This geometrical distortion from a geometry with more square pyramidal character than trigonal bipyramidal is also reflected by the τ_5 values[19]: 0.30 for **3**·$2H_2O$ (141°) < 0.40 for **3**·$1.5CH_3CN$ (151°) < 0.42 for **3**·$1.5CH_3CN$ (141°) < 0.68 for **6**·$2H_2O$ (180°).

While the Cu···Cu non-bonding distance in **6**·$2H_2O$ is 0.2-0.4 Å longer than in the analogous **3**·$2H_2O$ and **3**·$1.5CH_3CN$, the Cu-O-Cu angle is larger by approximately 30-40°, resulting in Cu-O-Cu angle of 180°. This unique arrangement promotes unusually strong antiferromagnetic superexchange interactions, with $-J$ = 808 cm^{-1}. The "broken-symmetry" DFT calculations showed that the overlap integral is larger than the ones

previously reported[6] for $[Cu_2(\mu\text{-}X)(\mu\text{-}\mathbf{L_m}^*)_2](BF_4)_3$ X = F^-, Cl^-, and it is close to the Br^- bridged analogue, where the Cu-X-Cu angle is fixed at 180° (0.125, 0.187, 0.228 respectively *vs.* 0.203 for **6**·$2H_2O$ in the triplet state). The spin delocalization towards the bridging oxygen s (0, 0.0053, 0.0055 respectively *vs.* 0.0061) and p_x (0.072, 0.096, 0.116 respectively *vs.* 0.123) orbitals is larger than any of the halide bridged compounds, probably also a result of the unusual linearity of the Cu-O-Cu angle.

In this work the magnetic data for copper(II) could be compared only with the magnetic properties of analogous cobalt(II) complexes. The lower -*J*, ca. 50 cm^{-1}, for the cobalt(II) hydroxide complexes **2**·CH_3CN and **4** versus the copper(II) hydroxide complexes was supported by the DFT calculations and was expected given that -*J* values decrease with the square of the number of unpaired electrons on the metal.[17] The –*J* values for copper(II) and cobalt(II) complexes observed here as well as in reference 6a roughly obey that rule. For both $[Cu_2(\mu\text{-}OH)(\mu\text{-}\mathbf{L_m}^*)_2]^{3+}$/$[Cu_2(\mu\text{-}F)(\mu\text{-}\mathbf{L_m}^*)_2]^{3+}$ and $[Co_2(\mu\text{-}OH)(\mu\text{-}\mathbf{L_m}^*)_2]^{3+}$/$[Co_2(\mu\text{-}F)(\mu\text{-}\mathbf{L_m}^*)_2]^{3+}$ pairs, the ratio of the -*J* values is similar, at about 1.5, showing that both the copper(II) and the cobalt(II) hydroxide complexes have stronger antiferromagnetic interactions than the analogous fluoride bridged complexes.

Five coordinate, dinuclear copper(II) compounds with a single hydroxide bridge connecting the metal centers, for which both structural and magnetic data is available, are shown in Table 3.11. These complexes are listed in order of increasing -*J* and show the general trends described above, however Table 3.11 contains exceptions to the trends for which there are currently no explanations.

In the two recent studies that summarize the magnetostructural correlations in monohydroxide bridged copper(II) complexes,[29,30] it was argued that the main structural

feature affecting the geometry and thus the magnitude of the intramolecular exchange coupling constant (-*J*) is the Cu-O-Cu angle.

The compound $[Cu_2(L^{21})(OH)](CF_3SO_3)_3 \cdot H_2O$, L^{21} = amino-cryptand, (Table 3.11) with Cu-O-Cu angle of 174.0˚, synthesized by Nelson *et al.*[28], exhibits strong antiferromagnetic behavior, with $-J = 865\ cm^{-1}$. The geometry around the metal centers is trigonal bipyramidal and the Jahn-Teller axes are pointing at each other. This arrangement allows the most advantageous overlap of the copper(II) d_z^2 and the oxygen p_z orbitals and explains the efficient antiferromagnetic superexchange. On the contrary, in **6**·$2H_2O$ while the geometry is also trigonal bipyramidal, the Jahn-Teller axes are perpendicular to the Cu···Cu direction. Interestingly, this arrangment, where the d_{z2} orbital is overlapping the bridging group with the "doughnut" portion, still results in unexpectedly high exchange coupling constants, $-J = 808\ cm^{-1}$, comparable with -*J* for Nelson's compound.

The -*J* values for the copper(II) compounds where the monohydroxide bridge is in the equatorial plane of the trigonal bipyramid, similarly to **6**·$2H_2O$, varies between 86 and 322 cm^{-1}. The larger energy gap, $-J = 322\ cm^{-1}$, measured for $[Cu_2(L^7)_4(OH)](ClO_4)_3$ (L^7 = 2,2'-bipyridine),[36] is a very special case where one copper(II) center is trigonal bipyramidal with the hydroxide in the equatorial position, but the other copper(II) is in a square pyramidal geometry. This unusual arrangement cannot be compared directly to **6**·$2H_2O$. The only monohydroxide bridged compound with the exact same geometry as **6**·$2H_2O$ is $[Cu_2(L^1)(OH)](ClO_4)_3 \cdot 2H_2O$ (L^1 = 1,4,8,11-tetrakis(2-pyridylmethyl)-1,4,8,11-tetraazacyclotetradecane),[31] with Cu-O-Cu angle 134.6˚. This compound is weakly

Table 3.11. Structural and Magnetic Data ($\hat{H} = -J\,\hat{S}_1\hat{S}_2$) for Five Coordinate Dicopper(II) Complexes with a Single Hydroxide Bridge.

Formula[a]	Cu···Cu (Å)	Cu-O-Cu (°)	Geometry[b]	τ_5	$-J$ (cm^{-1})	Ref.
$[Cu_2(L^1)(OH)](ClO_4)_3 \cdot 2H_2O$	3.71	134.6	TBPeq	0.51	86	Asato[31]
$[Cu_2(L^2)(OH)](ClO_4)2 \cdot H_2O$	3.03	103.7	SP	0.16/0.17	100	Neves[32]
$[Cu_2(L^3)_2(OH)(ClO_4)(MeCN)]ClO_4$	3.29	117.5	SP	0.15/0.08	220	Meyer[33]
$[Cu_2(L^4)(OH)(ClO_4)]ClO_4$	2.90	98.1	SP	0.19/0.34	238	Neves[32]
$[Cu_2(L^5)(OH)(H_2O)(ClO_4)](ClO_4)_2$	3.57	141.7	SP	0.26	240	Drew[34]
$[Cu_2(L^6)(OH)](NO_3)_2(H_2O)_2]NO_3$	3.10	109.3	SP	0.04/0.18	308	Thompson[35]
$[Cu_2(L^7)_4(OH)](ClO_4)_3$	3.65	141.6	TBPeq/SP	0.71/0.32	322	Hendrickson[36]
$[Cu_2(L^8)_2(OH)](ClO_4)_3$	3.66	139.8	SP	0.17	330	Spiccia[37]
$[Cu_2(L^9)(dpm)(OH)](ClO_4)_3 \cdot 2H_2O$	3.66	137.9	SP	0.14	365[c]	Spodine[38]
$[Cu_2(L^{10})(OH)(NO_3)(H_2O)](NO_3) \cdot 2H_2O$	3.28	117.5	SP	0.30/0.33	395	Thompson[39]
$[Cu_2(L^{11})(OH)](CF_3SO_3)(BPh_4)_2$	3.89	166.1	SP	0.10/0.13	430	Nelson[40]
$[Cu_2(L^{10})(OH)(H_2O)_2](ClO_4)_2 \cdot H_2O$	3.31	117.9	SP	0.14/0.11	443	Thompson[39]
$[Cu_2(L^{12})(OH)](ClO_4)_3 \cdot 1.5H_2O$	3.74[d]	150.6[d]	SP	0.16[d]	510	Adams[41]
$[Cu_2(L^{13})(OH)(H_2O)](ClO_4)_2$	3.01	102.9	SP/SPl	0.05	529	Kitagawa[42]
$[Cu(L^{14})(L^{15})(OH)](ClO_4) \cdot H_2O$	3.57	138.2	SP	0.003	550	Spiccia[43]
$[Cu_2(L_m)_2(OH)](ClO_4)_3 \cdot 2H_2O$ (3·2H_2O)	3.87	141.0	SP	0.29/0.30	560	this work
$[Cu_2(L_m)_2(OH)](ClO_4)_3 \cdot 1.5CH_3CN$ (3·1.5CH_3CN)	3.64	141.2/151.0	SP	0.42/0.40	649	this work
$[Cu_2(L^{16})(OH)](ClO_4)_3 \cdot H_2O$	3.76	156.0	TBPax	0.83	691	Reedijk[29]
$[Cu_2(L^{17})_2(OH)](ClO_4)_3$	3.64	136.5	TBPax	0.66	760	Duan[44]
$[Cu(L^{18})Br]_2(OH)(pz)$	3.38	123.9	SP	0.26/0.42	770	Escrivà[45]
$[Cu_2(L^{19})(OH)](ClO_4)_3 \cdot CH_3CN$	3.76	155.6	TBPax/SP	0.83/0.42	795	Nelson[46]
$[Cu_2(L_m^*)_2(OH)](ClO_4)_3 \cdot 2H_2O$ (5·2H_2O)	4.05	180.0	TBPeq	0.68	808	this work
$[Cu_2(L^{20})(OH)](BF_4)_3$	3.38	132.2	SP	0.13	850[c]	Osborn[47]
$[Cu_2(L^{21})(OH)](CF_3SO_3)_3 \cdot H_2O$	3.90	174.0	TBPax	0.88/0.95	865	Nelson[29]
$[Cu_2(L^{22})(OH)(ClO_4)](ClO_4)_2 \cdot CHCl_3$	3.64	143.7	SP	0.23	>1000	Lippard[48]
$[Cu_2(L^{23})(OH)][ClO_4]_2 \cdot (CH_3)_2CO$	3.53	136.7	SP	0.30/0.11	~1000	Wang[49]
$[Cu_2(L^{24})(OH)](ClO_4)_3$	3.39	123.0	SP/Oh	0.08	1146	Brooker[50]

[a]L^1 = 1,4,8,11-tetrakis(2-pyridylmethyl)-1,4,8,11-tetraazacyclotetradecane; L^2 = 6-amino-6-methylperhydro-1,4-diazepine; L^3 = 3,5-[3-bis(2-pyridyl)pyrazole-1-ylmethyl]pyrazole; L^4 = 2-[N,N-di(pyridine-2ylmehtyl)-aminomethyl]-4-methyl-6-[(6-methyl-[1,4]-diazepan-6-yl)imino-methyl]-phenol; L^5 = Shiff base of 2,6-diacetylpyridine and 3,6-dioxaoctane-1,8-diamine; L^6 = 1,4-bis(2-pyridylthio)phthalazine; L^7 = 2,2'-bipyridine; L^8 = 1-(2-Guanidinoethyl)-1,4,7-triazacyclononane; L^9 = 1,1,2,2-tetrakis-(2-pyridyl)ethylene, dpm = di(2-pyridyl)methane; L^{10} = N'3,N'6-dibenzylidenepyridazine-3,6-bis(carbohydrazonate); L^{11} = partially hydrolyzed Schiff base of 2,6-diacetylpyridine and tris(2-aminoethyl)amine, and tpmc = 1,4,8,11-tetrakis(2-pyridylmethyl)-1,4,8,11-tetraazacyclotetradecane; L^{12} = condensation of tris(2-aminoethyl)amine and 2,5-diformylfuran with $Ba(ClO_4)_2$; L^{13} = 2,6-bis[((4-imidazolylethyl)imino)methyl]-4-methylphenolate, L^{14} = 1,3-bis(1,4,7-triazacyclonon-1-ylmethyl)benzene; L^{15} = 4-nitrophenyl phosphate; L^{16} = 9,22-bis(pyridine-2'-ylmethyl) 1,4,9,14,17,22,27,28,29,30 decaazapentacyclo[22.2.$1^{4,7}$.$1^{11,14}$.$1^{17,20}$]triacontane 5,7(28),11(29),12,18,20(30), 2(27),25-octaene; L^{17} = tris(2-aminoethyl)-amine; L^{18} = 4-methoxy-2-(5-methoxy-3-methyl-1*H*-pyrazol-1-yl)-6-methylpyrimidine, pz = pyrazolate; L^{19} = 1,4,8,11,14,18,23,27-octaazabicyclo[9.9.9]nonacosane (amino-cryptand); L^{20} = 1,4-bis[(1-oxa-4,10-dithia-7-azacyclododecan-7-yl)methyl]-benzene; L^{21} = condensation of tris(2-aminoethyl)amine and 2,5-diformylfuran; L^{22} = 1,4,7,13,16,19-hexaaza-10,22-dioxatetracosane; L^{23} = N,N'-bis(8-quinolylmethy1)-1,4,10,13-tetraoxa-7,16-diazacyclooctadecane ; L^{24} = bis(pyridine-armed) acyclic Schiff base synthesized from 3,6-diformylpyridazine and two equivalents of 2-(2-aminoethyl)pyridine; [b]SP = square pyramidal (bridging O in equatorial position), TBPeq = trigonal bipyramidal with the bridge in an equatorial position, TBPax = trigonal bipyramidal with the bridge in an axial position, SPl = square planar; Oh = Octahedral. [c]this value is an average of three runs; [d]this value is an average due to two independent cations in the unit cell.

antiferromagnetic, $-J = 86$ cm^{-1}, the singlet-triplet energy gap is ten times smaller than the one measured for **6**·2H_2O, $-J = 808$ cm^{-1}. These results support our original statement above, that the strength of the antiferromagnetic interaction for **6**·2H_2O must be a consequence of the unusual linearity of the Cu-O-Cu angle, 180˚, which provides the most efficient superexchange pathway for this type of geometry. The other two new copper(II) complexes reported here have lower angles and lower $-J$ values, but clearly other geometric factors, reflected by τ_5, influence the strength of the interaction. The literature presents numerous examples of monohydroxide bridged compounds where the five coordinate copper(II) is in square pyramidal geometry (Table 3.11). The magnitude of the antiferromagnetic coupling constant varies in a large interval, $-J = 220$ to 1146 cm^{-1}. More commonly $-J$ seems to adopt a value between 300 and 600 cm^{-1}.

The data in Table 3.11 are in agreement with $-J$ measured for **3**·2H_2O and **3**·1.5CH_3CN, 555 and 649 cm^{-1} respectively. In the case of square pyramidal geometry significant superexchange interaction through the hydroxide bridge can be expected if the $d_{x^2-y^2}$ orbitals of copper(II) have the right orientation to overlap with p_x orbital of the hydroxide. For most examples with square pyramidal geometry, shown in Table 3.11, a change in the M-O-M angle (analogues to the in plane rotation of the $d_{x^2-y^2}$ orbitals) would still result in significant overlap of these two orbitals (reflected by $-J$). The very large $-J$ values (>1000 cm^{-1}) for some square pyramidal complexes[46,47-50] were explained by relatively large Cu-O-Cu angles, very short Cu-O bond lengths and/or the cooperative effect of the hydroxide and other auxiliary ligands.

A characteristic feature of the spin Hamiltonian parameters of the copper(II) complexes studied here is the large E/D ratio e.g. 0.62 in **6**·2H_2O.[51] The zfs parameters in

dinuclear copper(II) complexes depend on exchange interactions in excited states of the dinuclear complex, in which one of the copper(II) ions is in its ground state, and the other is in an excited state, like $J_{x^2-y^2,xy}$ in the formulas shown below, that was derived by Maurice *et al*. for the copper(II) paddlewheel complexes [copper(II) has $d_{x^2-y^2}$ ground state].[52]

An exchange interaction like $J_{x^2-y^2,xy}$ can only contribute to the zfs if there exists a non-zero matrix element of the angular momentum operator **L** between corresponding metal orbitals, for example $\langle d_{x^2-y^2}|\mathbf{L}_z|d_{xy}\rangle = 2i$.

Conclusions

The first extensive series of metal complexes containing single hydroxide bridges with large M-O-M angles, ranging from 141° to exactly 180°, of the formula $[M_2(\mu\text{-}OH)(\mu\text{-}\mathbf{L}_m)_2](ClO_4)_3$ [M = Fe(II), Co(II), Cu(II)] and $[M_2(\mu\text{-}OH)(\mu\text{-}\mathbf{L}_m\mathbf{*})_2](ClO_4)_3$ [M = Co(II), Ni(II), Cu(II)] have been prepared. As the M-O-M angle decreases, the geometry about the metal changes from distorted trigonal bipyramidal to square pyramidal. The two cobalt(II) complexes show moderate antiferromagnetic coupling, $-J$ = 48-56 cm^{-1}. The copper(II) complexes show strong antiferromagnetic coupling, $-J$ = 555-808 cm^{-1} where the exchange interactions were found to increase with the linearity of the Cu-O-Cu bridge and the d_z^2 character of the copper(II) ground state, a conclusion supported by DFT calculations. The EPR parameters of the copper(II) complexes show strong "rhombicity," which may be qualitatively understood by considering the interactions between the ground state of one copper(II) ion with the excited states of the other.

References

(1) Selected reviews: (a) Chakrabarty, R.; Mukherjee, P. S.; Stang, P. J. *Chem. Rev.* **2011,** 111, 6810. (b) Braga, D. J.; Brammer, L.; Champness, N. R. *CrystEngComm.* **2005**, *7*, 1. (c) Zaworotko, M. J. *Cryst. Growth and Des.* **2007**, *7*, 1740. (d) Zhao, D.; Timmons, D. J.; Yuan, D.; Zhou, H.-C. *Acc. Chem. Res.* **2011**, *44*, 123. (e) Chen, C.-L.; Zhang, J.-Y.; Su, C.-Y. *Eur. J. Inorg. Chem.* **2007**, 2997. (f) Northrop, B. H.; Yang, H.-B.; Stang, P. J. *Chem. Commun.* **2008**, *45*, 5896. (g) Lee, S. J.; Lin, W. *Acc. Chem. Res.* **2008**, *41*, 521. (h) Holliday, B. J.; Mirkin, C. A. *Angew. Chem. Int. Ed.* **2001**, *40*, 2022.

(2) Trofimenko, S. *J. Am. Chem. Soc.* **1970**, *92*, 5118.

(3) (a) Titze, C.; Hermann, J.; Vahrenkamp, H. *Chem. Ber.* **1995**, *128*, 1095. (b) Reger, D. L.; Grattan, T. C.; Brown, K. J.; Little, C. A.; Lamba, J. J. S.; Rheingold, A. L.; Sommer, R. D. *J. Organomet. Chem.* **2000**, *607*, 120. (c) Vahrenkamp, H. *Acc. Chem. Res.* **1999**, *32*, 589. (d) Vahrenkamp, H. *Dalton Trans.* **2007**, 4751.

(4) (a) Reger, D. L.; Gardinier, J. R.; Semeniuc, R. F.; Smith, M. D. *J. Chem. Soc. Dalton Trans.* **2003**, 1712. (b) Reger, D. L; Watson, R. P.; Gardinier, J. R.; Smith, M. D.; Pellechia, P. J. *Inorg. Chem.* **2006**, *45*, 10088. (c) Reger, D. L.; Foley, E. A.; Semeniuc, R. F.; Smith, M. D. *Inorg. Chem.* **2007**, *46*, 11345. (d) Reger, D. L.; Foley, E. A.; Smith, M. D. *Inorg. Chem.* **2009**, *48*, 936.

(5) Reger, D. L.; Foley, E. A.; Watson, R. P.; Pellechia, P. J.; Smith, M. D., Grandjean, F.; Long, G. J. *Inorg. Chem*. **2009**, *48*, 10658.

(6) (a) Reger, D. L.; Pascui, A. E.; Smith, M. D.; Jezierska, J.; Ozarowski A. *Inorg. Chem.* **2012**, *51*, 11820. (b) Reger, D. L.; Pascui, A. E.; Smith, M. D.; Jezierska, J.; Ozarowski A. *Inorg. Chem.* **2012**, *51*, 7966. (c) Reger, D. L.; Pascui, A. E.; Pellechia, P. J.; Smith, M. D. *Inorg. Chem.* **2013**, *52*, 11638.

(7) (a) Kahn, O. *Molecular Magnetism*; VCH Publishers, Inc.: New York, 1993. (b) Hay, P. J.; Thibeault, J. C.; Hoffmann, R. *J. Am. Chem. Soc.* **1975**, *97*, 4884.

(8) (a) Barrios, A. M.; Lippard, S. J. *J. Am. Chem. Soc.* **2000**, 122, 9172. (b) Thomann, H.; Bernardo, M.; McCormick, J. M.; Pulver, S.; Andersson, K. K.; Lipscomb, J. D.; Salomon, E. I. *J. Am. Chem. Soc.* **1993**, 115, 8881. (c) Yoon, J.; Fujii, S.; Solomon, E. I. *Proc. Natl. Acad. Sci*. **2009**, *106*, 6585. (d) Claus, H.; Decker, H. *Syst. App. Microbiol.* **2006**, *29*, 3. (e) Li, Y.; Wang, Y.; Jiang, H.; Deng, J. *Proc. Natl. Acad. Sci*. **2009**, *106*, 17002. (f) Gerdemann, C.; Eicken, C.; Krebs, B. *Acc. Chem. Res.* **2002**, *35*, 183. (g) Eicken, C.; Krebs, B.; Sacchetini, J. C. *Curr. Opin. Struct. Biol.* **1999**, *9*, 677. (h) Peisach, J.; Aisen, P.; Blumberg, W. E. *The Biochemistry of Copper*; Academic Press: New York, 1966.

(9) Hassan, A. K.; Pardi, L. A.; Krzystek, J.; Sienkiewicz, A.; Goy, P.; Rohrer, M.; Brunel, L.-C. *J. Magn. Reson.* **2000**, *142*, 300.

(10) (a) O'Connor, C. J. *Prog. Inorg. Chem.* **1982**, *29*, 203; (b) Bain, G. A.; Berry, J. F. *J. Chem. Ed.* **2008**, *85*, 532.

(11) (a) Barbour, L. J *J. Supramol. Chem.* **2003**, *1*, 189. (b) *POV-RAY 3.6*, **2006**, Persistence of Vision Raytracer Pty Ltd, Williamstown, Vic., Australia. (c) Laaksonen, L. gOpenMol version 3.00 www.csc.fi/english/pages/g0penMol.

(12) Wolsey, W. C. *J. Chem. Educ.* **1973**, *50*, A335-A337.

(13) SMART Version 5.630, SAINT+ Version 6.45. Bruker Analytical X-ray Systems, Inc., Madison, Wisconsin, USA, **2003**.

(14) SADABS Version 2.10. Bruker Analytical X-ray Systems, Inc., Madison, Wisconsin, USA, **2003**.

(15) CellNow, and TWINABS. Bruker Analytical X-ray Systems, Inc., Madison, Wisconsin, USA, **2003**.

(16) (a) Sheldrick, G.M. SHELXTL Version 6.14, Bruker Analytical X-ray Systems, Inc., Madison, Wisconsin, USA, **2000**. (b) Sheldrick, G.M. *Acta Cryst*. **2008**, A64, 112.

(17) Dolomanov, O. V.; Bourhis, L. J.; Gildea, R. J.; Howard J. A. K.; Puschmann, H. OLEX2: a complete structure solution, refinement and analysis program. *J. Appl. Cryst.* **2009**, *42*, 339.

(18) Shannon, R. D. *Acta Crystallogr.* **1976**, *A32*, 751.

(19) Addison, A. W.; Rao, T. N.; Reedijk, J.; Van Rijn, J.; Verschoor, G. C. *J. Chem. Soc. Dalton Trans*. **1984**, 1349. $\tau_5 = \frac{(\beta - \alpha)}{60°}$ Where α and β are the two largest angles measured around the metal centers. Perfect square pyramid: τ_5 = 0; Perfect trigonal bipyramid: τ_5 = 1.

(20) (a) Telser, J.; Ozarowski, A.; Krzystek, J. *Electron Paramag. Reson.* **2013**, *23*, 209. (b) Zadrozny, J. M.; Long, J. R. *J. Am. Chem. Soc.* **2011**, 133, 20732.

(21) (a) Neese, F. *ORCA - An ab initio, Density Functional and Semiempirical Program Package*, Version 2.9.1, **2012**. (b) Neese, F. - The ORCA program system WIREs, *Comput. Mol. Sci.* **2012**, *2*, 73.

(22) (a) Becke, D. A. *Phys. Rev. A* **1988**, *38*, 3098. (b) Perdew, J. P. *Phys. Rev. B* **1986**, *33*, 8822. (c) Perdew, J. P. *Phys. Rev. B.* **1986**, *34*, 7406. (d) Kendall, R. A.; Früchtl, H.A. *Theor. Chem. Acc.* **1997**, *97*, 158.

(23) (a) Schaefer, A.; Horn, H.; Ahlrichs, R. *J. Chem. Phys.* **1992**, *97*, 2571. (b) Ahlrichs, R. *et al*., unpublished results. The Ahlrichs auxiliary basis sets were obtained from the TurboMole basis set library under ftp.chemie.uni-karlsruhe.de/pub/jbasen.

(24) (a) Reinen, D.; Friebel, C. *Inorg. Chem.* **1984**, *23*, 791. (b) Arriortua, M. I.; Mesa, J. L.; Rojo, T.; Debaerdemaeker, T.; Beltrán-Porter, D.; Stratemeier, H.; Reinen, D. *Inorg. Chem.* **1987**, *27*, 2976. (c) Bianchi, A.; Fallani, D. G.; Ghilardi, C. A.; Sacconi, L. *J. Chem. Soc. Dalton Trans.* **1973**, 641.

(25) (a) Bersuker, I. B. in "*The Jahn–Teller Effect*" Univ. Press Cambridge, UK, 2006. (b) Harrison, D.; Kennedy D.; Hathaway, B. *Inorg. Nucl. Chem. Lett*. **1981**, *17*, 87.

(26) Selected publications: (a) Shakya, R.; Powell, D. R.; Houser, R. P. *Eur. J. Inorg. Chem.* **2009**, 5319. (b) Drabent, K.; Ciunik, Z., Ozarowski, A. *Inorg. Chem.* **2008**, *47*, 3358. (c) Ray, N. A.; Neves, A.; De Almeida, W. B.; Dos Santos, H. F.; Costa, L. A. S. *Int. J. Quantum Chem.* **2010**, *110*, 1432. (d) Wikstrom, J. P.; Filatov, A. S.; Mikhalyova, E. A.; Shatruk, M.; Foxman, B. M.; Rybak-Akimova, E. V. *Dalton Trans.* **2010**, *39*, 2504. (e) Wang, L.; Lu, S.; Zhou, Y.; Guo, X.; Lu, Y.; He, J.; Evans, D. G. *Chem. Commun.* **2011**, *47*, 11002. (f) Curtis, N. F.; Morgan, K. R.; Rickard, C. E. F.; Waters, J. M. *Polyhedron* **2010**, *29*, 1279. (g) Manzur, J.; Vega, A.; Garcia A. M.; Acuňa C.; Sieger, M.; Sarkar, B.; Niemeyer, M.; Lissner, F.; Schleid T.; Kaim, W. *Eur. J. Inorg. Chem.* **2007**, 5500. (h) Bruijnincx, P. C. A.; Buurmans, I. L. C.; Huang, Y.; Juhász, G.; Viciano-Chumillas, M.; Quesada, M.; Reedijk, J.; Lutz, M.; Spek, A. L.; Münck, E.; Bominaar, E. L.; Klein Gebbink, R. J. M. *Inorg. Chem.* **2011**, *50*, 9243. (i) Graham, B.; Hearn, M. T. W.; Junk, P. C.; Kepert, C. M.; Mabbs, F. E.; Moubaraki, B.; Murray, K.; Spiccia, L. *Inorg. Chem.* **2001**, *40*, 1536. (j) Incarvito, C.; Rheingold, A. L.; Gavrilova, A. L.; Qin, C. J.; Bosnich, B. *Inorg. Chem.* **2001**, *40*, 4101. (k) Plieger, P. J.; Downard, A. J.; Moubaraki, B.; Murray, K. S.; Brooker, S. *Dalton Trans.* **2004**, 2157. (l) He, C.; Lippard, S. J. *J. Am. Chem. Soc.* **2000**, *122*, 184. (m) Melnik, M *Coord. Chem. Rev.* **1982**, *42*, 259. (n) Tanase, S.; van Son, M.; van Albada, G. A.; de Gelder, R.; Bouwman, E.; Reedijk, J. *Polyhedron* **2006**, *25*, 2967. (o) Gutierrez, L.; Alzuet, G.; Real, J. A.; Cano, J; Borrás, J.; Casteñieras A. *Inorg. Chem*. **2000**, *39*, 3609. (p) Prescimone, A.; Sanchez-Benitez, J; Kamenev, K. K.; Moggach, S. A.; Warren, J. E.; Lennie, A. R.; Murrie, M.; Parsons, S.; Brechin, E. K. *Dalton Trans.* **2010**, *39*, 113. (q) References from Table 3.11.

(27) (a) Evans, D. R.; Mathur, R. S.; Heerwegh, K.; Reed. C. A.; Xie, Z. *Angew. Chem. Int. Ed.* **1997**, *36*, 1335. (b) Cheng, B.; Fries, P. H.; Marchon, J.-C.; Scheidt, W. R. *Inorg. Chem.* **1996**, *35*, 1024. (c) Scheidt, W. R.; Cheng, B.; Safo, M. K.; Cukiernik, F.; Marchon, J.-C.; Debrunner, P. G. *J. Am. Chem. Soc.* **1992**, *114*, 4420.

(28) (a) Lu, Q.; Latour, J. -M.; Harding, C. J.; Martin, N.; Marrs, D. J.; McKee, V.; Nelson, J. *J. Chem. Soc. Dalton Trans.* **1994**, 1471. (b) Harding, C. J.; McKee, V.; Nelson, J.; Lu, Q. *J. Chem. Soc. Dalton Trans.* **1993**, 1768.

(29) Koval, I. A.; van der Schilden, K.; Schuitema, A. M.; Gamez, P.; Belle, C.; Pierre, J.; Lüken, M.; Krebs, B.; Roubeau, O.; Reedijk, J. *Inorg. Chem.* **2005**, *44*, 4372.

(30) Patra, A.; Ray, M.; Mukherjee, R. *Polyhedron*, **2000**, 1423.

(31) Asato, E.; Toftlund, H.; Kida, S. *Inorg. Chim. Acta* **1989**, *165*, 207.

(32) Rey, N. A.; Neves, A.; Bortoluzzi, A. J.; Haase, W.; Tomkowicz, Z. *Dalton Trans.* **2012**, *41*, 7196.

(33) Singh, A. K.; van der Vlugt, J. I.; Demeshko, S.; Dechert, S.; Meyer, F. *Eur. J. Inorg. Chem.* **2009**, 3431.

(34) Drew, M. G. B.; McCann, M.; Martin-Nelson, M. *J. Chem. Soc. Dalton Trans.* **1981**, 1868.

(35) Chen, L.; Thompson, L. K.; Bridson, J. N. *Inorg. Chem.* **1993**, *32*, 2938.

(36) Haddad, M. S.; Wilson, S. R.; Hodgson, D. J.; Hendrickson, D. N. *J. Am. Chem. Soc.* **1981**, *103*, 384.

(37) Tjioe, L.; Joshi, T.; Forsyth, C. M.; Moubraki, B.; Murray, K. S.; Brugger, J.; Graham, B.; Spiccia, L. *Inorg. Chem.* **2012**, *51*, 939.

(38) Spodine, E.; Manzur, J.; Garland, M. T.; Kiwi, M.; Peña, O.; Grandjean, D.; Toupet, L. *J. Chem. Soc. Dalton Trans.* **1991**, 365.

(39) Dey, S. K.; Abedin, T. S. M.; Dawe, L. N.; Tandon, S. S.; Collins, J. L.; Thompson, L. K.; Postnikov, A. V.; Alam, M. S.; Müller, P. *Inorg. Chem.* **2007**, *46*, 7767.

(40) Harding, C. J.; Lu, Q.; Malone, J. F.; Marrs, D. J.; Martin, N.; McKee, V.; Nelson, J. *J. Chem. Soc. Dalton Trans.* **1995**, 1739.

(41) Adams, H.; Bailey, N. A.; Collinson, S. R.; Fenton, D. E.; Harding, C. J.; Kitchen, S. J. *Inorg. Chim. Acta.* **1996**, *246*, 81.

(42) Maekawa, M.; Kitagawa, S.; Munakata, M.; Masuda, H. *Inorg. Chem.* **1989**, *28*, 1904.

(43) Fry, F. H.; Spiccia, L.; Jensen, P.; Moubaraki, B.; Murray, K. S.; Tieknik, E. R. T. *Inorg. Chem.* **2003**, *42*, 5594.

(44) Duan, C.-y.; Lu, Z.-l; You, X.-z. *Trans. Met. Chem.* **1998**, *23*, 77.

(45) Escrivà, E.; García-Lozano, J.; Martínez-Lillo, J.; Nuñez, H.; Server-Carrió, J.; Soto, L.; Carrasco, R.; Cano, J. *Inorg. Chem.* **2003**, *42*, 8328.

(46) Chin, A.; Edgar, M.; Harding, C. J.; McKee, V.; Nelson, J. *Dalton Trans.* **2009**, 6315.

(47) Burk, P. L.; Osborn, J. A.; Youinou, M. *J. Am. Chem. Soc.* **1981**, *103*, 1273.

(48) Coughlin, P. K.; Lippard, S. J. *J. Am. Chem. Soc.* **1981**, *103*, 3228.

(49) Wang, D.; Xiang, H.; Wang, G.; Han, Z.; Yang, X.; Hu, H.; Yu, K. *J. Chem. Soc. Dalton Trans.* **1994**, 3325.

(50) Plieger, P. G.; Downard, A. J.; Moubaraki, B.; Murray, K. S.; Brooker, S. *Dalton Trans.* **2004**, 2157.

(51) *D* and *E* values reported here refer to the system of coordinates in which the Z direction is along the trigonal bipyramid axis. It is possible to convert them to obey the convention $E<=D/3$ by renaming the coordinate axes.

(52) (a) Maurice, R.; Sivalingam, K.; Ganyushin, D.; Guihery, N.; de Graaf, C.; Neese, F. *Inorg. Chem.* **2011**, *50*, 6229. (b) Ozarowski, A. *Inorg. Chem*. **2008**, *47*, 9760. (c) Ozarowski, A.; Szymanska, I. B.; Muziol, T.; Jezierska, J. *J. Am. Chem. Soc*. **2009**, *131*, 10279. (d) Reger, D. L.; Debreczeni, A.; Smith, M. D.; Jezierska, J. *Inorg. Chem*. **2012**, *51*, 1068.

Chapter IV

Synthesis and Structure–Magnetic Property Correlations in Solution and Solid State of Chloride and Bromide Bridged Dinuclear Metallacycles and Related Compounds[4]

[4]Partially adapted with permission from Reger, D. L.; Pascui, A. E.; Smith, M. D.; Jezierska, J.; Ozarowski, A. *Inorg. Chem.* **2012**, *51*, 7966-7968. DOI:10.1021/ic301321r

Introduction

Multinuclear complexes of magnetic metal centers are of current interest.[1] In order to understand the magnetic properties of complicated metallic clusters scientist must earn fundamental understanding of the magnetic behavior of simpler units. Significant attention was given to dinuclear systems where the metal centers are directly linked by small anions such as hydroxide[2], fluoride[3], chloride[4] and bromide[5]. While in the case of copper(II) dihydroxide bridged systems it was shown that the magnitude of the antiferromagnetic superexchange interaction expressed in terms of *J* (exchange coupling constant) corresponding to the singlet-triplet energy gap, correlates linearly with the Cu-O-Cu angle,[6] similar simple magneto-structural correlations were not found for the chloride bridged compounds.[7] The singlet-triplet energy gap seems to be dependent on M-Cl-M bond angles divided by the longer M-Cl bond length. This parameter follows a smooth curve.[7] Uncontrolled variations in the coordination sphere around the metal centers and a limited number of model compounds further complicate the observation of magneto-structural correlations.

Much of our current efforts are centered around the syntheses of metal complexes with third generation bis(pyrazolyl)methane ligands that control the overall structure of metal complexes by functionalization at the non-coordinating "back" position.[8] A relevant class of these ligands links two bis(pyrazolyl)methane units into a single molecule. Related to the work reported here, it was demonstrated that linking two bis(pyrazolyl)methane units through a 1,3-substituted arene spacer (Scheme 4.1) triggers the formation of dinuclear metallacycles (Scheme 4.2).[9] When the syntheses are carried out with metals in the 2+ oxidation state, the metallacycles form with small anions

bridging the two metals. This connection establishes a direct communication pathway between the metal centers, leading to antiferromagnetic superexchange interactions for metal systems with unpaired electrons.[1a]

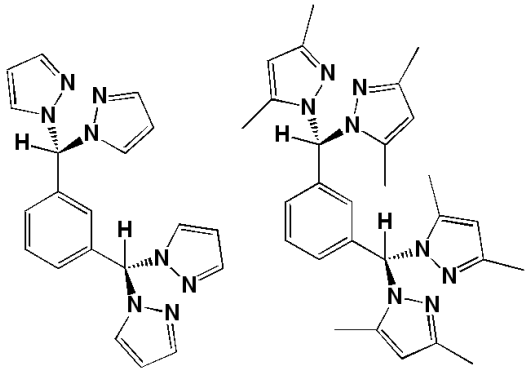

Scheme 4.1. Schematic representation of the ligands, $\mathbf{L}_m$ and $\mathbf{L}_m$*****.

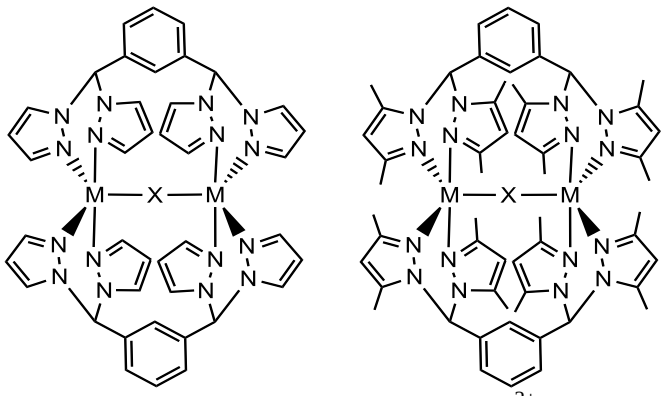

Scheme 4.2. Schematic representation of a $[Cu_2(\mu\text{-}X)(\mu\text{-}\mathbf{L})_2]^{3+}$ cation, X = F^-, OH^-. Left **L** = $\mathbf{L}_m$, right **L** = $\mathbf{L}_m$*****.

Of particular interest is the preparation of complexes that retain the metallacyclic structure, supported by $\mathbf{L}_m$ or $\mathbf{L}_m$***** while varying the bridging monoanions, in an effort to gain fundamental understanding of the magnetic properties of these systems.[9,10] The strength of the superexchange within the dinuclear units is altered by modification of the small, bridging anionic groups or the ligand ($\mathbf{L}_m$ or $\mathbf{L}_m$*****), which result in changes in the M···M distance and/or M-X-M angle. Changes in this angle may also result in

modifications in the geometry around the metal centers: trigonal bipyramidal *vs.* square pyramidal.[11] Previous chapters present results for complexes where the bridging group is fluoride or hydroxide, here analogous complexes of chloride or bromide are discussed.

Experimental Section

General Considerations. For the synthesis of the compounds standard Schlenk techniques were used. The solvents were not dried prior to use unless otherwise mentioned. The ligands, $\mathbf{L}_{m}$*[9a] and $\mathbf{L}_{m}$,[8b] were prepared following reported procedures. All other chemicals were purchased from Sigma-Aldrich or Strem Chemicals and used as received.

Crystals used for elemental analysis and mass spectrometry were removed from the mother liquor, rinsed with ether, and dried under vacuum, a process that removes solvent of crystallization, if present.

Mass spectrometric measurements were obtained on a MicroMass QTOF spectrometer in an acid-free environment. Elemental analyses were performed on vacuum-dried samples by Robertson Microlit Laboratories (Ledgewood, NJ).

^{1}H, ^{13}C and ^{113}Cd NMR spectra were recorded on a Varian Mercury/VX 300, Varian Mercury/VX 400, or Varian INOVA 500 spectrometer. All chemical shifts are in ppm and were referenced to residual undeuterated solvent signals (^{1}H), deuterated solvent signals (^{13}C), or externally to $CdCl_2$ (^{113}Cd).

High-field, high-frequency EPR spectra to determine *g*-factor at temperatures ranging from ca. 6K to 290 K were recorded on a home-built spectrometer at the EMR facility of the NHMFL.[12] The instrument is a transmission-type device in which microwaves are propagated in cylindrical lightpipes. The microwaves were generated by

a phase-locked Virginia Diodes source generating frequency of 13 ± 1 GHz and producing its harmonics of which the 2nd, 4th, 6th, 8th, 16th, 24th and 32nd were available. A superconducting magnet (Oxford Instruments) capable of reaching a field of 17 T was employed. The powder samples were not constrained and showed no magnetic torqueing at high magnetic fields.

Magnetic susceptibility measurements over the temperature range 1.8-300 K were performed at a magnetic field of 0.5 T using a Quantum Design SQUID MPMSXL-5 magnetometer. Correction for the sample holder, as well as the diamagnetic correction χ_D which was estimated from the Pascal constants[13] was applied.

XSEED, POV-RAY, MestReNOVA and GOpenMol were used for the preparation of figures.[14]

Caution! *Although no problems were encountered during this work with the perchlorate salts, these compounds should be considered potentially explosive!*[15]

$[Fe_2(\mu\text{-}Cl)(\mu\text{-}L_m^*)_2](ClO_4)_3$, 1. The iron(II) salts, $Fe(ClO_4)_2 \cdot 6H_2O$ (0.183 g, 0.504 mmol) and $FeCl_2$ (0.022 g, 0.17 mmol) were dissolved in 4 mL of methanol. Separately, **L_m*** (0.324 g, 0.672 mmol) was dissolved in 12 mL methanol and was transferred by cannula into the iron(II) solution. The reaction mixture was stirred for 5 h, after which time the system was filtered by cannula, the remaining solid was washed with Et_2O (10 mL) and dried under vacuum overnight, affording 0.200 g (42%) of the crude product. Single crystals suitable for X-ray studies were grown by the vapor diffusion of Et_2O into 1 mL acetonitrile solutions of **1**. Anal. Calcd.(Found) for $C_{56}H_{68}Cl_4Fe_2N_{16}O_{12}$: C, 47.68 (47.98); H, 4.86 (4.88); N, 15.89 (16.27). MS ESI(+) *m*/*z* (rel. % abund.) [assgn]: 1311

(2) $[Fe_2(\mathbf{L_m^*})_2Cl(ClO_4)_2]^+$, 605 (38) $[Fe_2(\mathbf{L_m^*})_2Cl(ClO_4)]^{2+}$, 483 (30) $[\mathbf{L_m^*} + H]^+$, 370 (100) $[Fe_2(\mathbf{L_m^*})_2Cl]^{3+}$.

$[Co_2(\mu\text{-}Cl)(\mu\text{-}L_m^*)_2](ClO_4)_3$, 2. Compound **2** was prepared similarly to compound **1** starting from $Co(ClO_4)_2 \cdot 6H_2O$ (0.184 g, 0.504 mmol) and $CoCl_2 \cdot 6H_2O$ (0.040 g, 0.17 mmol). The reaction afforded 0.194 g (40%) of a pink solid. Single crystals suitable for X-ray studies were grown by the vapor diffusion of Et_2O into 1 mL acetonitrile solutions of **2**. Anal. Calcd.(Found) for $C_{56}H_{68}Cl_4Co_2N_{16}O_{12}$: C, 47.47 (47.69); H, 4.84 (4.79); N, 15.82 (15.85). MS ESI(+) *m*/*z* (rel. % abund.) [assgn]: 1315 (2) $[Co_2(\mathbf{L_m^*})_2Cl(ClO_4)_2]^+$, 608 (20) $[Co_2(\mathbf{L_m^*})_2Cl(ClO_4)]^{2+}$, 372 (100) $[Co_2(\mathbf{L_m^*})_2Cl]^{3+}$.

$[Co_2(\mu\text{-}Cl)(\mu\text{-}L_m^*)_2](BF_4)_3$, 3. Under N_2, $[Co_2(\mu\text{-}F)(\mu\text{-}\mathbf{L_m^*})_2](BF_4)_3$ (0.166 g, 0.121 mmol) was dissolved in 10 mL dry acetonitrile and cooled to 0°C for 30 mins. The $(CH_3)_3SiCl$ (0.013 g, 0.12 mmol) was added all at once to the cobalt(II) solution. The solution immediately changed color from pink to blue. The reaction flask was removed from the cooling bath, allowed to warm to room temperature and stirred for 12 h. The solvent was removed by rotary evaporation and the product was recrystallized by vapor diffusion of Et_2O into 1 mL acetonitrile solutions of the blue solid. The resulting pink crystals were identified as **3**, 0.050 g (30%). Anal. Calcd.(Found) for $C_{56}H_{68}ClCo_2N_{16}B_3F_{12}$: C, 48.78 (48.20); H, 4.97 (4.57); N, 16.25 (16.17). MS ESI(+) *m*/*z* (rel. % abund.) [assgn]: 1291 (2) $[Co_2(\mathbf{L_m^*})_2Cl(BF_4)_2]^+$, 602 (30) $[Co_2(\mathbf{L_m^*})_2Cl(BF_4)]^{2+}$, 372 (100) $[Co_2(\mathbf{L_m^*})_2Cl]^{3+}$. From the same vapor diffusion tubes that contain **3**, blue crystals of **$Co_2(\mu\text{-}L_m^*)Cl_4$, 4** were also isolated. The two types of crystals were hand separated. MS ESI(+) *m*/*z* (rel. % abund.) [assgn]: 705 (8) $[Co_2(\mathbf{L_m^*})Cl_3]^+$, 602 (9) $[Co_2(\mathbf{L_m^*})_2Cl(BF_4)]^{2+}$, 483 $[\mathbf{L_m^*} + H]^+$, 372 (100) $[Co_2(\mathbf{L_m^*})_2Cl]^{3+}$.

[$Co_2(\mu\text{-}L_m)(\mu\text{-}Cl)_4$], 5. The methanolic solution of the ligand, L_m (0.185 g, 0.500 mmol), was transferred by cannula to the solution of $CoCl_2 \cdot 6H_2O$ (0.238 g, 1.00 mmol) in methanol to yield 0.205 g (65%) of blue precipitate. Single crystals of **5** were isolated upon slow evaporation of an acetonitrile/N,N-dimethylformamide solution of the blue precipitate at 5°C. Anal. Calcd.(Found) for $C_{20}H_{18}Co_2N_8Cl_4$: C, 38.12 (38.40); H, 2.88 (3.07); N, 17.78 (17.50). Crystals of **5** were first isolated from a similar reaction to the synthesis of **2** followed by recrystallization of the precipitate from methanol.

[$Ni_2(\mu\text{-}Cl)(\mu\text{-}L_m*)_2](ClO_4)_3$, 6. Compound **6** was prepared similarly to compound **1** starting from $Ni(ClO_4)_2 \cdot 6H_2O$ (0.184 g, 0.504 mmol) and $NiCl_2 \cdot 6H_2O$ (0.040 g, 0.17 mmol). The reaction afforded 0.160 g (33%) of a green solid. An additional 0.165 g (35%) of **6** can be isolated from the mother liquor by rotary evaporation of the solvent. Single crystals suitable for X-ray studies were grown by the vapor diffusion of Et_2O into highly diluted 1 mL acetonitrile solutions of **5**. Anal. Calcd.(Found) for $C_{56}H_{68}Cl_4Ni_2N_{16}O_{12}$: C, 47.49 (47.42); H, 4.84 (4.73); N, 15.82 (15.63). MS ESI(+) *m*/*z* (rel. % abund.) [assgn]: 1315 (2) $[Ni_2(\mathbf{L_m*})_2Cl(ClO_4)_2]^+$, 608 (25) $[Ni_2(\mathbf{L_m*})_2Cl(ClO_4)]^{2+}$, 483 (30) $[\mathbf{L_m*} + H]^+$, 372 (100) $[Ni_2(\mathbf{L_m*})_2Cl]^{3+}$.

[$Cu_2(\mu\text{-}Cl)(\mu\text{-}L_m*)_2](ClO_4)_3$, 7. Compound **7** was prepared similarly to compound **1** starting from $Cu(ClO_4)_2 \cdot 6H_2O$ (0.117 g, 0.316 mmol) and $CuCl_2 \cdot 2H_2O$ (0.018 g, 0.10 mmol). The reaction afforded 0.260 g (87 %) of a green solid. Single crystals suitable for X-ray studies were grown by the vapor diffusion of Et_2O into 1 mL acetonitrile solutions of **7**. Anal. Calcd.(Found) for $C_{56}H_{68}Cl_4Cu_2N_{16}O_{12}$: C, 47.16 (46.99); H, 4.81 (4.93); N, 15.71 (15.66). MS ESI(+) *m*/*z* (rel. % abund.) [assgn]: 1325 (20) $[Cu_2(\mathbf{L_m*})_2Cl(ClO_4)_2]^+$,

1062 (2) $[Cu(\mathbf{L}_m\mathbf{*})_2Cl]^+$, 644 (60) $[Cu_2(\mathbf{L}_m\mathbf{*})_2(ClO_4)_2]^{2+}$, 613 (55) $[Cu_2(\mathbf{L}_m\mathbf{*})_2Cl(ClO_4)]^{2+}$, 545 (100) $[Cu(\mathbf{L}_m\mathbf{*})]^+$, 514 (20) $[Cu(\mathbf{L}_m\mathbf{*})_2]^+$, 376 (80) $[Cu_2(\mathbf{L}_m\mathbf{*})_2Cl]^{3+}$.

$[Cu_2(\mu\text{-}Cl)(\mu\text{-}\mathbf{L}_m\mathbf{*})_2](BF_4)_3$, 8. Compound **8** was prepared similarly to compound **3** starting from $[Cu_2(\mu\text{-}F)(\mu\text{-}\mathbf{L}_m\mathbf{*})_2](BF_4)_3$ (0.183 g, 0.133 mmol) and $(CH_3)_3SiCl$ (0.015 g, 0.13 mmol). The reaction afforded 0.157 g (85 %) of a green solid. Single crystals suitable for X-ray studies were grown by the vapor diffusion of Et_2O into 1 mL acetonitrile solutions of **8**. Anal. Calcd.(Found) for $C_{56}H_{68}Cl_4Cu_2N_{16}O_{12}$: C, 48.45 (48.37); H, 4.94 (4.98); N, 16.14 (16.12). MS ESI(+) *m*/*z* (rel. % abund.) [assgn]: 1301 (22) $[Cu_2(\mathbf{L}_m\mathbf{*})_2Cl(BF_4)_2]^+$, 1062 (2) $[Cu(\mathbf{L}_m\mathbf{*})_2Cl]^+$, 1028 (2) $[Cu(\mathbf{L}_m\mathbf{*})_2]^+$, 645 (20) $[Cu_2(\mathbf{L}_m\mathbf{*})_2Cl]^+$, 607 (40) $[Cu_2(\mathbf{L}_m\mathbf{*})_2Cl(BF_4)]^{2+}$, 580 (35) $[Cu(\mathbf{L}_m\mathbf{*})Cl]^+$, 564 (25) $[Cu_2(\mathbf{L}_m\mathbf{*})_2Cl]^{2+}$, 545 (100) $[Cu(\mathbf{L}_m\mathbf{*})]^+$, 514 (15) $[Cu(\mathbf{L}_m\mathbf{*})_2]^+$, 376 (65) $[Cu_2(\mathbf{L}_m\mathbf{*})_2Cl]^{3+}$.

$[Cu_2(\mu\text{-}Cl)(\mu\text{-}\mathbf{L}_m)_2](ClO_4)_3$, 9. Compound **9** was prepared similarly to compound **1** starting from $Cu(ClO_4)_2\cdot 6H_2O$ (0.139 g, 0.370 mmol), $CuCl_2\cdot 2H_2O$ (0.022 g, 0.12 mmol) and $\mathbf{L}_m$ (0.185 g, 0.500 mmol). The reaction afforded 0.227 g (76 %) of a green solid. Single crystals suitable for X-ray studies were grown by the vapor diffusion of Et_2O into 1 mL acetonitrile solutions of **9** and yielded two solvates, **9**·1.5CH_3CN and **9**·2CH_3CN. Anal. Calcd.(Found) for $C_{40}H_{36}Cl_4Cu_2N_{16}O_{12}$: C, 39.98 (39.61); H, 3.02 (2.96); N, 18.65 (18.30). MS ESI(+) *m*/*z* (rel. % abund.) [assgn]: 1101 (1) $[Cu_2(\mathbf{L}_m)_2Cl(ClO_4)_2]^+$, 1002 (1) $[Cu_2(\mathbf{L}_m)_2Cl(ClO_4)+H]^+$, 967 (1) $[Cu(\mathbf{L}_m)_2(ClO_4)]^+$, 903 (2) $[Cu_2(\mathbf{L}_m)_2Cl]^+$, 838 (10) $[Cu(\mathbf{L}_m)_2Cl]^+$, 803 (19) $[Cu(\mathbf{L}_m)_2]^+$, 433 (100) $[Cu(\mathbf{L}_m)]^+$, 300 (35) $[Cu_2(\mathbf{L}_m)_2Cl]^{3+}$.

$[Cu_2(\mu\text{-}Cl)(\mu\text{-}\mathbf{L}_m)_2](BF_4)_3$, 10. Compound **10** was prepared similarly to compound **3** starting from $[Cu_2(\mu\text{-}F)(\mu\text{-}\mathbf{L}_m)_2](BF_4)_3$ (0.266 g, 0.230 mmol) and $(CH_3)_3SiCl$ (0.025 g, 0.230 mmol). The reaction afforded 0.227 g (84 %) of a green solid. Single crystals of

10·3CH_3CN can be grown by the vapor diffusion of Et_2O into 1 mL dry acetonitrile solutions under N_2 atmosphere. Anal. Calcd.(Found) for $C_{40}H_{36}B_3ClCu_2F_{12}N_{16}$: C, 41.28 (40.92); H, 3.12 (3.07); N, 19.26 (18.89). MS ESI(+) *m*/*z* (rel. % abund.) [assgn]: 890 (2) $[Cu(\mathbf{L}_m)_2(BF_4)]^+$, 838 (1) $[Cu(\mathbf{L}_m)_2Cl]^+$, 822 (1) $[Cu(\mathbf{L}_m)_2F]^+$, 803 (3) $[Cu(\mathbf{L}_m)_2]^+$, 468 (16) $[Cu_2(\mathbf{L}_m)_2Cl_2]^{2+}$, 452 (18) $[Cu_2(\mathbf{L}_m)_2Cl]^{2+}$, 300 (34) $[Cu_2(\mathbf{L}_m)_2Cl]^{3+}$.

$[Zn_2(\mu\text{-}Cl)(\mu\text{-}L_m^*)_2](ClO_4)_3$, 11. Compound **11** was prepared similarly to compound **1** starting from $Zn(ClO_4)_2·6H_2O$ (0.188 g, 0.504 mmol) and $ZnCl_2$ (0.023 g, 0.17 mmol). The reaction afforded 0.320 g (67 %) of a white solid. Single crystals suitable for X-ray studies were grown by the vapor diffusion of Et_2O into 1 mL diluted acetonitrile solutions of **11** at 5 ºC and were isolated as **11**·5CH_3CN. ^{1}H NMR (300 MHz, acetonitrile-d_3): δ 7.58 (s, 4H, $CH(pz)_2$), 7.49 (t, *J* = 9.0 Hz, 2H, 5-H C_6H_4), 6.88 (d, *J* = 9.0 Hz, 4H, 4,6-H C_6H_4), 6.29/6.08 (s/s, 4H/4H, 4-H pz), 4.91 (s, 1H, 2-H C_6H_4), 2.59/2.39 (s/s, 12H/12H, 5-CH_3) 1.76/1.29 (s/s, 12H/12H, 3-CH_3). ^{13}C NMR (75.5 MHz, acetonitrile-d_3): δ 154.6/151.5/147.5/144.7 (3,5-C pz), 135.9 (1,3-C C_6H_4), 130.5 (5-C C_6H_4), 128.3 (4,6-C C_6H_4), 125.9 (2-C C_6H_4), 109.0/107.7 (4-C pz), 68.7 ($CH(pz)_2$), 14.8/11.6 (3-CH_3), 11.5/10.6 (5-CH_3). Anal. Calcd.(Found) for $C_{56}H_{68}Cl_4Zn_2N_{16}O_{12}$: C, 47.04 (46.95); H, 4.79 (4.70); N, 15.71 (15.67). MS ESI(+) *m*/*z* (rel. % abund.) [assgn]: 1329 (2) $[Zn_2(\mathbf{L}_m^*)_2Cl(ClO_4)_2]^+$, 615 (18) $[Zn_2(\mathbf{L}_m^*)_2Cl(ClO_4)]^{2+}$, 483 (30) $[\mathbf{L}_m^* + H]^+$, 377 (50) $[Zn_2(\mathbf{L}_m^*)_2Cl]^{3+}$.

$[Zn_2(\mu\text{-}Cl)(\mu\text{-}L_m)_2](ClO_4)_3$, 12. Compound **12** was prepared similarly to compound **1** starting from $Zn(ClO_4)_2·6H_2O$ (0.208 g, 0.558 mmol), $ZnCl_2$ (0.039 g, 0.19 mmol) and $\mathbf{L}_m$ (0.276 g, 0.744 mmol). The reaction afforded 0.310 g (69 %) of a white solid. Single crystals suitable for X-ray studies were grown by layering acetone and Et_2O on top of a

concentrated solution of **12** in acetonitrile to yield **12**·2$(CH_3)_2O$. ^{1}H NMR (300 MHz, acetonitrile-d_3): δ 8.43, 8.14, 7.58, 7.47, 6.64, 6.53, 5.53, 5.16, 4.78. Anal. Calcd.(Found) for $C_{42}H_{42}Cl_4Zn_2N_{16}O_{12}$: C, 40.31 (40.68); H, 3.38 (3.12); N, 17.91 (17.98). MS ESI(+) *m*/*z* (rel. % abund.) [assgn]: 971 (2) $[Zn_2(\mathbf{L}_m)_2(ClO_4)]^+$, 839 (12) $[Zn(\mathbf{L}_m)_2Cl]^+$, 433 (50) $[Zn(\mathbf{L}_m)]^+$, 402 (100) $[Zn(\mathbf{L}_m)_2]^{2+}$, 371 (30) $[\mathbf{L}_m + H]^+$, 302 (50) $[Zn_2(\mathbf{L}_m)_2Cl]^{3+}$.

$[Cd_2(\mu\text{-}Cl)(\mu\text{-}L_m^*)_2](ClO_4)_3$, 13. Compound **13** was prepared similarly to compound **1** starting from $Cd(ClO_4)_2\cdot 6H_2O$ (0.133 g, 0.316 mmol), $CdCl_2$ (0.019 g, 0.10 mmol) in 3 mL THF and 1 mL MeOH and $\mathbf{L}_m$* (0.203 g, 0.421 mmol) in 10 mL THF. The reaction afforded 0.214 g (67 %) of a white solid. Single crystals grown by the vapor diffusion of Et_2O into acetonitrile solutions of **13** were highly disordered. By growing single crystals with the same crystallization method, but changing acetonitrile to acetone resulted in crystals of **13**, similarly, if methanol is used crystals of **13**·3.8CH_3OH was isolated. ^{1}H NMR (300 MHz, acetonitrile-d_3): δ 7.58 (s, 4H, $CH(pz)_2$), 7.49 (t, J = 9.0 Hz, 2H, 5-H C_6H_4), 6.78 (d, J = 9.0 Hz, 4H, 4,6-H C_6H_4), 6.32/6.12 (s/s, 4H/4H, 4-H pz), 5.07 (s, 1H, 2-H C_6H_4), 2.54/2.44 (s/s, 12H/12H, 5-H CH_3) 1.98/1.67 (s/s, 12H/12H, 3-H CH_3). ^{13}C NMR (75.5 MHz, acetonitrile-d_3): δ 154.4/152.0/148.0/145.1 (3,5-C pz, $J_{C\text{-}Cd}$ = 5-7 Hz), 136.7 (1,3-C C_6H_4), 130.8 (5-C C_6H_4), 128.5 (4,6-C C_6H_4), 126.0 (2-C C_6H_4), 108.4/107.3 (4-C pz), 68.8 ($CH(pz)_2$), 14.3/12.3 (3-C CH_3), 11.4/10.7 (5-C CH_3). ^{113}Cd NMR (88.8 MHz, acetonitrile-d_3): δ 133.4 (s). Anal. Calcd.(Found) for $C_{56}H_{68}Cl_4Cd_2N_{16}O_{12}$: C, 44.14 (44.52); H, 4.50 (4.63); N, 14.71 (14.78). MS ESI(+) *m*/*z* (rel. % abund.) [assgn]: 1425 (2) $[Cd_2(\mathbf{L}_m^*)_2Cl(ClO_4)_2]^+$, 1113 (5) $[Cd(\mathbf{L}_m^*)_2Cl]^+$, 695 (5) $[Cd(\mathbf{L}_m^*)(ClO_4)]^+$, 662 (50) $[Cd_2(\mathbf{L}_m^*)_2Cl(ClO_4)]^{2+}$, 631 (50) $[Cd(\mathbf{L}_m)Cl]^+$, 408 (100) $[Cd_2(\mathbf{L}_m^*)_2Cl]^{3+}$.

$[Cu_2(\mu\text{-}Br)(\mu\text{-}L_m^*)_2](ClO_4)_3$ 14. The copper(II) salts, $Cu(ClO_4)_2 \cdot 6H_2O$ (0.187 g, 0.504 mmol) and $CuBr_2$ (0.038 g, 0.168 mmol) were dissolved in 4 mL MeOH. The ligand, $\mathbf{L}_m^*$ (0.324 g, 0.672 mmol), dissolved in 10 mL MeOH, was transferred by cannula into the copper salt solution. A dark green precipitate formed instantly. The reaction mixture was stirred for 5 h, after which time the system was filtered by cannula, washed with 5 mL ether and dried in vacuum overnight, affording 0.335 g (68%) of the crude product. Single crystals suitable for X-ray and other studies were grown by layering Et_2O on top of a concentrated acetonitrile solution of **3** and a buffer layer of pure acetonitrile, crystals of $\mathbf{3}\cdot 2CH_3CN$ formed. Anal. Calcd.(Found) for $C_{56}H_{68}Cl_3BrCu_2N_{16}O_{12}$: C, 45.74 (45.57); H, 4.66 (4.63); N, 15.24 (15.39). MS ESI(+) *m*/*z* (rel. % abund.) [assgn]: 1371 (3) $[Cu_2(\mathbf{L}_m^*)_2(Br)(ClO_4)_2]^+$, 1108 (2) $[Cu(\mathbf{L}_m^*)_2Br]^+$, 635 (25) $[Cu_2(\mathbf{L}_m^*)_2Br(ClO_4)]^{2+}$, 545 (100) $[Cu(\mathbf{L}_m^*)]^+$, 514 (50) $[Cu(\mathbf{L}_m^*)_2]^{2+}$, 483 (65) $[\mathbf{L}_m^*+H]^+$, 390 (52) $[Cu_2(\mathbf{L}_m^*)_2Br]^{3+}$.

$Co_2(\mu\text{-}L_m^*)Br_4$ 15. Compound **15** was synthesized similarly to **3** starting from $[Co_2(\mu\text{-}F)(\mu\text{-}\mathbf{L}_m^*)_2](BF_4)_3$ (0.104 g, 0.076 mmol) and $(CH_3)_3SiBr$ (0.012 g, 0.076 mmol). The resulting blue solution was stirred for 12 h. The blue solution was crystallized by vapor diffusion of Et_2O into the acetonitrile solution. The resulting blue crystals were identified as **15**, 0.010 g (57%). Anal. Calcd.(Found) for $C_{28}H_{34}Co_2N_8Br_4$: C, 36.55 (36.87); H, 3.72 (3.45); N, 12.18 (12.04).

Crystallographic studies. X-ray diffraction intensity data for compounds **1-15** was measured on a Bruker SMART APEX CCD-based diffractometer (Mo Kα radiation, λ = 0.71073 Å).[16] Raw area detector data frame processing was performed with the SAINT+ and SADABS programs.[16] Final unit cell parameters were determined by least-squares

refinement of large sets of strong reflections taken from each data set. Direct methods structure solutions, difference Fourier calculations and full-matrix least-squares refinements against F^2 were performed using SHELXS and SHELXL, implemented in OLEX2[17]. Non-hydrogen atoms were in general refined with anisotropic displacement parameters, the exception being disordered species, which were refined isotropically. Prevalent anion and solvent disorder was modeled with the aid of 1,2 and 1,3 distance restraints, or with a disorder component restrained to adopt a similar geometry as an ordered anion in the structure (SHELX SAME instructions). Hydrogen atoms were placed in geometrically idealized positions and included as riding atoms. Details of the data collections and refinements are given in Tables 4.1-4.4.

During preliminary examinations at different temperatures, compounds **1**, **2**, **3**, **6**, **7** and **8** were observed to undergo a phase transition. The phase change is signaled by the appearance of additional peaks in the diffraction pattern when the crystals are cooled, and is accompanied by enlargement of the unit cell. The transitions are of the order-disorder type, caused by ordering of the anions at lower temperatures. All transitions occur without a change in crystal system (triclinic) or loss of space group symmetry. The space group *P-1* is retained throughout the transition as the symmetry group of both the high and low-temperature forms. The transitions are therefore a special case of the klassengleiche type transition with an isomorphic subgroup, and do not require the occurrence of twinning.

High-temperature structures of compounds **1**, **2**, **3**, **6**, **7** and **8**: Above the transition temperatures, compounds **1**, **2**, **3**, **6**, **7** and **8** are isostructural, adopting a triclinic structure with a unit cell volume near 1600 $Å^3$. The asymmetric unit of the high-temperature forms

consists of half of one metal complex, which is located on a crystallographic inversion center, and 1.5 (formally) perchlorate (**1**, **2**, **6**, **7**) or tetrafluoroborate (**3, 8**) anions. One of the anions (e.g. Cl1A/Cl1B or B1A/B1B) is disordered over an inversion center, and was modeled in each case with two independent, equally populated (25%) components. The second independent anion (Cl2 or B2) in each structure is disordered about a general position, and was modeled with three distinct components. The bridging chloride atom Cl1 was refined with either (a) one position, located on the inversion center or (b) disordered across the inversion center over two equally populated sites. Treatment of the bridging chloride atom depended on the degree of prolateness of the chlorine atom anisotropic displacement parameter if refined on the inversion center, as quantified by the U_3/U_1 ratio. Details of the disorder modeling and bridging chloride atom refinement are given below.

Compound **1**. **296 K form**: Populations of the three-fold disordered perchlorate anion Cl2 refined to Cl2A/Cl2B/Cl2C = 0.338(4) / 0.422(9) / 0.240(9), respectively (constrained to sum to unity). The bridging chlorine Cl1 was refined on the inversion center (Cl1 U_3/U_1 = 2.4). **100 K form**: At 100K the triclinic unit cell has doubled in size. The asymmetric unit consists of one complete iron complex located on a general position and three independent perchlorate anions. Two perchlorate anions (Cl2 and Cl3) are disordered over two positions with occupancies Cl2A/Cl2B = 0.826(5)/0.174(5) and Cl3A/Cl3B = 0.777(5)/0.223(5). The bridging chlorine Cl1 is disordered over two general positions with refined populations A/B = 0.76(5)/0.24(5). Both components were refined with a common anisotropic displacement parameter. A single chlorine position resulted in a strongly prolate ellipsoid with U_3/U_1 = 5.2.

Compound **2**. **295 K form**: Populations of the three-fold disordered perchlorate anion Cl2 refined to Cl2A/Cl2B/Cl2C = 0.368(4)/0.235(7)/0.397(7), respectively (constrained to sum to unity). The bridging chlorine Cl1 was refined on the inversion center (Cl1 U_3/U_1 = 3.2). **100 K form**: At 100K the triclinic unit cell has doubled in size, and is the same structure as the low-temperature form of **1**. The asymmetric unit consists of one complete cobalt complex located on a general position and three independent perchlorate anions. The perchlorate anions do not display any significant disorder. The bridging chlorine Cl1 was refined with a single chlorine position (Cl1 U_3/U_1 = 3.0).

Compound **3**. **296 K form**: Populations of the three-fold disordered BF_4^- anion B2 refined to B2A/B2B/B2C = 0.232(4)/0.453(7)/0.315(7), respectively (constrained to sum to unity). The bridging chlorine Cl1 was refined on the inversion center (Cl1 U_3/U_1 = 3.0). **100 K form**: The unit cell at 100 K has tripled in size. The asymmetric unit consists of one complete cobalt complex located on a position of general crystallographic symmetry (atom label suffixes "A"), half of another cation located on an inversion center (atom label suffixes "B"), and 4.5 (formally) tetrafluoroborate anions. Bridging chlorine Cl1B is located on the inversion center. Tetrafluoroborate anion B5 is disordered about an inversion center and therefore only half is present per asymmetric unit. Anions B3 and B4 are mildly disordered and were modeled with minor components having population fractions B3B = 0.104(4) and B4B = 0.079(3). Disordered BF_4^- anions were restrained to have a similar geometry as the ordered anion B1 (SHELX SAME instruction, 150 total restraints). The two bridging chlorine atoms were each refined with a single position (U_3/U_1 ratios are Cl1A = 3.0, Cl1B = 2.7).

Compound **4** crystallizes in the monoclinic space group $P2_1/c$ as determined by the pattern of systematic absences in the intensity data. The asymmetric unit consists of one molecule of **4**.

Compound **5** crystallizes in the orthorhombic space group *Pbca* as determined uniquely by the pattern of systematic absences in the intensity data. The asymmetric unit consists of two cobalt atoms, four chlorine atoms and one ligand (one polymeric repeating unit).

Compound **6**. **296 K form**: Populations of the three-fold disordered perchlorate anion Cl2 refined to Cl2A/Cl2B/Cl2C = 0.306(4) / 0.231(7) / 0.463(8), respectively (constrained to sum to unity). A moderately prolate anisotropic displacement parameter (U_3/U_1 = 4.2) was observed for the bridging chlorine with chlorine placed on the inversion center between the nickel atoms. A model refining the chlorine slightly displaced from the inversion center resulted in a crystallographically stable and physically reasonable model, and a more spherical displacement parameter (U_3/U_1 = 2.9). This model entails a split position with two half-occupied chlorine atoms disordered across the inversion center. Ni-Cl bond distances are similar (2.367(16) Å and 2.375(16) Å vs. 2.361 Å for Cl1 on the inversion center), but the Ni1-Cl1-Ni1' angle is 169.4(4)º (vs. 180º). **100 K form**: At 100K the triclinic unit cell has doubled in size, and is the same structure as the low-temperature forms of **1** and **2**. The asymmetric unit consists of one complete nickel complex located on a general position and three independent perchlorate anions. Two of the three perchlorate ions (Cl2 and Cl3) were refined with a minor disorder component (0.098(3) occupancy for Cl2B and 0.154(4) occupancy for Cl3B). The bridging chlorine Cl1 is disordered over two general positions with refined

populations 0.72(3) / 0.28(3). Both components were refined with a common anisotropic displacement parameter. A single chlorine position resulted in a strongly prolate ellipsoid with U_3/U_1 = 6.2.

Compound **7**. **296 K form.** Populations of the three-fold disordered perchlorate anion Cl2 refined to Cl2A/Cl2B/Cl2C = 0.317(4)/0.205(7)/0.478(8), respectively (constrained to sum to unity). The bridging chlorine Cl1 was refined with a single chlorine position (Cl1 U_3/U_1 = 2.9). **100 K form**. At 100 K the triclinic unit cell has doubled in size. The asymmetric unit consists of half of two centrosymmetic $[Cu_2(\mu\text{-}Cl)(\mu\text{-}\mathbf{L}_m\mathbf{*})_2]^{3+}$ cations and three independent perchlorate anions. The two cations were numbered identically except for the label suffix "A" or "B". The bridging chlorine atoms Cl1A and Cl1B were both refined with a single position, located on the inversion center (Cl1A U_3/U_1 = 2.7; Cl1B U_3/U_1 = 3.0). One perchlorate anion (Cl2) is disordered and was refined with two components having refined populations of 0.775(4)/ 0.225(4), using 10 geometric restraints. Oxygen atoms of the minor component were refined with a common isotropic displacement parameter. For consistency, the position of anion Cl1 is the same relative to the copper cations in the 296 K and 100 K structures. The disordered anion Cl2 in the 296 K structure splits into Cl2A/Cl2B and Cl3 at 100 K.

Compound **8. 200 K form**. Populations of the three-fold disordered BF_4^- anion B2 refined to B2A/B2B/B2C = 0.232(4)/0.453(7)/0.315(7), respectively (constrained to sum to unity). The bridging chlorine Cl1 was refined on the inversion center (Cl1 U_3/U_1 = 3.0). **100 K form**: At 100 K the triclinic unit cell has doubled in size, and is the same as the low-temperature form of **7**. The transition temperature is approximately 175 K. The asymmetric unit consists of half each of two independent cations, both on inversion

centers, and three independent tetrafluoroborate anions. The two cations were numbered identically except for the label suffix “A” or “B”. The anions are fully ordered at low-temperature. For consistency, the position of anion B1 is the same relative to the copper cations in the 200 K and 100 K structures. The disordered anion B2 in the 200 K structure splits into B2 and B3 at 100 K.

Two kinds of single crystals were isolated in the same vapor diffusion tube for **9**: **9**·1.5CH_3CN (bars, yield > ~95%) and **9**·2CH_3CN (parallelograms, minor product). The major product **9**·1.5CH_3CN crystallizes in the monoclinic space group $P2_1/m$ as determined by the pattern of systematic absences in the intensity data and by the successful solution and refinement of the structure. The asymmetric unit consists of half each of two independent $[Cu_2(\mu\text{-Cl})(\mu\text{-}\mathbf{L}_{\boldsymbol{m}})_2]^{3+}$ cations, three independent perchlorate anions and 1.5 independent acetonitrile molecules. Cation Cu1 is located on a crystallographic inversion center; cation Cu2 is located on a crystallographic mirror plane. The half-acetonitrile lies in a mirror plane. The bridging chloride atom Cl1 of the centrosymmetric cation Cu1 is disordered across the inversion center and was refined as half-occupied. This resulted in a acceptably spherical displacement parameter (U_3/U_1 = 2.7). The U_3/U_1 value for bridging chloride Cl2 is 2.4. Perchlorate anion Cl21 is disordered and was modeled with two distinct orientations with refined populations Cl21/Cl22 = 0.691(8)/0.309(8). Perchlorate anion Cl31 is also disordered and was modeled with three distinct orientations with refined populations Cl31/Cl32/Cl33 = 0.332(4)/0.425(8)/0.244(8). The geometry of all disordered ClO_4^- components was restrained to be similar to that of the ordered perchlorate Cl11 (67 total restraints). Compound **9**·2CH_3CN crystallizes in the space group *P-1* of the triclinic system. The

asymmetric unit consists of half each of two $[Cu_2(\mu\text{-}Cl)(\mu\text{-}\mathbf{L}_{\boldsymbol{m}})_2]^{3+}$ cations, both located on crystallographic inversion centers, three perchlorate anions and two acetonitrile molecules. Both bridging chloride atoms were refined with a single position located on the inversion centers giving good U_3/U_1 values of Cl1 = 3.5 and Cl2 = 2.9.

Compound **10**·$3CH_3CN$ crystallizes in the space group *P*-1 of the triclinic system. The asymmetric unit consists of half each of two independent, centrosymmetric $[Cu_2(\mu\text{-}Cl)(\mu\text{-}\mathbf{L}_{\boldsymbol{m}})_2]^{3+}$ cations, three tetrafluoroborate anions, and three acetonitrile molecules of crystallization. The bridging chloride ligands in both cations are located on crystallographic inversion centers, with U_3/U_1 values of Cl1 = 2.4 and Cl2 = 3.2.

The asymmetric unit of **11**·$5CH_3CN$ consists of half each of two independent, centrosymmetric $[Zn_2(\mu\text{-}Cl)(\mu\text{-}\mathbf{L}_{\boldsymbol{m}}\mathbf{*})_2]^{3+}$ cations, three perchlorate anions and five independent acetonitrile molecules. The bridging chloride ligands in both zinc cations are located on the inversion centers (U_3/U_1 values are: Cl1A = 3.1; Cl1B = 3.0). One perchlorate (Cl3) is disordered and was modeled using three distinct orientations, with refined fractional populations A/B/C = 0.387(4)/0.281(6)/0.331(7). The total site population was constrained to sum to unity. One acetonitrile is disordered over two closely separated positions with fractional populations N4S/N5S = 0.53(2)/0.47(2). A total of 40 distance restraints were used to maintain chemically reasonable geometries for the disordered species.

The asymmetric unit of **12**·$2(CH_3)_2O$ consists of half of one $[Zn_2(\mu\text{-}Cl)(\mu\text{-}\mathbf{L}_{\boldsymbol{m}})_2]^{3+}$ cation located on a crystallographic inversion center, 1.5 (formally) perchlorate anions and one acetone molecule of crystallization. The bridging chloride ligand of the dizinc complex was refined with a split position just off the inversion center. Placing this atom

on the inversion center (Zn1-Cl1-Zn1' = 180º) resulted in a badly elongated displacement parameter with U_3/U_1 = 6.6. The split position model (Zn1-Cl1-Zn1' = 169.9(2)º) refined stably, and gave a more physically reasonable displacement parameter with U_3/U_1 = 3.3. One perchlorate (Cl2) is located on an inversion center and as such only half is present per asymmetric unit. This anion is disordered over two independent positions within the asymmetric unit, with refined occupancies of Cl2A / Cl2B = 0.280(5) / 0.220(5). The acetone molecule is also disordered over three independent positions near an inversion center, with occupancies O51/O52/O53 = 0.403(3)/0.367(8)/0.230(8), respectively.

The asymmetric unit of **13** consists of half each of two independent $[Cd_2(\mu\text{-}Cl)(\mu\text{-}\mathbf{L}_m\mathbf{*})_2]^{3+}$ cation, and three independent perchlorate anions. Both cadmium complexes are located on crystallographic inversion centers. The bridging chloride ligand in each cation is located slightly off the inversion center, and was refined as disordered across the inversion center with half-occupancy. The asymmetric unit of **13**·3.8CH_3OH consists of half of one $[Cd_2(\mu\text{-}Cl)(\mu\text{-}\mathbf{L}_m\mathbf{*})_2]^{3+}$ cation, 1.5 (formally) perchlorate ions, an ordered methanol molecule and a region of diffuse electron density modeled as additional methanol molecules. The cadmium complex is located on a crystallographic inversion center. The bridging chloride ion is disordered across the inversion center. One perchlorate (Cl21) is disordered about a two-fold axis of rotation, and as such only half is present per asymmetric unit. This group was refined with half-occupancy with its geometry restrained to be similar to that of the ordered perchlorate Cl11. A group of disordered electron density peaks located near Cl21 was modeled as four partially occupied methanol molecules O2S-O5S. These are also disordered about a C_2 axis. Populations were initially refined, but were later fixed at physically sensible values (i.e.

not more than 100% total site occupancy), and all component atoms were refined with a common displacement parameter. The disordered perchlorate and methanol molecules were refined with the aid of 14 distance restraints.

Compound **14**·2CH_3CN crystallizes in the space group *C2/c* as determined by the pattern of systematic absences in the intensity data and by the successful solution and refinement of the structure. The asymmetric unit consists of half of one $[Cu_2(\mu\text{-Br})(\mu\text{-}\mathbf{L_m*})_2]^{3+}$ cation, which is located on a crystallographic inversion center, 1.5 (formally) perchlorate anions and one acetonitrile molecule. The bromine atom is located on the inversion center (U_3/U_1 = 2.41). Perchlorate anion Cl2 is disordered about a two-fold axis of rotation and as such only half is present in a given asymmetric unit. The geometry of this group was restrained to be similar to that of the ordered perchlorate Cl1 by means of a SHELX SAME instruction.

Compound **15** crystallizes in the space group $P2_1/c$ as determined by the pattern of systematic absences in the intensity data. The asymmetric unit consists of one molecule.

Table 4.1. Selected Crystal Data and Structure Refinement for the High Temperature Structure of the Phase Changing Compounds: **1**, **2**, **3**, **6**, **7** and **8**.

	1	**2**	**3**	**6**	**7**	**8**
Formula	$C_{56}H_{68}Cl_4$ $Fe_2N_{16}O_{12}$	$C_{56}H_{68}Cl_4$ $Co_2N_{16}O_{12}$	$C_{56}H_{68}B_3Cl$ $Co_2F_{12}N_{16}$	$C_{56}H_{68}Cl_4$ $Ni_2O_{12}N_{16}$	$C_{56}H_{68}Cl_4$ $Cu_2N_{16}O_{12}$	$C_{56}H_{68}B_3Cl$ $Cu_2F_{12}N_{16}$
Fw, g·mol^{-1}	1410.76	1416.92	1379.00	1416.48	1426.14	1388.22
Cryst. Syst.	Triclinic	Triclinic	Triclinic	Triclinic	Triclinic	Triclinic
Space group	P $\bar{1}$	P $\bar{1}$	P $\bar{1}$	P $\bar{1}$	P $\bar{1}$	P $\bar{1}$
T, K	296(2)	295(2)	296(2)	296(2)	295(2)	200(2)
***a*, Å**	11.5470(7)	11.5648(5)	11.2707(5)	11.5982(12)	11.5965(5)	11.2590(5)
***b*, Å**	12.7713(8)	12.7207(5)	12.6503(5)	12.7154(13)	12.6931(5)	12.5195(5)
***c*, Å**	13.6555(8)	13.5429(6)	13.6992(6)	13.4415(14)	13.4508(5)	13.5517(6)
***α*, deg**	117.689(1)	116.980(1)	117.740(1)	116.563(2)	116.296(1)	106.005(1)
***β*, deg**	100.091(1)	100.121(1)	100.654(1)	100.456(2)	101.606(1)	114.226(1)
***γ*, deg**	104.991(1)	105.531(1)	103.841(1)	105.718(2)	105.039(1)	102.968(1)
***V*, Å^3**	1616.49(17)	1604.91(12)	1575.64(12)	1597.8(3)	1595.86(11)	1545.34(11)
Z	1	1	1	1	1	1
R1 (I >2σ(I))	0.0548	0.0488	0.0556	0.0485	0.0551	0.0529
wR2 (I >2σ(I))	0.1438	0.1437	0.1611	0.1376	0.1528	0.1391

Table 4.2. Selected Crystal Data and Structure Refinement for the Low Temperature Structures of **1**, **2**, **3**, **6**, **7** and **8**.

	1	**2**	**3**	**6**	**7**	**8**
Formula	$C_{56}H_{68}Cl_4$ $Fe_2N_{16}O_{12}$	$C_{56}H_{68}Cl_4$ $Co_2N_{16}O_{12}$	$C_{56}H_{68}B_3Cl$ $Co_2F_{12}N_{16}$	$C_{56}H_{68}Cl_4$ $Ni_2N_{16}O_{12}$	$C_{56}H_{68}Cl_4$ $Cu_2N_{16}O_{12}$	$C_{56}H_{68}B_3Cl$ $Cu_2F_{12}N_{16}$
Fw, g·mol^{-1}	1410.76	1416.92	1379.00	1416.48	1426.14	1388.22
Cryst. Syst.	Triclinic	Triclinic	Triclinic	Triclinic	Triclinic	Triclinic
Space group	P $\bar{1}$	P $\bar{1}$	P $\bar{1}$	P $\bar{1}$	P $\bar{1}$	P $\bar{1}$
T, K	100(2)	100(2)	100(2)	100(2)	100(2)	100(2)
***a*, Å**	12.5895(12)	12.5738(6)	12.4854(7)	12.5479(12)	11.4245(5)	11.2345(8)
***b*, Å**	13.7272(13)	13.7181(6)	13.6318(7)	13.6618(13)	12.5062(5)	12.4229(9)
***c*, Å**	19.0556(19)	19.0076(9)	28.1186(15)	18.9760(17)	22.5208(9)	22.4871(16)
***α*, deg**	92.483(2)	92.539(1)	82.544(1)	92.415(2)	84.710(1)	84.710(1)
***β*, deg**	99.578(2)	99.042(1)	88.073(1)	98.573(2)	82.970(1)	83.774(1)
***γ*, deg**	104.833(2)	105.562(1)	74.441(1)	105.896(2)	75.285(1)	76.530(1)
***V*, Å^3**	3126.3(5)	3106.2(2)	4571.4(4)	3081.9(5)	3082.5(2)	3026.8(4)
Z	2	2	3	2	2	2
R1 (I >2σ(I))	0.0606	0.0368	0.0461	0.0510	0.0482	0.0413
wR2 (I >2σ(I))	0.1559	0.0937	0.1082	0.1337	0.1215	0.0984

Table 4.3. Selected Crystal Data and Structure Refinement for the Low Temperature Structures of **11**·5CH_3CN, **13**, **13**·3.8CH_3OH and **14**·2CH_3CN.

	11·5CH_3CN	**13**	**13**·3.8CH_3OH	**14**·2CH_3CN
Formula	$C_{66}H_{83}Cl_4Zn_2N_{21}O_{12}$	$C_{56}H_{68}Cl_4Cd_2N_{16}O_{12}$	$C_{59.80}H_{83.20}Cl_4Cd_2N_{16}O_{15.80}$	$C_{60}H_{74}BrCl_3Cu_2N_{18}O_{12}$
Fw, g·mol^{-1}	1635.07	1523.86	1645.62	1552.71
Cryst. Syst.	Triclinic	Monoclinic	Monoclinic	Monoclinic
Space group	P $\bar{1}$	$P2_1/c$	C2/c	C2/c
T, K	100(2)	100(2)	100(2)	100(2)
***a*, Å**	12.9848(7)	20.7244(11)	25.3217(14)	23.9421(17)
***b*, Å**	13.6965(8)	15.9031(9)	13.5025(7)	12.3031(9)
***c*, Å**	22.0090(12)	19.5139(10)	22.8451(12)	23.6249(17)
***α*, deg**	78.948(1)	90	90	90
***β*, deg**	85.295(1)	95.496(1)	114.810(1)	103.640(2)
***γ*, deg**	86.641(1)	90	90	90
***V*, Å^3**	3825.0(4)	6401.9(6)	7090.0(7)	6762.7(8)
Z	2	4	4	4
R1 (I >2σ(I))	0.0438	0.0367	0.0379	0.0350
wR2 (I >2σ(I))	0.0924	0.0884	0.0903	0.0861

Table 4.4. Selected Crystal Data and Structure Refinement for **4**, **5**, **9**·1.5CH_3CN, **9**·2CH_3CN, **10**·3CH_3CN, **12**·2$(CH_3)_2O$ and **15**.

	4	**5**	**9**·1.5CH_3CN	**9**·2CH_3CN	**10**·3CH_3CN	**12**·2$(CH_3)_2O$	**15**
Formula	$C_{28}H_{34}Cl_4Co_2N_8$	$C_{20}H_{18}Cl_4Co_2N_8$	$C_{43}H_{40.50}Cl_4Cu_2N_{17.50}O_{12}$	$C_{44}H_{42}Cl_4CuN_{18}O_{12}$	$C_{46}H_{45}B_3ClCu_2F_{12}N_{19}$	$C_{46}H_{48}Cl_4Zn_2N_{16}O_{14}$	$C_{28}H_{34}Br_4Co_2N_8$
Fw, g·mol^{-1}	742.29	630.08	1263.31	1283.84	1286.97	1321.54	920.13
Cryst. Syst.	Monoclinic	Othorhombic	Monoclinic	Triclinic	Triclinic	Monoclinic	Monoclinic
Space group	$P2_1/c$	Pbca	$P2_1/m$	$P\bar{1}$	$P\bar{1}$	$P2_1/m$	$P2_1/c$
T, K	100(2)	250(2)	150(2)	150(2)	150(2)	100(2)	100(2)
***a*, Å**	8.5328(4)	15.3807(6)	10.3088(6)	10.2560(4)	10.0411(7)	11.2243(9)	8.7243(6)
***b*, Å**	31.0199(13)	14.2441(6)	42.585(2)	12.8684(6)	13.0618(10)	17.0686(14)	31.462(2)
***c*, Å**	12.3447(5)	21.9973(9)	12.0443(7)	21.3259(9)	22.0678(17)	14.0062(12)	12.4239(9)
***α*, deg**	90	90	90	99.532(1)	94.615(2)	90	90
***β*, deg**	96.339(1)	90	103.343(1)	91.382(1)	92.400(1)	93.943(1)	96.772(2)
***γ*, deg**	90	90	90	111.324(1)	109.962(1)	90	90
***V*, Å^3**	3247.5(2)	4819.3(3)	5144.7(5)	2574.75(19)	2704.1(3)	2677.0(4)	3386.3(4)
Z	4	8	4	2	2	2	4
R1 (I >2σ(I))	0.0404	0.0327	0.0494	0.0389	0.0402	0.0360	0.0503
wR2 (I >2σ(I))	0.0915	0.0668	0.1160	0.0934	0.1037	0.0955	0.0923

Results

Synthesis. The monochloride bridged dinuclear metallacycles were synthesized from the direct reaction of the building blocks, $M(ClO)_4 \cdot 6H_2O$, MCl_2 and the ligand, $\mathbf{L}_m$ or $\mathbf{L}_m$*, according to the reaction below.

L = L_m* M = Fe (1) x = 0, Co (2) x = 6, Ni (6) x = 6, Cu (7) x = 2, Zn (11) x = 0, Cd (13) x = 6
L = L_m M = Cu (9) x = 2, Zn (12) x = 0

Similar assemblies were isolated for copper(II) by exchange reactions of the corresponding fluoride bridged metallacycle with $(CH_3)_3SiCl$, as shown below. The precursor was synthesized according to reported procedures.[9a] These reactions result in the BF_4^- derivatives of the chloride bridged metallacycle, rather than the ClO_4^-.

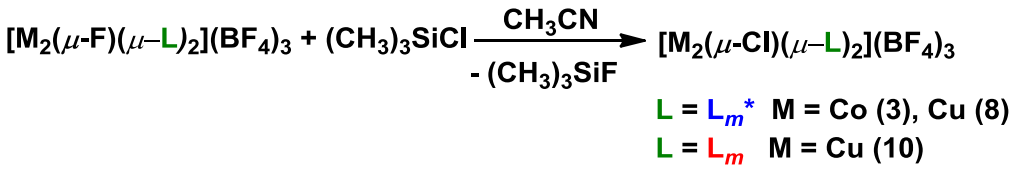

L = L_m* M = Co (3), Cu (8)
L = L_m M = Cu (10)

This reaction with $[Co_2(\mu\text{-F})(\mu\text{-}\mathbf{L}_m\text{*})_2](BF_4)_3$ yielded two different species, compound **3**, the metallacycle, which was isolated in significantly lower yield than the copper(II) species, and $Co_2(\mu\text{-}\mathbf{L}_m\text{*})Cl_4$ (**4**), a different dinuclear compound where the metal centers are bridged by only one ligand (*vide infra*) and the charge neutrality is achieved by coordination of additional chloride ions. $[Co_2(\mu\text{-}\mathbf{L}_m)(\mu\text{-Cl})_4]$, **5**, was first isolated as one of the products of the reaction of $Co(ClO_4)_2 \cdot 6H_2O$, $CoCl_2 \cdot 6H_2O$ and $\mathbf{L}_m$ using the stoichiometry of the first reaction, and was subsequently synthesized by the stoichiometric reaction of $CoCl_2 \cdot 6H_2O$ and $\mathbf{L}_m$ in better yield.

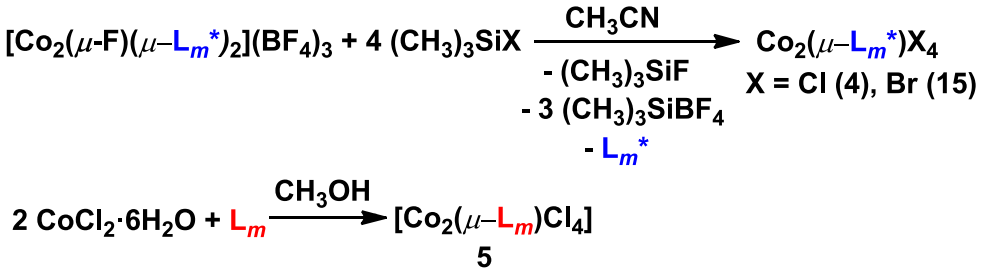

The bromide bridged copper(II) metallacycle, **14**, was similarly synthesized to the analogous chloride bridged compounds. A similar reaction in the presence of cobalt(II) resulted in $Co_2(\mu$-**L**$_m$***)**Br_4, **15**, analogous to **4**.

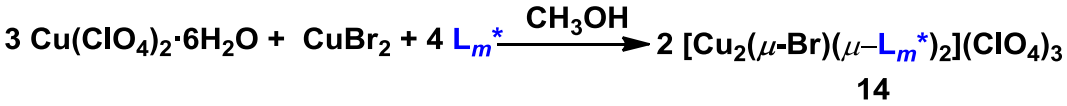

Mass spectrometry. Positive-ion electrospray mass spectra (ESI^+-MS) of all the metallacyclic species are similar. For $[M_2(\mu$-X$)(\mu$-**L**$_m$***)**$_2](ClO_4)_3$, X = Cl^- or Br^- (**1**, **2**, **6**, **7**, **11**, **13** and **14**) clusters, such as $[M_2($**L**$_m$***)**$_2X(ClO_4)_2]^+$, $[M_2($**L**$_m$***)**$_2X(ClO_4)]^{2+}$ and $[M_2($**L**$_m$***)**$_2X]^{3+}$, where M = Fe(II), Co(II), Ni(II), Cu(II), Zn(II), Cd(II), were observed in all spectra. The ESI^+-MS spectra of **3** and **8** shows similar peaks with the corresponding BF_4^- counterions. In several cases (**1**, **2**, **6**, **13**) the base peak in the spectrum is $[M_2($**L**$_m$***)**$_2Cl]^{3+}$; for the copper(II) compounds it also has relatively high intensity, but the base peak is $[Cu($**L**$_m$***)**$]^+$. For compound **12** the base peak is $[Zn($**L**$_m)_2]^{2+}$. The data indicates that the metallacycles are highly stable even in the gas phase, especially the **L**$_m$*** compounds. These observations are in good agreement with the structures determined in solid state and for **11** and **13** in solution.

Solid State Structures. The symmetry of the metallacyclic compounds differ, despite the similar cationic units. Relevant bond lengths and bond angles are shown in Table 4.5 and 4.6. Figure 4.1 shows the structure of the cationic unit of **1** at 296K (a) and

at 100K (b). Most of the chloride bridged compounds with $\mathbf{L_m}$* undergo a phase change at lower temperatures, which is caused by the partial ordering of the counter anions. The numbering scheme on Figure 4.1a for compound **1** is also correct for the high temperature structure of compounds **2**, **3**, **6**, **7**, **8** and **13**·3.8CH_3OH. These cationic units at high temperature are located on an inversion center. The phase change results in the loss of the inversion center. Figure 4.1b shows the low temperature structure for **2** and **6**. Compound **7** and **8** at low temperature have two centrosymmetic cations (Figure 4.2). For compounds **11** and **13** there are two independent cationic units in the structure. These cations are numbered the same way as the low temperature structure of **7** (Figure 4.2). The cationic units of **3** at 100K are shown in Figure 4.3, one cation is located at a general crystallographic position and the other one is on an inversion center.

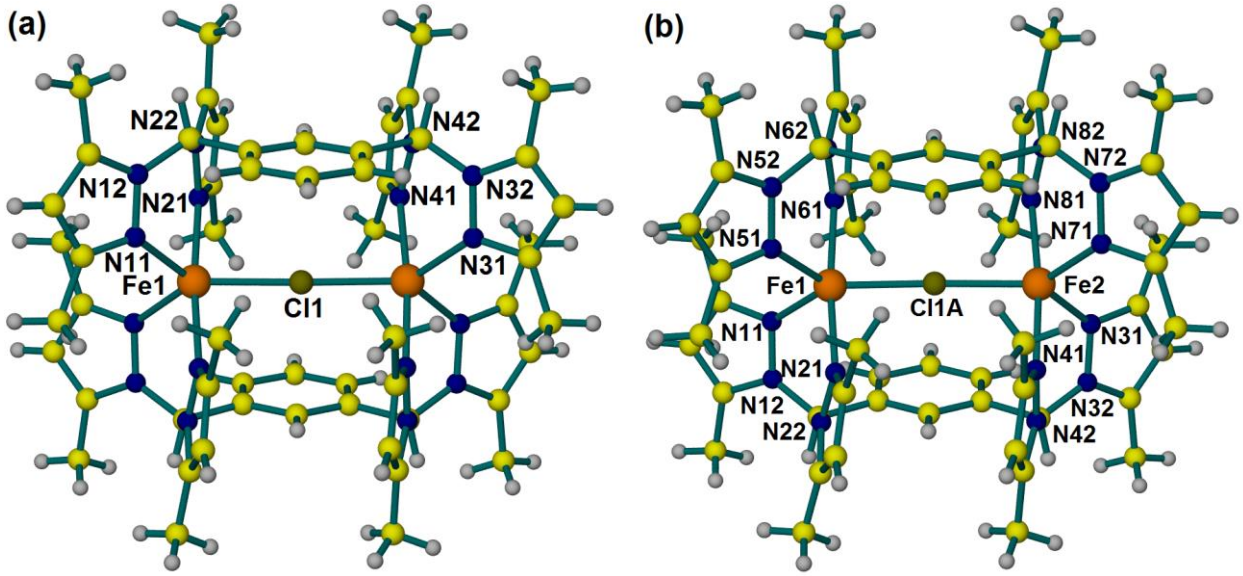

Figure 4.1. Structure of the cationic unit of $[Fe_2(\mu\text{-Cl})(\mu\text{-}\mathbf{L_m}^*)_2](ClO_4)_3$, **1**, at 296 K (a) and at 100 K (b). At 100 K the inversion center is lost. Disordered atoms are removed for clarity.

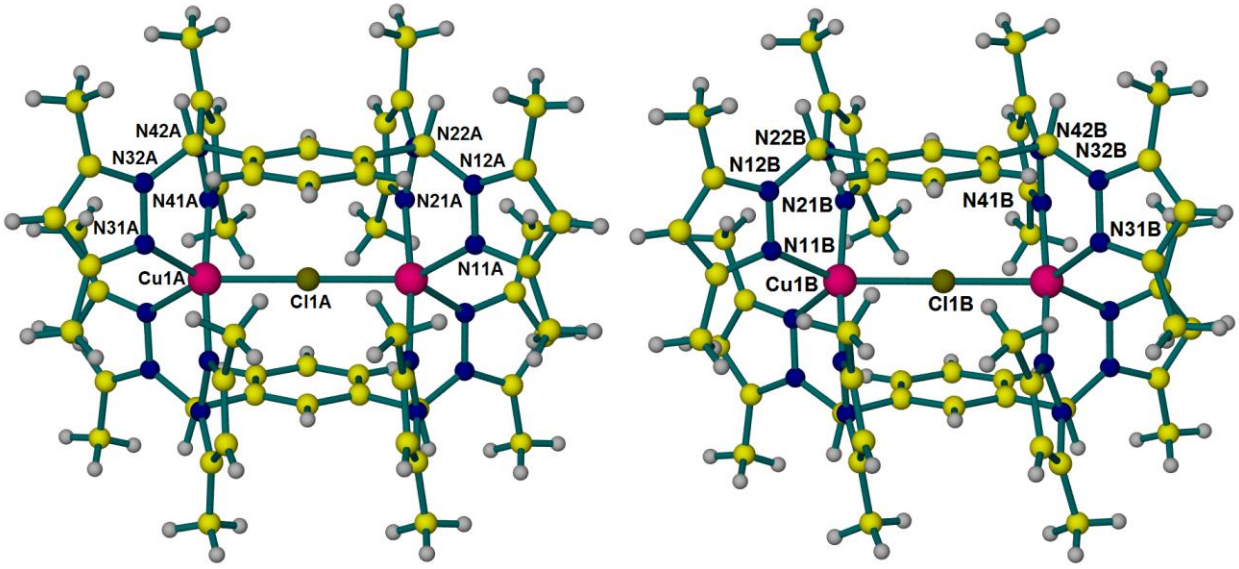

Figure 4.2. Structure of the two independent cationic units of $[Cu_2(\mu\text{-Cl})(\mu\text{-}\mathbf{L_m}^*)_2](ClO_4)_3$, **7**, at 100 K.

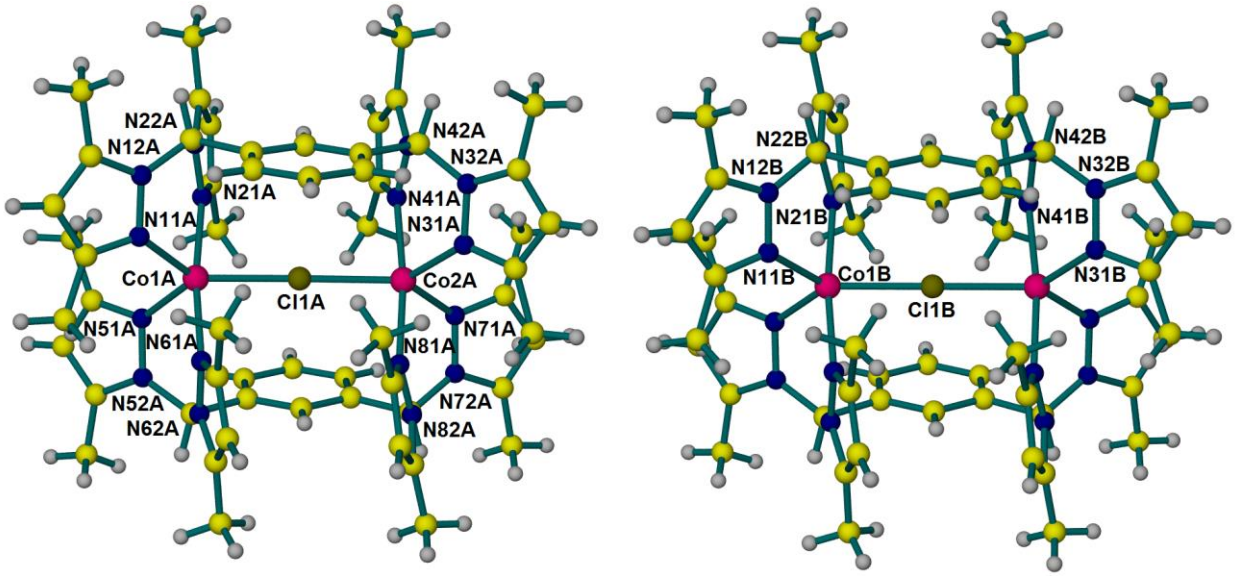

Figure 4.3. Structure of the two independent cationic units of $[Co_2(\mu\text{-Cl})(\mu\text{-}\mathbf{L_m}^*)_2](BF_4)_3$, **3** at 100 K.

Both **9**·1.5CH_3CN (bars) and **9**·2CH_3CN (parallelograms) are isolated from the same crystallization tube – **9**·1.5CH_3CN corresponds to approximately 95% of the crystals. Figure 4.4 shows the two independent cationic units of **9**·1.5CH_3CN, where cation Cu1 is located on a crystallographic inversion center and cation Cu2 is located on a

crystallographic mirror plane. The cation of compound **12**, also located on an inversion center, is numbered as cation Cu1 from the structure of **9**·1.5CH_3CN. Similarly, Figure 4.5 shows the cationic units of **9**·2CH_3CN, where both crystallographically independent cations are located on crystallographic inversion centers. The numbering scheme is also correct for the two independent cations of **10**·3CH_3CN.

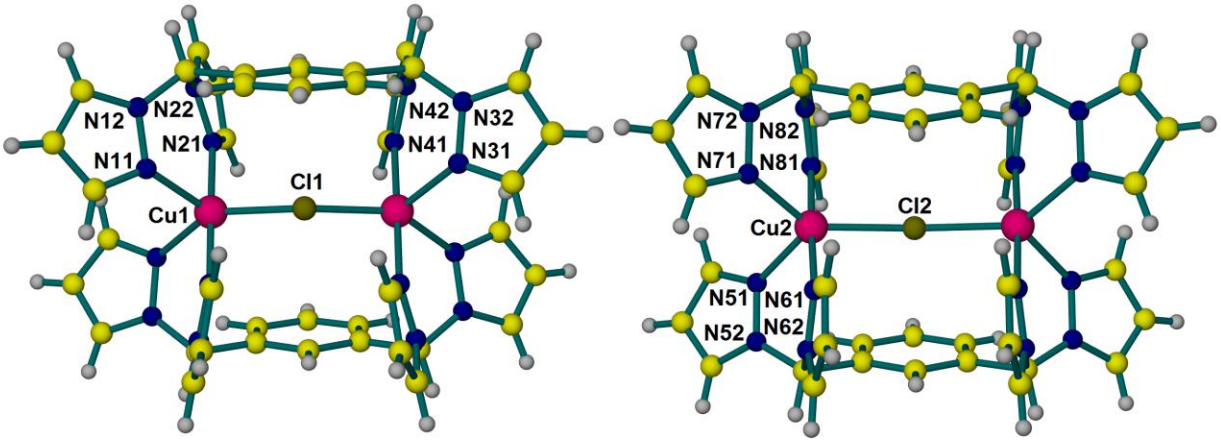

Figure 4.4. Structure of the two independent cationic units of $[Cu_2(\mu\text{-Cl})(\mu\text{-}\mathbf{L_m})_2](ClO_4)_3$·1.5$CH_3CN$, **9**·1.5$CH_3CN$ at 150 K. Disordered atoms are removed for clarity.

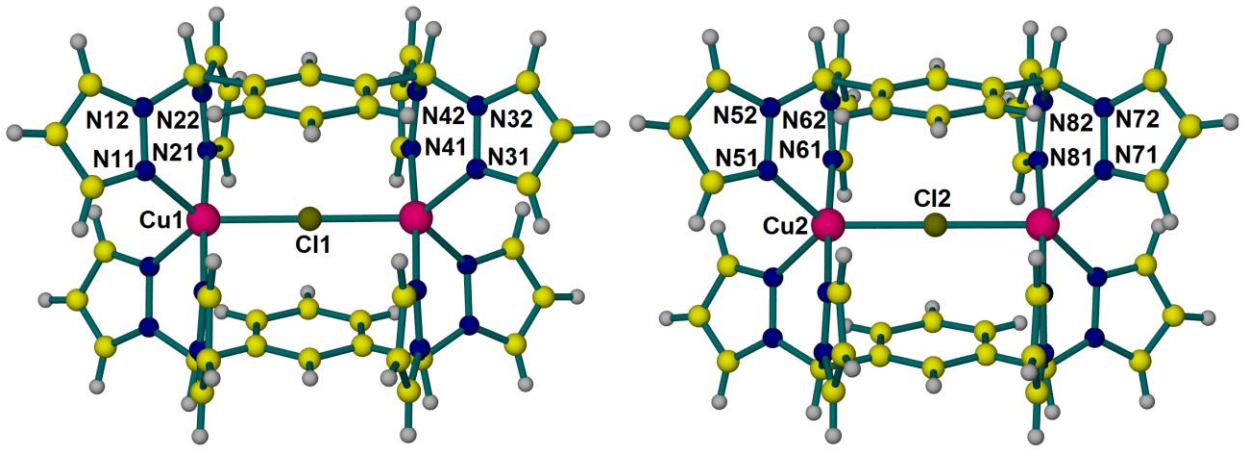

Figure 4.5. Structure of the two independent cationic units of $[Cu_2(\mu\text{-Cl})(\mu\text{-}\mathbf{L_m})_2](ClO_4)_3$·2$CH_3CN$, **9**·2$CH_3CN$ at 150 K.

Table 4.5. Selected Bond lengths and Bond Angles for Compounds $[Fe_2(\mu\text{-}Cl)(\mu\text{-}\mathbf{L_m}^*)_2](ClO_4)_3$ (**1**), $[Co_2(\mu\text{-}Cl)(\mu\text{-}\mathbf{L_m}^*)_2](ClO_4)_3$ (**2**), $[Co_2(\mu\text{-}Cl)(\mu\text{-}\mathbf{L_m}^*)_2](BF_4)_3$ (**3**), $[Ni_2(\mu\text{-}Cl)(\mu\text{-}\mathbf{L_m}^*)_2](ClO_4)_3$ (**6**), $[Cu_2(\mu\text{-}Cl)(\mu\text{-}\mathbf{L_m}^*)_2](ClO_4)_3$ (**7**), $[Cu_2(\mu\text{-}Cl)(\mu\text{-}\mathbf{L_m}^*)_2](BF_4)_3$ (**8**), $[Zn_2(\mu\text{-}Cl)(\mu\text{-}\mathbf{L_m}^*)_2](ClO_4)_3{\cdot}5CH_3CN$ (**11**$\cdot 5CH_3CN$), $[Cd_2(\mu\text{-}Cl)(\mu\text{-}\mathbf{L_m}^*)_2](ClO_4)_3$ (**13**).

Complex	T(K)	L	Metal centers	M-X-M Angle (deg)	M-X distance (Å)	Average M-N distance, Å	M⋯M distance, Å	τ_5[b]
1	296(2)	$\mathbf{L_m}^*$	Fe(1)-Fe(1')[a]	169.5(6)	2.37(2)/2.39(2)	2.121	4.73	0.65
1	100(2)	$\mathbf{L_m}^*$	Fe(1)-Fe(2)[a]	174.3(9) 167.1(12)	2.358(5)/ 2.371(19) 2.358(5)/ 2.370(19)	2.114 2.113	4.71	0.62 0.68
2	295(2)	$\mathbf{L_m}^*$	Co(1)-Co(1')	180.0	2.3786(3)	2.081	4.76	0.69
2	100(2)	$\mathbf{L_m}^*$	Co(1)-Co(2)	177.14(3)	2.3610(5) 2.3610(5)	2.073 2.073	4.72	0.70 0.68
3	296(2)	$\mathbf{L_m}^*$	Co(1)-Co(1')	180.0	2.3785(4)	2.081	4.76	0.70
3	100(2)	$\mathbf{L_m}^*$	Co(1A)-Co(2A) Co(1B)-Co(1B)	178.12(4) 179.999(1)	2.3527(7)/ 2.3587(7) 2.3703(3)	2.074/ 2.071 2.073	4.71 4.74	0.71 0.70
6	296(2)	$\mathbf{L_m}^*$	Ni(1)-Ni(1')[a]	169.4(4)	2.367(16)/2.375(16)	2.044	4.72	0.60
6	100(2)	$\mathbf{L_m}^*$	Ni(1)-Ni(2)[a]	172.3(5) 168.8(6)	2.342(4)/ 2.380(10) 2.327(10)/ 2.353(4)	2.032 2.032	4.68	0.58 0.62
7	295(2)	$\mathbf{L_m}^*$	Cu(1)-Cu(1')	180.0	2.3308(4)	2.041	4.66	0.70
7	100(2)	$\mathbf{L_m}^*$	Cu(1A)-Cu(1A) Cu(1B)-Cu(1B)	180.0 180.0	2.3170(3) 2.3201(3)	2.031 2.029	4.63 4.64	0.73 0.63
8	200(2)	$\mathbf{L_m}^*$	Cu(1)-Cu(1')	180.000(17)	2.3453(3)	2.034	4.69	0.70
8	100(2)	$\mathbf{L_m}^*$	Cu(1A)-Cu(1A) Cu(1B)-Cu(1B)	180.0 180.0	2.3384(3) 2.3396(3)	2.029 2.030	4.68 4.68	0.71 0.62
11$\cdot 5CH_3CN$	100(2)	$\mathbf{L_m}^*$	Zn(1A)-Zn(1A) Zn(1B)-Zn(1B)	180.0 179.998(1)	2.3841(4) 2.4092(4)	2.091 2.100	4.77 4.82	0.72 0.66
13	100(2)	$\mathbf{L_m}^*$	Cd(1A)-Cd(1A)[a] Cd(1B)-Cd(1B)[a]	167.73(16) 158.01(10)	2.462(8)/ 2.471(8) 2.451(2)/ 2.511(2)	2.318 2.272	4.91 4.87	0.70 0.65
13$\cdot 3.8CH_3OH$	100(2)	$\mathbf{L_m}^*$	Cd(1)-Cd(1')[a]	162.74(9)	2.473(3)/ 2.489(3)	2.286	4.91	0.74

[a]Disordered chloride bridge. [b]See ref. 18.

Table 4.6. Selected Bond Lengths and Bond Angles for Compounds $Co_2(\mu\text{-}\mathbf{L_m}\text{*})_2Cl_4$ (**4**), $[Co_2(\mu\text{-}\mathbf{L_m})_2Cl_4]$ (**5**), $[Cu_2(\mu\text{-}Cl)(\mu\text{-}\mathbf{L_m})_2](ClO_4)_3\cdot 1.5CH_3CN$ (**9**$\cdot 1.5CH_3CN$), $[Cu_2(\mu\text{-}Cl)(\mu\text{-}\mathbf{L_m})_2](ClO_4)_3\cdot 2CH_3CN$ (**9**$\cdot 2CH_3CN$), $[Cu_2(\mu\text{-}Cl)(\mu\text{-}\mathbf{L_m})_2](BF_4)_3$ (**10**$\cdot 3CH_3CN$), $[Zn_2(\mu\text{-}Cl)(\mu\text{-}\mathbf{L_m})_2](ClO_4)_3\cdot 2(CH_3)_2O$ (**12**$\cdot 2(CH_3)_2O$), $[Cu_2(\mu\text{-}Br)(\mu\text{-}\mathbf{L_m}\text{*})_2](ClO_4)_3\cdot 2CH_3CN$ (**14**$\cdot 2CH_3CN$), $Co_2(\mu\text{-}\mathbf{L_m}\text{*})_2Br_4$ (**15**).

Complex	T(K)	L	Metal centers	M-X-M Angle (deg)	M-X distance (Å)	Average M-N distance, Å	M⋯M distance, Å	τ_5 [b]
9$\cdot 1.5CH_3CN$	150(2)	$\mathbf{L_m}$	Cu(1)-Cu(1')[a]	138.53(13)	2.235(2)/ 2.248(2)	2.041	4.19	0.54
			Cu(2)-Cu(2')	167.79(7)	2.3392(5)	2.033	4.65	0.72
9$\cdot 2CH_3CN$	150(2)	$\mathbf{L_m}$	Cu(1)-Cu(1')	180.0	2.3530(3)	2.022	4.70	0.83
			Cu(2)-Cu(2')	180.0	2.3757(3)	2.037	4.75	0.82
10$\cdot 3CH_3CN$	150(2)	$\mathbf{L_m}$	Cu(1)-Cu(1')	180.0	2.3633(3)	2.038	4.73	0.73
			Cu(2)-Cu(2')	180.0	2.3400(3)	2.037	4.68	0.80
12$\cdot 2(CH_3)_2O$	100(2)	$\mathbf{L_m}$	Zn(1)-Zn(1')[a]	169.93(19)	2.346(8)/2.358(8)	2.094	4.70	0.75
4	100(2)	$\mathbf{L_m}$*	Co(1)-Co(2)	-	2.2607(8)/ 2.2098(9) 2.2459(8)/ 2.2126(7)	2.029	7.07	-
5	296(2)	$\mathbf{L_m}$	Co(1)-Co(2)	96.27(3)/ 93.65(3)	2.5981(8)/ 2.2901(7)/ 2.2750(8) 2.3286(7)/ 2.5357(7)/ 2.2874(7)	2.095 2.113	3.60/ 8.20	0.90 0.72
14$\cdot 2CH_3CN$	100(2)	$\mathbf{L_m}$*	Cu(1)-Cu(1')	180.0	2.4733(3)	2.033	4.95	0.64
15	100(2)	$\mathbf{L_m}$*	Co(1)-Co(2)	-	2.4048(12)/ 2.3395(12) 2.3796(12)/ 2.3449(11)	2.028	7.08	-

[a]Disordered chloride bridge. [b]See ref. 19.

The overall structures of the $[M_2(\mu\text{-Cl})(\mu\text{-}\mathbf{L})_2]^{3+}$ complexes, **L** = $\mathbf{L}_m$ or $\mathbf{L}_m$*****, are very similar. In all metallacyclic structures, the geometry around the metal centers is highly distorted trigonal bipyramidal. The equatorial (*e*) angles are distorted from the ideal values, e.g. $[Co_2(\mu\text{-Cl})(\mu\text{-}\mathbf{L}_m\text{*})_2](ClO_4)_3$ (**2**) at 295 K: *ee*-N-Co-N 102.82(9)˚; *ee*-N-Co-Cl 126.04(6)˚, 131.14(7)˚. Similarly, the atoms in the axial (*a*) positions form distorted angles, e.g. **2** at 295 K: *aa*-N-Co-N 172.80(8); *ae*-N-Co-N: 86.34(9)˚- 97.92(9)˚; *ae*-N-Co-Cl: 86.01(6)˚, 86.81(6)˚. For most metals, the equatorial bond lengths are shorter than the axial bond lengths, e.g. **2** at 295 K: *e*-N-Co 2.050(2) and 2.053(2) Å; *a*-N-Co 2.103(2) and 2.119(2) Å. This trend is reversed in the case of the copper(II) compounds as a result of pseudo Jahn-Teller distortion,[18] e.g. $[Cu_2(\mu\text{-Cl})(\mu\text{-}\mathbf{L}_m\text{*})_2](ClO_4)_3$ (**7**) at 295K: *e*-Cu-N 2.088(3) and 2.099(3)Å; *a*-Cu-N 1.984(3) and 1.993(2) Å. In addition, the τ_5[19] values, 0.58-0.83, summarized in Table 4.5 and 4.6, support the trigonal bipyramidal geometry around the metal centers ($\tau_5 > 0.5$) with various degree of distortion towards a square pyramidal geometry.

In most metallacycles, the M-Cl-M angles (Table 4.5 and 4.6) are linear or nearly linear, 168-180°. One notable exception is one of the forms of $[Cu_2(\mu\text{-Cl})(\mu\text{-}\mathbf{L}_m)_2](ClO_4)_3\cdot 1.5CH_3CN$ (**9**$\cdot 1.5CH_3CN$) where the angle drops to 138.53(13)°, with the other form in that structure at 167.79(7)°. The angles are also consistently lower in the two different solvates of $[Cd_2(\mu\text{-Cl})(\mu\text{-}\mathbf{L}_m\text{*})_2](ClO_4)_3$, 158.01(10)°-167.73(16)°, where the metal has a larger ionic radius than in the other structures.

The order/disorder type phase change for **1-3** and **5-7** does not result in significant structural modifications. The induced changes upon cooling of the samples are not bigger than ±3˚ for the N-M-N and N-M-Cl bond angles and ± 0.02 Å for the *a*-M-N, ± 0.05 Å

for the *e*-M-N and ± 0.02 Å for the M-Cl bond lengths. This small change in the crystal structure still induces dramatic color change in $[Co_2(\mu\text{-}Cl)(\mu\text{-}\mathbf{L}_m\mathbf{*})_2](ClO_4)_3$ (**2**) upon change in the temperature from 295(2) K (red/purple crystals) to 100(2) K (green crystals), Figure 4.6.

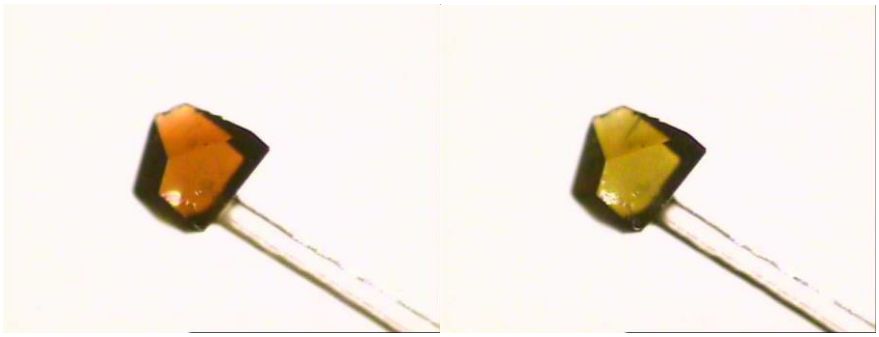

Figure 4.6. Crystals of $[Co_2(\mu\text{-}Cl)(\mu\text{-}\mathbf{L}_m\mathbf{*})_2](ClO_4)_3$ (**2**). Left 295(2) K, right 100(K).

Counter anion exchange from ClO_4^- to BF_4^- also results in only a small change of ± 0.02 Å in the M-Cl bond lengths as demonstrated by the copper(II) compounds **7** and **8** with $\mathbf{L}_m\mathbf{*}$, similarly **9**·1.5CH_3CN, **9**·2CH_3CN and **10**·3CH_3CN with $\mathbf{L}_m$ (Table 4.5 and 4.6). The Cu-Cl bond lengths are slightly longer for the BF_4^- compounds for both $\mathbf{L}_m$ and $\mathbf{L}_m\mathbf{*}$, e.g. **9**·1.5CH_3CN: Cu-Cl 2.235/ 2.248(2) and 2.3392(5) Å; **9**·3CH_3CN: Cu-Cl 2.3633(3) and 2.3400(3) Å. A similar trend was observed for analogous fluoride bridged compound, $[Cu_2(\mu\text{-}F)(\mu\text{-}\mathbf{L}_m\mathbf{*})_2](A)_3$, A = BF_4^- or ClO_4^-.[9a,10]

The bromide bridged compound, $[Cu_2(\mu\text{-}Br)(\mu\text{-}\mathbf{L}_m\mathbf{*})_2](ClO_4)_3$·2$CH_3CN$ (**14**·2CH_3CN), Figure 4.7, is similar to the chloride bridged analogue, **7**, the geometry around the metal centers is still distorted trigonal bipyramidal, $\tau_5 > 0.64$. Exchange of the chloride bridge to bromide results in larger Cu···Cu nonbonding distance, 4.95 Å vs. 4.66 Å, while the linearity of the bridge is retained, Cu-Br-Cu angle is 180°.

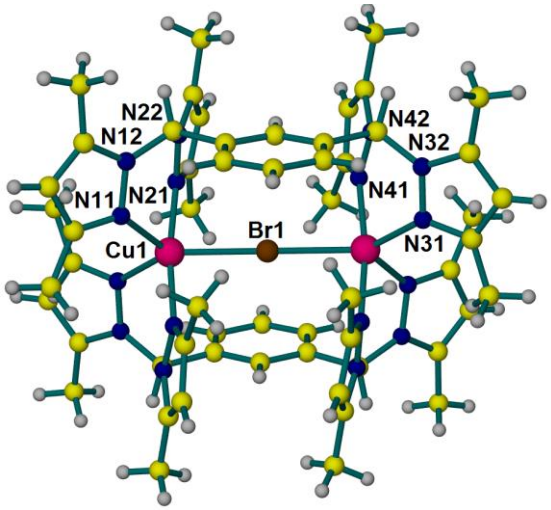

Figure 4.7. Structure of the cationic unit of $[Cu_2(\mu\text{-Br})(\mu\text{-}\mathbf{L}_m\mathbf{*})_2](ClO_4)_3\cdot 2CH_3CN$, **14**$\cdot 2CH_3CN$ at 100 K.

In the acyclic structure of $Co_2(\mu\text{-}\mathbf{L}_m\text{*})Cl_4$ (**4**), and analogous $Co_2(\mu\text{-}\mathbf{L}_m\text{*})Br_4$ (**15**) the ligand, $\mathbf{L}_m\mathbf{*}$, adopts *anti*-conformation, the two bis(pyrazolyl)methane units point towards opposite sides of the plane defined by the phenylene spacer, and chelates two cobalt(II) centers (Figure 4.8). Further coordination of two chloride or bromide ions to each cobalt(II), results in a distorted tetrahedral coordination environment around the metal centers with N-Co-N angles 91.96(9)º and 92.78(10)º, N-Co-Cl angles between 107.08º-118.38º and Cl-Co-Cl angles 109.74(3)º and 112.23(3)º. Compound $Co_2(\mu\text{-}\mathbf{L}_m\text{*})Br_4$ (**15**) is analogous to **4**, with N-Co-N angles 92.4(2)º and 93.1(2)º, N-Co-Br angles between 107.69º-118.83º and Br-Co-Br angles 108.82(4)º and 111.55(4)º.

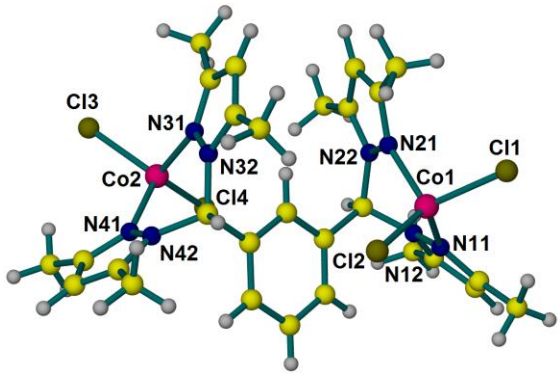

Figure 4.8. Structure of $Co_2(\mu\text{-}\mathbf{L}_m\mathbf{*})Cl_4$, **4**.

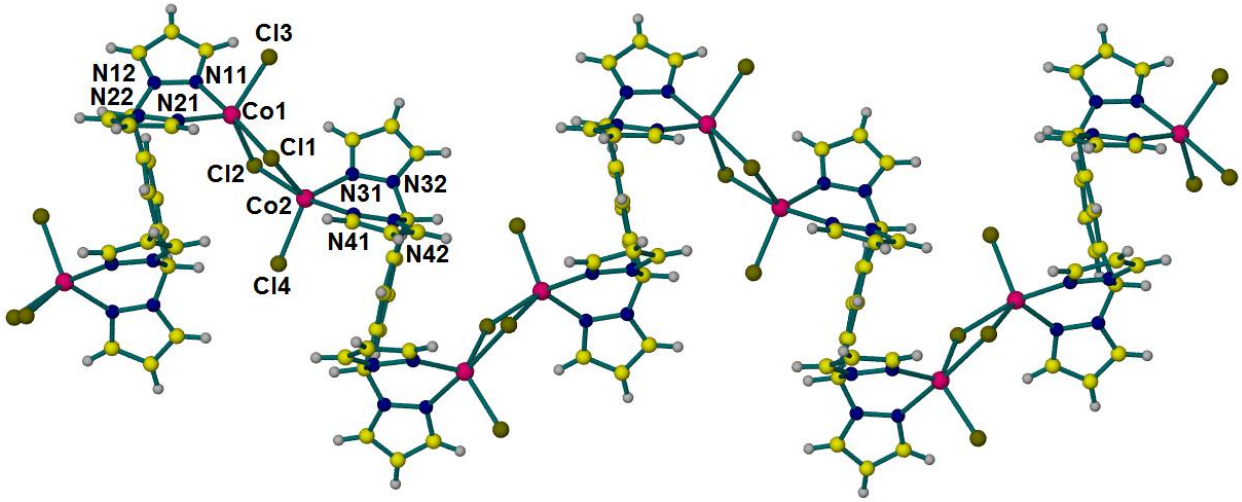

Figure 4.9. Structure of $[Co_2(\mu\text{-}\mathbf{L}_m)Cl_4]$, **5**.

Similarly to dinuclear $Co_2(\mu\text{-}\mathbf{L}_m\mathbf{*})Cl_4$ (**4**), in the structure of polymeric $[Co_2(\mu\text{-}\mathbf{L}_m)Cl_4]$ (**5**) the ligand, $\mathbf{L}_m$, is in *anti*-conformation bridging two cobalt(II) centers. Two chlorides (Cl1, Cl2), terminal in compound **4**, further bridge two cobalt(II) centers to generate the polymeric chain (Figure 4.9). The coordination number around cobalt(II) increases from four to five by further coordination of a terminal chloride (Cl3, Cl4) to each crystallographically independent cobalt(II) center (Co1 and Co2) resulting in a trigonal bipyramidal geometry. The equatorial positions of this trigonal bipyramid around Co1 are occupied by N21, Cl2, Cl3 and the axial positions are occupied by N11 and Cl1. The axial bond lengths are longer, than the equatorial ones: Co1-N11 2.141(2) Å, Co-N21 2.048(2) Å, Co1-Cl1 2.5981(8) Å, Co1-Cl2 2.2901(7) Å and Co1-Cl3 2.2750(8) Å. The coordination sphere around Co2 is very similar, Co2-N31 2.082(2) Å, Co2-N41 2.144(2) Å, Co2-Cl4 2.2874(7) Å, Co2-Cl1 2.3286(7) Å, Co2-Cl2 2.5357(7) Å. The τ_5 values are 0.90 and 0.72, respectively. The parallel polymeric chains participate in weak intra- and interchain CH···Cl interactions,[20] Figure 4.10: C-H···Cl 2.599(2) Å 172.37° and 2.453(2) Å 165.31°.

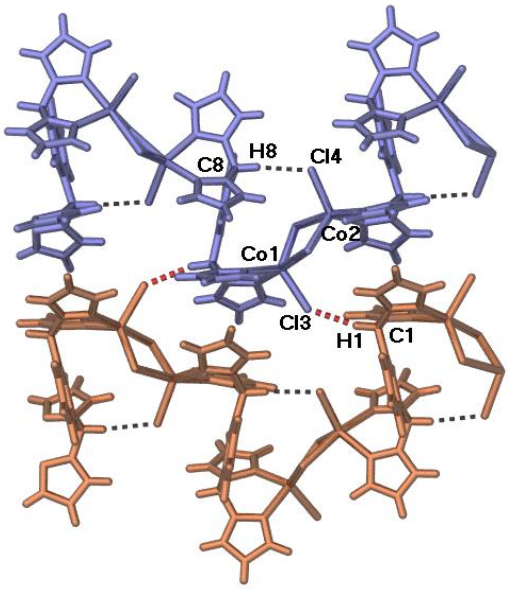

Figure 4.10. Weak intra- and interchain C-H···Cl interactions in the parallel polymeric chains of $[Co_2(\mu\text{-}\mathbf{L}_m)Cl_4]$, **5**.

NMR. The ^{1}H NMR spectra of $[Zn_2(\mu\text{-}Cl)(\mu\text{-}\mathbf{L}_m\mathbf{*})_2](ClO_4)_3$ (**11**) and $[Cd_2(\mu\text{-}Cl)(\mu\text{-}\mathbf{L}_m\mathbf{*})_2](ClO_4)_3$ (**13**) in acetonitrile (Figure 4.11) show the same characteristics as analogous fluoride bridged metallacycles, $[M_2(\mu\text{-}F)(\mu\text{-}\mathbf{L}_m\mathbf{*})_2]^{3+}$, M = Zn(II) or Cd(II).[9a]

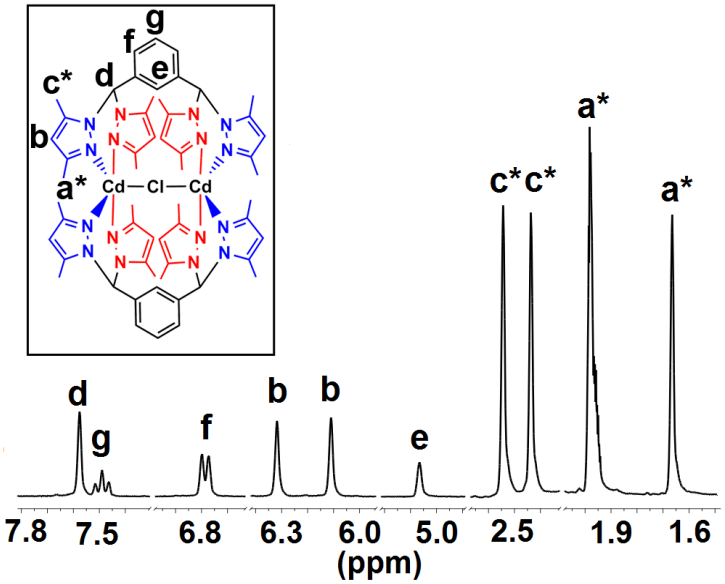

Figure 4.11. Ambient temperature ^{1}H NMR spectra of $[Cd_2(\mu\text{-}Cl)(\mu\text{-}\mathbf{L}_m\mathbf{*})_2](ClO_4)_3$, (**13**). Red axial, blue equatorial pyrazolyl rings.

Only one set of resonances can be observed for the *m*-phenylene spacers (*e, f, g*) and the methine (*d*) hydrogens. In contrast, the pyrazolyl methyl groups (*a** and *c**) and the pyrazolyl *b* hydrogen show two equal intensity resonances for each position, indicating two sets of non-equivalent pyrazolyl rings (*c** **11**: 2.59/ 2.39 ppm, **13**: 2.54/ 2.44 ppm; *a** **11**: 1.76/ 1.29 ppm, **13**: 1.98/ 1.67 ppm; *b* **11**: 6.29/ 6.08 ppm, **13**: 6.32/ 6.12 ppm). The ^{1}H NMR spectra of $[Zn_2(\mu\text{-Cl})(\mu\text{-}\mathbf{L_m})_2](ClO_4)_3$ (**12**) shows severe linewidth broadening, even at -40°C, assignment of the resonances was not possible.

Similarly to the ^{1}H NMR, in the ^{13}C NMR spectra there is one set of resonances for each type of carbon atom of the linking groups, but two sets of resonances are observed for the 3,5-dimethylpyrazolyl carbons. The *a**, *c**-methyl group carbons on the pyrazolyl rings are at 14.8, 11.6, 11.5, 10.6 ppm for **11** and 14.3, 12.3, 11.4, 10.7 ppm for **13**. The four distinct *a*, *c*-pyrazolyl ring carbon resonances are at 154.6, 151.5, 147.5, 144.7 ppm for **11** and 154.4, 152.0, 148.0, 145.1 ppm for **13**. For these pyrazolyl resonances in the spectra of compound **13**, cadmium(II) satellites were observed with $J_{C\text{-}Cd}$ between 5 and 7 Hz. The ^{113}Cd NMR spectrum of **13** shows a single relatively broad resonance at 133.4 ppm.

The results above indicate that the dinuclear structures shown in the solid state (*vide infra*) are retained in acetonitrile for both **11** and **13**. The solid state structures predict that if similar $[M_2(\mu\text{-Cl})(\mu\text{-}\mathbf{L_m}\text{*})_2]^{3+}$, M = Zn(II) or Cd(II), cationic units are present in solution two pairs of resonances should be observed for each hydrogen and carbon of the pyrazolyl rings: one set for those oriented along the M–Cl–M axis, equatorial (Figure 4.11, blue), and another set for those perpendicular to it, axial (red) pyrazolyl rings of the trigonal bipyramidal geometry. In contrast, each type of hydrogen and carbon atom in the

m-phenylene spacers and the methine group should be equivalent, again as observed in solid state.

Magnetic Properties of the Copper(II) Compounds. The magnetic susceptibility data for the copper(II) compounds, **7**, **9**·xCH_3CN and **14**·2CH_3CN, were interpreted using the Heisenberg-Dirac-van Vleck Hamiltonian in the form $\hat{\mathbf{H}} = -J\hat{\mathbf{S}}_1\hat{\mathbf{S}}_2$ which results in the Bleaney-Bowers expression for the magnetic susceptibility (per dimer):

$$\chi_d = \frac{Ng^2\mu_B^2}{3kT}\frac{6\exp(J/kT)}{1+3\exp(J/kT)}$$

The total susceptibility (per dimer) is: $\chi = (1-f)\,\chi_{dimer} + 2f\,\chi_{monomer}$, where f is a fraction of monomeric impurity and $\chi_{monomer} = (Ng^2\mu_B{}^2/3kT)\cdot S(S+1)$ with $S = 1/2$. Accordingly $\chi_{dimer} = (\chi - 2f\,\chi_{monomer}) / (1-f)$.

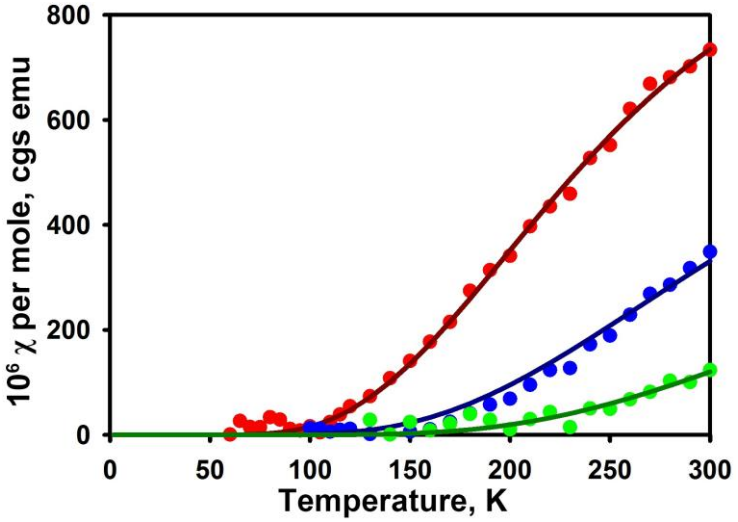

Figure 4.12. Magnetic susceptibility data for [Cu_2(μ-Cl)(μ-$\mathbf{L}_m$)$_2$](ClO_4)$_3$·xCH_3CN, **9**·xCH_3CN (red) and [Cu_2(μ-Cl)(μ-$\mathbf{L}_m$*****)$_2$](ClO_4)$_3$, **7** (blue), [Cu_2(μ-Br)(μ-$\mathbf{L}_m$*)$_2$](ClO_4)$_3$·2CH_3CN, **14**·2CH_3CN (green).

The experimental susceptibilities shown on Figure 4.12 were obtained by choosing f manually so that the low-temperature χ_{dimer} becomes constant. If that constant was not zero, the deviation was interpreted as to be due to imperfect Pascal constant and was subtracted from the data. This approach is justified as a small inaccuracy in the Pascal

contribution has a very large influence on the very low temperature susceptibilities of these compounds. The χ_{dimer} data obtained in this way were fitted. For all three compounds the magnetic susceptibility decreases, and below 100 K are close to 0. Data fitted in the standard way result in similar -*J* values.

The magnetic data, Table 4.7, demonstrate very strong antiferromagnetic exchange coupling between the copper(II) ions. The smallest magnetic moment at 300 K was observed for **14**·2CH_3CN, and resulted in extremely large -*J*, 945 cm^{-1}. One of the *g*-values is smaller than the other two, for example **7** g_z = 1.999, indicating that the unpaired electron on each copper(II) center is located on an orbital with predomintly d_{z^2} character.

Table 4.7. Spin Hamiltonian Parameters from the Magnetic Data for **7**, **9**·xCH_3CN and **14**·2CH_3CN.

Complex	**7**	**9**·xCH_3CN	**14**·2CH_3CN
$-J$, cm^{-1}	720(10)	536	945(20)
g_x	2.18[a]	2.19	2.15[b]
g_y	2.25	2.23	2.15
g_z	1.99	2.00	1.99
|D|, cm^{-1}	0.18	0.18	0.25
|E|, cm^{-1}	0.05	0.04	0.06

[a]High–field EPR, 305 K. [b]Q–Band, 295 K.

For the magnetic measurements on compound **9** a mixture of two solvates was used as both **9**·1.5CH_3CN and **9**·2CH_3CN are isolated from the same crystallization tube (see above) in approximately 95% to 5% ratio. The bent species (Cu-Cl-Cu 138.53° and 167.79°) dominate the sample and the weighted average of the Cu-Cl-Cu angle for 9·xCH_3CN is 154.46°. This angle is significantly smaller than the one in analogous **7**, 180.0°, therefore the antiferromagnetic interaction is stronger in the $\mathbf{L}_m$***** system than in the $\mathbf{L}_m$ system, $-J = 720$ cm^{-1} vs. $-J = 536$ cm^{-1}.

Discussion and Conclusions

A large family of monochloride bridged metallacycles of the type $[M_2(\mu\text{-Cl})(\mu\text{-}\mathbf{L})_2]^{3+}$ were synthesized with third-generation bis(pyrazolyl)ligands where **L** = $\mathbf{L}_m$ M = Cu(II), Zn(II) or $\mathbf{L}_m$* M = Fe(II), Co(II), Ni(II), Cu(II), Zn(II), Cd(II). In addition, $[Cu_2(\mu\text{-Br})(\mu\text{-}\mathbf{L}_m\text{*})_2](ClO_4)_3\cdot 2CH_3CN$ (**14**$\cdot 2CH_3CN$) was successfully isolated. The ESI^+-MS of all of these complexes and NMR spectroscopy of the zinc(II) and cadmium(II) compounds, as well as the isolation of $[Co_2(\mu\text{-}\mathbf{L}_m)Cl_4]$ (**5**) with $\mathbf{L}_m$, while the same reaction with $\mathbf{L}_m$* results in both $[Co_2(\mu\text{-Cl})(\mu\text{-}\mathbf{L}_m\text{*})_2](BF_4)_3\cdot$(**3**) and $Co_2(\mu\text{-}\mathbf{L}_m)Cl_4$ (**4**), suggest that the dimethyl substituted ligand, $\mathbf{L}_m$*, increases the stability of the metallacyclic structure.

To synthesize the chloride bridged metallacycles two distinct synthetic methods were used: the first is the direct reaction of the metallacycles building blocks and the second starts from the previously reported fluoride bridged analogues which are reacted with $(CH_3)_3SiCl$. The first method proved to be superior, the second method is successful only in the case of copper(II). Utilizing the first method $[Cu_2(\mu\text{-Br})(\mu\text{-}\mathbf{L}_m\text{*})_2](ClO_4)_3\cdot 2CH_3CN$, **14**$\cdot 2CH_3CN$ was also isolated. Upon attempts to expand the bromide bridged series to other metals $Co_2(\mu\text{-}\mathbf{L}_m\text{*})Br_4$, **15** was isolated.

In all metallacyclic structures the ligand $\mathbf{L}_m$ and $\mathbf{L}_m$* adopt *syn* conformation, with both bis(pyrazolyl)methane units on the same side of the phenylene spacer. Crystallographic studies show that the geometry around the metal centers is highly distorted, but it is closer to being trigonal bipyramidal than square pyramidal. For the copper(II) compounds as a result of the pseudo Jahn-Teller distortion the axial bond

lengths are shorter than the equatorial ones, similarly to the fluoride and hydroxide bridged analogues.[9-11]

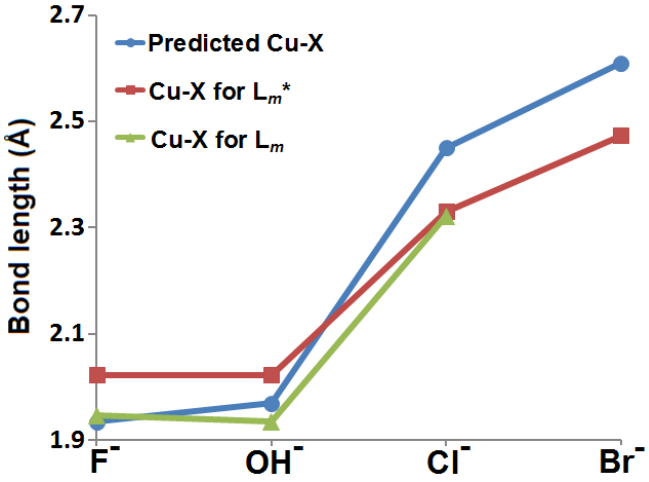

Figure 4.13. Plot of predicted (blue) and measured Cu–X (X = F^-, OH^-, Cl^-, Br^-) bond lengths (red for the $\mathbf{L_m}$* and green for the $\mathbf{L_m}$ compounds) vs. the bridging anions listed in order of increasing ionic radii.

Extensive data for copper(II) allows determination of the impact of the two supporting ligands, $\mathbf{L_m}$ and $\mathbf{L_m}$*, on the Cu-X bond distances. The $\mathbf{L_m}$* ligand has a moderating effect on the Cu–X bond lengths, Figure 4.13. The average Cu-F 2.03 Å, and Cu-O(H) 2.02 Å bond lengths are slightly longer, while the Cu-Cl 2.33 Å and Cu-Br 2.47 Å are shorter than predicted by the sum of the ionic radii of the corresponding atoms (1.94 Å, 1.97 Å, 2.45 Å and 2.61 Å, respectively).[21] In contrast to the longer than predicted Cu-F and Cu-OH distances in $[Cu_2(\mu\text{-}X)(\mu\text{-}\mathbf{L_m}^*)_2]^{3+}$ complexes, in analogous $\mathbf{L_m}$ compounds the Cu-X bond lengths (avg. Cu-F 1.947 Å and avg. Cu-OH 1.935 Å) are similar or slightly shorter than predicted, Figure 4.13. Interestingly, the average Cu-Cl bond length in $[Cu_2(\mu\text{-}Cl)(\mu\text{-}\mathbf{L_m})_2]^{3+}$ is 2.32 Å, shorter than predicted, 2.45 Å, and virtually the same as for $[Cu_2(\mu\text{-}Cl)(\mu\text{-}\mathbf{L_m}^*)_2]^{3+}$. Thus, for the small bridging anions F^- and OH^- the size of the "pocket" generated by the metallacycle $[Cu_2(\mu\text{-}\mathbf{L_m})_2]$ is just about correct for unsubstituted $\mathbf{L_m}$, but the steric effects of the addition of the methyl groups in

L*m** enforce longer Cu-X distances. For the bigger anions, Cl^- and Br^-, the pocket is smaller for both ligands causing mild compression of the M-X distances. Clearly the larger X groups render the steric interactions introduced by the bulkier **L*m**** ligand less relevant.

Magnetic susceptibility data for the Cl^- and Br^- bridged copper(II) metallacycles showed strong antiferromagnetic interactions, **7** $-J = 705\ cm^{-1}$, **9**·xCH_3CN $-J = 536\ cm^{-1}$ and **14**·2CH_3CN $-J = 945\ cm^{-1}$. The magnitude of the $-J$ values is particularly surprising, given that the geometry of complexes has the interaction being transmitted through overlap of the "doughnut" portion of the magnetic d_{z2} orbital with the bridging halides p_x orbital. Large $-J$ values have been observed previously when a bridging group with relatively large Cu–X–Cu angles overlaps with the magnetic d_{x2-y2} orbital in square planar or pyramidal geometry or along the z-axis of a trigonal bipyramid.[22] For the one known complex with a linear bridge, a bridge oriented similarly to those reported here, $[Cu_2(tet–b)_2Cl](ClO_4)_3$, the $-J$ value was reported to be 288 cm^{-1},[23] substantially smaller than the 720 cm^{-1} value observed for **7**, or even **9**·xCH_3CN with an weighted average Cu-X-Cu angle of 154.46°. Compound **14**·2CH_3CN exhibits one of the strongest antiferromagnetic interaction observed in a dinuclear compound, with $-J = 945\ cm^{-1}$, only a couple of other compounds have $-J$ above 1000 cm^{-1}.[24]

The large size of the Cl^- and Br^-, as well as the resulting compression of the metallacyclic pockets, Figure 4.13, is probably increasing the strength of the antiferromagnetic interactions in comparison to analogous F^- and OH^- bridged compounds, by increasing the overlap between the magnetic orbitals and the delocalization of unpaired spins towards the bridging halides. Based on the structure of

the $[Cu_2(\mu\text{-}X)(\mu\text{-}\mathbf{L}_m\text{*})_2]^{3+}$ series, X= F^-, Cl^-, OH^-, Br^-, where the overall metallacyclic structures are very similar, and even the Cu-X-Cu angle is fixed at 180° the following trend can be established: the strength of the antiferromagnetic superexchange interactions increase in the sequence F^- < Cl^-< OH^-< Br^-, where for Br^-, and even OH^-, the interaction is so strong that the magnetic moment is close to zero even at room temperature, Figure 4.14.

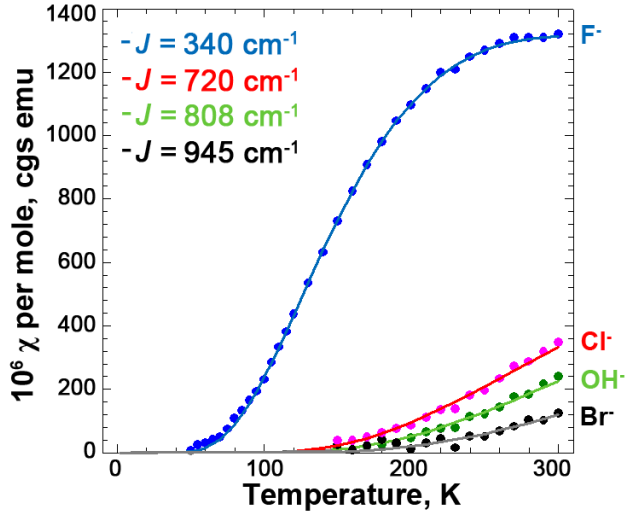

Figure 4.14. Magnetic susceptibility. Dots represent experimental data with the monomer impurity contribution subtracted. Solid lines are calculated with -*J* values shown.

In conclusion, in the copper(II) chloride bridged compounds, similarly to any other antiferromagnetically coupled dinuclear compound with small anionic bridge, the strength of the superexchange interactions largely depends on the bridging angle, but it is also influenced by the M-Cl distance.

References

(1) (a) Kahn, O. *Molecular Magnetism* VCH Publishers, Inc., New York 1993. (b) Gatteschi, D.; Fittipaldi, M.; Sangregorio, C.; Sorace, L. *Angew. Chemie Int. Ed.* **2013**, *51*, 4792. (c) Gatteschi, D.; Comia, A.; Mannini, M.; Sessoli, R. *Inorg. Chem.* **2009**, *48*, 3408. (d) Miller, J. S. *Dalton Trans.* **2006**, 2742. (e) Christou, G. *Polyhedron*, **2005**, *24*, 2065.

(2) Selected examples: (a) Shakya, R.; Powell, D. R.; Houser, R. P. *Eur. J. Inorg. Chem.* **2009**, 5319. (b) Drabent, K.; Ciunik, Z., Ozarowski, A. *Inorg. Chem.* **2008**, *47*, 3358. (c) Ray, N. A.; Neves, A.; De Almeida, W. B.; Dos Santos, H. F.; Costa, L. A. S. *Int. J. Quant. Chem.* **2010**, *110*, 1432. (d) Wikstrom, J. P.; Filatov, A. S.; Mikhalyova, E. A.; Shatruk, M.; Foxman, B. M.; Rybak-Akimova, E. V. *Dalton Trans.* **2010**, *39*, 2504. (e) Wang, L.; Lu, S.; Zhou, Y.; Guo, X.; Lu, Y.; He, J.; Evans, D. G. *Chem. Commun.* **2011**, *47*, 11002. (f) Koval, I. A.; van der Schilden, K.; Schuitema, A. M.; Gamez, P.; Belle, C.; Pierre, J.; Lüken, M.; Krebs, B.; Roubeau, O.; Reedijk, J. *Inorg. Chem.* **2005**, *44*, 4372. (g) Patra, A.; Ray, M.; Mukherjee, R. *Polyhedron*, **2000**, 1423, (h) Coughlin, P. K.; Lippard, S. J. *J. Am. Chem. Soc.* **1981**, *103*, 2338. (i) Turowski, P. N.; Armstrong, W. H.; Liu, S.; Brown, S. N.; Lippard S. J. *Inorg. Chem.* **1994**, *33*, 636. (j) Incarvito, C.; Rheingold, A. L.; Gavrilova, A. L.; Qin, C. J.; Bosnich, B. *Inorg. Chem.* **2001**, *40*, 4101.

(3) Selected examples: (a) Nadeem, M. A.; Bhadbhade, M; Stride, J. A. *Dalton Trans.* **2010**, *39*, 9860. (b) Ding, K.; Dugan, T. R.; Brennessel, E. B.; Holland, P. L. *Organometallics* **2009**, *28*, 6650. (c) Vela, J.; Smith, J. M.; Yu, Y.; Ketterer, N. A.; Flaschenriem, C. J.; Lachicotte, R. J.; Holland, P. L. *J. Am. Chem. Soc.* **2005**, *127*, 7857. (d) Zhu, Q.; Nelson, K. J.; Shum, W. W.; DiPasquale, A.; Rheingold, A. L.; Miller, J. S. *Inorg. Chim. Acta* **2009**, *362*, 595. (e) Birk, T.; Magnussen, M. J.; Piligkos, S.; Weihe, H.; Holten, A.; Benidx, J. *J. Fluorine Chem.* **2010**, *131*, 898. (f) Tomat, E.; Cuesta, L.; Lynch, V. M.; Sessler, J. L. *Inorg. Chem.* **2007**, *46*, 6224. (g) Casellas, H.; Pevec, A.; Kozlevčar; Gamez, P.; Reedijk, J. *Polyhedron* **2005**, *24*, 1549. (h) Wang, C.-M.; Liao, C.-H.; Kao, H.-M.; Lii, K.-H. *Inorg. Chem.* **2005**, *44*, 6294. (i) Leo, R.; Massa, W.; Pebler, J. *J. Fluorine Chem.* **2004**, *125*, 923. (j) Choudhury, A.; Rao, C. N. R. *J. Struct. Chem.* **2002**, *43*, 632. (k) Worm, K.; Chu, F.; Matsumoto, K; Best, M. D.; Lynch, V.; Anslyn, E. V. *Chem. Eur. J.* **2003**, *9*, 741. (l) Blake, A. J., Devillanova, F. A.; Garau, A.; Harrison, A.; Isaia, F.; Lippolis, V.; Tiwary, S. K.; Schröder, M.; Verani, G.; Whittaker, G. *J. Chem. Soc. Dalton Trans.* **2002**, 4389. (m) Westerheide, L.; Muller, F. K.; Than, R.; Krebs, B.; Dietrich, J.; Schindler, S. *Inorg. Chem*. **2001**, 40, 1951. (n) Hao, H.; Cui, C.; Herbert, W.; Bai, G.; Schmidt, H.-G.; Noltemeyer, M. *Chem. Commun.* **2001**, 1118. (o) Yu, P.; Muller, P.; Roesky, H. W.; Noltemeyer, M.; Demsar, A.; Uson, I. *Angew. Chem., Int. Ed*. **1999**, *38*, 3319.

(4) (a) Hay, J. P.; Thibeault, J. C.; Hoffmann, R. *J. Am. Chem. Soc.* **1975**, *97*, 4884. (b) Roundhill, S. G. N.; Roundhill, D. M.; Bloomquist, D. R.; Landee, C; Willettt, R. D.; Dooley, D. M.; Gray, H. B. *Inorg. Chem.* **1979**, *18*, 831. (c) Marsh, W. E.; Patel, K. C.; Hatfield, W. E.; Hodgson, D. J. *Inorg. Chem.* **1983**, *22*, 551. (d) Woo, A.; Lee, Y. H.; Hayami, S. Lindoy, L. F.; Thuéry, P; Kim, Y *J. Incl. Phenom. Macrocycl. Chem.* **2011**,

71, 409. (e) Grove, H.; Sletten, J.; Julve, M.; Lloret, F. *J. Chem. Soc., Dalton Trans.* **2001**, 1029. (f) Du, M.; Guo, Y.; Bu, X.; Ribas, J.; Monfort, M. *New. J. Chem.* **2002**, *26*, 939. (g) Seeber, G.; Kariuki, B. M.; Cronin, L.; Kögerler, P. *Polyhedron*, **2005**, 1651. (h) Żurowska, B.; Mroziński, J.; Ciunik, Z. *Polyhedron*, **2007**, 3085. (i) Bauer, R. A.; Robinson, W. R.; Margerum, D. W. *J. Chem. Soc. Dalton Trans.* **1973**, 1227. (j) Aznar, E.; Ferrer, S.; Borrás, J.; Lloret, F.; Liu-González, M.; Rodríguez-Prieto, H.; García-Granda, S. *Eur. J. Inorg. Chem.* **2006**, 5115. (k) Ferlay, S.; Jouaiti, A.; Loï, M.; Hosseini, M. W.; De Cian, A.; Turek, P. *New J. Chem.* **2003**, *27*, 1801. (l) Song, Y.; Massera, C.; Roubeau, O.; Lanfredi, A. M. M.; Reedijk, J. *Polyhedron* **2005**, *24*, 1599.

(5) (a) Landee, C. P.; Greeney, R. E. *Inorg. Chem.* **1986**, *25*, 3771. (b) Wang, P.; Wang, Y.-Y.; Chi, Y.-H.; Wei, W.; Zhang, S.-G.; Cottrill, E.; Shi, Y.-M. *J. Coord. Chem.* **2013**, *66*, 3092.

(6) (a) Crawford, V. H.; Richardson, H. W.; Wasson J. R.; Hodgson D. J.; Hatfield, W. E. *Inorg. Chem.* **1976**, *15*, 2107. (b) Hodgson, D. *J. Inorg. Chem.* **1976**, *15*, 3174.

(7) (a) Towle, D. K.; Hoffmann, S. K; Hatfield, W. E.; Singh, P.; Chaudhuri, P.; Wieghardt, K. *Inorg. Chem.* **1985**, *24*, 4393. (b) Hodgson, D. J. *Prog. Inorg. Chem.* **1975**, *19*, 173. (c) Hatfield, W. E. *A.C.S.,Symp. Ser.* **1974**, *5*, 108.

(8) (a) Reger, D. L.; Foley, E. A.; Smith, M. D. *Inorg. Chem. Comm.* **2010**, *13*, 568. (b) Reger, D. L; Watson, R. P.; Smith, M. D.; Pellechia, P. J. *Organometallics* **2005**, *24*(7), 1544.

(9) Reger, D. L.; Foley, E. A.; Watson, R. P.; Pellechia, P. J.; Smith, M. D., Grandjean, F.; Long, G. J. *Inorg. Chem.* **2009**, *48*, 10658.

(10) Reger, D. L.; Pascui, A. E.; Smith, M. D.; Jezierska, J.; Ozarowski, A. *Inorg. Chem.* **2012**, *51*, 7966.

(11) Reger, D. L.; Pascui, A. E.; Smith, M. D.; Jezierska, J.; Ozarowski, A. *Inorg. Chem.* **2013**.

(12) Hassan, A. K.; Pardi, L. A.; Krzystek, J.; Sienkiewicz, A.; Goy, P.; Rohrer, M.; Brunel, L.-C. *J. Magn. Reson.* **2000**, *142*, 300.

(13) (a) O'Connor, C. J. *Prog. Inorg. Chem.* **1982**, *29*, 203; (b) Bain, G. A.; Berry, J. F. *J. Chem. Ed.* **2008**, *85*, 532.

(14) (a) Barbour, L. J. *J. Supramol. Chem.* **2003**, *1*, 189. (b) *POV-RAY*, 3.6; Persistence of Vision Raytracer Pty Ltd: Williamstown, Victoria, Australia, **2006**. (c) MestReNOVA v.5.2.5; Mestrelab Research S.L.: Santiago de Compostela, Spain, **2008**. (d) Laaksonen, L. gOpenMol version 3.00; CSC - IT Center for Science Ltd.: Espoo, Finland, **2005**; available at www.csc.fi/english/pages/g0penMol.

(15) Wolsey, W. C. *J. Chem. Educ.* **1973**, *50*, A335-A337.

(16) SMART Version 5.630, SAINT+ Version 6.45. Bruker Analytical X-ray Systems, Inc., Madison, Wisconsin, USA, **2003**.

(17) G.M. Sheldrick, SHELXTL Version 6.14, Bruker Analytical X-ray Systems, Inc., Madison, Wisconsin, USA, **2000**.

(18) (a) Reinen, D.; Friebel, C. *Inorg. Chem.* **1984**, *23*, 791. (b) Arriortua, M. I.; Mesa, J. L.; Rojo, T.; Debaerdemaeker, T.; Beltrán-Porter, D.; Stratemeier, H.; Reinen, D. *Inorg. Chem.* **1987**, *27*, 2976. (c) Bersuker, I. B. in "*The Jahn–Teller Effect*" Univ. Press Cambridge, UK, 2006.

(19) Addison, A. W.; Rao, T. N.; Reedijk, J.; Van Rijn, J.; Verschoor, G. C. *J. Chem. Soc. Dalton Trans*. **1984**, 1349. $\tau_5 = \frac{(\beta - \alpha)}{60°}$ Where α and β are the two largest angles measured around the metal centers. Perfect square pyramid: $\tau_5 = 0$; Perfect trigonal bipyramid: $\tau_5 = 1$.

(20) Steed, J. W.; Atwood J. L. in "*Supramolecular Chemistry"*, 2nd Ed., John Wiley & Sons, UK, 2009.

(21) Shannon, R. D. *Acta Crystallogr.* **1976**, *A32*, 751.

(22) Lee, S. C.; Holm, R. H. *Inorg. Chem.* **1993**, *32*, 4745.

(23) Duggan, D. M.; Jungst, R. G.; Mann K. R.; Stucky, G. D.; Hendrickson, D. N. *J. Am. Chem. Soc.* **1974**, *96*, 3443.

(24) (a) Coughlin, P. K.; Lippard, S. J. *J. Am. Chem. Soc.* **1981**, *103*, 3228. (b) Wang, D.; Xiang, H.; Wang, G.; Han, Z.; Yang, X.; Hu, H.; Yu, K. *J. Chem., Soc. Dalton Trans.* **1994**, 3325. (c) Plieger, P. G.; Downard, A. J.; Moubaraki, B.; Murray, K. S.; Brooker, S. *Dalton Trans.* **2004**, 2157. (d) Agnus, Y.; Louis, R.; Weiss, R. *J. Am. Chem. Soc.* **1979**, *101*, 3381.

Chapter V

Syntheses and Structural Studies of Cyanide and Azide Monobridged Dinuclear Copper(II) Complexes

Introduction

Dinuclear copper(II) complexes bridged by a single anion can serve as model compounds for the treatment of superexchange interactions in more complicated systems.[1] The linearly bridged complexes of the type $[Cu_2(\mu\text{-}X)(\mu\text{-}\mathbf{L}_m\mathbf{*})_2](ClO_4)_3$ where X = F^-, Cl^-, OH^-, Br^- and $\mathbf{L}_m\mathbf{*}$ = *m*-bis[bis(3,5-dimethyl-1-pyrazolyl)methyl]benzene, Scheme 5.1, show that this system supports extremely strong antiferromagnetic superexchange interactions, with $-J$ = 340, 720, 808 and 945 cm^{-1}, respectively ($\hat{\mathbf{H}} = -J\,\hat{\mathbf{S}}_1\hat{\mathbf{S}}_2$).[2]

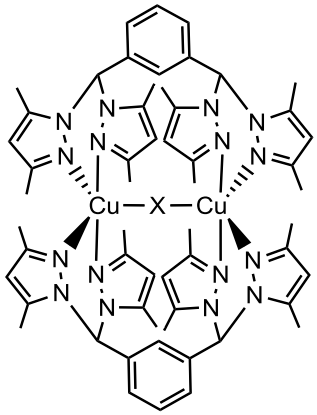

Scheme 5.1. Schematic representation of the metallacycle $[Cu_2(\mu\text{–}X)(\mu\text{–}\mathbf{L}_m\mathbf{*})_2]^{3+}$.

The unusual $[Cu_2(\mu\text{-}X)(\mu\text{-}\mathbf{L}_m\mathbf{*})_2](ClO_4)_3$ system, where the structure is held relatively constant, presents the first example of the syntheses of a series of complexes that consistently promote the linear Cu-X-Cu (180°) bridging arrangement. Even though the theoretical basis for the antiferromagnetic interactions in dinuclear compounds is well developed,[3] the linear Cu-X-Cu arrangement is virtually unstudied prior to our work due to the lack of compounds of this type. In the $[Cu_2(\mu\text{-}X)(\mu\text{-}\mathbf{L}_m\mathbf{*})_2](ClO_4)_3$ series, the magnetic orbitals have predominantly d_z^2 character, as a result of the pseudo Jahn-Teller distorted, axially compressed trigonal bipyramidal geometry around copper(II), where the

Cu-X-Cu axis is defined as the x-axis, and the axial direction as the z-axis. The large –*J* values, increasing from F^- to the Br^- in the halide bridged series, are explained by increasingly stronger interaction between the valence p orbital of the bridging group with the "doughnut" portion of the d_z^2 orbitals in the antibonding antisymmetric combination than the lower lying s orbital in the symmetric combination. Therefore the energy of the antisymmetric orbital rises faster and the singlet state is stabilized. The very large -*J* value for the OH^- bridged complex is a result of the unusually large overlap integral of the magnetic orbitals and the large spin delocalization towards the p orbital in comparison to the fluoride bridged compound.

This chapter focuses on complexes containing more complex bridges, end-on (μ-1,1) N_3^- and end to end CN^- in similar metallacyclic compounds of $\mathbf{L}_m$, *m*-bis[bis(1-pyrazolyl)methyl]benzene, and $\mathbf{L}_m$*****. Even though several dinuclear copper(II) compounds with doubly bridged N_3^- have been reported,[4] the number of compounds with a single end-on (μ-1,1) N_3^- exclusively mediating the superexchange interaction is small,[5] and in these examples the Cu-N-Cu bridging angle is relatively low, ~90-115°. The CN^- bridged dinuclear compounds are even less extensively studied as a result of the reducing character of these anions in the presence of copper(II).[6] The structure of the pentametallic copper(I) I^- bridged compound is also discussed. This compound was isolated in an attempt to synthesize the I^- bridged dinuclear metallacycle – the reducing effect of iodide on copper(II) is well known and only a few successful attempts are documented where species with copper(II)-iodide bond were isolated.[7]

Experimental Section

General Considerations. The syntheses of the compounds were carried out under nitrogen atmosphere using standard Schlenk techniques and a Vacuum Atmospheres HE-493 drybox unless otherwise mentioned. All solvents were dried and purified prior to use following standard techniques. The metal salts were purchased from Sigma-Aldrich or Strem Chemicals and were used as received. The complexes $[Cu_2(\mu\text{-}F)(\mu\text{-}\mathbf{L_m})_2](BF_4)_3$, $[Cu_2(\mu\text{-}F)(\mu\text{-}\mathbf{L_m}\mathbf{*})_2](ClO_4)_3$ and $[Cu_2(\mu\text{-}Cl)(\mu\text{-}\mathbf{L_m}\mathbf{*})_2](ClO_4)_3$ were prepared according to reported procedures.[8]

Crystals used for elemental analysis and mass spectrometry were removed from the mother liquor, rinsed with ether, and dried under vacuum. Elemental analyses were performed on samples dried to constant weight by Robertson Microlit Laboratories (Ledgewood, NJ). Mass spectrometric measurements were obtained on a MicroMass QTOF spectrometer in an acid-free environment.

Caution: Although no problems were encountered with perchlorate salts during this work, these compounds should be considered potentially explosive!

High-field, high-frequency EPR spectra at temperatures ranging from ca. 6K to 290 K were recorded on a home-built spectrometer at the EMR facility of the NHMFL.[9] The instrument is a transmission-type device. The microwaves were generated by a phase-locked Virginia Diodes source generating frequency of 13 ± 1 GHz. A superconducting magnet capable of reaching a field of 17 T was employed. The powder samples were not constrained and showed no magnetic torqueing at high magnetic fields.

Magnetic susceptibility measurements over the temperature range 1.8-300 K were performed at a magnetic field of 0.5 T using a Quantum Design SQUID MPMSXL-5

magnetometer. Correction for the sample holder, as well as the diamagnetic correction χ_D, which was estimated from the Pascal constants,[10] was applied.

$[Cu_2(\mu\text{-}CN)(\mu\text{-}L_m)_2](ClO_4)_3$, 1. The copper salt, $Cu(ClO_4)_2 \cdot 6H_2O$ (0.186 g, 0.503 mmol) and NaCN (0.016 g, 0.25 mmol) were dissolved in MeOH (6 mL). The ligand, $\mathbf{L}_m$ (0.186 g, 0.503 mmol), dissolved in MeOH (8 mL), was transferred by cannula into the copper(II) salt solution. A deep blue precipitate formed immediately. The reaction mixture was stirred for 6 h, after which time the system was filtered by cannula, washed with 5 mL ether and dried in vacuum overnight, affording 0.273 g (75%) of the crude product. Single crystals suitable for X-ray and other studies were grown by vapor diffusion of Et_2O into concentrated 1 mL acetonitrile solutions of **1** and were isolated as $\mathbf{1} \cdot 3CH_3CN$. Anal. Calcd (Found) for $C_{41}H_{36}Cl_3Cu_2N_{17}O_{12}$: C, 41.30 (41.08); H, 3.04 (2.87); N, 19.97 (19.67). MS ESI(+) *m*/*z* (rel. % abund.) [assgn]: 1092 (2) $[Cu_2(\mathbf{L}_m)_2(CN)(ClO_4)_2]^+$, 497 (10) $[Cu_2(\mathbf{L}_m)_2(CN)(ClO_4)]^{2+}$, 433 (100) $[Cu(\mathbf{L}_m)]^+$, 371 (18) $[\mathbf{L}_m + H]^+$, 298 (60) $[Cu_2(\mathbf{L}_m)_2(CN)]^{3+}$.

$[Cu_2(\mu\text{-}N_3)(\mu\text{-}L_m)_2](BF_4)_3$, 2. In the drybox, $[Cu_2(\mu\text{-}F)(\mu\text{-}\mathbf{L}_m)_2](BF_4)_3$ (0.150 g, 0.131 mmol) was dissolved in CH_3CN (5 mL). Upon addition of 0.02 mL (0.018 g, 0.15 mmol) of $(CH_3)_3SiN_3$ the blue solution turned green. Vapor diffusion of Et_2O into the green solution, further diluted with a small amount of CH_3CN, resulted in crystals 0.080 g (52%) of $\mathbf{2} \cdot 2.25CH_3CN$. Anal. Calcd (Found) for $C_{40}H_{36}B_3Cu_2N_{19}F_{12}$: C, 41.05 (41.22); H, 3.10 (2.85); N, 22.74 (22.51). MS ESI(+) *m*/*z* (rel. % abund.) [assgn]: 1082 (2) $[Cu_2(\mathbf{L}_m)_2(N_3)(BF_4)_2]^+$, 498 (2) $[Cu_2(\mathbf{L}_m)_2(N_3)(BF_4)]^{2+}$, 433 (100) $[Cu(\mathbf{L}_m)]^+$, 371 (40) $[\mathbf{L}_m + H]^+$, 303 (50) $[Cu_2(\mathbf{L}_m)_2(N_3)]^{3+}$.

$[Cu_2(\mu\text{-}CN)(\mu\text{-}L_m^*)_2](ClO_4)_3$, 3. Compound **3** was synthesized similarly to compound **1** starting from $Cu(ClO_4)_2 \cdot 6H_2O$ (0.190 g, 0.514 mmol), NaCN (0.017 g, 0.26 mmol) and $\mathbf{L}_m^*$ (0.248 g, 0.514 mmol). The solution went through a series of color changes followed by the formation of a blueish green precipitate, 0.273 g (75%). Single crystals were grown by vapor diffusion of Et_2O into concentrated 1 mL acetonitrile solutions of **3** and were isolated as **3**·$2CH_3CN$. Anal. Calcd (Found) for $C_{57}H_{68}Cl_3Cu_2N_{17}O_{12}$: C, 48.32 (47.97); H, 4.84 (4.58); N, 16.81 (16.59). MS ESI(+) *m*/*z* (rel. % abund.) [assgn]: 1316 (8) $[Cu_2(\mathbf{L}_m^*)_2(CN)(ClO_4)_2]^+$, 609 (20) $[Cu_2(\mathbf{L}_m^*)_2(CN)(ClO_4)]^{2+}$, 545 (100) $[Cu(\mathbf{L}_m^*)]^+$, 483 (55) $[\mathbf{L}_m^*+H]^+$, 373 (95) $[Cu_2(\mathbf{L}_m^*)_2(CN)]^{3+}$.

$[Cu_2(\mu\text{-}L_m^*)(\mu\text{-}N_3)_2(N_3)_2]$, 4. The complex $[Cu_2(\mu\text{-}Cl)(\mu\text{-}\mathbf{L}_m^*)_2](ClO_4)_3$ (0.020 g, 0.014 mmol) was dissolved in CH_3CN (2 mL). To this solution, NaN_3 (0.005 g, 0.08 mmol) dissolved in CH_3CN (1 mL) and MeOH (1 mL) was added dropwise. The solution immediately turned dark green. Single crystals suitable for X-ray and the other studies were grown by vapor diffusion of Et_2O into this dark green solution and resulted in 0.009 g (83%) crystals of **4**. Anal. Calcd.(Found) for $C_{28}H_{34}Cu_2N_{20}$: C, 43.24 (41.88); H, 4.41 (4.06); N, 36.02 (36.51).

$[Cu_5(\mu\text{-}I_4)(\mu\text{-}L_m^*)_2](I_3)$, 5. In the drybox, $[Cu_2(\mu\text{-}F)(\mu\text{-}\mathbf{L}_m^*)_2](ClO_4)_3$ (0.150 g, 0.106 mmol) was dissolved in 5 mL CH_3CN. Upon addition of three drops of $(CH_3)_3SiI$, the green solution turned brown. Vapor diffusion of Et_2O into the brown solution resulted in single crystals 0.030 g (31%) of **5**. Anal. Calcd.(Found) for $C_{56}H_{68}Cu_5N_{16}I_7$: C, 30.98 (31.41); H, 3.16 (2.78); N, 10.32 (10.21). MS ESI(+) *m*/*z* (rel. % abund.) [assgn]: 2045

(1) $[Cu_5(\mathbf{L}_m^*)_2(I_6)]^+$, 1027 (2) $[Cu(\mathbf{L}_m^*)_2]^+$, 959 (1) $[Cu_5(\mathbf{L}_m\mathbf{*})_2(I_5)]^{2+}$, 737 (100) $[Cu_4(\mathbf{L}_m^*)_2(I_2)]^{2+}$, 596 (1) $[Cu_5(\mathbf{L}_m^*)_2(I_4)]^{3+}$, 545 (92) $[Cu(\mathbf{L}_m\mathbf{*})]^+$, 483 (20) $[\mathbf{L}_m\mathbf{*}+H]^+$.

Crystallographic studies. X-ray diffraction intensity data for compounds **1-4** were measured on a Bruker SMART APEX CCD-based diffractometer (Mo Kα radiation, λ = 0.71073 Å).[11] The raw area detector data frame processing was performed with the SAINT+ and SADABS programs.[12] Final unit cell parameters were determined by least-squares refinement of large sets of strong reflections taken from each data set. Direct methods structure solution, difference Fourier calculations and full-matrix least-squares refinement against F^2 were performed with SHELXS/L^2 as implemented in OLEX2.[13] Non-hydrogen atoms were refined with anisotropic displacement parameters, the exception being disordered species. The hydrogen atoms were placed in geometrically idealized positions and included as riding atoms. Details of the data collection are given in Table 5.1.

Table 5.1. Selected Crystal Data and Structure Refinement for **1**·3CH_3CN, **2**·2.25CH_3CN, **3**·2CH_3CN, **4** and **5**.

	1·3CH_3CN	**2**·2.25CH_3CN	**3**·2CH_3CN	**4**	**5**
Formula	$C_{47}H_{45}Cl_3$ $Cu_2N_{20}O_{12}$	$C_{44.50}$ $H_{42.75}$ B_3 Cu_2 F_{12} $N_{21.25}$	C_{61} H_{74} Cl_3 Cu_2 N_{19} O_{12}	C_{28} H_{34} Cu_2 N_{20}	C_{56} H_{68} Cu_5 I_7 N_{16}
Fw, g mol^{-1}	1315.46	1262.79	1498.82	777.83	2171.66
Cryst. Syst.	Triclinic	Monoclinic	Monoclinic	Monoclinic	Monoclinic
Space group	*P*-1	$P2_1$	*C*2/c	*C*2/c	*C*2/m
T, K	100(2)	100(2)	100(2)	100(2)	100(2)
a, Å	10.0369(18)	12.8682(18)	23.910(7)	23.0409(12)	19.632(2)
b, Å	13.096(2)	13.9995(19)	12.374(4)	8.7757(5)	21.904(3)
c, Å	22.234(4)	15.841(2)	23.705(7)	19.4868(10)	8.5445(10)
α, deg	94.415(4)	90	90	90	90
β, deg	93.120(5)	111.853(3)	103.733(6)	118.2850(10)	96.768(2)
γ, deg	109.393(4)	90	90	90	90
V, $Å^3$	2738.5(9)	2648.7(6)	6813(4)	3469.8(3)	3648.8(7)
Z	2	2	4	4	2
R1(I >2σ (I))	0.0497	0.0550	0.0376	0.0366	0.0427
wR2(I >2σ (I))	0.0773	0.1326	0.0944	0.0901	0.1065

For compound **1**·3CH_3CN the asymmetric unit consists of half of two independent $[Cu_2(\mu\text{-}CN)(\mu\text{-}\mathbf{L}_{\boldsymbol{m}})_2]^{3+}$ cations, three independent perchlorate anions and three independent acetonitrile molecules. The two independent cations are located on crystallographic inversion centers, imposing disorder on the bridging CN^- groups. For refinement, a single atomic position with a 50/50 population of carbon and nitrogen was used for each cation. With this model, the C2/N2 anisotropic displacement parameters are slightly elongated, suggesting a disorder somewhat beyond a single scrambled C/N position. However this disorder was too small to be modeled well crystallographically. One perchlorate anion (Cl3) is disordered and was modeled with two components. The major disorder fraction is Cl3A = 0.909(6). The geometry of the minor component was restrained to be similar to the major (SHELX SADI instruction). The largest residual electron density peak of 0.59 $e^-/Å^3$ in the final difference map is located 0.08 Å from Cu2.

For compound **2**·2.25CH_3CN the space groups $P2_1$ and $P2_1/m$ were consistent with the pattern of systematic absences in the intensity data. $P2_1$ was established as the correct space group as by structure solution. The ADDSYM program in PLATON found no missed symmetry elements.[14] The asymmetric unit consists of one $[Cu_2(\mu\text{-}N_3)(\mu\text{-}\mathbf{L}_{\boldsymbol{m}})_2]^{3+}$ cation, three tetrafluoroborate anions and a region of disordered acetonitrile solvent molecules. Each BF_4^- anion is disordered over two closely separated positions with occupancies B1A/B1B = 0.79(1)/0.21(1), B2A/B2B = 0.65(1)/0.35(1), B3A/B3B = 0.71(1)/0.29(1). Total site occupancy was constrained to sum to unity. B-F and F-F distance restraints were applied to maintain chemically reasonable geometries for each component. The acetonitrile disorder was modeled with four molecules of variable

occupancy: N1S = 0.88(1), N2S = N4S = 0.5 and N3S = 0.38(1). Occupancies of acetonitrile molecules N2S and N4S were fixed to avoid physically nonsensical values, and C-N and C-C distance restraints were applied. The largest residual electron density peak of 0.62 $e^-/Å^3$ in the final difference map is located 1.0 Å from Cu1. The final absolute structure (Flack) parameter refined to 0.004(14).

For compound **3**·2CH_3CN the asymmetric unit consists of half of one $[Cu_2(\mu\text{-}CN)(\mu\text{-}\mathbf{L}_m\mathbf{*})_2]^{3+}$ cation located on an inversion center, 1.5 perchlorate anions and one acetonitrile molecule. The bridging cyano group is disordered and was modeled with one atomic position consisting of 50% carbon and 50% nitrogen. Perchlorate anion Cl2/O21-O24 is disordered about a C_2 axis of rotation and therefore only half of this anion is present per asymmetric unit. This perchlorate is further disordered over two independent positions within the asymmetric unit. The occupancies of the disordered groups are A/B = 0.057(2) / 0.443(2), which were constrained to sum to 0.5. Geometries of the two independent disordered groups were restrained to be similar to that of the ordered perchlorate Cl1/O11-O14 with SHELX SAME instructions (30 restraints).

The asymmetric unit of compound **4** consists of one copper atom, half of one ligand which is located on a two-fold axis of rotation, and two azide ions. The two-fold axis passes through phenyl ring atoms C4 and C5 of the $\mathbf{L_m}$***** ligand.

For **5** there is disorder of both the cation and the two independent anion sites in the crystal; trial solutions in the space groups *C*2 and *C*m also resulted in the same disorder discussed below. The asymmetric unit in *C*2/m consists of ¼ of one $[Cu_5(\mu\text{-}I_4)(\mu\text{-}\mathbf{L}_m\mathbf{*})_2]^+$ cation, which has crystallographic C_{2h} point symmetry, and two regions of triiodide anions. The cation consists of two independent copper(I) sites, two bridging iodide atoms

and half of one $\mathbf{L}_m$* ligand. Atoms I1, C4 and C5 sit on a mirror plane; atoms Cu2 and I2 reside on the C_2 axis perpendicular to the mirror. Atom Cu2 is disordered across the nearby mirror plane and was refined with half-occupancy. Refining Cu2 with full occupancy results in a very short Cu2-Cu2' distance of ca. 2.1 Å and an unacceptably large displacement parameter. Triiodide anion I4/I5 consists of two independent iodine atoms and also has C_{2h} point symmetry. I4 is located on the C_{2h} site, and I5 is disordered about the C_2 axis over two positions. The displacement parameters of atoms I4 and I5 became unreasonably large when refined with full occupancy. Allowing their site occupancies to refine decreased the *R*1 value by ca. 2% and gave acceptable displacement parameters. The final population of the I4/I5 anion is 84%. The deficit of negative charge caused by the partial occupancy of I4/I5 is compensated by the second independent anion region, which is severely disordered about a crystallographic site with C_{2h} point symmetry. No chemically recognizable species could be found. Instead, an essentially continuous linear distribution of electron density extending along the *y*-axis from $y = 0.3$ to $y = 0.7$ was observed. This was interpreted as disordered I_3^- species. For refinement, six electron density peaks found in this region were assigned as iodine atoms I5-I10, and their occupancy values was allowed to vary freely. These atoms were all assigned a fixed displacement parameter of 0.07 $Å^2$, which was chosen because it gave a final composition of three iodine atoms per $[Cu_5(\mu\text{-}I_4)(\mu\text{-}\mathbf{L}_m\mathbf{*})_2]^+$ unit, *i.e.* an electro-neutral crystal. The chemical occupancies of the individual iodine atom peaks are low, *ca.* 3%. It is likely that when these atoms are not present in a given asymmetric unit, a linear guest molecule such as the crystallization solvent acetonitrile is present, but this could not be identified because of the disorder.

Results

Synthesis. The reactions of $Cu(ClO_4)_2$ with NaCN and the ligands $\mathbf{L}_m$ or $\mathbf{L}_m$***** result in the cyanide bridged metallacycles **1** and **3** respectively. Compound **2** was synthesized starting from the previously reported F^- bridged metallacycle of the ligand $\mathbf{L}_m$.[8] The bridging F^- is exchanged with the N_3^- in the presence of $(CH_3)_3SiN_3$. The driving force of this reaction is the formation of strong Si-F bonds. The reaction of the building blocks of the metallacycle: $Cu(ClO_4)_2 \cdot 6H_2O$, NaN_3 and $\mathbf{L}_m$ results in both the azide bridged compound, $[Cu_2(\mu\text{-}N_3)(\mu\text{-}\mathbf{L}_m)_2](ClO_4)_3$ and the analogous hydroxide bridged compound.The reactions are shown in Scheme 5.2.

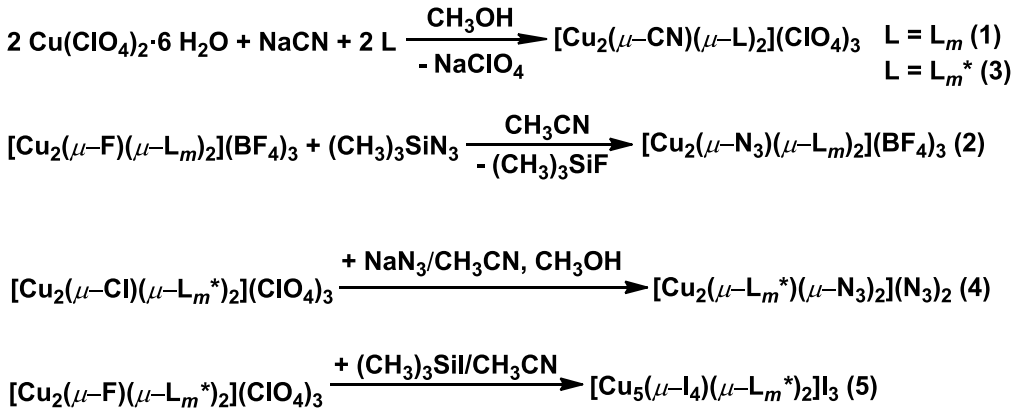

Scheme 5.2. Synthesis of compounds **1**-**5**.

Upon the reaction of $[Cu_2(\mu\text{-}Cl)(\mu\text{-}\mathbf{L}_m\mathbf{*})_2](ClO_4)_3$ with a large excess of the polymeric structure $[Cu_2(\mu\text{-}\mathbf{L}_m\mathbf{*})(\mu\text{-}N_3)_2(N_3)_2]$ (**4**) was isolated; stoichiometric azide did not yield the desired $[Cu_2(\mu\text{-}N_3)(\mu\text{-}\mathbf{L}_m\mathbf{*})_2](ClO_4)_3$ complex.

Attempts to synthesize the I^- bridged dinuclear copper(II) metallacycle failed, instead a pentametallic species, $[Cu_5(\mu\text{-}I_4)(\mu\text{-}\mathbf{L}_m\mathbf{*})_2]I_3$ (**5**) was isolated upon the reaction of the fluoride bridged metallacycle with $(CH_3)_3SiI$. The copper(II) centers of the starting material were reduced to copper(I) during this reaction.

Solid State Structures. Figure 5.1 shows the two independent cationic units in the crystal structure of $[Cu_2(\mu\text{-}CN)(\mu\text{-}\mathbf{L}_m)_2](ClO_4)_3\cdot 3CH_3CN$, **1**·3$CH_3CN$. Similarly, Figure 5.2 shows the structure for the cationic units of $[Cu_2(\mu\text{-}N_3)(\mu\text{-}\mathbf{L}_m)_2](BF_4)_3\cdot 2.25CH_3CN$, **2**·2.25$CH_3CN$ and $[Cu_2(\mu\text{-}CN)(\mu\text{-}\mathbf{L}_m\mathbf{*})_2](ClO_4)_3\cdot 2CH_3CN$, **3**·2$CH_3CN$, respectively. Selected structural parameters are shown in Table 5.2.

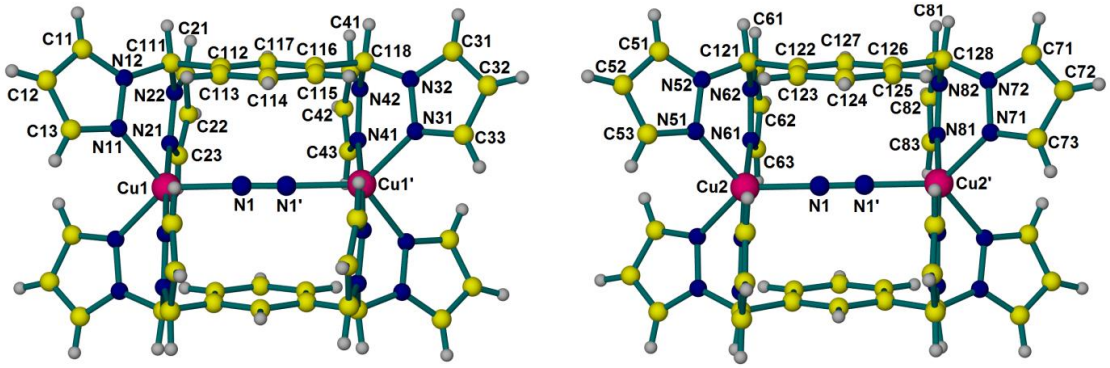

Figure 5.1. The structure of the two independent cationic units of $[Cu_2(\mu\text{-}CN)(\mu\text{-}\mathbf{L}_m)_2](ClO_4)_3\cdot 3CH_3CN$ (**1**·3CH_3CN). The atoms in the disordered CN^- bridge were modeled as 50% carbon and 50% nitrogen.

The single end-on bridging cyano group of **1**·3CH_3CN and **3**·2CH_3CN are disordered about the inversion center, effectively scrambling the carbon and nitrogen atoms. This group was modeled with one atomic position consisting of 50% carbon and 50% nitrogen; on Figure 5.1 and 5.2b it is labeled N1. The Cu-N(C)-N(C)-Cu' torsion angle is 180.0° in both compounds. The two atoms labeled N1 are slightly displaced with respect to the Cu-Cu axis, one being slightly in front, and the other being at the back of the Cu-Cu axis, the Cu-N(C)-N(C) angles are 176.9° and 173.9° for **1**·3CH_3CN and 173.0° for **3**·2CH_3CN. The geometry around copper(II) is an intermediate between trigonal bipyramidal and square pyramidal geometries in both **1**·3CH_3CN and **3**·2CH_3CN. The geometry is more disstorted towards a square pyramid in **3**·2CH_3CN, the τ_5 values[15] are 0.76/0.79 for **1**·3CH_3CN and 0.61 for **3**·2CH_3CN.

For **1**·3CH_3CN, the axial positions are occupied by N21, N41 (N21-Cu1-N41 177.70°) for one of the two independent cations in the unit cell and N61, N81 (N61-Cu2-N81 177.29°) for the second cation. The atoms N1, N11, N31, and N2, N51, N71 reside in the equatorial plane, with angles in the 104.18-132.00° range. The pyrazolyl Cu-N bond lengths show a slightly compressed trigonal bipyramidal geometry, axial Cu-N bonds are between 1.98 and 2.01 Å, equatorial Cu-N bond lengths are between 2.06 and 2.09 Å.

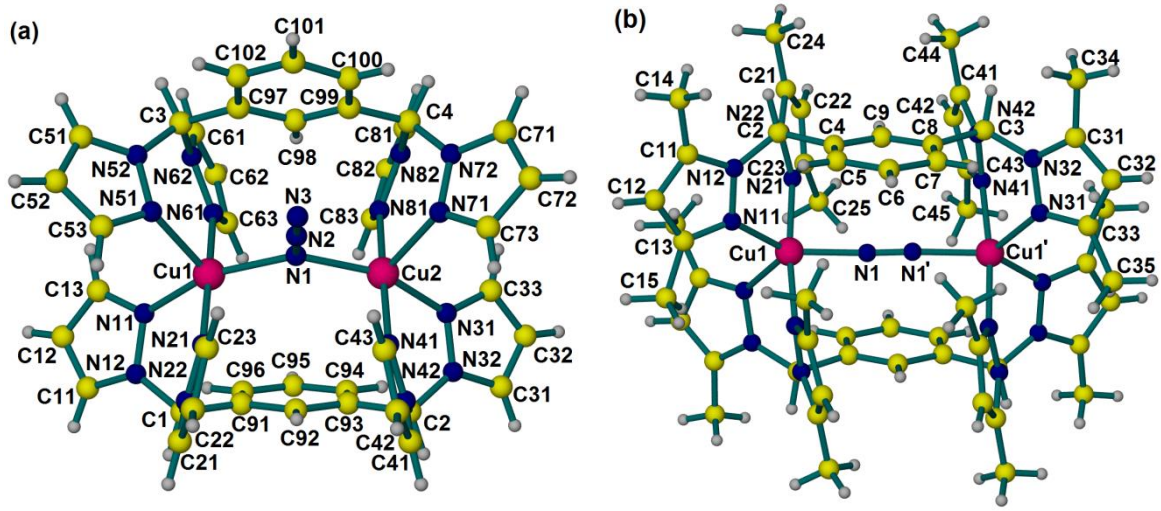

Figure 2. The structure of the cationic unit of (a) $[Cu_2(\mu\text{-}N_3)(\mu\text{-}\mathbf{L}_m)_2](BF_4)_3\cdot 2.25CH_3CN$ (**2**·2.25CH_3CN) (b) $[Cu_2(\mu\text{-}CN)(\mu\text{-}\mathbf{L}_m\mathbf{*})_2](ClO_4)_3\cdot 2CH_3CN$ (**3**·2CH_3CN).

For **3**·2CH_3CN the axial positions are occupied by N21, N41 (N21-Cu1-N41 173.56°), while N1, N11, N31 reside in the equatorial plane, these angles being 103.59°, 119.29° and 137.11° approximating a trigonal bipyramid. Conversely, by analyzing the Cu-N bond lengths the geometry resembles more a distorted square pyramidal geometry, with axial N31 (Cu1-N31 2.1297 Å) and equatorial N1, N11, N21 and N41, these latter

Table 5.2. Important Structural Parameters for $[Cu_2(\mu\text{-}CN)(\mu\text{-}\mathbf{L}_m)_2](ClO_4)_3\cdot 3CH_3CN$ (**1**·3CH_3CN) $[Cu_2(\mu\text{-}N_3)(\mu\text{-}\mathbf{L}_m)_2](BF_4)_3\cdot 2.25CH_3CN$ (**2**·2.25CH_3CN), $[Cu_2(\mu\text{-}CN)(\mu\text{-}\mathbf{L}_m\mathbf{*})_2](ClO_4)_3\cdot 2CH_3CN$ (**3**·2CH_3CN) and $[Cu_2(\mu\text{-}\mathbf{L}_m\mathbf{*})(\mu\text{-}N_3)_2(N_3)_2]$ (**4**).

	1·3CH_3CN	**2**·2.25CH_3CN	**3**·2CH_3CN	**4**
Temp, K	100(2)	100(2)	100(2)	100(2)
Metal centers	Cu(1)-Cu(2)	Cu(1)-Cu(2)	Cu(1)-Cu(1)'	Cu(1)-Cu(1)'
Bridging Cu-N-Cu or Cu-N(C)-N(C), deg	176.92/173.90	138.0(2)	173.0(3)	113.31(1)/122.1(1)
Cu-N1 or Cu-N33, Å	1.946(4)/ 1.926(4)	2.054(4)/ 2.059(4)	1.948(2)	2.3825(19)
Cu-N11/ Cu-N51, Å	2.092(4)/2.090(4)	2.017(5)/ 2.195(5)	2.0368(17)	2.0393(17)
Cu-N21/ Cu-N61, Å	1.997(4)/1.995(4)	2.005(4)/ 1.988(5)	2.0355(16)	2.0169(18)
Cu-N31/ Cu-N71, Å	2.055(4)/2.056(4)	2.036(5)/ 2.176(5)	2.1297(17)	1.9799(18)
Cu-N41/ Cu-N81, Å	1.981(4)/2.006(4)	2.004(5)/ 2.007(5)	2.0365(17)	1.974(2)
τ_5	0.76/0.79	0.30/0.26	0.61	0.11
Cu···Cu, Å	5.049/5.009	3.084	5.024	4.881

four bond lengths being 0.1 Å shorter than Cu1-N31 (Table 5.2), as expected for pseudo Jahn-Teller distorted square pyramidal geometries.[16]

The single bridging azide in **2**·2.25CH_3CN adopts end-on coordination mode, by bridging the two copper(II), Cu1-N1-Cu2 being 138.0° and the Cu1-Cu2 non-bonding distance 3.084 Å. The nitrogen donor atoms around the metal centers are in pseudo Jahn-Teller distorted square pyramidal geometry, with axial Cu1-N51 2.195 Å, and Cu2-N71 2.176 Å. The equatorial Cu-N bond lengths vary between 1.988 and 2.059 Å, the longest being those involving the azide, N1.

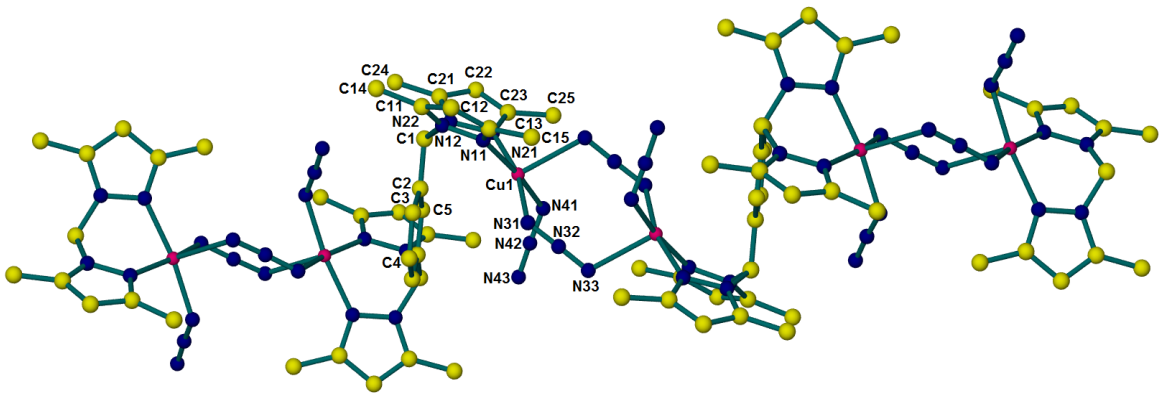

Figure 5.3. The polymeric structure of [Cu_2(μ-**L**$_m$*****)(μ-N_3)$_2$(N_3)$_2$] (**4**). Hydrogen atoms are omitted for clarity.

Figure 5.3 and Table 5.2 contains information related to the structure of [Cu_2(μ-**L**$_m$*****)(μ-N_3)$_2$(N_3)$_2$] (**4**). The copper(II) centers are still five coordinate, by coordination of two ligand nitrogens and three azide nitrogens. The geometry is square pyramidal, τ_5 = 0.11. The azide N31-N32-N33 is end-to-end coordinated and N33 becomes the axial ligand, Cu1-N33 being 2.383 Å. The equatorial positions are occupied by N11, N21, N31 and N41, the average of these bonds is 2.00 Å. The Cu-N bonds involving the ligand are slightly shorter then the azide Cu-N bonds by approximately 0.04 Å. The ligand **L**$_m$***** adopts *anti* conformation, with two bis(pyrazolyl)methane units being on the opposite

side of the phenylene spacer. The infinite parallel polymeric chains, formed by $\mathbf{L}_{m}$* and two end-to-end azides alternatively bridging two copper(II) centers, run along the crystallographic [101] direction.

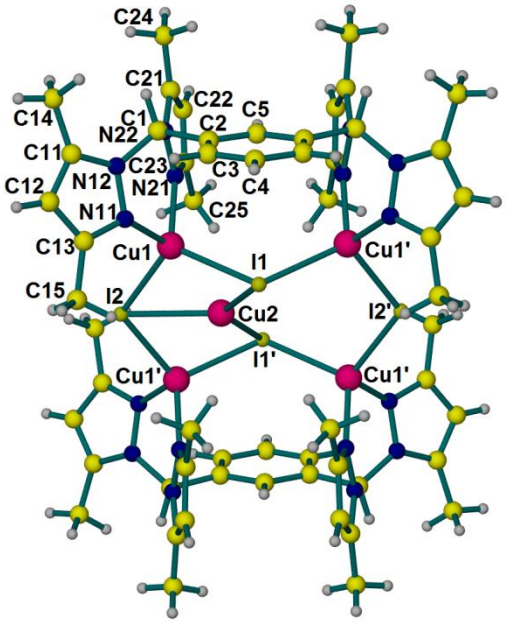

Figure 5.4. The structure of the cationic unit of $[Cu_5(\mu\text{-}I_4)(\mu\text{-}\mathbf{L}_{m}\text{*})_2]I_3$ (**3**); Cu2, is disordered across the mirror plane and is refined with half-occupancy (only one of the two Cu2 sites is shown).

Figure 5.4 presents the structure of $[Cu_5(\mu\text{-}I_4)(\mu\text{-}\mathbf{L}_{m}\text{*})_2]I_3$ (**5**) and Table 5.3 contains selected structural parameters for this compound. The asymmetric unit contains ¼ of one cation, therefore all four identical Cu1 centers are in distorted tetrahedral coordination environment where the N11-Cu1-N21 angle is 93.78°, the I1-Cu1-I2 angle is 110.76° and the N-Cu1-I angles vary between 110.02° and 116.31°. Two pairs of Cu1 centers are bridged by the ligand $\mathbf{L}_{m}$* and I1, with Cu1-I1-Cu1 bridging angle 120.34°. The two pairs of Cu1 centers are connected via I2 bridges with a Cu1-I2-Cu1 angle of 116.21°. The Cu2 cation resides in this cavity formed by the four Cu1 ions alternating with two I1 and two I2 ions. The Cu2 cation is disordered across a mirror plane and is refined with

half-occupancy. The geometry around Cu2 is more unusual, trigonal planar with I1-Cu2-I1 131.11° and I1-Cu2-I2 114.45° and torsion angle I1-Cu2-I2-I1 180.0°.

Table 5.3. Selected Structural Parameters for $[Cu_5(\mu\text{-}I_4)(\mu\text{-}\mathbf{L}_m\mathbf{*})_2]I_3$ (**4**).

Temp, K	100(2)
Cu1-I1-Cu1	120.34
Cu1-I2-Cu1	116.21
Cu1-I1-Cu2	59.35
Cu1-I2-Cu2	58.11
I1-Cu1-I2	110.76(3)
I1-Cu1-N11	110.76(14)
I1-Cu1-N21	116.31(13)
I2-Cu1-N11	110.02(14)
I2-Cu1-N21	113.95(14)
N11-Cu1-N21	93.78(18)
I1-Cu2-I1	131.11(7)
I1-Cu2-I2	114.45(4)
Cu1-I1, Å	2.6411(7)
Cu1-I2, Å	2.6305(8)
Cu2-I1, Å	2.5219(9)
Cu2-I2, Å	2.6374(19)
Cu-N11, Å	2.047(5)
Cu-N21, Å	2.041(4)
Cu1···Cu1', Å	2.5581(11)
Cu1···Cu2, Å	2.5581(11)

Discussion

The family of monoatomic bridged $[Cu_2(\mu\text{-}X)(\mu\text{-}\mathbf{L})_2]^{3+}$ compounds, where X = F^-, Cl^-, Br^-, OH^- and **L** = $\mathbf{L}_m$ or $\mathbf{L}_m$***** was successfully expanded by synthesizing $[Cu_2(\mu\text{-}CN)(\mu\text{-}\mathbf{L})_2](ClO_4)_3\cdot x CH_3CN$ (**1**·3CH_3CN, **3**·2CH_3CN) and $[Cu_2(\mu\text{-}N_3)(\mu\text{-}\mathbf{L}_m)_2](BF_4)_3\cdot 2.25CH_3CN$ (**2**·2.25CH_3CN). There are a number of important differences between the structures of these compounds and the previously reported metallacycles.[2,8,17]

Although our earlier chemistry with non-bridged $[Ag_2(\mu\text{-}\mathbf{L}_m)_2]^{2+}$ complexes had indicated the Ag···Ag nonbonding distance is flexible over the range 4.83-5.31 Å,[18] the

CN^- bridged complexes **1**·3CH_3CN and **3**·2CH_3CN have the largest Cu1···Cu1' non-bonding distances, 5.02 - 5.05 Å, of all the $[Cu_2(\mu\text{-}X)(\mu\text{-}\mathbf{L})_2]^{3+}$ type compounds. Complex **2**·2.25CH_3CN, with end-on coordination of the bridging azide, is the first with nuclei attached to the bridging group other than a hydrogen. To accomodate this orientation of the bridging azide, the angle between the two mean planes of the phenylene spacers is 33.37°, while analogous angles for $[Cu_2(\mu\text{-}F)(\mu\text{-}\mathbf{L}_m)_2]^{3+}$ vary between 0° and 2.32°.[8b] This difference is clearly shown in the space filling models in Figure 5.5 a and b. In addition, this change in geometry leads to the the smallest Cu1-N1-Cu2 bridging angle, 138.0°, found for all of the metallacycles of the type $[Cu_2(\mu\text{-}X)(\mu\text{-}\mathbf{L})_2]^{3+}$.[2,8,17] In the case of $[Cu_2(\mu\text{-}OH)(\mu\text{-}\mathbf{L}_m)_2](ClO_4)_3\cdot 2H_2O$ the bending of the bridging Cu-X-Cu angle (<180°) changes the geometry about the metals from trigonal bipyramidal toward square pyramidal geometry;[17a] therefore **2**·2.25CH_3CN has square pyramidal geometry. Interestingly, although this Cu1-N1-Cu2 angle is small in comparison to other $[Cu_2(\mu\text{-}X)(\mu\text{-}\mathbf{L})_2]^{3+}$ metallacycles, this angle is still large in comparison to other dinuclear complexes containing a single azide bridge.[5]

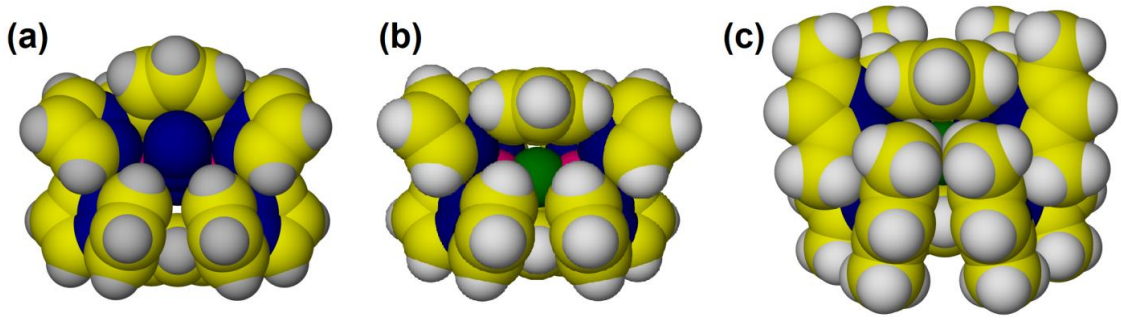

Figure 5.5. Space filling model of the cations (a) $[Cu_2(\mu\text{-}N_3)(\mu\text{-}\mathbf{L}_m)_2]^{3+}$, (b) $[Cu_2(\mu\text{-}F)(\mu\text{-}\mathbf{L}_m)_2]^{3+}$ and (c) $[Cu_2(\mu\text{-}F)(\mu\text{-}\mathbf{L}_m\mathbf{*})_2]^{3+}$.

This unusual tilted orientation of one of the phenylene spacers in **2**·2.25CH_3CN supports the plausibility of the previously reported mechanism proposed for the dynamic behavior of [Zn_2(μ-OH)(μ-$\mathbf{L}_m$)$_2$](ClO_4)$_3$.[17b] This mechanism involves the 180° flip of the phenylene spacers along the $C_{methine}$-$C_{phenylene}$ bonds in a concerted mechanism with the Berry pseudorotation of the pyrazolyl rings at both zinc(II) sites - the two bis(pyrazolyl)methane units coordinated to each zinc(II) rotate in opposite directions, the pivot ligand is the bridging hydroxide group. These combined motions were termed "Carolina twist and flip" mechanism.

In the presence of excess azide the zig-zag polymeric structure [Cu_2(μ-$\mathbf{L}_m$*)(μ-N_3)$_2$(N_3)$_2$] forms, similar to [Cu(μ-$\mathbf{L}_p$)(CH_3OH)](BF_4)$_2$·(CH_3OH)$_{0.62}$,[19] where the bis(pyrazolyl)methane units are also on opposite sides of the phenylene spacer, *anti* comformation. The formation of the polymeric structure is not surprising in the light of the space filling model of the previously reported fluoride bridged metallacycles,[2,8] Figure 5.5 b and c. In the metallacyclic system with $\mathbf{L}_m$, the ligand allows enough space for the end-on coordination of a bridging azide, Figure 5.5a. The $\mathbf{L}_m$* system blocks this position, as a result of the 3,5-methyl substitution of the pyrazolyl rings and it is not flexible enough to accomodate an end-to-end (μ-1,3) bridging azide.

Conclusions

The dinuclear metallacyclic system is flexible enough to accomodate not only one, but two bridging atoms by the preparation of the cyanide bridged compounds [Cu_2(μ-CN)(μ-$\mathbf{L}$)$_2$](ClO_4)$_3$, but not an end-to-end coordinated azide, involving three bridging atoms. The metallacycle with the ligand $\mathbf{L}_m$ provides enough space for the end-on coordination of N_3^-, thus avoiding further strain in the system. As the bulkier ligand, $\mathbf{L}_m$*,

blocks the end-on coordination mode of N_3^- a polymeric structure forms, the metallacycle does not form. The I^- ion reduces copper(II) prohibiting the isolation of an iodide bridged metallacycle.

References

(1) (a) Kahn, O. *Inorg. Chim. Acta* **1982**, *62*, 3. (b) Bleaney, B.; Bowers, K. D. *Proc. Roy. Soc. London, A* **1952**, *214*, 451. (c) Lee, S. C.; Holm, R. H. *Inorg. Chem.* **1993**, *32*, 4745. (d) Koval, I. A.; van der Schilden, K.; Schuitema, A. M.; Gamez, P.; Belle, C.; Pierre, J.; Lüken, M.; Krebs, B.; Roubeau, O.; Reedijk, J. *Inorg. Chem.* **2005**, *44*, 4372 and references therein. (e) Marino, N.; Armentano, D.; De Munno, G.; Cano, J.; Lloret, F.; Julve, M. *Inorg. Chem.* **2012**, *51*, 4323. (f) Kahn, O. *Molecular Magnetism*, 1993 VCH Publishers Inc. New York. (g) Saito, T.; Yasuda, N.; Nishihara, S.; Yamanaka, S.; Kitagawa, Y.; Kawakami, T.; Okumura, M.; Yamaguchi, K. *Chem. Phys. Lett.* **2011**, *505*, 11.

(2) Reger, D. L.; Pascui, A. E.; Smith, M. D.; Jezierska, J.; Ozarowski A. *Inorg. Chem.* **2012**, *51*, 7966.

(3) Hay, J. P.; Thibeault, J. C.; Hoffmann, R. *J. Am. Chem. Soc.* **1975**, *97*, 4884.

(4) (a) Adhikary, C.; Koner, S. *Coord. Chem. Rev.* **2010**, *254*, 2933. (b) Escuer, A.; Aromí, G *Eur. J. Inorg. Chem.* **2006**, 4721. (c) Cabrero, J.; de Graaf, C.; Bordas, E.; Caballol, R.; Malrieu, J.-P. *Chem. Eur. J.* **2003**, *9*, 2307. (d) Banerjee, A.; Singh, R.; Colacio, E.; Rajak, K. K. *Eur. J. Inorg. Chem.* **2009**, 277. (e) Ravikumar, I.; Suresh, E.; Ghosh, P. *Inorg. Chem.* **2006**, *45*, 10046. (f) Amendola, C.; Fabbrizzi, L.; Mangano, C.; Pallavicini, P.; Michele, Z. *Inorg. Chim. Acta* **2002**, *337*, 70. (g) Xie, Y.; Liu, Q.; Jiang, H.; Du, C.; Xu, X.; Yu, M.; Zhu, Y. *New J. Chem.* **2002**, *26*, 176. (h) Benzekri, A.; Dubourdeaux, P.; Latour, J.-M.; Laugier, J.; Rey, P. *Inorg. Chem.* **1988**, *27*, 3710. (i) Chou, J.-L.; Horng, D.-N.; Chyn, J.-P.; Lee, K.-M.; Urbach, F. L.; Lee, G.-H.; Tsai, H.-L. *Inorg. Chem. Comm.* **1999**, 392. (j) Matsumoto, K.; Ooi, S.; Mori, W.; Nakao, Y. *J. Chem. Soc. Dalton Trans.* **1990**, 3117. (k) Benzekri, A.; Dubourdeaux, P.; Latour, J.-M.; Rey, P.; Laugier, J. *J. Chem. Soc. Dalton Trans.* **1991**, 3359. (l) Chattopadhyay, P.; Sabnam Banu, K.; Banerjee, A.; Ribas, J.; Majee, A.; Nethaji, M.; Das, D. *J. Molec. Struc.* **2007**, *833*, 13. (m) Tandon, S. S.; Thompson, L. K.; Manuel, M. E.; Bidson, J. M. *Inorg. Chem.* **1994**, *33*, 5555. (n) Thompson, L. K.; Tandon, S. S.; Manuel, M. E. *Inorg. Chem.* **1995**, *34*, 2356. (o) Murase, I.; Ueda, I.; Marubayashi, N.; Mikuriya, M. *J. Chem. Soc. Dalton Trans.* **1990**, 2763. (p) Plieger, P. G.; Downard, A. J.; Moubaraki, B.; Murray, K. S.; Brooker, S. *Dalton Trans.* **2004**, 2157. (q) McLachlan, G. A.; Fallon, G. D.; Martin, R. L.; Moubaraki, B.; Murray, K. S.; Spiccia, L. *Inorg. Chem.* **1994**, *33*, 4663. (r) Shen, Z.; Zuo, J.-L.; Gao, S.; Song, Y.; Che, C.-M.; Fun, H.-K.; You, X.-Z. *Angew. Chem. Int. Ed.* **2000**, *39*, 3633. (s) Hall, G. R.; Duggan, D. M.; Hendrickson, D. N. *Inorg. Chem.* **1975**, *14*, 1956.

(5) (a) Harding, C. J.; Mabbs, F. E.; MacInnes, E. J. L.; McKee, V.; Nelson, J. *J. Chem. Soc. Dalton Trans.* **1996**, 3227. (b) Naiya, S.; Biswas, C.; Drew, M. G. B.; Gómez-García, C. J.; Clemente-Juan, J. M.; Ghosh, A. *Inorg. Chem.* **2010**, *49*, 6616. (c) Lin, X.– J.; Shen, Z.; Song, Y.; Xu, J.-H.; Li, Y.-Z.; You, X.-Z. *Inorg. Chim. Acta* **2005**, *358*, 1963.

(6) (a) Jungst, R.; Stucky, G. *Inorg. Chem.* **1974**, *13*, 2404. (b) Atanasov, M.; Comba, P.; Hanson, G. R.; Hausberg, S.; Helmle, S.; Wadepohl, H. *Inorg. Chem.* **2011**, *50*, 6890. (c) Bond, A. D.; Derossi, S.; Harding, C. J.; McInnes, E. J. L.; McKee, V.; McKenzie, C. J.;

Nelson, J.; Wolowska, J. *Dalton Trans.* **2005**, 2403. (d) Parker, R. J.; Spiccia, L.; Moubaraki, B.; Murray, K. S.; Skelton, B. W.; White, A. H. *Inorg. Chim. Acta* **2000**, *300-302*, 922. (e) Flay, M.-L.; Vahrenkamp, H. Eur. J. *Inorg. Chem.* **2003**, 1719. (f) Rodríguez-Fortea, A.; Alemany, P.; Alvarez, S.; Ruiz, E.; Scuiller, A.; Decroix, C.; Marvaud, V.; Vaissermann, J.; Verdaguer, M.; Rosenman, I.; Julve, M. *Inorg. Chem.* **2001**, *40*, 5868. (g) Lu, T.; Zhuang, X.; Li, Y.; Chen, S. *J. Am. Chem. Soc.* **2004**, *126*, 4760. (h) Lim, B. S.; Holm, R. H. *Inorg. Chem.* **1998**, *37*, 4898. (i) Scott, M. J.; Lee, S. C.; Holm, R. H. *Inorg. Chem.* **1994**, *33*, 4651. (j) Xu, F.; Huang, W.; You, X.-Z. *Dalton Trans.* **2010**, *39*, 10652. (k) Thaler, F.; Hubbard, C. D.; Heinemann, F. W.; van Eldik, R.; Schindler, S.; Fábián, I.; Dittler-Kingemann, A. M.; Hahn, F. E.; Orvig, C. *Inorg. Chem.* **1998**, *37*, 4022.

(7) (a) Chaudhuri, B.; Winter, M.; Flörke, U.; Haubt, H. J. *Inorg. Chim. Acta* **1995**, *232*, 125. (b) Lobana, T. S.; Khanna, S.; Butcher, R. J. *Dalton Trans.* **2012**, *41*, 4845. (c) Zhou, X.-P.; Li, D.; Zheng, S.-L.; Zhang, X.; Wu, T. *Inorg. Chem.* **2006**, *45*, 7119. (d) Johnson, J. E.; Jacobson, R. A. *J. Chem . Soc. Dalton Trans.* **1973**, 580.

(8) (a) Reger, D. L.; Pascui, A. E.; Smith, M. D.; Jezierska, J.; Ozarowski A. *Inorg. Chem.* **2012**, *51*, 11820. (b) Reger, D. L.; Foley, E. A.; Watson, R. P.; Pellechia, P. J.; Smith, M. D. *Inorg. Chem*. **2009**, *48*, 10658.

(9) Hassan, A. K.; Pardi, L. A.; Krzystek, J.; Sienkiewicz, A.; Goy, P.; Rohrer, M.; Brunel, L.-C. *J. Magn. Reson.* **2000**, *142*, 300.

(10) (a) O'Connor, C. J. *Prog. Inorg. Chem*. **1982**, *29*, 203. (b) Bain, G. A.; Berry, J. F. *J. Chem. Ed.* **2008**, *85*, 532.

(11) SMART Version 5.631, SAINT+ Version 6.45 and SADABS Version 2.10. Bruker Analytical X-ray Systems, Inc., Madison, Wisconsin, USA, 2**003**.

(12) Sheldrick, G.M. *Acta Cryst*. **2008**, A64, 112.

(13) Dolomanov, O. V.; Bourhis, L. J.; Gildea, R. J.; Howard, J. A. K.; Puschmann, H. OLEX2: a complete structure solution, refinement and analysis program. *J. Appl. Cryst.* **2009**, *42*, 339.

(14) (a) LePage, Y. *J. Appl. Crystallogr.* **1987**, *20*, 264. (b) Spek, A. L. *J. Appl. Crystallogr.*, **1988**, *21*, 578. (c) Spek, A. L. *Acta Crystallogr., Sect A* **1990**, *46*, C34. (d) PLATON, A Multipurpose Crystallographic Tool, Utrecht University, Utrecht, The Netherlands, Spek, A. L. **1998**.

(15) The τ_5 values in Table 1 were calculated according to: $\tau_5 = \frac{(\beta - \alpha)}{60°}$, where α and β are the two largest angles measured around the metal centers. Perfect square pyramid: $\tau_5 = 0$; Perfect trigonal bipyramid: $\tau_5 = 1$. Addison, A. W.; Rao, T. N.; Reedijk, J.; Van Rijn, J.; Verschoor, G. C. *J. Chem. Soc., Dalton Trans*. **1984**, 1349.

(16) (a) Bersuker, I. B. "*The Jahn–Teller Effect*" Univ. Press Cambridge, UK, 2006. (b) Harrison, D.; Kennedy D.; Hathaway, B. *Inorg. Nucl. Chem. Lett*. **1981**, *17*, 87. (c) Kepert, D. L. "*Inorganic Chemistry Concepts*" Springer-Verlag, New York 1982, Vol. *6*, 36.

(17) (a) Reger, D. L.; Pascui, A. E.; Pellechia, P. J.; Smith, M. D. *Inorg. Chem.* **2013**, *52*, 11638.

(18) Reger, D. L.; Watson, R. P.; Smith, P. J. *Inorg. Chem.* **2006**, *45*, 10077.

(19) Reger, D. L.; Pascui, A. E.; Smith, M. D. *Eur. J. Inorg. Chem.* **2012**, *29*, 4593.

Chapter VI

NMR Investigations of Dinuclear, Single-Anion Bridged Copper(II) Metallacycles: Structure and Antiferromagnetic Behavior in Solution[5]

[5]Adapted with permission from Reger, D. L.; Pascui, A. E.; Smith, M. D.; Jezierska, J.; Ozarowski, A. *Inorg. Chem.* **2013**, *52*, 12741-12748. DOI: 10.1021/ic402016m.

Introduction

The study of dinuclear copper(II) complexes formed from ligands containing nitrogen donor atoms[1] as models for type-3 active sites of copper enzymes[2] (e.g. tyrosinase, oxyhemocyanin, laccases, ascorbate oxidase, ceruloplasmin) is extensive. In these systems, histidine residues are coordinated to the copper(II) centers with at least one small bridging group directly connecting the metal centers and mediating strong antiferromagnetic superexchange interactions between the two S = ½ metal centers. In addition to the solid state structural and magnetic information, the characterization of these models in solution is important because of possible applications as biomimetic catalysts[4] and/or molecular magnets.[5]

Paramagnetic copper(II) complexes usually have long electronic relaxation times and give broad NMR signals, thus impeding characterization in solution.[6] In contrast, dinuclear, antiferromagnetically coupled copper(II) complexes give relatively narrow NMR signals, however there are only a limited number of examples in the literature that demonstrate the use of this method as a means of characterization in solution.[7,8] In these studies, the small bridging ligand responsible for the antiferromagnetic coupling of the copper(II) centers is usually an OH^- group. Currently there are no solution studies of an extensive series of dinuclear copper(II) compounds where the structure is held relatively constant while the small bridging anions are varied. Very few examples of these types of copper(II) complexes have been characterized by 2D NMR techniques (^1H-^1H COSY)[8] and apparently there are no examples of ^{13}C NMR and ^1H-^{13}C correlation studies.

Series of five coordinate dinuclear copper(II) metallacycles supported by the ligands *m*-bis[bis(1-pyrazolyl)methyl]benzene **(L_m)** and *m*-bis[bis(3,5-dimethyl-1-

pyrazolyl)methyl]benzene ($\mathbf{L}_m^*$) of the formula $[Cu_2(\mu\text{-}X)(\mu\text{-}\mathbf{L})_2](A)_3$ ($\mathbf{L}_m$: X = F^- A = BF_4^-; X = Cl^-, OH^- A = ClO_4^-; $\mathbf{L}_m$***:** X = CN^-, F^-, Cl^-, OH^-, Br^- A = ClO_4^-) were recently synthesized.[9]

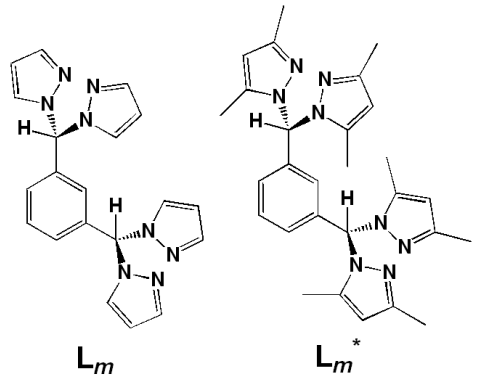

Scheme 6.1. Schematic representation of the ligands, $\mathbf{L}_m$ and $\mathbf{L}_m$*****.

Scheme 6.1 shows the structure of the two ligands, which differ by the methyl substitution of the pyrazolyl rings, and Figure 6.1 shows the structure of the $[Cu_2(\mu\text{-}F)(\mu\text{-}\mathbf{L}_m^*)_2]^{3+}$ cation. The $\mathbf{L}_m$***** complexes have unusual structural features, such as the linear Cu-X-Cu bridging arrangement and axially compressed trigonal bipyramidal geometry around the metal centers. This arrangement,[9] where the bridging X^- ligand occupies an equatorial site of the coordination sphere, results in strong antiferromagnetic superexchange interactions in the solid state, $-J$ = 160(CN^-), 340(F^-), 720(Cl^-), 808(OH^-) and 945(Br^-) cm^{-1} respectively ($\hat{\mathbf{H}} = -J\,\hat{\mathbf{S}}_1\hat{\mathbf{S}}_2$, $-J$ = exchange coupling constant) as a result of the overlap of the "donut" shaped portion of the spin rich copper(II) d_z^2 orbitals with the bridging anions orbitals. The magnitude of $-J$ correlates with the size of the bridging halides and it is unusually large for the OH^-.[9a] "Broken-Symmetry" ORCA calculations showed that as the size of the bridging halide increases, the energy of the triplet state increases faster than the energy of the singlet state, resulting in larger singlet-triplet energy gaps. The hydroxide singlet-triplet gap is between that of the Cl^- and Br^- bridged

compounds. The exchange integral and the spin delocalization of unpaired spin density toward the bridging group also increase as the size of the bridging halide is increasing.

The F^- bridged complex of the $\mathbf{L}_m$ ligand has the same trigonal bipyramidal geometry as the analogous $\mathbf{L}_m$* compound, with an almost linear Cu-F-Cu bridging angle (164-180° depending on the solvent content of the crystals),[9b] and subsequently the -*J* value is similar, 365 cm^{-1} vs. -340 cm^{-1}. The Cu-X-Cu bridging angle in the Cl^{-}[10] and OH^- analogues is smaller (153.2° and 141.0°) than in the $\mathbf{L}_m$* analogues (180°), resulting in weaker superexchange interactions in the $\mathbf{L}_m$ series (-*J* = 536 and 555 cm^{-1}, respectively) when compared to analogous $\mathbf{L}_m$* compounds (720 and 808 cm^{-1}, respectively) in solid state.

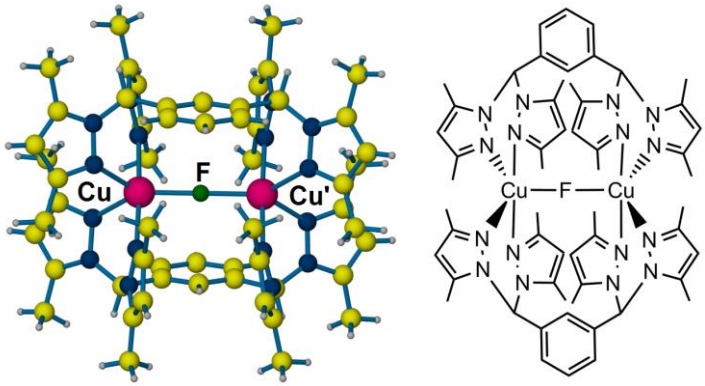

Figure 6.1. Solid state structure and drawing of $[Cu_2(\mu\text{-}F)(\mu\text{-}\mathbf{L}_m\text{*})_2]^{3+}$.

This chapter presents and discusses the determination of the structures in solution, using 1- and 2D NMR techniques, as well as T_1 measurements for the calculation of Cu···H distances, of this first extensive series of dinuclear copper(II) metallacycles, where the X^- bridges promote strong antiferromagnetic interactions, and where these bridges are systematically varied. Variable temperature (VT) ^{1}H NMR studies give insight into the magnitude of the exchange coupling constant (-*J*) in solution.

Experimental Section

^{1}H, ^{13}C NMR and the 2D NMR (^{1}H-^{1}H COSY, ^{1}H-^{13}C HSQC, ^{1}H-^{13}C HMBC) spectra were recorded on a Varian Mercury/VX 400 or a Bruker Avance-III HD 400 with broadband Prodigy Cryoprobe. All chemical shifts are in ppm and were referenced to residual undeuterated solvent signals (^{1}H) and deuterated solvent signals (^{13}C). The 2D NMR experiments were run with gradient coherence selection pulse sequences that were included with the vendor supplied software (VNMRJ version 2.2C or Topspin 3.1). The VT experiments were carried out in the temperature range -40 to 75°C (233 to 348K) in acetonitrile-d_3. A standard Varian L900 variable-temperature controller was utilized in these experiments. The longitudinal relaxation times (T_1) were determined by standard inversion-recovery experiments. For the calculated Cu···H distances, from the crystal structures, equivalent hydrogen atoms were averaged. If the two copper(II) centers were not equivalent in solid state, the Cu···H distances were measured from each copper(II) and then were averaged. MestReNova and SigmaPlot was used for the preparation of figures.[11]

Syntheses, single crystal structures of the copper(II) metallacycles and J values in solid state, calculated from fitting the magnetic susceptibilities to the Bleaney-Bowers equation, were previously reported or prepared and measured by analogous procedures.[9]

Caution: *Although no problems were encountered during this work with the perchlorate salts, these compounds should be considered potentially explosive!*

Results and Discussion

NMR Assignments and Confirmation of Structure in Solution. Solid state magnetic susceptibility measurements demonstrated that the dinuclear copper(II) complexes, $[Cu_2(\mu\text{-}X)(\mu\text{-}\mathbf{L}_m)_2](A)_3$ (X = F^- A = BF_4^-; X = Cl^-, OH^- A = ClO_4^-) and $[Cu_2(\mu\text{-}X)(\mu\text{-}\mathbf{L}_m\mathbf{*})_2](ClO_4)_3$ (X = F^-, Cl^-, Br^-, OH^-, CN^-), show strong antiferromagnetic coupling,[9] while the ^1H NMR spectra of analogous dinuclear Zn(II) and Cd(II) compounds, e.g. $[Cd_2(\mu\text{-}F)(\mu\text{-}\mathbf{L}_m\mathbf{*})_2](ClO_4)_3$, showed that the single anion bridged, metallacyclic structure is retained in solution.[9] For these reasons, relatively sharp ^1H NMR resonances were anticipated for these copper(II) compounds, with small hyperfine shifts. The ^1H NMR resonances, in CD_3CN at 20°C, are indeed relatively sharp and in a very narrow chemical shift range for copper(II) complexes: $[Cu_2(\mu\text{-}F)(\mu\text{-}\mathbf{L}_m)_2](ClO_4)_3$ 2 to 30 ppm, $[Cu_2(\mu\text{-}Cl)(\mu\text{-}\mathbf{L}_m)_2](ClO_4)_3$ 4 to 25 ppm, $[Cu_2(\mu\text{-}OH)(\mu\text{-}\mathbf{L}_m)_2](ClO_4)_3$ 4 to 17 ppm, $[Cu_2(\mu\text{-}CN)(\mu\text{-}\mathbf{L}_m\mathbf{*})_2](ClO_4)_3$ -5 to 20 ppm, $[Cu_2(\mu\text{-}F)(\mu\text{-}\mathbf{L}_m\mathbf{*})_2](ClO_4)_3$ -2 to 27 ppm, $[Cu_2(\mu\text{-}Cl)(\mu\text{-}\mathbf{L}_m\mathbf{*})_2](ClO_4)_3$ 0 to 13 ppm, $[Cu_2(\mu\text{-}OH)(\mu\text{-}\mathbf{L}_m\mathbf{*})_2](ClO_4)_3$ 0 to 10 ppm and $[Cu_2(\mu\text{-}Br)(\mu\text{-}\mathbf{L}_m\mathbf{*})_2](ClO_4)_3$ 1 to 8 ppm.

A series of NMR experiments were carried out in order to assign these resonances. First the VT-^1H NMR spectra was recorded in the temperature range -40 to 75˚C in acetonitrile-d_3. The shape and position of the resonances are dependent on the population distribution between the diamagnetic singlet S = 0 (ground) and the triplet S = 1 (excited) states, that is they are essentially a function of the strength of the antiferromagnetic interaction. To facilitate the interpretation of the ^1H NMR data the ^{13}C NMR, ^1H-^1H COSY, ^1H-^{13}C HSQC spectra of the compounds and for $[Cu_2(\mu\text{-}OH)(\mu\text{-}\mathbf{L}_m\mathbf{*})_2](ClO_4)_3$ the ^1H-^{13}C HMBC spectrum were also recorded.

To complete and/or confirm the assignments of the ^{1}H NMR resonances, the T_1 spin-lattice relaxation times were measured. Assuming a predominantly paramagnetic dipolar relaxation mechanism[7] for the metallacyclic protons, the distance between the closest paramagnetic copper(II) center and the hydrogen atoms can be determined according to the following equation: $d_i = d_{ref}(T_{1i}/T_{1ref})^{1/6}$, where d_i and T_{1i} are the Cu···H crystallographic distances and spin-lattice relaxation time of proton *i*, similarly d_{ref} and T_{1ref} are the Cu···H distance and spin-lattice relaxation time of a reference hydrogen. The results of this analysis usually have a 20% error margin.

As the strength of the antiferromagnetic interaction decreases, the assignment of the resonances becomes harder; the 2D NMR experiments, as a result of short nuclear relaxation times, provide less or no useful information. In these cases, the integrals of the deconvoluted resonances and similarities between the spectra of the more weakly and strongly coupled copper(II) complexes were taken into consideration along with the spectra of the d^{10} analogues. The shape and the temperature dependent behavior of the resonances also facilitate the assignments. The assignments are shown in Table 6.1, while Figure 6.2 shows the ^{1}H NMR spectrum of $[Cu_2(\mu\text{-Br})(\mu\text{-}\mathbf{L}_m\mathbf{*})_2](ClO_4)_3$ at -40˚C along with a labeled drawing. The labeling scheme shown on the left side of Figure 6.2 is correct for all $\mathbf{L}_m\mathbf{*}$ compounds; the $\mathbf{L}_m$ compounds are labeled analogously except there are no *a** and *c** methyl groups attached to the pyrazolyl rings.

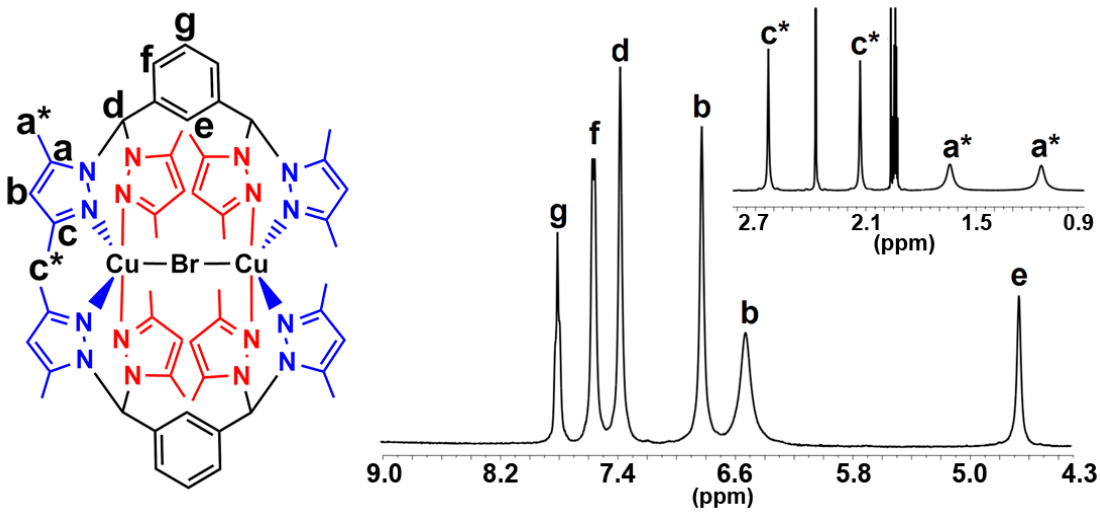

Figure 6.2. ^{1}H NMR spectrum of $[Cu_2(\mu\text{-Br})(\mu\text{-}\mathbf{L}_m\mathbf{*})_2](ClO_4)_3$ at -40˚C. Red axial, blue equatorial pyrazolyl rings.

The ^{1}H and ^{13}C NMR spectra of $[Cu_2(\mu\text{-Br})(\mu\text{-}\mathbf{L}_m\mathbf{*})_2](ClO_4)_3$ at -40˚C show a single resonance for the methines (*d*) and the resonances corresponding to the nonequivalent positions of the phenylene spacers (*e*, *f*, *g* and *ipso*-*C*). For the *a**, *c** and *b*-pyrazolyl resonances, two distinct environments are observed (^{13}C resonances for ring carbon atoms are not observed for the compounds with $\mathbf{L}_m\mathbf{*}$) corresponding to the axial and equatorial pyrazolyl rings of the trigonal bipyramidal geometry around copper(II) observed in the solid state.

Table 6.1. Chemical shifts and assignments of the ^{1}H NMR and ^{13}C NMR resonances of $[Cu_2(\mu\text{-}X)(\mu\text{-}\mathbf{L_m})_2](A)_3$ (X = F^- A = BF_4^-; X = Cl^-, OH^- A = ClO_4^-) and $[Cu_2(\mu\text{-}X)(\mu\text{-}\mathbf{L_m}^*)_2](ClO_4)_3$ (X = CN^-, F^-, Cl^-, OH^-, Br^-) at 20˚C. See Figure 2 for the labeling scheme of individual hydrogen and carbon atoms. Multiple resonances that were not clearly assigned are shown in one cell.

	$[Cu_2(\mu\text{-}X)(\mu\text{-}\mathbf{L_m})_2]^{3+}$						$[Cu_2(\mu\text{-}X)(\mu\text{-}\mathbf{L_m}^*)_2]^{3+}$									
X	**F^-**		**Cl^-**		**OH^-**		**CN^-**		**F^-**		**Cl^-**		**OH^-**		**Br^-**	
	^{1}H	^{13}C	^{1}H	^{13}C	^{1}H	^{13}C	^{1}H	^{13}C	^{1}H	^{13}C	^{1}H	^{13}C	^{1}H	^{13}C	^{1}H	^{13}C
a* **or *a*** [a]	9.35[b]	184.9 198.2	10.96	-	7.88	184.6[b]	-2.82	-	-0.82	-	0.75[e]	11.0	0.19	9.8	1.49	15.7
a* **or *a*** [a]	24.14[b,c]		17.86		[12].44	201.9[b]	-4.17	10.1	-1.15[c]	7.3		19.5	1.66	20.5	1.15	10.6
c* **or *c*** [a]	18.62		14.18		9.31	-	-0.30	19.4	1.13	34.2	1.93	18.3	1.95	16.2	2.18	12.6
c* **or *c*** [a]	15.35		15.92		12.10	136.4	1.68	23.8	3.31	21.1	2.70	14.8	2.84	13.1	2.69	11.7
b	24.58		19.83		12.99	162.4	3.42	48.6	9.83	136.1	9.66	125.6[d]	7.63	124.1	7.56	-
b	29.70		24.55		16.98	168.7	4.44	105.8	26.85	-	12.10	-	9.77	-	8.00[c]	
d	4.82	59.8	5.39	62.5	7.08	70.3	9.42	128.5	10.95	-	6.31	64.3	7.13	66.0	7.13	66.5
f	10.52	128.0	8.43[c]	127.5	8.38	129.6	10.77	129.6	16.79[e]	132.3	8.19[e]	130.3	8.52[e]	131.1	7.68	128.5
g	9.80	134.6	8.56	131.5	8.81	133.2	13.00	134.3				131.9		133.1	7.91	130.1
e	2.67[b]	123.0	4.17	122.9[d]	4.03	123.2[d]	17.66	141.5	4.03	-	4.00	-	3.95	-	4.69	125.4
***ipso*-C**		137.7		135.6[d]		138.2				140.2		136.7		138.0		135.1

[a] *a**, *c** for the compounds with the ligand $\mathbf{L_m}^*$ and *a*, *c* for the $\mathbf{L_m}$ compounds; [b]Broad resonance. [c]Shoulder. [d]Tentative assignment (no correlation was found in the ^{1}H-^{13}C HSQC spectra). [e]Two resonances merged.

The VT-^{1}H NMR spectra of $[Cu_2(\mu\text{-Br})(\mu\text{-}\mathbf{L_m}^*)_2](ClO_4)_3$, Figure 6.3, shows the temperature dependent behavior of the resonances. Most resonances move to lower shielding as the temperature is increased, except the *d* and *a** resonances. The *b*-pyrazolyl resonances are the most affected by the temperature change, especially the broader *b*-resonance, which shifts to lower shielding by more than 3 ppm. The temperature dependent hyperfine shifts correlate with -*J*, this issue is discussed in detail later.

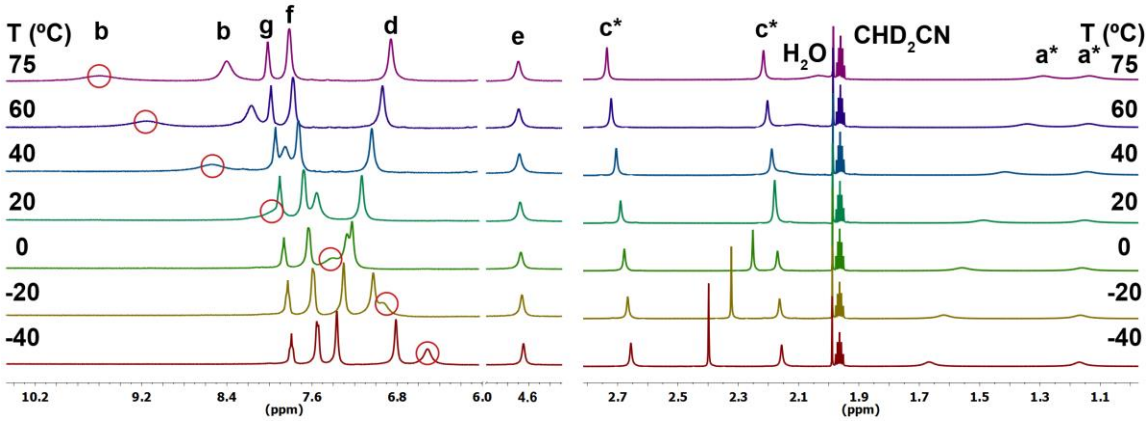

Figure 6.3. Variable temperature ^{1}H NMR spectra of $[Cu_2(\mu\text{-Br})(\mu\text{-}\mathbf{L_m}^*)_2](ClO_4)_3$. The red circles mark the position of one of the two nonequivalent *b*-pyrazolyl resonances at each temperature. This resonance was used for the calculation of -*J* in solution. The resonance for the small amount of H_2O (δ = 2.40 ppm at -40°C) present in CD_3CN broadens with increasing temperature and overlaps with one *c** resonance at 20°C.

The line widths of *a** and one of the *b*-pyrazolyl resonances are much larger than the *c** and the other *b*-pyrazolyl resonances, presumably due to an increase in paramagnetic relaxation effects causing shorter spin-spin relaxation times. The *a** resonances are closer (ca. 3.7 Å) to the metal centers than the *c** resonances (ca. 5.9 Å) and even though the *b*-pyrazolyl resonances in both the axial and equatorial positions are about 5.0 - 5.2 Å away from the copper(II) centers, the broad *b*-pyrazolyl resonances can

be tentatively assigned to the axial pyrazolyl rings, which are oriented towards the "dumbbell" shaped region of the spin rich d_z^2 orbitals of copper(II).

The assignments above are corroborated by the Cu···H distances determined from T_1 measurements at room temperature, Table 6.2. The *f* resonance was chosen as reference for the calculation of Cu···H distances, because in the ^{1}H-^{1}H COSY spectrum of the $[Cu_2(\mu\text{-}X)(\mu\text{-}\mathbf{L_m^*})_2](ClO_4)_3$ X = CN^-, F^-, Cl^-, Br^-, OH^- compounds, the only peaks, other than the diagonal peaks, expected and observed are the *f* and *g* peaks, δ(7.68,7.91) and δ(7.91,7.68), making the assignments definitive, Figure 6.4.

Table 6.2. Spin-lattice (longitudinal) relaxation times (T_1), Cu···H distances calculated from T_1 in solution and Cu···H distances from the single crystal X-ray diffraction structures for $[Cu_2(\mu\text{-}Br)(\mu\text{-}\mathbf{L_m^*})_2](ClO_4)_3$. Axial and equatorial assignments are tentative.

δ (ppm) 20°C	T_1 (ms) -40°C	$d_{Cu\cdots H}$ NMR (Å)	$d_{Cu\cdots H}$ cryst (Å)	Assignments
1.49	16.87	3.80	3.78	*a** (eq)
1.15	15.04	3.73	3.69	*a** (ax)
2.18	116.90	5.26	5.84	*c** (ax)
2.69	138.00	5.40	5.91	*c** (eq)
7.56	70.66	4.83	5.06	*b* (ax)
8.00	75.52	4.89	5.17	*b* (eq)
7.13	30.46	4.20	4.25	*d*
4.69	20.91	3.94	4.07	*e*
7.91	92.73	5.06	5.76	*g*
7.68	38.67	used as ref.	4.37	*f*

As shown in Table 6.2, the distances determined by NMR match those measured by X-ray crystallography quite well. This match in values demonstrates that the structure of $[Cu_2(\mu\text{-}Br)(\mu\text{-}\mathbf{L_m^*})_2](ClO_4)_3$ in solution is similar to the solid state structure.[9b] Analogous tables for the other compounds can be found in the Supporting Information (Table 6.3-6.6) demonstrating that the *correlation of solid and solution structures is general for this class of complexes*.

Table 6.3. Longitudinal relaxation times (T_1), Cu···H distances calculated from T_1 in solution and Cu···H distances from the single crystal X-ray diffraction structures for $[Cu_2(\mu\text{-OH})(\mu\text{-}\mathbf{L}_m\mathbf{*})_2](ClO_4)_3$. Axial and equatorial assignments are tentative.

δ (ppm) 20°C	T_1 (ms) -40°C	$d_{Cu\cdots H}$ NMR (Å)	$d_{Cu\cdots H}$ cryst (Å)	Assignments
1.66	6.77	3.79	3.66	*a** (ax)
0.19	9.51	4.01	3.94	*a** (eq)
1.95	67.34	5.56	5.84	*c** (ax)
2.84	74.37	5.65	5.93	*c** (eq)
7.63	42.14	5.14	5.25	*b* (eq)
9.77	34.89	4.98	5.06	*b* (ax)
7.13	13.42	used as ref.	4.25	*d*
3.95	5.27	3.63	4.07	*e*
8.52	20.67	4.56	4.86	*g+f*

Table 6.4. Longitudinal relaxation times (T_1), Cu···H distances calculated from T_1 in solution and Cu···H distances from the single crystal X-ray diffraction structures for $[Cu_2(\mu\text{-Cl})(\mu\text{-}\mathbf{L}_m\mathbf{*})_2](ClO_4)_3$. Axial and equatorial assignments are tentative.

δ (ppm) 20°C	T_1 (ms) -40°C	$d_{Cu\cdots H}$ NMR (Å)	$d_{Cu\cdots H}$ cryst (Å)	Assignments
0.75	5.26	3.80	3.74	*a**
1.93	48.07	5.49	5.82	*c** (ax)
2.70	52.38	5.57	5.89	*c** (eq)
9.66	23.77	4.88	5.14	*b* (eq)
12.10	25.37	4.94	5.04	*b* (ax)
6.31	9.84	used as ref.	4.22	*d*
4.00	5.51	3.83	3.95	*e*
8.19*	18.89	4.70	5.07	*g+f*

Table 6.5. Longitudinal relaxation times (T_1), Cu···H distances calculated from T_1 in solution and Cu···H distances from the single crystal X-ray diffraction structures for $[Cu_2(\mu\text{-F})(\mu\text{-}\mathbf{L}_m\mathbf{*})_2](ClO_4)_3$. Axial and equatorial assignments are tentative.

δ (ppm) 20°C	T_1 (ms) -40°C	$d_{Cu\cdots H}$ NMR (Å)	$d_{Cu\cdots H}$ cryst (Å)	Assignments
-0.82	3.11	3.83	3.91	*a** (eq)
-1.15 sh	2.05	3.58	3.68	*a**(ax)
1.13	25.19	5.43	5.85	*c** (ax)
3.31	27.20	5.50	5.96	*c** (eq)
9.83	14.43	4.95	5.24	*b* (eq)
26.85	13.43	4.89	5.04	*b* (ax)
10.95	5.62	used as ref.	4.23	*d*
4.03	4.23	4.03	3.73	*e*
16.79	14.20	4.94	5.08	*g+f*

Table 6.6. Longitudinal relaxation times (T_1), Cu···H distances calculated from T_1 in solution and Cu···H distances from the X-ray diffraction structures for $[Cu_2(\mu\text{-CN})(\mu\text{-}\mathbf{L}_m\mathbf{*})_2](ClO_4)_3$. In this case the quality of data did not allow the assignment of the resonances.

δ (ppm)	T_1 (ms)	$d_{Cu\text{-}H}$ NMR (Å)	$d_{Cu\text{-}H}$ cryst (Å)	Assignments
-2.82	0.61	3.56	3.74	*a** (ax)
-4.17	0.89	used as ref.	3.79	*a** (eq)
-0.30	8.42	5.52	5.87	*c** (ax)
1.68	8.29	5.50	5.90	*c** (eq)
13.00	5.59	5.15	5.12	*b* (ax)
17.66	5.77	5.18	5.18	*b* (eq)
9.42	5.07	5.07	4.24	*d*
10.77	1.59	4.18	4.04	*e*
3.42	10.47	5.72	5.71	*g*
4.44	11.02	5.77	4.31	*f*
			5.01	*g*+*f*

The ^{1}H-^{13}C HSQC spectra of $[Cu_2(\mu\text{-Br})(\mu\text{-}\mathbf{L}_m\mathbf{*})_2](ClO_4)_3$, recorded at 20°C, clearly correlate the proton and carbon resonances (Figure 6.4). No correlations were found for the *b*-pyrazolyl resonances, probably a result of short nuclear relaxation times. These *b*-pyrazolyl resonances are also absent in the ^{13}C NMR spectra.

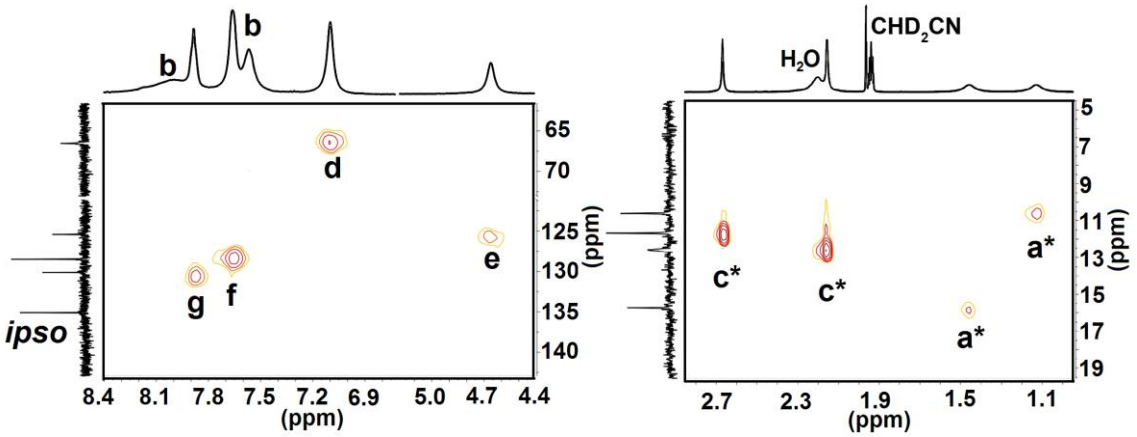

Figure 6.4. ^{1}H-^{13}C HSQC spectra of $[Cu_2(\mu\text{-Br})(\mu\text{-}\mathbf{L}_m\mathbf{*})_2](ClO_4)_3$ at 20˚C.

Similar assignments were made for $[Cu_2(\mu\text{-OH})(\mu\text{-}\mathbf{L}_m\mathbf{*})_2](ClO_4)_3$, the VT-NMR spectra is shown in Figure 6.5.

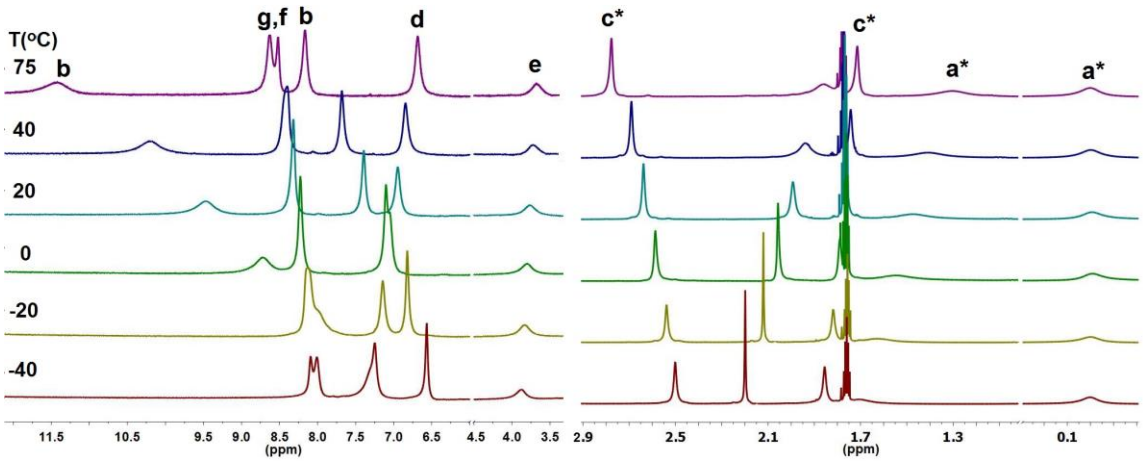

Figure 6.5. VT-^{1}H NMR spectra of $[Cu_2(\mu\text{-}OH)(\mu\text{-}\mathbf{L}_{\boldsymbol{m}}\mathbf{*})_2](ClO_4)_3$.

The ^{1}H-^{13}C HSQC spectra at 20°C confirms that the *g* and *f* resonances are merged in the ^{1}H NMR spectrum (8.52 ppm). The most prominent difference in the ^{1}H-^{13}C HSQC spectra of the bromide and the hydroxide bridged compounds is a cross peak at δ(7.57,124.1) that can be assigned to one of the *b*-pyrazolyl resonances (allowing the assignment of one ^{13}C *b* resonance in Table 6.1), while the proton-carbon cross peak for resonance *e* disappears (Figure 6.6). The proof that δ(7.57,124.1) corresponds to a *b*-pyrazolyl resonance, and not the *e*, comes from the ^{1}H-^{13}C HSQC experiment at -40°C, where this cross peak shifts to δ(6.72,115.4) and the ^{1}H-^{13}C HMBC experiment which correlates the ^{13}C resonance at 115.4 ppm with one *c**-pyrazolyl resonance at 2.67 ppm (Figure 6.7, blue circle). The Cu···H distances calculated from T_1 also confirm that the resonance at 7.57 ppm corresponds to *b* ($d_{Cu\cdots H}$ NMR vs. cryst: 5.14 vs. 5.25 Å), while the resonance at 3.95 ppm corresponds to *e* ($d_{Cu\cdots H}$ NMR vs. cryst: 3.63 vs. 4.07 Å), Table 6.3.

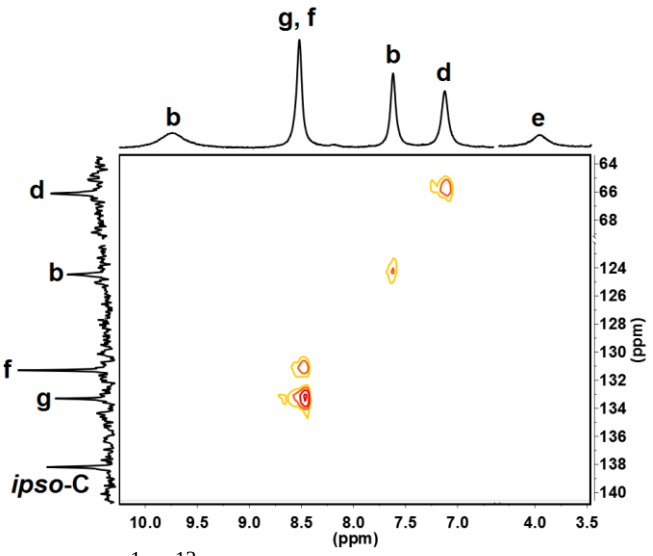

Figure 6.6. Fragment of the ^{1}H-^{13}C HSQC spectrum of $[Cu_2(\mu\text{-OH})(\mu\text{-}\mathbf{L}_m\mathbf{*})_2](ClO_4)_3$ at 20˚C.

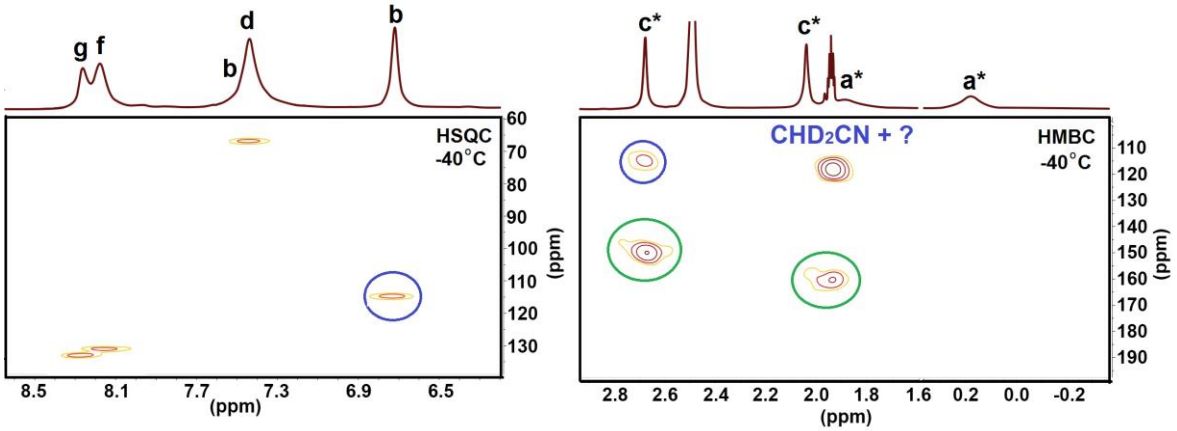

Figure 6.7. Fragments of the ^{1}H-^{13}C HSQC and ^{1}H-^{13}C HMBC spectra of $[Cu_2(\mu\text{-OH})(\mu\text{-}\mathbf{L}_m\mathbf{*})_2](ClO_4)_3$ at -40˚C. The cross peak δ(6.72,115.4) in the ^{1}H-^{13}C HSQC and δ(2.67,114.5) in the ^{1}H-^{13}C HMBC spectra are marked by a blue circle (a second cross peak around 115 ppm might be overlapped by the solvent, CH_3CN, cross peak). The green circles show the two bond correlation of the *a**, *c**-pyrazolyl proton resonances with *a* and *c*-pyrazolyl ^{13}C resonances (these ^{13}C resonances could not be observed at 20°C).

In the ^{13}C NMR spectra of the $[Cu_2(\mu\text{-X})(\mu\text{-}\mathbf{L}_m\mathbf{*})_2](ClO_4)_3$ series the quaternary *a*, *c* and some of the *b*-pyrazolyl carbon resonances could not be observed at 20°C, but the ^{1}H-^{13}C HMBC spectrum of $[Cu_2(\mu\text{-OH})(\mu\text{-}\mathbf{L}_m\mathbf{*})_2](ClO_4)_3$ at -40°C indicates that these resonances have chemical shifts in a similar range as $[Cd_2(\mu\text{-F})(\mu\text{-}\mathbf{L}_m\mathbf{*})_2](BF_4)_3$, 145-154

ppm, Figure 6.7, green circles. These resonances would be more shifted for the more weakly antiferromagnetically coupled compounds.

For $[Cu_2(\mu\text{-Cl})(\mu\text{-}\mathbf{L}_m\mathbf{*})_2](ClO_4)_3$, the ^{1}H-^{13}C HSQC spectrum shows a cross peak for the merged *g* and *f* resonances δ(8.19,130.3), δ(8.19,131.9) and two cross peaks for the *c** resonances δ(2.73,14.8), δ(1.95,18.3). The other resonances can be assigned based on the assignments for the $[Cu_2(\mu\text{-Br})(\mu\text{-}\mathbf{L}_m\mathbf{*})_2](ClO_4)_3$, the VT-^{1}H NMR spectra (Figure 6.8) and T_1 measurements.

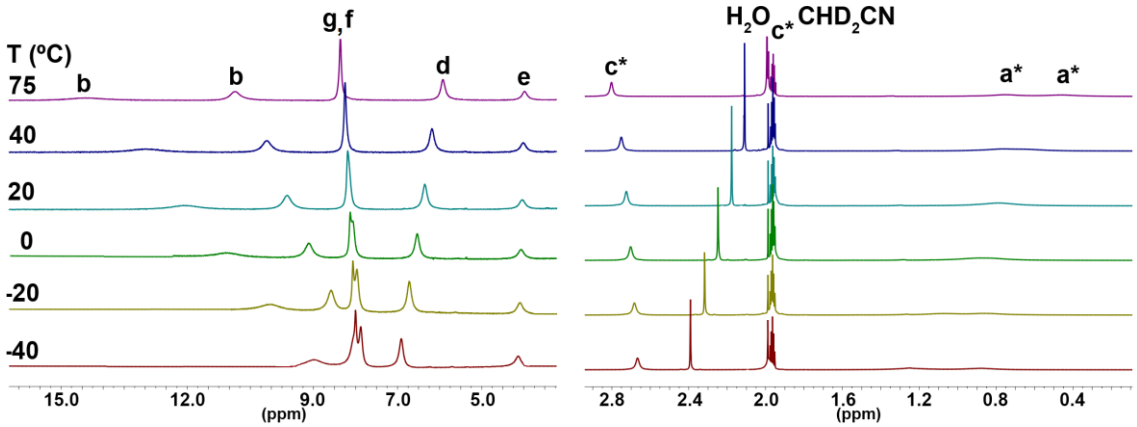

Figure 6.8. VT-^{1}H NMR spectra of $[Cu_2(\mu\text{-Cl})(\mu\text{-}\mathbf{L}_m\mathbf{*})_2](ClO_4)_3$. At 20°C the two *a** resonances merged.

The compound $[Cu_2(\mu\text{-F})(\mu\text{-}\mathbf{L}_m\mathbf{*})_2](ClO_4)_3$ behaves similarly to $[Cu_2(\mu\text{-Cl})(\mu\text{-}\mathbf{L}_m\mathbf{*})_2](ClO_4)_3$. For $[Cu_2(\mu\text{-CN})(\mu\text{-}\mathbf{L}_m\mathbf{*})_2](ClO_4)_3$, the NMR data and T_1 measurements are inconclusive regarding the assignment of the resonances.

The VT-^{1}H NMR spectra of $[Cu_2(\mu\text{-X})(\mu\text{-}\mathbf{L}_m)_2](A)_3$ (X = F^- A = BF_4^-; X = Cl^-, OH^- A = ClO_4^-) are shown in Figure 6.9, 6.10 and 6.11.

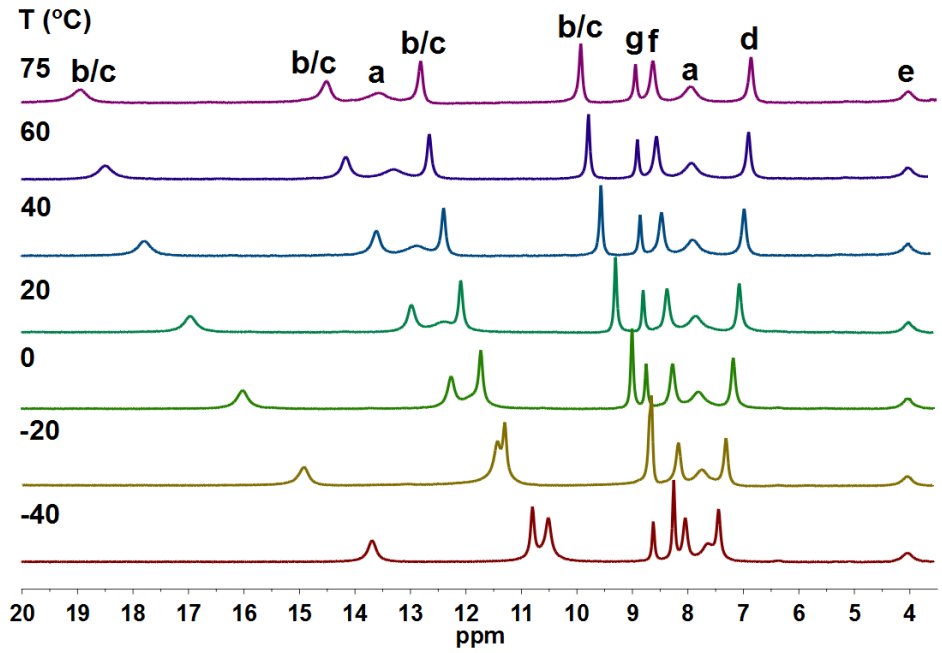

Figure 6.9. VT ^{1}H NMR spectra of $[Cu_2(\mu\text{-OH})(\mu\text{-}\mathbf{L}_m)_2](ClO_4)_3$.

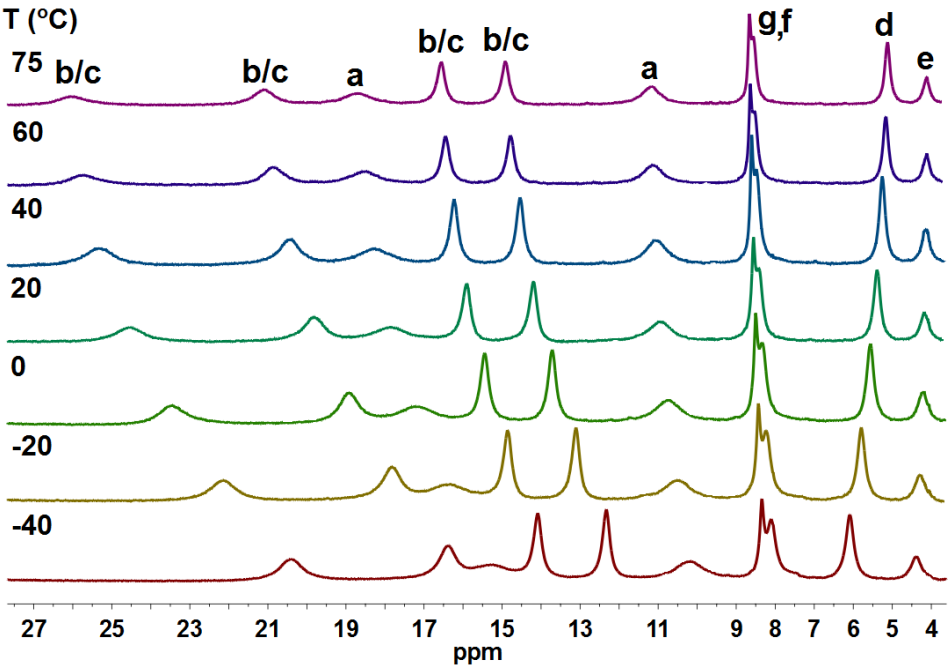

Figure 6.10. VT ^{1}H NMR spectra of $[Cu_2(\mu\text{-Cl})(\mu\text{-}\mathbf{L}_m)_2](ClO_4)_3$.

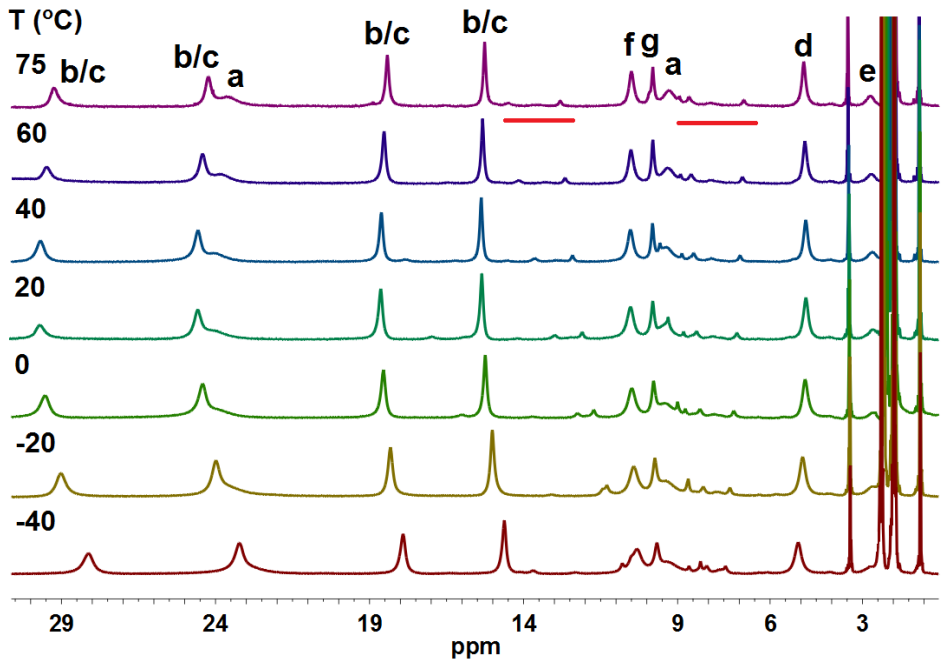

Figure 6.11. VT ^{1}H NMR spectra of $[Cu_2(\mu\text{-}F)(\mu\text{-}\mathbf{L}_m)_2](BF_4)_3$. The $[Cu_2(\mu\text{-}OH)(\mu\text{-}\mathbf{L}_m)_2]^{3+}$ resonances are underlined in red at 75 °C.

These compounds behave similarly to their analogues with the $\mathbf{L}_m$***** ligand, except the unsubstituted pyrazolyl ring resonances make the assignments more difficult because they are observed in the same region as the other resonances; the T_1 measurements become crucial (Table 6.7-6.9).

Table 6.7. Longitudinal relaxation times (T_1), Cu···H distances calculated from T_1 in solution and Cu···H distances from the single crystal X-ray diffraction structures for $[Cu_2(\mu\text{-}OH)(\mu\text{-}\mathbf{L}_m)_2](ClO_4)_3$.

δ (ppm)	Integrals	T_1 (ms)	$d_{Cu\text{-}H}$ NMR (Å)	$d_{Cu\text{-}H}$ cryst (Å)	Assignments
16.98	~3	25.44	4.93	5.15 or 5.08	*b* or *c*
12.99	4	24.12	4.89	5.15 or 5.08	*b* or *c*
12.44	4	3.15	3.48	3.34	*a*
12.10	4	25.00	4.92	5.15 or 5.08	*b* or *c*
9.31	4	33.66	5.17	5.15 or 5.08	*b* or *c*
8.81	2	23.36	4.87	5.57	*g*
8.38	4	9.91	4.22	4.40	*f*
7.88	4	3.46	3.54	3.34	*a*
7.08	4	11.04	used as ref.	4.29	*d*
4.03	2	4.27	3.66	3.92	*e*

Table 6.8. Longitudinal relaxation times (T_1), Cu···H distances calculated from T_1 in solution and Cu···H distances from the single crystal X-ray diffraction structures for $[Cu_2(\mu\text{-}Cl)(\mu\text{-}\mathbf{L}_m)_2](ClO_4)_3$.

δ (ppm)	T_1 (ms)	$d_{Cu\text{-}H}$ NMR (Å)	$d_{Cu\text{-}H}$ cryst (Å) Cu-Cl-Cu Bent**	$d_{Cu\text{-}H}$ cryst (Å) Cu-Cl-Cu Linear*	Assignments
24.55	12.14	4.93	5.08 or 5.01	5.11 or 5.02	*b* or *c*
19.83	11.13	4.86	5.08 or 5.01	5.11 or 5.02	*b* or *c*
17.86	1.10	3.30	3.28	3.31	*a*
15.92	10.57	4.82	5.08 or 5.01	5.11 or 5.02	*b* or *c*
14.18	12.55	4.96	5.08 or 5.01	5.11 or 5.02	*b* or *c*
10.96	0.95	3.22	3.28	3.31	*a*
8.56	9.72	4.75	5.38	5.03	*g*
8.43	4.15	4.12	4.14	3.75	*f*
5.39	5.00	used as ref.	4.25	4.21	*d*
4.17	3.30	3.97	3.99	4.24	*e*

* two cations in the unit cell: one is linearly bridged, the other has a bent Cl^- bridge.

Table 6.9. Longitudinal relaxation times (T_1), Cu···H distances calculated from T_1 in solution and Cu···H distances from the single crystal X-ray diffraction structures for $[Cu_2(\mu\text{-}F)(\mu\text{-}\mathbf{L}_m)_2](ClO_4)_3$.

δ (ppm)	T_1 (ms)	$d_{Cu\text{-}H}$ NMR (Å)	$d_{Cu\text{-}H}$ cryst (Å) Cu-F-Cu Bent*	$d_{Cu\text{-}H}$ cryst (Å) Cu-F-Cu Linear*	Assignments
29.70	11.14	4.97	5.11 or 5.02	5.15 or 5.05	*b* or *c*
24.58	9.17	4.81	5.11 or 5.02	5.15 or 5.05	*b* or *c*
24.14	-	-	3.30	3.35	*a*
18.62	9.81	4.86	5.11 or 5.02	5.15 or 5.05	*b* or *c*
15.35	12.57	5.07	5.11 or 5.02	5.15 or 5.05	*b* or *c*
10.52	3.47	4.09	4.05	3.73	*f*
9.80	6.78	4.57	5.21	4.89	*g*
9.35	1.17	3.41	3.30	3.35	*a*
4.82	4.12	used as ref	4.24	4.21	*d*
2.67	~1.60	3.60	3.90	4.03	*e*

* two cations in the unit cell: one is linearly bridged, the other has a bent F^- bridge.

The pyrazolyl rings also show two very broad pyrazolyl resonances in the ^{13}C NMR spectra of the OH^- and F^- bridged compounds (Table 6.1). The ^1H-^{13}C HSQC experiment shows five correlations for $[Cu_2(\mu\text{-}OH)(\mu\text{-}\mathbf{L}_m)_2](ClO_4)_3$ corresponding to the *d*, *f*, *g* and two pyrazolyl hydrogen atoms despite the weaker antiferromagnetic interactions (Figure

6.12), for $[Cu_2(\mu\text{-}Cl)(\mu\text{-}\mathbf{L}_m)_2](ClO_4)_3$ three correlations, *d*, *f* and *g*, while for $[Cu_2(\mu\text{-}F)(\mu\text{-}\mathbf{L}_m)_2](ClO_4)_3$ four correlations, *d*, *f*, *g* and a pyrazolyl hydrogen. ^{1}H-^{1}H COSY experiments failed for these compounds. In three different sample of $[Cu_2(\mu\text{-}F)(\mu\text{-}\mathbf{L}_m)_2](ClO_4)_3$, the resonances of $[Cu_2(\mu\text{-}OH)(\mu\text{-}\mathbf{L}_m)_2](ClO_4)_3$ were identified (Figure 6.11). These resonances grow over time, suggesting that the water in the solvent is promoting the exchange of the F^- and OH^- bridges in solution.

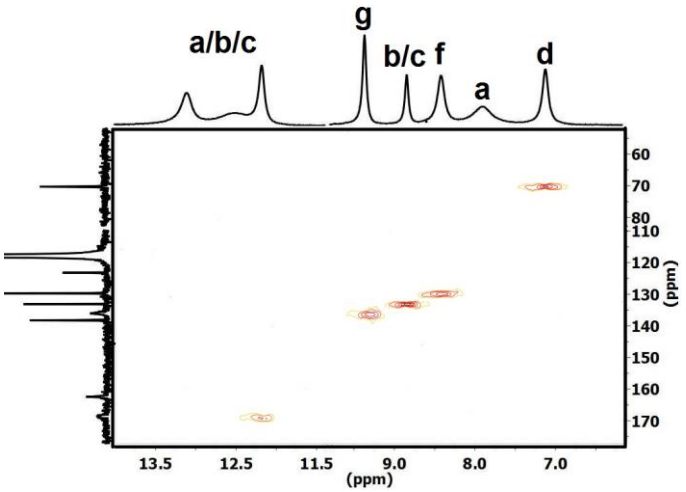

Figure 6.12. ^{1}H-^{13}C HSQC spectrum of $[Cu_2(\mu\text{-}OH)(\mu\text{-}\mathbf{L}_m)_2](ClO_4)_3$.

Determination of the Exchange Coupling Constant (-*J*) from VT-NMR. The population of the paramagnetic triplet (S = 1) and diamagnetic singlet (S = 0) states is temperature dependent, a change that impacts on the ^{1}H NMR spectra. The energy difference between these states corresponds to -*J*, where $\hat{\mathbf{H}} = -J\,\hat{\mathbf{S}}_1\hat{\mathbf{S}}_2$. The temperature dependent hyperfine shifts correlate with -*J* according to the following equation: $\delta_{iso} = A\frac{g\beta}{g_N\beta_N k}\frac{e^{J/kT}}{T(1+3e^{J/kT})} + \delta_0$,[7e,g,12] where δ_{iso} is the chemical shift of any ^{1}H NMR resonance, *g* is the *g*-factor determined for the compounds in solid state (~2.15), β is the Bohr magneton, g_N is the nuclear *g*-factor and β_N is the nuclear magneton, *A* is the

hyperfine coupling constant, k is the Boltzmann constant, T is the temperature and δ_0 is the hypothetical very low temperature position of the resonance chosen for the analyses. The chemical shifts of the resonances that show the largest temperature dependence (in all but one case the *b*-pyrazolyl resonance, see Figure 6.3) were used for the analysis. After estimating δ_0 by letting it vary freely for $[Cu_2(\mu\text{-Br})(\mu\text{-}\mathbf{L_m}\text{*})_2](ClO_4)_3$, δ_0 was fixed at 5.6 ppm for the $\mathbf{L_m}$* and 6.1 ppm for $\mathbf{L_m}$ compounds, close to the chemical shift of the *b*-pyrazolyl resonance in the ligands $\mathbf{L_m}$* (5.8 ppm)[9c] and $\mathbf{L_m}$ (6.3 ppm)[9d] at room temperature.[13] The parameters -J and A were simultaneously fit (Table 6.10, Figure 6.13) to the equation above with the software SigmaPlot. Observed and calculated chemical shifts are shown in Table 6.11.

Table 6.10. Results of the fitting procedure for $[Cu_2(\mu\text{-X})(\mu\text{-}\mathbf{L_m})_2](A)_3$ (X = F^- A = BF_4^-; X = Cl^-, OH^- A = ClO_4^-) and $[Cu_2(\mu\text{-X})(\mu\text{-}\mathbf{L_m}\text{*})_2](ClO_4)_3$ (X = CN^-, F^-, Cl^-, OH^-, Br^-).

Compound	δ_{iso} (ppm) at 20°C[a]	A (MHz) Solution[b]	-J (cm^{-1}) solution[b]	-J (cm^{-1}) solid
$[Cu_2(\mu\text{-F})(\mu\text{-}\mathbf{L_m})_2](BF_4)_3$	29.71	1.68(±0.2)	338(±2)	365
$[Cu_2(\mu\text{-Cl})(\mu\text{-}\mathbf{L_m})_2](ClO_4)_3$	24.55	1.99(±0.3)	460(±3)	536
$[Cu_2(\mu\text{-OH})(\mu\text{-}\mathbf{L_m})_2](ClO_4)_3$	14.92	1.63(±0.2)	542(±3)	555
$[Cu_2(\mu\text{-CN})(\mu\text{-}\mathbf{L_m}\text{*})_2](ClO_4)_3$	17.66[c]	0.45 (±0.3)	128(±12)	160
$[Cu_2(\mu\text{-F})(\mu\text{-}\mathbf{L_m}\text{*})_2](ClO_4)_3$	26.85	1.47(±0.3)	329(±2)	340
$[Cu_2(\mu\text{-Cl})(\mu\text{-}\mathbf{L_m}\text{*})_2](ClO_4)_3$	12.10	2.04(±0.3)	717(±4)	720
$[Cu_2(\mu\text{-OH})(\mu\text{-}\mathbf{L_m}\text{*})_2](ClO_4)_3$	9.77	1.98(±0.6)	823(±7)	808
$[Cu_2(\mu\text{-Br})(\mu\text{-}\mathbf{L_m}\text{*})_2](ClO_4)_3$	8.00	2.15(±0.4)	944(±4)	945

[a]Resonances assigned to the *b*-pyrazolyl hydrogens except for $[Cu_2(\mu\text{-CN})(\mu\text{-}\mathbf{L_m}\text{*})_2](ClO_4)_3$ where the assignment is not possible, but is not the *b*-pyrazolyl based on the A value. [b]R_{fit}^2 = 0.97-0.99. [c]δ_0 = 7.07 ppm.

Table 6.11. Experimental and calculated chemical shifts for the fitted data of $[Cu_2(\mu\text{-}X)(\mu\text{-}L_m)_2](A)_3$ (X = F^- A = BF_4^-; X = Cl^-, OH^- A = ClO_4^-) and $[Cu_2(\mu\text{-}X)(\mu\text{-}\mathbf{L_m}\mathbf{*})_2](ClO_4)_3$ (X = CN^-, F^-, Cl^-, OH^-, Br^-).

$[Cu_2(\mu\text{-}X)(\mu\text{-}\mathbf{L_m}\mathbf{*})_2]^{3+}$										
T(K)	**CN^-, L_m***		**F^-, L_m***		**Cl^-, L_m***		**OH^-, L_m***		**Br^-, L_m***	
	Exp.	**Calcd.**	**Exp.**	**Calcd.**	**Exp.**	**Calcd.**	**Exp.**	**Calcd.**	**Exp.**	**Calcd.**
233.15	19.53	19.52	25.68	25.76	8.97	9.03	7.32	7.36	6.51	6.52
253.15	18.83	18.84	26.40	26.37	10.05	10.02	7.98	8.00	6.93	6.93
273.15	18.20	18.21	26.76	26.69	11.04	11.03	8.71	8.70	7.41	7.41
293.15	17.68	17.64	26.85	26.80	12.04	12.02	9.47	9.43	7.94	7.95
313.15	17.11	17.12	26.75	26.74	12.98	12.97	10.22	10.18	8.55	8.53
333.15	16.62	16.64	26.54	26.57	-	-	-	-	9.14	9.13
348.15	16.31	16.30	26.32	26.38	14.47	14.49	11.41	11.45	9.58	9.59

$[Cu_2(\mu\text{-}X)(\mu\text{-}\mathbf{L_m})_2]^{3+}$						
T(K)	**F^-, L_m**		**Cl^-, L_m**		**OH^-, L_m**	
	Exp.	**Calcd.**	**Exp.**	**Calcd.**	**Exp.**	**Calcd.**
233.15	28.12	28.21	20.40	20.52	13.69	13.66
253.15	29.02	28.99	22.15	22.12	14.92	14.91
273.15	29.53	29.44	23.48	23.43	16.03	16.03
293.15	29.69	29.64	24.56	24.45	16.97	17.00
313.15	29.69	29.64	25.32	25.24	17.80	17.82
333.15	29.48	29.50	25.76	25.82	18.49	18.50
348.15	29.24	29.33	26.03	26.13	18.96	18.92

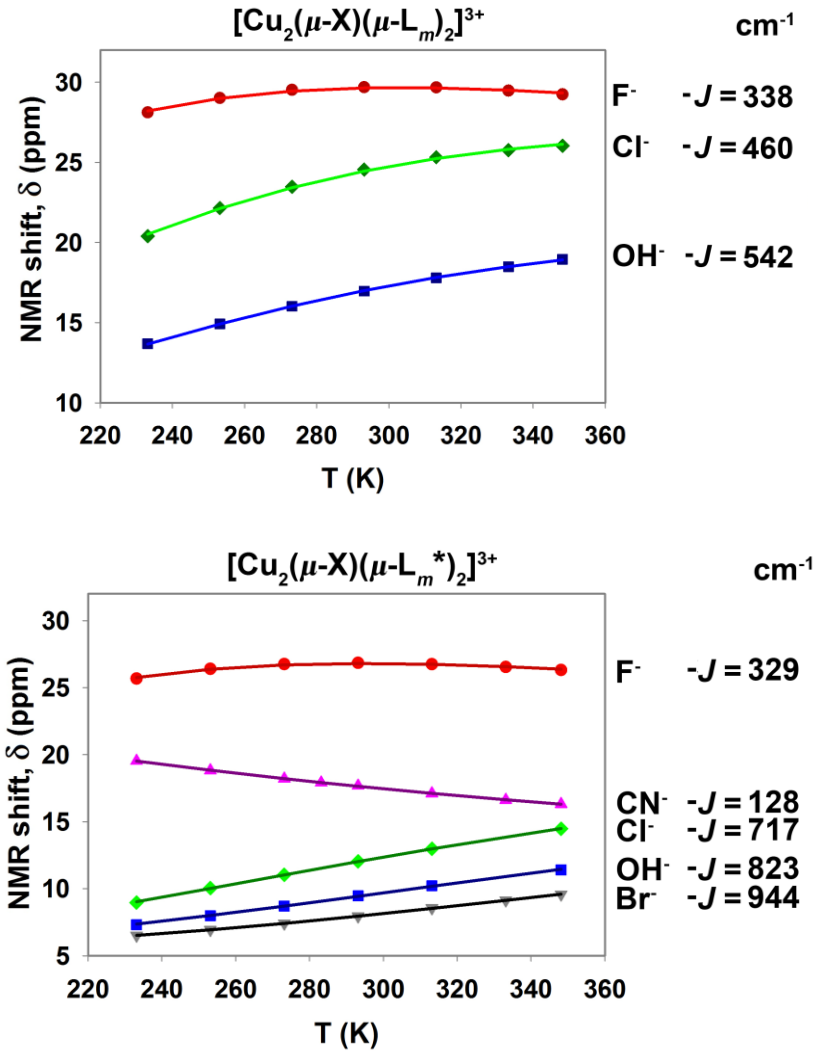

Figure 6.13. Plot of chemical shifts (δ) of the *b*-pyrazolyl resonances vs. the temperature (233 to 348 K). In case of $[Cu_2(\mu\text{-CN})(\mu\text{-}\mathbf{L_m}^*)_2](ClO_4)_3$, the plotted resonance could not be identified. Fitting of the experimental data (represented by the symbols) results in the solid lines (R_{fit}^2 = 0.97-0.99). The -*J* values are shown on the right side of the plots.

The fitting procedure was repeated for each compound with other resonances and similar –*J* values were obtained in each case, for example in the case of the *d* methine resonance of $[Cu_2(\mu\text{-Br})(\mu\text{-}\mathbf{L_m}^*)_2](ClO_4)_3$, with δ_0 fixed at 7.53 ppm, the fit results in -*J* = 930(±6) cm^{-1}, *A* = -0.34(±0.4) MHz, Figure 6.14. The *A* values match the literature values for other copper(II) compounds.[14]

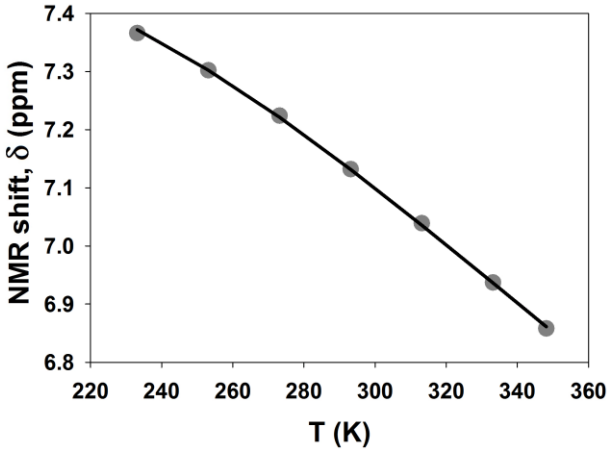

Figure 6.14. Chemical shift vs. temperature plot for the *d* methine resonance of $[Cu_2(\mu\text{-}Br)(\mu\text{-}\mathbf{L}_m\mathbf{*})_2](ClO_4)_3$, with δ_0 at 7.53 ppm. Dots: experimental data, solid line: fitted data.

Although the freezing and boiling point of the solvent restrict the data collection to a relatively narrow temperature range, the error margins are relatively small (Table 6.10). The results of the fit are in good agreement with the -*J* values determined in solid state, the difference between the solid state and solution -*J* values being between 1 to 32 cm^{-1}, except for $[Cu_2(\mu\text{-}Cl)(\mu\text{-}\mathbf{L}_m)_2](ClO_4)_3$. This good agreement between the -*J* values indicates that the linear or near linear Cu-X-Cu angle in solid state is retained for most compounds and the overall geometry around the copper(II) centers remain largely unchanged. The successful determination of -*J* in solution for this extensive series of complexes in which the bridging group is varied demonstrates the *power of the method and provides an alternative route for the correlation of solid and solution structures*.

The data for $[Cu_2(\mu\text{-}OH)(\mu\text{-}\mathbf{L}_m)_2](ClO_4)_3$ is especially interesting in the light of the bent Cu-O-Cu angle in solid state (142°), resulting in a geometry around copper(II) that is better described as distorted axially elongated square pyramidal than trigonal bipyramidal. The excellent agreement between -*J* in solution (542 cm^{-1}) and in solid state

(555 cm^{-1}) for $[Cu_2(\mu\text{-}OH)(\mu\text{-}\mathbf{L_m})_2](ClO_4)_3 \cdot 2H_2O$ suggests that the bridging angle and distorted square pyramidal geometry is retained in solution.

The solution -*J* value for $[Cu_2(\mu\text{-}Cl)(\mu\text{-}\mathbf{L_m})_2](ClO_4)_3$ differs by 76 cm^{-1} from the solid state value, a difference larger than for the other compounds, and what can be explained by experimental error. A possible explanation is that in this case the solution structure is different from that in solid state. In the crystal structure there are two independent molecules in 1:1 ratio,[10] one with a bent Cu-Cl-Cu angle of 138.5° and the other more linearly bridged, 167.8°. It is likely that in the solution state there is a difference in the bridging angle compared to the average angle in the solid state, resulting in lower *J* value in solution.

Density Functional Theory calculations were performed on $[Cu_2(\mu\text{-}Br)(\mu\text{-}\mathbf{L_m}^*)_2](ClO_4)_3$ with the software ORCA[15] to estimate the magnitude of *A* for the *b*-pyrazolyl hydrogens. The calculated *A* values for all other compounds should be similar to that of $[Cu_2(\mu\text{-}Br)(\mu\text{-}\mathbf{L_m}^*)_2](ClO_4)_3$, because the spin densities on the corresponding hydrogens are similar.[9a] Ahlrichs-type basis set TZVPP for copper(II) and SVP for other atoms were used, combined with the B3LYP functional.[16] Ahlrichs polarisation functions from basis H - Kr R and auxiliary bases from the TurboMole library were also used.[17] The Br^- bridged molecule was simplified by removal of the methyl groups on the pyrazolyl fragments, as well as the benzene rings, and hydrogen atoms were placed appropriate positions. All remaining atoms were retained at the positions determined by X-ray crystallography. The calculations result in an average *A*[18] value of 0.65 MHz for the equatorial and 1.43 MHz for the axial *b*-pyrazolyl hydrogens, in line with literature

data.[14] The fitting of the experimental data, Teble 6.11, results in a similar *A* value, 2.15(±0.4) MHz (Table 6.10), for the axial *b*-pyrazolyl hydrogens,

An important note is that the *d* methine hydrogens should have negative *A* values, as the resonance of the *d* hydrogen is moving to higher shielding with increase in temperature in the VT ^{1}H NMR spectra, Figure 6.3. The $[Cu_2(\mu\text{-Br})(\mu\text{-}\mathbf{L}_m\mathbf{*})_2](ClO_4)_3$ data using the *d* hydrogens was fitted and the resulting *A* = -0.34 MHz, Figure 6.14, is similar to the one calculated by ORCA, *A* = -0.30 MHz.

Conclusions

The ^{1}H and ^{13}C NMR in combination with 2D NMR correlation spectroscopy and T_1 relaxation time measurements have been used to study the structure and properties of antiferomagnetically coupled, dinuclear copper(II) compounds *in solution*, despite the large variation in the strength of the antiferromagnetic interactions. Even though the nuclear relaxation times are short, the ^{1}H-^{1}H COSY and especially the ^{1}H-^{13}C HMBC experiments result in limited, but clearly useful information for compounds with $-J > 700$ cm^{-1}, particularly at lower temperatures. Correlations in the ^{1}H-^{13}C HSQC spectra were observed for compounds with $-J > 500$ cm^{-1}. The T_1 measurements accurately determine the Cu··H distances in these molecules. The analyses of the data lead to the conclusion that the dinuclear structure and the unusual axially compressed trigonal bipyramidal geometry are retained in CD_3CN for the $\mathbf{L}_m\mathbf{*}$ series, complexes that have the linear Cu-X-Cu arrangement. The structures in solution of the $\mathbf{L}_m$ complexes, which have bent Cu-X-Cu bridges, are also similar to the solid state, although for $[Cu_2(\mu\text{-Cl})(\mu\text{-}\mathbf{L}_m)_2](ClO_4)_3$ there may be some variation.

This study is the first where the VT-NMR method was used for determination of -*J* in solution for an extended series of antiferomagnetically coupled, dinuclear paramagnetic copper(II) compounds, where the bridging anion (X) was systematically varied. The solution and solid state -*J* values are very similar, showing that these compounds retain their solid state structures in solution. The VT-NMR method was shown to be extremely useful for the determination of solution state -*J* values over a large range of antiferromagnetic interactions with different strengths from 944 to 128 cm^{-1}.

References

(1) (a) Rolff, M.; Schottenheim, J.; Decker, H.; Tuczek, F. *Chem. Soc. Rev.* **2011**, *40*, 4077. (b) Koval, I. A.; Gamez, P.; Belle, C.; Selmeczi, K.; Reedijk J. *Chem. Soc. Rev.* **2006**, *35*, 814. (c) Rolff, M.; Schottenheim, J.; Tuczek, F. *J. Coord. Chem.* **2010**, *63*, 2382. (d) Coughlin, P. K.; Lippard, S. J. *J. Am. Chem. Soc.* **1981**, *103*, 3228. (e) Selmeczi, K.; Règlier, M.; Giorgi, M.; Speier, G. *Coord. Chem. Rev.* **2003**, *245*, 191.

(2) (a) Yoon, J.; Fujii, S.; Solomon, E. I. *Proc. Natl. Acad. Sci*. **2009**, *106*(16), 6585. (b) Claus, H.; Decker, H. *Syst. Appl. Microbiol* **2006**, *29*, 3. (c) Li, Y.; Wang, Y.; Jiang, H.; Deng, J. *Proc. Natl. Acad. Sci*. **2009**, *106*(40), 17002. (d) Gerdemann, C.; Eicken, C.; Krebs, B. *Acc. Chem. Res.* **2002**, *35*, 183. (e) Eicken, C.; Krebs, B.; Sacchetini, J. C. *Curr. Opin. Struct. Biol.* **1999**, *9*, 677. (f) Peisach, J.; Aisen, P.; Blumberg, W. E. *The Biochemistry of Copper*; Academic Press: New York, **1966**. (g) Zaballa, M.-E.; Ziegler, L.; Kosman, D. J.; Vila A. J. *J. Am. Chem. Soc.* **2010**, *132*, 11191. (h) Abriata, L. A.; Ledesma, G. N.; Pierattelli, R.; Vila A. J. *J. Am. Chem. Soc.* **2009**, 131, 1939. (i) Fernández, C. O.; Vila A. J. in "Paramagnetic NMR of Electron Transfer Copper Proteins" *Paramagnetic Resonance of Metallobiomolecules*, *ACS Symposium Series* **2003**, *858*, 287. (j) Donaire, A.; Jiménez, B.; Fernández, C. O.; Pierattelli, R.; Niizeki, T.; Moratal, J.-M.; Hall, J. F.; Kohzuma, T.; Hasnain, S. S.; Vila A. J. *J. Am. Chem. Soc.* **2002**, 124, 13698.

(3) (a) Kahn, O. *Molecular Magnetism*; VCH Publishers, Inc.: New York, 1993. (b) Hay, P. J.; Thibeault, J. C.; Hoffmann, R. *J. Am. Chem. Soc.* **1975**, *97*, 4884.

(4) (a) Pinkowicz, D.; Chorąży, S.; Olaf, S. *Science Progress* **2011**, *94*(2), 139. (b) Miller, J. S.; Gatteschi D. *Chem. Soc. Rev.* **2011**, *40*, 3065. (c) Leuenberger, M. N.; Loss, D. *Nature* **2001**, *410*, 789-793. (d) Kahn, O. *Acc. Chem. Res.* **2000**, *33*(10), 647. (e) Wernsdorfer, W.; Aliaga–Alcalde, N.; Hendrickson, D. N.; Christou, G. *Nature* **2002**, *416*, 406.

(5) (a) Nùñez, C.; Bastida, R.; Macías, A.; Valencia, L.; Neuman, N. I.; Rizzi, A. C.; Brondino, C. D.; González, P. J.; Capelo, J. L.; Lodeiro, C. *Dalton Trans.* **2010**, *39*, 11654. (b) Mutti, F. G.; Zoppellaro, G.; Gulotti, M.; Santagostini, L.; Pagliarin, R.; Andersson, K. K.; Casella, L. *Eur. J. Inorg. Chem.* **2009**, 554 and references therein. (c) Solomon, E. I.; Ginsbach, J. W.; Heppner, D. E.; Kieber–Emmons, M. T.; Kjaergaard, C. H.; Smeets, P. J.; Tian, L.; Woertink, J. S. *Faraday Discuss.* **2010**, *148*, 11. (d) Battaini, G.; Granata, A.; Monzani, E.; Gullotti, M.; Casella, L. *Adv. Inorg. Chem.* **2006**, *58*, 185. (e) Siegbahn, P. E. M. *Faraday Discuss.* **2003**, *124*, 289. (f) Pirngruber, G. D.; Frunz, L.; Lüchinger, M. *Phys. Chem. Chem. Phys.* **2009**, *11*, 2928. (g) Bertini, I.; Gray, H. B.; Lippard, S. J.; Valentine, J. S. *Bioinorganic Chemistry*; University Science Books: Mill Valley, CA, 1994. (h) Liu, H. Y.; Scharbert, B.; Holm, R. H. *J. Am. Chem. Soc.* **1991**, *113*, 9529.

(6) (a) Bertini, I.; Turano, P.; Vila, A. J. *Chem.Rev.* **1993**, *93*, 2833. (b) Machonkin, T. E.; Westler, W. M.; Markley, J. L. *Inorg. Chem.* **2005**, *44*, 779. (c) Holm, R. H.; Abbott, E. H. In *Coordination Chemistry*; Martell, A. E., Ed.; Van Nostrand Reinhold Company: New York, **1971**, *2*, 264. (d) Clementi, V.; Luchinat, C. *Acc. Chem. Res.* **1998**, *31*, 351.

(7) (a) Tanase, S.; Koval, I . A.; Bouwman, E.; de Gelder, R.; Reedijk, J. *Inorg. Chem.* **2005**, *44*, 7860. (b) Satcher, J. H.; Balch, A. L. *Inorg. Chem.* **1995**, *34*(13), 3371. (c) Holz, R. C.; Bradshow, J. M.; Bennett, B. *Inorg. Chem.* **1998**, *37*, 1219. (d) Holz, R. C.; Brink, J. M.; Gobena, F. T.; O'Connor, C. J. *Inorg. Chem.* **1994**, *33*, 6086. (e) Maekawa, M.; Kitagawa, S.; Munakata, M.; Masuda, H. *Inorg. Chem.* **1989**, *28*(10), 1904. (f) Mandal, P. K.; Manoharan, P. T. *Inorg. Chem.* **1995**, *34*, 270. (g) Asokan, A.; Varghese, B.; Manoharan, P. T. *Inorg. Chem.* **1999**, *38*, 4393. (h) Gupta, R.; Mukherjee, S.; Mukherjee, R. *J. Chem. Soc. Dalton Trans.* **1999**, 4025.

(8) (a) Koval, I. A.; van der Schilden, K.; Schuitema, A. M.; Gamez, P.; Belle, C.; Pierre, J.-L.; Lüken, M.; Krebs, B.; Roubeau, O.; Reedijk, J. *Inorg. Chem.* **2005**, *44*, 4372. (b) Mohanta, S.; Adhikary, B.; Baitalik, S.; Nag, K. *New J. Chem.* **2001**, *25*, 1466. (c) Murthy, N. N.; Karlin, K. D.; Bertini, I.; Luchinat, C. *J. Am. Chem. Soc.* **1997**, *119*, 2156. (d) Lubben, M.; Hage, R.; Meetsma, A.; Bÿma, K.; Feringa, B.L. *Inorg. Chem.* **1995**, *34*, 2217. (e) Brink, J. M.; Rose, R. A.; Holz, R. C. *Inorg. Chem.* **1996**, *35*, 2878. (f) Holz, R. C.; Brink, J. M. *Inorg. Chem.* **1994**, *33*, 4609.

(9) (a) Reger, D. L.; Pascui, A. E.; Smith, M. D.; Jezierska, J.; Ozarowski, A. *Inorg. Chem.* **2012**, *51*, 7966. (b) Reger, D. L.; Foley, E. A.; Watson, R. P.; Pellechia, P. J.; Smith, M. D. Grandjean, F.; Long, G. J. *Inorg. Chem.* **2009**, *48*, 10658. (c) Reger, D. L.; Pascui, A. E.; Smith, M. D.; Jezierska, J.; Ozarowski, A. *Inorg. Chem.* **2012**, *51*, 11820. (d) Reger, D. L.; Watson, R. P.; Smith, M. D.; Pellechia, P. J. *Organometallics*, **2005**, *24*, 1544. (e) Reger, D. L.; Pascui, A. E.; Pellechia, P. J.; Smith, M. D. *Inorg Chem.* **2013**, *52*, 11638.

(10) The crystallographic unit cell of these acetonitrile solvated compounds contain two independent $[Cu_2(\mu\text{-Cl})(\mu\text{-}\mathbf{L_m})_2]^{3+}$ cations.

(11) (a) *MestReNOVA* 5.2.5, Mestrelab Research S. L. **2008**. (b) SigmaPlot 11.0, Systat Software Inc. **2008**.

(12) Pfirrmann, S.; Limberg, C.; Herwig, C.; Knispel, C.; Braun, B.; Bill, E.; Stösser, R. *J. Am. Chem. Soc.* **2010**, *132*, 13684.

(13) For the compounds with large -*J*, e.g. $[Cu_2(\mu\text{-Br})(\mu\text{-}\mathbf{L_m}^*)_2](ClO_4)_3$, the temperature dependence of the chemical shifts is very small and δ_0 becomes critical.

(14) Sharples, K. M.; Carter, E.; Hughes, C. E.; Harris, K. D. M.; Platts, J. A.; Murphy, D. M. *Phys. Chem. Chem. Phys.* **2013**, *15*, 15214.

(15) (a) Neese, F. *ORCA - An ab initio, Density Functional and Semiempirical Program Package*, Version 2.9.1, **2012**. (b) Neese, F. - The ORCA program system WIREs, *Comput. Mol. Sci.* **2012**, *2*, 73.

(16) (a) Becke, D. A. *Phys. Rev. A* **1988**, *38*, 3098. (b) Perdew, J. P. *Phys. Rev. B* **1986**, *33*, 8822. (c) Perdew, J. P. *Phys. Rev. B.* **1986**, *34*, 7406. (d) Kendall, R. A.; Früchtl, H.A. *Theor. Chem. Acc.* **1997**, *97*, 158.

(17) (a) Schaefer, A.; Horn, H.; Ahlrichs, R. *J. Chem. Phys.* **1992**, *97*, 2571. (b) Ahlrichs, R. *et al*., unpublished results. The Ahlrichs auxiliary basis sets were obtained from the TurboMole basis set library under ftp.chemie.uni-karlsruhe.de/pub/jbasen.

(18) ORCA calculates two values for both axial and equatorial *b*-pyrazolyl hydrogens as the two sides of copper(II) coordination sphere are not equal in the X-Ray structure. The molecule is more symmetric in solution than in solid state; one axial (4H, red Figure 6.2) and one equatorial (4H, blue) *b*-pyrazolyl resonance is observed.

Chapter VII

Zinc(II) and Cadmium(II) Monohydroxide Bridged, Dinuclear Metallacycles:

A Unique Case of Concerted Double Berry Pseudorotation[6]

[6]Adapted with permission from Reger, D. L.; Pascui, A. E.; Pellechia, P. J.; Smith, M. D. *Inorg Chem.* **2013**, *52*, 11638-11649. DOI: 10.1021/ic402073d. Copyright 2013 American Chemical Society.

Introduction

The structure and molecular motion of self-assembled complexes of diamagnetic metal centers are of considerable interest.[1] The quest for the creation of artificial molecular machineries stimulated the design and synthesis of numerous organic molecules that resemble macroscopic machineries, such as rotors, motors and gyroscopes.[2] Recently it was proposed that metal-organic frameworks (MOFs) and discrete metallacyclic rotors might have superior properties compared to the more conventional organic rotors, in the sense that the conformational dynamics can be easily controlled using supramolecular metal-directed approaches.[3] Garcia-Garibay and co-workers recently studied the lattice dynamics of MOF-5, $Zn_4O(BDC\text{-}NH_2)_3$ (BDC = 1,4-benzenedicarboxylate), with the goal to control the internal dynamics of such systems, which ultimately "may open opportunities for the development of functional materials and artificial molecular machines."[4] In addition, there is major interest in the structure and solution behavior of zinc(II) and cadmium(II) hydroxide bridged dinuclear systems,[5] which stems from the existence of similar units in several dinuclear metallohydrolases.[6]

Over the past years I gained significant understanding of the solid state structure and magnetostructural correlations in single anion (F^-, Cl^-, Br^-, OH^-) bridged dinuclear metallacycles supported by bis(pyrazolyl)methane ligands, $\mathbf{L}_{\boldsymbol{m}}$, *m*-bis[bis(1-pyrazolyl)methyl]benzene and $\mathbf{L}_{\boldsymbol{m}}$*****, *m*-bis[bis(3,5-dimethyl-1-pyrazolyl)methyl]benzene (Scheme 7.1).[7,8] Reported are the synthesis, structure (both in solid state and solution) of three monohydroxide bridged metallacycles with these bis(pyrazolyl)methane ligands and the complex molecular motion of these compounds in solution, as studied by ^{1}H variable temperature (VT) NMR and saturation transfer experiments. The effect of trace amounts

of water in the solvent and the impact of methyl-substitution of the ligand on the conformational dynamics of the system is highlighted.

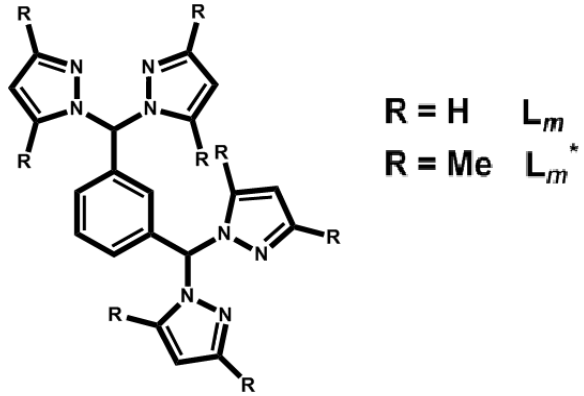

Scheme 7.1. Schematic drawing of the structure of $\mathbf{L}_m$ and $\mathbf{L}_m$*****. The ligands contain two bis(pyrazolyl)methane units connected by a 1,3-phenylene spacer.

Experimental Section

General Considerations. Standard Schlenk techniques were used for the synthesis of the hydroxide bridged compounds. The solvents were not dried prior to use. The ligands, $\mathbf{L}_m$[9] and $\mathbf{L}_m$*****[7a], were prepared following reported procedures. All other chemicals were purchased from Sigma-Aldrich or Strem Chemicals and used as received.

Crystals used for elemental analysis and mass spectrometry were removed from the mother liquor, rinsed with ether, and dried under vacuum, a process that removes the solvent of crystallization, if present.

^{1}H, ^{13}C and ^{113}Cd NMR spectra were recorded on a Varian Mercury/VX 300, Varian Mercury/VX 400, or Varian INOVA 500 spectrometer. All chemical shifts are in ppm and were referenced to residual nondeuterated solvent signals (^{1}H), deuterated solvent signals (^{13}C), or externally to $CdCl_2$ (^{113}Cd). To test the accuracy of the saturation transfer experiment a sample of N,N-dimethylacetamide diluted in toluene-d_8, was used to calculate k (rate constant), and $\Delta G^{\ddagger}$ for the rotational barrier about the amide bond. The

calculated values (25.0˚C: k = 0.53 s^{-1}, $\Delta G^{\ddagger}$ = 17.8 kcal/mol) are comparable with literature values (22.5˚C: k = 0.61 s^{-1}, $\Delta G_{OH}^{\ddagger}$ = 17.7 kcal/mol).[10]

Mass spectrometric measurements were obtained on a MicroMass QTOF spectrometer in an acid-free environment. Elemental analyses were performed on vacuum-dried samples by Robertson Microlit Laboratories (Ledgewood, NJ).

XSEED[11], POV-RAY[11] and MESTRENOVA[12] were used for the preparation of figures.

CAUTION! *Although no problems were encountered during this work with the perchlorate salts, these compounds should be considered potentially explosive!*[13]

$[Zn_2(\mu\text{-}OH)(\mu\text{-}L_m)_2](ClO_4)_3$, 1. To a methanolic solution (10 mL) of the ligand $\mathbf{L_m}$ (0.19 g, 0.51 mmol), NEt_3 (0.07 mL, 0.5 mmol) was added. The $Zn(ClO_4)_2 \cdot 6H_2O$ (0.19 g, 0.51 mmol) was dissolved in 4 mL of methanol and the ligand/amine solution was transferred by cannula into the zinc(II) salt solution. A white precipitate formed immediately. The reaction mixture was stirred for 5 hours. The crude product, 0.145 g (48%), was collected by cannula filtration, washed with 5 mL ether and dried under vacuum overnight. Single crystals suitable for X-ray studies were grown by vapor diffusion of Et_2O into 1 mL acetonitrile solutions of **1** and were mounted directly from the mother liquor as $\mathbf{1} \cdot CH_3CN$ (major form) and $\mathbf{1} \cdot 1.5CH_3CN$ (minor form). ^{1}H NMR (400 MHz, acetonitrile-d_3) at 20°C: δ 8.40/8.19 (s/s, 4H/4H, 5-H pz) 8.15 (s, 4H, $CH(pz)_2$), 7.56 (t, J = 8.0 Hz, 2H, 5-H C_6H_4), 7.48/6.64 (s/s, 4H/4H, 3-H pz), 6.63 (d, J = 12.0 Hz, 4H, 4,6-H C_6H_4), 6.52/6.42 (s/s, 4H/4H, 4-H pz), 4.75 (s, 2H, 2-H C_6H_4), -0.66 (s, 1H, Zn-(O)H-Zn). ^{13}C NMR (100.6 MHz, acetonitrile-d_3) at 20°C: δ 144.6 (broad, 3-C pz), 137.4 (1,3-C C_6H_4), 138.0/136.3 (5-C pz), 130.8 (5-C C_6H_4), 128.9 (4,6-C C_6H_4),

124.5 (2-C C_6H_4), 108.4 (4-H pz), 75.2 ($CH(pz)_2$). ^{13}C NMR (100.6 MHz, acetonitrile-d_3) at -40°C: δ 143.7/ 142.9 (3-C pz), 136.2 (1,3-C C_6H_4), 137.0/135.2 (5-C pz), 129.5 (5-C C_6H_4), 128.0 (4,6-C C_6H_4), 123.6 (2-C C_6H_4), 107.1/107.0 (4-H pz), 73.8 ($CH(pz)_2$). Anal. Calcd.(Found) for $C_{40}H_{37}Cl_3Zn_2N_{16}O_{13}$: C, 40.49 (40.15); H, 3.14 (3.21); N, 18.88 (18.75). MS ES(+) *m*/*z* (rel. % abund.) [assgn]: 1087 (1) $[Zn_2(\mathbf{L}_m)_2(OH)(ClO_4)_2]^+$, 903 (13) $[Zn(\mathbf{L}_m)_2(ClO_4)]^+$, 533 (30) $[Zn_2(\mathbf{L}_m)_2(ClO_4)_2]^{2+}$, 494 (27) $[Zn_2(\mathbf{L}_m)_2(OH)(ClO_4)]^{2+}$, 451 (10) $[Zn\mathbf{L}_mOH]^+$, 402 (100) $[Zn(\mathbf{L}_m)_2]^{2+}$, 371 (19) $[\mathbf{L}_m + H]^+$, 296 (48) $[Zn_2(\mathbf{L}_m)_2(OH)]^{3+}$.

$[Zn_2(\mu\text{-}OH)(\mu\text{-}L_m^*)_2](ClO_4)_3$, 2, was prepared similarly to compound **1** starting from $\mathbf{L}_m^*$ (0.25 g, 0.51 mmol), NEt_3 (0.070 mL, 0.51 mmol) and $Zn(ClO_4)_2{\cdot}6H_2O$ (0.19 g, 0.51 mmol). The reaction afforded 0.100 g of a white precipitate. Single crystals were grown the same way as crystals of **1**. The samples of crystals of **2** are contaminated by a poorly crystalline material that was not identified, and from which it could not be separated. The NMR spectra of these crystals of **2** indicates ca. 20% impurity, but the resonances of **2** can be assigned based on the NMR spectra of **1**, **3** and related compounds. ^{1}H NMR (300 MHz, acetonitrile-d_3) at 20°C: δ 7.68 (s, 4H, $CH(pz)_2$), 7.59 (t, J = 12 Hz, 2H, 5-H C_6H_4), 6.98 (d, J = 6 Hz, 4H, 4,6-H C_6H_4), 6.14/6.08 (s/s, 4H/4H, 4-H pz), 5.11 (s, 1H, 2-H C_6H_4), 2.57/2.42 (s/s, 12H/12H/, 5-H CH_3), 1.81/0.73 (s/s, 12H/12H/, 3-H CH_3), -1.15 (s, 1H, Zn-(O)H-Zn). ^{13}C NMR (100.6 MHz, acetonitrile-d_3) at 20°C: δ 153.7/151.7/146.4/144.9 (3,5-C pz), 135.4 (1,3-C C_6H_4), 130.2 (5-C C_6H_4), 128.4 (4,6-C C_6H_4), 124.2 (2-C C_6H_4), 108.8/106.9 (4-C pz), 67.5 ($CH(pz)_2$), 15.3/10.4 (3-CH_3), 10.0/9.9 (5-CH_3). Anal. Calcd.(Found) for $C_{56}H_{69}Cl_3Zn_2N_{16}O_{13}$: C, 47.66 (45.43); H, 4.93 (4.73); N, 15.88 (15.13). MS ES(+) *m*/*z* (rel. % abund.) [assgn]: 1311 (1)

$[Zn_2(\mathbf{L_m}^*)_2(OH)(ClO_4)_2]^+$, 606 (8) $[Zn_2(\mathbf{L_m}^*)_2(OH)(ClO_4)]^{2+}$, 514 (20) $[Zn(\mathbf{L_m}^*)_2]^{2+}$, 483 (92) $[\mathbf{L_m}^* + H]^+$, 371 (25) $[Zn_2(\mathbf{L_m}^*)_2(OH)]^{3+}$. HRMS: ES^+ (*m/z*): $[Zn_2(\mathbf{L_m}^*)_2(OH)(ClO_4)_2]^+$ calcd. for $[C_{56}H_{68}Cl_2Zn_2O_9N_{16}]^+$ 1311.3358; found 1311.3331.

$[Cd_2(\mu\text{-}OH)(\mu\text{-}L_m^*)_2](ClO_4)_3$, 3, was prepared similarly to compound **2,** in a total of 15 mL tetrahydrofuran (THF) solution, starting from $Cd(ClO_4)_2{\cdot}6H_2O$ (0.22 g, 0.51 mmol). The reaction afforded 0.240 g (62%) of crude product. Single crystals were grown similarly as crystals of **2** and were mounted directly from the mother liquor as **3**·$4CH_3CN$. ^{1}H NMR (400 MHz, acetonitrile-d_3) at 20°C: 7.66 (s, 4H, $CH(pz)_2$), 7.59 (t, J = 8.0 Hz, 2H, 5-H C_6H_4), 6.88 (d, J = 8.0 Hz, 4H, 4,6-H C_6H_4), 6.20/6.11 (s/s, 4H/4H, 4-H pz), 5.27 (s, 2H, 2-H C_6H_4), 2.55/2.46 (s/s, 12H/12H, 5-H CH_3), 2.02/1.25 (s/s, 12H/12H, 3-H CH_3), -2.43 (s, $J_{Cd\text{-}H(O)}$ = 24 Hz, 1H, Cd-(O)H-Cd). ^{13}C NMR (100.6 MHz, acetonitrile-d_3) at 20°C: δ 154.0/152.1/146.4/145.7 (3,5-C pz, $J_{C\text{-}Cd}$ = 4-8 Hz), 136.4 (1,3-C C_6H_4), 130.8 (5-C C_6H_4), 129.3 (4,6-C C_6H_4), 125.7 (2-C C_6H_4), 108.4/107.2 (4-C pz), 68.4 ($CH(pz)_2$), 14.6/11.4 (3-CH_3), 11.0/10.7 (5-CH_3). ^{113}Cd NMR (88.8 MHz, acetonitrile-d_3) at 20°C: δ 79.9 (d, $J_{Cd\text{-}H(O)}$ = 29 Hz, $J^{111}{}_{Cd\text{-}}{}^{113}{}_{Cd}$ = 174 Hz); proton decoupled spectra δ 79.9 (s, $J^{111}{}_{Cd\text{-}}{}^{113}{}_{Cd}$ = 172 Hz). Anal. Calcd.(Found) for $C_{56}H_{69}Cl_3Cd_2N_{16}O_{13}$: C, 44.68 (44.63); H, 4.62 (4.38); N, 14.93 (14.91). MS ES(+) *m/z* (rel. % abund.) [assgn]: 1405 (2) $[Cd_2(\mathbf{L_m}^*)_2OH(ClO_4)_2]^+$, 653 (30) $[Cd_2(\mathbf{L_m}^*)_2OH(ClO_4)]^{2+}$, 402 (100) $[Cd_2(\mathbf{L_m}^*)_2OH]^{3+}$.

Crystallographic Studies. X-ray diffraction intensity data were collected on a Bruker SMART APEX CCD-based diffractometer (Mo Kα radiation, λ = 0.71073 Å)[14]. Raw area detector data frame processing was performed with the SAINT+ and SADABS programs.[14] Final unit cell parameters were determined by least-squares refinement of

large sets of strong reflections taken from each data set. Direct methods structure solution, difference Fourier calculations and full-matrix least-squares refinement against F^2 were performed with SHELXTL[15]. Non-hydrogen atoms were refined with anisotropic displacement parameters, the exception being disordered species. The hydrogen atoms were placed in geometrically idealized positions and included as riding atoms. Details of the data collection are given in Table 7.1.

Table 7.1. Selected Crystal Data and Structure Refinement for **1-3.**

	1·CH$_3$CN	**1·1.5CH$_3$CN**	**2**	**3·4CH$_3$CN**
Formula	$C_{42}H_{40}Cl_3N_{17}O_{13}Zn_2$	$C_{43}H_{41.50}Cl_3N_{17.50}O_{13}Zn_2$	$C_{56}H_{69}Cl_3N_{16}O_{13}Zn_2$	$C_{64}H_{81}Cl_3N_{20}O_{13}Cd_2$
Fw, g mol^{-1}	1228.0	1248.53	1411.36	1669.64
Cryst. Syst.	Triclinic	Monoclinic	Triclinic	Triclinic
Space group	$P\ \bar{1}$	$P\ 2_1/m$	$P\ \bar{1}$	$P\ \bar{1}$
T, K	150(2)	150(2)	295(2)	100(2)
a, Å	14.2332(5)	10.3497(9)	11.3390(7)	10.8807(5)
b, Å	16.8433(6)	42.817(4)	12.8304(8)	13.4098(6)
c, Å	21.8771(8)	11.9166(9)	13.3422(8)	13.9681(7)
α, deg	97.669(1)	90	116.578(1)	78.558(1)
β, deg	102.779(1)	101.797(2)	99.107(1)	70.097(1)
γ, deg	94.881(1)	90	105.748(2)	85.428(1)
V, Å^3	5033.3(3)	5169.2(7)	1580.12(17)	1878.08(15)
Z	4	4	1	1
R_1 ($I > 2\sigma(I)$)	0.0602	0.0679	0.0503	0.0347
wR_2 ($I > 2\sigma(I)$)	0.1418	0.1516	0.0935	0.0926

Crystals of **1**·CH_3CN (major product) and **1**·$1.5CH_3CN$ (minor product) were found in the same crystallization tube. Compound **1**·CH_3CN crystallizes in the triclinic system. The space group $P\ \bar{1}$ was determined by the successful solution and refinement of the structure. The asymmetric unit consists of two crystallographically independent $[Zn_2(\mu\text{-OH})(\mu\text{-}\mathbf{L_m})_2]^{3+}$ cations, six independent perchlorate anions and two independent acetonitrile molecules. Atoms of both cations were labeled similarly, distinguished by the label suffixes A or B. The hydroxide protons of the bridging OH^- groups (O1A and O1B)

could not be located by Fourier difference synthesis, and were not calculated. There are several small electron density peaks around each bridging oxygen atom, but none could be reasonably refined. These hydroxide protons may be disordered. The bridging hydroxide oxygen atom of cation "B" (O1B) showed an elongated displacement ellipsoid if refined with a single position (U_3/U_1 = 5.5) and was modeled as being split equally over two positions (O1B1 and O1B2). Positional disorder was modeled for two of the six perchlorates, using geometric restraints. Their total populations were constrained to sum to unity. Compound **1**·1.5CH_3CN crystallizes in the space group $P2_1/m$ of the monoclinic system. The asymmetric unit consists of half of each of two independent $[Zn_2(\mu\text{-}OH)(\mu\text{-}\mathbf{L}_{\boldsymbol{m}})_2]^{3+}$, three independent perchlorate anions and 1.5 independent acetonitrile molecules. Cation Zn1 is located on a crystallographic inversion center; cation Zn2 is located on a crystallographic mirror plane. The half-acetonitrile lies in a mirror plane. The hydroxide group of the centrosymmetric cation is disordered across the inversion center and was refined as half-occupied. Two disordered perchlorate anions were refined with two distinct orientations with the aid of geometric restraints. The bridging hydroxyde protons (O1 and O2) could not be located by Fourier difference synthesis, and were not calculated.

Compound **2** crystallizes in the triclinic system. The space group P $\bar{1}$ was determined by the successful solution and refinement of the structure. The asymmetric unit consists of half of one $[Zn_2(\mu\text{-}OH)(\mu\text{-}\mathbf{L}_{\boldsymbol{m}}\mathbf{*})_2]^{3+}$ cation located on an inversion center, one disordered ClO_4^- anion on a general position (Cl2), and half of another ClO_4^- anion which is disordered across an inversion center (Cl1). Perchlorate Cl2 was refined with three disorder components. The sum of the occupancies of the three components initially

refined to near unity; subsequently the occupancies were fixed near those values. Because of its location on an inversion center, only half of perchlorate Cl1 is present in the asymmetric unit. Cl1 was refined with two components, each with a fixed occupancy of 0.25. Cl-O and O-O distance restraints were used to maintain a chemically reasonable geometry for each component. Upon cooling to 100 K, there is a visible change in the diffraction pattern. Some diffraction maxima appear split, and some very weak additional peaks appear. However, because of the small size and weak diffracting power of the available crystals, the low-temperature form could not be structurally characterized.

Compound **3**·4CH_3CN crystallizes in the triclinic system. The space group P $\bar{1}$ was confirmed by the successful solution and refinement of the structure. The asymmetric unit consists of half of one [Cd_2(μ-OH)(μ-$\mathbf{L}_{m}$*)$_2$] cation, (formally) 1.5 perchlorate ions, and a total of two acetonitrile molecules. The complex is located on an inversion center. The bridging oxygen atom O(1) is disordered across the inversion center and was refined with half-occupancy. A good position for the hydroxide proton H(1A) was located in a difference map and refined isotropically with a d(O-H) = 0.82(2) Å distance restraint, and half-occupancy. One of the two perchlorate ions is disordered across an inversion center and is therefore only half-occupied per asymmetric unit. This ion is further disordered within the asymmetric unit, and was modeled with two 1/4-occupied components [Cl(2)/Cl(3)]. The geometries of these components were restrained to be similar to that of the ordered perchlorate Cl(1). One of the two acetonitrile molecules is also disordered across an inversion center, and was modeled with three components with refined occupancies near 1/3. The total site occupancy was constrained to sum to unity.

Results

Synthesis. The metallacycles are synthesized from the corresponding metal perchlorate hexahydrate, $M(ClO_4)_2 \cdot 6H_2O$ [M = Zn(II), Cd(II)], and the ligand (**L**$_m$ or **L**$_m$*****) in the presence of a base, triethylamine (Scheme 7.2). Monohydroxide bridged compounds are isolated in all cases, even in the presence of excess NEt_3. Single crystals suitable for X-ray studies were grown by vapor diffusion of Et_2O into 1 mL acetonitrile solutions. For compound **1**, both **1**$\cdot CH_3CN$ (major) and **1**$\cdot 1.5CH_3CN$ (minor) form in this procedure. Compound **2**, while crystalline, could not be completely separated from a slight impurity.

$$2\ Zn(ClO_4)_2 \cdot 6\ H_2O + 2\ L_m \xrightarrow[-\ (HNEt_3)(ClO_4)]{+\ NEt_3} [Zn_2(\mu\text{-}OH)(\mu\text{–}L_m)_2](ClO_4)_3 \quad (1)$$

$$2\ M(ClO_4)_2 \cdot 6\ H_2O + 2\ L_m^* \xrightarrow[-\ (HNEt_3)(ClO_4)]{+\ NEt_3} [M_2(\mu\text{-}OH)(\mu\text{–}L_m^*)_2](ClO_4)_3 \quad M = Zn\ (2),\ Cd\ (3)$$

Scheme 7.2. Synthesis of the hydroxide bridged metallacycles.

Mass spectrometry. Positive-ion electrospray mass spectra (ESI^+-MS) of the three complexes are similar. In all spectra, clusters, such as $[M_2(\mathbf{L})_2OH(ClO_4)_2]^+$, $[M_2(\mathbf{L})_2OH(ClO_4)]^{2+}$ and $[M_2(\mathbf{L})_2OH]^{3+}$, [M = Zn(II) where **L** = **L**$_m$ and M = Zn(II), Cd(II) where **L** = **L**$_m$*****] corresponding to the complete hydroxide bridged metallacycles are observed, demonstrating the highly stable nature of these species.

Solid State Structures. Figure 7.1 presents the two independent cationic units of **1**$\cdot CH_3CN$. Similarly Figure 7.2 shows the two independent cationic units of compound **1**$\cdot 1.5CH_3CN$, one rests on a plane of symmetry whereas the other resides on an inversion center. The structure and numbering scheme for the cationic unit of **3**$\cdot 4CH_3CN$ is shown

in Figure 7.3; the overall structure and numbering scheme of **2** are the same. Selected bond lengths and bond angles are shown in Table 7.2.

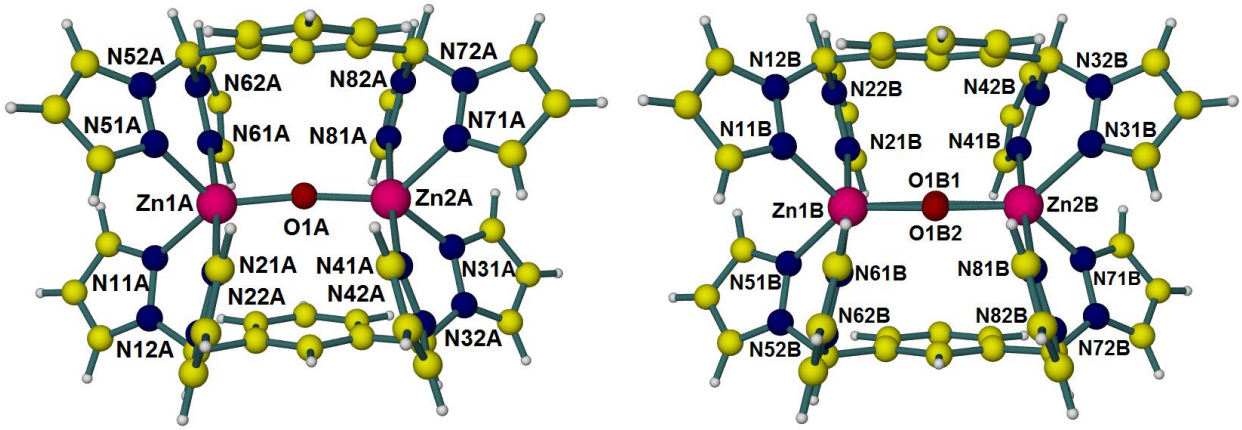

Figure 7.1. Structure of the two independent cationic unit of $[Zn_2(\mu\text{-OH})(\mu\text{-}\mathbf{L}_{\boldsymbol{m}})_2](ClO_4)_3\cdot CH_3CN$, **1**·$CH_3CN$.

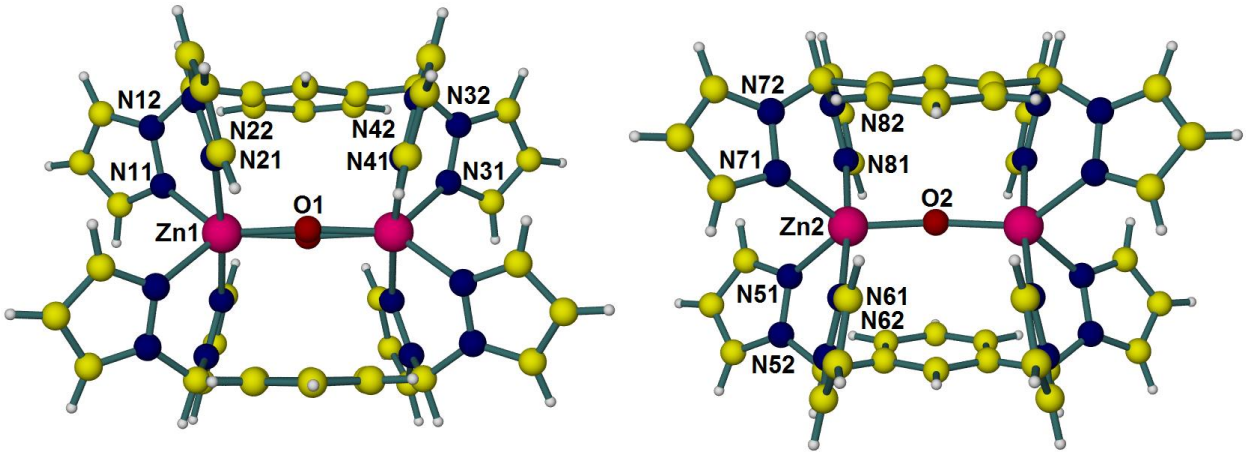

Figure 7.2. Structure of the two independent cationic units of $[Zn_2(\mu\text{-OH})(\mu\text{-}\mathbf{L}_{\boldsymbol{m}})_2](ClO_4)_3\cdot 1.5CH_3CN$, **1**·$1.5CH_3CN$.

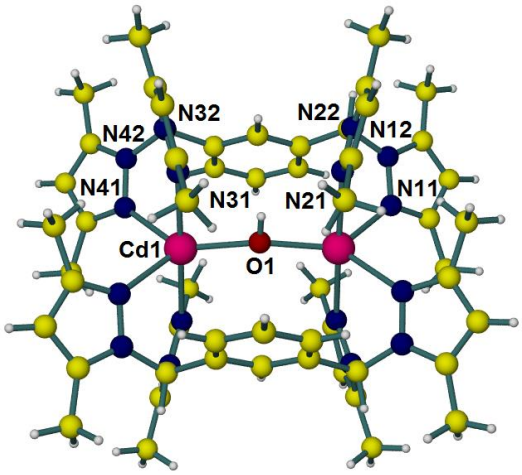

Figure 7.3. Structure of the cationic units of $[Cd_2(\mu\text{-}OH)(\mu\text{-}\mathbf{L}_m\mathbf{*})_2](ClO_4)_3\cdot 4CH_3CN$, $\mathbf{3}\cdot 4CH_3CN$. The 2-fold disorder of the bridging hydroxide is removed for clarity.

The structures of the three metallacycles are very similar regardless of the bis(pyrazolyl)methane ligand used (Figure 7.4). The geometry around the metal centers in these complexes are distorted trigonal bipyramidal, as supported by the M-N bond lengths [e.g. $\mathbf{1}\cdot CH_3CN$, equatorial: Zn(1A)-N 2.085(4) Å, 2.101(5) Å; axial: Zn(1A)-N, 2.137(4) Å, 2.198(4) Å, bond angles [e.g. $\mathbf{1}\cdot CH_3CN$**,** axial-axial: N-Zn(1A)-N 175.12(18)˚; equatorial-equatorial: N-Zn(1A)-N 98.57(18)˚; N-Zn(1A)-O(1A) 128.35(18)˚, 132.23(18)˚, equatorial-axial: N-Zn(1A)-N 84.93(17)˚, 89.51(17)˚, 92.93(17)˚, 86.47(17)˚] and τ_5[16] values (0.63-0.73).

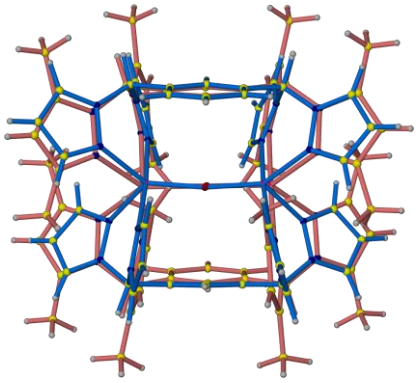

Figure 7.4. Superimposed cationic units of $[Zn_2(\mu\text{-}OH)(\mu\text{-}\mathbf{L}_m)_2](ClO_4)_3$ and $[Zn_2(\mu\text{-}OH)(\mu\text{-}\mathbf{L}_m\mathbf{*})_2](ClO_4)_3$.

Table 7.2. Selected bond lengths and bond angles for $[Zn_2(\mu\text{-}OH)(\mu\text{-}\mathbf{L}_m)_2](ClO_4)_3\cdot CH_3CN$, **1**·$CH_3CN$; $[Zn_2(\mu\text{-}OH)(\mu\text{-}\mathbf{L}_m)_2](ClO_4)_3\cdot 1.5CH_3CN$, **1**·$1.5CH_3CN$; $[Zn_2(\mu\text{-}OH)(\mu\text{-}\mathbf{L}_m\mathbf{*})_2](ClO_4)_3$, **2**; $[Cd_2(\mu\text{-}OH)(\mu\text{-}\mathbf{L}_m\mathbf{*})_2](ClO_4)_3\cdot 4CH_3CN$, **3**·$4CH_3CN$.

Complex	**1·CH$_3$CN**	**1·1.5CH$_3$CN**	**2**	**3·4CH$_3$CN**
Temp, K	150(2)	150(2)	295(2)	100(2)
Metal Centers	Zn(1A)-Zn(2A) Zn(1B)-Zn(2B)	Zn(1)-Zn(1) Zn(2)-Zn(2)	Zn(1)-Zn(1)	Cd(1)-Cd(1)
M-O-M angle, deg	163.6(3) 164.8[a]	162.4(7) 167.2(5)	180	161.36(14)
M-O length, Å	1.961(4)/ 1.934(4) 1.960/ 1.967[b]	1.939[b] 1.9737(13)	2.0407(6)	2.1505[b]
Predicted M-O length, Å[c]	2.0	2.0	2.0	2.19
Average M-N length, Å	2.130/ 2.133 2.143/ 2.137	2.139 2.134	2.135	2.337
M···M distance, Å	3.855 3.889	3.831 3.923	4.0814	4.244
τ_5	0.72/0.73 0.63/0.68	0.65 0.65	0.72	0.72

[a]Average bond angle, due to disorder. [b]Average bond length, due to disorder. [c]Shannon radii, ref. 17.

The predicted values for the M-O(H) distances were calculated by summing the ionic radius of each metal center with the ionic radius of the hydroxide ion.[17] The calculated values are in good agreement with the measured M-O(H) distances. The Zn-O(H) distances for the $\mathbf{L}_m$ compound is slightly shorter than predicted, while the bulkier ligand $\mathbf{L}_m$***** compounds have longer bond lengths than predicted by 0.071-0.102 Å. These deviations indicate that the M-O(H) distances are influenced by the steric properties of the bis(pyrazolyl)methane ligand. The M-O-M angles, 163.6(3)/164.8˚ for **1**·CH_3CN, 162.4(7)/167.2(5)˚ for **1**·$1.5CH_3CN$, 180° for **2** and 161.36(14)˚ for **3**·$4CH_3CN$, are very large for a bridging hydroxide (commonly between 90-120˚).[5a,c] The ligands $\mathbf{L}_m$ and $\mathbf{L}_m$***** support the metallacyclic structures and influence the M···M nonbonding distance, resulting in large M-O-M angles.

Ambient Temperature NMR Studies. The ambient temperature ^{1}H and ^{13}C NMR spectra of **1-3** revealed that the dinuclear structure remains intact in acetonitrile solution, as reported previously with the fluoride bridged metallacycles, $[Zn_2(\mu\text{-}F)(\mu\text{-}\mathbf{L})_2](BF_4)_3$ (**L** = $\mathbf{L}_m$ or $\mathbf{L}_m$*).[6] The presence of a highly symmetric species is indicated by the ^{1}H NMR spectra in Figure 7.5 of $[Zn_2(\mu\text{-}OH)(\mu\text{-}\mathbf{L}_m)_2](ClO_4)_3$, **1** (a) and $[Cd_2(\mu\text{-}OH)(\mu\text{-}\mathbf{L}_m\text{*})_2](ClO_4)_3$, **3** (b), which show three resonances for the ligand 1,3-substituted phenylene spacer (e.g. **1**: 7.56, 6.63 and 4.75 ppm) and one for the methine hydrogens (e.g. **1**: 8.15 ppm).

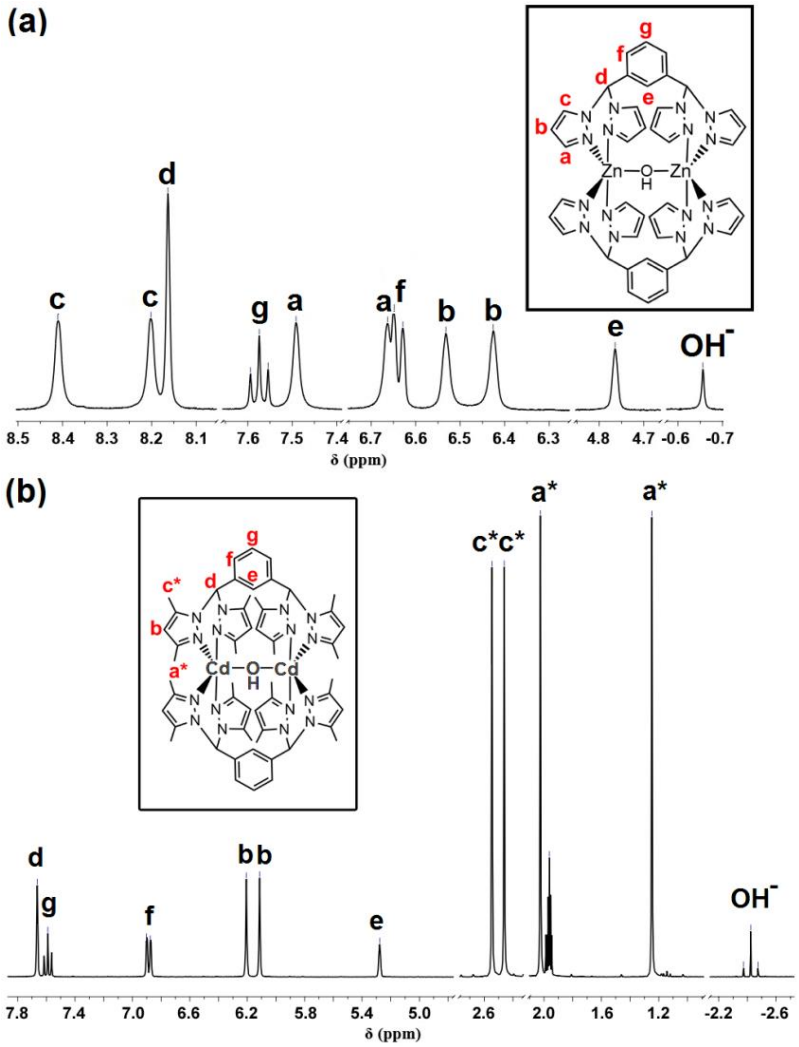

Figure 7.5. Ambient temperature ^{1}H NMR spectra of $[Zn_2(\mu\text{-}OH)(\mu\text{-}\mathbf{L}_m)_2](ClO_4)_3$, **1** (a) and $[Cd_2(\mu\text{-}OH)(\mu\text{-}\mathbf{L}_m\text{*})_2](ClO_4)_3$, **3** (b).

For the pyrazolyl-ring hydrogen atoms, two distinct sets of equal intensity resonances are observed. The 4(*b*)-pyrazolyl hydrogens of **1** can be found at 6.52 and 6.42 ppm, the 5(*c*)-pyrazolyl hydrogens are at 8.40 and 8.19 ppm, while the 3(*a*)-pyrazolyl hydrogens are at 7.48 and 6.64 ppm. The resonances for the *c**- and *a**-methyl groups are at 2.57, 2.42, 1.81 and 0.73 ppm for **2**, and at 2.55, 2.46, 2.02 and 1.25 ppm for **3** respectively. For all compounds, one pyrazolyl resonance is highly shielded. These hydrogens correspond to one of the axial pyrazolyl hydrogens or methyl groups that are pointing toward the phenylene spacers (Figure 7.6). This assignment makes the 3(*a*)/*a**- and 5(*c*)/*c**- positions distinguishable by ^{1}H NMR spectroscopy.

The resonances corresponding to the bridging OH^- are located at -0.66 ppm (**1**), -1.15 ppm (**2**) and -2.43 ppm (**3**). Similar assignments were made in Co(III) dimers by Bosnich *et al.*, where the hydroxide resonance was found in the range 0.57 to -2.42 ppm in CD_3CN solution.[18]

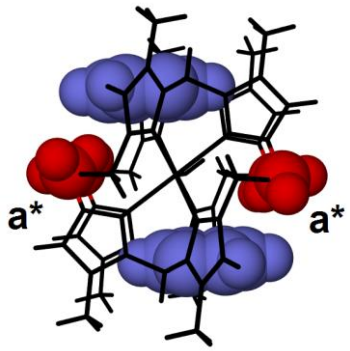

Figure 7.6. Shielded *a** methyl groups in the structure of $[Cd_2(\mu\text{-}OH)(\mu\text{-}\mathbf{L_m*})_2](ClO_4)_3$, **3** (red = methyl group; blue = phenylene spacer).

The retention of the solid state structure in solution was also confirmed by measuring the diffusion coefficient for complex **1** by pulsed field-gradient spin-echo NMR (PFGSE NMR).[19] The hydrodynamic radius based on the diffusion coefficient from

this experiment is 8.93 Å, similar to the maximum radius for the dinuclear unit, calculated from the crystal structure of **1**, 8.20 Å.

At room temperature, the ^{13}C NMR spectrum of **1** shows that the pyrazolyl resonances are very broad and the 5(*c*), 144.6 ppm, as well as the 4(*b*), 108.4 ppm, pyrazolyl resonances coalesced. At -40°C two sharp resonances are observed for each pyrazolyl hydrogen: 5(*c*) 143.7/142.9 ppm, 3(*a*) 137.00/135.22 ppm, 4(*b*) 107.14/107.00 ppm (Figure 7.7).

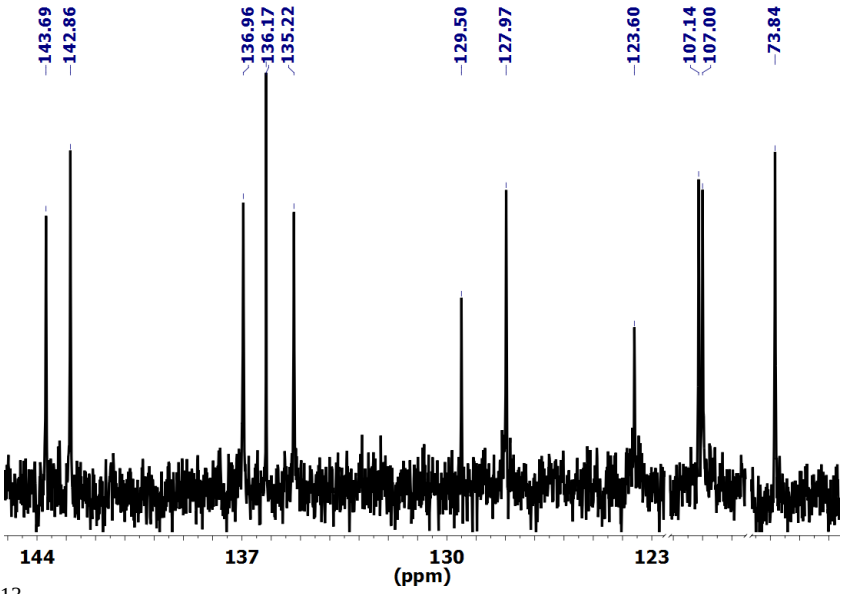

Figure 7.7. ^{13}C NMR spectra of $[Zn_2(\mu\text{-}OH)(\mu\text{-}\mathbf{L}_{\boldsymbol{m}})_2](ClO_4)_3$ at -40°C.

The ^{13}C and ^{113}Cd NMR spectra of **3** demonstrate several interesting features. The ^{13}C NMR spectrum shows coupling of the 3(*a*)- and 5(*c*)-pyrazolyl carbons with the cadmium(II) centers, $J_{C\text{-}Cd}$ = 4-8 Hz, while in the ^{113}Cd NMR spectrum the coupling of the cadmium(II) centers to the bridging hydroxide hydrogen can be observed (Figure 7.8). Without proton decoupling a doublet is observed at 79.9 ppm; the coupling constant, $J_{Cd\text{-}H(O)}$ = 29 Hz, is the same as the coupling constant observed for the cadmium(II) satellites in the ^{1}H NMR spectrum, $J_{(O)H\text{-}Cd}$ = 32 Hz (Fig. 7.8b). The proton decoupled

^{113}Cd NMR spectra of **3** shows only a singlet. Particularly interesting and important features are the $^{111/113}$Cd satellites in both coupled and decoupled spectra ($J^{111}_{Cd-}{}^{113}_{Cd}$ = 173 Hz, both of these spin ½ isotopes are about 13% abundant).

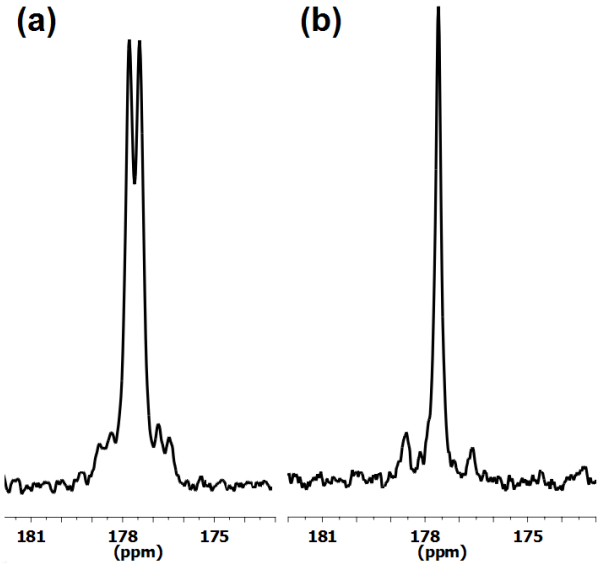

Figure 7.8. ^{113}Cd NMR of $[Cd_2(\mu\text{-}OH)(\mu\text{-}\mathbf{L}_m\mathbf{*})_2](ClO_4)_3$, **3**: (a) proton coupled, (b) proton decoupled.

Variable-temperature ^{1}H NMR Studies. The broad or coalesced pyrazolyl hydrogen resonances observed at ambient temperature in the ^{1}H and ^{13}C NMR spectra of **1** are indicative of a dynamic process in solution. The variable-temperature ^{1}H NMR spectra of **1** over the liquid range of CD_3CN, Figure 7.9, show major changes, confirming that the complex is indeed dynamic on the NMR time scale in solution. A trace amount of H_2O, present in the deuterated solvent, was observed in all spectra. The relative amount of water in these experiments, an important issue (vide infra), was defined as the integral of the H_2O resonance divided by the integral of the *e* resonance at 25°C, a ratio that is equal to 5 for the data in Figure 7.9. Under similar conditions, the resonances in the ^{1}H NMR spectra of compounds **2** and **3** remain sharp up to 75°C, indicating the lack of a similar dynamic process in these complexes.

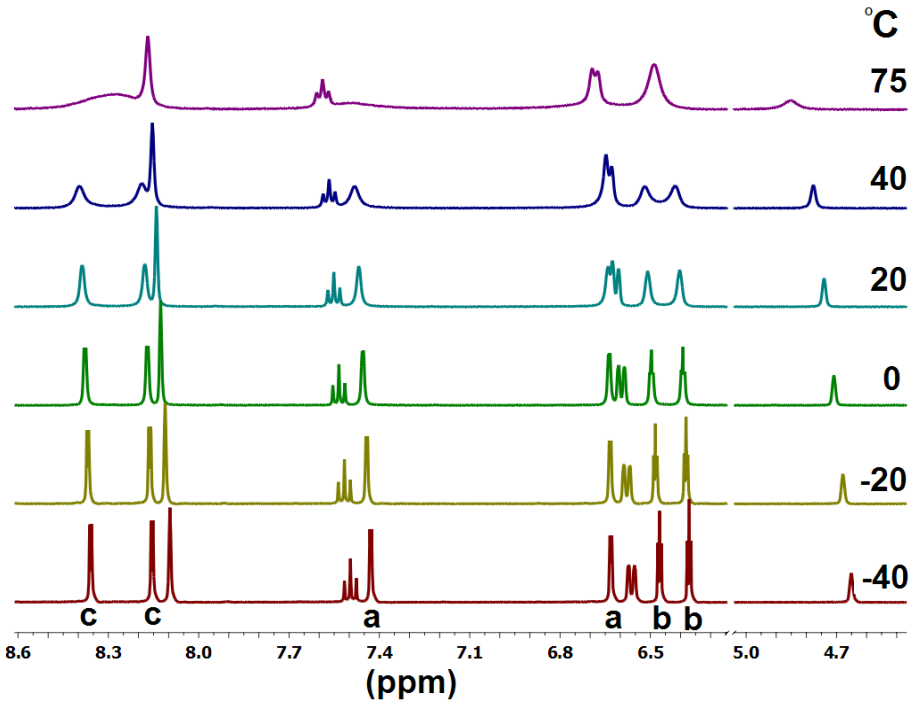

Figure 7.9. Variable temperature ^{1}H NMR spectra of $[Zn_2(\mu\text{-}OH)(\mu\text{-}\mathbf{L}_m)_2](ClO_4)_3$ (**1**) from -40 to 75˚C in CD_3CN.

For **1**, the pyrazolyl resonances assigned to the 3(*a*)/5(*c*) positions were resolved as doublets and the 4(*b*) positions as triplets upon cooling the sample to -40˚C. At high temperature (75°C), the resonances corresponding to the nonequivalent pyrazolyl rings average, only one set of 4(*b*) and 5(*c*) and two very broad 3(*a*) resonances could be observed. The limiting high temperature spectrum could not be reached as the boiling point of CD_3CN is 81.6 ˚C.

The rate constant (k_{pz}) for the exchanging pyrazolyl resonances was calculated two different ways:[20]

(a) from the experimental data measuring the broadening in excess of the natural line width ($W_{1/2}$) before coalescence via eq 1 (Figure 7.10, left);

$$k = \pi \cdot W_{1/2} \qquad (1)$$

(b) by simulation of the exchanging resonances using the program DNMR as implemented in Spinworks[21] (Figure 7.10, right). The exchange of the 5(*c*)-pyrazolyl hydrogen atoms were simulated.

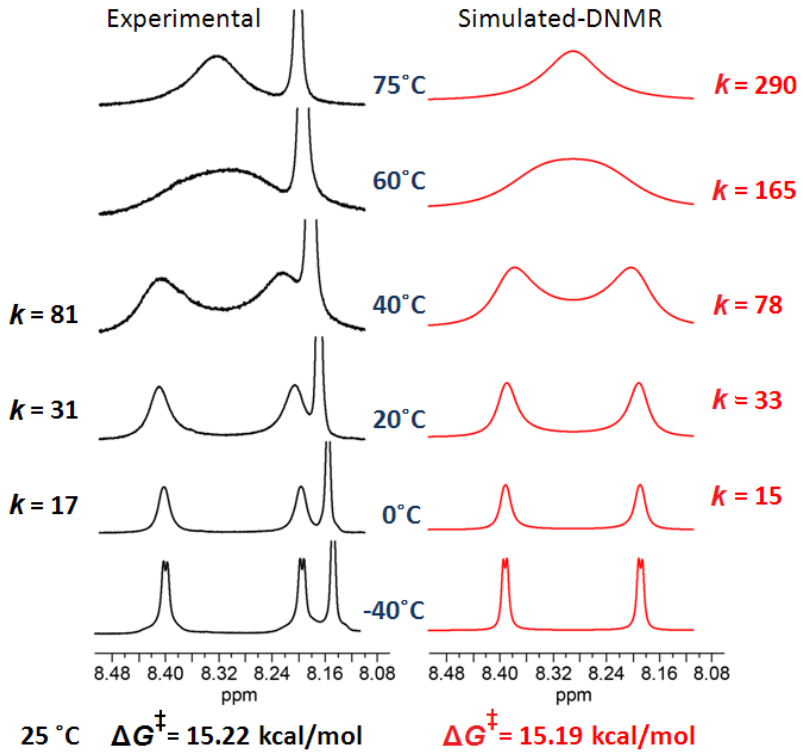

Figure 7.10. The 5(*c*)-pyrazolyl proton resonances of $[Zn_2(\mu\text{-OH})(\mu\text{-}\mathbf{L}_{\boldsymbol{m}})_2](ClO_4)$ (**1**). Left: experimental spectra, showing the rate constants at different temperatures and the calculated $\Delta G^{\ddagger}$ in black as determined using method (a). Right: simulated ^{1}H NMR spectra, corresponding rate constants and calculated $\Delta G^{\ddagger}$ shown in red using method (b).

The Gibbs energy of activation, $\Delta G_{pz}^{\ddagger}$, was calculated by applying the modified Eyring equation (eq 2) to the rate constants, where R is the universal gas constant and T is the temperature. The two methods (a, b) resulted in identical $\Delta G_{pz}^{\ddagger}$ values, 15.2(±0.2) kcal/mol at 25˚C.

$$\Delta G^{\ddagger} = RT\left(23.759 + \ln\frac{T}{k}\right) \qquad (2)$$

The enthalpy of activation, $\Delta H_{pz}^{\ddagger}$, 6.6 (±0.1) kcal/mol, and entropy of activation, $\Delta S_{pz}^{\ddagger}$, -28.8 (±0.4) cal/mol·K, were calculated from the Eyring plot (Figure 7.11). More than half of the value for $\Delta G_{pz}^{\ddagger}$ comes from the $T{\cdot}\Delta S_{pz}^{\ddagger}$ term (when $\Delta G_{pz}^{\ddagger} = \Delta H_{pz}^{\ddagger} - T{\cdot}\Delta S_{pz}^{\ddagger}$). The negative entropy value indicates that the transition state is highly organized.[22]

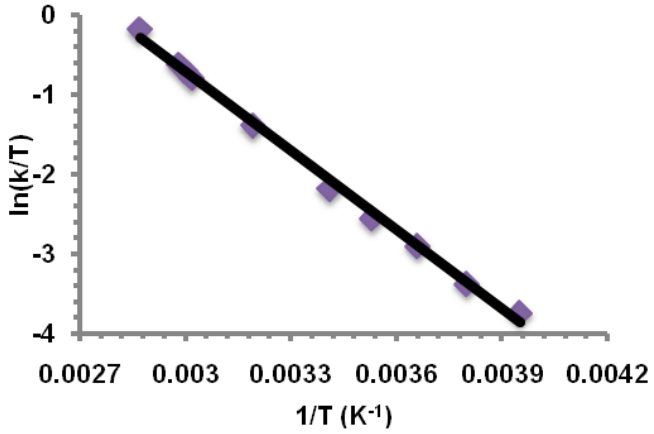

Figure 7.11. Eyring plot based on k_{pz} values from the simulation of the 5(*c*)-pyrazolyl resonances of $[Zn_2(\mu\text{-OH})(\mu\text{-}\mathbf{L}_{\boldsymbol{m}})_2](ClO_4)_3$ at different temperatures, where the slope = $-\Delta H^{\ddagger}/R$; and the intercept = $\Delta S^{\ddagger}/R + 23.759$. The data points were fitted to y = -3324.5x + 9.2673 (R^2 = 0.9968).

Impact of water concentration on the VT-NMR spectra. Similar VT-NMR studies were carried out on 5 different samples of **1**, where the concentration of the zinc(II) complex was maintained constant (3 mg in 800 μL CD_3CN), but the concentration of H_2O in the CD_3CN was varied. At 25˚C the line widths of the phenylene resonances are not affected significantly by the concentration of H_2O in the sample, but the pyrazolyl resonances undergo severe line width broadening in the presence of increased amounts of H_2O. As a consequence, the $\Delta G_{pz}^{\ddagger}$ is dependent on the concentration of trace amounts of water in the sample (Figure 7.12). Since the absolute concentration of the water is unknown, it is expressed as the ratio of the integral of the

H_2O resonance divided by the integral of the $\mathbf{L}_{m}$ ligand *e* resonance at 25ºC. Drying the CD_3CN by vacuum distillation from P_2O_5 yielded the lowest ratio of 0.6.

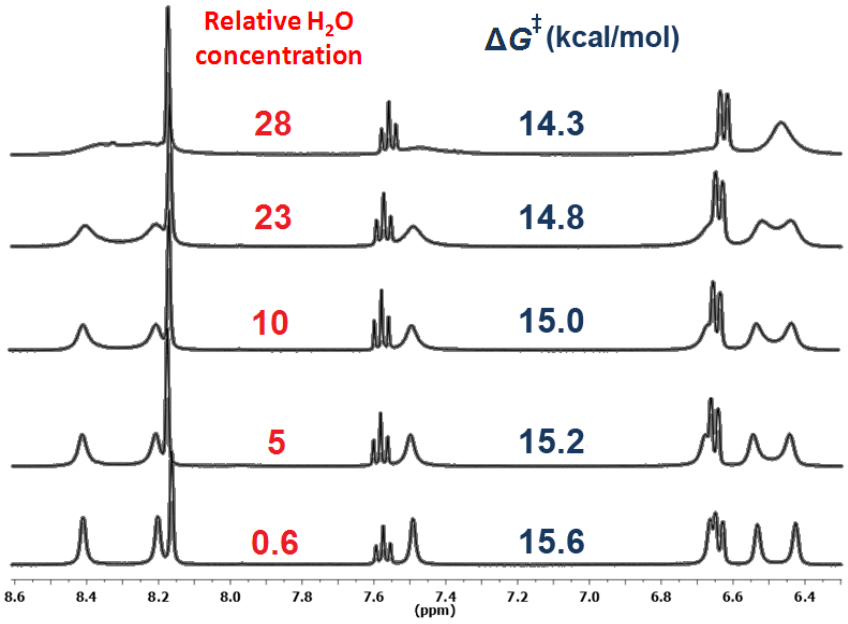

Figure 7.12. Fragment of the ^{1}H NMR spectra of five different samples of $[Zn_2(\mu\text{-}OH)(\mu\text{-}\mathbf{L}_{m})_2](ClO_4)_3$ (**1**) in CD_3CN at 25˚C that differ only in the relative H_2O concentration.

The plot of $\Delta G_{pz}^{\ddagger}$ vs. the relative water concentration reveals a linear relationship (Figure 7.13). This dependence of $\Delta G_{pz}^{\ddagger}$ on the water concentration in the sample indicates that water acts to accelerate the process. The $\Delta H_{pz}^{\ddagger}$ and $\Delta S_{pz}^{\ddagger}$ were found by creating the Eyring plot from the variable temperature data for each sample, these activation parameters are shown in Table 7.3.

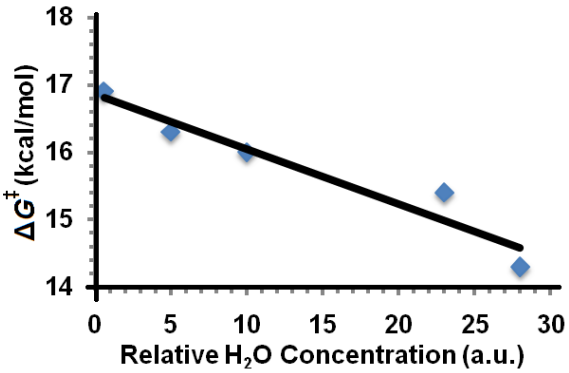

Figure 7.13. Relationship between the relative H_2O concentration (five samples) and $\Delta G_{pz}^{\ddagger}$ for $[Zn_2(\mu\text{-OH})(\mu\text{-}\mathbf{L}_m)_2](ClO_4)_3$ (**1**) at 25˚C. The data points were fitted to y = -0.0811x + 16.86 (R^2 = 0.9278).

Table 7.3. Activation parameters at 25˚C calculated based on Eyring plot of simulated k_{pz} values for the pyrazolyl exchange in $[Zn_2(\mu\text{-OH})(\mu\text{-}\mathbf{L}_m)_2](ClO_4)_3$ (**1**) at five different H_2O concentrations [$c(H_2O)_{rel}$ = integral of H_2O resonance divided by integral of *e* resonance at 25˚C]. Also shown are the coalescence temperatures of the 5(*c*)-resonances, T_c.

Sample	$c(H_2O)_{rel}$	$\Delta H_{pz}^{\ddagger}$ (kcal/mol)	$\Delta S_{pz}^{\ddagger}$ (cal/mol·K)	$\Delta G_{pz}^{\ddagger}$ (kcal/mol)	T_c (ºC)
1	28	5.6 (±0.2)	-29.5 (±0.4)	14.3 (±0.3)	25
2	23	6.1 (±0.1)	-29.5 (±0.4)	14.8 (±0.2)	45
3	10	6.4 (±0.1)	-29.0(±0.3)	15.0 (±0.2)	56
4	5	6.6 (±0.1)	-28.8 (±0.4)	15.2 (±0.2)	62
5	0.6	7.1 (±1.2)	-28.7 (±4.4)	15.6 (±2.5)	70

Saturation Transfer NMR Experiments. Samples of complexes **1-3** in CD_3CN were subject to two different saturation transfer experiments. First the exchange of the axial and equatorial 3(*a*)-pyrazolyl hydrogens were targeted in **1** [$c(H_2O)_{rel}$ = 5], the same process studied in the VT-NMR experiments. In the second experiment the exchange of the H_2O hydrogens (from solvent) with the hydrogen of the bridging hydroxide group was studied in all three complexes.

During the saturation transfer experiments pairs of exchanging resonances are followed, for example in the first experiment the axial and equatorial 3(*a*)-pyrazolyl resonances of **1**. Saturation of one of the exchanging resonances results in a decrease in the intensity of the other resonance. This decrease in intensity is a function of irradiation

time. In the experiments, the irradiation time is increased in 0.25 second intervals until the intensity of the second resonance remains constant. The natural logarithm of this decrease in intensity is proportional to the rate constant (*k*).

Following literature methods,[23] the values of $\ln(I_i - I_\infty)$ against the irradiation time (*t*) were plotted, as seen on Figure 7.14, where I_i is the residual intensity of the exchanging resonance after intermediate amounts of irradiation times and I_∞ is the residual intensity of the exchanging resonance after complete saturation. The slope of this straight line gives $-(1/\tau_{1a})$, where τ_{1a} is the overall lifetime of the process, which includes the spin-lattice relaxation time (T_{1a}) and the lifetime of the equatorial 3(*a*)-pz proton in the axial 3(*a*)-pz site (τ_a). A standard inversion recovery experiment results in values of T_{1a}. By substitution of the known values into eq 3, $1/\tau_a$ was calculated, which is equal to *k* (eq. 4) if the equilibrium is first order. The $\Delta G^{\ddagger}$ was calculated by applying the modified Eyring equation to *k*.

$$\frac{1}{\tau_{1a}} = \frac{1}{\tau_a} + \frac{1}{T_{1a}} \qquad (3)$$

$$k = \frac{1}{\tau_a} \qquad (4)$$

The saturation transfer experiments targeting the pyrazolyl exchange was carried out at -40˚C, in order to study sharp and clearly separated resonances (Figure 7.14). The resulting $\Delta G_{pz}^{\ddagger}$ at -40˚C for the pyrazolyl exchange, 13.1(±0.2) kcal/mol, is in very good agreement with the one calculated from the VT-NMR experiment, $\Delta G_{pz}^{\ddagger}$ = 13.2(±0.2) kcal/mol at -40ºC for the same sample.

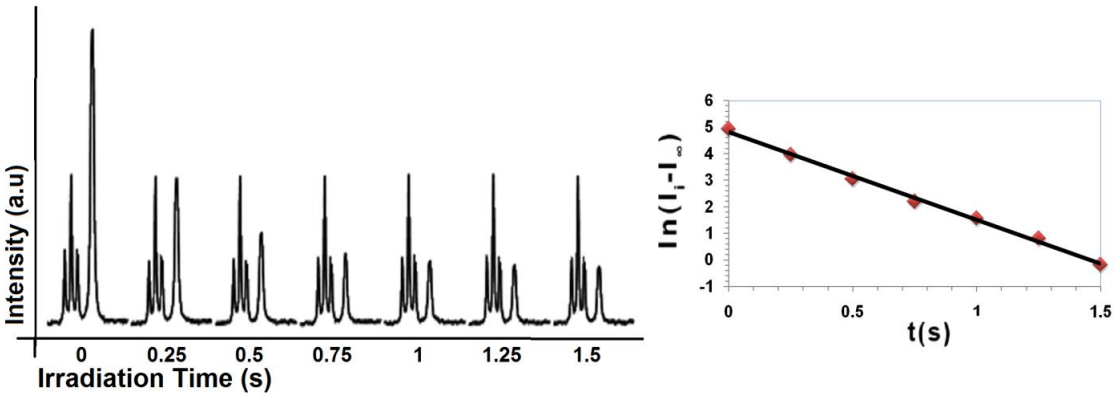

Figure 7.14. Saturation transfer experiment targeting the axial-equatorial pyrazolyl exchange in $[Zn_2(\mu\text{-}OH)(\mu\text{-}\mathbf{L}_{\boldsymbol{m}})_2](ClO_4)_3$ (**1**) at -40˚C. Left: decrease of one of the 3(*a*)-pz resonances as a function of the irradiation time of the other 3(*a*)-pz resonance. As the height of the pyrazolyl resonance decreases upon increased saturation, the height of the neighboring phenylene triplet (resonance *g*) remains constant, as it is not part of the exchange process. Right: linear plot of the natural logarithm of the 3(*a*)-pz resonance intensities vs. irradiation time. Data fitted to y = -3.3055x + 4.8098 (R^2 = 0.9965).

The second spin saturation experiment demonstrates the exchange of the hydrogens between H_2O, present in the solvent, and the bridging hydroxide (Figure 7.15). Upon complete saturation of the H_2O resonance, the bridging hydroxide resonance almost disappears at 25˚C.

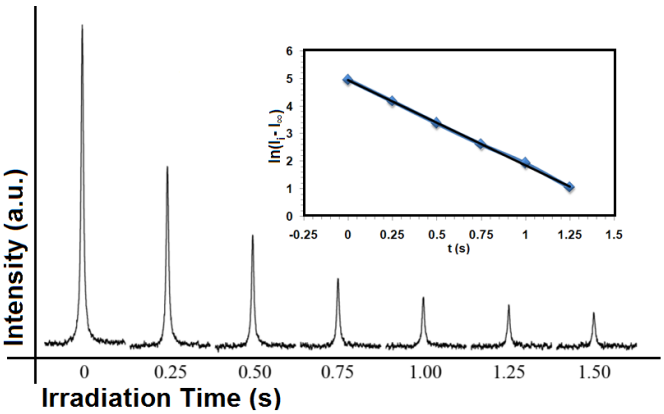

Figure 7.15. Saturation transfer experiment targeting the exchange of hydrogen between H_2O and OH^- for $[Zn_2(\mu\text{-}OH)(\mu\text{-}L_m)_2](ClO_4)_3$ (**1**) at 25˚C. The intensity of the bridging OH^- resonance decreases as a function of irradiation time at the H_2O site. Inset: linear plot of the natural logarithm of the OH^- resonance intensity vs. the irradiation time. Data fitted to y = -3.0839x + 4.944 (R^2 = 0.9994).

The $\Delta G_{OH}^{\ddagger}$ calculated from the saturation transfer experiment for the exchange of hydrogen from water and the bridging hydroxide is 16.8(±0.2) kcal/mol at 25˚C. For comparison, $\Delta G_{pz}^{\ddagger}$ is 15.2(±0.2) kcal/mol at 25˚C from the VT-NMR data shown in Figure 7.9. To directly compare $\Delta G_{OH}^{\ddagger}$ and $\Delta G_{pz}^{\ddagger}$ from saturation transfer experiments, the experiment performed at 25˚C was repeated at -40º C, resulting in $\Delta G_{OH}^{\ddagger}$ = 14.4(±0.2) kcal/mol (Figure 7.16). This value for $\Delta G_{OH}^{\ddagger}$ is larger by 1.3 kcal/mol compared to $\Delta G_{pz}^{\ddagger}$ = 13.1(±0.2) kcal/mol, as determined above.

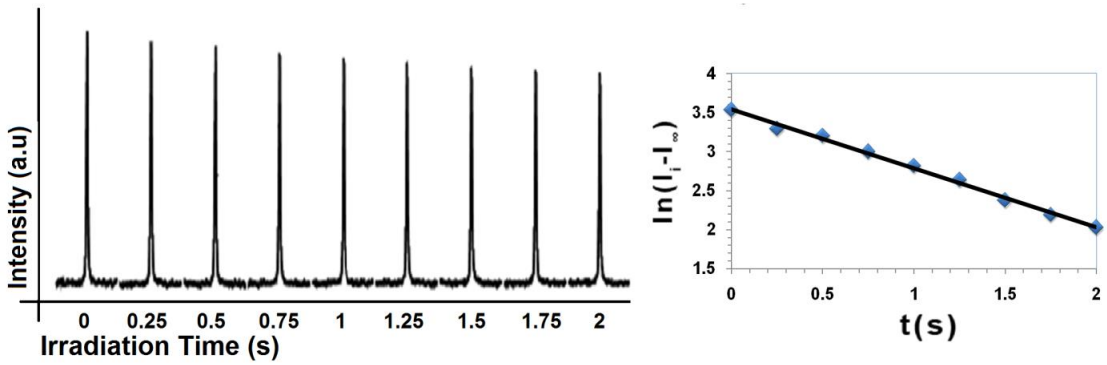

Figure 7.16. Saturation transfer experiment targeting the exchange of the hydrogens from H_2O and OH^- in $[Zn_2(\mu\text{-}OH)(\mu\text{-}\mathbf{L}_m)_2](ClO_4)_3$ (**1**) at -40˚C. Left: decrease of the OH^- resonance as a function of irradiation time at the H_2O site. Right: linear plot of the natural logarithm of the OH^- resonance intensities vs. irradiation time. Data fitted to y = -0.7581x + 3.5429 (R^2 = 0.9952).

Room temperature pyrazolyl saturation transfer experiments for **2** and **3** show that the pyrazolyl rings are not exchanging, but the H_2O-OH^- hydrogen exchange can be followed. The rate constants (**2**: k_{OH} = 0.70 s^{-1}; **3**: k_{OH} = 0.47 s^{-1}) at 25 ºC show that the hydrogen exchange is slower for $\mathbf{L}_m$***** compounds than for $\mathbf{L}_m$ compounds (**1**: k_{OH} = 2.85 s^{-1}). Consequently $\Delta G_{OH}^{\ddagger}$ increases by 1.0-1.3 kcal/mol (**2**, $\Delta G_{OH}^{\ddagger}$ = 17.7(±0.2) kcal/mol; **3**, $\Delta G_{OH}^{\ddagger}$ = 17.9(±0.2) kcal/mol vs. **1,** $\Delta G_{OH}^{\ddagger}$ = 16.8(±0.2) kcal/mol).

Discussion

Three diamagnetic monohydroxide bridged Zn(II) and Cd(II) complexes, of the type $[M_2(\mu\text{-OH})(\mu\text{-}\mathbf{L})_2](ClO_4)_3$, **L** = $\mathbf{L}_m$ or $\mathbf{L}_m$*****, were isolated. Coordination of the four pyrazolyl nitrogens from two different ligands oriented in a *syn* conformation [both bis(pyrazolyl)methane units on the same side of the linking phenylene ring] to two metal centers with a hydroxide directly connecting the metal centers results in the monobridged metallacyclic structures, with metal centers in distorted trigonal bipyramidal geometry.

These complexes were shown to retain this structure in solution and in gas phase according to ^{1}H, ^{13}C and ^{113}Cd NMR and positive-ion ESI^{+}-MS studies, respectively. For example, the observation in the ^{1}H NMR spectra of one type of phenylene and methine resonances and two types of pyrazolyl signals (two distinct sets of resonances for each type of pyrazolyl ring) are in complete agreement with the solid state structure, where the pyrazolyl rings are in the equatorial and axial plane of the trigonal bipyramidal arrangement around the metal centers. The bridging hydroxide proton resonances are characteristically located in the interval -0.66 to -2.43 ppm,[18] and in the case of **3** shows coupling to cadmium(II).

VT-NMR experiments often give important structural details about molecular motion in solution.[24] In this work, complex **1** was shown to be dynamic in solution by this method. Two sets of broad pyrazolyl resonances for each type of ring hydrogen can be observed at room temperature, which broaden and/or coalesce at higher temperatures. This behavior corresponds to the exchange of the axial and equatorial pyrazolyl rings. The activation parameters derived from the Eyring plot at different temperatures are $\Delta G_{pz}^{\ddagger}$ = 15.2(±0.2) kcal/mol, $\Delta H_{pz}^{\ddagger}$ = 6.6(±0.1) kcal/mol and $\Delta S_{pz}^{\ddagger}$ = -28.8(±0.4)

cal/mol·K at 25˚C. Most notably, this large negative $\Delta S_{pz}^{\ddagger}$ is unusual for most fluxional processes[24] and is indicative of a highly organized transition state.[22]

Saturation transfer experiments were also used to study the dynamics of **1.** Saturation of one pyrazolyl resonance of the exchanging pairs results in a decrease in the intensity of the second corresponding pyrazolyl resonance. This experiment was best carried out at -40˚C in order to avoid resonance overlap and to carry out the intensity measurements on narrow resonances, yielding $\Delta G_{pz}^{\ddagger}$ = 13.1(±0.2) kcal/mol, a value comparable to $\Delta G_{pz}^{\ddagger}$ from VT-NMR experiment of 13.2(±0.2) kcal/mol at -40˚C. These results show that this experiment is advantageous for the study of mutual-site exchange kinetics, especially when the coalescence temperature exceeds the boiling point of the solvent or the limiting low temperature spectra cannot be reached, basically allowing the analyses of *k* in the range ~10^{-3} to 10^{2} s^{-1}.

The most plausible mechanism for this relatively low barrier dynamic process, which exchanges the axial and equatorial pyrazolyl rings in the trigonal bipyramidal arrangement around the metal centers, involves the Berry pseudorotation at *both metal sites* using the bridging oxygen atom as the pivot ligand, coupled with the rotation of the ligands phenylene spacer by 180˚ (ring flip) along the $C_{methine}$-C_{Ph} bond (Figure 7.17). This movement results in the exchange of the axial (left, 1, 1*) and equatorial (left, 2, 2*) pyrazolyl rings through an approximately square pyramidal transition state at each metal, where the square bases are occupied by the interchanging pyrazolyl groups. The two, originally equatorial ligands move to the axial sites, reestablishing the trigonal bipyramidal geometry.[25] The main advantages of this mechanism are that no bond cleavage is necessary and relatively small bond angle changes are required around the

central zinc(II) ions, which support a relatively low $\Delta H_{pz}^{\ddagger}$. The transition state involves a distorted square pyramidal arrangement around each zinc(II), where the four pyrazolyl rings are approximately in the same plane, explaining the relatively large negative $\Delta S_{pz}^{\ddagger}$. Following the precedence of Chisholm *et al.*, describing the mechanism of a rearrangement for a very different dinuclear dynamic system ("Bloomington Shuffle"),[26] this new mechanism was termed the "*Columbia Twist and Flip*."

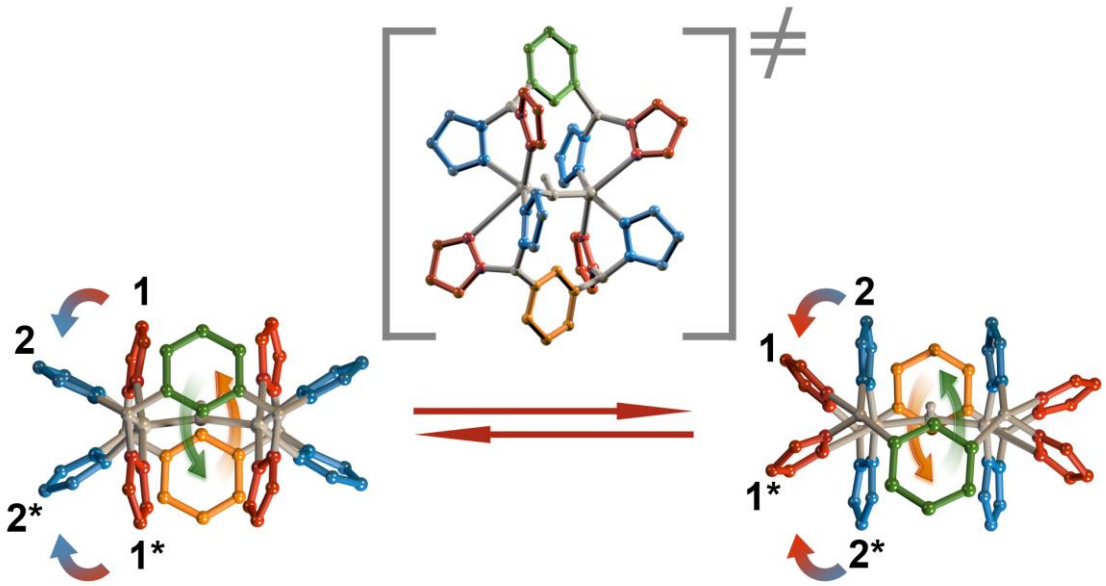

Figure 7.17. "Columbia Twist and Flip" involving the concerted double Berry pseudorotation of the pyrazolyl rings and the accompanied 180° flip of the phenylene linkers for $[Zn_2(\mu\text{-OH})(\mu\text{-}\mathbf{L_m})_2](ClO_4)_3$ (**1**). The 1 and 1* pz rings exchange with the 2 and 2* pz rings through a square pyramidal intermediate. The proposed intermediate (in brackets) is rotated 90° to show the approximate square pyramidal geometry around copper(II). Phenylene spacer top = green, bottom = orange; left side: axial pyrazolyl rings = red, equatorial pyrazolyl rings = blue, right side: axial pyrazolyl rings = blue, equatorial pyrazolyl rings = red.

The energy barrier for the Berry pseudorotation in PF_5 is ~3.1 kcal/mol.[27] The Columbia Twist and Flip is energetically more demanding than the unhindered rotation of fluorine atoms, because of the size of the pyrazolyl rings and the rigidity of the dinuclear

unit, leading to a barrier of 15.2(±0.2) kcal/mol. A mononuclear case similar to the dynamic behavior of $[Zn_2(\mu\text{-}OH)(\mu\text{-}\mathbf{L}_m)_2](ClO_4)_3$ (**1**) was studied by Moore *et al.*, $[ZnCl(\mathbf{L}_c)]ClO_4$ where L_c = 1,4,8,11-tetramethyl-1,4,8,11-tetra-azacyclotetradecane.[28] The zinc(II) center is five coordinate with four nitrogen donors and a chloride. In solution, as revealed by the ^{13}C NMR, the geometry is trigonal bipyramidal. Similarly to $[Zn_2(\mu\text{-}OH)(\mu\text{-}\mathbf{L}_m)_2](ClO_4)_3$, two ligand nitrogen atoms occupy axial and two equatorial sites. The compound undergoes Berry pseudorotation to equilibrate the nonequivalent sites with activation parameters, $\Delta G^{\ddagger}$ = 13.0(±1.0) kcal/mol, $\Delta H^{\ddagger}$ = 14.1(±0.7) kcal/mol and $\Delta S^{\ddagger}$ = 3.6 (±2.9) cal/mol·K at 25°C. The contribution to $\Delta G^{\ddagger}$ from the $\Delta S^{\ddagger}$ term for this mononuclear complex is low, indicating that in the case of **1** the large negative $\Delta S^{\ddagger}$ contribution is a result of the dinuclear structure and the rigidity of the system.

A somewhat similar dynamic process in a dinuclear system has been reported by Gardinier *et al.*,[29] for four-coordinate silver(I) metallacycles, such as $[Ag_2(\mu\text{-}\mathbf{L}_l)_2](BF_4)_2$, $\mathbf{L}_l$ = α,α,α',α'-tetra(pyrazolyl)lutidine. In this system, the data indicate that monomeric complexes are present in solution and are responsible for the dynamic behavior. While the results of the PFGSE NMR in their case supports this hypothesis, for compound **1** the calculated hydrodynamic radius based on the diffusion coefficient supports the dinuclear structure in solution, as do the observation of $[Zn_2(\mathbf{L}_m)_2(OH)(ClO_4)_2]^+$ and $[Zn_2(\mathbf{L}_m)_2(OH)(ClO_4)]^{2+}$ peaks in the mass spectrometric measurements. In addition, the $^{113}Cd/^{111}Cd$ coupling in **3** (Figure 7.8) definitively shows this sterically more hindered complex does not rapidly dissociate into monomers in solution.

The spectra of compounds **2** and **3** do not change at different temperatures. The space filling models of $[Zn_2(\mu\text{-}OH)(\mu\text{-}\mathbf{L}_m)_2](ClO_4)_3$ and $[Zn_2(\mu\text{-}OH)(\mu\text{-}\mathbf{L}_m\mathbf{*})_2](ClO_4)_3$,

Figure 7.18, illustrates that the substitution of the pyrazolyl rings in the 3(*a*) and 5(*c*) positions causes steric crowding. The methyl groups sterically restrict the rotation of the pyrazolyl rings; a square pyramidal transition state is very unlikely in this case. Similar tuning of the molecular motion is observed in molecular rotors, where substitution of bulky groups on the stator or rotator hinders the motion.[2-4]

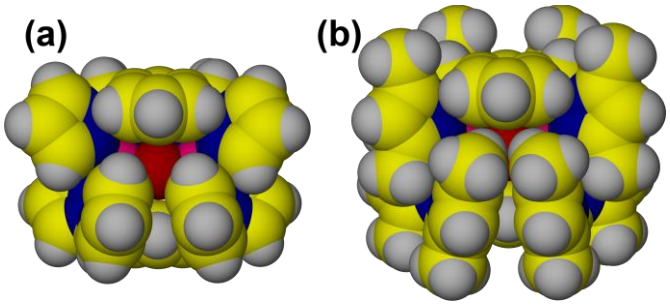

Figure 7.18. Space-filling representation of $[Zn_2(\mu\text{-}OH)(\mu\text{-}\mathbf{L}_{\boldsymbol{m}})_2](ClO_4)_3$ (a) and $[Zn_2(\mu\text{-}OH)(\mu\text{-}\mathbf{L}_{\boldsymbol{m}}\mathbf{*})_2](ClO_4)_3$ (b).

The pseudorotation is influenced by the concentration of trace amounts of water present in the solution of **1** in CD_3CN. The ^1H NMR spectra of samples with increased relative water concentration, at 25˚C, are broader, resulting in different activation parameters. There is a linear relationship between the water concentration and $\Delta G_{pz}^{\ddagger}$; as the water concentration is increasing $\Delta G_{pz}^{\ddagger}$ is decreasing (Figure 7.12 and 7.13).

Saturation transfer experiments demonstrated the exchange of the hydrogens between the water in the sample and the bridging hydroxide group, with $\Delta G_{OH}^{\ddagger}$ = 16.8(±0.2) kcal/mol at 25 ºC. This value is much larger than the barriers measured for the deprotonation of weak acids (1-2 kcal/mol)[30] and similar to, but clearly larger than the barrier of $\Delta G_{pz}^{\ddagger}$ = 15.2(±0.2) kcal/mol for the fluxional process. Supporting the contention that the two processes are independent is the observation of a similar exchange process of the water and the bridging hydroxide group hydrogens in **2** and **3**,

complexes for which no exchange of the pyrazolyl rings is observed by NMR. While independent, the two processes are likely related, especially given the similarity of the $\Delta G_{pz}^{\ddagger}$ values for **1**. Clearly the water stabilizes the intermediate in the pseudorotation process more than the ground state, and this interaction could also be involved in the hydrogen exchange.

The $[Zn_2(\mu\text{-}OH)(\mu\text{-}\mathbf{L_m})_2]^{3+}$ complex illustrates that more than one molecular motion can be incorporated into a single molecule (pseudorotation and arene ring flip) through coordination of organic building blocks to metal centers and that these motions can be controlled, similarly to purely organic rotors,[2-4] by substitution of the organic building blocks with bulky groups. In this case, the methyl substitution of the pyrazolyl rings effectively locks the geometry around the metal centers (compounds **2** and **3**). This metallacyclic system also allows the fine tuning of the barrier to the molecular motion, through careful control of the water concentration in the sample, as water influences the barrier to pseudorotation of the pyrazolyl rings.

Conclusions

The VT-NMR and saturation transfer experiments of $[Zn_2(\mu\text{-}OH)(\mu\text{-}\mathbf{L_m})_2](ClO_4)_3$ revealed an *unprecedented example of a concerted double Berry pseudorotation for a dinuclear complex*. As imposed by the ligand design, this pseudorotation must be accompanied by the 2-fold flip of the ligand's phenylene spacer along the $C_{methine}$-C_{Ph} bond – termed the Columbia Twist and Flip mechanism. The dynamic process that equilibrates the pyrazolyl rings is influenced by the concentration of water in the solvent; in addition, saturation transfer experiments demonstrate that the water hydrogen atoms exchange with the bridging hydroxide hydrogen. Saturation transfer experiments are a

valuable method in the determination of $\Delta G^{\ddagger}$ for the fluxional process that equilibrates the pyrazolyl rings in $[Zn_2(\mu\text{-}OH)(\mu\text{-}\mathbf{L}_{\boldsymbol{m}})_2](ClO_4)_3$. This method is of general use for the study of coordination compounds that show dynamic processes that may not be completely studied by more conventional variable temperature methods. Compounds $[Zn_2(\mu\text{-}OH)(\mu\text{-}\mathbf{L}_{\boldsymbol{m}}\mathbf{*})_2](ClO_4)_3$ and $[Cd_2(\mu\text{-}OH)(\mu\text{-}\mathbf{L}_{\boldsymbol{m}}\mathbf{*})_2](ClO_4)_3$ do not show the dynamic process involving the pyrazolyl-rings in solution because of steric crowding caused by the methyl group substitution, but do show the exchange between the water in the solvent and the bridging hydroxide group.

References

(1) Selected reviews: (a) Piguet, C. *Chem. Commun.* **2010**, *46*, 6209. (b) Zhang, J.-P.; Huang, X.-C.; Chen, X.-M *Chem. Soc. Rev.* **2009**, *38*, 2385. (c) Moulton, B.; Zaworotko, M. J. *Chem. Rev.* **2001**, *101*, 1629. (d) Garcia-Garibay, M. A. *Proc. Natl. Acad. Sci.* **2005**, *102*(31), 10771. (e) Mann, S. *Nat. Mater.* **2009**, *8*, 781.

(2) (a) Kottas, G. S.; Clarke, L. I.; Horinek, D.; Michl, L. *Chem. Rev.* **2005**, *105*, 1281. (b) Skopek, K.; Hershberger, M. C.; Gladysz, J. A. *Coord. Chem. Rev.* **2007**, *251*, 1723. (c) Shirai, Y.; Morin, J.-F.; Sasaki, T.; Guerrero, J. M.; Tour, J. M. *Chem. Soc. Rev.* **2006**, *35*, 1043. (d) Kay, E. R.; Leigh, D. A.; Zerbetto, F. *Angew. Chem. Int. Ed.* **2007**, *46*, 72.

(3) (a) Thanasekaran, P.; Lee, C.-C.; Lu, K.-L. *Acc. Chem. Res.* **2012**, *45*(9), 1403. (b) Rajakannu, P.; Shankar, B.; Yadav, A.; Shanmugam, R.; Gupta, D.; Hussain, F.; Chang, C.-H.; Sathiyendiran, M.; Lu, K.-L. *Organometallics* **2011**, *30*, 3168. (c) Gardinier, J. R.; Pellechia, P. J.; Smith, M. D. *J. Am. Chem. Soc.* **2005**, *127*, 12448. (d) Caskey, D. C.; Michl, J. *J. Org. Chem.* **2005**, *70*, 5442.

(4) (a) Morris, W.; Taylor, R. E.; Dybowski, C.; Yaghi, O. M.; Garcia-Garibay, M. A. *J. Mol. Struct.* **2011**, *1004*, 94. (b) Gould, S. L.; Tranchemontagne, D.; Yaghi, O. M.; Garcia-Garibay, M. A. *J. Am. Chem. Soc.* **2008**, *130*, 3246.

(5) (a) He, C.; Lippard, S. J. *J. Am. Chem. Soc.* **2000**, *122*, 184. (b) Ingle, G. K.; Makowska-Grzyska, M. M.; Arif, A. M.; Berreau, L. M. *Eur. J. Inorg. Chem.* **2007**, 5262. (c) Berreau, L. M.; Allred, R. A.; Makowska-Grzyska, M. M.; Arif, A. M. *Chem. Commun.* **2000**, 1423. (d) Allred, R. A.; McAlexander, L. H.; Arif, A. M.; Berreau, L. M. *Inorg. Chem.* **2001**, *41*, 6790. (e) Bergquist, C.; Parkin, G. *Inorg. Chem.* **1999**, *38*, 422.

(6) (a) Sträter, N.; Lipscomb, W. N.; Klabunde, T.; Krebs, B. *Angew. Chem. Int. Ed.* **1996**, *35*, 2024. (b) Lipscomb, W. N.; Sträter, N. *Chem. Rev.* **1996**, *96*, 2375. (c) Wilcox, D. E. *Chem. Rev.* **1996**, *96*, 2435. (d) Mulder, F. A. A.; Mittermaier, A.; Hon, B.; Dahlquist, F. W.; Kay, L. E. *Nat. Struct. Biol.* **2001**, *8*, 932.

(7) (a) Reger, D. L.; Pascui, A. E.; Smith, M. D.; Jezierska, J.; Ozarowski, A. *Inorg. Chem.* **2012**, *51*, 11820. (b) Reger, D. L.; Foley, E. A.; Watson, R. P.; Pellechia, P. J.; Smith, M. D., Grandjean, F.; Long, G. J. *Inorg. Chem.* **2009**, *48*, 10658. (c) Reger, D. L; Watson, R. P.; Gardinier, J. R.; Smith, M. D.; Pellechia, P. J. *Inorg. Chem.* **2006**, *45*, 10088.

(8) Reger, D. L.; Pascui, A. E.; Smith, M. D.; Jezierska, J.; Ozarowski, A. *Inorg. Chem.* **2012**, *51*, 7966.

(9) Reger, D. L; Watson, R. P.; Smith, M. D.; Pellechia, P. J. *Organometallics* **2005**, *24*, 1544.

(10) Jarek, R. L.; Flesher, R. J.; Shin, S. K. *J. Chem. Educ.* **1997**, *74*, 978.

(11) (a) Barbour, L. J *J. Supramol. Chem.* **2003**, *1*, 189. (b) *POV-RAY 3.6* , Persistence of Vision Raytracer Pty Ltd, Williamstown, Victoria, Australia, **2006**.

(12) *MestReNOVA* v.5.2.5, Mestrelab Research S. L.: Santiago de Compostela, Spain, **2008**.

(13) Wolsey, W. C. *J. Chem. Educ.* **1973**, *50*, A335-A337.

(14) SMART Version 5.630, SAINT+ Version 6.45. Bruker Analytical X-ray Systems, Inc.,Madison, Wisconsin, USA, 2003.

(15) G.M. Sheldrick, SHELXTL Version 6.14, Bruker Analytical X-ray Systems, Inc., Madison, Wisconsin, USA, **2000**.

(16) Addison, A. W.; Rao, T. N.; Reedijk, J.; Van Rijn, J.; Verschoor, G. C. *J. Chem. Soc., Dalton Trans*. **1984**, 1349. $\tau_5 = \frac{(\beta - \alpha)}{60°}$ Where α and β are the two largest angles measured around the metal centers. Perfect square pyramid: τ_5 = 0; Perfect trigonal bipyramid: τ_5 = 1.

(17) Shannon, R. D *Acta Crystallogr.* **1976**, *A32*, 751.

(18) Gavrilova, A. L.; Qin, C. J.; Sommer, R. D.; Rheingold, A. L.; Bosnich, B. *J. Am. Chem. Soc.* **2002**, *124*, 1714.

(19) (a) Valentini, M.; Pregosin, P. S.; Rüegger, H. *Organometallics* **2000**, *19*, 2551. (b) Stilbs, P. *Prog. NMR Spectrosc.* **1987**, *19*, 1.

(20) Sandström, J. *Dynamic NMR Spectroscopy*, London & New York **1982**.

(21) Marat, K. *SPINWORKS 3* v.3.1.8.2, University of Manitoba: Winnipeg, Manitoba, Canada, **2011**.

(22) (a) Fernández-Moreira, V.; Thorp-Greenwood, F.; Arthur, R. J.; Kariuki, B. M.; Jenkins, R. L.; Coogan, M. P. *Dalton Trans.* **2010**, *39*, 7493. (b) Guerrero, A.; Jalón, F. A.; Manzano, B. R.; Rodríguez, A.; Claramunt, R. M.; Cornago, P.; Milata, V.; Elguero, J. *Eur. J. Inorg. Chem.* **2004**, 549.

(23) (a) Forsén, S.; Hoffman, R. A. *J. Chem. Phys.* **1963**, *39*, 2892. (b) Babailov, S. P.; Krieger, Y. G. *J. Struct. Chem.* **2001**, *42*, 305. (c) DiFranco, S. A.; Maciulis, N. A.; Staples, R. J.; Batrice, R. J.; Odom, A. L. *Inorg. Chem.* **2012**, *51*, 1187. (d) Faller, J. W.; Wilt, J. C. *Organometallics* **2005**, *24*, 5076. (e) Ashby, M. D.; Govindan, G. N.; Grafton , A. K. *J. Am. Chem. Soc.* **1994**, *116*, 4801. (f) Wik, B. J.; Lersch, M.; Krivokapic, A.; Tilset, M. J. Am. Chem. Soc. **2006**, *128*, 2682. (g) Rybtchinski, B.; Cohen, R.; Ben-David Y.; Martin, J. M. L.; Milstein, D. *J. Am. Chem. Soc.* **2003**, *125*, 11041.

(24) Selected references: (a) Pastor, A.; Martínez-Viviente, E. *Coord. Chem. Rev.* **2008**, *252*, 2314. (b) Sabiah, S.; Varghese, B.; Murthy, N. N. *Dalton Trans.* **2009**, 9770. (c) Schalley, C. A.; Müller, T.; Linnartz, P.; Witt, M.; Schäfer, M.; Lützen, A. *Chem. Eur. J.* **2002**, *8*(15), 3538. (d) Weilandt, T.; Troff, R. W.; Saxell, H.; Rissanen, K.; Schalley, C. A. *Inorg. Chem.* **2008**, *47*, 7588. (e) Uehara, K.; Kasai, K.; Mizuno, N. *Inorg. Chem.* **2010**, *49*, 2008. (f) Jensen, T. B.; Scopelliti, R.; Bünzli, J.-C. G. *Chem. Eur. J.* **2007**, *13*, 8404. (g) Ferrer, M.; Pedrosa, A.; Rodríguez, L.; Rossell, O.; Vilaseca, M. *Inorg. Chem* **2010**, *49*, 9438. (h) Habermehl, N. C.; Eisler, D. J.; Kirby, C. W.; Yue, N. L.-S.; Puddephatt, R. J *Organometallics* **2006**, *25*, 2921. (i) Bachechi, F.; Burini, A.; Galassi, S.; Pietroni, B. R.; Tesei, D. *Eur. J. Inorg. Chem.* **2002**, 2086.

(25) (a) Berry, R. S. *J. Chem. Phys.*, **1960**, *32*, 933. (b) Cass, M. E.; Hii, K. K.; Rzepa, H. S. *J. Chem. Educ.* **2006**, *83*, 336.

(26) Chisholm, M. H.; Clark, D. L.; Hampden-Smith, M. J. *J. Am. Chem. Soc.* **1989**, *111*, 574.

(27) (a) Bernstein, L. S.; Kim, J. J.; Pitzer, K. S.; Abramowitz, S.; Levin, I. W. *J. Chem. Phys.* **1975**, *62*, 3671. (b) Bernstein, L. S.; Abramowitz, S.; Levin, I. W. *J. Chem. Phys.* **1976**, *64*, 3228. (c) Caliginana, A., Aquilanti, V., Burcl, R., Handy, N. C., Tew. D. P. *Chem. Phys. Lett.*, **2003**, *369*, 335. (d) Wasada, H., Hirao, K. *J. Am. Chem. Soc.* **1992**, *114*, 16.

(28) Alcock, N. W.; Herron, N.; Moore, P. *J. Chem. Soc., Dalton Trans.* **1978**, 1282.

(29) Morin, T. J.; Merkel, A.; Lindeman, S. V.; Gardinier, J. R. *Inorg. Chem*. **2010**, *49*, 7992.

(30) (a) Li, S. H.; Rasaiah, J. C. *J. Chem. Phys.* **2011**, *135*, 124505. (b) Rose, M. C.; Stuehr, J. E. *J. Am. Chem. Soc.* **1974**, *94*, 5532. (c) Bučko, T.; Benco, L.; Hafner, J.; Ángyán, J. G. *J. Catal.* **2007**, *250*, 171. (d) Chernyshev, A.; Cukierman, S. *Biophys. J.* **2002**, *82*, 182.

Chapter VIII

Hydroxide Bridged Cubane Core Complexes of Nickel(II) and Cadmium(II):

Magnetic and Unusual Dynamic Properties

Introduction

Polynuclear complexes of magnetic metal centers are viable candidates for applications in various fields, such as biomimetic systems used for the study of enzyme active sites and multi-electron transfers,[1] or magnetic materials for applications in the field of molecular nanotechnology.[2] The magnetic exchange between paramagnetic metal ions is important not only from a theoretic point of view,[3] which aims to understand the fundamental correlation between the structure and magnetic properties, but also targets the development of single molecule magnets (SMM).[4] One promising motif for SMM is based on nickel-hydroxy cubane-type tetrametallic clusters (Figure 8.1), which recently received increased attention.[5]

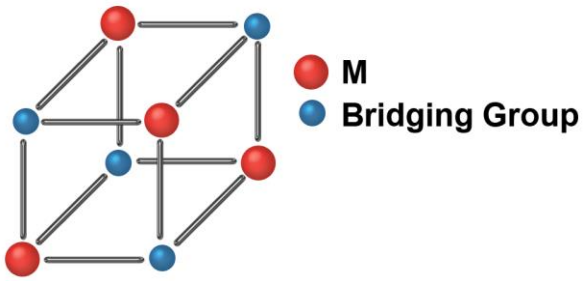

Figure 8.1. Schematic representation of a cubane cluster.

In these systems the metallic centers are usually in an octahedral coordination environment, where three sites are occupied by small bridging atoms. The literature presents two types of cubane core clusters supported by polydentate ligands with oxygen and/or nitrogen donors:[5,6] (i) donor atoms in the polydentate ligand occupy the bridging cubane positions, each bridging three metal centers - depending on the nature of the ligand, the remaining metal sites are occupied by other ligand donor atoms, anions or solvent molecules; (ii) more commonly the sole role of the ligand is to stabilize the

coordination sphere of the metal centers, the core is generated by triply bridged anions, especially methoxide or other small ligands such as azide, halides, sulfides and hydroxide.

This chapter discusses nickel(II) and cadmium(II) cubane core tetrametallic compounds of the second type with triply bridging hydroxide linking the metal centers, which are also stabilized by third-generation poly(pyrazolyl)methane ligands. There are only a few magnetically characterized structures known where the nickel(II) cubane core is generated by triple bridging of the hydroxide groups[6] and no analogues cadmium(II) compounds were found in the literature. The small number of cubane core cadmium(II) compounds that are known contain triple bridging chloride[7] and di-2-pyridyl ketone and/or carboxylates.[8]

A series of monofluoride bridged dinuclear metallacyclic compounds of the type $[M_2(\mu\text{-}F)(\mu\text{-}\mathbf{L}_{\boldsymbol{m}})_2](BF_4)_3$, M = Fe(II), Co(II), Cu(II), Zn(II), where $\mathbf{L}_{\boldsymbol{m}}$ is *m*-bis[bis(1-pyrazolyl)methyl]benzene (*m*-[*C*H(pz)$_2$]$_2$C$_6$H$_4$, pz = pyrazolyl ring, Scheme 8.1) were recently synthesized.[9] Interestingly, syntheses of analogous to those used in these preparations with the metals Ni(II) and Cd(II) generated *difluoride* bridged compounds, $[M_2(\mu\text{-}F)_2(\mu\text{-}\mathbf{L}_{\boldsymbol{m}})_2](BF_4)_2$.

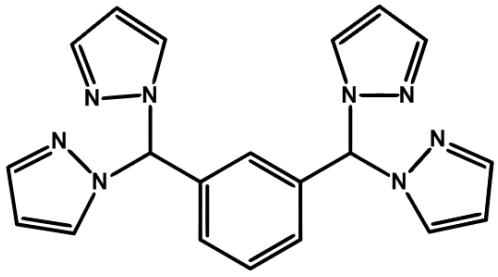

Scheme 8.1. Schematic drawing of the structure of $\mathbf{L}_{\boldsymbol{m}}$.

Analogous hydroxide bridged complexes $[M_2(\mu\text{-}OH)(\mu\text{-}\mathbf{L}_{\boldsymbol{m}})_2](ClO_4)_3$, [M = Fe(II), Co(II), Cu(II), Zn(II)] were also synthesized using triethylamine as the base to generate the hydroxide ligands from water molecules present in the syntheses.[10] As observed with the fluoride bridged complexes, in this chapter it is shown that analogous reactions where M = Ni(II) or Cd(II) lead to different types of products, hydroxide bridged complexes with cubane core, $[Ni_4(\mu\text{-}OH)_4(\mu\text{-}\mathbf{L}_{\boldsymbol{m}})_2(DMF)_4](ClO_4)_4\cdot DMF\cdot EtOH$ and $[Cd_4(\mu\text{-}OH)_4(\mu\text{-}\mathbf{L}_{\boldsymbol{m}})_2(ACE)_2(H_2O)_2](ClO_4)_4\cdot 2ACE$ (ACE = acetone); as characterized by X-ray crystallography. The magnetic and EPR properties of the nickel(II) complex were studied as well as detailed NMR investigations were carried out with the cadmium(II) hydroxide bridged cubane core complex, showing a unique dynamic behavior in solution.

Experimental Section

General Considerations. For the synthesis of the cubane core compounds standard Schlenk techniques were used. The solvents were not dried prior to use. The ligand, $\mathbf{L}_{\boldsymbol{m}}$, was prepared following reported procedures.[9c] All other chemicals were purchased from Sigma-Aldrich or Strem Chemicals and used as received.

Crystals used for elemental analysis and mass spectrometry were removed from the mother liquor, rinsed with ether, and dried under vacuum.

^1H, ^{13}C and ^{113}Cd NMR spectra were recorded on a Varian Mercury/VX 300, Varian Mercury/VX 400, or Varian INOVA 500 spectrometer. All chemical shifts are in ppm and were referenced to residual undeuterated solvent signals (^1H), deuterated solvent signals (^{13}C), or externally to $CdCl_2$ (^{113}Cd). In order to test the accuracy of the spin saturation transfer experiment, a sample of N,N-dimethylacetamide diluted in toluene-d_8 was used for VT NMR studies and k and $\Delta G^{\ddagger}$ were calcuclated for the rotational barrier

about the amide bond. The calculated values (25.0˚C: k = 0.53 s^{-1}, $\Delta G^{\ddagger}$ = 17.8 kcal/mol) are comparable with literature values (22.5˚C: k = 0.61 s^{-1}, $\Delta G^{\ddagger}$ = 17.7 kcal/mol).[11]

Mass spectrometric measurements were obtained on a MicroMass QTOF spectrometer in an acid-free environment. For all reported peaks, the isotopic patterns match those calculated for the assignment. Elemental analyses were performed on vacuum-dried samples by Robertson Microlit Laboratories (Ledgewood, NJ).

XSEED[12], POV-RAY[12] and MESTRENOVA[13] were used for the preparation of figures.

High-field, high-frequency EPR spectra at temperatures ranging from ca. 6K to 290 K were recorded on a home-built spectrometer at the EMR facility of the NHMFL.[14] The instrument is a transmission-type device in which microwaves are propagated in cylindrical lightpipes. The microwaves were generated by a phase-locked Virginia Diodes source generating frequency of 13 ± 1 GHz and producing its harmonics of which the 2nd, 4th, 6th, 8th, 16th, 24th and 32nd were available. A superconducting magnet (Oxford Instruments) capable of reaching a field of 17 T was employed. The powder samples were not constrained and showed no magnetic torqueing at high magnetic fields.

Magnetic susceptibility measurements over the temperature range 1.8-300 K were performed at a magnetic field of 0.5 T using a Quantum Design SQUID MPMSXL-5 magnetometer. Correction for the sample holder, as well as the diamagnetic correction χ_D which was estimated from the Pascal constants[15] was applied.

Caution! *Perchlorate salts of metal complexes with organic ligands are potentially explosive.*[16]

$[Ni_4(\mu\text{-}OH)_4(\mu\text{-}L_m)_2(DMF)_4](ClO_4)_4\cdot DMF\cdot EtOH$, 1. The ligand $\mathbf{L}_m$ (0.444 g, 1.2 mmol) was dissolved in 16 mL methanol, then NEt_3 (0.17 mL, 1.2 mmol) was added. The $Ni(ClO_4)_2\cdot 6H_2O$ (0.439 g, 1.2 mmol) was dissolved in 4 mL of methanol and the ligand/amine solution was transferred by cannula into the nickel salt solution. The reaction mixture was stirred for 24 hours, after which time the system was filtered by cannula. The resulting green solid (0.210 g) was washed with 5 mL ether and dried in vacuum overnight. Layering a buffer layer of pure EtOH and then Et_2O on top of the DMF solution of the crude product afforded 0.100 g of **[**$Ni_4(\mu\text{-}OH)_4(\mu\text{-}\mathbf{L}_m)_2(DMF)_4](ClO_4)_4\cdot DMF\cdot EtOH$ single crystals suitable for X-ray studies. The use of MeOH instead of EtOH resulted in crystals of $[Ni_4(\mu\text{-}OH)_4(\mu\text{-}\mathbf{L}_m)_2(DMF)_2\{(H_2O)_{0.79}(MeOH)_{0.21}\}_2](ClO_4)_4\cdot 2(DMF)\cdot\{(MeOH)_{0.79}(DMF)_{0.21}\}_2$, **2**. Anal. Calcd.(Found) for $C_{52}H_{68}Cl_4Ni_4N_{20}O_{24}$: C, 36.02 (36.25); H, 3.95 (4.22); N, 16.16 (15.90). MS ES(+) *m*/*z* (rel. % abund.) [assgn]: 1341 (15) $[Ni_4(\mathbf{L}_m)_2(OH)_4(ClO_4)_3]^+$, 662 (13) $[Ni_4(\mathbf{L}_m)_2(OH)_3(ClO_4)_3]^{2+}$, 621 (100) $[Ni_4(\mathbf{L}_m)_2(OH)_4(ClO_4)_2]^{2+}$, 527 (25) $[Ni_2(\mathbf{L}_m)_2(ClO_4)_2]^{2+}$, 445 (7) $[Ni\mathbf{L}_mOH]^+$, 378 (80) $[Ni_4(\mathbf{L}_m)_2(OH)_4(ClO_4)]^{3+}$, 371 (22) $[\mathbf{L}_m + H]^+$, 292 (92) $[Ni_2(\mathbf{L}_m)_2(OH)]^{3+}$.

$[Cd_4(\mu\text{-}OH)_4(\mu\text{-}L_m)_2(ACE)_2(H_2O)_2](ClO_4)_4\cdot 2ACE$, 3. The cadmium compound was synthesized similarly starting from $\mathbf{L}_m$ (0.190 g, 0.514 mmol), NEt_3 (0.070 mL, 0.514 mmol) and $Cd(ClO_4)_2\cdot 6H_2O$ (0.215 g, 0.514 mmol). Vapor diffusion of Et_2O into the diluted acetonitrile solution of the crude product at 5 ºC afforded 0.148 g (44%) transparent single crystals and white microcrystalline solid. ^{1}H NMR (300 MHz, acetonitrile-d_3): 8.40/8.37 (s/s, 2H/2H, 5-pz), 8.20/8.16/8.13 (s/s/s, 12H, 5-pz + 3-pz + $CH(pz)_2$), 7.56 (t, J = 9 Hz, 2H, 5-H C_6H_4), 6.94/6.91 (d/s, 6H, 4,6-H C_6H_4 + 3-pz), 6.76

(d, 2H, 4,6-H C_6H_4), 6.70 (s, 2H, 4-H pz), 6.52 (s, 6H, 4-H pz), 5.01 (s, 2H, 2-H C_6H_4), 2.59 (s, 2H, Cd-OH-Cd), -2.11 (s, 2H, Cd-OH-Cd). ^{1}H NMR (400 MHz, acetone-d_3): 8.65 (s br, 8H, 5-pz + C*H*$(pz)_2$), 8.38 (s br, 8H, 5-pz + 3-pz), 8.29 (s, 2H, 3-pz), 7.67 (t, *J* = 8 Hz, 2H, 5-H C_6H_4), 7.23 (s, 2H, 3-pz), 7.02 (d, 2H, 4,6-H C_6H_4), 6.84 (d, 2H, 4,6-H C_6H_4), 6.69 (s, 2H, 4-H pz), 6.58 (s, 6H, 4-H pz), 5.19 (s, 2H, 2-H C_6H_4), -1.50 (s, 2H, Cd-OH-Cd). ^{13}C NMR (100.6 MHz, acetone-d_6): δ 146.1/145.7/145.0 (5-C pz), 139.0 (1,3-H C_6H_4), 136.8/136.6/136.2/135.8 (3-C pz), 130.6 (5-C C_6H_4), 128.8 (4,6-C C_6H_4), 125.4 (2-C C_6H_4), 108.1/107.9/107.7/107.6 (4-C pz), 75.2 ($CH(pz)_2$). ^{113}Cd NMR (88.8 MHz, acetone-d_6): δ 3.1/1.7 (s/s). Anal. Calcd.(Found) for $C_{40}H_{40}Cl_4Cd_4N_{16}O_{20}$: C, 29.01 (29.50); H, 2.43 (2.35); N, 13.53 (13.44). MS ES(+) *m*/*z* (rel. % abund.) [assgn]: 1556 (2) $[Cd_4(\mathbf{L}_m)_2(OH)_4(ClO_4)_3]^+$, 1181 (2) $[Cd_2(\mathbf{L}_m)_2(OH)(ClO_4)_2]^+$, 953 (8) $[Cd(\mathbf{L}_m)_2(ClO_4)]^+$, 729 (30) $[Cd_4(\mathbf{L}_m)_2(OH)_4(ClO_4)_2]^{2+}$, 583 (100) $[Cd(\mathbf{L}_m)(ClO_4)]^+$, 519 (90) $[Cd(\mathbf{L}_m)(OH)_2 + H]^+$, 501 (15) $[Cd_2(\mathbf{L}_m)_2(OH)_2]^+$, 427 (25) $[Cd(\mathbf{L}_m)_2]^{2+}$, 371 (22) $[\mathbf{L}_m + H]^+$, 326 (10) $[Cd_2(\mathbf{L}_m)_2(OH)]^{3+}$.

Crystallographic studies. X-ray diffraction intensity data for compounds **1-3** were measured on a Bruker SMART APEX CCD-based diffractometer (Mo Kα radiation, λ = 0.71073 Å)[17]. Raw area detector data frame processing was performed with the SAINT+ and SADABS programs.[17] Final unit cell parameters were determined by least-squares refinement of large sets of strong reflections taken from each data set. Direct methods structure solution, difference Fourier calculations and full-matrix least-squares refinement against F^2 were performed with SHELXTL.[18] Non-hydrogen atoms were refined with anisotropic displacement parameters, the exception being disordered species.

The hydrogen atoms were placed in geometrically idealized positions and included as riding atoms. Details of the data collection are given in Table 8.1.

Table 8.1. Selected Crystal Data and Structure Refinement for **1-3.**

	1	**2**	**3**
Formula	$C_{57}H_{81}Cl_4N_{21}Ni_4O_{26}$	$C_{55.67}H_{83.34}Cl_4N_{20}Ni_4O_{28}$	$C_{52}H_{68}Cl_4Cd_4N_{16}O_{26}$
Fw, g mol^{-1}	1853.07	1857.51	1924.62
Cryst. Syst.	Triclinic	Monoclinic	Monoclinic
Space group	P $\bar{1}$	C 2/c	$P2_1/c$
T, K	150(2)	150(2)	100(2)
***a*, Å**	12.7195(6)	21.7442(12)	13.5923(7)
***b*, Å**	14.3046(7)	17.5713(10)	21.1444(11)
***c*, Å**	21.7466(10)	22.1788(12)	24.2774(12)
***α*, deg**	91.8090(10)	90	90
***β*, deg**	93.0850(10)	115.8900(10)	90.1170(10)
***γ*, deg**	106.2300(10)	90	90
***V*, Å^3**	3789.1(3)	7623.4(7)	6977.3(6)
Z	2	4	4
R1 (I >2σ (I))	0.0569	0.0497	0.0374
wR2 (I >2σ (I))	0.1542	0.1314	0.0927

Compound **1** crystallizes in the space group P $\bar{1}$ of the triclinic system. The asymmetric unit consists of one $[Ni_4(\mu\text{-}OH)_4(\mu\text{-}\mathbf{L}_{\boldsymbol{m}})_2(DMF)_4]^{4+}$ cation, four independent perchlorate anions, and one DMF and one ethanol molecule of crystallization. Two of the coordinated DMF molecules (associated with O5 and O8) are disordered over two orientations. These species were refined with the aid of a "same geometry" restraint (SHELX SAME instruction), which restrained their geometries to be similar to that of the well-behaved DMF (O7, N7, C74-C76). The atoms of the disordered DMF molecules and both guest solvent species were refined with isotropic displacement parameters. The electron density map in the vicinity of the non-coordinated DMF and EtOH molecules suggest additional orientations of these species; however no sensible disorder model

could be obtained; the reported coordinates reflect only the major orientation of each of these species. The four bridging hydroxyl hydrogens were located in difference maps and refined isotropically with their O-H distances restrained to be approximately equal. The ethanolic hydrogen could not be located and was not calculated.

Compound **2** crystallizes in the space group C2/c. The asymmetric unit consists of half of one $[Ni_4(\mu\text{-}OH)_4(\mu\text{-}\mathbf{L_m})_2(DMF)_2\{(H_2O)_{0.79}(MeOH)_{0.21}\}_2]^{4+}$ cation located on a two-fold axis of rotation, two perchlorate anions, one non-coordinated DMF molecule and an interstitial region of disordered electron density which was modeled as a mixture of diethyl ether and methanol. The structure is afflicted with pervasive disorder. The DMF molecule coordinated to Ni2 is disordered over two closely separated, equally populated positions. Interpretation of the electron density map around Ni1 was not straightforward, but eventually this coordination site was modeled as a disordered mixture of 79% water and 21% methanol. Reasonable positions for the water hydrogens were located in a difference map. These were included with d(O-H) = 0.85(2) Å and d(H···H) = 1.40(2) Å distance restraints and U(iso,H) = 1.5U(eq,O). The total population of this site was constrained to sum to unity. The methanolic hydrogen was not located or calculated. Perchlorate Cl1 is disordered and was modeled with two orientations; perchlorate Cl2 shows some elongated displacement ellipsoids but was acceptably modeled with only one orientation. The interstitial region modeled as MeOH / Et_2O is severely disordered and the model employed should be regarded as approximate. The occupation factors were tied to those of the water/MeOH molecules bonded to Ni1, such that water molecule O3A and MeOH molecule O1S are present in together in a given asymmetric unit, and coordinated MeOH O3B and Et_2O molecule O2S are present

together. The two independent hydroxyl hydrogens H1A and H2A were located and refined isotropically with d(O-H) = 0.85(2) Å distance restraints. The largest residual electron density peaks are in the vicinity of the disordered methanol/ether molecules, indicating the limitations of the model used.

Crystals of **3** formed as colorless irregular twinned masses. X-ray intensity data was measured from a cleaved fragment. The crystals decompose in air on a timescale of hours. Compound **3** crystallizes in the space group $P2_1/c$. The asymmetric unit consists of one $[Cd_4(\mu\text{-}OH)_4(\mu\text{-}\mathbf{L}_{\boldsymbol{m}})_2(H_2O)_2(acetone)_2]^{4+}$ cation, four perchlorate anions and two acetone molecules of crystallization. Two perchlorate anions (Cl3 and Cl4) are disordered and were modeled with two closely spaced positions having occupancies Cl3A/Cl3B = 0.53(2) / 0.47(2) and Cl4A/Cl4B = 0.779(7)/0.221(7). Total site occupancy was constrained to sum to unity. Geometries of each disorder component were restrained to be similar to that of the ordered perchlorate Cl1. The hydroxyl and water hydrogen atoms were located in difference maps and refined isotropically with a d(O-H) = 0.85(2) Å distance restraint.

Results

Syntheses. Non-crystalline samples were prepared through the reaction of separate methanolic solutions of $\mathbf{L}_{\boldsymbol{m}}$ and $M(ClO_4)_2{\cdot}6H_2O$, M = Ni(II), Cd(II), Scheme 8.2. These products contain $[M_4(\mu\text{-}OH)_4(\mu\text{-}\mathbf{L}_{\boldsymbol{m}})_2]^{4+}$ units according to ESI^+-MS spectra of the nickel(II) compound and ^1H NMR spectra of the cadmium(II) compound. As the formation of $[M_2(\mu\text{-}OH)(\mu\text{-}\mathbf{L}_{\boldsymbol{m}})_2](ClO_4)_3$ type complexes was anticipated initially, analogous to those observed with other transition metals,[10] these reactions were carried out with equimolar amounts of ligand and metal salts. Crystals of compound **1**, $[Ni_4(\mu\text{-}$

$OH)_4(\mu\text{-}\mathbf{L}_m)_2(DMF)_4](ClO_4)_4\cdot DMF\cdot EtOH$ were isolated by layering EtOH and ether on top of a DMF solution of the initial green powder. The use of MeOH instead of EtOH resulted in crystals of **2,** $[Ni_4(\mu\text{-}OH)_4(\mu\text{-}\mathbf{L}_m)_2(DMF)_2\{(H_2O)_{0.79}(MeOH)_{0.21}\}_2](ClO_4)_4 \cdot 2(DMF)\cdot\{(MeOH)_{0.79}(DMF)_{0.21}\}_2$. Crystals of compound **3**, $[Cd_4(\mu\text{-}OH)_4(\mu\text{-}\mathbf{L}_m)_2(ACE)_2(H_2O)_2](ClO_4)_4\cdot 2ACE$, were isolated upon the vapor diffusion of diethyl ether into a diluted acetone solution of the initial white powder, at 5°C.

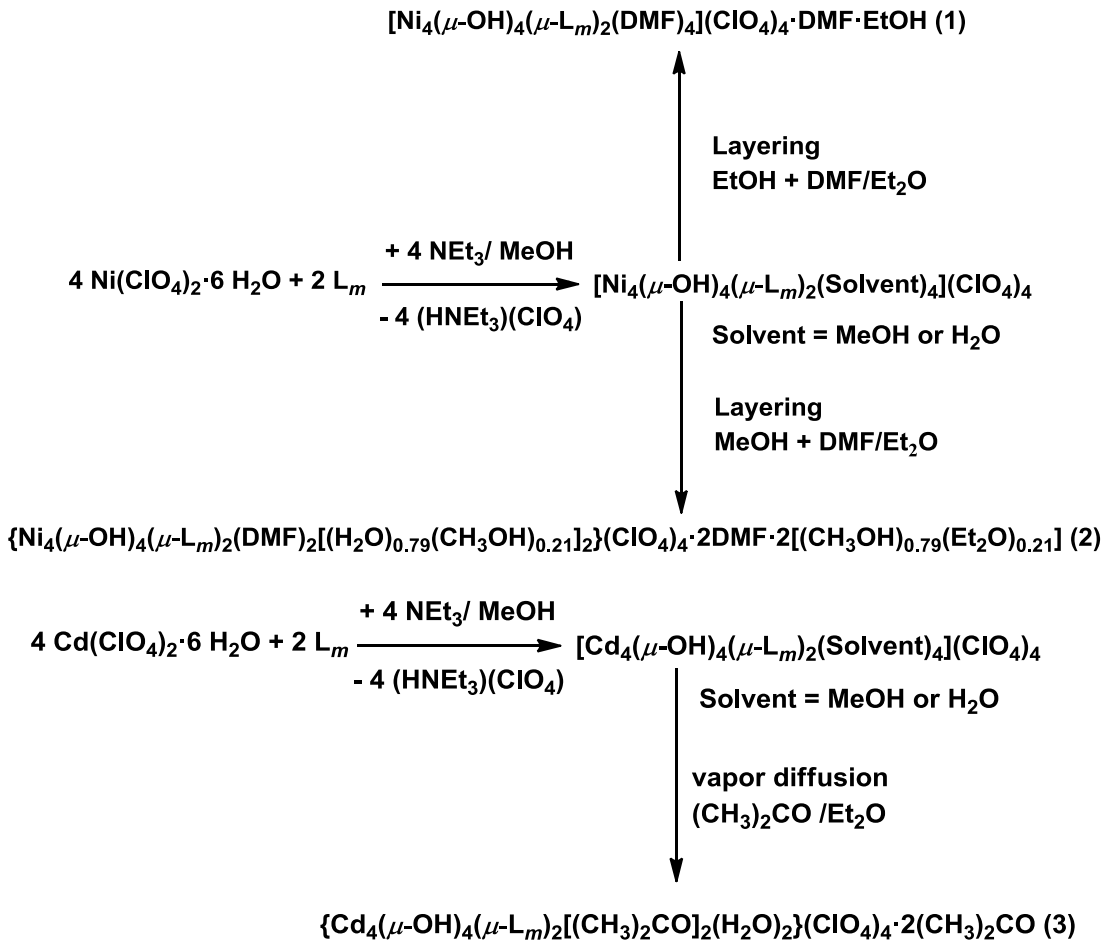

Scheme 8.2. Synthesis of the cubane compounds, **1**-**3**.

Mass spectrometry. Positive-ion electrospray mass spectra (ESI^+-MS) of the nickel(II) and cadmium(II) complexes are similar. Clusters, such as

$[M_4(\mathbf{L}_m)_2(OH)_4(ClO_4)_3]^+$ and $[M_4(\mathbf{L}_m)_2(OH)_4(ClO_4)_2]^{2+}$ can be observed for both compounds. In the spectrum of **1**, the base peak is $[Ni_4(\mathbf{L}_m)_2(OH)_4(ClO_4)_2]^{2+}$ and even $[Ni_4(\mathbf{L}_m)_2(OH)_4(ClO_4)]^{3+}$ could be identified. The base peak for **3** is $[Cd(\mathbf{L}_m)(ClO_4)]^+$. Peaks corresponding to clusters containing the coordinated solvent molecules are not observed in the spectra.

Solid State Structures. Figure 8.2 presents the cationic units of **1**, the numbering scheme is correct for both **1** and **3**. Figure 8.3 shows the cationic unit of compound **2**, which resides on a twofold axis of rotation. Selected bond lengths and bond angles are shown in Table 8.2.

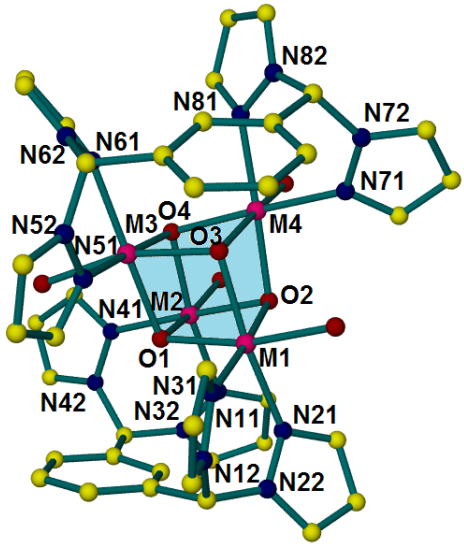

Figure 8.2. Structure of cationic unit in $[Ni_4(\mu\text{-}OH)_4(\mu\text{-}\mathbf{L}_m)_2(DMF)_4](ClO_4)_4\cdot DMF\cdot EtOH$, **1**. Hydrogen atoms are omitted for clarity. For the DMF molecules only the oxygen atoms are shown.

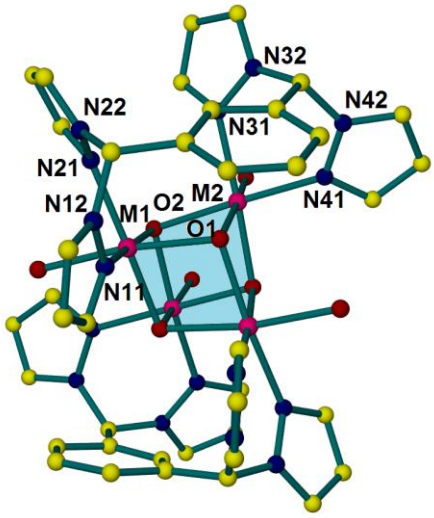

Figure 8.3. Structure of the cationic unit in $\{Ni_4(\mu\text{-}OH)_4(\mu\text{-}\mathbf{L}_m)_2(DMF)_2[(H_2O)_{0.79}(MeOH)_{0.21}]_2\}$ $(ClO_4)_4 \cdot 2(DMF) \cdot 2[(MeOH)_{0.79}(DMF)_{0.21}]$, **2**. Hydrogen atoms are omitted for clarity. For the coordinated solvent molecules only the oxygen atoms are shown.

In all structures, the geometry around the metal centers is distorted octahedral. The coordination sites of the metal centers are occupied by three hydroxides, two nitrogen atoms from one of the two bis(pyrazolyl)units of the ligand $\mathbf{L}_m$, and one oxygen atom from a coordinated solvent molecule. The bond angles are distorted with adjacent N-M-N bond angles around 84.83 - 94.95º, N-M-O angles around 78.85 - 99.75º and O-M-O angles around 77.24 -80.82º.

Four octahedral metal centers alternating with four triply bridged hydroxide groups at the eight corners of a cube generate a cubane core. The ligand, $\mathbf{L}_m$, adopts a *syn* conformation with both bis(pyrazolyl)methane units on the same side of the phenylene linker with each ligand supporting the arrangement of the core by connecting two metal ions. The octaherdal coordination in the solid state is completed by coordination of a solvent molecule (DMF, MeOH, H_2O or acetone). The weakly coordinated solvent molecules form longer Ni-O (2.092 - 2.115 Å) and Cd-O (2.325 - 2.440 Å) bonds than the bridging hydroxide groups (Ni-O 2.039 - 2.076 Å, Cd-O 2.231 - 2.291Å).

Table 8.2. Selected Bond Lengths and Bond Angles for $[Ni_4(\mu\text{-}OH)_4(\mu\text{-}\mathbf{L_m})_2(DMF)_4](ClO_4)_4\cdot DMF\cdot EtOH$, **1**, $\{Ni_4(OH)_4(\mathbf{L_m})_2(DMF)_2[(H_2O)_{0.79}(MeOH)_{0.21}]_2\}(ClO_4)_4\cdot 2(DMF)\cdot 2[(MeOH)_{0.79}(DMF)_{0.21}]$, **2**, $[Cd_4(\mu\text{-}OH)_4(\mu\text{-}\mathbf{L_m})_2(ACE)_2(H_2O)_2](ClO_4)_4\cdot 2$ ACE, **3**.

	T (K)	Metal	O-M-O Angle Interval (deg)	M-O-M Angle Interval (deg)	M-O Distance Interval (Å)	Predicted M-O Distance, (Å)[a]	Average M-N Distance (Å)	M···M Distance Interval (Å)
1	150	Ni(1)	77.91-80.41	97.93-101.46	2.049-2.063	1.97	2.105	3.122-3.171
		Ni(2)	79.22-80.61		2.050-2.076		2.116	3.122-3.166
		Ni(3)	77.96-80.22		2.039-2.069		2.118	3.128-3.171
		Ni(4)	78.85-80.56		2.062-2.072		2.119	3.128-3.167
2	150	Ni(1)	77.73-80.73	98.06-101.44	2.056-2.060	1.97	2.102	3.117-3.180
		Ni(2)	78.45-80.89		2.067-2.070		2.111	
3	100	Cd(1)	77.28-80.82	98.05-101.74	2.251-2.284	2.21	2.336	3.458-3.503
		Cd(2)	78.24-80.82		2.265-2.303		2.348	3.454-3.473
		Cd(3)	77.91-80.45		2.231-2.272		2.323	3.442-3.503
		Cd(4)	78.90-80.95		2.263-2.291		2.375	3.442-3.478

[a]Shannon Radii, Ref. 19.

The values for the M-O(*H*) distances are larger than predicted by summing the ionic radii of the corresponding metal centers and hydroxide by 0.04-0.08 Å, suggesting that structures **1-3** are strained. Two of the four triply bridging hydroxide groups are oriented towards the phenylene linker forming weak O-H···π interactions [d(H···centroid) = 2.31 – 2.74 Å, O-H···centroid 143.32 - 167.85°].[20]

NMR of $[Cd_4(\mu\text{-}OH)_4(\mu\text{-}L_m)_2(ACE)_2(H_2O)_2](ClO_4)_4\cdot 2ACE$, 3. The cadmium(II) compound was characterized in acetonitrile (ACN) and acetone (ACE) solutions. The slightly different spectra in the two solvents helped the identification of several resonances that have very similar chemical shifts and are superimposed in one or the other solvent, Figure 8.4.

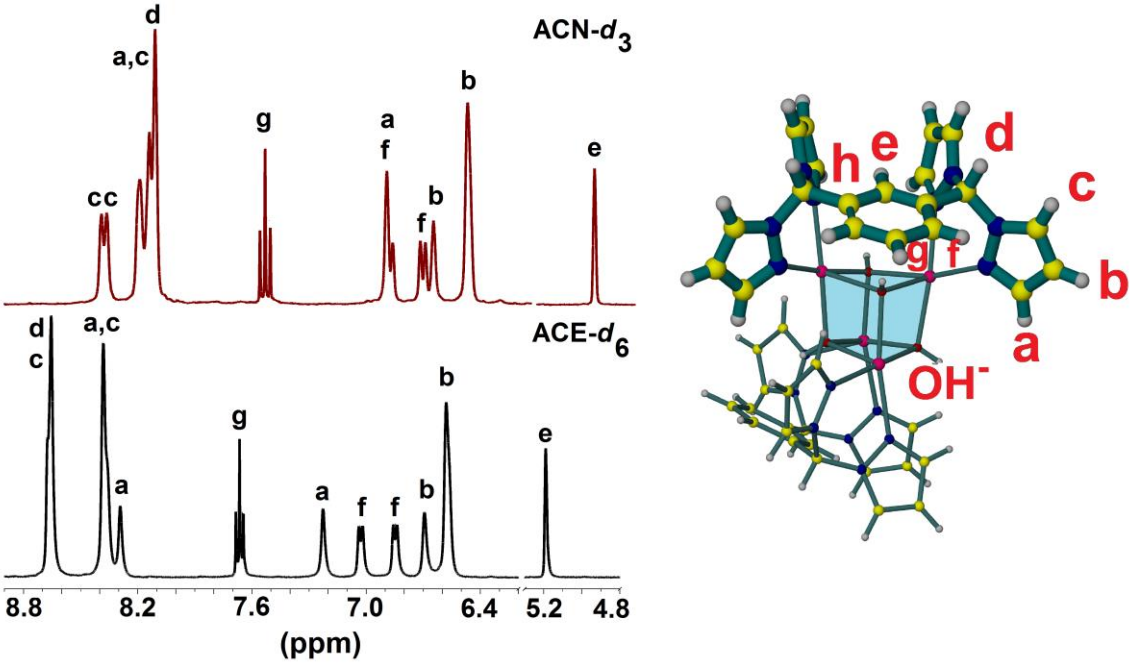

Figure 8.4. ^{1}H NMR spectra of **3** in acetonitrile (top) and acetone (bottom), more shielded resonances for the OH^- groups are omitted for clarity. labeling scheme for the hydrogens is shown on the right: *a*, *b*, *c* – pyrazolyl hydrogens, *d* – methine hydrogen, *e*, *f*, *g* – phenylene hydrogens, *h* – ipso carbon.

The ambient temperature ^{1}H and ^{13}C NMR spectra of **3** are complicated and the resonances broader than anticipated. To fully interpret these spectra the HSQC (^{1}H-^{13}C Heteronuclear Single Quantum Coherence), HMBC (^{1}H-^{13}C Heteronuclear Multiple Bond Correlation) and COSY (^{1}H-^{1}H Correlation) NMR spectra of **3** in acetone and acetonitrile (Figure 8.5) were recorded. Variable temperature (VT) NMR studies were also performed to complete the analyses.

In the ^{1}H-NMR spectra of compound **3**, a single resonance can be observed for both the *g* (ACN-d_3 7.56 ppm; ACE-d_6 7.67 ppm) and *e* (ACN-d_3 5.01 ppm; ACE-d_6 5.19 ppm) positions of the phenylene linker, but there are two distinct doublets observed for the *f* position (ACN-d_3 6.91 and 6.76 ppm; ACE-d_6 7.02 and 6.84 ppm). In contrast, metallacyclic compounds of the type $[M_2(\mu\text{-}F)(\mu\text{-}\mathbf{L})_2](BF_4)_3$ (M = Zn(II) or Cd(II), **L** = $\mathbf{L_m}$ or $\mathbf{L_m}$***)**[9a,21] $[Zn_2(\mu\text{-}OH)(\mu\text{-}\mathbf{L_m})_2](ClO_4)_3$ and $[M_2(\mu\text{-}OH)(\mu\text{-}\mathbf{L_m}*)_2](ClO_4)_3$, M = Zn(II) or Cd(II), $\mathbf{L_m}$* = *m*-$[CH(3,5\text{-}Me_2pz)_2]_2C_6H_4$, pz = pyrazolyl ring,[10] show only one set of three resonances for the two phenylene linkers: *e*, *f* and *g* hydrogens. Although the ^{13}C NMR spectrum of **3** shows one resonance for each of the *e*, *f* and *g* carbons, the single carbon *f* resonance is clearly correlated with the two distinct resonances assigned to the *f* hydrogens in the HSQC and HMBC experiments (Figure 8.5a and 8.5b, ^{13}C NMR spectra is shown on the Y axes of the 2D NMR experiments).

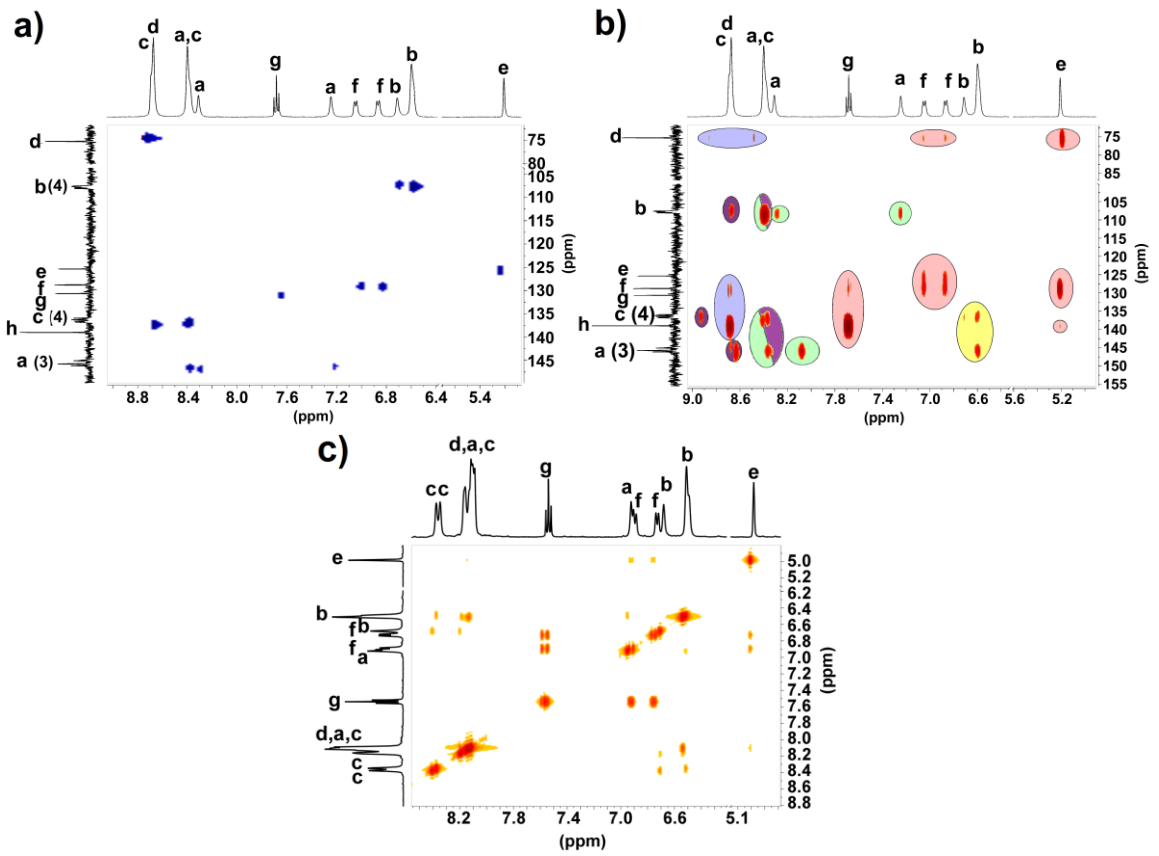

Figure 8.5. Two dimensional **(**2D) NMR experiments of **3**: HSQC spectrum in ACE-d_6 (a), HMBC spectrum in ACE-d_6 (b) - color code: correlations of the phenylene spacer resonances are colored pink, methine blue, *b*-pyrazolyl yellow, *a*-pyrazolyl green, *c*-pyrazolyl violet; and COSY in ACN-d_3 (c).

The ^{13}C NMR resonances for the pyrazolyl rings (*a*, *b* and *c*) of **3** indicate four nonequivalent rings out of a total of eight, as opposed to the previously reported dinuclear species $[Zn_2(\mu\text{-OH})(\mu\text{-}\mathbf{L}_m)_2](ClO_4)_3$, where only two distinct environments were observed. The ^{13}C NMR spectra of **3** in acetone show three signals for the *c*-pyrazolyl carbons (146.1, 145.7, 145.0 ppm) and four signals for both the *a*- (136.8, 136.6, 136.2, 135.8 ppm) and *b*- (108.1, 107.9, 107.7, 107.6 ppm) pyrazolyl carbons. This differentiation cannot be clearly observed in the ^{1}H NMR spectrum, indicating that some of the pyrazolyl resonances are superimposed. The *b*-pyrazolyl resonances [ACN-d_3 6.70

(2H)/ 6.52 (6H) ppm; ACE-d_6 6.69 (2H)/ 6.58 (6H) ppm] integrate 1:3, consistent with four types of pyrazolyl rings in the solution structure.

Another interesting feature in the ^{1}H NMR spectrum is that one of the *a*- or *c*-position pyrazolyl resonances is unusually shielded (6.94 ppm in ACN-d_3 and 7.23 ppm in ACE-d_6) when compared to the other *a*- and *c*-pyrazolyl resonances (8.40 – 8.13 ppm in ACN-d_3 and 8.65 - 8.29 ppm in ACE-d_6). This shielded resonance can be assigned as an *a*-pyrazolyl hydrogen because in the solid state structure two *a* hydrogens are pointing towards the phenylene linkers and are shielded by the π-aromatic electrons (Figure 8.6), an effect noted previously with $[Zn_2(\mu\text{-OH})(\mu\text{-}\mathbf{L_m})_2](ClO_4)_3$.[10] This assignment makes the *a*- and *c*-positions distinguishable by ^{1}H NMR spectroscopy (Figure 8.4), when coupled with the variable temperature data (vide infra).

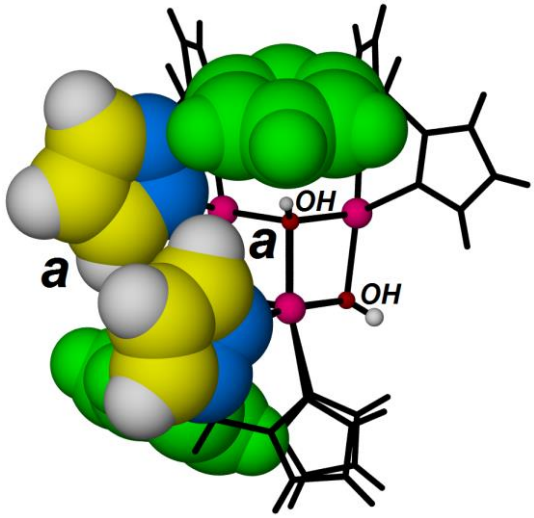

Figure 8.6. Two *a*-pyrazolyl hydrogens and one of the two visible triply bridging hydroxides point towards the π-electron cloud of the phenylene linkers. Phenylene linkers are shown in green.

The HSQC and HMBC spectra (Figure 8.5a and 8.b) show that in acetone at 8.65 ppm the methine resonances are superimposed with four *c*-pyrazolyl hydrogen resonances, similarly at 8.38 ppm the remaining four *c*-pyrazolyl hydrogen resonances

are superimposed with four *a*-pyrazolyl hydrogen resonances. The integrals of these signals are in conformity with these assignments. The remaining *a*-pyrazolyl hydrogen resonances can be observed at 8.29 ppm, and at 7.23 ppm, both corresponding to two hydrogens. Based on the COSY spectra (Figure 8.5c) and the assignments above the spectra of **3** in acetonitrile can be interpreted: the resonances at 8.39 ppm can be assigned to four *c*-pyrazolyl hydrogens, the complicated multiplet centered at 8.16 ppm corresponds to 14 hydrogens: 4 methine, 4 *c*-pyrazolyl and 6 *a*-pyrazolyl hydrogens, while the multiplet at 6.91 ppm is the signal of the remaining 2 *a*-pyrazolyl hydrogens superimposed with the signal of one set (two hydrogens) of *f*-phenylene resonances.

The ^{1}H NMR resonances at -2.11 ppm in acetonitrile and at -1.50 ppm in acetone correspond to two bridging OH^- hydrogens,[10,22] also shielded by the π-electron cloud of the phenylene linker (Figure 8.6). In ACN-d_3 another resonance, also integrating for two hydrogens, can be observed at 2.6 ppm, most clearly at lower temperatures (Figure 8.8, vide infra). This resonance is assigned to the other two bridging hydroxide groups, which are not located below the phenylene linkers. Similarly, the proton decoupled ^{113}Cd NMR spectrum of **3** shows two distinct cadmium resonances at 3.1 and 1.7 ppm (Figure 8.7).

All of these NMR data demonstrate that the solid state cubane core structure is retained in solution. If, as expected, the weakly coordinated solvents observed in the solid state structures are displaced by the NMR solvent that is itself rapidly exchanging on the NMR time scale and thus does not influence the spectra, one expects four types of pyrazolyl rings and two types of "cubane" positions for the hydroxide and cadmium vertices, a structure similar to that shown in Figure 8.3 for nickel(II) with the coordinated solvent removed (drawing in Figure 8.4). For example, two types of hydroxide groups are

present, one with the hydrogens pointing at the phenylene linker (O1) and the other at the back side of this bridging ligand (O2). The two sets of hydroxide groups and cadmium(II) cations, together with the pyrazolyl rings of each $\mathbf{L}_{\boldsymbol{m}}$ ligand are equilibrated by the two fold rotation axis passing through the middle of the cubane core, similar to that observed for the solid state structure of compound **2**.

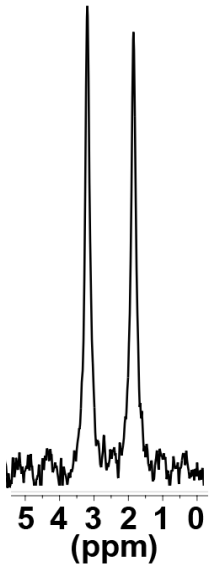

Figure 8.7. Proton decoupled ^{113}Cd NMR spectrum of $[Cd_4(\mu\text{-}OH)_4(\mu\text{-}\mathbf{L}_{\boldsymbol{m}})_2(ACE)_2(H_2O)_2](ClO_4)_4$, **3**.

Results of the diffusion experiment, PFGSE (Pulsed Field-Gradient Spin Echo), also support the presence of the tetrameric form in solution. The hydrodynamic radius of **3** in acetonitrile, calculated based on the diffusion coefficient measured by PFGSE NMR, was determined as 8.4 Å. This number agrees with the maximum radius (also 8.4 Å) calculated from the X-Ray structure for a hypothetical sphere generated around the cubane compound.

Variable temperature ^{1}H NMR (VT-NMR). As observed previously with $[Zn_2(\mu\text{-}OH)(\mu\text{-}\mathbf{L}_{\boldsymbol{m}})_2](ClO_4)_3$, a molecule that was shown to display a very unusual fluxional

process,[10] the pyrazolyl hydrogen resonances of **3** are broad at room temperature. Upon increasing the temperature of the sample of **3** the pyrazolyl resonances broaden substantially and start to equilibrate, indicating that this molecule is also fluxional.[23] To study this process, the VT ^{1}H NMR spectra of **3** was recorded over the liquid range of ACN-d_3, as shown on Figure 8.8.

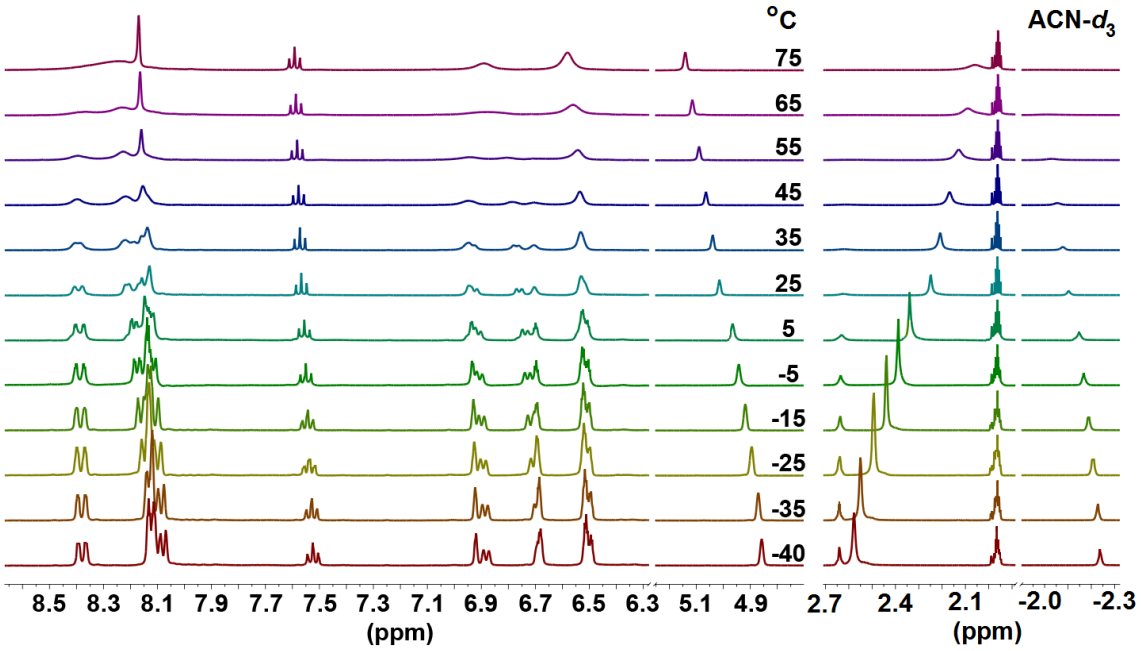

Figure 8.8. The ^{1}H VT-NMR spectra of **3** over the liquid range of ACN-d_3.

Even though the temperature range accessible in ACN-d_3 is relatively narrow (-40 to 75°C) and the limiting high temperature spectra could not be reached, the data indicate that the four resonances for each type of pyrazolyl hydrogens, the two *f*-position resonances and the two hydroxide resonances observed at lower temperatures coalesce at higher temperatures. The rate constant for the pyrazolyl exchange (k_{Lm}) was modeled successfully by simulation of the *c*-pyrazolyl resonance linewidths using DNMR as implemented in Spinworks.[24] The linewidths of the *c*-pyrazolyl resonance were simulated because that set was most clearly separated from other resonances. The Gibbs energy of

activation, $\Delta G_{Lm}^{\ddagger}$, enthalpy of activation, $\Delta H_{Lm}^{\ddagger}$, and entropy of activation, $\Delta S_{Lm}^{\ddagger}$, were calculated based on the Eyring plot (Figure 8.9). The $\Delta H_{Lm}^{\ddagger}$ based on the Eyring plot is 10.1±0.5 kcal/mol, while the $\Delta S_{Lm}^{\ddagger}$ is -19.2±1.0 cal/mol·K. The Gibbs energy of activation was calculated based on the fundamental equation: $\Delta G_{Lm}^{\ddagger} = \Delta H_{Lm}^{\ddagger} - T \cdot \Delta S_{Lm}^{\ddagger}$ and gave $\Delta G_{Lm}^{\ddagger}$ = 15.8±0.8 kcal/mol at 25°C.

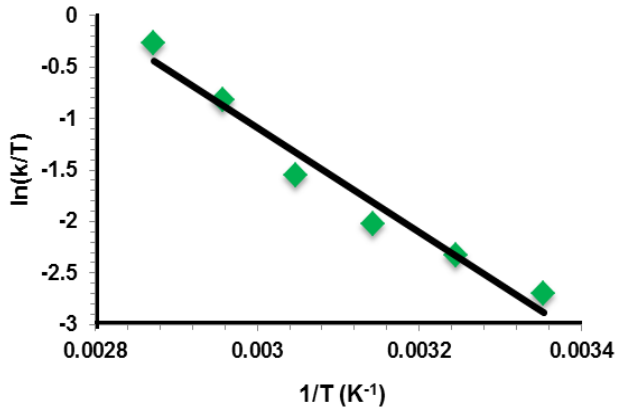

Figure 8.9. Eyring plot based on simulated k_{Lm} values for **3**, where slope = - $\Delta H_{Lm}^{\ddagger}$/R; intercept = $\Delta S_{Lm}^{\ddagger}$/R +23.7600. Green squares: experimental data, Black line: least squares fit, R^2 = 0.96.

For the VT-NMR experiment a different sample was used than for the room temperature NMR studies, which resulted in different trace amounts of H_2O in the sample (from ACN-d_3). The shape of the pyrazolyl resonances (at the same temperature) was affected by this change in the H_2O concentration and as a consequence the magnitude of the rate constant changed. Since the absolute concentration of the water is unknown, it was expressed as the ratio of the integral of H_2O divided by the integral of the *e*-position of the ligand signal at 25ºC. The relative H_2O concentration in the sample used for room temperature NMR studies is 1.8 and in the sample used for VT-NMR experiments it is 2.3. At the same temperature, the pyrazolyl resonances in the sample with more water (2.3) are broader than the same resonances in the sample with less water (1.8), indicating

that the rate of the pyrazolyl exchange increases at higher concentrations of H_2O. The *f*-resonances of the phenylene linker also change, but the *g*- and *e*-resonances are not affected by the change in the H_2O concentration.

Saturation Transfer Experiments. Two different saturation transfer experiments were performed on an ACN-d_3 sample of **3**. The first experiment targeted the exchange process between the nonequivalent *a*-pyrazolyl hydrogens – the same process studied by VT-NMR, while in the second experiment the exchange of the trace amount of H_2O with the bridging hydroxide groups was studied.

During these experiments, one of the exchanging resonances is saturated and the effect on the intensity of the second resonance is monitored. To determine the rate constant for the exchange the decrease in the intensity of the exchanging resonance as a function of increased saturation times at the site of the other exchanging resonance was measured. The saturation time was increased by 0.25 second until the intensity of the resonance remains constant. The plot of the values of $\ln[I_i - I_\infty]$ (I_i - residual intensity after intermediate amounts of saturation times and I_∞ - final intensity) against the saturation time (t) results in a straight line. The slope of this line permits the determination of the rate constant, if the process is first order.[25]

In the first experiment, the overlapping *a*-pyrazolyl hydrogen resonances (~8.16 ppm) were saturated, while the effect of this saturation on the shielded *a*-pyrazolyl resonance (6.94 ppm) was monitored. Since in this case the extra chemical shift difference between the two exchanging *a*-pyrazolyl resonances is an advantage, the *a*-pyrazolyl resonances were used for the experiment, instead of the *c* resonances used for the VT-NMR. To avoid cross saturation of the pyrazolyl resonances the sample was

cooled to 0˚C. Data collected during the saturation transfer experiment is shown on Figure 8.10, left.

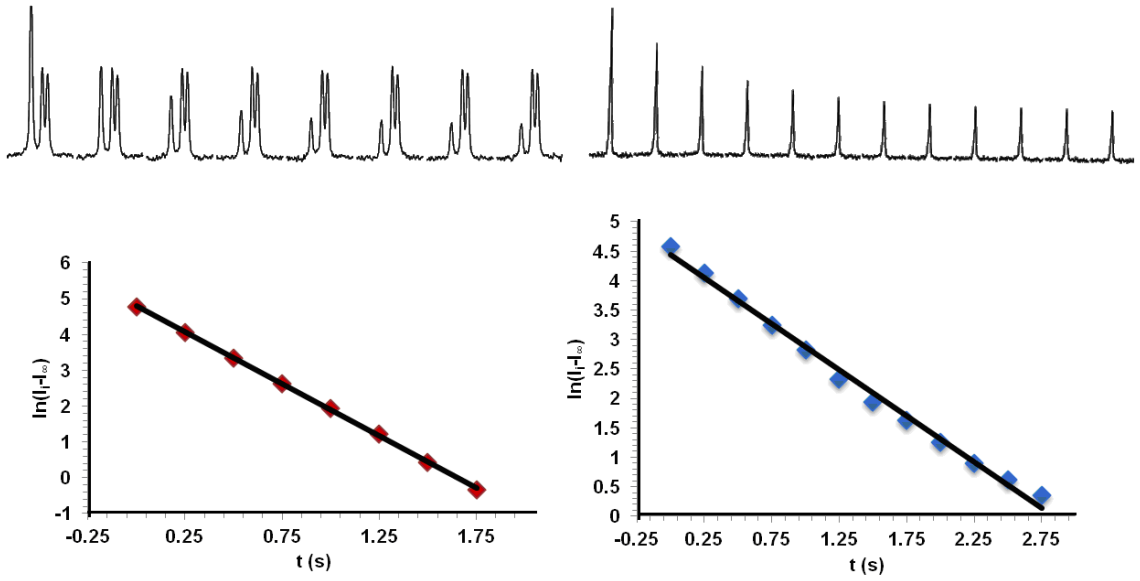

Figure 8.10. Saturation transfer experiment at 0ºC for **3**. Top left: decrease of the *a*-pz resonance as a function of saturation time. For the *a*-pyrazolyl exchange the phenylene doublet (*f*) was included in the figure. As the height of the pyrazolyl resonance decreases upon increased saturation times, the height of the doublet is constant, since the *f* hydrogens are not exchanging with the other *a*-pyrazolyl hydrogens. Bottom left: linear plot of the saturation time vs. the natural logarithm of the a-pz resonance intensities. Top right: decrease of the OH^- resonance as a function of saturation time. Bottom right: linear plot of the saturation time vs. the natural logarithm of the OH^- resonance intensities. Red and blue squares: experimental data; black line: least squares fit, $R^2 = 0.99$.

In the second experiment the H_2O hydrogen resonance (~2.35 ppm) was saturated. The decrease in the intensity of the shielded bridging OH^- hydrogen resonance (-2.15 ppm) as a function of increased saturation times was monitored (Figure 8.10, right).

At 0˚C, for the *a*-pyrazolyl exchange the calculated k_{Lm} is 2.18(±0.1) s^{-1} and $\Delta G_{Lm}^{\ddagger}$ is 15.5(±0.3) kcal/mol. For the water-hydroxide exchange the k_{OH} is 1.16(±0.1) s^{-1} and the $\Delta G_{OH}^{\ddagger}$ is 15.9±(0.3) kcal/mol. The rate constants and activation barriers calculated for the pyrazolyl exchange from the saturation transfer measurements are in very good

agreement with the analogous value calculated from VT-NMR experiments ($\Delta G_{Lm}^{\ddagger}$ = 15.3(±0.8) kcal/mol at 0ºC for the same sample).

Magnetic Properties of $[Ni_4(\mu\text{-}OH)_4(\mu\text{-}L_m)_2(DMF)_4](ClO_4)_4\cdot DMF\cdot EtOH$, 1. The effective magnetic moment (Figure 8.11), calculated per entire tetranuclear molecule is 6.53 BM at 300 K, somewhat higher than that expected for 4 non-interacting nickel(II) ions with a g value of about 2.2 ($\mu_{\text{eff}} = g\sqrt{4S(S+1)} = 6.22$). Upon lowering the temperature, μ_{eff} increases to reach a maximum of 9.75 BM at 5.5 K and then decreases to 8.74 at 1.8 K. The maximum μ_{eff} value is close to that expected for a tetranuclear nickel(II) system with only the S = 4 state populated ($\mu_{\text{eff}} = g\sqrt{S(S+1)} = 9.84$). This behavior indicates weak ferromagnetic interactions between the nickel ions. The magnetic moment decrease at the lowest temperatures is caused by the Zeeman splitting plus the zero-field splitting becoming comparable to the thermal energy, kT. The structure of the molecular core (Figure 8.2) reveals that each nickel(II) ion is connected to its three neighbors by three oxygen atoms. If the core had been a perfect cube, with all Ni-O-Ni angle around 90°, all six exchange integrals J_{ij} would be equal. However, upon closer examination, two types of Ni-O-Ni angles may be distinguished: in the first group, the Ni-O-Ni angle are in the range 97.9 to 98.9° (Ni1-Ni2, Ni2-Ni4 and Ni3-Ni4), while the angles are slightly larger in the second group, 100.1 to 100.5° (Ni1-Ni3, Ni1-Ni4 and Ni2-Ni3). Two kinds of exchange interactions are expected, the one in the first group being more ferromagnetic. It should be emphasized that this is an approximation to obtain a manageable model, while in fact all six exchange integrals are likely to be different. The Heisenberg-Dirac-VanVleck Hamiltonian for the isotropic exchange interactions will have the form:

$$\hat{\boldsymbol{H}}_{\mathrm{HDVV}} = -J_1(\hat{\boldsymbol{S}}_1\hat{\boldsymbol{S}}_2 + \hat{\boldsymbol{S}}_2\hat{\boldsymbol{S}}_4 + \hat{\boldsymbol{S}}_3\hat{\boldsymbol{S}}_4) - J_2(\hat{\boldsymbol{S}}_1\hat{\boldsymbol{S}}_3 + \hat{\boldsymbol{S}}_1\hat{\boldsymbol{S}}_4 + \hat{\boldsymbol{S}}_2\hat{\boldsymbol{S}}_3) \qquad (1)$$

The total spin of our tetranuclear system is defined as

$$\hat{\boldsymbol{S}}_{\mathrm{T}} = \hat{\boldsymbol{S}}_1 + \hat{\boldsymbol{S}}_2 + \hat{\boldsymbol{S}}_3 + \hat{\boldsymbol{S}}_4 \qquad (2)$$

Exchange interactions result in one $S_T = 4$ state, 3 $S_T = 3$ states, 6 $S_T = 2$ states, 6 $S_T = 1$ states and 3 $S_T = 0$ states. If $J_1 = J_2$ in eq (1) above then all states with a given S_T have the same energy, but are split otherwise.

Non-negligible zero-field splitting (zfs) effects are also expected. In polynuclear transition metal systems there are three sources of zfs: the magnetic dipole-dipole interactions, the anisotropic exchange interactions and the zero-field splitting on individual ions, if their spin is larger than ½. The third contribution should be the most important in our case, as nickel(II) is known to exhibit large *D* and *E* parameters corresponding to the spin Hamiltonian

$$\hat{\boldsymbol{H}}_{\mathrm{i}}^{\mathrm{zfs}} = D_{\mathrm{i}}[\hat{\boldsymbol{S}}_{\mathrm{zi}}^{2} - S_{\mathrm{i}}(S_{\mathrm{i}}+1)/3] + E_{\mathrm{i}}(\hat{\boldsymbol{S}}_{\mathrm{xi}}^{2} - \hat{\boldsymbol{S}}_{\mathrm{yi}}^{2}) \qquad (3)$$

where the index i = 1 to 4 [nickel(II) ions]. A full spin Hamiltonian to describe the magnetic properties as well as the electron paramagnetic resonance spectra is:

$$\hat{\boldsymbol{H}} = \hat{\boldsymbol{H}}_{\mathrm{HDVV}} + \hat{\boldsymbol{H}}_1^{\mathrm{zfs}} + \hat{\boldsymbol{H}}_2^{\mathrm{zfs}} + \boldsymbol{H}_3^{\mathrm{zfs}} + \hat{\boldsymbol{H}}_4^{\mathrm{zfs}} + \mu_{\mathrm{B}}B(\{\boldsymbol{g}_1\}\hat{\boldsymbol{S}}_1 + \{\boldsymbol{g}_2\}\hat{\boldsymbol{S}}_2 + \{\boldsymbol{g}_3\}\hat{\boldsymbol{S}}_3 + \{\boldsymbol{g}_4\}\hat{\boldsymbol{S}}_4)$$

(4)

The last term represents the Zeeman interaction. The $\{\boldsymbol{g}_{\mathrm{i}}\}$, D_{i} and E_{i} values will be assumed equal for all four nickel(II) ions, but the $\{\boldsymbol{g}_{\mathrm{i}}\}$ and zfs tensors are not coaxial.

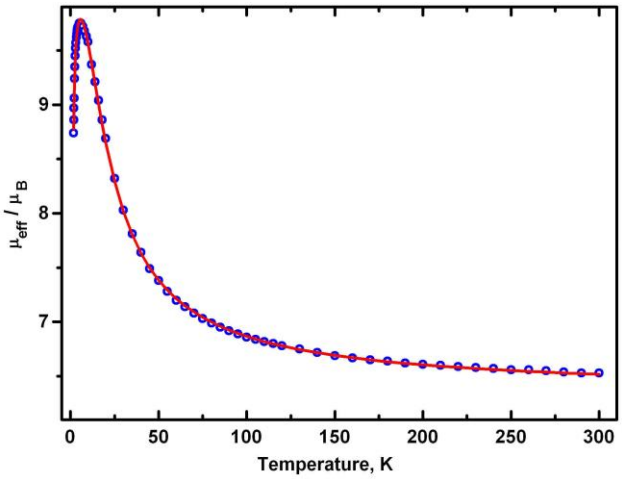

Figure 8.11. The experimental effective magnetic moments (circles) and calculated (solid line) referred to four nickel(II) ions. The fitting procedure resulted in g_{ave} = 2.24, D_i = 5.8 cm^{-1}, E = 2.3 cm^{-1} (g, D and E assumed to be the same for all four metal ions, but their orientations in space are different), J_1 = 9.1 cm^{-1}, J_2 = 2.1 cm^{-1}.

EPR Spectra of $[Ni_4(\mu\text{-}OH)_4(\mu\text{-}L_m)_2(DMF)_4](ClO_4)_4\cdot DMF\cdot EtOH$, 1. Well resolved spectra coming from the ground S_T = 4 state of the tetranuclear molecule were observed at high microwave frequencies ca. 50-430 GHz at low temperatures. (Figure 8.12). No spectra of excited spin states could be observed at any temperature. The temperature dependence of the spectra allowed determination of the sign of the zero-field splitting parameters D and E, which is negative. The coupled-spin state Hamiltonian with S = 4 was used in the EPR simulations:

$$\hat{\boldsymbol{H}}_{S=4} = \mu_B B(\{\boldsymbol{g}\}\hat{\boldsymbol{S}} + D\,[\hat{\boldsymbol{S}}_z^{\,2} - S(S_i+1)/3] + E(\hat{\boldsymbol{S}}_x^{\,2} - \hat{\boldsymbol{S}}_y^{\,2}) + B_4^{\,0}O_4^{\,0} + B_4^{\,2}O_4^{\,2} + B_4^{\,4}O_4^{\,4} \quad (5)$$

The more correct procedure using the spin Hamiltonian (4) is prohibitively difficult with respect to the calculation time and many needed parameters cannot be predicted, like the orientations of the g and zfs tensors of the four nickel ions. The simulation procedures resulted in the parameter set for S = 4: g_x = 2.205, g_y = 2.157, g_z = 2.204, D = -0.299 cm^{-1}, E = -0.036 cm^{-1}, $B_4^{\,0}$ = -3.7·10^{-5} cm^{-1}, $B_4^{\,2}$ = 4.2·10^{-4} cm^{-1}, $B_4^{\,4}$ = -1.6·10^{-4} cm^{-1}.

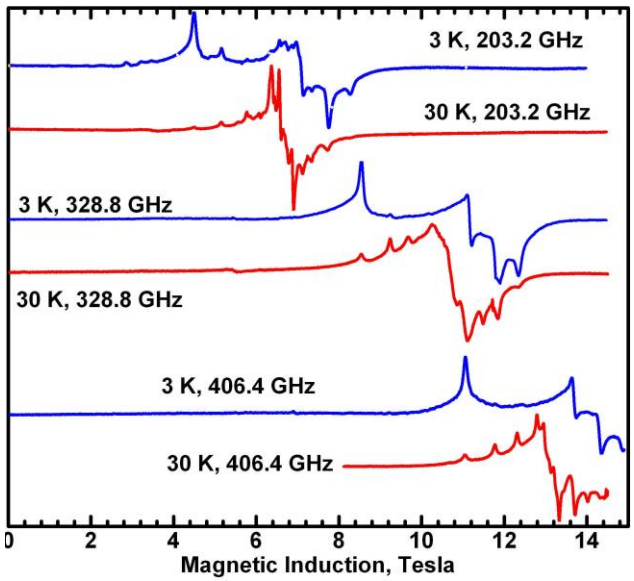

Figure 8.12. EPR spectra of **1** at temperatures and microwave frequencies as indicated. The intense transition at the low field in the three 3 K spectra is the first (of 8) "allowed" parallel (Z) transitions in the $S = 4$ spin state, occurring between the $M_S = -4$ and $M_S = -3$ states. The $M_S = -4$ state is the only one significantly populated at 3 K and at the high magnetic field (see SI). More transitions appear at 30 K as the states $M_S = -3$, -2 etc. become populated. The highest-field feature in the 203.2 and 328.8 GHz spectra is the Y transition. The intensity relations allow the determination of the negative sign of the D parameter in the spin Hamiltonian for $S = 4$.

The necessity of including the fourth order spin operators in the EPR simulations may be an artifact caused by the mixing of the levels belonging to different S_T states by the zero-field splitting and the Zeeman interactions. Similar effects have been observed before.[26]

The relationship between the zfs parameters D and E of the single-ion Hamiltonian (3) and the D and E parameters of the "giant spin" Hamiltonian (5) are known.[27] For example, in case of a nickel(II) tetramer, in which the zfs tensors on all individual ion are parallel and equal, a D_i value of Hamiltonian (3) would result in $D = D_i/7$ in the spin Hamiltonian (5) for the $S = 4$ state. However, in the present case, the D and E values of the four nickel(II) ions are unlikely to be equal, and moreover, their orientations are impossible to predict. Determining zfs on individual nickel ions from the spin

Hamiltonian parameters found for the coupled $S = 4$ state is therefore impossible. Spin Hamiltonian (5) was successfully used here to simulate the EPR spectra as well as the field dependence of the magnetization at 2 K.

Discussion and Conclusions

Nickel(II) and cadmium(II) compounds with cubane core were synthesized where the corners of the "cube" are occupied by four metal centers alternating with four hydroxide bridges. This arrangement is supported by the bis(pyrazolyl)methane ligand $\mathbf{L}_{\boldsymbol{m}}$ and additional solvent molecules from the crystallization procedure in the solid state to give compounds of the type $[M_4(\mu\text{-}OH)_4(\mu\text{-}\mathbf{L}_{\boldsymbol{m}})_2(\text{solvent})_4](ClO_4)_4$, with octahedral metal centers. The cubane core is highly stable in gas phase and solution as indicated by ESI^+-MS and NMR experiments. While several cubane cored coordination compounds are known, this type of cluster is rarely generated by triply bridging hydroxide groups.[5,6]

The cubane core can be seen as being assembled from two bridged dinuclear units of the type $[M_2(\mu\text{-}OH)_2(\mu\text{-}\mathbf{L}_{\boldsymbol{m}})(\text{solvent})_2]^{2+}$, with the ligand $\mathbf{L}_{\boldsymbol{m}}$, in the *syn* conformation, and two hydroxide bridging the two metals. The connection between two of these $[M_2(\mu\text{-}OH)_2(\mu\text{-}\mathbf{L}_{\boldsymbol{m}})(\text{solvent})_2]^{2+}$ units is realized through further coordination of the hydroxide bridges to the metal centers of another $[M_2(\mu\text{-}OH)_2(\mu\text{-}\mathbf{L}_{\boldsymbol{m}})(\text{solvent})_2]^{2+}$ unit to generate a cubane core. From this view of the cubane compounds, it is straightforward to envisage a C_2 axis of rotation passing through the middle of the "cube", and bilateral symmetry as observed for compound **2** in the solid state (Figure 8.13) and for compound **3** in solution.

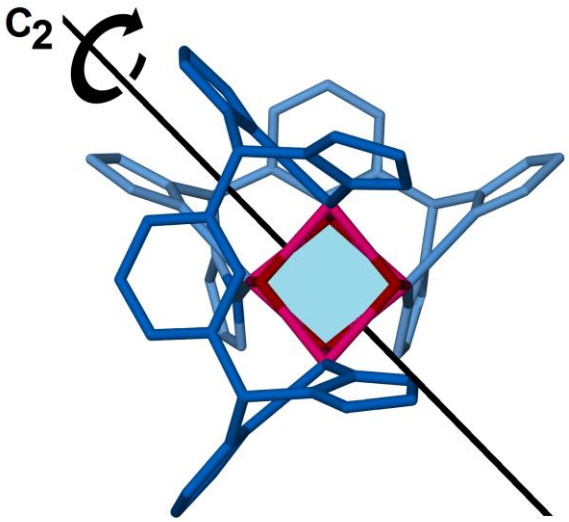

Figure 8.13. A C_2 axis passing through the cation $[Cd_4(\mu\text{-}OH)_4(\mu\text{-}\mathbf{L}_{\boldsymbol{m}})_2]^{4+}$ in solution, making two cadmium(II) centers and the two ligands symmetry equivalent. The figure is based on the crystal structure of **3**. Hydrogen atoms are omitted for clarity of the figure. Color code: $\mathbf{L}_{\boldsymbol{m}}$ blue, cadmium(II) pink, OH^- oxygen red. Darker shades of blue are on the top of the "cube", lighter shades in the back.

The cadmium(II) compound was characterized by a series of NMR experiments in solution that support the cubane structure in acetonitrile and acetone solutions. The 2D NMR experiments (HSQC, HMBC and COSY) facilitated the assignment of the complicated ^{1}H NMR resonances, some resonances of which are accidentally superimposed (isochronous). Two nonequivalent sites of cadmium(II) centers and hydroxides were observed, while there are four different types of pyrazolyl rings in the solution structure, and the phenylene linker has two inequivalent *f* hydrogens, all in agreement with a cubane core with a C_2 axis of rotation on average in solution (Figure 8.13).

The ^{1}H VT-NMR and saturation transfer experiments show that each type of pyrazolyl hydrogen are exchanging, as well as the *f* positions of the phenylene linkers. The four broad pyrazolyl resonances for each type of ring hydrogen and the two *f*

phenylene resonance and bridging hydroxide resonances broaden and/or coalesce at higher temperatures. In the case of the zinc(II) metallacycle, $[Zn_2(\mu\text{-}OH)(\mu\text{-}\mathbf{L}_{\boldsymbol{m}})_2](ClO_4)_3$, it was shown that the two sets of nonequivalent pyrazolyl rings [axial and equatorial in a trigonal bipyramidal geometry around zinc(II)] exchange through a Berry pseudorotation mechanism at *both metal sites* accompanied by the simultaneous 180° ring flip of the phenylene linkers, a rearrangement process termed the "Columbia Twist and Flip."

Similarly for **3** the cubane core is retained in solution despite the fast exchange of weakly coordinated solvent molecules on the NMR timescale, resulting in effectively five coordinate cadmium(II) centers on average. In this system, three oxygen positions are fixed in the cubane core, while the remaining two positions are occupied by the $\mathbf{L}_{\boldsymbol{m}}$ pyrazolyl rings. In order to explain the NMR behavior of **3** presented here, a similar rearrangement process is proposed, where pairs of pyrazolyl rings at each of the two metals linked by $\mathbf{L}_{\boldsymbol{m}}$ twist (about 90°) with the simultaneous 180° flip of the phenylene linker along the C_{methine}-C_{Ph} bond according to Figure 8.14, the Columbia Twist and Flip mechanism. The twist of the pyrazolyl rings accompanied by the ring flip of the phenylene linker equilibrates the red and blue/pink and teal pairs of pyrazolyl rings. In order to equilibrate all four inequivalent pyrazolyl ring; the second $\mathbf{L}_{\boldsymbol{m}}$ ligand must undergo the same Columbia Twist and Flip motion. These combined motions result in the exchange of the nonequivalent pyrazolyl rings and the *f* positions of the phenylene linkers, as well as the two nonequivalent cadmium(II) and hydroxide sites (Figure 8.8), while the overall structure remains unchanged. The $\Delta G_{\text{L}m}^{\ddagger}$ for the combined motion of the $\mathbf{L}_{\boldsymbol{m}}$ ligands is 15.8 kcal/mol at 25°C, similar to the one measured for $[Zn_2(\mu\text{-}OH)(\mu\text{-}\mathbf{L}_{\boldsymbol{m}})_2](ClO_4)_3$ of 15.2 kcal/mol at 25°C.

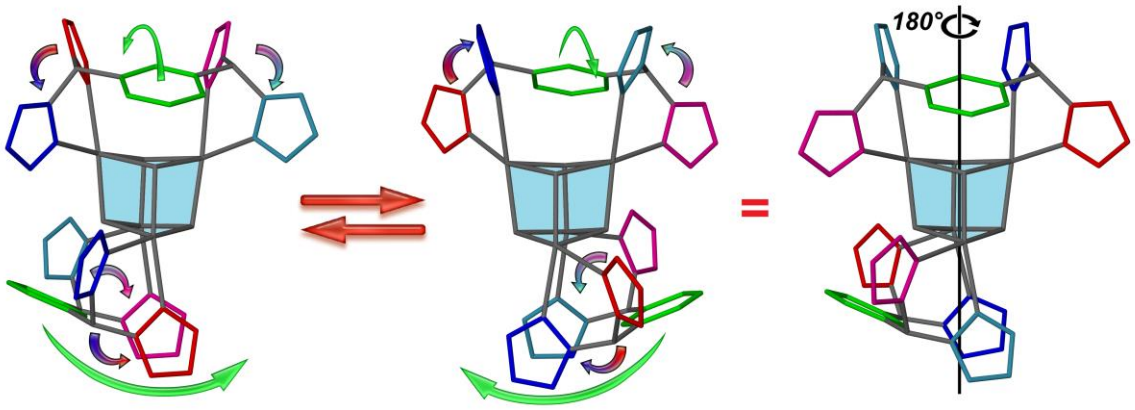

Figure 8.14. The exchange of the inequivalent (red, pink, blue and teal) pyrazolyl rings of **3** through 90° twist of the pyrazolyl rings, accompanied by the 180° flip of the phenylene linkers (left and middle molecules). Rotation of the middle structure by 180°, after both ligands have undergone the Columbia Twist and Flip motion, results in the view on the right side, which is in a similar orientation to the one on the left with the rings and cubane core positions exchanged.

The linewidths of the exchanging resonances are dependent on the water (from ACN-d_3) concentration in the sample; the more water is in the sample, the broader the *a*, *b* and *c*-pyrazolyl and *f*-phenylene resonances become in the room temperature ^{1}H NMR spectra. In addition, saturation transfer experiments at 0°C show that the hydroxide and water hydrogen exchange, $\Delta G_{OH}^{\ddagger}$ is 15.9 kcal/mol. This process has a slightly higher energy barrier than the pyrazolyl exchange, 15.3 kcal/mol at 0°C, as observed with $[Zn_2(\mu\text{-}OH)(\mu\text{-}\mathbf{L}_m)_2](ClO_4)_3$. Considering the experimental results above, the twist and flip motion of $\mathbf{L}_m$ in the cubane compounds and the water-hydroxide exchange are probably independent but related processes.

The compound $[Ni_4(\mu\text{-}OH)_4(\mu\text{-}\mathbf{L}_m)_2(DMF)_4](ClO_4)_4\cdot DMF\cdot EtOH$, **1**, was magnetically characterized. Temperature dependence of the magnetic susceptibility was fitted using spin Hamiltonian (4) with two triads of equal *J* values and assuming a model with the zfs tensors of all nickel(II) ions equal and their Z orientation chosen along the respective Ni-O_{DMF} directions. The fitting of the experimental data to this model (Figure

8.11) resulted in two strongly different J values and strongly non-axial zfs parameters for the nickel(II) ions (g_{ave} = 2.24, D_i = 5.8 cm^{-1}, E = 2.3 cm^{-1}, J_1 = 9.1 cm^{-1} and J_2 = 2.1 cm^{-1}).

"Broken symmetry" Density Functional Theory (DFT) were performed to get more insight into the exchange interactions in this system. The tetranuclear molecule was simplified by converting DMF into formamide. To calculate the exchange integral between a pair of nickel(II) ions, the remaining two nickel(II) were replaced by zinc(II). One calculation was performed for the pair in which the Ni-O-Ni angles were larger and another for a pair with smaller Ni-O-Ni angles. The calculation was indeed able to distinguish between these situations, although the calculated exchange integrals (J_1 = 9.2 cm^{-1}, J_2 = 5.0 cm^{-1}) were less different than those found from the magnetic susceptibility. The magnetic orbitals are shown in Figure 8.15. Ferromagnetic interactions were found in each case, which were weaker with larger Ni-O-Ni angles, as expected.

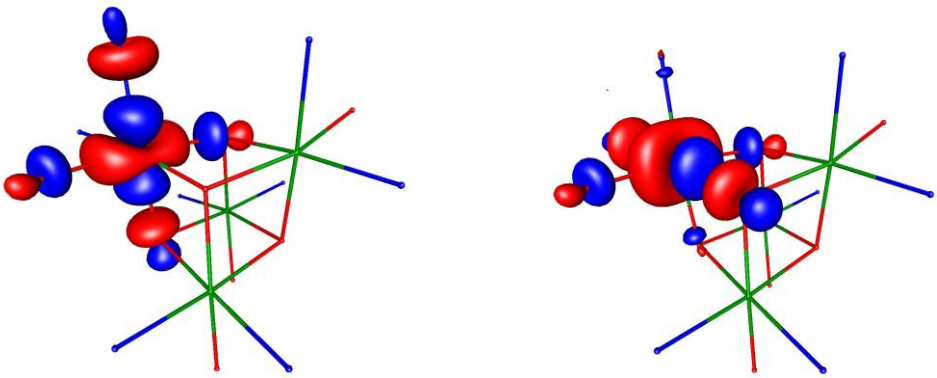

Figure 8.15. Magnetic orbitals of one of the nickel(II) ions calculated from DFT. Only the metal atoms and the coordinated ligand atoms are shown. Left: the $d_{x^2-y^2}$ type orbital; right: the d_{z^2}-type orbital. Corresponding orbitals of the same shape are located on another nickel(II) ion in an interacting pair. The overlap integrals of the $d_{x^2-y^2}$ type magnetic orbitals are 0.038 and 0.047 for the pairs with smaller Ni-O-Ni angles (around 98-99°) and larger angles (around 100°), respectively. The overlaps of the d_{z^2}-type magnetic orbitals are 0.014 and 0.016, respectively.

References

(1) (a) Halcrow, M. A.; Christou, G. *Chem. Rev.* **1994**, *94*, 2421. (b) Fukuyama, K. "*Handbook of Metalloproteins*" Wiley, Chichester, UK, 2001, 543. (c) Carter, C. W. "*Handbook of Metalloproteins"* Wiley, Chichester, UK, 2001, 602.

(2) (a) Urdempilleta, M.; Klyatskaya, S.; Cleuziou, J.-P.; Ruben, M.; Wernsdorger, W. *Nature Mat.* **2011**, *10*, 502. (b) Zhu, L.; Yao, K. L.; Liu, Z. L. *Appl. Phys. Lett.* **2010**, *96*, 082115.

(3) Venegas-Yazigi, D.; Cano, J.; Ruiz, E.; Alvarez, S. *Phys. B* **2006**, *384*, 123.

(4) (a) Bogni, L.; Wernsdorfer, W. *Nature Mat.* **2008**, *7*, 179. (b) Glaser, T. *Chem. Commun.* **2011**, *47*, 116. (c) Affronte, M.; Troiani, F.; Ghirri, A.; Candini, A.; Evangelisti, M.; Corradini, V.; Carretta, S.; Santini, P.; Amoretti, G.; Tuna, F.; Timco, G.; Winpenny, R. E. P. *J. Phys. D: Appl. Phys.* **2007**, *40*, 2999. (d) Enders, A.; Skomski, R.; Honolka, J. *J. Phys.: Condens. Matter.* **2010**, *22*, 433001.

(5) Publications listed cronologically: (a) Zhang, S.-H.; Zhang, Y. D.; Zou, H. H.; Guo, J. J.; Li, H. P.; Song, Y.; Liang, H. *Inorg. Chim. Acta* **2013**, *396*, 119. (b) Das, A.; Klinke, F. J.; Demeshko, S.; Meyer, S.; Dechert, S, Meyer, F. *Inorg. Chem.* **2012**, *51*, 8141. (c) Feng, X.; Ma, L.-F.; Zhao, J.-S. *Inorg. Chem. Comm.* **2011**, *14*, 584. (d) Zhang, W.-H.; Sulaiman, N. B.; Tio, S. P. X.; Hor, A. T. S. *CrystEngComm* **2011**, *13*, 2915. (e) Zhang, S.-H.; Li, N.; Ge, C.-M.; Feng, C.; Ma, L.-F. *Dalton Trans.* **2011**, *40*, 3000. (f) Yu, G.-M.; Zhao, L.; Zou, L.-F.; Guo, Y.-N.; Xu, G.-F.; Li, Y.-H.; Tang, J. *J. Chem. Crystallogr.* **2011**, *41*, 606. (g) Wang, F.-M.; Lin, J.-G.; Xing, Y.-Y.; Liu, Y.-M.; Lu, C.-S.; Meng, Q.-J. J. *Coord. Chem.* **2010**, *63*, 3431. (h) Moro, F.; Piga, F.; Krivokapic, I.; Burgess, A.; Lewis, W.; McMaster, J.; van Slageren J. *Inorg. Chim. Acta* **2010**, *363*, 4329. (i) Fomina, I. G.; Dobrokhotova, Z. V.; Aleksandrov, G. G.; Proshenkina, O. Yu.; Kovba, M. L.; Bogomyakov, A. S.; Ikorskii, V. N.; Novotortsev, V. M.; Eremenko, I. L. *Russ. Chem. Bull. Int. Ed.* **2009**, *58*, 11. (j) Mandal, D.; Hong, C. S.; Kim, H. C.; Fun, H.-K.; Ray, D. *Polyhedron* **2008**, 27, 2372. (k) Lin, Z.; Li, Z.; Zhang, H. *Cryst. Gr. Des.* **2007**, *7*, 589. (l) Isele, K.; Gigon, F.; Williams, A. F.; Bernardinelli, G.; Franz, P.; Decurtins, S. *Dalton Trans.* **2007**, 332. (m) Alley, K. G.; Bircher, R.; Güdel, H. U.; Moubaraki, B.; Murray, K. S.; Abrahams, B. S.; Boskovic, C. *Polyhedron* **2007**, *26*, 269. (n) Song, X.-Y.; Xu, Y; Li, L.; Liao, D.; Jiang, Z. *Inorg. Chim. Acta* **2007**, 2039. (o) Abrahams, B. F.; Hudson , T. A.; Robson, R. *Chem. Eur. J.* **2006**, *12*, 7095. (p) Yang, E.-C.; Wernsdorfer, W.; Zakharov. L. N.; Karaki, Y.; Yamaguchi, A.; Isidro, R. M.; Lu, G.-D.; Wilson, S. A.; Rheingold, A. L.; Ishimoto, H.; Hendrickson, D. N. *Inorg. Chem.* **2006**, *45*, 529. (q) Li, Y.-M.; Zhang, J.-J.; Fu, R.-B.; Xiang, S.-C.; Sheng, T.-L.; Yuan, D.-Q.; Huang, X.-H.; Wu, X.-T *Polyhedron*, **2006**, *25*, 1618. (r) Sieber, A.; Boskovic, C.; Bircher, R.; Waldmann, O.; Ochsenbein, S. T.; Chaboussant, G.; Güdel, H. U.; Kirchner, N.; van Slageren, J.; Wernsdorfer, W.; Neels, A.; Stoeckli-Evans, H.; Janssen, S.; Juranyi F.; Mutka, H. *Inorg. Chem.* **2005**, *44*, 4315. (s) Moragues-Canovas, M.; Helliwell, M.; Ricard, L.; Riviere, E.; Wernsdorfer, W.; Brechin, E.; Mallah, T. Eur. J. *Inorg. Chem.* **2004**, 2219. (t) Yang, E.-C.; Wernsdorfer, W.; Hill, S.; Edwards, R. S.; Nakano, M.;

Maccagnano, M.; Zakharov, L. N.; Rheingold, A. N.; Christou, G.; Hendrickson, D. N. *Polyhedron* **2003**, *22*, 1727. (u) Clemente-Juan, J. M.; Chansou, B.; Donnadieu, B.; Tuchagues, J. P. *Inorg. Chem.* **2000**, *39*, 5515 and references therein. (v) Escuer, A.; Font-Bardía, M.; Kumar, S. B.; Solans, X.; Vicente, R. *Polyhedron* **1999**, *18*, 909.

(6) (a) Wikstrom, J. P.; Nazarenko, A. Y.; Reif, W. A.; Rybak-Akimova, E. V. *Inorg. Chim. Acta* **2007**, *360*, 3733. (b) Ballester, L.; Coronado, E.; Gutierrez A.; Monge, A.; Perpinan, M. F.; Pinilla, E.; Rico, T. *Inorg. Chem.* **1992**, *31*, 2053. (c) Boyd, P. D. W.; Martin, R. L.; Schwarzenback, G. *Aust. J. Chem.* **1988**, *41*, 1449. (d) Aurivillius, B. *Acta Chem. Scand.* **1977**, *31*, 501.

(7) (a) Zhu, R.-Q. *Acta Cryst.* **2011**, *E67*, m1416. (b) Lee, C.-J.; Wei, H.-H; Lee, G.-H.; Wang, Y. *Inorg. Chem. Comm.* **2000**, *3*, 690.

(8) (a) Chen, Z.; Liang, F.; Zhou, S.; Xia, C.; Hu, R. *J. Mol. Struc.* **2007**, *827*, 20. (b) Suen, M.-C.; Wang, J.-C. *Inorg. Chem. Comm.* **2006**, *9*, 478. (c) Tong, M.-L.; Lee, H. K.; Zheng, S.-L.; Chen, X.-M. *Chem. Lett.*, **1999**, 1087.

(9) (a) Reger, D. L.; Watson, R. P.; Smith, P. J. *Inorg. Chem.* **2006**, *45*, 10077. (b) Reger, D. L.; Foley, E. A.; Watson, R. P.; Pellechia, P. J.; Smith, M. D., Grandjean, F.; Long, G. J. *Inorg. Chem.* **2009**, *48*, 10658. (c) Reger, D. L; Watson, R. P.; Smith, M. D.; Pellechia, P. J. *Organometallics* **2005**, *24*, 1544.

(10) Reger, D. L.; Pascui, A. E.; Pellechia, P. J.; Smith, M. D. *Inorg. Chem.* **2013**, *52*, 11638.

(11) Jarek, R. L.; Flesher, R. J.; Shin, S. K. *J. Chem. Ed.* **1997**, *74*, 978.

(12) a) Barbour, L. J *J. Supramol. Chem.* **2003**, *1*, 189. (b) *POV-RAY 3.6*, **2006**, Persistence of Vision Raytracer Pty Ltd, Williamstown, Vic., Australia.

(13) MestReNOVA v.5.2.5, Mestrelab Research S. L. **2008**.

(14) Hassan, A. K.; Pardi, L. A.; Krzystek, J.; Sienkiewicz, A.; Goy, P.; Rohrer, M.; Brunel, L.-C. *J. Magn. Reson.* **2000**, *142*, 300.

(15) (a) O'Connor, C. J. *Prog. Inorg. Chem.* **1982**, *29*, 203; (b) Bain, G. A.; Berry, J. F. *J. Chem. Ed.* **2008**, *85*, 532.

(16) Wolsey, W. C. *J. Chem. Educ.* **1973**, *50*, A335-A337.

(17) SMART Version 5.630, SAINT+ Version 6.45. Bruker Analytical X-ray Systems, Inc.,Madison, Wisconsin, USA, **2003**.

(18) G.M. Sheldrick, SHELXTL Version 6.14, Bruker Analytical X-ray Systems, Inc., Madison, Wisconsin, USA, **2000**.

(19) Shannon, R. D. *Acta Cryst.* **1976**, *A32*, 751.

(20) Steed, J. W.; Atwood J. L. in "*Supramolecular Chemistry"* 2nd Ed., John Wiley & Sons, UK, 2009.

(21) D. L. Reger, A. E. Pascui, M. D. Smith, J. Jezierska, A. Ozarowski *Inorg. Chem.* **2012**, *51*, 11820.

(22) Gavrilova, A. L.; Qin, C. J.; Sommer, R. D.; Rheingold, A. L.; Bosnich, B. *J. Am. Chem. Soc.* **2002**, *124*, 1714.

(23) Sandström, J. *Dynamic NMR Spectroscopy*, London & New York **1982**.

(24) SPINWORKS 3 v.3.1.8.2, Kirk Marat **2011**.

(25) (a) Forsén, S.; Hoffman, R. A. *J. Chem. Phys.* **1963**, *39*, 2892. (b) Babailov, S. P.; Krieger, Y. G. *J. Struct. Chem.* **2001**, *42*, 305. (c) DiFranco, S. A.; Maciulis, N. A.; Staples, R. J.; Batrice, R. J.; Odom, A. L. *Inorg. Chem.* **2012**, *51*, 1187. (d) Faller, J. W.; Wilt, J. C. *Organometallics* **2005**, *24*, 5076. (e) Ashby, M. D.; Govindan, G. N.; Grafton , A. K. *J. Am. Chem. Soc.* **1994**, *116*, 4801. (f) Wik, B. J.; Lersch, M.; Krivokapic, A.; Tilset, M. J. Am. Chem. Soc. **2006**, *128*, 2682. (g) Rybtchinski, B.; Cohen, R.; Ben-David Y.; Martin, J. M. L.; Milstein, D. *J. Am. Chem. Soc.* **2003**, *125*, 11041.

(26) (a) Burdinski, D.; Bill, E.; Birkelbach, F.; Wieghardt, K.; Chaudhuri, P. *Inorg. Chem.* **2001**, *40*, 1160. (b) Semenaka, V. V.; Nesterova, O. V.; Kokozay, V. N.; Dyakonenko, V. V.; Zubatyuk, R. I.; Shishkin, O. V.; Boca, R.; Jezierska, J.; Ozarowski, A. *Inorg. Chem.* **2010**, *49*, 5460.

Appendix A: Copyright Permissions

Title: "NMR Investigations of Dinuclear, Single-Anion Bridged Copper(II) Metallacycles: Structure and Antiferromagnetic Behavior in Solution"
Author: Daniel L. Reger, Andrea E. Pascui, Perry J. Pellechia, and Andrew Ozarowski
Publication: Inorganic Chemistry
Publisher: American Chemical Society
Date: Nov 1, 2013

Title: "Zinc(II) and Cadmium(II) Monohydroxide Bridged, Dinuclear Metallacycles: A Unique Case of Concerted Double Berry Pseudorotation"
Author: Daniel L. Reger, Andrea E. Pascui, Perry J. Pellechia, and Mark D. Smith
Publication: Inorganic Chemistry
Publisher: American Chemical Society
Date: Sep 1, 2013

Title: "Dinuclear Complexes Containing Linear M-F-M [M = Mn(II), Fe(II), Co(II), Ni(II), Cu(II), Zn(II), Cd(II)] Bridges: Trends in Structures, Antiferromagnetic Superexchange Interactions, and Spectroscopic Properties"
Author: Daniel L. Reger, Andrea E. Pascui, Mark, D. Smith, Julia Jezierska and Andrew Ozarowski
Publication: Inorganic Chemistry
Publisher: American Chemical Society
Date: Nov 1, 2012

Title: "Halide and Hydroxide Linearly Bridged Bimetallic Copper(II) Complexes: Trends in Strong Antiferromagnetic Superexchange Interactions"
Author: Daniel L. Reger, Andrea E. Pascui, Mark, D. Smith, Julia Jezierska and Andrew Ozarowski
Publication: Inorganic Chemistry
Publisher: American Chemical Society
Date: Aug 1, 2012

PERMISSION/LICENSE IS GRANTED FOR YOUR ORDER AT NO CHARGE
This type of permission/license, instead of the standard Terms & Conditions, is sent to you because no fee is being charged for your order. Please note the following:

- Permission is granted for your request in both print and electronic formats, and translations.
- If figures and/or tables were requested, they may be adapted or used in part.
- Please print this page for your records and send a copy of it to your publisher/graduate school.
- Appropriate credit for the requested material should be given as follows: "Reprinted (adapted) with permission from (COMPLETE REFERENCE CITATION). Copyright (YEAR) American Chemical Society." Insert appropriate information in place of the capitalized words.
- One-time permission is granted only for the use specified in your request. No additional uses are granted (such as derivative works or other editions). For any other uses, please submit a new request.

JOHN WILEY AND SONS LICENSE TERMS AND CONDITIONS
Sep 16, 2013

This is a License Agreement between Andrea E Pascui ("You") and John Wiley and Sons ("John Wiley and Sons") provided by Copyright Clearance Center ("CCC"). The license consists of your order details, the terms and conditions provided by John Wiley and Sons, and the payment terms and conditions.

License Number: 3230821316376
License date: Sep 16, 2013
Licensed content publisher: John Wiley and Sons
Licensed content publication: European Journal of Inorganic Chemistry
Licensed content title: Structural Variations in Copper(II) Complexes of a Bitopic Bis(pyrazolyl)methane Ligand
Licensed copyright line: Copyright 2012 WILEY-VCH Verlag GmbH & Co. KGaA, Weinheim
Licensed content author: Daniel L. Reger, Andrea E. Pascui, Mark D. Smith
Licensed content date: May 25, 2012
Start page: 4593
End page: 4604
Type of use: Dissertation/Thesis
Requestor type: Author of this Wiley article
Format: Print and electronic
Portion: Full article
Will you be translating? No